(61)

Experimental Investigation of Flow Distortion Effects on the Performance of Radial Discrete-Passage Diffusers

by

Victor G. Filipenco

GTL Report #206 September 1991

Major funding for this project was provided by General Electric Aircraft Engines (GEAE). Additional support was provided by the US Army Research Office and the AFRAPT Program of the Air Force Office of Scientific Research.

EXPERIMENTAL INVESTIGATION OF FLOW DISTORTION EFFECTS ON THE PERFORMANCE OF RADIAL DISCRETE-PASSAGE DIFFUSERS

by

VICTOR GREGORY FILIPENCO

ABSTRACT

A swirling-radial-flow generator has been developed for the study of fluid-dynamic phenomena in radial passage- and vaneless-diffusers. A unique feature of the swirling-flow generator is the capability of providing a wide range of diffuser inlet flow conditions. This is accomplished by means of a very-high-solidity rotating radial-outflow nozzle cascade in conjunction with annular cross-flow injection/suction slots in the flow-path walls immediately upstream and downstream of the rotor blading. The rotor generates a shockless and weak-wake axisymmetric transonic swirling flow which can be tailored to provide a desired level of diffuser inlet flow-field axial distortion by means of cross-flow injection and/or suction through the annular slots. A complete test-facility was designed and constructed based on this concept and was utilized to study effects of inlet flow-field axial distortion on the pressure-recovery performance and stability of a modern high-performance gas-turbine-engine radial discrete-passage diffuser.

It was shown that the diffuser pressure-recovery coefficient, if based on the inlet availability-averaged total pressure, correlates well with the diffuser inlet momentum-averaged flow angle independent of flow-field axial distortion and Mach number over the wide flow parameter range investigated. It was argued that the generally accepted high sensitivity of diffuser pressure recovery performance to inlet flow distortion and boundary-layer blockage is largely due to inappropriate quantification of the diffuser inlet flow-field parameters.

Time resolved pressure measurements in the vaneless space between the rotor and diffuser showed that the diffuser operating range is limited by the onset of rotating stall triggered by the loss of flow stability in the diffuser, independent of the rotor operating point (if overall compression system instability did not occur first). It was found that the loss of flow stability in the diffuser occurred at a critical value of the diffuser inlet momentum-averaged flow angle and corresponding overall-diffuser pressure recovery coefficient (based on the availability-averaged total pressure), independent of inlet flow-field distortion and Mach number, over the wide flow parameter range investigated.

A simple analytical consideration of an idealized diffuser consisting of a constant-area mixing duct followed by an isentropic-flow diffuser was used to show that the observed insensitivity of the diffuser pressure-recovery performance to inlet flow-field distortion can be attributed to rapid mixing of the flow. It was shown that measurements of the static pressure distribution along the centerline of an individual diffuser-passage support this hypothesis.

ACKNOWLEDGEMENTS

Over the years of this effort, so much support and encouragement was given to me by so many that it is difficult to know where to begin.

First, I would like to thank my thesis advisor, Professor Greitzer, who put up with many of my anomalies and stuck with me to the end. His encouragement, guidance, suggestions, motivation, and especially his patience and understanding were well beyond the ordinary. Professor Greitzer's enthusiasm for expanding the limits of knowledge in the turbomachinery and propulsion fields is humbling and truly inspirational. It was also Professor Greitzer who proposed the idea for this thesis.

Another guilty party in this thesis is Professor David Gordon Wilson, whose enthusiasm for turbomachinery and engineering in general proved to be very contagious. Starting with his turbomachinery-design course which I took in the early 80's, Professor Wilson's obviously genuine interest in engineering has provided much inspiration for me. During the course of this research, Professor Wilson has more than once kept me from jumping overboard and has provided much advice for which I am grateful.

I wish also to thank Professor Kerrebrock for his support and suggestions and especially for his constructive criticism and thought-provoking comments. I am very grateful that Professor Kerrebrock was able to find time in his busy schedule to offer help and guidance especially since I always somehow managed to catch him at the most inconvenient times (like in the middle of his vacation).

Also very inspiring and motivating was Professor Gyftopoulos, whose rational approach to the science of thermodynamics and his ability to explain the principles involved on a level which I was able to understand has proven to be invaluable to me. For this and for Professor Gyftopoulos' persistent encouragement and support at the most critical moments of my stay at M.I.T., I am very grateful.

During my stay at the G.T.L., many words of encouragement and confidence also came from Professor Belgacem Jery and I would like to offer my gratitude to him. He boosted my spirit immeasurably on many occasions.

A great deal of credit for the success of this thesis must go to Viktor Dubrowski. Without his ingenuity and talent for manufacturing precision mechanical components, making the necessary tools as he goes along, and at a moments notice, this thesis would not have been possible. Viktor's sense of humor, lively philosophical discussions, and his always-cheerful attitude brightened many critical moments.

I also appreciate Roy Andrews' help with the welding and would like to thank Jim Nash for pointing me in the right direction at the right time on many occasions. Jim Nash's assistance in interfacing with outside contractors was also invaluable.

Special thanks also goes to Warren Wu for procuring most of the components of the bearing lubrication system and for helping with its assembly. Many encouraging words were also provided by Warren at the right times.

On the administrative front, I would like to thank Holly Rathbun, who performed miracles in managing the file cabinets of paperwork associated with this thesis and who was always on hand to handle the unusual predicaments which I managed to get my self into whenever trying to interface with the real world. Holly also provided much appreciated advice on topics far outside of the envelope of this thesis. Many thanks also to Karen Hemmick for cheerfully getting me whatever I needed right away and for her sense of humor and to Diana Park for her view-graph artistry.

Leslie Regan and her team at the M.I.T. Mechanical Engineering Graduate Office deserve special thanks for putting up with me and letting me get away with doing things my own way. Leslie especially went well outside of the expected limits of her job and showed genuine concern for my progress. Her always cheerful and good humored attitude did much to cheer me up.

Over the years of my stay at M.I.T., many colleagues at the G.T.L. made it all worthwhile. Much thanks must go to my friend Dave Fink, who gave me much valuable advice right from the start of my stay at the G.T.L. and whose constant assurances that the rotor disc will not fail (any time soon) convinced me that I should stop repeating the stress calculations and go on with the job at hand. If it weren't for him, I'd still be trying to calculate how much concrete a ruptured disc would take out of the test-cell wall. It's also a good thing that Dave talked me out of destroying my model airplane when I couldn't get it to fly properly. I will never forget the many enjoyable and humorous hours of flying (well, sort of) that followed on Brigg's field. (The bouncing-off of the tennis bubble, Dave's runaway flight around the tennis bubble, and the splash-down on the M.I.T. solar-demonstrator house are just a few examples.) Dave's technical advice and suggestions, especially on the finer points of the Kulites, are much appreciated and his excitement about turbomachinery and many other kinds of interesting devices certainly played a significant role in maintaining my interest in this thesis project. I will also never forget the kindness given to me by Dave's family.

Flying isn't everything however, as proven by the fact that even though another G.T.L. inmate, Jon Simon is not a model aircraft enthusiast (yet), I consider him a very valued friend. Many hours of stimulating conversations with Jon on a wide range of topics ranging from the technical to the philosophical, proved more educational for me than some of my course experiences at M.I.T. and I have learned that I must weigh Jon's opinions very seriously before taking action. Jon has also been able to pull me from the depths of despair and set me back on track many times. I am grateful for all of this (even though Jon does not want to help me take the world speed record in steam powered model hydroplanes).

My latest flying-field friend (victim), Jim Paduano helped me survive at M.I.T. in many ways. Jim has given me many valued suggestions and advice and I am especially grateful to him for talking me into, and helping me build the Electricus. Jim's and his wife Ching's kindness and friendship also did much to keep me going.

Many other G.T.L. colleagues were always on hand to brighten an otherwise dull moment. Cell-mates Knox Millsaps with his "Veeeektorrr, how's it going?", Doug Loose, Seung Jin Song, and Scott Barton all put up with many of my stale jokes and un-witty sayings. Long-since graduated Steve Koff and Phil Lavrich were always willing to lend an ear, listen to my whining, and give advice back in the early days of this project. My newest office mates, Joel Haynes and Fred Newman have added another positive dimension to my stay at M.I.T. Fred always comes up with a good story for every occasion and Joel never refuses to listen to any of mine. Fred also deserves much credit for giving me many useful "pointers" during the writing of this thesis. In addition, G.T.L. cohorts Eric Strang and Laurent Bonnaure also did their share by being ready at all times to agree with me on any issue.

Much credit for my success at M.I.T. should also go to many off-campus friends who kept me in-line. The encouragement, support, and friendship given me by my longest-time and best friend, Andy Yu and his wife Maggie is very rare. I will always remember the excursions that they took me on through New York's China Town and the many occasions on which they went well out of their way to cheer me up in the darkest of moments. Andy's interest in cars, aviation, watches, and many other things provided many hours of stimulating and enjoyable conversation. The knowledge that people like this still exist in the world was one of the things that kept me from giving up the ghost. I would like to thank my good friends, (Professors) Miles Greiner and Andy Tangborn, for their genuine interest in my progress at M.I.T. and for their continued advice and support. Even though they have long since graduated from M.I.T. and have moved on to bigger and better things, they did not forget me and my struggles. Much thanks also goes to my good friend Charles Thomas who on many occasions pointed out that all is not as bad as it seems. Charles also offered much valued advice and introduced me to many facets of classical music which I was not familiar with.

This research was made possible (funded that is) by our good friends at General Electric, where good things, (like aircraft gas-turbine engines), come to life. I would especially like to thank Les King of General Electric for providing the test diffuser and for his continued faith in this effort at M.I.T. Dr. Rudy Markytan of General Electric also deserves special thanks for his friendship, humor, and encouragement, and for his patience in listening to my sob stories over the phone about how difficult it is to buy fasteners, shims, and gaskets these days. Some additional support was also provided by the General Electric Turbomachinery Research Fund. In the final stages of this project, partial support was also provided by the Army Research Office under Grant DAAL 03-90-G-0138, Dr. T. Doligalski, Program Manager. This support is also appreciated. The Air Force Office of Scientific Research provided funding for my studies at M.I.T. through the Air Force Research in Aero Propulsion Technology (AFRAPT) Program and I would also like to thank them for this. I would also like to acknowledge Dr. Carol Russo of General Electric for invaluable help in the initial stages of this project and encouragement throughout its course.

I would like to express my appreciation to Dr. Dave Japikse of Concepts ETI, Inc. and Bharatan Patel of Creare Inc. for providing data on the performance of a swirl generator developed at Creare, employing forward-leaning blading. This information proved very helpful in setting this thesis effort on course.

Last but not least, I would like to thank my sister, Larisa and brother-in-law, Jim Childs for their understanding and their putting up with a lot of bad moods. No one has expressed more hope for my success than they have.

TABLE OF CONTENTS

LIST OF TABLES

LIST OF FIGURES

LIST OF PHOTOGRAPHS

NOMENCLATURE

Symbols

a	acoustic-wave propagation speed
A	area
Bl_b	rotor blade blockage
b	rotor blade height; vaneless diffuser width
C	flow velocity vector magnitude in laboratory frame of reference
C_L	blade lift-coefficient
C_p	specific heat at constant pressure
Cpr	pressure recovery coefficient
Cpr_ψ	pressure recovery coefficient based on availability-averaged diffuser inlet dynamic pressure
Cpr_a	pressure recovery coefficient based on maximum dynamic pressure at diffuser inlet
Cpr_b	pressure recovery coefficient based on the area averaged diffuser inlet dynamic pressure
Cpr_c	pressure recovery coefficient base on the diffuser inlet dynamic pressure defined in terms of the diffuser inlet area averaged static density and area-averaged absolute velocity
d	diameter
d_t	diffuser throat diameter
C_v	specific heat at constant volume
e	$\equiv \tan\gamma$
E	modulus of elasticity
F	force
G	shearing modulus of elasticity
h	enthalpy per unit mass
i	incidence angle
J	second polar moment of area
k_{br}	bearing radial stiffness
k_{ba}	bearing axial stiffness

l	diffuser passage length, from point of tangency of passage centerline to base circle to the diffuser exit
$\dot{m}$	mass flow rate
M	Mach number, Moment
N	rotor rotational speed, revolutions per minute
P	pressure
Pr	Prandtl number
P_{t_ψ}	availability-averaged total pressure
r	radius or radial coordinate, orthogonal to x and θ
R	gas constant for air in equation of state $P\upsilon=RT$
$\mathcal{R}$	recovery factor
Re	Reynolds number
s	entropy per unit mass; streamwise coordinate
sf	fractional distance along the camber line of the rotor blade, measured from the leading edge
t	time; thickness
tn	thickness, normal
T	temperature
Tq	torque
u	meridional velocity in boundary layer; radial displacement of blisk due to strain
U	blade speed
$\hat{U}$	meridional velocity at boundary-layer edge
υ	specific volume
V	magnitude of velocity
w	circumferential velocity in boundary layer
W	flow velocity vector magnitude in rotor frame of reference
$\dot{W}$	power
$\hat{W}$	circumferential velocity at boundary-layer edge
x	linear coordinate in axial direction of machine
Z	number of blades
z	local coordinate normal to duct wall

α	flow angle, relative to radial or meridional direction, in laboratory frame of reference
α_{n}	flow angle non-uniformity
α_{s}	flow angle skew
β	flow angle, relative to radial direction in rotor frame of reference
β_{b}	blade angle, relative to radial direction
γ	ratio of specific heats, $C_{\mathrm{p}}/C_{\mathrm{v}}$; angle between velocity vector at wall and at boundary-layer edge
δ	boundary layer thickness
δ_T	thermal boundary layer thickness
ζ	local linear coordinate normal to diffuser passage centerline, (orthogonal to x and ξ)
η_{diff}	diffuser effectiveness
$\eta_{\mathrm{tt}_{\mathrm{p}}}$	total-to-total polytropic compression efficiency
θ	angular coordinate, orthogonal to x and r, positive in rotor rotation-direction
θ_{b}	rotor blade camber-line wrap angle
κ	torsional stiffness
μ	viscosity
ν	Poisson's ratio
ξ	distance along diffuser passage centerline, measured from point of tangency of centerline to base circle
ξ_{ke}	kinetic-energy-flux skew
ξ_{m}	mass-flux skew
ξ_{p}	momentum-flux skew
Π_{ts}	swirl-generator total-to-static pressure ratio
Π_{tt}	swirl-generator total-to-total pressure ratio
ρ	density
σ	blade solidity; normal stress
σ_{ke}	kinetic-energy-flux deficit
σ_{m}	mass-flux deficit
σ_{p}	momentum-flux deficit
τ	shear stress
τ_{w_s}	streamwise component of wall shear stress
τ_{w_θ}	tangential component of wall shear stress

φ	local angle between tangent to wall surface in meridional plane and the axial direction
ψ	blade loading coefficient
ψ_d	circumferential static pressure distortion parameter
$\dot{\Psi}$	thermodynamic availability flux, relative to reference state
Ω	rotor rotational speed, radians per second

Subscripts

Al	pertaining to aluminum
amb	ambient conditions
d_t	at diffuser throat or based-on diffuser throat diameter
Hg	pertaining to mercury
r	in radial direction or radial component
ref	reference condition
rel	relative to rotor frame of reference
st	static condition
t	total condition; tangential component
x	in x-direction or x-component
δ	based on boundary-layer thickness
θ	in θ-direction or θ-component
0	at rotor inlet (at leading edge) or at duct wall
$1'$	at vaneless space or vaneless diffuser inlet (same as rotor exit)
1	at discrete-passage diffuser inlet (same as vaneless-space exit) or pertaining to profile control slot number 1 as defined in figure 2.15
2	at diffuser exit or pertaining to profile control slot number 2 as defined in figure 2.15
3	pertaining to profile control slot number 3 as defined in figure 2.15
4	pertaining to profile control slot number 4 as defined in figure 2.15

CHAPTER 1

INTRODUCTION AND BACKGROUND

1.1 Introduction

The centrifugal compressor is a widely-utilized device ranging in applications from vacuum cleaners to commercial air-conditioning systems to high-performance gas-turbine aircraft engines. The centrifugal pump, a close relative of the centrifugal compressor, has perhaps an even wider range of applications, ranging from the rather crude designs used in washing machines and other household devices to the space-shuttle main-engine high-pressure propellant feed pumps, the highest-power-density rotating machinery ever built. An important component of these centrifugal machines is the radial diffuser, the purpose of which is to reduce the velocity of the flow leaving the impeller, ideally reversibly, to that required by the downstream components.

In many applications it is required that the velocity of the fluid entering the component immediately downstream of the compressor be much lower than that leaving the impeller. In these cases the diffuser plays a critical role in establishing the overall efficiency and total-to-static pressure-flow characteristic of the stage. In addition, depending on the design of the impeller and its matching to the diffuser, the diffuser can be the key component limiting the operating range of the compressor between choke and stall.

Radial diffusers of many different configurations have been applied to centrifugal compressors. These can be grouped into two general classes: vaneless diffusers and discrete-passage diffusers. The highest-performance compressors and pumps make use of discrete-passage diffusers as these generally exhibit a higher pressure-recovery coefficient than the vaneless type, although over a relatively narrower flow range about the design point, and have a smaller discharge-radius for a given level of diffusion.

An application of particular current interest illustrating the crucial role of the centrifugal-compressor radial diffuser is the high-performance gas-turbine engine. Some current and proposed applications of gas-turbine engines utilizing centrifugal compressors (often as the last stage of a multi-stage axi-centrifugal compressor) include fixed- and rotary-winged aircraft propulsion, remotely piloted vehicles, military surface-vehicle propulsion, airborne auxiliary-power units, ship propulsion, automotive and locomotive propulsion, electric-power generation for spacecraft (closed Brayton cycle with concentrated solar-energy source), and many others.

In these applications, specific fuel-consumption (more appropriately "efficiency" in cases such as the above mentioned spacecraft application) and specific weight and specific volume are critical. Accordingly, the current trend in engine design is toward increasing overall compressor pressure-ratio and pressure-ratio per stage, requiring impeller-exit Mach numbers in excess of unity. Since the gas-turbine combustor requires a much lower inlet Mach-number, on the order of M=0.1 (burning kerosene), an efficient diffuser is absolutely necessary for high overall-engine-efficiency.

In addition to high design-point-efficiency, many compressor applications require that the compressor be able to operate over a range of flow rate. The maximum flow-rate is limited by the occurrence of choking (sonic velocity) in some throughflow component of the compressor while operation below the design-point flow rate is usually limited by the onset of local and/or system instability as described in detail by Greitzer [25]. The limitation of flow rate due to choking simply dictates the sizing of a compressor to the specific application. That due to the onset of flow instability is more difficult to design for, as it is not completely understood in terms of the flow processes occurring within the individual compressor-components. Since the radial diffuser plays a major roll in the overall pressure rise characteristics of a high performance centrifugal compressors, an in-depth understanding of the flow mechanisms occurring within radial diffusers is essential for the prediction of the compressor stage efficiency and stability characteristics.

1.2 Background

Of the different common radial-diffuser configurations, the vaneless diffuser has been the most extensively studied followed by the vane-island type, with the least amount of data available for the pipe configuration.

A centrifugal-compressor designer would like to be able to predict the fluid-dynamic characteristics of a particular diffuser configuration as a function of the flow field entering the diffuser (i.e. that provided by the impeller) to optimize the impeller/diffuser combination. As pointed out by Wilson [61], one of the biggest problems in designing centrifugal- compressor diffusers is that the flow at the exit of a centrifugal-compressor impeller is typically very distorted (see Eckardt [17] for example) and unique to that particular impeller design. This often requires much cut-and-try before a good-performing diffuser/impeller combination is obtained. It is not clear how, or if, available diffuser-performance-data obtained with essentially ad-hoc diffuser-inlet conditions can be used to predict the fluid dynamic behavior of a diffuser operating with a specific centrifugal-compressor impeller. The testing of a specific impeller/diffuser combination certainly establishes the performance characteristics of that particular combination but any generalization of the observed diffuser behavior is difficult to make due to the ambiguous effect of the highly distorted impeller exit flow on the diffuser performance.

Previous studies of radial transonic diffusers utilized either actual centrifugal-compressor impellers [48,32,5], stationary radial-outflow-nozzles [20,57], or "vortex nozzle" swirl-generators [2,3,4,15] as a means of generating the inlet flow to the diffuser. None of these approaches has proven to be entirely suitable for obtaining an in-depth and generalized understanding of radial-diffuser flow mechanisms.

The so-called "vortex nozzle" approach to generating the diffuser inlet flow as used by Baghdadi [2] and later by Dutton et al. [15], was originally intended to provide a uniform, well-defined swirling-flow field for basic radial-diffuser studies with the added advantage of mechanical simplicity. In both of these attempts however, the diffuser inlet flow produced by the "vortex nozzle" was very distorted, in fact separated on one wall at the diffuser entrance.

Faulders [20] and Stenning et al. [57] used radial-outflow nozzle cascades to generate the diffuser inlet flow. The main objection to this approach is that stationary wakes (and shocks at off-design conditions in the case of transonic diffuser studies) result at the inlet to the diffuser. This inlet condition is not representative of actual centrifugal-compressor applications.

The difficulty in studying radial transonic diffusers in a controlled manner was again illustrated by a recent unique but unsuccessful attempt to develop a radial-diffuser test rig with a means for providing controlled diffuser-inlet-conditions. The device, based on a variant of the stationary radial-outflow-nozzle concept, produced a diffuser-inlet flow field which was judged to be of "unsatisfactory" uniformity [60].

Many basic diffuser studies have been made using single (individual) diffuser-channels [49,63,43,1,6]. Runstadler and Dean [49] extensively investigated the performance of flat-wall channel-type diffusers as a function of diffuser geometry over a range of diffuser-inlet Mach numbers from 0.2 to 1.0 and boundary-layer blockage from ~1 to ~14 %. In their study, the inlet flow-field consisted of a potential core surrounded by the wall boundary-layer. Other studies [63,43,1,6] investigated the effects of non-uniform diffuser-inlet-conditions on diffuser performance. These data, although providing some insight into the important flow mechanisms governing channel- diffuser performance, can not by themselves be used to obtain a complete understanding of radial discrete-passage diffuser fluid-dynamic phenomena.

Since the radial discrete-passage diffuser consists of an array of several diffuser passages acting in parallel, mutual fluid-dynamic interactions involving several passages (such as rotating stall) can occur. Such phenomena obviously cannot be directly studied using a single diffuser-passage. Similarly, data obtained using a single diffuser-passage do not give any information on the flow mechanisms within the vaneless or quasi-vaneless space of a radial discrete-passage diffuser. Previous investigators have suggested that the flow phenomena in this region are critical factors in the overall diffuser stability and pressure recovery [18] and, as pointed out by Kerrebrock [39], the swept-back nature of the leading edges of pipe diffuser passages may account for the relatively good transonic performance of this type of radial diffuser. Individual-diffuser-passage data are however extensively relied upon for radial-diffuser design, primarily for setting the passage cross section area distribution downstream of the throat.

Another consideration in interpreting existing diffuser data is that various investigators have correlated their data in terms of different parameters, some of which have ambiguous physical significance or make general use of the data difficult or impossible. In [50] and [51] for example (where [51] is an extensive compilation of channel-diffuser performance data) the diffuser pressure recovery coefficient is base on the diffuser-inlet centerline total-pressure, with boundary-layer blockage used as a correcting parameter. Other popular approaches [63] include basing the diffuser pressure recovery coefficient on a dynamic head calculated form the diffuser inlet static pressure and mass averaged or area-averaged total pressure or on a diffuser inlet dynamic head based on the area-average diffuser inlet velocity (for incompressible-flow cases) [41]. As pointed out by Klein [40], most researchers did not include the necessary information for converting from one definition to another, limiting the generality of the available data.

1.3 Research Objectives

The deficiencies of previous diffuser-studies described above, in conjunction with current high-performance gas turbine engine design trends, suggested that the following objectives and questions, divided into two main parts, be addressed in the current research:

1.) <u>Development of an Improved Radial Diffuser Test Facility</u>

A principal objective of the present research is the development of an improved means for the experimental study of radial centrifugal-compressor transonic diffusers, encompassing the following capabilities:

- The apparatus should include means for controlling the diffuser inlet boundary-layer blockage, velocity profile axial-distortion, Mach No., and swirl angle. The base case of an axially-uniform velocity profile with minimum boundary-layer blockage no greater than 5% should be attainable.
- The test rig is to be designed and built to study a radial discrete-passage diffuser representing actual high-performance engine-geometry. (The hardware used was supplied by the General-Electric Company). The diffuser used should be generic enough so that data on the flow mechanisms in the diffuser will be of general value.
- For the specific case of the G.E. discrete-passage diffuser, the test rig is to be capable of providing a diffuser inlet Mach-number of at least 1.0, a swirl-angle range of 65 to 75 degrees (measured from the radial direction), and a boundary-layer-blockage range of ~5 to ~25 percent. Means for introducing significant flow-field skew at the diffuser inlet should be provided. These ranges cover those encountered in actual engine operation. In addition, the swirl generator itself should not generate shocks nor stationary wakes, nor introduce any circumferential non-uniformity of the flow field.

2.) <u>Investigation of the Performance Characteristics of Radial Discrete-Passage Diffusers</u>

The basic questions concerning the fluid-dynamic characteristics of radial discrete-passage diffusers addressed in this thesis include:

- What are the pressure-recovery characteristic of the G.E. discrete-passage diffuser as a function of inlet Mach number, swirl angle, and blockage?
- What is the sensitivity of the pressure-recovery coefficient of this diffuser to the axial distortion of the Mach number and swirl-angle profiles?
- What is the nature of stable-flow breakdown in the diffuser? Do flow mechanisms within the quasi-vaneless space play a key role in this? Does rotating stall occur? How is the onset of the flow breakdown affected by

boundary-layer blockage and flow-field skew at the diffuser inlet?

- What are the most appropriate diffuser performance characterization parameters in the general case of an axially non-uniform diffuser inlet flow-field?
- What are the specific flow-mechanisms within the diffuser responsible for the observed behavior?

1.4 Experimental Approach

1.4.1 Experimental Options Considered

At the initiation of this thesis research-project, an extensive investigation was undertaken to determine the best approach to take to meet the above stated experimental objectives.

The conventional approach of using an actual centrifugal compressor impeller to generate the required diffuser-inlet flow field was rejected early in the investigation due to the difficult-to-control distorted velocity profile produced by conventional impellers and also due to the high power which would be required to produce transonic flow at the inlet of the test diffuser. (The power required could be reduced by using a suitable working fluid in a closed loop arrangement, but this complexity also seemed undesirable.) The use of stationary radial-outflow nozzles was rejected due to the undesirable stationary shocks and wakes which would result.

The mechanical simplicity of the vortex nozzle swirl generator initially developed by Baghdadl [2,3,4] for studying radial vaned diffusers, made it an appealing approach for the present investigation. A schematic diagram of the apparatus, (taken from [2]) is shown in figure 1.1a and a similar device, later used by Dutton et al. [15] is shown in figure 1.1b. The basic approach here is to produce a swirling flow inside a cylindrical "vortex chamber" by means of stationary radial-inflow swirl nozzles. An axisymmetric radial outlet from this vortex chamber, located at a smaller radius than the exit of the radial inflow nozzles, supplies flow to the test diffuser. If the radius ratio between the exit of the radial inflow nozzles and the inlet of the test diffuser is high enough, a test diffuser inlet Mach of unity or greater can be achieved with a subsonic Mach number at the exit of the radial inflow swirl-nozzles as a result of conservation of angular momentum. The basic advantage of this is that since the swirl nozzle exit Mach number is subsonic and the meridional Mach number in the chamber is also subsonic throughout, shocks can not be produced by the swirl generator. In addition, since the flow-path distance between the exit of the radial-inflow nozzles and the inlet to the test section is many times greater than the nozzle pitch, the nozzle-vane wakes will be mixed out before the flow reaches the test section inlet. Due to unanticipated flow mechanisms in the vortex chamber however, the test section inlet flow field obtained by these investigators was highly distorted as shown in figures 1.2a and 1.2b. This was considered unacceptable for the present study. It was thought however that the concept might be improved upon by guiding the flow from the radial-inflow nozzles to the test-diffuser inlet by means of an appropriately contoured axisymmetric duct as depicted schematically in figure 1.3. Because the flow must undergo significant diffusion from the lowest-radius point of the duct to the test-diffuser inlet, analysis of the boundary layer behavior in this region was required before attempting to implement this concept. The approach taken implemented a simplified inviscid streamline curvature analysis technique using the computer code ANDUCT [36] in conjunction with a momentum-integral boundary layer analysis scheme patterned after a technique developed by Senoo et al. [54] for predicting boundary-layer behavior in radial vaneless diffusers. In the present investigation, the boundary layer analysis technique was generalized to the case of an axi-symmetric duct defined by arbitrary surfaces of revolution. The details of this analysis are given in appendix A.

Figure 1.4 shows the Mach number, static pressure, and swirl angle distributions obtained using the inviscid analysis for a typical duct design at an operating point corresponding to test-diffuser inlet conditions of $M = 1.0$ and $\alpha = 75^{\circ}$. Although the radius ratios and flow area distributions were chosen to minimize the diffusion required in the axial-to-radial portion of the duct, the diffusion is still substantial, as can be seen from figure 1.4. The corresponding calculated boundary-layer thickness and wall flow angle distributions are shown in figure 1.5.

As can be seen from figure 1.5, the boundary layer remains at an essentially constant thickness in the favorable static-pressure gradient region of the duct but begins to grow very rapidly upon encountering the adverse pressure gradient in the axial to radial portion. In interpreting these results, it should be noted that the boundary layer solution and the inviscid streamline curvature solutions were not coupled. These results suggest however that separation of the boundary layer would be a severe problem, and it was decided that development of the radial-inflow/radial-outflow axisymmetric-duct concept posed an unacceptably high risk in the context of this thesis effort.

It is interesting to note that in [8], unknown to me at the time of the present analysis, a similar survey of swirl generator concepts is reported. Although the method of analysis in [8] appears to be somewhat different, the conclusions reached are essentially the same as reached here. Much later, I also learned of an axisymmetric duct corresponding to the axial-to-radial portion of the duct shown in figure 1.3, used as a diffuser downstream of an axial-cascade tester [13]. According to [13], the flow in fact did separate.

One possible approach to overcoming the separation problem might be to use boundary-layer suction through porous or perforated duct walls. After consideration of this technique, it was concluded that although it can not be completely ruled out for future investigations, the high development risk involved was also not appropriate for a thesis project.

1.4.2 The VHS-RRONC Swirling-Flow-Generator Concept

After determining that the radial-inflow-nozzle/axi-symmetric duct swirl generator concept is inappropriate for the present study, it was decided to use a very-high-solidity rotating radial-outflow nozzle-cascade (VHS-RRONC) to generate the required diffuser inlet swirling flow-field. The concept employs a rotor driven by a variable speed electric motor. An independent downstream compressor is used to control the flow rate through the test section, independently of the swirl generator rotor speed. Air was chosen as the working fluid in an open-loop arrangement with atmospheric inlet, eliminating the complexity of a closed-loop system.

A feature of the VHS-RRONC swirling flow generation technique is that the blade exit relative Mach number is always kept at, or below, unity. The diffuser-inlet absolute Mach-number greater than unity is obtained as a result of the rotor rotation as shown in figure 1.6. This precludes the possibility of shocks due to the rotor blading itself while the static pressure drop through the nozzle blading, in conjunction with the very-high blade solidity, results in a rotor-exit flow field with very narrow wakes which would be expected to mix out rapidly. In addition, the very high solidity makes the rotor-exit flow-field insensitive to the rotor-inlet incidence and distortion, allowing for a wide operating range. It also results in an "integrated-throttle" effect, producing losses which tend to compensate for the de-stabilizing positively-sloped total-pressure *vs.* flow characteristic typical of forward-leaning blading. Other advantages of the VHS-RRONC concept include low required shaft-power and a high level of design confidence as a result of the favorable static-pressure gradient.

The type of rotor blading employed here belongs to the general class of total-pressure-increasing turbomachines with forward-leaning rotor blades. Blading of this type is often used in various blowers in applications such as heating, ventilating, and air-conditioning systems and equipment cooling. Forward-leaning blading has also been applied to a variety of experimental compressors. Reference [24] describes a supersonic axial impulse-type compressor with forward-leaning blading and an extensive experimental program to develop a supersonic radial-compressor with forward leaning blading is described in [19]. In [8], a radial-outflow rotor with forward-leaning blading having velocity diagrams believed to be similar to that employed in the present research was used to generate a radial swirling flow for vaneless diffuser and return-channel studies. It is believed however that forward-leaning radial compressor blading was for the first time exploited in conjunction with the advantages of very-high blade-solidity as described above, in the present research.

A unique feature of the swirl generator developed in the present work is the means by which control of the diffuser inlet boundary-layer blockage and profile distortion is achieved. This scheme implements annular cross-flow-injection/suction slots immediately upstream and downstream of the rotor blading in the walls defining the vaneless space as depicted schematically in figure 1.7 (four slots total). Each of the profile control slots (PCS) is independently connected through an array of passages and flow distribution chambers to a flow-control system. With this system, mass (air) can be either injected into or removed from the main flow (through control of the manifold pressure). In the injection mode, the annular cross-flow enters the vaneless space without any tangential or radial momentum, and generally with a different total pressure from rotor exit flow. If the rotor exit flow is uniform, the diffuser inlet flow will be axially distorted as a result of local mixing of the main flow with the cross flow. It was also thought that the cross-flow injection through the annular slots immediately upstream of the rotor blading would result in an axially-distorted flow entering the rotor and secondary flow within the rotor blading, and thus axially-distorted flow at the test diffuser inlet. As will be discussed in section 3.3.2 however, the rotor exit flow proved to be insensitive to axial flow-field distortion at the rotor inlet due to effective mixing within the high solidity rotor blading. The effect of cross flow injection in the vaneless space downstream of the rotor was however as expected.

In the suction mode, boundary-layer fluid upstream and downstream of the rotor may be removed, allowing for the control of the boundary layer thickness at the test diffuser inlet.

Through a combination of flow injection and/or suction though the slots, a wide range of diffuser-inlet blockage and velocity-profile distortion can be obtained. In addition, removal of mass flow from the main flow in the vaneless space allows for the variation of the diffuser inlet flow angle independently of the rotor operating point as a result of continuity and conservation of angular momentum between the rotor exit and test diffuser inlet. This allows for the isolation of phenomena specific to the rotor or diffuser.

A complete diffuser test facility was designed and constructed based on the VHS-RRONC/PCS swirl-generator concept. The detailed facility-design considerations are discussed in chapter 2.

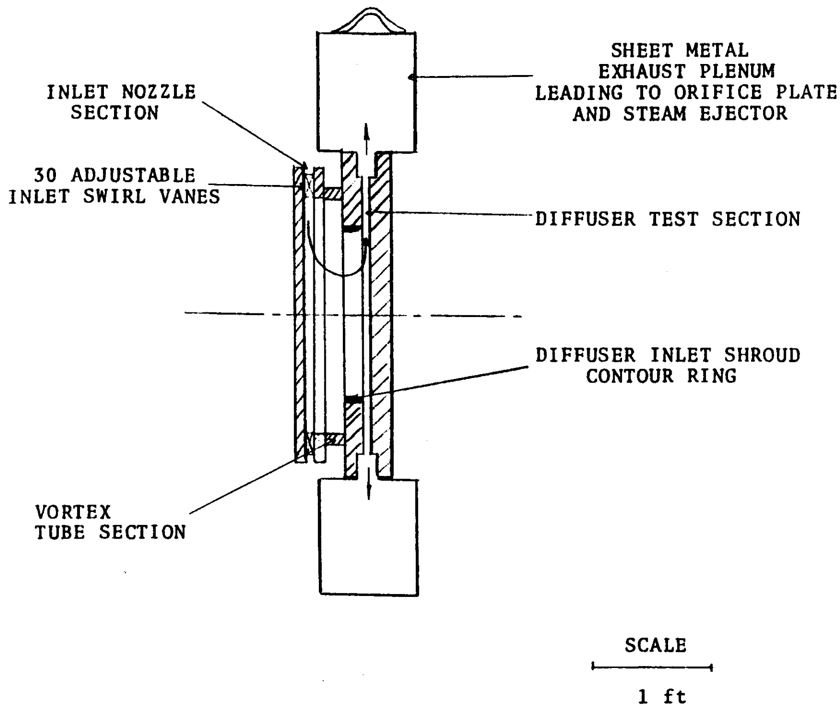

Fig. 1.1a "Vortex-Nozzle" Diffuser Test Rig Concept, from [2]

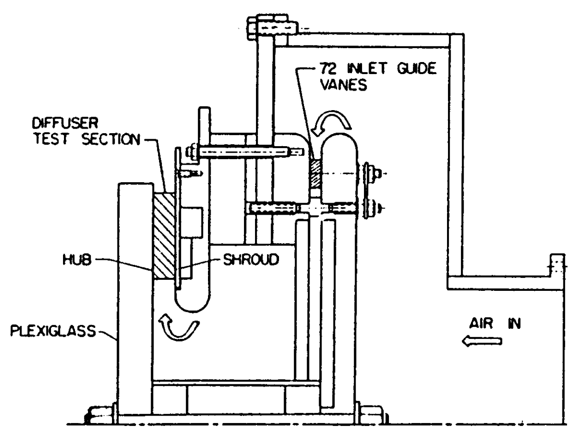

Fig. 1.1b Texas A&M "Vortex-Nozzle" Diffuser Test Rig, from [15]

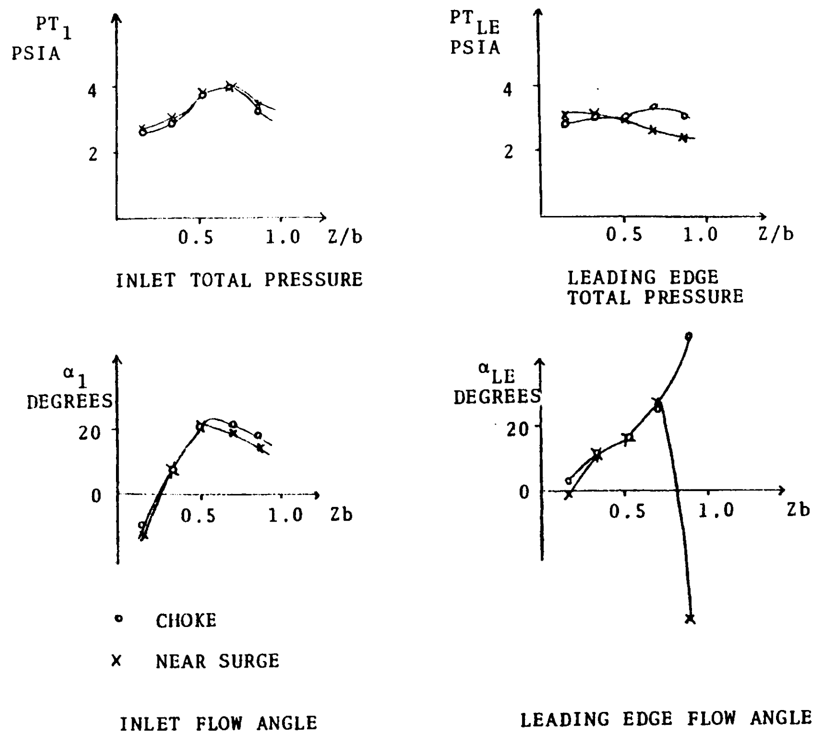

Fig. 1.2a Diffuser Inlet and Leading Edge Total Pressure and Flow Angle* Axial Distributions Produced by Rig of Fig. 1.1a, from [2]

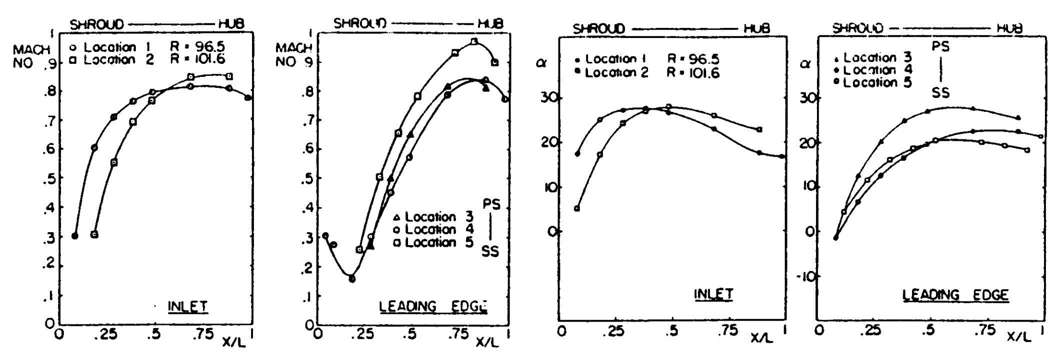

Fig. 1.2b Diffuser inlet and leading Edge Mach Number and Flow Angle* Axial Distributions Produced by Rig of Fig. 1.1b, from [15]

* Flow angle measured from the tangential direction

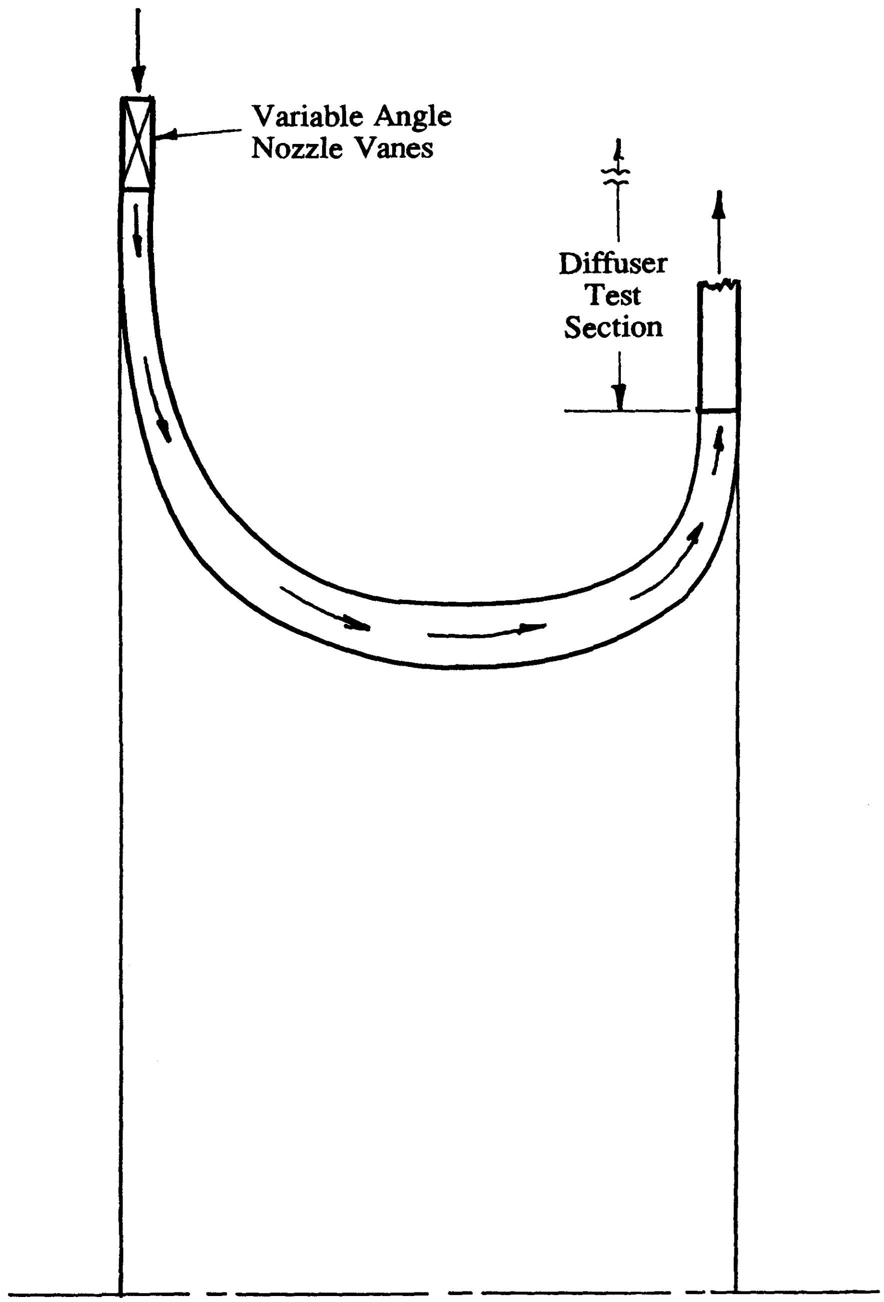

Fig. 1.3 Schematic of the Vortex-Nozzle/Contoured-Duct Swirl-Generator Concept

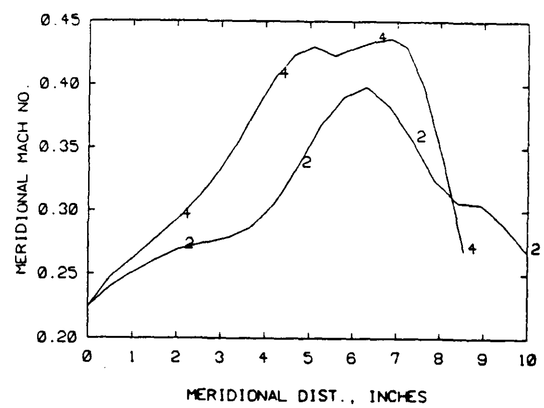

a) Meridional Mach Number

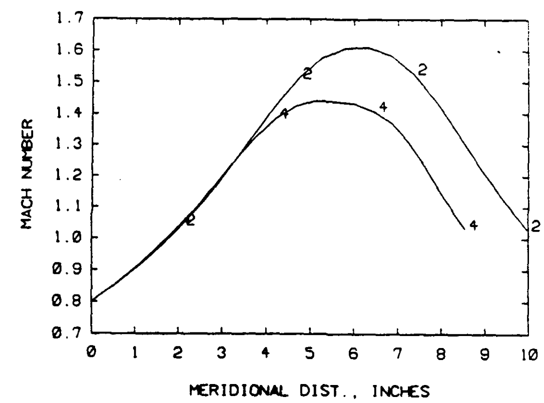

b) Total Mach Number

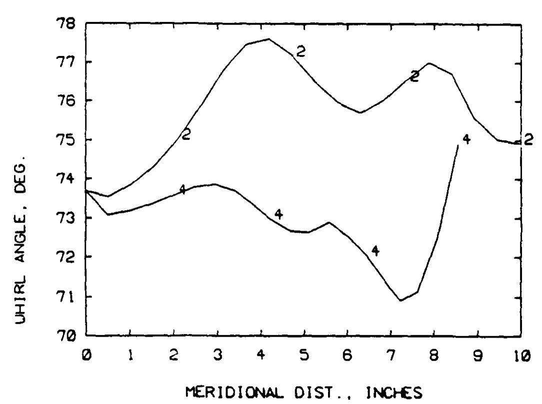

c) Swirl Angle

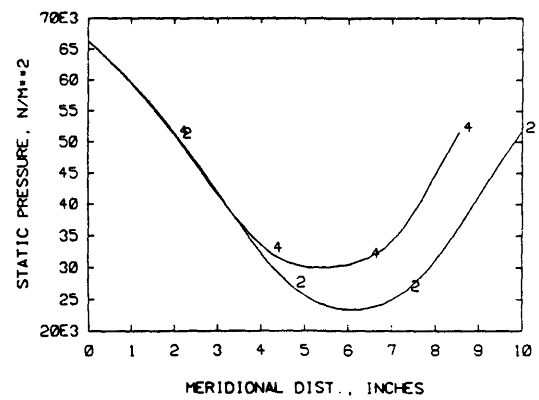

d) Static Pressure

Fig. 1.4 Calculated Distributions of a) Meridional Mach Number, b) Total Mach Number, c) Swirl Angle, and d) Static Pressure Distributions for the Vortex-Nozzle/Contoured-Duct Swirl Generator.
2≡Hub Surface, 4≡Shroud Surface

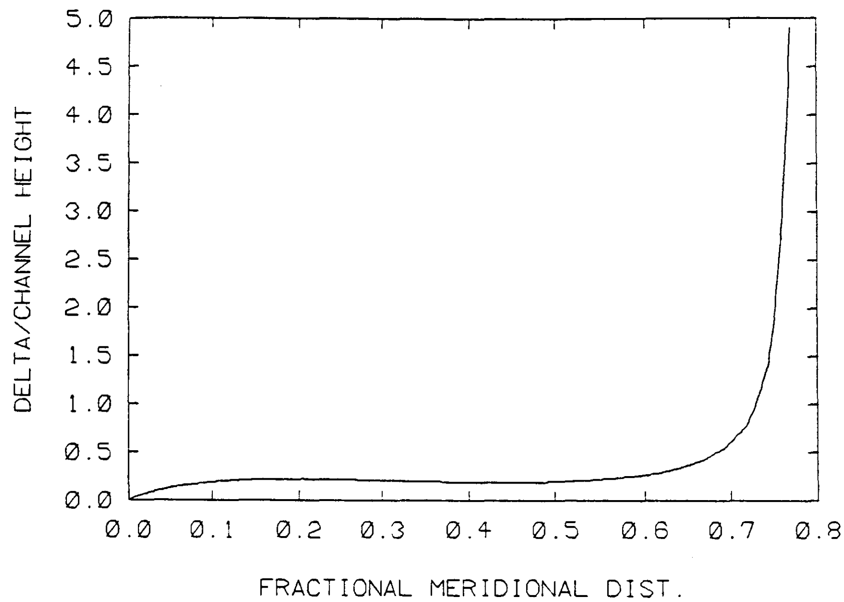

a) Boundary Lay Thickness (Hub Surface)

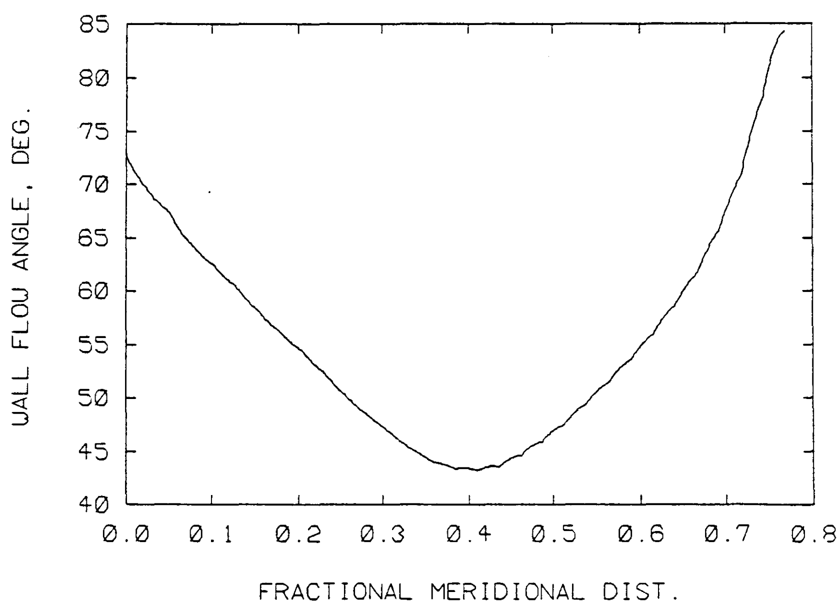

b) Wall Flow Angle (Hub Surface)

Fig. 1.5 **Boundary Layer Analysis Results for the Contoured-Duct Swirl Generator. a) Hub Boundary Layer Thickness, b) Hub Wall Flow Angle**

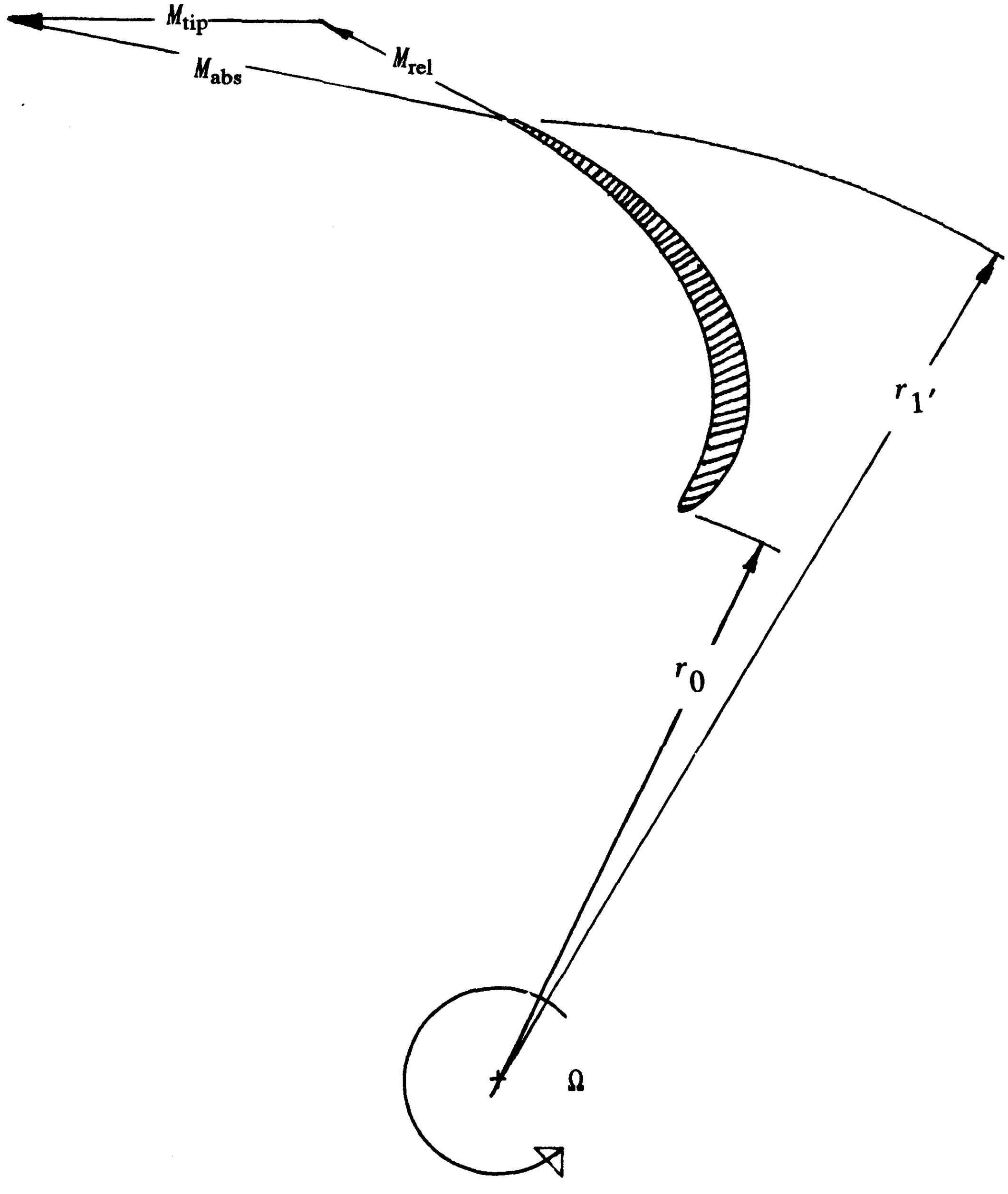

Fig. 1.6 VHS-RRONC Mach-Number Vector Diagram

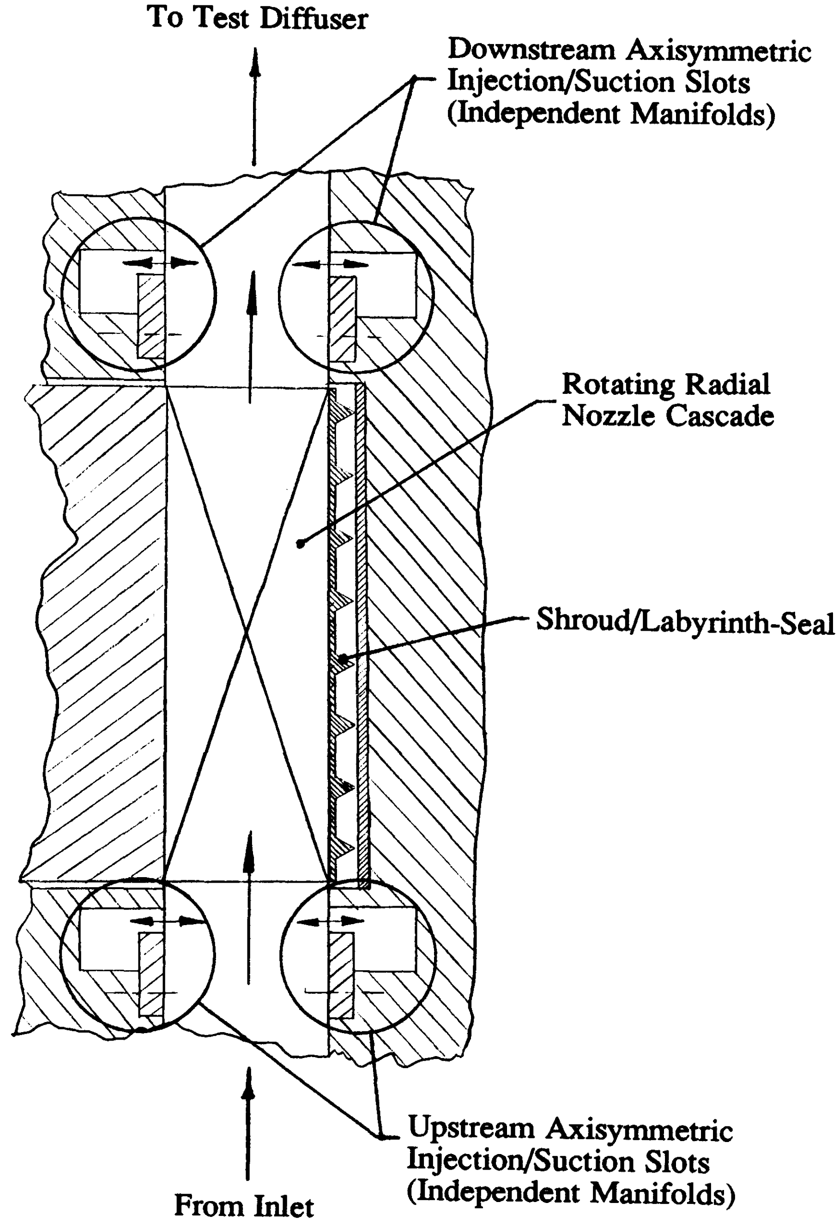

Fig. 1.7 Schematic Diagram of Injection/Suction Profile-Control-Slot Concept (not to scale)

CHAPTER 2

THE EXPERIMENTAL TEST FACILITY: DESIGN AND FEATURES

2.1 Preliminary Swirling-Flow-Generator Design Considerations

Once the VHS-RRONC/PCS swirl generator concept was selected as the most suitable approach for generating the diffuser-inlet swirling flow-field as described in chapter 1, an effort was undertaken to determine specific values of various aerodynamic and mechanical design parameters to best meet the experimental objectives of this thesis. The following sections describe this effort.

2.1.1 Preliminary Aerodynamic Design Considerations

Before beginning the detailed design of the test facility, the basic swirl-flow generator aerodynamic design-parameters had to be selected. These included the meridional shape of the blading and flow-path upstream and downstream of the rotor, the rotor inlet and exit diameters (setting the size of the vaneless space between the rotor and the discrete-passage diffuser inlet), the rotor inlet and exit relative Mach numbers and flow angles (which together with the rotor diameter determine the required rotor rotational-speed), and the blade solidity.

To simplify the aerodynamic and mechanical design of the rotor, it was decided early in the investigation that the bladed flow-path as viewed in the meridional plane would be purely radial (constant-span blade) and that the blade will have no twist, with axial leading and trailing edges. In addition, it was decided that the rotor blading should be shrouded to eliminate tip-leakage- and moving-wall-driven secondary flows within the rotor blading. A labyrinth seal incorporated into the shroud would reduce leakage around the outside of the shroud. The added mechanical design and manufacturing complexity of such a shroud is of course undesirable, but it was felt that the advantages well outweighed the disadvantages. The nominal span of the swirl-generator rotor blade and downstream vaneless space was selected to be 0.354 inches, the exit width of the matching impeller for the General Electric discrete-passage diffuser.

After initial selection of these design features, a parametric study was undertaken to determine appropriate values of the rotor exit relative Mach number, the vaneless-space radius ratio, the rotor blade exit-to-inlet radius ratio, the rotor pre-whirl flow angle, and the rotor inlet and exit blade angles. This parametric study was done for an operating point corresponding to the maximum-required discrete-passage diffuser inlet flow angle of 75° and a maximum Mach number of 1.0. The details of the analysis are presented in appendix B.

Figure 2.1a shows the calculated variation of the required blading-power with the vaneless space radius ratio and rotor-exit relative Mach number for the case without pre-whirl. Figure 2.1b shows the corresponding variation of rotational speed. These figures indicate that it is desirable to use the lowest possible vaneless-space radius-ratio and maximize the rotor exit relative Mach number to minimize the required shaft power and rotational speed.

The lowest possible vaneless space radius-ratio is determined by space requirements for the injection/suction slot system while the maximum allowable radius ratio is determined from stability considerations. A vaneless space radius-ratio of 1.10 was selected as being the best compromise between space requirements for the injection/suction system and the required shaft power. According to the results of the vaneless diffuser studies by Jansen [34], this low radius-ratio should not pose any stability problems over the required operating parameter range of the swirl generator. In setting the vaneless space radius ratio in actual compressor design, consideration is also typically given to the rotor-blade wake mixing-out distance. Since in the present case, very lightly-loaded blading with accelerating relative flow is used, this was not a major factor.

As discussed previously, a subsonic rotor-exit relative Mach number should be maintained over the entire operating range to prevent the possibility of shocks being introduced at the test diffuser inlet. Considering the variation of required blading power and rotational speed with rotor-exit relative Mach number as shown in figures 2.1a and 2.1b, a design point value of 0.80 was selected. This provides adequate margin for the uncertainty in rotor exit boundary-layer blockage while keeping the required blading power at acceptable levels.

The remaining parameter which specifies the rotor-blade meridional envelope is the blade trailing-edge to leading-edge radius ratio. This is selected based on blade-loading, leading-edge Mach number, and inlet-design considerations. Figure 2.2 shows the calculated variation of blade loading (in terms of a lift coefficient) and the leading edge Mach number as a function of rotor radius-ratio. From these results, and considering the space required for the axial-to-radial inlet (as discussed in section 2.2.2), a rotor blade radius-ratio of 1.4 was selected.

The use of pre-whirl was considered as a means of reducing the required shaft power. Figure 2.3 shows the calculated reduction of blading power as compared to the no pre-whirl case for a range of pre-whirl angles. The corresponding variation of required rotational-speed is less than 2%. It was decided that the reduction of shaft power within the range of acceptable pre-whirl angles is not large enough to justify the added mechanical and aerodynamic-matching complexity which adding pre-whirl vanes would introduce.

In the above preliminary-design analysis, a rotor total-to-total polytropic efficiency of 85.% was assumed. Since the swirl-flow generator design-objective was to achieve a specific diffuser-inlet Mach number and swirl-angle range (and not a specific overall-machine pressure ratio), a deviation of the actual blading efficiency from the assumed value is mainly important as far as it affects the required blading power and rotor-blade incidence angle. For the selected design parameters described above, figure 2.4a shows the calculated effect of rotor total-to-total polytropic efficiency on the required blading power and total pressure ratio and figure 2.4b shows the corresponding variation in the rotor incidence angle. The rotor speed required to maintain the desired diffuser-inlet Mach number and swirl angle does not change with deviation of efficiency from the assumed value. The blading power and total pressure ratio decrease with decreasing efficiency while the rotor-blade incidence angle increases. The sensitivity however is not severe and it was concluded that accurate prediction of rotor efficiency is not necessary in the present design analysis.

In summary, the basic swirl-generator aerodynamic design-parameters selected in the preliminary design study are:

Vaneless-Space Radius Ratio	1.10
Vaneless-Space and Rotor-Blade Width	0.354 inches
Rotor-Blade Radius Ratio	1.40
Rotor-Exit Radius	7.26 inches
Rotor-Exit Blade Angle	64.0°
Rotor-Inlet Blade Angle	-37.2°
Rotor Pre-Whirl Angle	0.0°
Rotor-Exit Relative Mach Number	0.80
Rotor-Inlet Relative Mach Number	0.42
Rotor Corrected-Speed	6003 RPM @ $T_0 = 518.69°R$

The estimated swirl-generator pressure-rise performance and exit (test-diffuser inlet)

Mach number and swirl-angle range are shown in figures 2.5a and 2.5b respectively.

As was mentioned in chapter 1, mass flow removal through the vaneless space slots by means of suction can be used to vary the test diffuser inlet flow angle independently of the rotor operating point (as a result of continuity and conservation of angular momentum). Figure 2.6 shows the calculated effect of suction through the vaneless-space slots on the swirl-angle range at the test-diffuser inlet at fixed diffuser inlet Mach number.

2.1.2 Preliminary Mechanical Design Considerations

Many preliminary mechanical-design decisions had to be made before progressing with the detailed facility-design. The main issues which had to be addressed include:

- Type of rotor configuration- Should a disk or some type of hybrid-drum arrangement (as in [8]) be used to support the blades? Should the blades be integrally machined or be individually mounted? Would an overhung wheel be best or should the rotor be supported between the bearings?
- Labyrinth seal- Integral? Brazed? Removable? Should there be a "straight-through" design or a more complicated "interlocking" design? What type of land surface should be used to handle the possibility of a rub?
- Method of rotor support- Type of bearings, stiffness required, etc.
- Rotor drive method- Electric motor?, turbine?, I.C. engine?, or?, and what specific type? Direct or indirect drive?
- Instrumentation requirements- What access is needed to the test section, and what type of probe mounting provisions are required?
- Test-section/rotor alignment tolerances required- (radial and axial)
- Mechanical requirements of, and constraints imposed by, the profile control injection/suction slots and manifolds
- Method of bearing lubrication, if required
- Mounting requirements for the discrete-passage diffuser
- Vaneless-diffuser interchangeability requirements

Other less critical mechanical design considerations included:

- Test-section housing configuration- Should the housing be axially or radially split? How does it integrate with the bearing housing?
- Type of bearing housing- Should the bearings be directly mounted or in a removable insert? Should the bearing housing be machined out of a

single piece of stock or built up? Axially split?

- Main plenum/collector configuration- Should the plenum be axially or radially split? Welded construction?
- Test section (centerline) orientation- Vertical, horizontal, or?
- Versatility required for assembly/disassembly
- Constraints imposed by available test-cell

Many of these points are obviously interrelated and many had to be addressed giving consideration to the rotor speed range requirements, the aerodynamic loading which would have to be withstood over the anticipated operating envelope of the machine, and other aerodynamic aspects of the swirl generator. For example, due to the fluid-dynamic uncertainties in selecting the most suitable vaneless space and injection/suction profile-control slot configurations, it was decided that the components forming both the vaneless space and injection/suction slots should be easily replaceable. The details of this feature are discussed in sections 2.2.4. and 2.4.

For the basic rotor configuration, it was decided to use an integrally-bladed disk (blisk) with an annular shroud brazed onto the blade tips. Knife edges machined into the outer surface of the shroud, in conjunction with a non-contact seal land, form an axial labyrinth-seal. It was felt that such a configuration would be relatively easy to manufacture and would have good mechanical integrity. The one-piece construction allows the required close tolerances to be relatively easily maintained. The material selected for both the disk and brazed-on shroud is 6061-T6 aluminum. This material has adequate strength and fatigue characteristics for the present application and is readily brazeable. For mechanical simplicity in integrating the diffuser test-section with the swirl generator, an overhung-disk arrangement is used, with the disk attached to a shaft by means of an interference fit and two diametrically-opposed keys. The shaft is supported by a system of axially pre-loaded angular-contact ball-bearings directly mounted in a one-piece housing. Figure 2.7 shows a conceptual schematic of the basic rotor/bearing-housing assembly as was envisioned at this stage in the facility development process.

After considering several alternative drive schemes, an AC induction-motor in a direct-drive arrangement, together with a variable-frequency power supply was selected as the most reliable and elegant means of driving the swirl-generator rotor. Induction motors with variable-frequency power supplies have become popular in the last ten years, replacing DC motors in many applications where variable speed is required. They are of acceptable cost, and are more reliable and relatively maintenance free as compared to brush-type DC motors. In many cases they are more compact, efficient, and can operate at higher shaft speed for long periods of time as compared to brush-type DC motors of the same power.

It was decided to drive the swirl-generator rotor directly (by means of a shaft coupling) as this is mechanically simple and results in a substantially more compact motor than if a low-speed motor of the same power was used with a speed-increaser. The high-speed motor (7200 RPM) itself is somewhat more expensive than a more conventional-speed (3600 RPM) type but this is offset by the lack of need for a speed increaser.

The swirl generator is mounted on a test stand with the shaft oriented horizontally. This gives good access to the test-section externally-mounted instrumentation and facilitates assembly/disassembly within the constraints imposed by the available test-cell. It was decided that both the test-diffuser housing and the main collector/plenum should be radially split as the components would be easier to manufacture, and a more distortion-free and hermetic assembly would result, as compared to axially-split configurations. Assembly (stacking) of such a test section however is much easier with the centerline in the vertical position. It was therefore also decided early in the design process that a device to allow vertical assembly of the test section must be developed.

More specific details on the design of the various swirl-generator components is given in section 2.2.

2.2 Detailed Design of the Swirling-Flow-Generator

2.2.1 Rotor-Blade Aerodynamic Design

After selecting the basic blade aerodynamic design parameters, as described in section 2.1.1, a simplified inverse design technique was developed to determine a suitable blade profile. The basic approach taken was to analytically specify the mean blade loading as a function of radius and an analytical normal thickness distribution as a function of a non-dimensional distance along the camber line from the leading edge to the trailing edge of the blade. It was assumed that the solidity was high enough so that the deviation of the flow within the blade passage from the local direction tangent to the camber line is negligible. Similarly, it was assumed that due to the low blade loading resulting from the high solidity, the flow parameters along the mean camber line can be adequately represented by the mean of the local pressure- and suction-surface values. The local blade thickness is represented as a bulk blockage.

The blading power for a radial element of the blade, dr , is:

$Z\Delta P_{st} br\Omega \, dr = \dot{m} \frac{dh_t}{dr} dr$, where ΔP_{st} is the static pressure difference between the pressure and suction surfaces at the given radius. Rearranging,

$$\frac{1}{r}\frac{dh_t}{dr} = \left[\frac{Z\Delta P_{st} b}{\dot{m}}\right] \Omega \tag{2.1}$$

The blade loading is specified by specifying $\frac{1}{r}\frac{dh_t}{dr}$ as a function of radius from the leading edge to the trailing edge.

Defining the loading coefficient $\psi(r) = \dfrac{h_t(r) - h_{t_0}}{r^2\Omega^2}$ and rearranging:

$$h_t(r) = r^2\Omega^2\psi + h_{t_0}$$

Differentiating with respect to r: $\frac{dh_t}{dr} = 2r\Omega^2\psi + r^2\Omega^2 \frac{d\psi}{dr}$ or,

$$\frac{1}{r}\frac{dh_t}{dr} = 2\Omega^2\psi + r\Omega^2 \frac{d\psi}{dr} \tag{2.2}$$

From equation 2.2, it is seen that a uniform distribution of $\frac{1}{r}\frac{dh_t}{dr}$ corresponds to the case of a uniform loading coefficient: $\frac{d\psi}{dr} = 0$. This also corresponds to the case of a constant pressure-to-suction surface ΔP_{st} as seen from equation 2.1. This, combined with the fact that the loading must go to zero at the leading and trailing edges serves as a basis for formulating a simple analytical specification of the loading distribution.

The loading distribution was specified analytically as depicted in figure 2.8. As seen in figure 2.8, the variation of $\frac{1}{r}\frac{dh_t}{dr}$ with r is chosen to be parabolic from the leading edge $(r = r_0)$ to a specified radius r_a followed by a linear variation between radius r_a and a specified radius r_b and then again parabolic from radius r_b to the trailing edge $(r = r_1')$. At radii r_a and r_b, the slopes of the parabolic and linear loading distributions are matched.

With this loading pattern and:

$$\int_{r_0}^{r_1'} \left[\frac{dh_t}{dr}\right] dr = (h_{t_1'} - h_{t_0}), \tag{2.3}$$

$$\left.\frac{1}{r_0}\frac{dh_t}{dr}\right|_{r_0} = \left.\frac{1}{r_1'}\frac{dh_t}{dr}\right|_{r_1'} = 0, \tag{2.4}$$

specification of r_0, r_1', r_a, r_b, $\dfrac{\left.\frac{1}{r_b}\frac{dh_t}{dr}\right|_{r_b}}{\left.\frac{1}{r_a}\frac{dh_t}{dr}\right|_{r_a}} \equiv \zeta$, and $(h_{t_1'} - h_{t_0})$ completely specifies the blade loading distribution. The design point value of $(h_{t_1'} - h_{t_0})$ was determined in the preliminary analysis as described in section 2.1.1 and shown in appendix B.

Once the loading distribution is specified as described above, the tangential velocity distribution, $C_\theta(r)$ can be obtained from Euler's equation:

$$h_t(r) - h_{t_0} = \Omega\,(rC_\theta(r) - r_0 C_{\theta_0}) \quad \text{or,}$$

$$C_\theta(r) = \frac{h_t(r) - h_{t_0}}{\Omega r} + \frac{r_0}{r} C_{\theta_0} \tag{2.5}$$

Also, if M is the mean absolute Mach number within the blade passage and α is the local absolute flow angle measured from the radial direction, from the definition of Mach number and basic compressible flow relations, it is seen that:

$$C_\theta(r) = \frac{\sqrt{\gamma R T_t}\; M \sin\alpha}{\sqrt{1 + \frac{\gamma - 1}{2} M^2}} \tag{2.6}$$

For a given C_θ distribution, M and α must be found to satisfy equation 2.6 and continuity:

$$\dot{m} = \frac{P_t}{RT_t} \frac{\sqrt{\gamma R T_t}\; M\; 2\pi r b(1 - B l_b) \cos\alpha}{\left[1 + \frac{\gamma - 1}{2} M^2\right]^{\frac{(\gamma+1)}{2(\gamma-1)}}} = const. \tag{2.7}$$

where P_t, T_t, and M are local absolute mean values of the total pressure, total temperature, and Mach number, respectively, and Bl_b is the local blade-blockage. P_t is related to T_t by:

$$\frac{P_t(r)}{P_{t_0}} = \left[\frac{T_t(r)}{T_{t_0}}\right]^{\frac{\gamma}{(\gamma-1)}\eta_{tt_p}} \tag{2.8}$$

The blade shape is defined by the camber line shape and a normal thickness distribution. The thickness distribution is specified analytically as a function of the fractional distance along the blade camber line as shown in figure 2.9. An elliptical distribution is used from the leading edge to a specified distance $sf = sf_{tan}$, followed by a linear distribution to the trailing edge. The slopes of the linear and elliptical portions are matched at $sf = sf_{tan}$. For structural reasons as will be discussed in section 2.2.5, the trailing edge thickness was selected to be 0.50 mm.

If the local radius of curvature of the camber line is much larger than the local blade normal thickness, t_n, the blade blockage can be approximated by:

$$Bl_b(r) = \frac{Zt_n}{2\pi r \cos \beta_b} \tag{2.9}$$

where $\beta_b = \beta_b(r)$ is the blade angle distribution obtained from the basic velocity triangle relation:

$$\beta_b(r) = \tan^{-1}\left[\frac{C_\theta - \Omega r}{Cr}\right] \tag{2.10}$$

Once the loading and normal thickness distributions are specified, equations 2.5 through 2.10 are solved simultaneously to determine $\alpha(r)$, $M(r)$, and $\beta_b(r)$. The blade camber-line wrap-angle distribution, as defined in figure 2.10, is then determined from:

$$\theta_b(r) = \int_0^r \frac{\tan \beta_b}{r}\, dr \tag{2.11}$$

which defines the camber line shape. This, combined with the normal thickness distribution, defines the blade pressure and suction surfaces:

$$r_p = \sqrt{\left[\frac{t_n}{2}\cos\beta_b\right]^2 + \left[r - \frac{t_n}{2}\sin\beta_b\right]^2} \tag{2.12a}$$

$$\theta_p = \theta_b + \sin^{-1}\left[\frac{t_n \cos\beta_b}{2r_p}\right] \tag{2.12b}$$

$$r_s = \sqrt{\left[\frac{t_n}{2}\cos\beta_b\right]^2 + \left[r + \frac{t_n}{2}\sin\beta_b\right]^2} \tag{2.12c}$$

$$\theta_s = \theta_b - \sin^{-1}\left[\frac{t_n \cos\beta_b}{2r_s}\right] \tag{2.12d}$$

The blade surface static pressure distributions were estimated assuming that:

$$P_{st_p}(r) = P_{st}(r) + \frac{\Delta P_{st}(r)}{2} \tag{2.13a}$$

and

$$P_{st_s}(r) = P_{st}(r) - \frac{\Delta P_{st}(r)}{2} \tag{2.13b}$$

for the pressure and suction surfaces respectively. Here, P_{st} is the mean static pressure in the blade passage at radius r, given by:

$$\frac{P_{st}}{P_{t_0}} = \frac{\left[\frac{T_t}{T_{t_0}}\right]^{\frac{\gamma}{(\gamma-1)}\eta_{tt_p}}}{\left[1 + \frac{\gamma-1}{2}M^2\right]^{\frac{\gamma}{(\gamma-1)}}} \tag{2.14}$$

The blade surface relative Mach number distributions were then estimated based on the assumption that the relative total pressure within the blade passage is dependent only on r (independent of θ). This would be exactly correct for the case of adiabatic-isentropic flow or if entropy was a function of r only, since due to the fact that rothalpy is constant within the blade passage, $T_{t_{rel}}$ is a function of r only (assuming adiabatic flow). The resulting expressions for the blade pressure and suction surface relative Mach number distributions are:

$$M_{rel_p} = \sqrt{\frac{2}{(\gamma-1)}\left[\left[\frac{P_{st}}{P_{st_p}}\right]^{\frac{\gamma-1}{\gamma}}\left[1+\frac{\gamma-1}{2}M_{rel}^2\right]-1\right]} \tag{2.15a}$$

$$M_{rel_s} = \sqrt{\frac{2}{(\gamma-1)}\left[\left[\frac{P_{st}}{P_{st_s}}\right]^{\frac{\gamma-1}{\gamma}}\left[1+\frac{\gamma-1}{2}M_{rel}^2\right]-1\right]} \tag{2.15b}$$

where M_{rel} is the mean relative Mach number related to M, α, and β_b, found as described above, by:

$$M_{rel} = M\frac{\cos\alpha}{\cos\beta_b} \tag{2.16}$$

as can be seen from figure 1.6.

The present blade design was obtained by trial and error by specifying loading and thickness distributions to obtain static pressure and relative Mach number distributions without any abrupt adverse static pressure gradients and with a subsonic relative Mach number throughout the blade passage.

Zweifel's loading criterion [14,61], which approximates the minimum-loss solidity for turbine blading, was used as a guide to selecting the number of rotor blades. According to Horlock, as reported in [14], this loading criterion is applicable to turbine cascades with outlet angles in the range of 60° to 70°. Since the present swirl generator blading is similar to reaction turbine blading (in that there is a static pressure drop through the blading) and the blade outlet angle is 65°, agreement with Zweifel's criterion should be adequate. As discussed in chapter 1 and shown in section 2.1.1 however, the blading efficiency is not a critical factor in the current application. A higher solidity than the optimum predicted by Zweifel's loading criterion was therefore selected to reduce the severity of the rotor blade wakes at the diffuser inlet, give a small "deviation" angle, and, help to counter the de-stabilizing effect of the positively-sloped total-pressure rise vs. flow-rate characteristic resulting from the forward-leaning blading.

In selecting the number of rotor blades, consideration was also given to the possibility of rotor/diffuser aero-elastic interactions and "sirening", to manufacturing feasibility and cost, and to stress and braze-fillet size. Since the discrete-passage diffuser which was tested as part of this thesis and another diffuser which is available and may be tested in the future both have an even number of passages (30 and 38 respectively), the rotor was selected to have 71 (a prime, odd number) blades. This eliminates the possibility of circumferential periodicity in the rotor-blade/diffuser-passage relative positions and gives a design-point blade lift coefficient of 0.23. This is a very light blade loading compared to the optimum lift coefficient value of 0.80 given by Zweifel's criterion.

The final blade shape obtained is shown in figure 2.11 and the pressure and suction surface coordinates are given in table 2.1. The calculated design point static pressure and relative Mach number distributions are given in figures 2.12a and 2.12b respectively. Figure 2.13 shows a scale diagram of all 71 blades positioned on the rotor, illustrating the very high blade solidity. The detailed mechanical drawings of the rotor assembly are shown in appendix F in figures F.3a through F.3c.

2.2.2 Inlet System Design

The swirl generator inlet system is an axi-symmetric assembly consisting of a double-contoured radial inflow cylindrical inlet transitioning into an axial-flow strut housing section followed by an axial-to-radial contoured duct leading to the rotor blading. The axial strut-housing is necessary to provide a means of support for the inner (hub) contour of the inlet system. Another array of struts is used to support the front section of the inlet system and a cylindrical anti-foreign-object screen at the inlet mouth. The overall arrangement can be seen in the swirl-generator assembly drawing shown in figure F.1.

The contours of the the entire inlet system were specified analytically. The front-section contour is a surface of revolution defined by the curve $r = const.$ while the remaining inlet duct contours are surfaces of revolution defined by a combination of cubic and linear sections. The contours were selected to provide a continuously accelerating flow from the inlet mouth to the rotor blading.

The axial-to-radial portion of the inlet duct was analyzed using the streamline-curvature analysis program "ANDUCT" [36] to insure that there will be no regions of severe adverse pressure gradient. The resulting design-point static pressure and Mach number distributions for the "hub" and "shroud" contours are shown in figure 2.14. As will be discussed in chapter 3, section 3.2 however, it was found that due to the high rotor blade solidity and the effect of mixing, the diffuser inlet flow-field is not sensitive to rotor inlet axial flow field distortion. The mechanical details of the inlet system components are given in appendix F, figures F.2a through F.2k.

2.2.3 Labyrinth-Seal Design

As discussed in section 2.1.1, a labyrinth seal was incorporated into the rotor-blading shroud to reduce leakage around the outside of the shroud to an acceptable level. Using references [44,58,62] as a guide, a basic straight-through seal configuration was selected, consisting of nine equal-height knife edges machined into the front surface of the rotor blading shroud as shown schematically in figure 1.7 (chapter 1). It was recognized that the more advanced seal configurations discussed in [58] offer higher sealing effectiveness than the straight-through configuration, but in the interest of mechanical simplicity and reliability, the straight-through design was selected. It was also recognized that since in rotating machinery, radial clearances are generally easier to maintain reliably than axial clearances, a radial labyrinth seal arrangement would be more desirable than the axial configuration selected. Due to the mechanical constraints of the blading and rotor configuration selected however, the axial seal configuration was chosen as the most appropriate arrangement in the present case, with the close-tolerance axial clearance being maintained by means of a very stiff bearing and casing design as described in sections 2.2.6 and 2.2.7.

In the present design, the seal land consists of an aluminum annular-plate coated with an abradable material, a fused aluminum/polyester powder (Metco-601), to safely handle the possibility of a seal rub. After application of the aluminum/polyester, the abradable surface was machined flat. Initially, a Teflon (polytetrafluoroethylene) seal land, as used in [19] and others, was tried but this proved to be a mistake as the Teflon tends to melt rather than abrade under the action of friction at high relative velocities.

One of the most critical parameters affecting the leakage through the seal is the seal clearance. For the present mechanical configuration, as discussed above, it was felt that the smallest clearance which could be reliably maintained is 0.010 inches (this in fact proved to be the case). This results in a knife-edge spacing to clearance ratio of 22 for the nine equally spaced knife edges. With this clearance, for the most severe anticipated pressure ratio of 0.60 (static exit to total inlet) across the seal, the theoretical corrected mass flow rate through the seal is calculated to be 0.069 Kg/second, which is 6.7% of the blading through flow rate at that operating condition. Using the results of [44], figure 11, the seal discharge coefficient was estimated to be 0.38. This discharge coefficient gives a maximum seal leakage of 2.5% of the blading through flow. It should be noted however that this is only an approximation, as the results of [44] are for a radial seal configuration and do not include the effect of rotation.

The mechanical details of the blading shroud/labyrinth seal are given in figure F.3c. Figure F.3a and photograph 1 show the rotor-shroud/seal assembly and the abradable-land ring is shown in figure F.4 and in photograph 2.

2.2.4 Injection/Suction-Slot Component Design

As described in chapter 1, a system of annular injection/suction slots was incorporated into the walls of the vaneless space between the rotor exit and test diffuser inlet, and also into the inlet duct just upstream of the rotor, to provide a means of controlling the axial distortion of the flow field at the inlet of the test diffuser. The basic configuration was shown schematically in figure 1.7.

Since no directly applicable data on the mixing of an annular cross-flow with the highly swirling, transonic rotor-exit flow was available and since this flow is very complex, no attempt at detailed analysis was made. Rather, the slots were designed for ease of modification so that several configurations could be tried if necessary.

For the initial design (which turned out to be the final design), the annular flow area of each vaneless-space slot was selected to be 5% of the main-flow through-flow area, requiring a slot width of 0.025 inches. At maximum rotor through-flow, this allows for a maximum theoretical suction flow rate (through both vaneless-space slots combined) of 33% of the rotor through-flow rate.

As shown schematically in figure 1.7, the annular slots are formed between the removable "slot-rings" which serve as covers to annular cavities machined into the flow-path end-walls upstream and downstream of the rotor blading, and one axial wall of these cavities. These rings fit into recesses machined into the flow path walls so that each slot-ring surface exposed to the main flow is flush with the basic contour of the main-flow path. This arrangement allows the radial slot-gap to be varied by using rings of different inside diameter (outside diameter in the case of the slots No.1 and No. 2, upstream of the rotor). The vaneless-space slots (slots No. 3 and No. 4) were located as close as mechanically feasible to the rotor exit to allow for some mixing of the slot flow and the main flow to occur before entry into the test diffuser. The annular cavity behind each of the slot-rings serves as a primary flow-collection/feed chamber and is connected through an array of circumferentially distributed passages (drillings) to a larger secondary collection/feed annular-chamber which in turn is connected to the external flow-injection/suction control system described in section 2.3.4.

The slot flow-path arrangement is somewhat different for the rotor-inlet hub slot (slot No.1). Through an array of circumferential passages, the primary flow-collection/feed annular-chamber for this slot is connected to a central cavity machined into the hub contour of the axial-to-radial section of the inlet duct. This cavity in turn is connected to a center flow-injection/suction tube by means of another array of circumferentially-distributed passages, with the tube serving as the connection to the external slot-flow control system. Figure 2.15 shows a schematic of the basic flow-collection/feed chamber and passage arrangement for the four independent slot systems.

To insure circumferential uniformity of the slot flow, the flow areas of all internal connecting passages were made as large as possible relative to the slot flow-area and an as high as mechanically possible circumferential density of passages connecting the primary and secondary collection/feed chambers was used. The area contraction from the primary annular-chamber behind each slot ring and the slot-gap itself is 10:1. In addition, low-porosity conical (annular in the axial projection) screen inserts were used in the secondary collection/feed annular-chambers (as shown in figure 2.15) to aid in maintaining circumferentially-uniform slot flow. Each screen insert consists of a perforated stainless steel ring formed into a conical section as shown in figure F.10. To decrease the porosity of the basic perforated plate material, a wire mesh screen made out of 0.013 inch diameter wire in a square pattern of 40 wires/inch, was spot-welded onto the perforated ring, resulting in a combined porosity of 9.2%.

The overall details of the slot flow-system can be seen in the swirl generator assembly drawing shown in figure F.1. The flow-passage arrays and secondary flow-collection/feed annular chambers are shown in the detailed drawings of the test section housing front-inner and rear plates in figures F.5a and F.5d respectively. The details of the rotor-inlet hub primary collection/feed chamber and connecting passages are shown in figure F.2e while the rotor-inlet shroud primary flow-collection/feed chamber is integral with the test section housing front inner plate as shown in figure F.5a. The primary collection/feed chambers and flow-passage arrays for the slots downstream of the rotor are integral with the removable front and rear vaneless-space and front and rear vaneless-diffuser rings, the drawings of which are shown in figures F.6a,b and F.7a,b respectively. The upstream and downstream slot rings are shown in figures F.8a and F.8b respectively and the secondary flow-collection/feed annular-chamber covers are shown in figures F.9a and F.9b. Figure F.2g shows the center injection/suction tube for the rotor-inlet hub slot (slot No. 1). Photograph 2 shows slot number 3 in the vaneless-space ring shown mounted on the front section of the test-diffuser housing.

2.2.5 Rotor-Blisk Mechanical Design

As was discussed in section 2.1.2, a bladed disk (blisk) rotor configuration was selected for the present application. In this rotor construction approach, the blades are machined integrally with the rotor disk. It was decided to support the blisk on a shaft in an overhung arrangement and attach it to the shaft by means of a simple double-keyed interference fit. The interference fit was achieved by machining a taper of 0.02 inches/inch on the blisk bore diameter and a corresponding taper on the shaft and then press fitting the blisk onto the shaft.

The overall mechanical configuration of the blisk was selected within the constraints imposed by the mechanical requirements of the inlet system, the profile control slot system, and the test section itself. Mass and moments of inertia were also considered as they affect critical speed (see appendix D).

A variable thickness disk cross-section was used to reduce the stress in the bore as compared to that resulting in a constant thickness design. Because of the indicated constraints and also for manufacturing simplicity, a simple linear taper of thickness with radius was selected. A drawing of the blisk is given in figure F.3a and photograph 1 shows a close-up view of the actual blisk installed in the test rig. The stress analysis of the blisk is given in appendix C.

2.2.6 Rotor-Spindle and Bearing-Housing Design

The rotor-spindle and bearing housing were designed to provide adequate support for the blisk over the expected operating envelope of the machine. The primary design requirements were:

- Axial stiffness sufficient to maintain the axial position of the blisk relative to the test diffuser to within ±0.002 inches.
- Radial positioning of the blisk relative to the test diffuser to within 0.001 inches.
- First shaft critical speed at least 30% greater than the 7200 RPM maximum operating speed.
- Adequate sealing to prevent infiltration of bearing lubricating oil into the test section.
- Bearing life (L-10) of at least 2000 hours.

The spindle designed to satisfy these requirements consists of a shaft with dual pre-loaded angular contact bearings (15° contact angle) in a tandem arrangement at the front (blisk) end of the shaft providing the required axial and radial stiffness and an identical but single angular contact bearing providing radial location at the rear (power input) end of the shaft. The shaft was machined from 4340 low-alloy steel, hardened to 50 Rockwell C, and precision-ground to final dimensions.

As indicated in section 2.2.5, the blisk was mounted on the shaft with an interference fit achieved by pressing the blisk onto the shaft. This is facilitated by a taper on the shaft diameter of 0.020 inches/inch and a matching taper on the blisk bore. Two diametrically-opposed keys are used to positively lock the blisk to the shaft. Positive axial location of the blisk on the shaft is achieved by means of a spacer-sleeve located between the blisk and the inner race of front bearing. The inner races of the tandem bearing package, the spacer-sleeve, and the blisk are clamped against a shoulder on the shaft by means of a locknut, lock-washer, and thrust washer. Since the thermal expansion coefficient for the aluminum blisk is higher than that for the steel shaft by a factor 1.6, positive clamping of the assembly is maintained over the operating temperature range of the machine. The length of the spacer-sleeve was selected to give an interference fit of 0.002 inches between the blisk and the shaft. This provides for a positive interference fit between the blisk and the shaft at the maximum operating speed of 7200 RPM. At this speed, if the blisk is not press-fitted onto the shaft, the growth of the blisk bore diameter due to centrifugal loading is estimated to be 1.64 mils as shown in appendix C.

Because of the high-precision required, ABEC-7 grade bearings were used. The main criteria which had to be met in selecting the bearings was adequate radial and axial stiffness and bearing life. An adequate radial stiffness is required to place the first critical speed of the spindle above the operating speed as shown in appendix D while an adequate axial stiffness is required to maintain the correct axial position of the rotor relative to the test diffuser as the axial load on the spindle varies. Bearing life is a function of the axial and radial loading on the bearings, the operating speed, the type of lubrication, and operating temperature.

The total radial load on the bearings is a combination of a static load due to the spindle weight and a dynamic load due to any radial imbalance of the spindle. The spindle was dynamically balanced to a tolerance of 0.05 inch-ounces resulting in a maximum dynamic radial load of 4.6 lbf at 7200 RPM. The total weight of the spindle is approximately 50 lbf. Due to the pressure imbalance between the front and rear surfaces of the blisk resulting primarily from the pressure drop through the rotor blading, there is an axial load on the disk of up to 1200 pounds force. Such axial force imbalances in turbomachinery (which in general also include the net effect all axial momentum fluxes in addition to the static pressure distributions) are generally handled in one of two ways. They can be either taken directly by the bearings or an attempt can be made to reduce the net axial force on the bearings by means of balance pistons, balance ribs, or labyrinth seals located at appropriate radii to tailor the pressure distribution over the disk to give a low net axial load. In some cases symmetric-flow designs are used ideally resulting in a zero net axial force on the bearings. All of these axial-force reducing approaches, although attractive in principle, introduce addition design complications undesirable in the present application. The feasibility of handling the entire axial pressure-imbalance force directly by the bearings was therefore investigated and it was determined that Fafnir type 2MM212WI bearings in the arrangement described above could fully handle the load at the maximum rotational speed of 7200 RPM with oil-jet lubrication. The radial load consisting of the spindle weight of 55 lbf and a maximum dynamic imbalance load of $\approx$5 lbf is negligible for these bearings. The lubrication system is described in section 2.3.2.

Since the axial and radial stiffness of the bearings increases with applied load, the bearings are pre-loaded to a level high enough to give a stiffness which would keep axial deflections to within the $\pm$0.002 inch limit while maintaining adequate bearing life. A pre-load of 320 pounds force was selected which from data supplied by the bearing manufacturer, results in an axial stiffness of 566000 lbf/inch for the tandem bearing pair and the radial stiffness of 3.42×10^6 lbf/inch for the pair. This results in an axial deflection of 0.0027 inches under the most severe axial loading of 1200 lbf from the pressure imbalance combined with the 320 lbf pre-load (1520 lbf total axial load), based on a conservative first-order estimate. The pre-load is supplied by a stack of wave-washer springs positioned in a recess within the bearing housing. The pre-load is applied to the outer race of the rear bearing by means of a precision-machined sleeve positioned between the rear bearing outer race and the wave-washer spring stack. The bearing housing bore for the rear bearing was designed such that the outer race of the rear bearing is free to slide axially. The spring load is therefore transmitted through the rear bearing, putting the shaft in tension and pre-loading the front tandem bearings. Figure I.1 shows the experimentally determined force v.s. displacement calibration curve for the wave-washer spring stack. The bearing life (L-10) at the most severe loading and speed described above was estimated to be in excess of 10000 hours with oil-jet lubrication, based on the manufacturers data.

In addition to the static deflections of the shaft, a critical design parameter closely related to the bearing stiffness, the critical speed(s), must also be considered. Turbomachinery is typically not designed to operate in steady state at or near a shaft critical speed as it is difficult to provide damping sufficient enough to maintain vibration levels within acceptable limits. The rotor and bearing system is therefore designed with stiffness adequate enough to put the first critical speed above the maximum operating speed. When this is either not feasible, or undesirable due to weight considerations, the rotor and bearing system is designed so that the normal operating speed range falls between critical speeds (typically between the first and second or sometimes between the second and third critical speeds). In the present case, to produce a continuous range of diffuser inlet conditions, it is desirable to be able to operate the swirl generator over a wide speed range without restriction. The rotor and bearing system was therefore designed with stiffness high enough to insure that the first shaft critical speed is at least 30% higher than the maximum operating speed of 7200 RPM. Obtaining the very-high shaft stiffness within the speed-x-diameter constraints imposed by the bearings required the closest possible spacing between the tandem bearing pair and the blisk, constraining the design of the oil seal as described below. This close bearing-blisk spacing was achieved in part by clamping the entire assembly of the tandem bearings, oil seal sleeve, and blisk against a shoulder on the shaft with a single lock nut (rather than providing a separate locking arrangement for the bearings). The high shaft stiffness required resulted in a very lightly loaded shaft, as shown in the stress analysis of the blisk and shaft in appendix C. The critical speed analysis is presented in appendix D.

As indicated above, oil-jet lubrication of the bearings was required. Since infiltration of this oil into the test section is undesirable, a precision magnetic carbon-face-seal was implemented between the front tandem bearings and the blisk. This type of contact seal consists of a stationary permanent-magnet lapped mating ring attached to the bearing housing and a ferromagnetic-steel ring containing the carbon sealing-element flexibly mounted on the shaft using O-rings and rotating with the shaft. The magnetic attraction between the two provides the sealing force. This seal design results in a more reliable and uniform seal-loading distribution and allows for a closer spacing between the blisk and the tandem bearings as compared to the more conventional spring-loaded type. One disadvantage of the magnetic face-seal is that the immediate components surrounding the seal elements can not be made out of ferromagnetic materials as this will "short-circuit" the magnetic flux around the seal preventing its operation.

In the present application there is a static pressure drop through the rotor blading of up to half an atmosphere while the pressure within the bearing housing always remains essentially atmospheric. The carbon face seal was therefore selected for operation with a pressure difference of up to 7.5 psid (low on the blisk side) at the maximum rotational speed of 7200 RPM. Since the seal mating surfaces are in contact with the bearing lubricating oil, long seal life is assured at this speed.

An oil seal was also required on the power input end of the shaft. Since the pressure within the bearing housing is essentially atmospheric, a simple lip-type elastomer oil seal was selected for this application.

The overall spindle design including the shaft, bearings, oil seals, and bearing pre-load arrangement can be seen in the swirl-generator assembly drawing shown in figure F.1. A detailed drawing of the shaft is given in figure F.11a and figures F.11b and F.11c show the blisk mounting keys and lock-nut thrust washer respectively. The bearing pre-load sleeve is shown in figure F.12. The rear oil-seal holder (which also serves as the bearing housing rear cover) is shown in figure F.13 and the front oil seal non-magnetic stainless-steel shaft-sleeve, which also serves as the bearing-to-blisk spacer as described above, is shown in figure F.14a. The magnet-ring holder is shown in figure F.14b and the threaded retaining ring used to secure the oil-seal assembly and tandem bearing package in the bearing housing is shown in figure F.14c.

In designing and constructing the bearing housing, special attention had to be given to maintaining accurate dimensions and concentricity of the bearing bores and squareness of the mating flanges. Since the bearing housing serves as the central structural element of the swirl-generator assembly, adequate stiffness of the bearing housing body and flanges was also a major concern. The bearing housing was machined as a single piece out of a 304 stainless steel round and plate, electron-beam welded together.

Included in the bearing-housing design are provisions for attaching the bearing housing to the test stand and mating the test-diffuser housing with the bearing housing. Appropriate apertures and mounting arrangements were provided for an oil-jet nozzle holder, an oil drain, a vibration transducer, an eddy-current blisk axial-displacement transducer, and three bearing temperature thermocouples (one for each bearing).

The overall features of the bearing housing and its structural function can be seen in the swirl generator assembly drawing shown in figure F.1 and a detailed drawing of the housing is given in figure F.15.

2.2.7 Test-Diffuser Housing Design

The following points summarize the functional requirements which had to be met in the design of the test-diffuser housing:

- The test-diffuser housing provides structural support for the test diffuser and vaneless-space elements to maintain their mutual alignment and their alignment with respect to the swirl-generator blisk. The tolerance goal was to maintain the error in spacing between the front and rear vaneless space elements to within ±0.002 inches and the mutual alignment error between the center plane of the discrete passage diffuser, the center plane of the vaneless space, and the mid-span plane of the rotor blading also to within ±0.002 inches. The labyrinth-seal land ring, described in section 2.2.3, must also be supported by the diffuser housing structure to within ±0.002 inches of the labyrinth seal knife edges on the blisk shroud.

- Appropriate passages and flow-collection/feed chambers for the diffuser-inlet profile control injection/suction slots had to be incorporated into the diffuser housing. Means for interfacing this internal flow-passage system with the external slot-flow-control system also had to be provided.
- Means for mounting probe holders and traverser mechanisms and means for the hermetic feed-through of transducer wiring and pressure-tap tubing had to be incorporated into the diffuser housing.
- The diffuser housing must provide an unobstructed flow path from the test-diffuser exit into the main collector/plenum without introducing circumferential diffuser-exit-flow distortion.
- The test-diffuser housing serves as the central structural support-element for the inlet and the main collector/plenum. This entire assembly is mated with and supported by the bearing housing. Means for the hermetic integration of these components had to be included in the design.

The test-diffuser housing designed to meet the above requirements consists of four main components: 1.) the front inner section, 2.) the front outer section, 3.) the cylindrical joiner "cage-ring" and, 4.) the rear plate. These components were machined out of 7075-T6 aluminum.

The front inner section of the diffuser housing contains the injection/suction flow passages and secondary flow-collection/feed chambers for the front upstream and downstream profile-control-slots (slots No. 2 and No. 3) and also has provisions for the mounting of the inlet, the labyrinth seal land ring, the vaneless-diffuser or vaneless-space front ring, and the secondary injection/suction flow-collection/feed annular-chamber cover (see section 2.2.4 for a description of the injection/suction flow-passage and flow-collection/feed chamber system). The primary flow-collection/feed annular-chamber for profile-control slot No. 2 is machined integrally with this section of the diffuser housing. In addition, a probe holder mount is attached to this section of the diffuser housing. This mount consists of a stainless steel annular plate and provides a hard surface for mounting probe holders or probe-actuator mechanisms at twelve circumferential positions at a radius corresponding to the G.E. discrete-passage diffuser inlet radius. The circumferential locations of the probe ports are given in table 2.3. Internal "O"-rings, retained with special plates shown in figure F.17, provide hermetic sealing of the probe body to the diffuser housing.

The front outer section of the diffuser housing provides structural support for the front inner section and was made separate from the inner section only for ease of manufacturing. A stainless steel probe-holder/actuator mount plate similar to that described for the front inner section above attaches to the front outer section and provides twelve circumferential probe mounting locations at a radius corresponding to the G.E. discrete passage diffuser exit radius. The circumferential locations of the test diffuser exit probe ports are the same as for the ports at the test diffuser inlet, as given in table 2.3.

Special probe holders and a actuator mount were designed and built for mounting stationary probes and the probe actuator mechanism described in section 2.5.1 onto the diffuser-housing mounting plates. The stationary probe mount is shown in figures F.18a and F.18b and the probe-actuator mount is shown in figure F.19. If a probe is not required at a specific probe-port, a dummy probe must be inserted into that port to seal the aperture. A drawing of the long dummy probe, for use in the diffuser inlet probe ports, and the short dummy probe, for use in the diffuser exit probe ports is shown in figure F.20. The retainer required to hold the dummy probes in place is shown in figure F.21.

The G.E. discrete passage diffuser mounts directly onto the rear plate of the diffuser housing by means of an existing flange on the diffuser. The rear plate of the diffuser housing also contains the injection/suction flow passages and secondary flow-collection/feed chamber for the rear downstream profile control slot (slot No. 4) and has provisions for the mounting of the rear vaneless-diffuser- or vaneless-space-ring.

The rear plate of the diffuser housing includes the means for attaching the diffuser housing to the bearing housing. This consists of twelve studs which are permanently fixed to the rear plate and mate with corresponding drillings in a flange on the bearing housing. Radial location of the diffuser housing relative to the bearing housing is provided by means of a shoulder on the bearing housing and a corresponding precision machined bore in the diffuser housing rear plate. Since this bore is larger than the diameter of the blisk, removal of the blisk is not required to separate the diffuser housing from the bearing housing. A hermetic seal between the diffuser and bearing housing is maintained by means of an O-ring on the bearing-housing shoulder.

Three ports for mounting pressure line feed-through blocks and two ports for electrical feed through fixtures are also provided in the rear diffuser housing plate. The pressure line feed-through block and electrical feed-through fixture are shown in figures F.22 and F.23 respectively.

Structural support between the front and rear sections of the diffuser housing is provided by means of a cylindrical joiner ring. Forty-eight equally-spaced, circumferentially-distributed slots were machined into this ring forming a "cage" around the diffuser to provide a flow path from the test diffuser exit into the main plenum/collector surrounding the diffuser housing. The relative angular location between all of the diffuser-housing elements is maintained by means of precision-ground hardened-steel dowel pins.

To minimize the influence of the cage-ring on the test-diffuser exit flow, the inside diameter of the ring was made larger than the exit diameter of the discrete-passage diffuser by a factor of 1.25, placing the "bars" of the cage-ring at a distance of 3.5 bar-widths downstream of the diffuser exit. Since significant streamline curvature in a flow approaching a grid of bars can be expected only within ~ 2 bar-widths upstream of the grid, the influence of the diffuser-housing cage-ring on the discrete-passage diffuser exit flow should be negligible.

The total flow-through area of the diffuser housing cage-ring is larger than the discrete-passage diffuser exit flow area by a factor of ~6, providing minimal flow resistance between the diffuser and the collector/plenum which surrounds the diffuser housing. The design of the cage-ring however facilitates the addition of a significant axisymmetric flow resistance between the test-diffuser exit and the plenum if this is desired to alter the dynamics of the flow system. This can be done by attaching a wire-mesh or perforated-plate screen of appropriate blockage to the inside surface of the cage-ring or an adjustable resistance can be introduced by various means. One option for providing an adjustable axi-symmetric flow resistance (throttle) at the exit of the diffuser housing is to mount an additional closely-fitting slotted ring over the existing cage-ring so that the angular position of the outer ring can be adjusted relative to that of the inner ring. Varying the degree of overlap of the slots of the two rings would vary the flow resistance. Another option would be to incorporate individual throttle-elements within the slots of the existing cage-ring.

Figures F.5a through F.5d show the diffuser housing front inner section, the front outer section, the cage-ring, and the rear section respectively. The cage-ring can be seen in photograph 3a which shows the disassembled diffuser housing with the discrete-passage diffuser mounted on the rear plate of the housing. Figures F.24 and F.25 show the outer and inner probe mount plates respectively. An estimate of the maximum deflection of the diffuser housing plates is given in appendix E.

2.2.8 Main Plenum/Collector Design

A flow collector surrounding the diffuser housing described in section 2.2.7 was required to provide a means for channeling the axisymmetric flow at the diffuser exit into a single downstream pipe. This allows for the control of the diffuser exit pressure by means of a combination of a downstream throttle and independent compressor and also allows the diffuser mass through-flow rate to be measured directly. (Since mass injection/suction upstream of the diffuser is used as a means for controlling the diffuser inlet profile, the determination of the diffuser flow-rate by means of a flow-meter positioned upstream of the swirl generator would require the accurate measurement of all injection/suction flow rates.)

Many radial compression-turbomachines use a "scroll" or "volute" flow collector surrounding the diffuser to provide a means for connecting the compressor to the external flow-circuit. This type of collector was judged to be unsuitable for the present application because of circumferential pressure-distortions that arise at off-design conditions [22,23]. For the present application, an oversized drum-type plenum/collector was designed to provide negligible circumferential pressure distortion at the diffuser exit over the entire operating range of the swirl generator.

The plenum/collector assembly consists of three separate components, the main body and two end covers. The body is a welded aluminum (6061-T6) structure, the main elements of which are a cylindrical shell and an internally-braced plenum to exit-flange transition "hood". The hood intersects the cylindrical shell over an arc of 120° and transitions to a standard eight-inch pipe flange. The end covers were machined out of 6061-T6 aluminum plate and serve as flanges joining the main body of the plenum /collector with the diffuser housing. To reduce pipe-loading of the plenum/collector assembly, a flexible bellows-type coupling is used to connect the plenum to the downstream piping.

An estimation of the maximum possible circumferential pressure distortion in the plenum was made to determine the appropriate size of the plenum. If it is assumed that the swirl of the diffuser exit flow is mostly removed by the diffuser housing cage ring (see section 2.2.7), then the flow within the plenum/collector will be symmetrical with respect to the principal meridional plane. In this case the maximum value of $\dot{m}/A_p$, where A_p is the local cross-section flow area of the plenum as measured in a meridional plane, occurs at the circumferential position of the junction of the cylindrical shell section and the plenum to exit-pipe transition hood, with one third of the diffuser exit flow passing through this section. Assuming uniform total pressure throughout the plenum, the minimum static pressure (maximum velocity) would be expected at this circumferential position in the plenum. The maximum possible pressure in the plenum would be the stagnation (total) pressure.

Defining the circumferential static pressure distortion parameter, ψ_d, as the ratio of the difference between the maximum and minimum static pressure in the plenum to the diffuser exit dynamic head and assuming incompressible, uniform total-pressure flow in the plenum,

$$\psi_d = \frac{P_{st_{max}} - P_{st_{min}}}{\frac{1}{2}\rho V_{d2}^2} = \frac{V_{max}^2 - V_{min}^2}{V_{d2}^2} \qquad 2.17$$

where V_{d2} is the diffuser exit flow velocity.

With the above stated assumptions, this reduces to:

$$\psi_d \approx \frac{\left[\frac{A_{dp}}{3}\right]^2}{A_{p_{crit}}^2} \qquad 2.18$$

where $A_{p_{crit}}$ is the cross-section flow area in the plenum at the circumferential location where $\dot{m}/A_p$ is maximum as discussed above and A_{d2} is the diffuser exit flow area.

For the present case, the effective exit flow area for the 30-passage G.E. diffuser is ~25.0 square inches while $A_{p_{crit}}$ is 110.0 square inches. This gives a value of ψ_d according to equation 2.18 equal to 0.0057 or 0.57%.

This crude estimate of the circumferential pressure non-uniformity in the plenum is adequate for design purposes in the present case because the design of the diffuser housing ring-cage facilitates the addition of an axi-symmetric flow resistance (a screen for example) as discussed in section 2.2.7. This can be used to reduce the circumferential pressure non-uniformity in the plenum as seen at the diffuser exit if required. As is shown in chapter 3 however, this proved to be unnecessary.

Figures F.26a and F.26b show drawings of the plenum/collector main body and a drawing of the end covers is given in figure F.27. A good general view of the plenum construction is provided in photograph 4.

2.2.9 Seals, Shims, and Fasteners

A critical and major effort in the development of the swirl generator was the design and selection of various seals, shims, and fasteners.

In addition to the custom-designed oil face-seal described in section 2.2.6, "O"-rings or flat elastomer gaskets were implemented between mating mechanical components where hermetic sealing was required. Static "O"-ring seals (nitrile synthetic rubber) were used at the following mechanical interfaces:

- At all flanges of the inlet components and at the mating journals of the central injection/suction tube (which is part of the inlet assembly).
- Between the discrete-passage diffuser front and rear flanges and the diffuser housing.
- Between the vaneless-diffuser and vaneless-space rings and the diffuser housing.
- At the interface between the diffuser housing front-inner and front-outer sections.
- Between the labyrinth-seal-land ring and the diffuser housing.
- At the interface between the diffuser housing rear-plate and the bearing housing.
- Between the stationary elements of the carbon face-seal assembly and the bearing housing and between the rotating element of the carbon face-seal and the shaft-sleeve and between the shaft-sleeve and the shaft.
- Between the blisk proximity-probe and oil-jet-nozzle holders and the bearing housing.

In addition, "O"-rings were used to provide sealing for all probe ports in the diffuser housing. These can serve either as static seals for stationary probes or as dynamic seals if probe motion is required for traversing the test section.

Flat elastomer-gaskets (neoprene) were selected for many static-sealing applications. These were used at the following locations:

- Between the mating flanges of the front and rear covers of the main collector/plenum and the plenum body-shell and at the junction of the plenum/collector assembly and the diffuser housing.
- At the seats for the injection/suction slot-rings.
- At the seat for the rear cover of the axial-to-radial-turn hub-section of the inlet assembly.
- At the seats of all pressure tube and electrical feed-through fixture ports in

the diffuser housing.

- At the seats of all injection/suction flow-distribution secondary-plenum covers.
- At the bearing housing rear-cover seat.

As discussed in section 2.2.7, the relative axial positions of various swirl-generator components must be accurately maintained. This can be achieved either by very accurate machining or through the use of shims at appropriate locations. Since the present construction involves the multiple stacking of several components, very close tolerances would be required on the dimensions of individual components for the required accuracy to be met without shimming, making the construction prohibitively expensive. The design approach therefore taken was to specify tolerances on all critical swirl-generator components in such a way that any resulting stacking error could be corrected through the use of shims during assembly of the swirl generator. Spring-steel shims of various thicknesses were made up for insertion, if required, at the following locations:

- Between the mating flanges of the diffuser housing front-inner and front-outer sections, to adjust for error in the spacing between the front and rear components forming the vaneless diffuser or the vaneless space.
- Under the mounting flange of the G.E. discrete-passage diffuser, to adjust its axial alignment with the vaneless-space components.
- Under the mounting flange of the inlet strut-housing, to adjust for the axial spacing between the axial-to-radial-turn components immediately upstream of the rotor.
- At the seat of the labyrinth-seal-land ring, to adjust for its proximity to the knife edges on the blisk shroud.
- Between the carbon-face-seal shaft sleeve and the inner race of the front bearing, to adjust the axial position of the blisk on the shaft.
- Between the mating flanges of the diffuser housing and the bearing housing, to correct for error in axial alignment between the blisk blading and the diffuser components.

In addition, shims were made up for use in the alignment of the motor and swirl generator on the test stand as described in section 2.3.3.

For simplicity, threaded fasteners were used throughout the swirl-generator assembly although the use of quick-release devices in several locations would have allowed for more convenient assembly/disassembly of the machine. The types of fasteners used includes threaded studs, nuts, bolts, machine screws, and threaded retaining-rings. Their application was standard and will not be discussed in detail here.

Machine screws and bolts were used at locations where piloting is not required and where frequent assembly/disassembly is not expected. In cases where the mating components are made out of aluminum and frequent assembly/disassembly of the components is required, stainless-steel studs were permanently fixed to one of the mating components with locking compound and nuts were then used to hold the components together. This eliminates wear of the relatively soft aluminum threads and provides piloting for ease of assembly.

2.3 Auxiliary Systems and Support Devices

Various systems and peripheral devices were required for operation of the swirl generator and for the acquisition of meaningful data. These are discussed in the following sections.

2.3.1 Variable-Speed Motor and Drive System

As discussed in section 2.1.2, a direct-drive induction motor in conjunction with a variable frequency power supply was selected to drive the swirl-generator rotor.

The motor was custom designed by the Electric Apparatus Company to operate continuously at any shaft speed between zero and 7200 RPM, with the maximum shaft power output of 100 H.P. at 7200 RPM. The motor is of the totally-enclosed type and is force-convection cooled by means of an external blower mounted on the motor and driven by and independent constant-speed 1 H.P. A.C. induction motor. Since the main motor bearings carry a much lighter load and have a smaller diameter than the swirl generator bearings, active lubrication of the motor bearings was not required. The direct coupling between the motor and swirl-generator shafts is accomplished by means of a continuous-sleeve gear-coupling (Sier-Bath Standard Coupling, size C-2.5).

The motor was modified to allow for rotation of the rotor in only one direction. This was done to prevent the possible reverse overspeed of the motor/swirl-generator rotor. Such an overspeed can occur if power to the drive motor is lost while a high flow rate continues to be maintained through the swirl-generator rotor by the downstream compressor. In such a case, the torque on the swirl generator rotor resulting from the momentum change of the flow through the forward-leaning blading will rapidly accelerate the rotor in a direction opposite to the normal direction of rotation. The final "runaway" speed in reverse rotation was estimated to be as high as 18,000 RPM in the worst case of choked flow in the rotor. At this speed, the blisk bore stress, calculated as shown in appendix C, would be greater than the 38,000 psi yield strength of the 6061-T6 aluminum at operating temperature.

The motor was constrained to rotate in only the normal swirl-generator mode direction by means of a one-way roller clutch (Torrington model number FC-25) retrofitted to the motor. The modification involved the addition of a shaft extension to the existing motor shaft on the end opposite to the power-takeoff end. The rollers of the clutch ride on a journal on the shaft extension which was case hardened to 58 Rockwell C to safely handle the maximum reverse torque estimated to be 490 inch-pounds. Rotational constraint for the outer element of the clutch is provided by means of a floating spider and mating socket-cap secured to the motor housing rear cover. A drawing of the shaft extension is given in figure F.28. The floating spider, the mating socket-cap, and the spider retainer are shown in figures F.29a through F.29c respectively. The required modification of the motor housing rear cover is shown in figure F.30 and the jig used to drill the motor shaft to accept the shaft extension is shown in figure F.31.

Control of the drive-motor speed is accomplished by means of an Emerson Electric Company model number AS5112 type 5VT-125 variable-frequency, 3-phase power supply. The power supply is microprocessor controlled, features a comprehensive diagnostics system, and can be programmed for either fixed torque or variable torque operation to match the motor load vs. speed requirements.

In the present application, since the swirl-generator input shaft-power varies approximately with the cube of the shaft speed (at constant throttle setting), the variable torque option was selected giving a linear variation of output voltage vs. frequency. However, because the downstream compressor can be used to produce a high flow rate through the swirl-generator rotor at low shaft speed which in turn would result in high shaft torque at low shaft speed (due to the forward leaning blading), the constant-torque option may have to be selected if operation in the high-flow, low-shaft-speed regime is required. The minimum and maximum speed limits are also programmable and were set to ~500 and ~7200 RPM respectively. The power supply output voltages corresponding to these speeds were set to 32 V RMS and 460 V RMS respectively.

Even though the output frequency of the power supply is established by an on-board oscillator, the speed of the motor varies with load as a result of slip (as opposed to being exactly determined by the frequency of the input power source as in the case of a synchronous motor). At present, the motor speed is set to the desired value in an open-loop mode by manually adjusting a dial on the power supply housing while monitoring the motor speed by means of a digital-readout tachometer. At constant load, the motor speed has been observed to remain constant to within 0.25% but can vary by as much as 2% between no load and full load if no manual compensation is made. A closed-loop control system can be easily incorporated into the present setup if manual correction of speed with changes in load is undesirable.

The main drive motor can be seen in photographs 5 and 6 and the variable-frequency motor power supply is shown in photograph 10.

2.3.2 Main-Bearing Lubrication System

Since the swirl-generator rotor bearings operate at high speed and are highly loaded, active lubrication of the bearings was required as discussed in section 2.2.6. Oil jet lubrication was selected for this purpose, using two oil nozzles positioned within the bearing housing by means of a fixture so that one of the nozzles provides a stream of oil to the front tandem bearing-package while the other nozzle provides oil to the rear bearing.

A closed-loop oil feed system is used to supply oil to the nozzles. The main components of the oil feed-system include an oil storage tank, an electric motor driven positive displacement (vane-type) oil pump, an oil-to-water heat exchanger, an oil filter, and a bypass-type oil-pressure-regulating valve. The entire oil feed system is mounted on the test stand described in section 2.3.3 below. The oil storage tank is mounted below the level of the bearing housing facilitating the gravity-driven return of oil from the oil drain at the bottom of the bearing housing back to the oil storage tank. A schematic of the bearing lubrication system is shown in figure J.1 and the actual system can be seen in the lower part of photograph 5. A drawing of the oil-jet nozzle holder is given in figure F.32.

2.3.3 Test stand

The swirl-generator assembly consisting of the bearing housing and rotor, the diffuser housing, and the main collector/plenum subassemblies, together with the drive motor are mounted on a specially-design test stand. The main structure of the stand consists of two longitudinally-oriented wide-flange beams joined together by three C-channels. The stand is mounted on six visco-elastic mounts which in turn are anchored to the test-cell floor and provide vibration isolation and damping. The swirl-generator assembly is attached to the stand by means of brackets at the front and rear of the bearing housing while the drive motor is mounted on a separate pedestal which in turn is bolted to the test stand. Relative alignment of the motor and swirl-generator shafts is achieved be means of shims. All of the structural elements of the test stand are made out of carbon steel and are either welded or bolted together. The bearing lubrication oil-feed system, described in section 2.3.2, is also mounted on the test stand.

Figure F.33a shows a drawing of the basic test-stand foundation assembly and figures F.33b, F.33c, and F.33d show the swirl-generator front bracket, swirl-generator rear bracket, and main motor pedestal respectively. The basic layout of the test stand can be seen in photograph 5.

2.3.4 Velocity-Profile-Control Flow Metering and Distribution System

The diffuser-inlet velocity profile control-scheme described in sections 1.4.2 and 2.2.4 requires an external flow control system to independently remove mass from or inject mass into the main flow through each of the four profile control slots (two upstream and two downstream of the rotor blading and designated as slot-systems 1 through 4 as shown in figure 2.15 for reference).

The system designed for this purpose incorporates two large plenums, one serving as the main "suction" plenum and the other (identical to the first mechanically) serving as the main "feed" plenum. The main suction plenum is connected to a steam-driven air ejector suction-line and the main feed plenum is supplied with air under pressure provided by a positive-displacement compressor through a pilot-operated pressure regulator. In addition to a main feed or main suction port connected accordingly to either the compressed air line or the air-ejector line, each of the main plenums has four ports on each of which is mounted a remotely-operated butterfly throttle valve (eight valves total). Each throttle valve on the main suction plenum is connected to one of four flow-distributors (one for each independent profile-control-slot system). Each of these distributors is connected, by means of flexible hoses (four hoses each for slot systems 2, 3, and 4 and a single hose for slot system 1), to the corresponding flow-collection/feed system, described in section 2.2.4, on the swirl generator. Similarly, each of the four throttle valves on the main feed plenum is also connected to one of the four flow distributors. This arrangement allows for the desired level of either "suction" or "pressure" to be applied to any of the four independent slot flow-collection/feed systems, in any combination by opening the appropriate combination of valves the appropriate amount.

Since all four profile control injection/suction slots are upstream of the test-diffuser inlet flow field profile-measurement location, accurate knowledge of any of the profile-control suction or injection flow rates is not required. However, the capability of repeating any combination of injection/suction flow rates is desirable and is obtained by measuring the pressure in the three secondary flow-collection/feed annular-chambers (for slot No's 2, 3, and 4) and in the central injection/suction tube which feeds slot No. 1 on the swirl generator. The measurement of these pressures also allows for the approximation of the actual injection and suction mass flow rates if desired. The injection-flow temperature was not measured in the present experiments because the matching of the injection flow stagnation temperature to the rotor exit flow stagnation would require a complicated heat-exchanger and control system. It was found however that in the worst case, the rotor-to-injection flow stagnation temperature ratio is only 1.24. As discussed in detail by Greitzer et al. [27], this should have a negligible effect on the Mach number and stagnation pressure distributions within the test diffuser.

The profile-control injection/suction pressures are measured by means of pressure taps in the flow-collection/feed chamber covers (see figures F.9a and F.9b) and a pressure tap-collar on the central injection/suction tube (see figures F.2g and F.2h). A single high-quality pressure transducer (Setra model number 271, ±15 psid range) is multiplexed to the individual pressure measuring points by means of remotely-operated solenoid valves. A schematic of the injection/suction flow distribution system is given in figure 2.23.

The capacity of the positive displacement compressor allows for an injection flow rate of over 50% of the maximum diffuser through flow rate. This is substantially greater than that attempted in the present investigation (see sections 3.2 and 4.2). The capacity of the steam-driven air ejector is sufficient to choke the two vaneless space profile-control slots, giving a theoretical maximum suction flow rate of ~33% of the maximum diffuser through-flow rate.

Figure F.34 shows a drawing of the main suction/feed plenum and the flow-distributor body and cover, which are used for slot systems No. 2, 3, and 4, are shown in figures F.35a and F.35b respectively. Since slot system No. 1 uses a single central injection/suction tube, a single flexible hose and a simple "Y" pipe connection is used to connect this slot system to the suction and injection throttle valves. The components of the slot-flow control system were mounted together on a frame and positioned next to the swirl-generator test stand as shown in photograph 7. The hose-connection arrangement between the slot-flow control system flow-distributors and the swirl-generator flow-collector/feed systems can be seen in photographs 4 and 6.

2.3.5 Main-Plenum Throttle Valve and Downstream Slave Compressor

The exit flow from the diffuser test rig plenum is passed through a throttle valve to the inlet of a separate slave compressor. This allows for the control of the flow rate through the test rig by a combination of the throttle valve position and the suction provide by the slave compressor, and gives access to test-rig operating regimes requiring sub-atmospheric pressure in the main collector/plenum. A venturi-type flow meter (see section 2.5.5) located in the pipe joining the test rig with the slave compressor provides a means for measuring the test diffuser mass flow rate.

The throttle valve is a standard eight-inch butterfly type and is operated remotely from the control panel described in section 2.3.7. The slave compressor is a five-stage centrifugal type manufactured by the DeLaval company (machine number 249698). This compressor is part of the G.T.L. facility and is well oversized for the present application. However, a re-circulation valve in conjunction with an air-to-water heat exchanger, both part of the DeLaval facility, allow for the operation of the DeLaval compressor away from its surge line while the diffuser test rig is operated anywhere from shutoff to choke.

The diffuser test rig was operated in conjunction with the Delaval compressor only when the flow rate required through the test diffuser could not be driven by the swirl-generator rotor itself. All operation of the diffuser test rig requiring the Delaval compressor was done with the Delaval compressor operating at a fixed true-speed of 3500 RPM and with the recirculation valve set to maintain the static pressure at the inlet to venturi flow meter in the range of -5.5 to -6.0 psig for all test rig exit throttle valve settings. It was found that operation of the Delaval compressor in this range is necessary to keep pressure fluctuations in the test-rig flow circuit at a minimum (less than one inch of water as measured at the venturi flow meter). At higher Delaval compressor flow rates, obtained by opening the recirculation valve, static pressure fluctuations of several inches of water were observed at the venturi flow meter inlet.

2.3.6 Operation-Monitoring and Auto Shutdown Safety System

Although the maximum tip speed of the swirl-generator blisk of 460 ft/sec. is considered to be low by modern turbomachinery standards, various catastrophic failure modes leading to serious damage to the facility are possible. Bearing failure for example can lead to a blisk rub which in turn could rapidly lead to the structural failure of the blisk and destruction of the machine. Overheating of various test section components can similarly lead to distortion or failure. (Another failure mode considered was the reverse overspeed of the swirl-generator rotor, as discussed in section 2.3.1.)

To insure adequate lubrication of the swirl generator main bearings, a low oil-pressure alarm was installed. The temperature of each bearing outer race, together with the supply oil temperature, are monitored by means of thermocouples and digital temperature readouts. Long term wear of the bearings is inferred by monitoring the axial position of the blisk by means of a non-contact eddy-current proximity probe (Indikon model number 590). This probe is positioned behind the swirl-generator blisk by means of a probe holder, shown in figure F.16, mounted in the swirl-generator bearing housing main flange as can be seen in the swirl-generator assembly drawing shown in figure F.1. In addition, the motor bearing temperatures are monitored by means of thermocouples and a digital readout thermometer in conjunction with a manual multiplexing switch. The locations of these thermocouples can also be seen in figure F.1.

A good indication of the degradation of the "health" of the rotating components of a turbomachine is an increase in the vibration level. For this reason the vertical component of the vibration of the swirl-generator bearing housing at the front bearings was monitored by means of a vibration transducer (Metrix model number 5484) mounted on the bearing housing. The output of this transducer is a standard 4 to 20 ma control loop current linearly corresponding to a vibration level range of 0.0 to 1.0 inches/sec. (peak).

Since degradation of the mechanical integrity of the machine can occur rapidly, an automatic drive-motor shutdown circuit was designed and built. The circuit, the schematics of which are shown in appendix K, automatically monitors the bearing housing vibration level and test-section temperature and shuts down the swirl-generator main drive motor if pre-set limits are exceeded. In addition, the circuit also can be set to shut down the drive motor if the flow rate through the swirl generator drops below a preset value or if the main downstream line pressure exceeds a preset value, indicating unexpected shutdown of the downstream slave compressor. The circuit features lockouts so that any of the four shutdown criteria can be deactivated and trigger indicators to facilitate failure isolation.

2.3.7 Remote-Operation Control Block

The operation of the test facility is done remotely. The main elements of the remote operation-control block are the main control panel, the data acquisition computer, and the variable frequency power supply for the main drive motor described in section 2.3.1.

The main control panel contains the operating controls and monitoring displays for the profile-control injection/suction system described in section 2.3.4, the auto-shutdown and operation monitoring system described in section 2.3.6, the lubrication system describe in section 2.3.2, the main plenum/collector throttle valve, and the downstream slave compressor described in section 2.3.5. Readouts for the venturi flow-meter flow temperature, the test section temperature, the ambient temperature, and the main plenum pressure are also provided on the main control panel and a manometer for measuring the pressure drop across the venturi flow meter is wall-mounted in close proximity to the panel. The data-acquisition computer is describe in section 2.6.

The main control panel is shown in photograph 9 and the data acquisition computer setup is shown in photograph 12. Photograph 10 shows the main motor variable frequency power supply.

2.3.8 Assembly/Disassembly Devices, Tools, and Accessories

Various devices and tools had to be designed and built for use in the assembly and disassembly of the diffuser test-rig. These include:

- The test-section to bearing-housing mate/de-mate pivot-stand.

  This stand allows the entire assembly consisting of the diffuser housing, inlet, and plenum to be mated or de-mated from the bearing housing containing the swirl-generator rotor assembly. Rollers mounted on the pivot stand allow the diffuser housing assembly to be moved away from the bearing housing. These rollers ride on flanges of the test stand described in section 2.3.3. Once separated from the bearing housing, retractable casters are lowered and the entire assembly can be moved away from the test stand. The diffuser housing/inlet/plenum assembly can then be rotated to put the centerline of the assembly into a vertical position by means of a manually operated worm-gear drive mechanism. Once in the vertical position, the individual components of the assembly can be easily de-stacked by means of simple lifting devices. The procedure is reversed for assembly.

  The pivot-stand can be seen in the front view of the diffuser test rig shown in photograph 4. Drawings of the individual components of the stand are shown in figures F.36a through F.36v.

- The auxiliary diffuser housing front-section assembly/disassembly stand.

  In addition to the main pivot-stand described above, an auxiliary stand was designed and constructed to aid in the assembly and disassembly of the front section of the diffuser housing. This stand is also design to allow rotation of the assembly to facilitate access to various components of the front section of the diffuser housing. Photograph 14 shows the auxiliary stand with the front section of the diffuser housing mounted in place. Figures F.37a through F.37d show drawings of the individual components of the stand.

- The hydraulic press.

A hydraulic press was designed and built for mounting the gear-coupling hubs onto the swirl-generator and motor shafts. In addition, the hydraulic cylinder of the press is used with the blisk mount/dismount devices described below.

- The swirl-generator blisk mount/dismount devices.

As discussed in section 2.2.6, an interference fit is used between the blisk and the shaft. This is achieved by pressing the blisk onto the slightly tapered shaft by means of a hydraulic cylinder and a specially designed loading device. Removal of the blisk from the shaft is similarly accomplished using the hydraulic cylinder and in conjunction with a blisk removal device designed to distribute the pull force uniformly around the rim of the blisk. To prevent the galling of the blisk bore during the mount/dismount operations, a thin layer of graphite powder was applied to shaft.

The components of the blisk mounting device are shown in the drawings of figures F.38a through F.38c and the blisk dismount components are shown in figures F.39a and F.39b.

- The inlet and instrumentation shield and noise suppressor.

A shield was designed and constructed to protect the test rig inlet and instrumentation from damage. This essentially comprises a large aluminum box constructed out of 0.25 inch thick aluminum plate on a Unistrut frame. To attenuate noise radiated from the inlet, the box was lined with sound-dampening foam.

The shield was designed to be mounted on top of the main pivot-stand described above but is removed in photograph 4 to show the details of the test rig. The shield is shown separately in photograph 8.

In addition to the devices described above, a wide range of lifting and small positioning accessories had to be designed and constructed. These, together with the blisk mount/dismount devices described above, are shown in photograph 13.

2.4 Description of The Test Diffusers

2.4.1 Vaneless Diffuser

A 1.20 radius-ratio vaneless diffuser immediately downstream of the swirl generator blisk was used for the initial swirl-generator performance verification tests as described in chapter 3. The diffuser is formed by the axial gap between two removable rings, one mounted on the front section of the diffuser housing and the other mounted on the rear section of the housing. These rings contain the primary velocity profile control flow distribution annular-chambers and flow passages and accept the rings which form the profile-control-slots as described in section 2.2.4. The vaneless diffuser has a sharp-corner exit and dumps into the diffuser-housing/collector-plenum assembly described in sections 2.2.7 and 2.2.8.

Static pressure taps are provided at four circumferential locations at a radius ratio of 1.10 and also at a radius ratio of 1.17 (relative to the swirl-generator rotor exit radius) on each vaneless diffuser ring. Traverse-probe apertures are provided at three circumferential locations at a radius ratio 1.10. The radius ratio of 1.10 corresponds to the discrete-passage diffuser inlet radius.

The overall vaneless-diffuser radius ratio of 1.2 was selected as a compromise between the vaneless-diffuser stability limit and the diffuser exit effects as seen at the traverse location. With a vaneless diffuser radius ratio of 1.20, the static-pressure-tap and traverse-probe positions at a radius ratio of 1.10 are over two vaneless-diffuser widths upstream of the vaneless diffuser exit and would not be affected by any axial flow-field distortion effects at the diffuser exit produced by the interaction of the diffuser exit flow with the main plenum/collector flow. As estimated from the vaneless diffuser data of Jansen [34], the 1.20 radius ratio vaneless diffuser with a width to inlet-radius ratio of 0.049 should exhibit stable operation up to an inlet angle of ≈80° at a Reynolds number on the order of 10^6 (based on the diffuser inlet radius and flow properties). This satisfies the requirements of the present experiment as discussed in section 1.3.

The vaneless diffuser static pressure tap and traverse-probe aperture locations are shown in figure 2.16 and drawings of the front and rear vaneless diffuser rings are shown in figures F.7a and F.7b respectively.

2.4.2 Discrete-Passage Diffuser and Vaneless-Space Elements

The primary test object of the current research program was a General Electric 30-passage discrete-passage radial diffuser, with a design-point inlet Mach number of 0.973 at a flow angle of 71.1° from the radial direction. As shown in figure 2.17, the diffuser design is characterized by straight centerline passages which are of circular cross-section from the diffuser inlet up to the throat but transition, unconventionally, to a semi-rectangular cross-section at the discharge. In the region from the inlet of the diffuser up to the throat, adjacent passages intersect, forming a "quasi-vaneless space". The actual diffuser mounted in the test-rig diffuser housing (with the front cover of the housing removed) is shown in photograph 3a and photograph 3b is a close-up view of the diffuser inlet and quasi-vaneless-space region.

One passage of the diffuser as supplied by G.E. was instrumented with an array of static pressure taps. The locations of those taps which were used in the present investigation are shown in figure 2.18 and table 2.2. Six additional static pressure taps were drilled in the front and rear walls of passages number 1, 6, 11, 16, 21, and 26 (12 taps total) on the axial projection of the passage centerlines at a radius ratio of 1.129 relative to the rotor exit radius. These were used to verify circumferential uniformity of the diffuser flow.

To allow for the axial traverse of the discrete-passage diffuser inlet by means of the P-total/flow-angle probe described in section 2.5.1, six probe-apertures were drilled through the front and rear walls of the diffuser at a radius ratio of 1.002 relative to the diffuser inlet radius. The circumferential locations of the apertures correspond to the first six (of twelve) probe port locations provided in the diffuser housing as given in table 2.3.

A 1.10 radius ratio vaneless space between the swirl-generator blisk exit and the discrete passage diffuser inlet contains the profile control slot elements identical, to within manufacturing tolerances, to those in the 1.20 radius ratio vaneless diffuser described in section 2.4.1. In addition, three high-frequency response pressure transducers (see section 2.5.2) are flush mounted in the vaneless space at a radius ratio of 1.077 relative to the rotor exit radius. The circumferential locations of these transducers in the vaneless space is shown in figure 2.19 and drawings of the front and rear vaneless-space rings are shown in figures F.6a and F.6b respectively.

2.5 Instrumentation and Calibration

2.5.1 Total-Pressure/Flow-Angle Probe and Actuator Mechanism

Since one of the principle objectives of the present research program was the investigation of the effect of the axial distortion of the diffuser inlet flow field on the diffuser performance, a means had to be provided for determining the actual diffuser inlet Mach number and flow angle profiles at various swirl-generator operating conditions. This was achieved by means of a cylindrical single-hole total-pressure/flow-angle probe (as described in [7] for example) axially spanning the inlet of the test diffuser as shown schematically in figure 2.20. A single hole probe was used for the present application to minimize the probe diameter and thereby minimize the effect of the probe on the diffuser inlet flow field.

The probe used in the present experiments consists of a 0.039 inch diameter stainless steel tube in which a 0.009 inch diameter sensing hole was radially-drilled through one wall. The tube is sealed on the free end and is supported by a stepped, hollow probe-body on the other end for structural support and to provide a means for transmitting the pressure signal to the external pressure transducer. A drawing of the P-total/flow-angle probe is shown in figure F.40.

With the probe positioned in a cross-flow, rotation of the probe about its principal axis produces an output pressure signal in accordance with the pressure distribution around a cylinder in a cross-flow (at the corresponding Reynolds number and Mach number). The maximum output pressure, occurring when the sensing hole is facing directly into the flow, indicates the total pressure of the flow (after corrections for viscous effects and/or shock loses, if applicable, are made). This allows the single hole cylindrical probe to be used for determining the flow total-pressure and flow angle of a 2-D flow in a plane normal to the probe axis.

Figure G.1 shows a calibration curve, obtained using a calibration jet, for the P-total/flow-angle probe used in the present experiments. The calibration curve shows the relationship between $\frac{P_{out}}{P_{t_{jet}}}$ and δ_α, where P_{out} is the output pressure signal from the probe, δ_α is the deviation angle of the sensing hole centerline from the calibration jet centerline, and $P_{t_{jet}}$ is the jet total pressure. Since $\frac{dP_{out}}{d\delta_\alpha} = 0$ at $\delta_\alpha = 0$, where δ_α is the angular offset of the flow vector from the sensing hole centerline in a plane normal to the probe axis, the flow angle α can not be determined accurately by simply searching for the peak of the P_{out} vs. α curve. Due to symmetry of the P_{out} vs. δ_α curve about δ_α=0 however, an accurate determination of the flow angle can be made by finding the centroid of the P_{out} vs. α curve. This was the approach taken in the present investigation as depicted schematically in figure 2.21.

The axial and angular positioning of the probe at the diffuser inlet was achieved by means of a L.C. Smith model number BBS-1-SM-180-SM probe actuator.

This actuator provides traverse/angle positioning of the probe using separate stepping-motor drives for each degree of freedom. The traverse range of the actuator is one inch and the angle range is 180°.

Rated angular positioning linearity is to within 0.1% of full scale, which for the present 180° range is 0.18°. Hysteresis is 0.2°. The rated traverse positioning linearity is also to within 0.1% of full scale or 0.001 inches for the 1.0 inch range with a hysteresis of 0.002 inches. In the present experiments, all traverse/angle set points were approached from the same direction to avoid hysteresis error. Photograph 4 shows the probe actuator mounted on the diffuser test rig.

2.5.2 Low-Frequency-Response Pressure Transducers

Measurements of steady static-pressure at all static taps in the diffuser test rig, including the vaneless-diffuser taps, the discrete-passage diffuser taps, and the main plenum pressure were made by means of a single Druck type PDCR-23D ±5, psid pressure transducer, multiplexed to the various pressure taps by means of a Scanivalve model number 48C9 pressure-transducer multiplexer. The rated combined non-linearity, hysteresis, and repeatability of this transducer is to within ±0.04% of full scale.

The velocity profile control-system injection/suction pressures and the venture flow meter upstream static pressure were measured by means of a Setra model number 271, ±15 psid pressure transducer. A manually-switched solenoid-valve multiplexer was built to connect the transducer to each of these pressure-measurement points as required. This transducer has excellent long term stability, with a rated repeatability to within ±0.02% of full scale and a rated accuracy to within ±0.05% of full scale.

Both the Druck and Setra pressure transducers were calibrated using a standard mercury manometer to set the applied pressure. The calibration curve for the Druck transducer is shown in figure G.2 and the calibration curve for the Setra transducer is given in figure G.3.

2.5.3 High-Frequency-Response Pressure Transducers

Three Kulite model number XCS-062, ±5 psid pressure transducers were flush mounted in the vaneless space between the swirl-generator rotor and the discrete passage diffuser at the positions shown in figure 2.19 for detection of rotating stall and any other unsteady pressure phenomena. These transducers have a rated combined non-linearity and hysteresis of better than ±0.50% of full scale and a repeatability to within ±0.10% of full scale. Since the natural frequency of the diaphragm in these transducers is ≈150kHz, negligible error in the frequency response can be conservatively expected to at least 15Khz. Calibration curves for the three transducers (serial numbers 1547-9-208, 1547-9-278, and 1547-9-284) mounted in the vaneless space, are shown in figures G.4a through G.4d respectively.

A Kulite model number XT-140, ±50psid pressure transducer was flush mounted in the main collector/plenum wall to detect pressure fluctuations in the plenum. (This transducer was used because of its availability, resulting in a higher than required range. The normal range of the plenum pressure is from ≈ -6.0 psig to ≈ +5.0 psig). The rated combined non-linearity and hysteresis of the transducer is to within ±0.5% of full scale and the repeatability is to within ±0.10% of full scale. A calibration curve for this transducer is shown in figure G.4c.

Reference pressure for the calibration of all of the pressure transducers was determined by means of a standard mercury manometer (properties of mercury from [31]).

2.5.4 Temperature Measurements

Flow temperature was measured in the test-section at the exit of the vaneless and discrete passage diffusers (at an axial location corresponding to the center plane of the diffuser), at the exit of the venturi flow-meter (see section 2.5.5 and appendix H), and at the swirl-generator inlet. Temperature was also measured at the swirl generator bearings and the main drive-motor bearings for diagnostic purposes.

The diffuser exit temperature was measured by means of a shielded type E (chromel/constantan) thermocouple probe, a drawing of which is shown in figure F.41, and an Omega Engineering model number 670 digital-readout temperature display. The temperature at the exit of the venturi flowmeter was measured using an Omega Engineering thermistor probe model THX-400-AP and an digital-readout thermometer model 651. Ambient air temperature at the swirl-generator inlet was measured by means of a type T (copper/constantan) thermocouple and an Omega Engineering model number 115 digital readout thermometer.

These temperature-measurements systems are standard and can typically be used uncalibrated to an accuracy of ±1.%. However, to verify proper operation and to insure that no installation-related errors have occurred, a two-point calibration of each system was made using a -1°C-50°C precision mercury thermometer (0.1°C resolution) at ice-bath and room-temperature reference points. The calibrations were carried out for the overall temperature-sensor to digital-readout systems, with all temperature-sensor wiring in the final installed configuration, giving a conservatively estimated overall accuracy to within ±1°R, or <0.2% over the temperature range of the present experiment (~525°R to ~610°R). Since the temperature measurements in the present experiment are used primarily for setting the corrected speed and for mass flow measurement, both of which depend on the square root of the absolute temperature, the measurement error of these parameters due to temperature measurement error is less than ±0.1% .

2.5.5 Mass Flow Meter

The mass flow rate through the test diffuser was determined by means of a BIF "universal venturi tube" [30], part number 0182-10-2291, located in the test-rig exit ten-inch, schedule 40 carbon-steel pipe. The rated uncalibrated accuracy of the flowmeter is ±1.0% of the true value [30].

A standard AGA-ASME tube-bundle type flow straightener located eleven (11) pipe diameters upstream of the venturi tube was used to reduce the required distance between the upstream pipe-elbow and the venturi. A drawing of the flowmeter piping layout is shown in figure F.42.

The mass flow rate was calculated directly without calibration as shown in appendix H.

2.5.6 Tachometer

The swirl generator rotor speed was measured by means of a Shimpo model number DT-5BC digital readout tachometer. This tachometer utilizes a built-in quartz-oscillator frequency reference resulting in a rated speed-readout-accuracy to within 0.008% of reading. The readout resolution is to 0.1 RPM.

The operation of the tachometer relies on a pulse-type input signal which was provided by means a magnetic proximity switch, Shimpo model DJ2-G, mounted near the motor/swirl-generator shaft-coupling outer sleeve. Eight circumferentially-equally-spaced circular cavities (0.25 inches in diameter) were radially cut into the outer surface of the coupling sleeve (0.188 inches deep) to provide eight output pulses from the proximity switch for every revolution of the swirl generator shaft. The tachometer is equipped with user-selectable multipliers for internal conversion from pulses/revolution to RPM.

A binary-coded-decimal digital output feature is built into this tachometer but was not implemented in the present setup of the data acquisition system. In the present experiments, the tachometer reading was manually entered into the data acquisition computer at the appropriate time in the data acquisition sequence, as prompted by the data acquisition program which will be described in section 2.6.2.

2.6 Data Acquisition System

2.6.1 Description of Data Acquisition Hardware

The main hardware elements of the data acquisition system include:

- IBM-PC-AT computer with a Metrabyte Dash-16F eight channel A/D converter board and a National Instruments GPIB-PC-2A communications interface board.

The Dash-16F A/D converter provides a 12-bit resolution and a maximum sampling rate of 100Khz to memory in the DMA (direct memory access) mode. The GPIB-PC-2A board provides communications with the Scanivalve digital interface unit and the L.C. Smith probe-actuator controller, both described below, using the GPIB (IEEE-488) standard.

- Pressure-transducer multiplexing unit, Scanivalve model number 48C9, and a Scanivalve digital interface unit model number SDIU-MK5.

The pressure-transducer multiplexing unit was used to switch a single pressure transducer to various pressure-measurement points as described in section 2.5.2. An on-board transducer signal conditioner, Scanivalve model number SCSG2/±5V/VG provides excitation voltage to the pressure transducer and amplification of the transducer output to ±5 volts full scale.

Control of the transducer multiplexer is provided by the SDIU-MK5 unit. This unit is operated automatically through the GPIB interface buss by the data acquisition software described in the following section. An on-board 16-bit A/D converter converts the transducer-signal-conditioner output to digital form for transmission to the IBM-PC-AT data acquisition computer through the GPIB interface buss.

- Probe-actuator controller and computer interface unit, L.C. Smith model number TAC-H-SM.

This unit controls the stepping motor probe-actuator (described in section 2.5.1), positioning the probe according to software commands received through the GPIB buss from the IBM-PC-AT computer.

- Signal conditioning amplifiers, Measurements Group, Instruments Division, model number 2310 (four units total). These units were used to provide excitation for the Kulite high frequency-response pressure transducers (see section 2.5.3) and amplification and filtering for the transducer output.

A schematic diagram of the overall data acquisition system is shown in figure

2.22. Photograph 11 shows the main hardware rack containing, from top to bottom, the TAC-H-SM probe-actuator controller unit, the signal conditioning amplifiers, the Scanivalve digital interface unit, and the Scanivalve pressure-transducer multiplexer. The lower panel of the rack contains the manually-switched solenoid-valve Setra pressure-transducer multiplexer described in section 2.5.2. The remote data-acquisition station is shown in photograph 12.

2.6.2 Description of Data Acquisition Software

Data acquisition is handled by a master operation-coordination computer program written in the ASYST$_{TM}$ programming language. The program includes options for various test sequences including the traverse of the test section with the P-total/flow-angle probe, acquisition of time-resolved data from the Kulite pressure transducers, and scan of selected Scanivalve channels. The program provides cues for manually entered data including the swirl-generator-rotor rotational speed, the profile control system flow-distribution chamber pressures, the venturi flow meter upstream pressure, the venturi flow meter upstream-to-throat pressure difference, the flow meter downstream temperature, and the ambient and test section temperatures. Data files appropriate for the selected test sequence are automatically created and all data is logged according to pre-determined formats. The modular structure of the program allows for easy additions and/or modifications.

2.7 Summary

A complete radial-diffuser test facility has been designed and constructed based on the very-high-solidity rotating radial-outflow nozzle-cascade swirl-generator/profile-control-slot (VHS-RRONC/PCS) concept described in chapter 1. The main elements of the facility include:

- The swirl-generator/diffuser-test-section assembly and main drive motor mounted on a test stand
- The velocity-profile-control flow metering and distribution system
- A remote operation-control and data acquisition station
- Various assembly/disassembly accessories

The swirl generator rotor is directly driven by a continuously-variable-speed electric motor and provides a diffuser inlet Mach number of up to 1.0 and a swirl angle range of ~66° to ~75°. Circumferential injection/suction slots built into the endwalls of the swirl-generator rotor inlet duct immediately upstream of the rotor and into the vaneless space walls downstream of rotor provide a means of controlling the axial distortion of the diffuser inlet profile.

An independent downstream centrifugal compressor allows for a wide flow-rate range through the test diffuser independent of the swirl-generator rotor operating speed.

An overall schematic of the facility swirl-generator/diffuser-test-section assembly and associated flow systems is shown in figure 2.23.

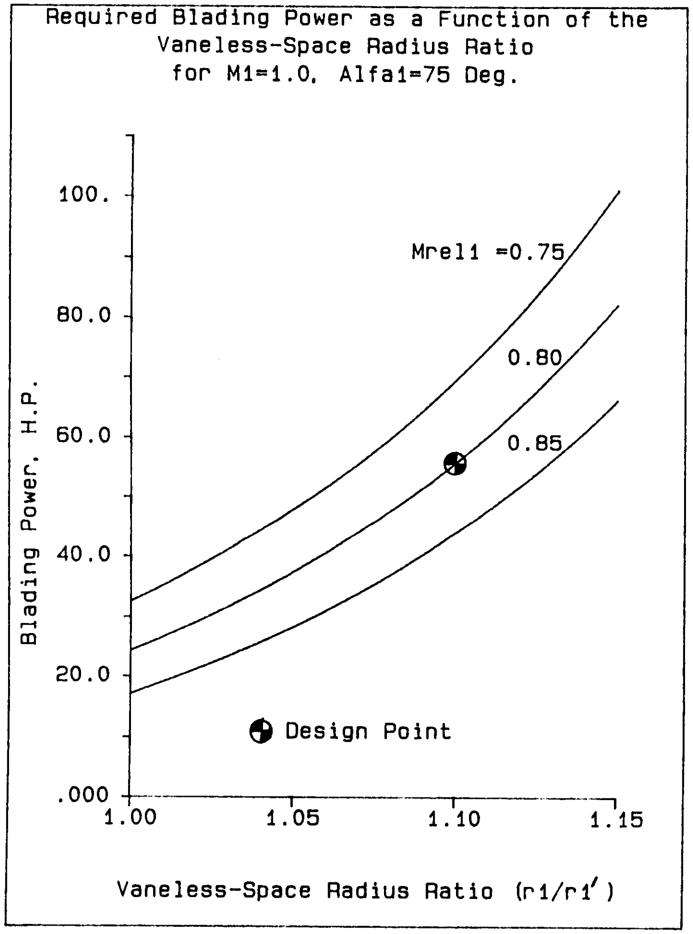

Fig. 2.1a Calculated Required Blading Power as a Function of Vaneless Space Radius Ratio and Rotor Exit Relative Mach Number

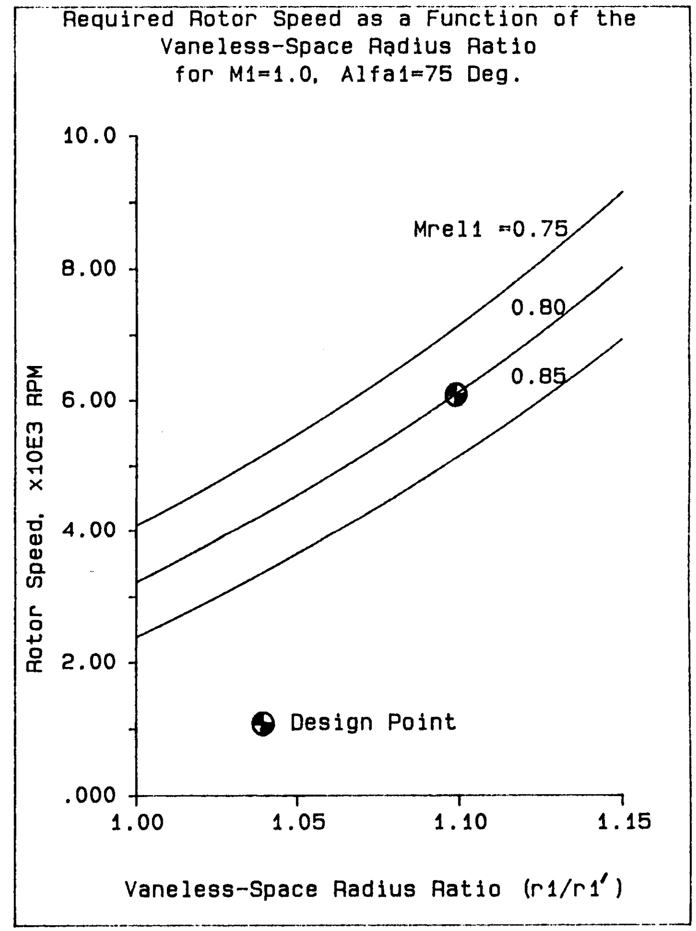

Fig. 2.1b Calculated Required Rotor Speed as a Function of Vaneless Space Radius Ratio and Rotor Exit Relative Mach number

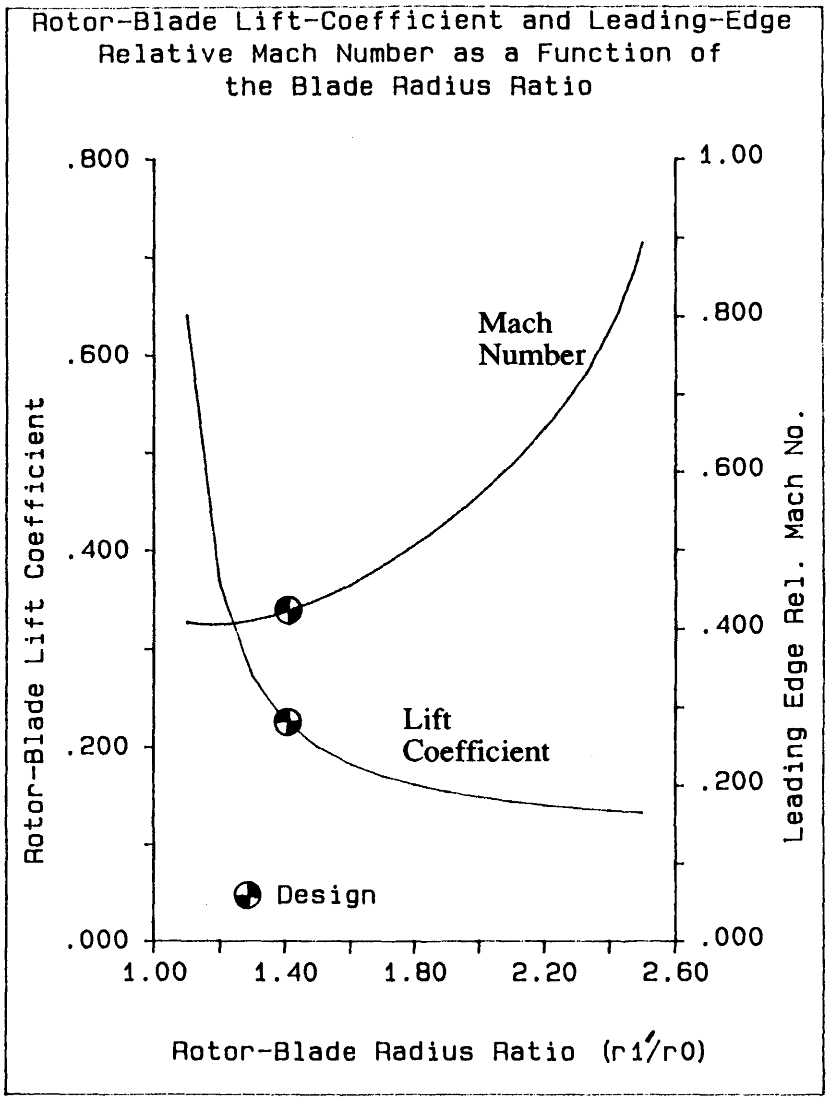

Fig. 2.2 Rotor-Blade Loading and Rotor-Inlet Relative Mach Number as a Function of the Blade Radius-Ratio

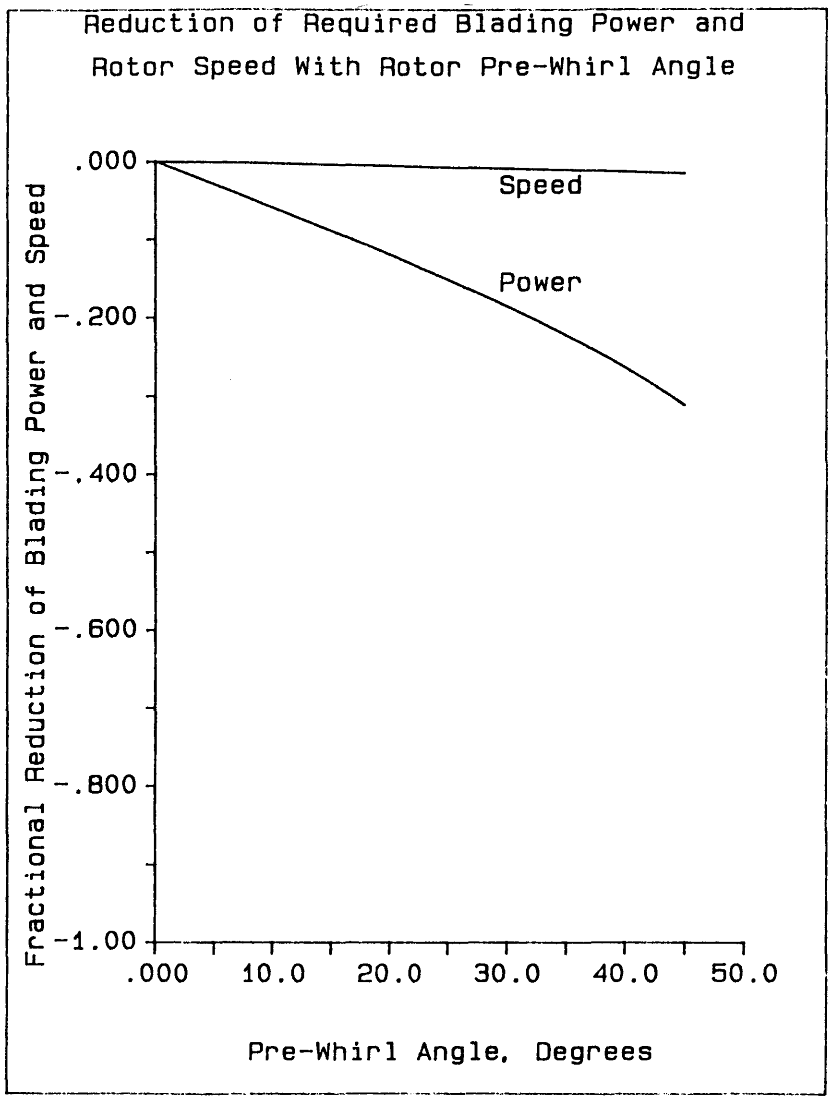

Fig. 2.3 Calculated Effect of Pre-Whirl on Required Blading Power and Rotor Speed

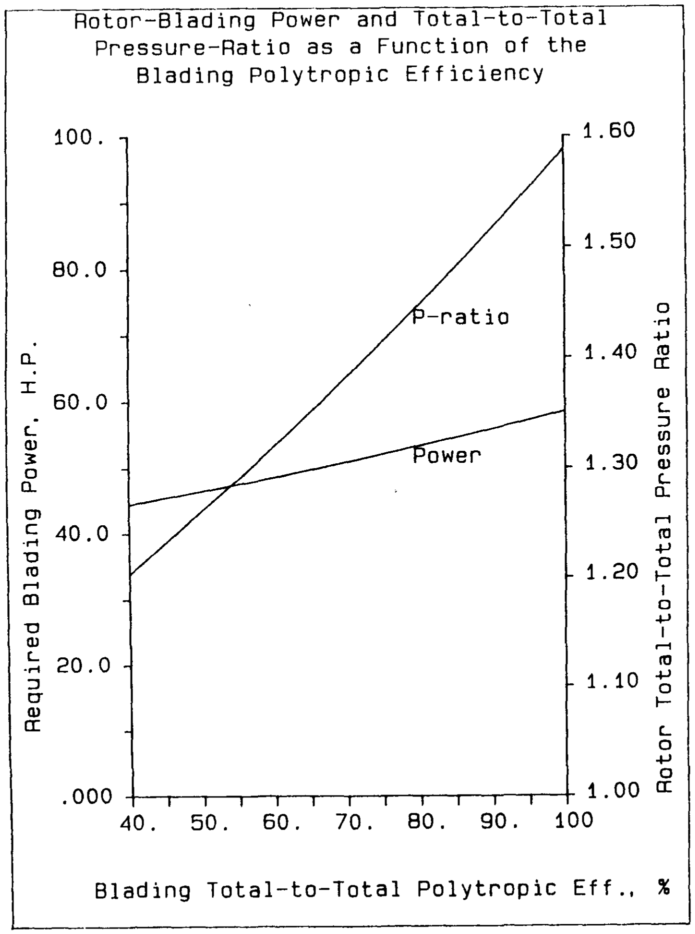

Fig. 2.4a Rotor-Blading Power and Total-Pressure-Ratio as a Function of the Rotor Total-to-Total Polytropic Efficiency

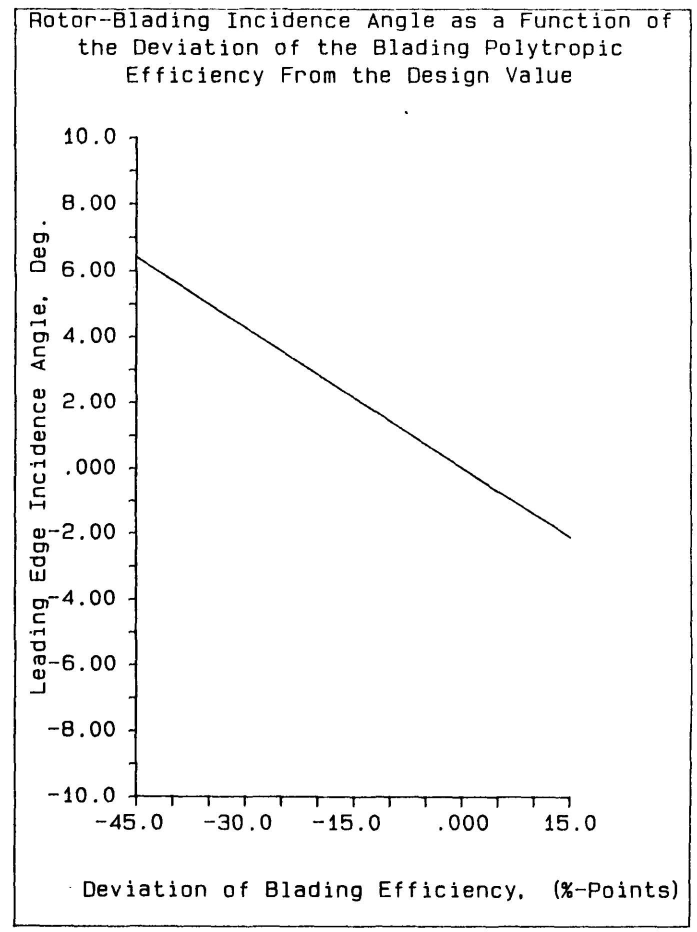

Fig. 2.4b Rotor Incidence Angle as a Function of Deviation of Rotor Efficiency From the Assumed Value

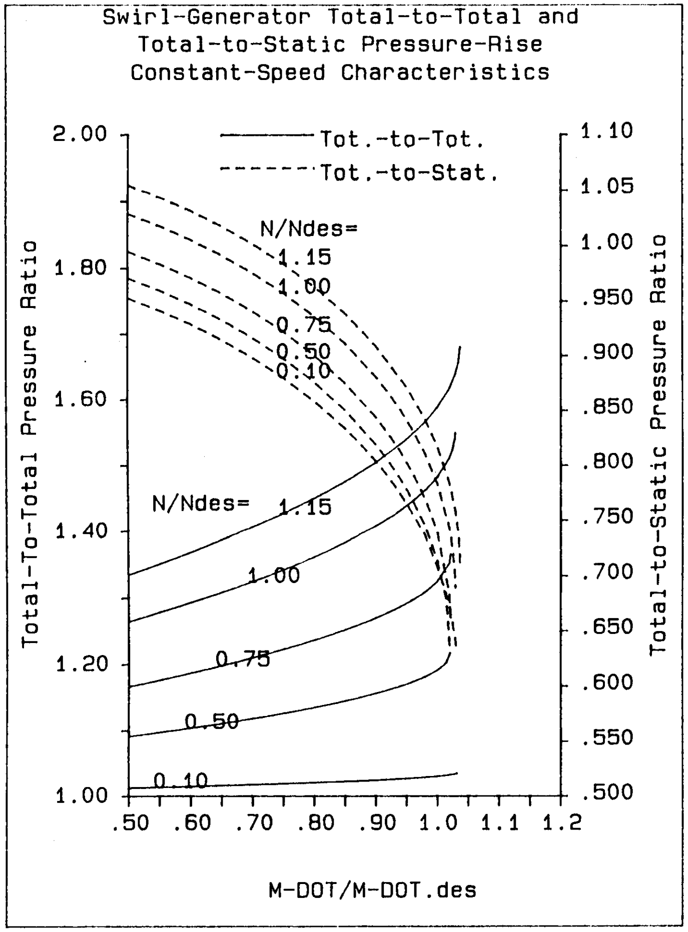

Fig. 2.5a Calculated Swirl-Generator Total-to-Total and Total-to-Static Pressure-Rise v.s. Mass Flow-Rate Characteristics

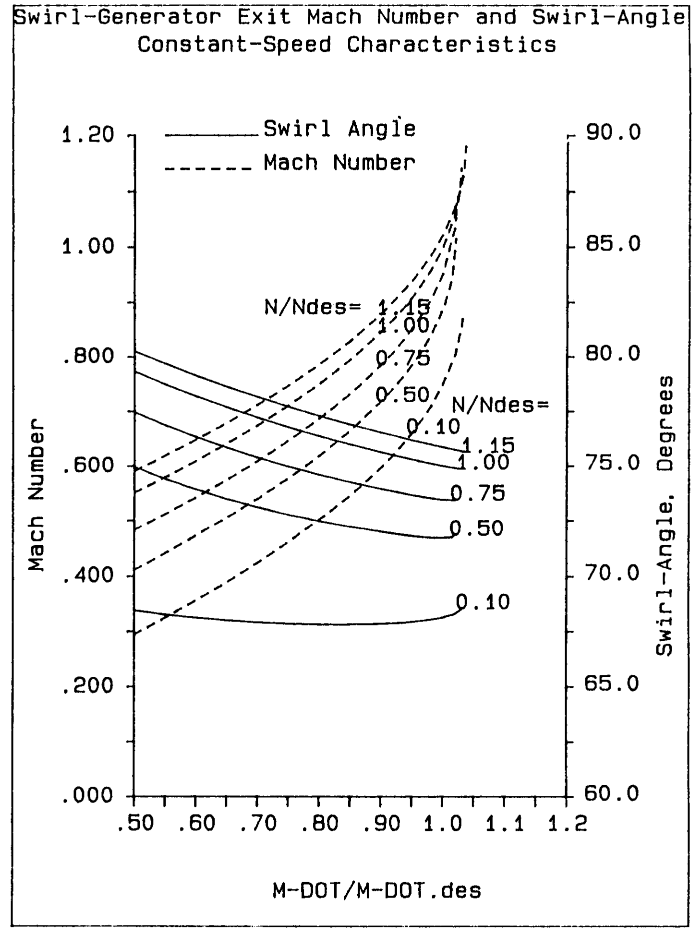

Fig. 2.5b Calculated Swirl-Generator Exit Mach-Number and Swirl Angle vs. Mass Flow-Rate Characteristics

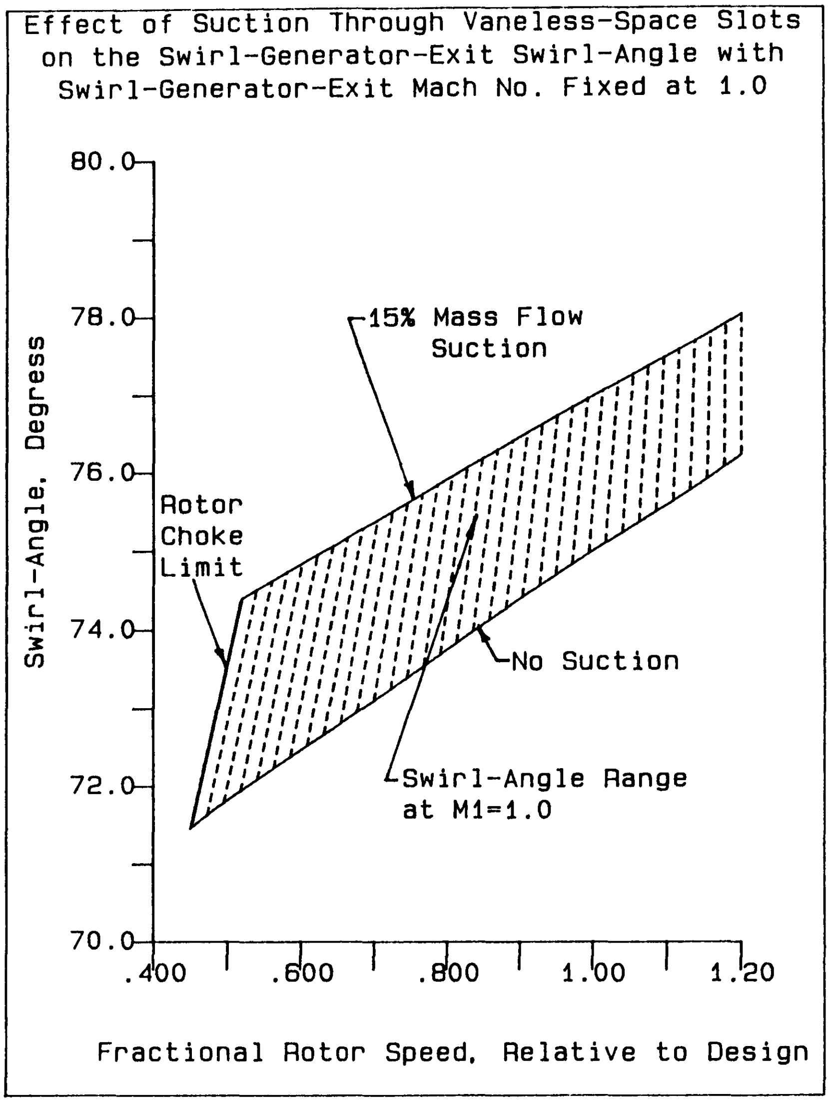

Fig. 2.6 Calculated Effect of Suction Through Vaneless Space Slots on the Swirl-Generator Exit Swirl Angle

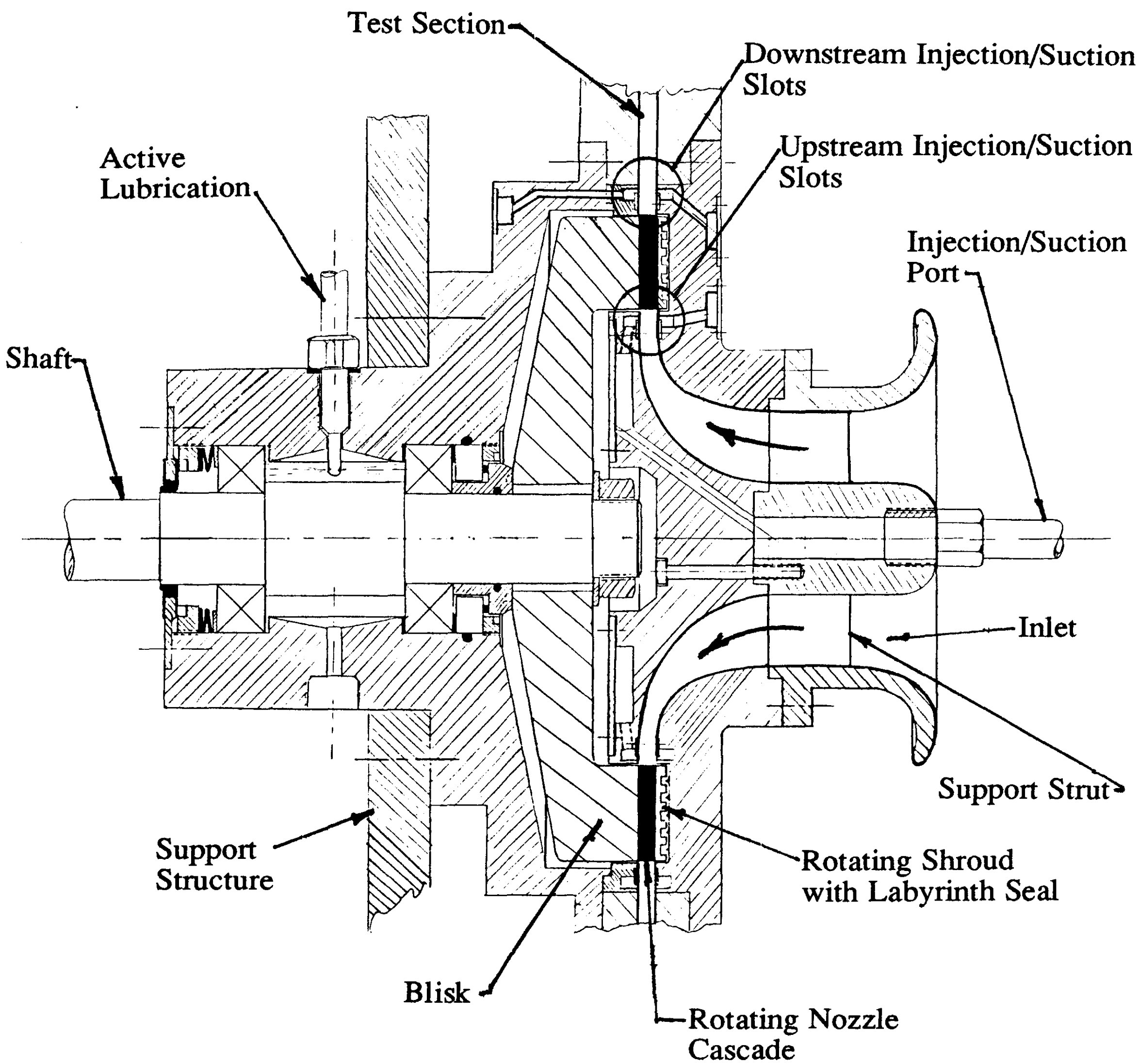

Fig. 2.7 Swirl Generator Mechanical-Concept Schematic

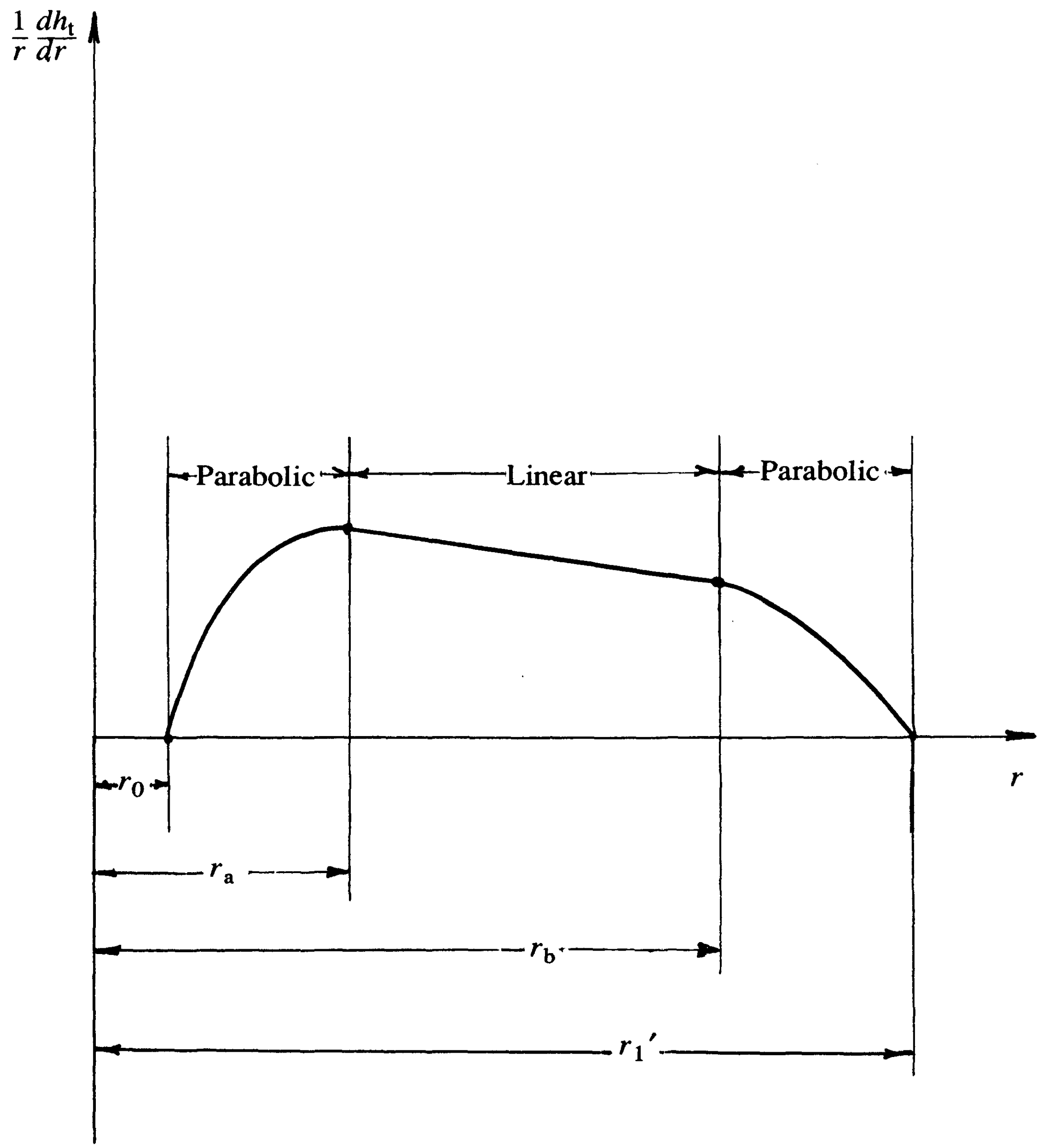

Fig. 2.8 Swirl Generator Blade Loading Specification Pattern

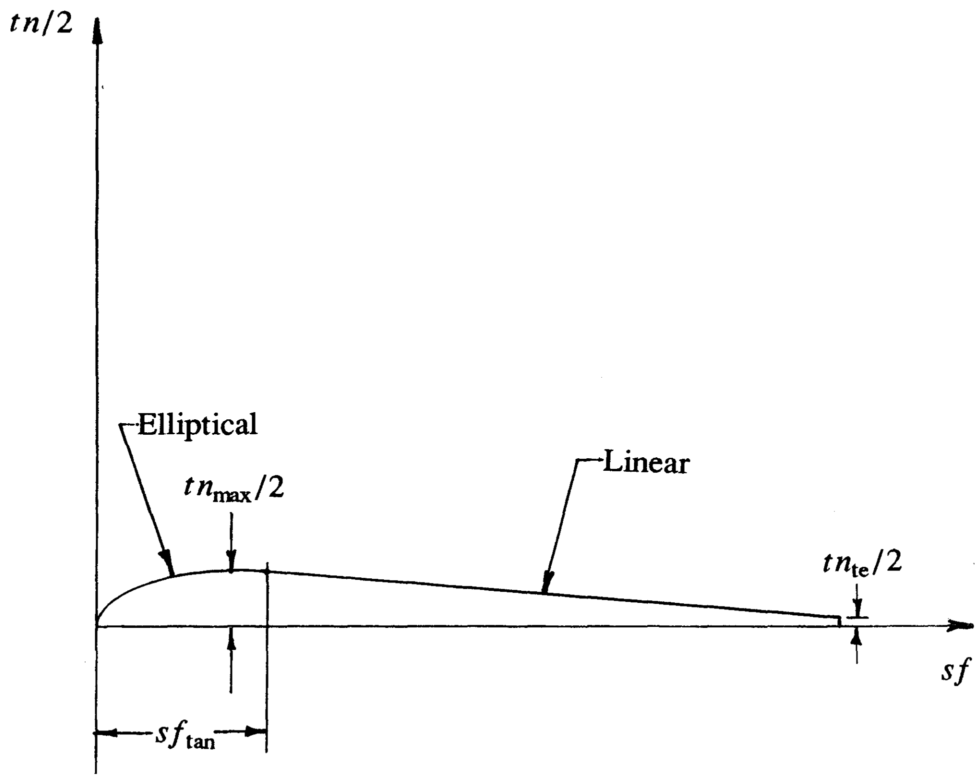

Fig. 2.9 Swirl Generator Blade Thickness Specification Pattern

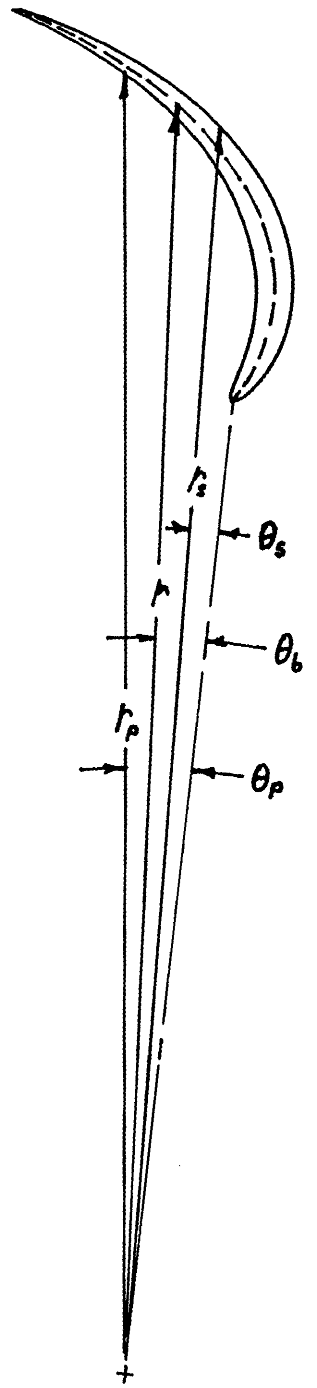

Fig. 2.10 Swirl Generator Blade Camber Line and Surface Definition Coordinates

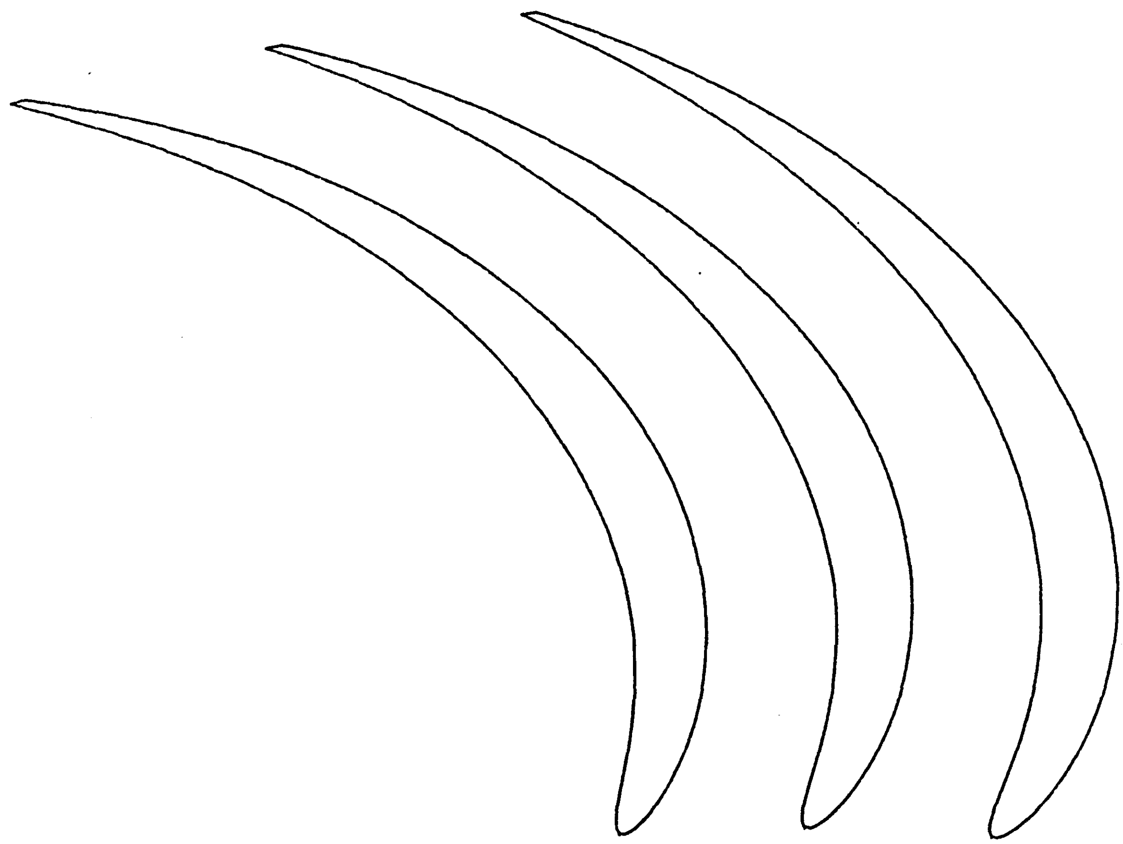

Fig. 2.11 Swirl Generator Blade Profile

Table 2.1- Swirl-Generator Blade Surface Coordinates

Pressure Surface		Suction Surface	
Radius (inches)	Wrap Angle (degrees)	Radius (inches)	Wrap Angle (degrees)
5.1948	.0000	5.1948	.0000
5.2071	.0680	5.1930	-.1525
5.2221	.0706	5.1988	-.3128
5.2289	.0626	5.2025	-.3807
5.2418	.0390	5.2105	-.5045
5.2541	.0099	5.2190	-.6176
5.2660	-.0219	5.2280	-.7232
5.2834	-.0719	5.2419	-.8710
5.3004	-.1230	5.2563	-1.0084
5.3169	-.1738	5.2709	-1.1371
5.3544	-.2869	5.2911	-1.2969
5.4011	-.4160	5.3378	-1.6133
5.4463	-.5240	5.3861	-1.8768
5.5054	-.6356	5.4519	-2.1559
5.5488	-.6951	5.5021	-2.3169
5.6060	-.7437	5.5699	-2.4731
5.6624	-.7580	5.6384	-2.5663
5.7184	-.7390	5.7074	-2.6002
5.7743	-.6875	5.7765	-2.5779
5.8302	-.6045	5.8457	-2.5028
5.8864	-.4908	5.9145	-2.3774
5.9430	-.3472	5.9830	-2.2047
6.0001	-.1742	6.0510	-1.9872
6.0578	.0276	6.1183	-1.7268
6.1309	.3194	6.2015	-1.3430
6.1904	.5846	6.2672	-.9897
6.2506	.8786	6.3320	-.5945
6.3117	1.2084	6.3959	-.1605
6.3734	1.5761	6.4592	.3077
6.4357	1.9816	6.5219	.8098
6.4987	2.4250	6.5840	1.3455
6.5622	2.9064	6.6455	1.9148
6.6263	3.4260	6.7065	2.5182
6.6908	3.9846	6.7670	3.1561
6.7395	4.4296	6.8121	3.6577
6.8049	5.0584	6.8718	4.3585
6.8542	5.5576	6.9163	4.9087
6.9038	6.0811	6.9605	5.4809
6.9536	6.6297	7.0044	6.0756
7.0037	7.2042	7.0481	6.6938
7.0541	7.8051	7.0916	7.3360
7.1047	8.4337	7.1348	8.0033
7.1386	8.8685	7.1634	8.4626
7.1726	9.3164	7.1920	8.9339
7.2238	10.0132	7.2346	9.6639
7.2581	10.4948	7.2628	10.1663
7.2753	10.7354	7.2769	10.4224

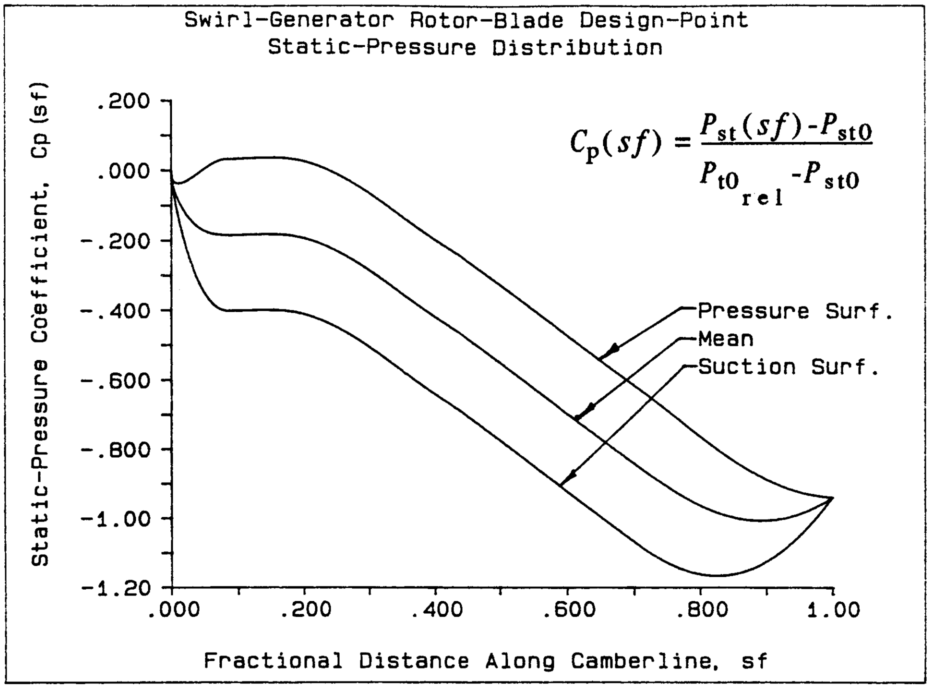

Fig. 2.12a Swirl Generator Blading Design-Point Calculated Static Pressure Distribution

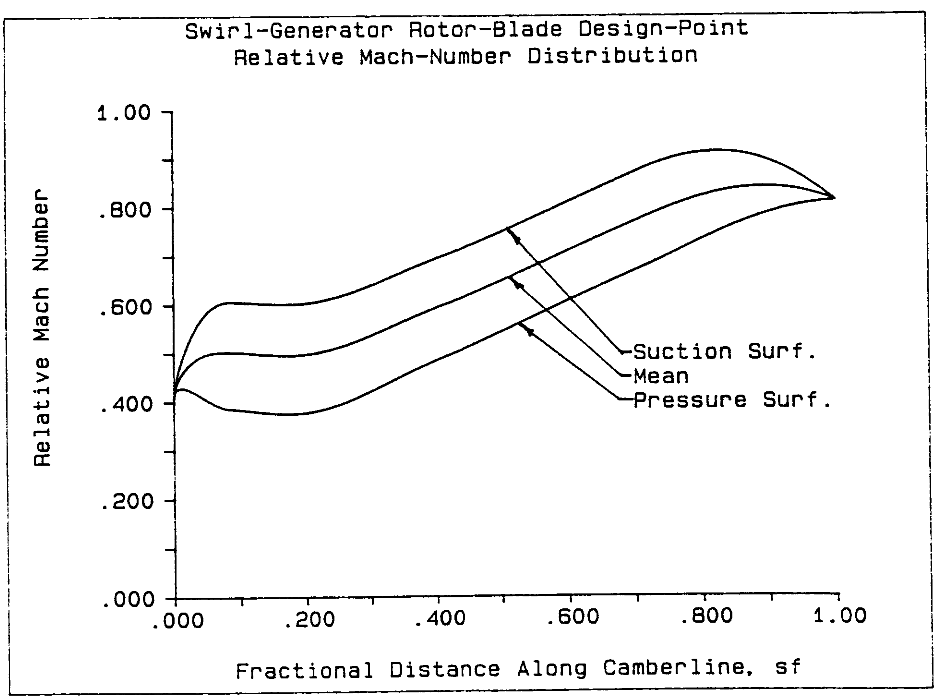

Fig. 2.12b Swirl Generator Blading Design-Point Relative Mach number Distribution

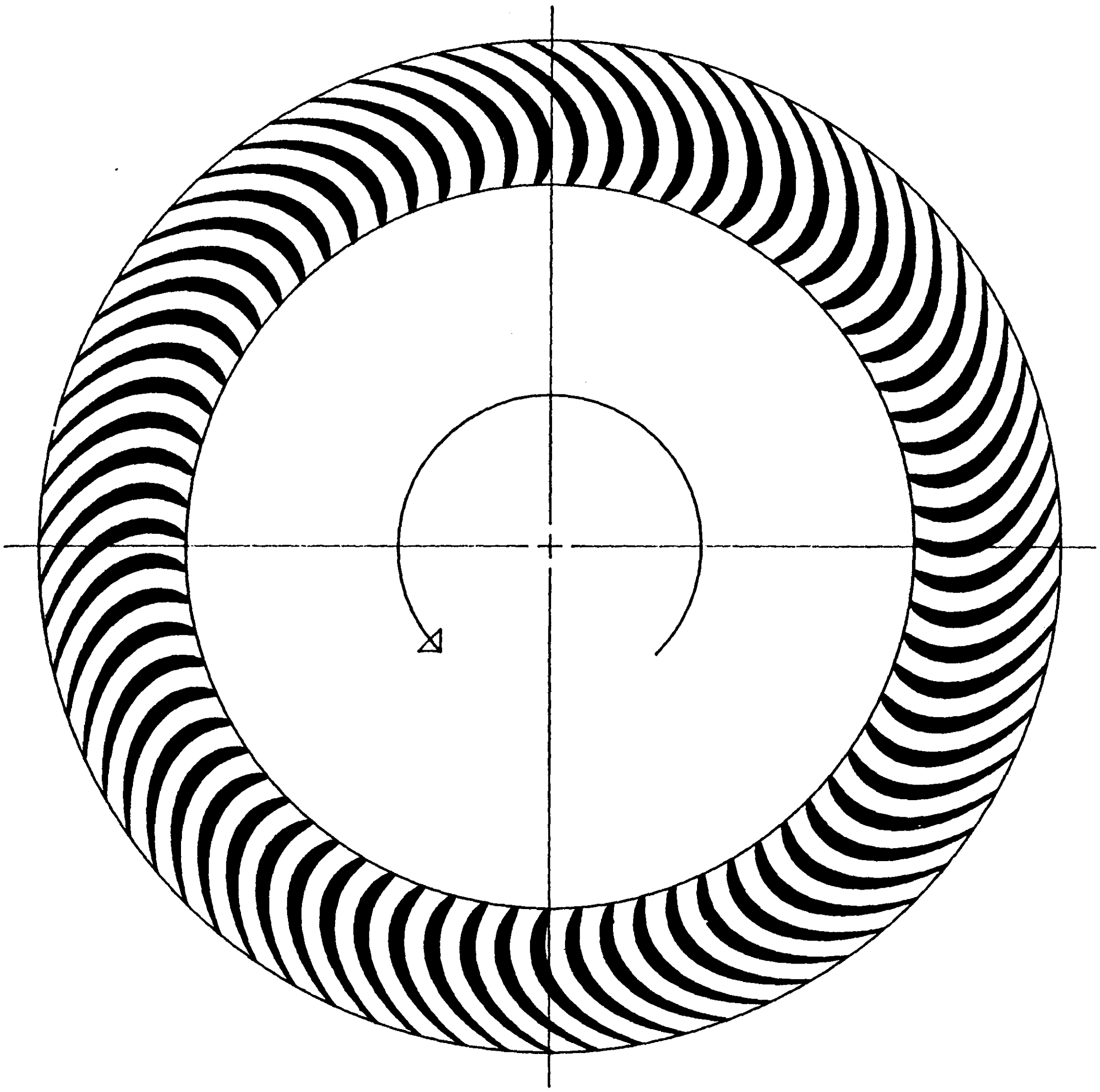

Fig. 2.13 Scale Diagram of Swirl Generator Blading Illustrating the High Blading-Solidity

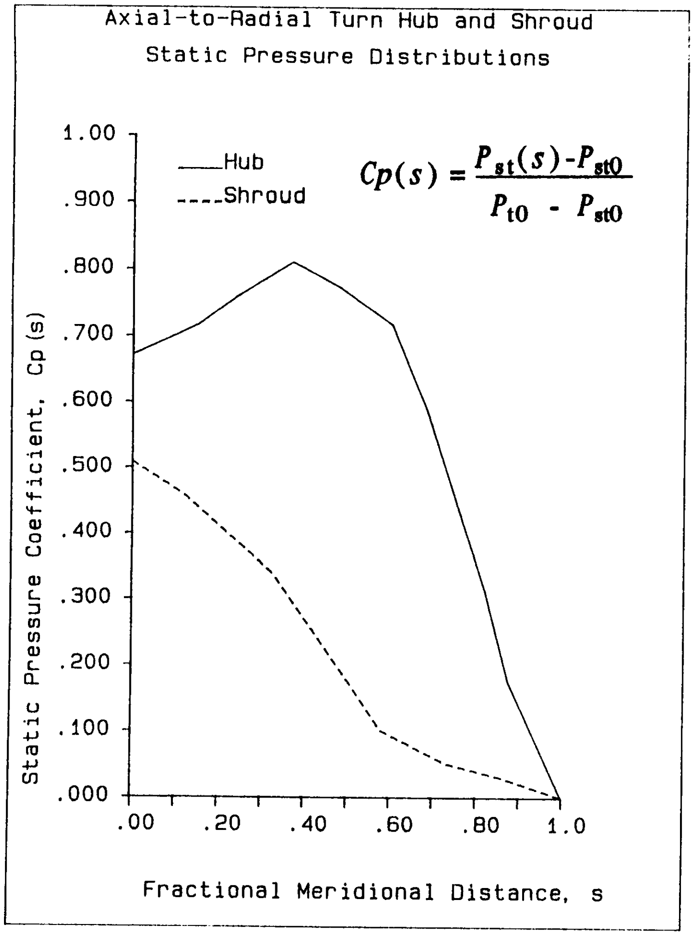

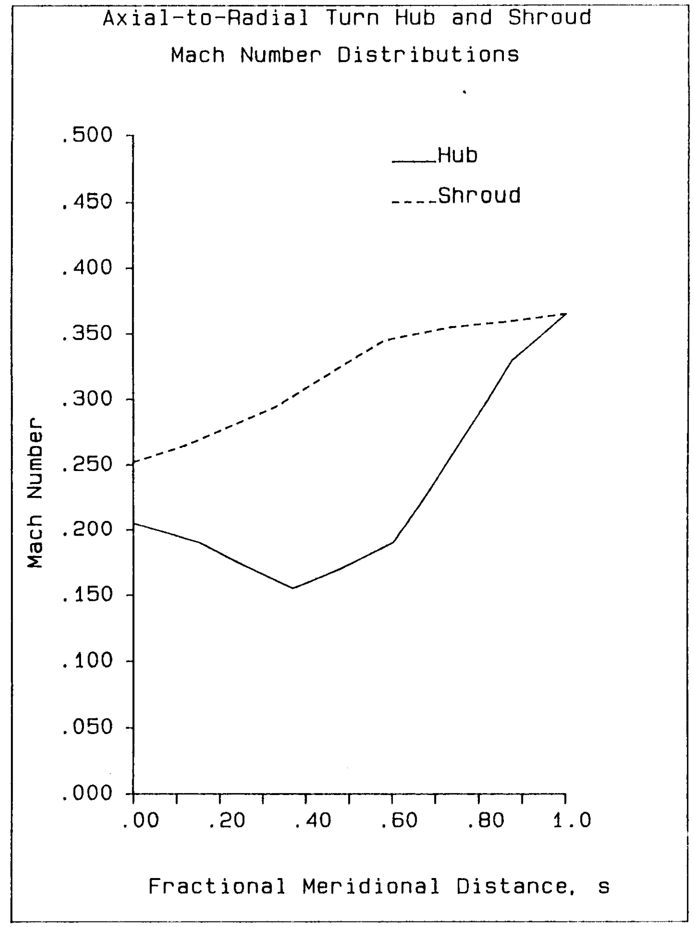

Fig. 2.14 Hub and Shroud Design-Point Static Pressure and Mach Number Distributions for the Axial-to-Radial Section of the Swirl Generator Inlet

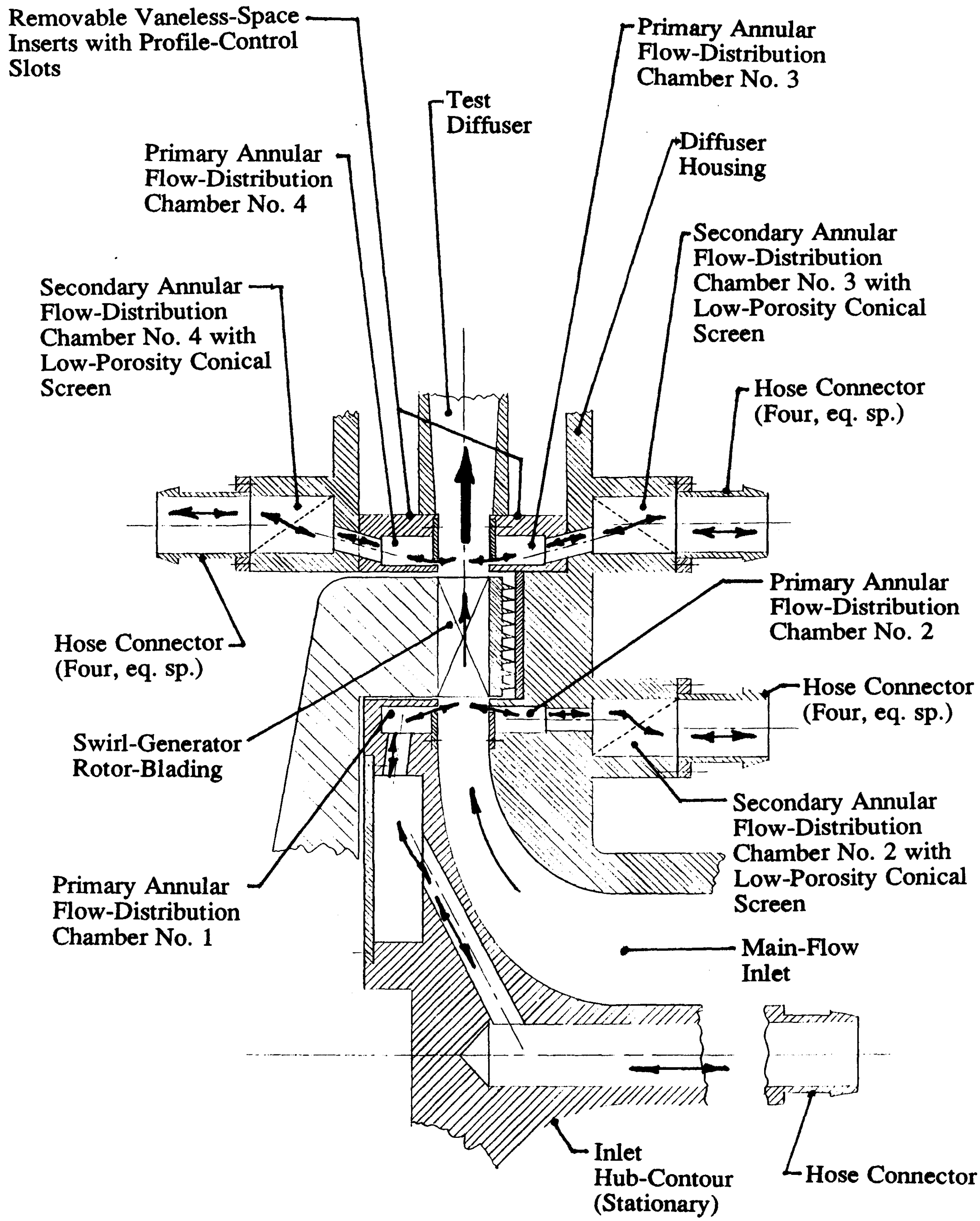

Fig. 2.15 Schematic of the Profile-Control-Slot Flow-Collection/Feed Chamber and Flow Passage Arrangement

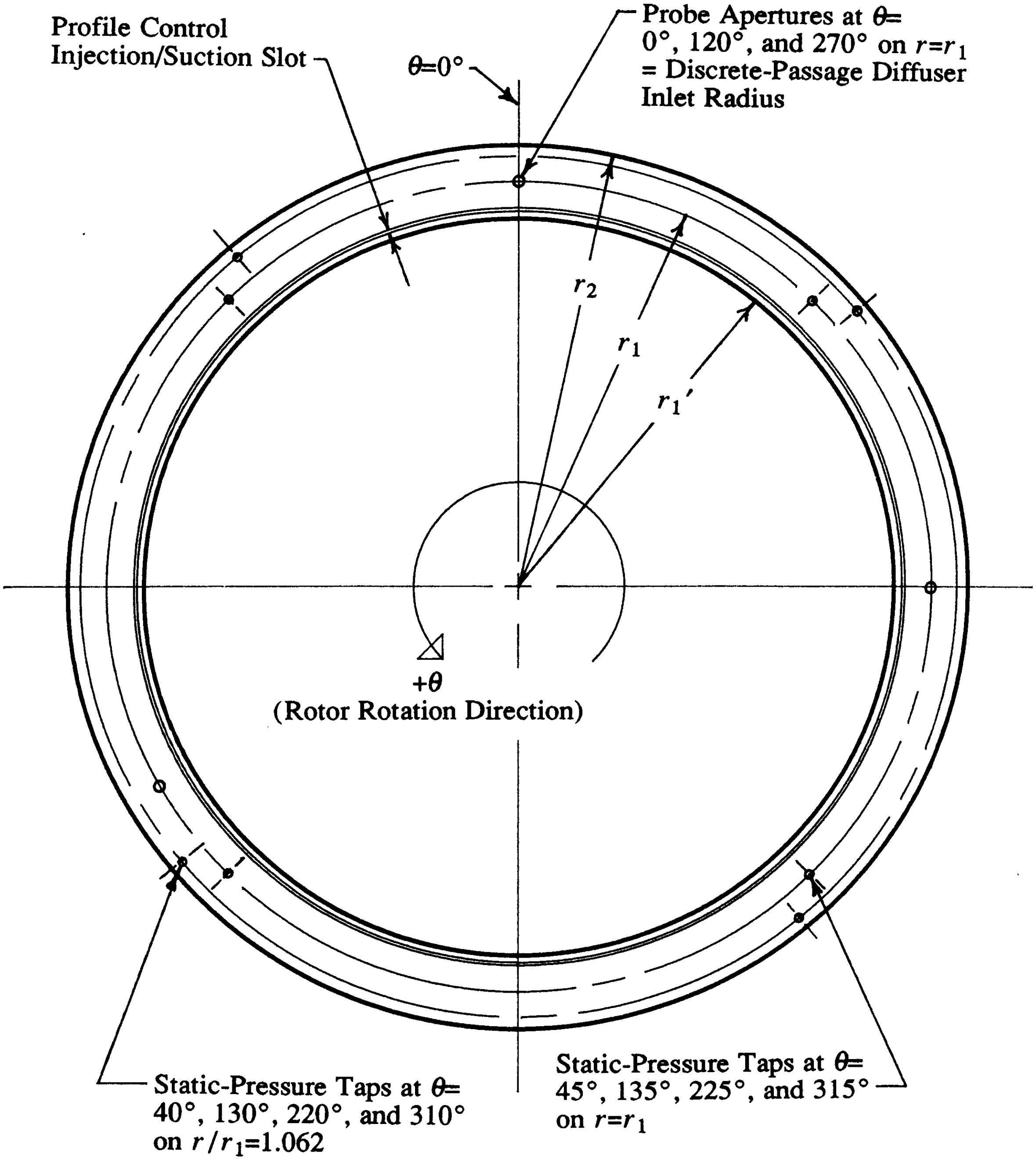

Fig. 2.16 Vaneless Diffuser Static Pressure-Tap and Probe-Aperture Locations

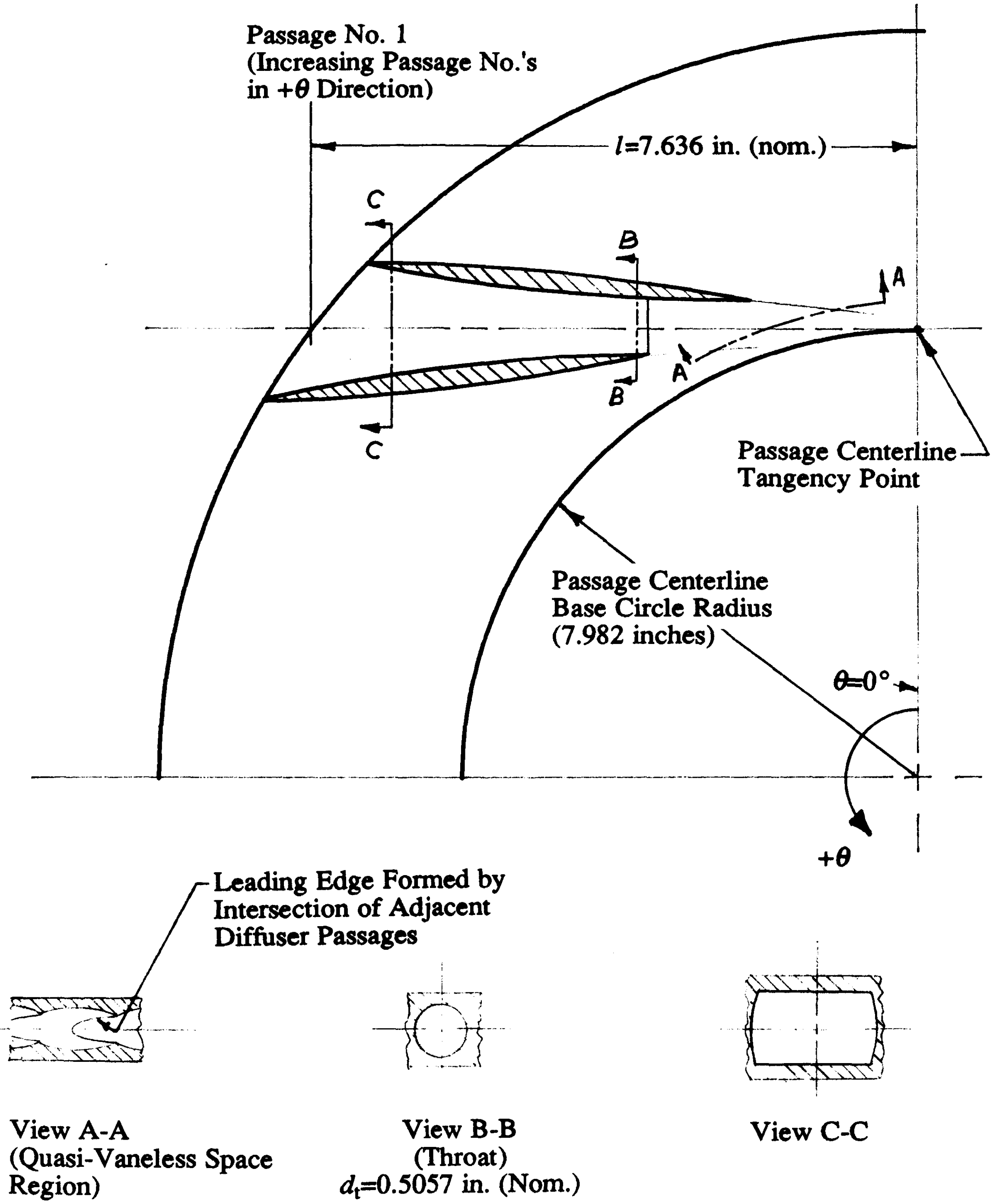

Diffuser Passage Throat-to-Exit Area Ratio = 4.29

Fig. 2.17 Discrete-Passage Diffuser Passage-Geometry Schematic

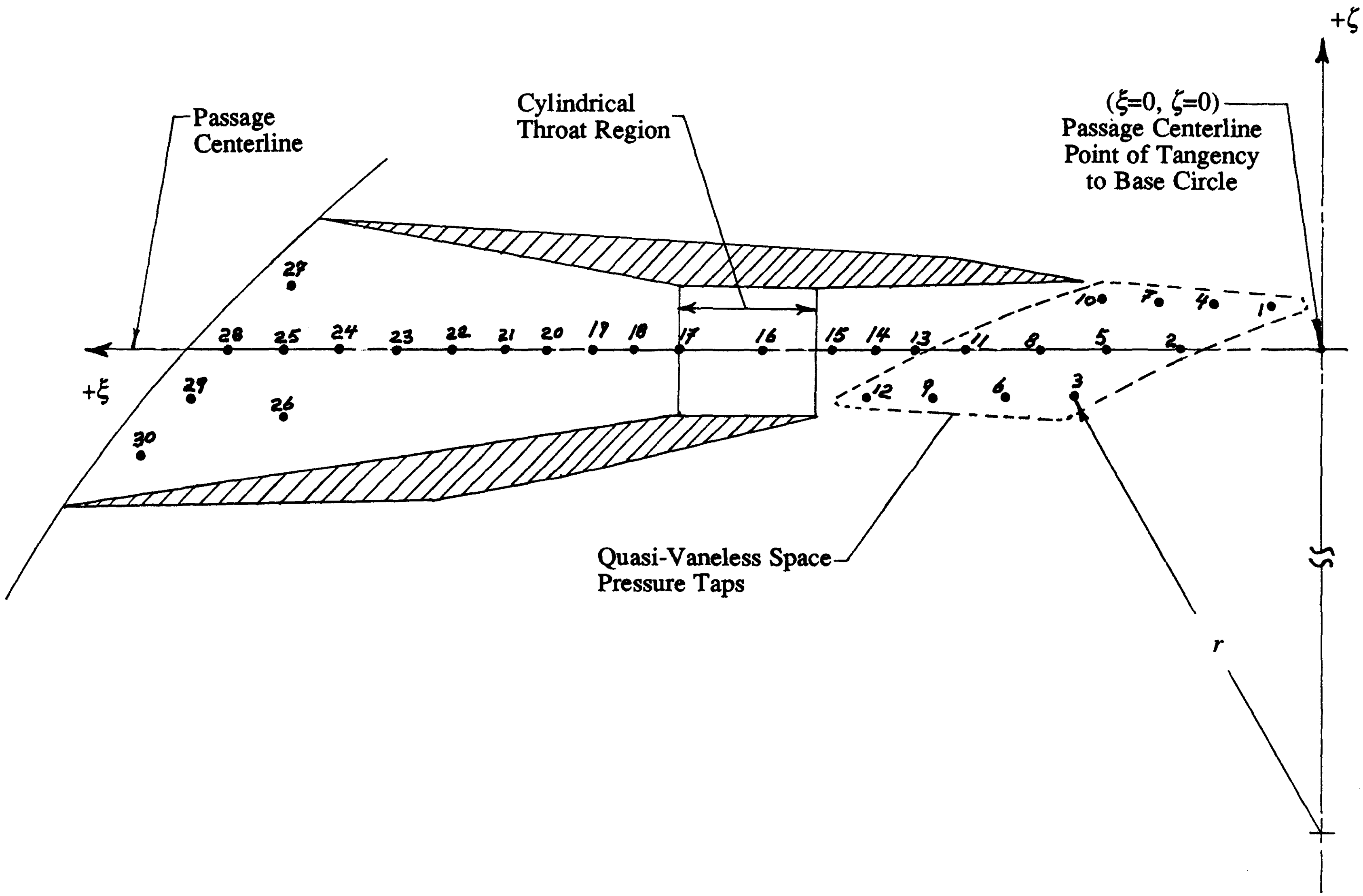

Fig. 2.18 Diffuser-Passage Static Pressure Tap Locations
(see table 2.3 for coordinates)

Table 2.2- Diffuser Passage Static Pressure-Tap Location Coordinates (see figure 2.18)

Tap Number	ξ (inches)	ζ (inches)	r (inches)
1	0.779	+0.059	8.079
2	1.250	0.0	8.079
3	1.659	-0.075	8.079
4	0.923	+0.086	8.121
5	1.498	0.0	8.121
6	1.892	-0.085	8.121
7	1.075	+0.117	8.170
8	1.745	0.0	8.170
9	2.134	-0.096	8.170
10	1.280	+0.145	8.227
11	1.993	0.0	8.227
12	2.450	-0.128	8.227
13	2.240	0.0	
14	2.512	0.0	
15	2.785	0.0	
16	3.058	0.0	
17	3.211	0.0	
18	3.697	0.0	
19	4.176	0.0	
20	4.654	0.0	
21	5.142	0.0	
22	5.621	0.0	
23	6.200	0.0	
24	6.717	0.0	
25	7.116	0.0	
26	7.116	-0.335	
27	7.116	+0.335	10.946
28	7.490	0.0	10.946
29	7.846	-0.350	10.946
30	8.172	-0.700	10.946

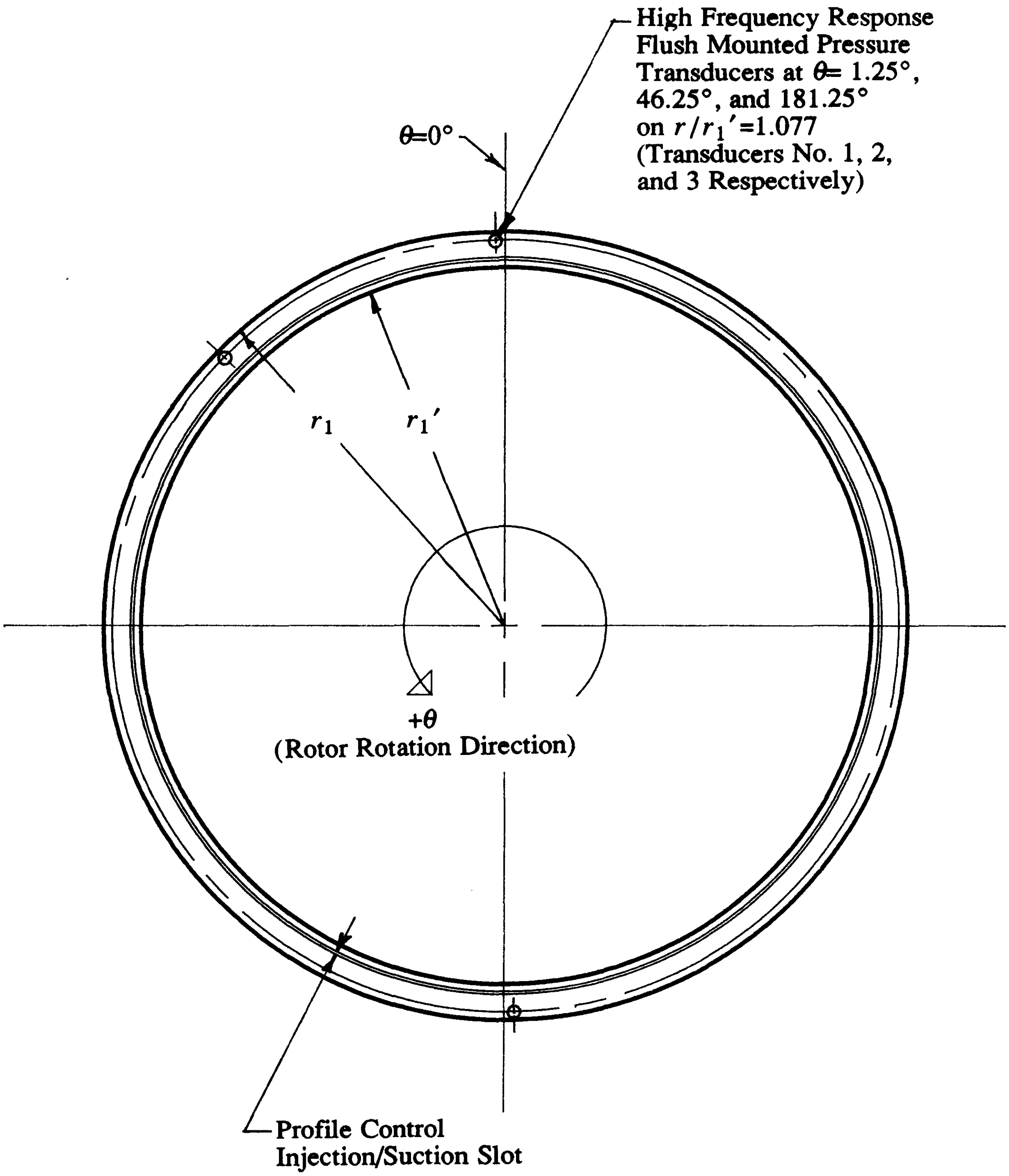

Fig. 2.19 High Frequency Response Pressure Transducer Locations in the Vaneless Space

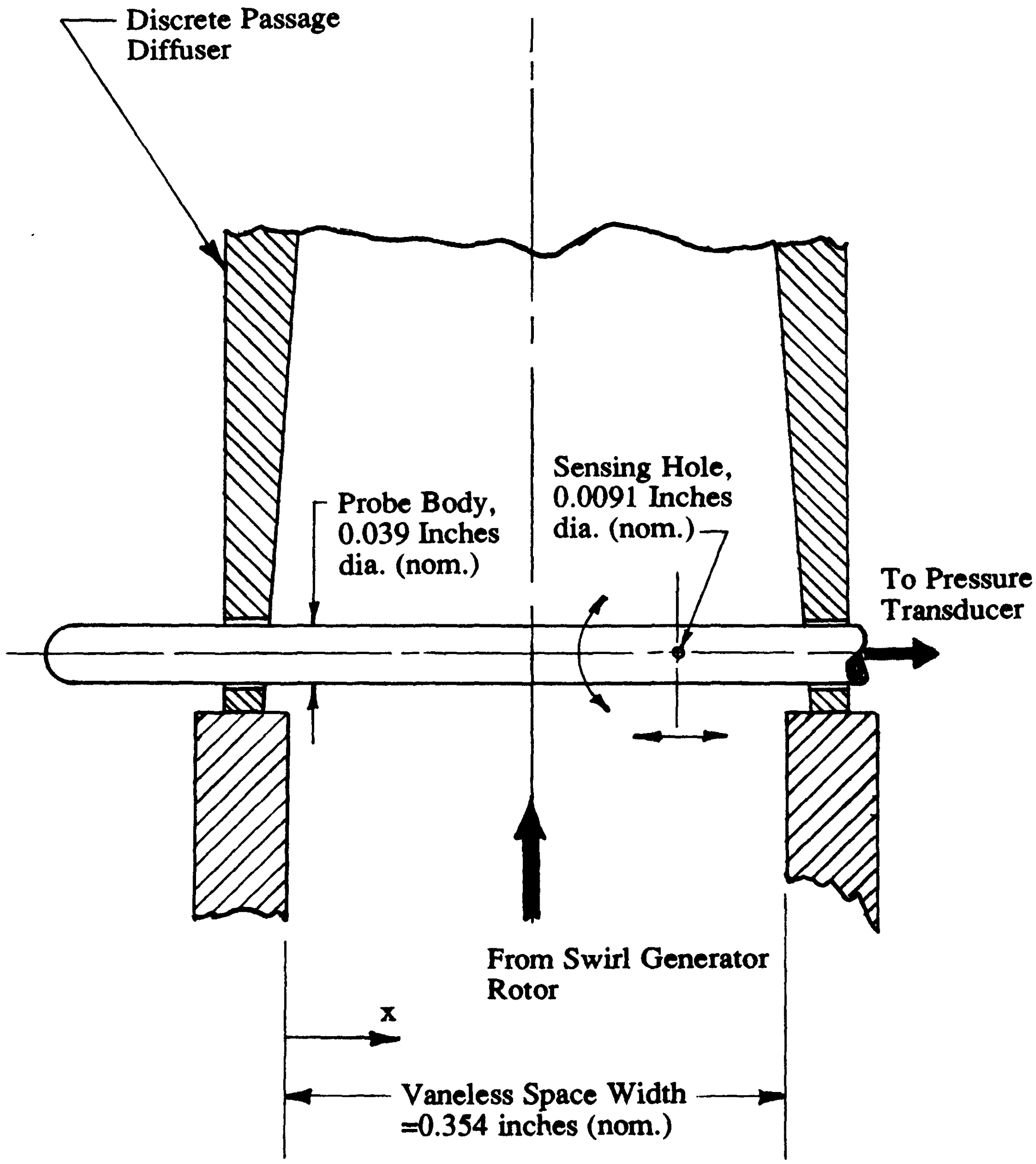

Fig. 2.20 Schematic Diagram of the *P*-Total/Flow-Angle Probe

Table 2.3- Diffuser Housing Probe-Port Circumferential Locations*

Port Number	Circumferential Position (Deg.)**
1	0.0
2	38.0
3	76.0
4	114.0
5	120.0
6	150.0
7	180.0
8	210.0
9	240.0
10	270.0
11	284.0
12	322.0

* Two ports at each circumferential position, one upstream of the test diffuser at $r = 8.001$ inches, and one downstream of the diffuser at $r = 11.200$ inches (24 ports total).

** Positive in direction of rotor rotation

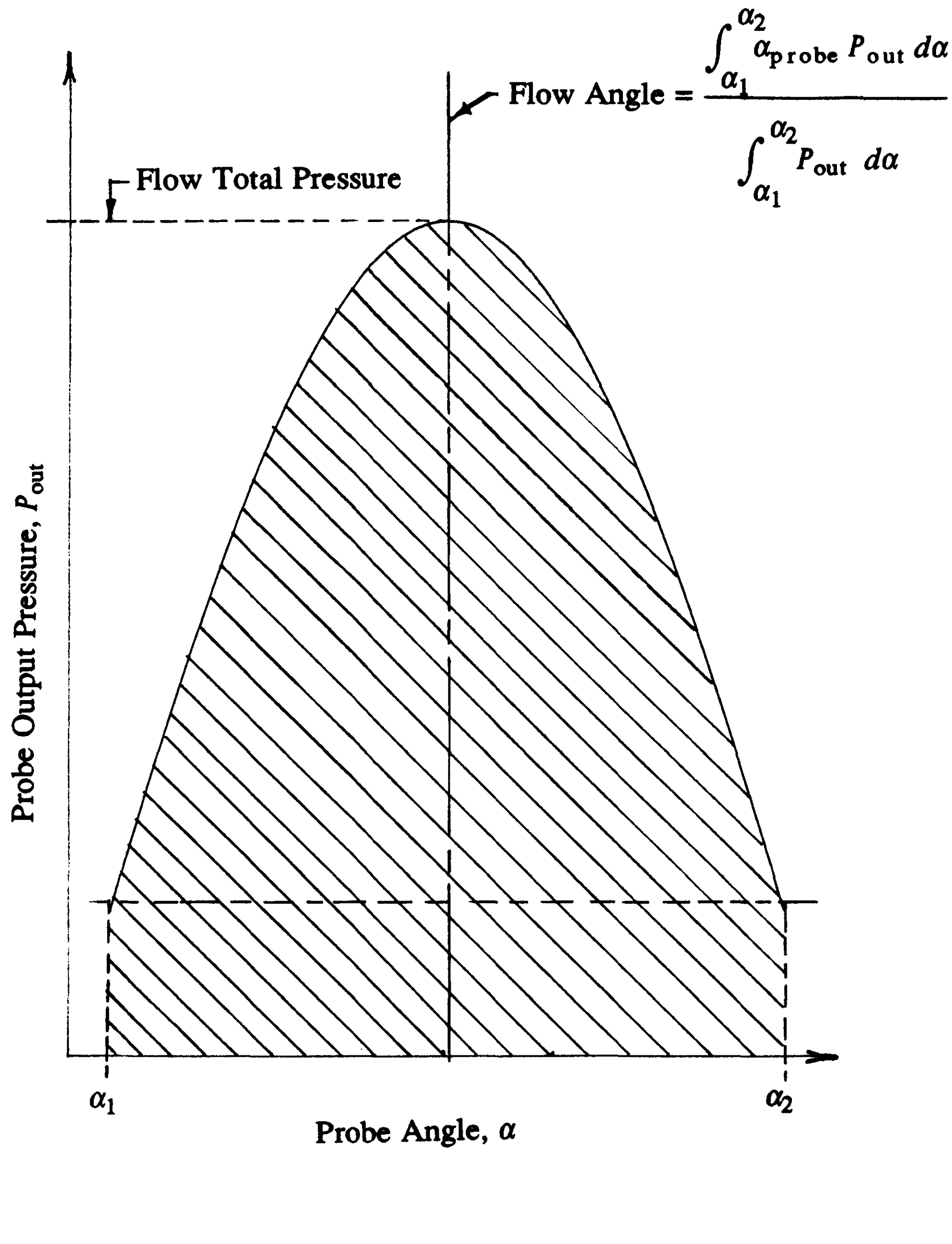

Fig. 2.21 Determination of Flow Angle From the P-total/Flow-Angle Probe Data

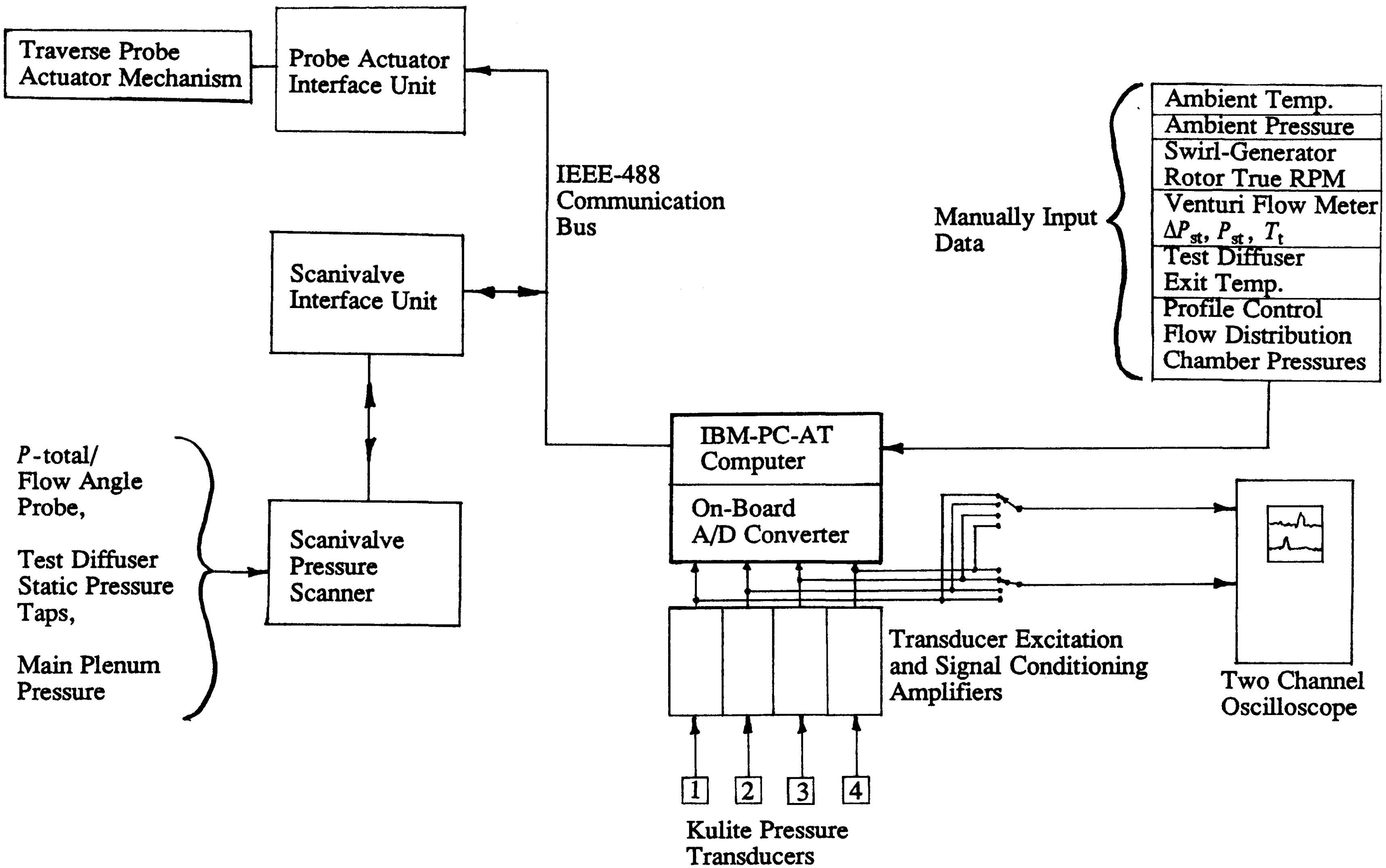

Fig. 2.22 Data Acquisition System Schematic

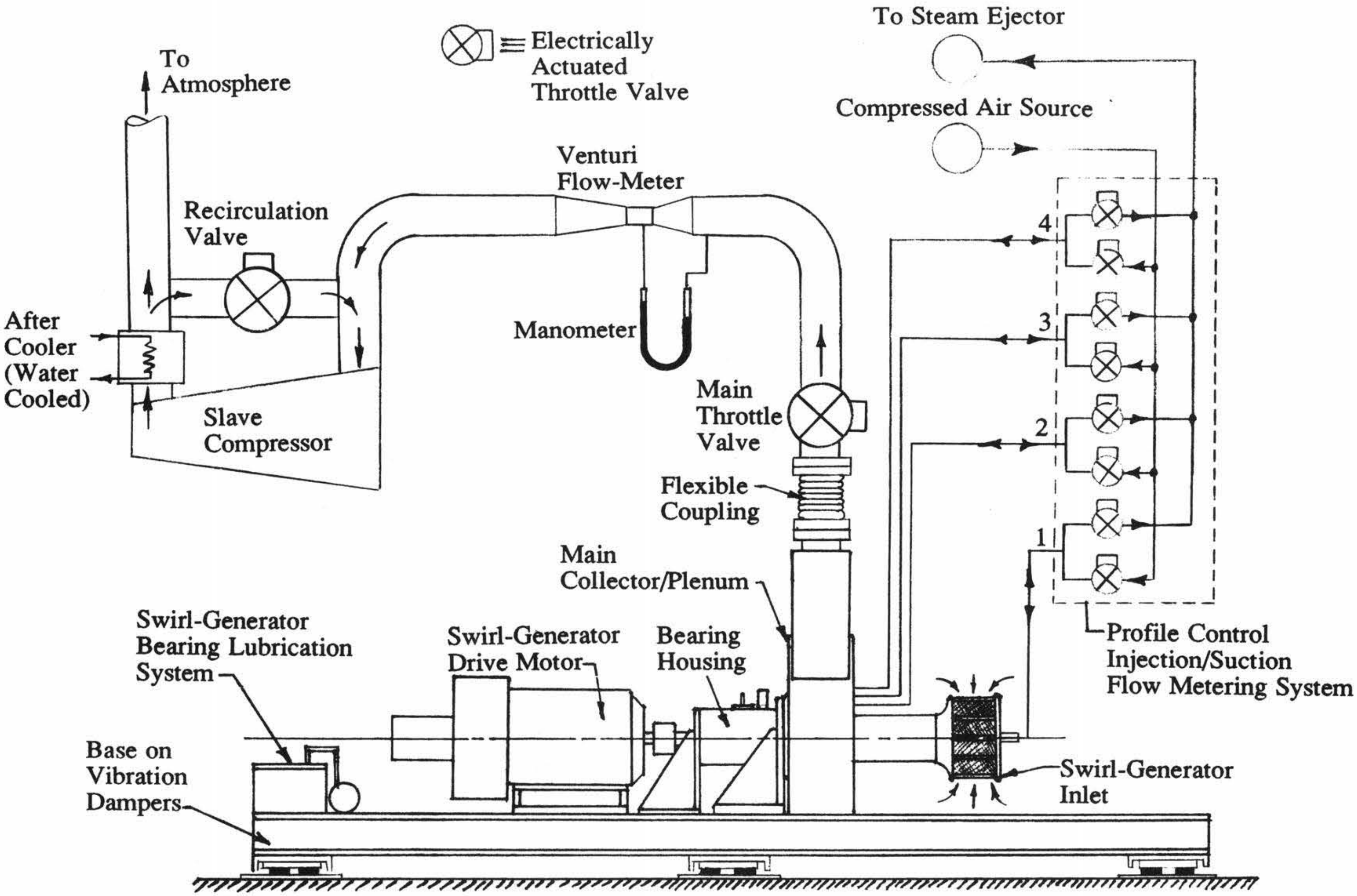

Fig. 2.23 Swirl-Generator/Diffuser-Test-Section Assembly and Flow-System Schematic

CHAPTER 3

FACILITY PERFORMANCE VERIFICATION WITH VANELESS DIFFUSER

3.1 Facility Performance Verification Configuration

The initial build of the swirl-generator was without the discrete-passage diffuser, but with a vaneless diffuser with a radius ratio 1.20. This allowed for measurement of the performance of the swirl generator alone (see section 2.4.1 for a description of the vaneless diffuser).

As described in section 2.4.1 and shown in figure 2.16, the vaneless diffuser was provided with circumferentially-distributed static pressure taps and axial-traverse probe apertures, the radial position of which corresponds to the discrete-passage diffuser inlet radius. This provides a means for measuring the swirl-generator exit flow field parameters that would be seen by the discrete-passage diffuser. The elements forming the vaneless diffuser are also provided with the profile control slot-system as described in section 2.2.4. (When the discrete-passage diffuser is mounted, elements forming a vaneless space with a radius ratio of 1.10 replace the 1.20 radius ratio vaneless-diffuser elements as described in section 2.4.2. The 1.10 radius-ratio vaneless space elements have profile-control slot systems which are identical, to within manufacturing tolerances, to those in the 1.20 radius ratio diffuser elements.)

The swirl-generator performance verification tests with the vaneless diffuser are described in the following sections.

3.2 Swirl-Generator Pressure-Ratio v.s. Flow-Rate Characteristics

With the vaneless diffuser mounted in the test section as described above, the constant-speed, steady-state pressure-ratio-v.s.-flow characteristics of the swirl generator were determined to establish the basic operating envelope of the machine.

Since the discrete passage diffuser inlet radius corresponds to the 1.10 radius ratio location relative to the swirl-generator rotor exit radius, the "swirl generator" is defined as the entire flow-system upstream of this location. Accordingly, the total-to-static pressure ratio of the swirl generator is defined as:

$$\Pi_{ts1} \equiv \frac{P_{st1}}{P_{amb}} \qquad 3.1$$

where P_{st1} is the absolute static pressure at the 1.10 radius ratio location downstream of the rotor and P_{amb} is the ambient pressure.

The flow through the swirl generator was expressed conventionally as a corrected mass flow rate:

$$\dot{m}_{corr} \equiv \frac{\sqrt{\dfrac{T_{amb}}{T_{ref}}}}{\dfrac{P_{amb}}{P_{ref}}}\dot{m}_{actual} \qquad 3.2$$

where T_{ref} is a reference temperature and P_{ref} is a reference pressure. In the present experiments, standard sea-level values were used:

$$T_{ref} = 518.69\ °\mathrm{R} \quad \text{and} \quad P_{ref} = 14.6958\ \mathrm{psia}$$

Similarly, the swirl-generator rotor speed was corrected for ambient temperature:

$$N_{corr} \equiv \sqrt{\frac{T_{ref}}{T_{amb}}}\, N_{actual} \qquad 3.3$$

P_{st1} was taken as the mean value of the pressure readings from the four vaneless diffuser static taps at r_1 (see figure 2.16 for tap locations):

$$\bar{P}_{st1} = \frac{1}{4}\sum_{n=1}^{4} P_{st1_n} \qquad 3.4$$

The individual pressures, P_{st1_n}, were measured using the Scanivalve-mounted Druck pressure transducer described in section 2.5.2 and the mass flow rate through the swirl generator was determined by means of the venturi flow meter as discussed in appendix H. Figure 3.1 shows the resulting experimentally determined swirl-generator pressure-ratio v.s. flow-rate constant-speed characteristics for several rotor corrected speeds in the range of zero to 6200 RPM.

The maximum flow through the swirl generator as shown in figure 3.1 is limited by the choking of the rotor blading. A minimum flow-rate limit (with the vaneless diffuser mounted) was not absolutely established as there was no positive indication of any flow instability and the accuracy of the flow-meter, as discussed in appendix H, is uncertain below ≈29% of the swirl-generator maximum (choke) flow rate of ≈2.2 lbm/sec. As can be seen from figure 3.1 however, the 6200 RPM corrected speed pressure rise characteristic shows a rising pressure ratio with decrease in flow rate and negligible scatter down to at least ≈45% of the maximum corrected flow of 2.2 lbm/sec and the range at lower speeds is at least as wide. This covers the entire stable flow range of the discrete-passage diffuser as will be discussed in chapter 4.

The atmosphere-to-plenum pressure ratio was used as an operating point reference for some of the data presented in sections 3.3 and 3.4. For reference, figure 3.2 shows the experimentally-determined atmosphere-to-plenum pressure-ratio (with the vaneless diffuser) v.s. corrected-mass-flow constant speed characteristics corresponding to the total-to-static, atmosphere to swirl-generator-exit ($r = r_1$) characteristics presented in figure 3.1.

3.3 Swirl-Generator-Exit Mach Number and Swirl-Angle Traverse-Data

The swirl generator exit Mach number and swirl-angle axial profiles were measured over a range of steady-state operating points to verify that the performance of the machine, including the profile-control system, meets the design requirements discussed in chapter 1.

A single-hole cylindrical total-pressure/angle probe was used to axially-traverse the swirl-generator exit to obtain the axial distributions of total pressure and swirl-angle as described in section 2.5.1. Assuming negligible streamline curvature in the meridional plane at the traverse location, the axial distribution of the static pressure is uniform and can be determined by means of static pressure wall-taps in the vaneless diffuser at the traverse radius. The Mach number axial profile can be calculated from the total-pressure distribution data using the basic compressible flow function:

$$M_1(x) = \left[\frac{2}{\gamma-1}\right]^{\frac{1}{2}} \left[\left[\frac{P_{t1}(x)}{P_{st\,1}}\right]^{\frac{\gamma-1}{\gamma}} - 1\right]^{\frac{1}{2}} \qquad 3.5$$

where P_{st1} is determined according to equation 3.4.

Similarly, assuming a uniform total temperature, measured by means of a thermocouple positioned at the exit of the diffuser at an axial location of $x=b/2$ as described in section 2.5.4, the static temperature distribution at the swirl-generator exit is calculated:

$$T_{st1}(x) = T_{t1}\left[1 + \frac{\gamma-1}{2}M_1^2(x)\right]^{-1} \qquad 3.6$$

where $M_1(x)$ is obtained from equation 3.5.

As will be shown in section 3.3.3, the agreement between the mass flow rate through the diffuser as determined by the venturi flow meter and by integration of the flow-field axial-traverse data at the swirl-generator exit was within 5%. This supports the basic assumptions described above.

For each axial traverse of the swirl-generator exit, the swirl angle and total pressure were measured at fifteen axially-distributed points, as a compromise between spatial resolution and measurement time. Since the gradients of the flow-field parameters are larger near the diffuser walls than near the center plane of the diffuser, closer spacing was used near the walls. This was accomplished using a power-law biasing scheme as follows:

Starting the axial traverse at a specified axial location x_a and ending the traverse at a specified location x_b, the intermediate measurement-point locations x_i are given by:

$$x_i = x_a + x_i' \left[\frac{x_i'}{(x_a-x_b)/2}\right]^n, \quad \text{for } x_i \leq (x_a-x_b)/2 \qquad 3.7$$

$$x_i = x_b - (x_b-x_i')\left[\frac{x_b-x_i'}{(x_a-x_b)/2}\right]^n, \quad \text{for } x_i > (x_a-x_b)/2 \qquad 3.8$$

where x_i' are the axial positions for equally-spaced measurement-points between x_a and x_b and n is a constant selected to be 0.40.

3.3.1 Swirl-Generator Mach Number and Swirl-Angle Axial Distributions Without Profile Control.

The swirl-generator exit (discrete-passage diffuser inlet) flow-field is established by setting six basic independent operating parameters: the swirl generator rotor speed, the swirl-generator flow-rate, and the pressures in the four injection/suction profile control flow-distribution chambers as described in section 2.3.4. This section shows the dependence of the swirl-generator exit Mach-number and swirl-angle axial-profiles on the swirl-generator flow-rate and rotor speed, without slot injection or suction. The effect of injection/suction through the four profile control slots is discussed in section 3.3.2.

Axial distributions of the absolute and radial Mach numbers at the swirl-generator exit are shown in figure 3.3 for corrected swirl-generator-rotor speeds of 1000, 4000, and 6000 RPM. The swirl-generator speed and flow ranges represented in the data cover the operating envelope of the swirl-generator without profile control injection/suction used to obtain the discrete-passage diffuser performance data in chapter 5. Figure 3.4 shows the corresponding swirl angle range. The effect of rotor speed on the swirl-generator exit Mach number and swirl angle distributions at fixed atmosphere-to-plenum pressure ratio is shown in figure 3.5. It can be concluded from figures 3.3 through 3.5 that the basic design objective, swirl generator exit Mach number of up to 1.0 and swirl angle of up to 75°, has been met. The minimum swirl-angle attained is ≈66°. This is adequately close to the target value of 65°.

Definitions of "average" flow field parameters and means of quantifying the swirl-generator exit flow field distortion will be discussed in chapter 5. It can be seen qualitatively from figures 3.3 through 3.5 however that the swirl-generator exit flow field is fairly symmetrical at low rotor speeds but develops a slight asymmetry with an increase in rotor speed at the higher flow rates. It is believed that this is primarily due to labyrinth seal leakage; although secondary flow in the rotor inlet flow field may also contribute. As is shown in section 3.3.2, a substantial improvement in the symmetry of the swirl generator exit flow field was obtained by means of suction through the downstream profile control slot on the labyrinth-seal side of the vaneless diffuser (slot number 3).

3.3.2 Effect of Slot-Injection/Suction on the Swirl-Generator Flow-Field Axial Distortion

Given that each of the four profile-control slots can be used for either flow injection, suction, or neither (inactive), there are 81 possible combinations of "injection" "suction" or "inactive" for the four slots combined as a profile control system. In addition, the level of injection and suction through each of the four slots can be adjusted. Since the development of a complete operating map covering all of these combinations was impractical and it was not known how sensitive the discrete passage diffuser will be to changes in the profile, so only several combinations of injection and suction only were initially attempted.

One of the objectives of the present investigation was the determination of the baseline performance of the discrete passage diffuser with as uniform an inlet profile as possible. An attempt was thus made to improve the uniformity of the profiles shown in figure 3.3 by means of suction through the profile control slots upstream and downstream of the rotor blading. Suction through the slots upstream of the rotor blading had a negligible effect on the swirl generator exit flow field while suction through the downstream slots provided a significant improvement in the swirl generator exit flow field uniformity. The most severe non uniformity in the swirl generator exit flow field without profile control occurs at the highest speeds and flow rates as can be seen from figures 3.3 and 3.5. Figure 3.6 shows the improvement obtained in the uniformity of these Mach number and swirl angle profiles by means of suction through the downstream slots.

The improvement in uniformity shown in figure 3.6 is the best which was achieved. Increases in suction beyond the level used in figure 3.6 made the non-uniformity worse because the geometry of the present slots requires a rapid readjustment of the main flow in the vicinity of the slots at high suction flow rates, resulting in local separation.

Axially-asymmetric flow injection through the downstream slots proved effective in producing significant skew in the swirl generator exit flow field, particularly in the radial Mach number distribution as shown in figure 3.7. Axially-symmetric injection through the downstream slots also had a significant effect on the non-uniformity of the profiles as shown in figure 3.8. In all of these cases, the theoretical injection/suction mass flow rates as based on the injection/suction annular feed chamber pressures is at most 15% of the rotor through flow rates.

In addition to changing the shape of the swirl generator exit profiles, the injection or suction of flow through the downstream slots can be used to control the swirl generator exit flow angle independently of rotor speed. This can be seen in figure 3.6 for example, where the swirl angle increases due to suction. The reason for this is that the radial component of velocity at the swirl generator exit decreases relative to the case of no suction while the tangential component of velocity, neglecting viscous effects, remains unchanged. The net result is an increase in the flow angle. Similarly, mass flow injection through the downstream slots results in a decrease in the flow angle as seen in figure 3.8. In the case of cross-flow injection, the radial component of velocity must increase (to satisfy conservation of mass flow) while the tangential component of velocity remains the same outside of the mixing regions and decreases within the mixing regions due to the fact that the injected flow enters without angular momentum. The overall result is a decrease in the average flow angle.

Cross flow injection through the upstream profile control slots (slots 1 and 2) provided a minimal influence on the swirl generator exit profile as shown in figure 3.9. At 6000 RPM, a cross flow injection through slot 1 of ≈13% of the through flow with a Mach number ratio M_{inj}/M_{thru} of ≈1.87 produced only a minor change in the swirl generator exit profiles as can be seen by comparing profiles 1 and 2 in figure 3.9 where profiles 1 are without suction/injection. A more severe cross-flow injection through upstream slot 2 of ≈30% of the through flow with a Mach number ratio M_{inj}/M_{thru} of ≈4.11 produced a larger effect on the swirl generator exit profiles at 4000 RPM (profiles 3 and 4) but this effect is still relatively small as compared to the effect of cross-flow injection downstream of the rotor. It is believed that the reason for this is effective mixing of the flow within the very high solidity rotor blading.

As a result of these experiments, the effect upstream injection/suction was not investigated further. All tests of the discrete passage diffuser as discussed in chapter 4 relied on profile control by means of the downstream slots. Means of quantifying the axial distortion of the swirl-generator exit flow field are presented in chapter 5.

3.3.3 Mass Flow Continuity Verification

To evaluate the validity of the assumption of negligible streamline curvature in the meridional plane at the traverse location ($r = r_1$) and to establish the integrity of the traverse data, a comparison was made between mass flow rate as measured by means of the venturi flow meter and as calculated by integration across the swirl-generator exit:

$$\dot{m} = 2\pi r_1 \int_0^b \rho_{st1}(x) V_1(x) dx \qquad 3.9$$

As described in section 3.3, each axial traverse of the swirl-generator exit involves the measurement of the total-pressure and swirl angle at locations x_i, $i=1,2....,15$. The data, together with the no-slip condition at the diffuser walls: ($V=0$ at $x=0$ and at $x=b$), are used to approximate integral 3.9 as a summation:

$$\dot{m} \approx 2\pi r_1 \sum_{j=1}^{16} \left[\frac{\rho_{st}(x_j)V(x_j)\cos\alpha(x_j) + \rho_{st}(x_{j-1})V(x_{j-1})\cos\alpha(x_{j-1})}{2} \right]_{r=r1} (x_j - x_{j-1}) \qquad 3.10$$

Figure 3.10 shows a comparison between the mass flow rate as determined according to equation 3.10 with the mass flow rate determined by means of the venturi flow-meter for all of the operating points shown in figure 3.3 and for additional data obtained at corrected speeds of 2000, 3000, 5000, and 6200 RPM. As can be seen from figure 3.10, the agreement is consistently to within 5%. This is quite good considering that at a swirl angle of 75°, a ±0.50° error in the measurement of the swirl angle results in an error of ±3.3% in the calculated mass flow rate:

$$\frac{\delta\dot{m}}{\dot{m}} \approx -\tan\alpha\ \delta\alpha = -\tan 75° \times \mp 0.50\ \pi/180 = \pm 0.0325 \qquad 3.11$$

Agreement between the mass flow rate as determined by means of the venturi flow meter and by integration of the swirl generator exit flow field according to equation 3.10 was somewhat worse for the case of the distorted profiles of figure 3.7 with a maximum error of ≈6.5% as shown in figure 3.11. As is discussed in section 3.4 however, this is likely the result of non-uniform injection due to circumferential variations in the injection slot width and was corrected for the discrete passage diffuser tests by hand-finishing the slot width to a tolerance of ±0.0005 inches (2% of the nominal width).

3.3.4 Swirl-Generator Total-to-Total Pressure-Ratio Characteristics

The traverse data described above was used to obtain the total-to-total pressure ratio characteristics of the swirl generator, with the total-to-total pressure ratio defined as:

$$\Pi_{tt1} = \frac{\hat{P}_{t1}}{P_{amb}} \qquad 3.12$$

Here, $\hat{P}_{t1}$ is the mass averaged total pressure at the swirl generator exit $(r = r_1)$

defined as:

$$\hat{P}_{t1} = \frac{1}{\dot{m}}\int_0^b P_{t1}(x)\rho_{st1}(x)V_1(x)\cos\alpha_1(x)2\pi r_1 dx \qquad 3.13$$

The traverse data was used to calculate the mass averaged total pressure according to equation 3.13 by approximating the integral in 3.13 as a summation:

$$\hat{P}_{t1} \approx \frac{2\pi r_1}{\dot{m}}\sum_{j=1}^{16}\left[\frac{P_t(x_j)\rho_{st}(x_j)V_r(x_j) + P_t(x_{j-1})\rho_{st}(x_{j-1})V_r(x_{j-1})}{2}\right]_{r=r1}(x_j - x_{j-1}) \qquad 3.14$$

where $V_r = V\cos\alpha$. The resulting experimentally determined total-to-total pressure ratio v.s. flow rate constant speed characteristics of the swirl generator are shown in figure 3.12 for corrected speeds of 1000, 4000, and 6200 RPM.

As can be seen from figure 3.12, at 1000 RPM, where the flow is primarily driven by the downstream slave compressor, the swirl generator behaves like a nozzle with an increasing total pressure loss with increasing flow. At the highest speed of 6200 RPM, where the flow is driven primarily by the swirl generator rotor itself, the total pressure ratio increases with increasing flow rate as a result of the energy exchange v.s. flow rate characteristics of the forward leaning rotor blading. At intermediate rotor speeds, these two effects cancel each other and the total-to-total pressure ratio of the swirl generator is essentially independent of the flow rate.

3.4 Establishment of Swirl-Generator Exit Flow-Field Circumferential Uniformity

Since the objective of the present research is the investigation of the effect of axial distortion of the diffuser inlet flow-field on diffuser performance, the inlet flow-field should ideally be axisymmetric. This allows the parameters of the test-diffuser inlet flow field to be quantified by an axial traverse of the diffuser inlet at one circumferential location.

The degree of circumferential non-uniformity of the diffuser inlet flow field was established by measuring the circumferential non-uniformity of the static pressure at the four circumferentially-distributed static pressure wall-taps in the vaneless diffuser at radius r_1 (see figure 2.16 for tap locations). A pressure non-uniformity parameter was defined to quantify the severity of the distortion:

$$\psi_d(\theta)_{r1} = \frac{P_{st1}(\theta) - \bar{P}_{st1}}{P_{t1_{ref}} - \bar{P}_{st1}}, \qquad 3.15$$

where $\bar{P}_{st1}$ is defined as in equation 3.4 and $P_{t1_{ref}}$ is a reference total pressure taken to be the mass-averaged total pressure obtained from an axial traverse of the diffuser inlet at circumferential position θ=0.0° as given by equation 3.14. As shown in the following, ψ_d, as defined in equation 3.15, approximates the circumferential non-uniformity of the diffuser inlet velocity field.

Since $\partial\Pi_{tt}/\partial\dot{m}$ << $\partial\Pi_{ts}/\partial\dot{m}$ over a wide portion of the operating range (compare figures 3.12 and 3.1), the circumferential total-pressure non-uniformity (say $P_{t1}(\theta)_{max} - P_{t1}(\theta)_{min}$) should be much less than the static pressure non-uniformity $P_{st1}(\theta)_{max} - P_{st1}(\theta)_{min}$, assuming a quasi-steady parallel-compressor model. Approximating the total pressure at the test diffuser inlet radius r_1 as being circumferentially uniform, the denominator of equation 3.15 represents the circumferentially-averaged dynamic pressure at r_1. Assuming low Mach number flow for purposes of illustration, the circumferentially-averaged dynamic pressure at r_1 is:

$$\bar{P}_{dyn1} = \frac{1}{2\pi}\int_0^{2\pi} \frac{1}{2}\rho V_1^2(\theta)d\theta = \frac{1}{2}\rho\overline{V_1^2} \qquad 3.16$$

Similarly, the static pressure at r_1 and circumferential position position θ can be expressed as:

$$P_{st1}(\theta) = P_{t1}(\theta) - \frac{1}{2}\rho V_1^2(\theta) \qquad 3.17$$

The circumferentially-averaged static pressure at r_1 is then:

$$\bar{P}_{st1} = \bar{P}_{t1} - \frac{1}{2}\rho\overline{V_1^2} \qquad 3.18$$

Substituting equations 3.16, 3.17, and 3.18 into 3.15 with the approximation that

$P_{t1}(\theta) \approx const.$ $(= P_{t1})$ as before, we obtain:

$$\psi_d(\theta) \approx \frac{\overline{V_1^2} - V_1^2(\theta)}{\overline{V_1^2}} \qquad 3.19$$

Defining:

$$V_1(\theta) = \bar{V}_1 + v(\theta) \ ,$$

it can be easily shown that for $v \ll \bar{V}_1$, as is expected to be the case here, $\overline{V^2} \approx \bar{V}^2$. Equation 3.19 can therefore be written as:

$$\psi_d(\theta) \approx \left[\frac{\bar{V}_1 - V_1(\theta)}{\bar{V}_1}\right]\left[\frac{\bar{V}_1 + V_1(\theta)}{\bar{V}_1}\right] \text{ or ,}$$

$$\psi_d(\theta) \approx 2\left[\frac{\bar{V}_1 - V_1(\theta)}{\bar{V}_1}\right] \qquad 3.20$$

Equation 3.20 shows that when the assumptions that P_{t1} is independent of θ and $v(\theta)/\bar{V}_1 \ll 1$ hold, ψ_d as defined by equation 3.15 gives a direct indication of the circumferential non-uniformity of the diffuser inlet velocity.

Figure 3.13 shows the experimentally-determined distortion parameter ψ_d plotted as a function of circumferential position for all of the operating points corresponding to the profile data shown in figure 3.3 and analogous additional data obtained at corrected speeds of 2000, 3000, 5000, and 6200 RPM. As can be seen from this figure, the circumferential distortion of the static pressure is consistently less than 1% of the dynamic pressure at the swirl-generator exit indicating adequate sizing of the plenum. The good agreement obtained between the mass flow rate as determined by the venturi flow-meter and by integrating the traverse data at the swirl generator exit also supports this conclusion since the traverse-data was obtained at one circumferential location. The circumferential pressure-distortion is somewhat worse, with a variation of over 1.5% of the dynamic pressure, for the operating points with cross-flow injection (figure 3.7) as can be seen in figure 3.14. It is believed that the reason for this is that the injection slot slot width was not circumferentially uniform for the vaneless diffuser tests, with circumferential variations of up to 0.002 inches. This is 8% of the of the nominal slot with of 0.025 inches. This error was reduced in the vaneless space elements used for the discrete passage diffuser tests by hand finishing the slot width after assembly to a tolerance of ±.0.0005 inches, or 2% of the nominal slot with.

3.5 Summary

A comprehensive survey of the swirl-generator operating envelope was made using a 1.2 radius ratio vaneless diffuser. Overall swirl-generator pressure ratio v.s. flow constant speed characteristics were determined and the swirl generator exit Mach number and swirl angle profiles were obtained with and without profile control injection/suction. The circumferential uniformity of the swirl-generator exit flow field was investigated and a mass flow continuity check between the traverse data and the venturi flow meter was made. The following points summarize the results of this survey.

- The swirl generator total-to-static pressure ratio constant speed characteristics exhibit a continuously increasing pressure ratio with decreasing flow rate down to at least 45% of the maximum (choke) flow rate of 2.2 lbm/sec at 6200 RPM and down to approximately 12% of the maximum flow of 2.05 lbm/sec. at 1000 RPM, covering the entire operating range as used for the discrete passage diffuser tests.
- The total-to-total pressure ratio constant speed characteristics of the swirl generator show an increase in total pressure ratio with increasing flow rate at the highest speed attempted of 6200 RPM and a decreasing pressure ratio with increasing flow rate at 1000 RPM. The total-to-total pressure ratio is insensitive to flow rate at an intermediate speed of 4000 RPM.
- Mach number and swirl angle profiles at the swirl generator exit show that the basic design objective of a swirl generator exit Mach number of up to 1.0 at a swirl angle of up to 75° has been met. The minimum swirl angle measured is ≈66°. This is considered to be acceptably close to the design objective of 65° for the present diffuser study.
- The degree of axial asymmetry in the swirl-generator exit flow field can be significantly affected by suction and/or injection using the profile control slots downstream of the rotor. Injection through the profile control slots upstream of the rotor produces a relatively minor change in the swirl-generator exit profiles. Means of quantifying the severity of the distortion of the flow field are discussed in chapter 5.
- Agreement of mass flow rate as determined by the venturi flow meter and by integration across the swirl generator exit was consistently to within 5% over the entire operating range of the swirl generator without profile control

injection/suction and within ≈6.5 % with cross flow injection downstream of the rotor.

- The maximum circumferential variation of the static pressure at the swirl generator exit over the entire operating range of the swirl generator without profile control injection/suction was approximately 1% of the dynamic pressure but increased to ≈1.5% with cross flow injection downstream of the rotor. It is believed that this is the result of circumferential non-uniformity of the injection slot width, which was found to be approximately 8% of the nominal width of 0.025 inches. This non-uniformity in the slot width was reduced in the vaneless space elements used in the discrete passage diffuser tests (see chapter 4) to ≈2% of the slot width by hand finishing.

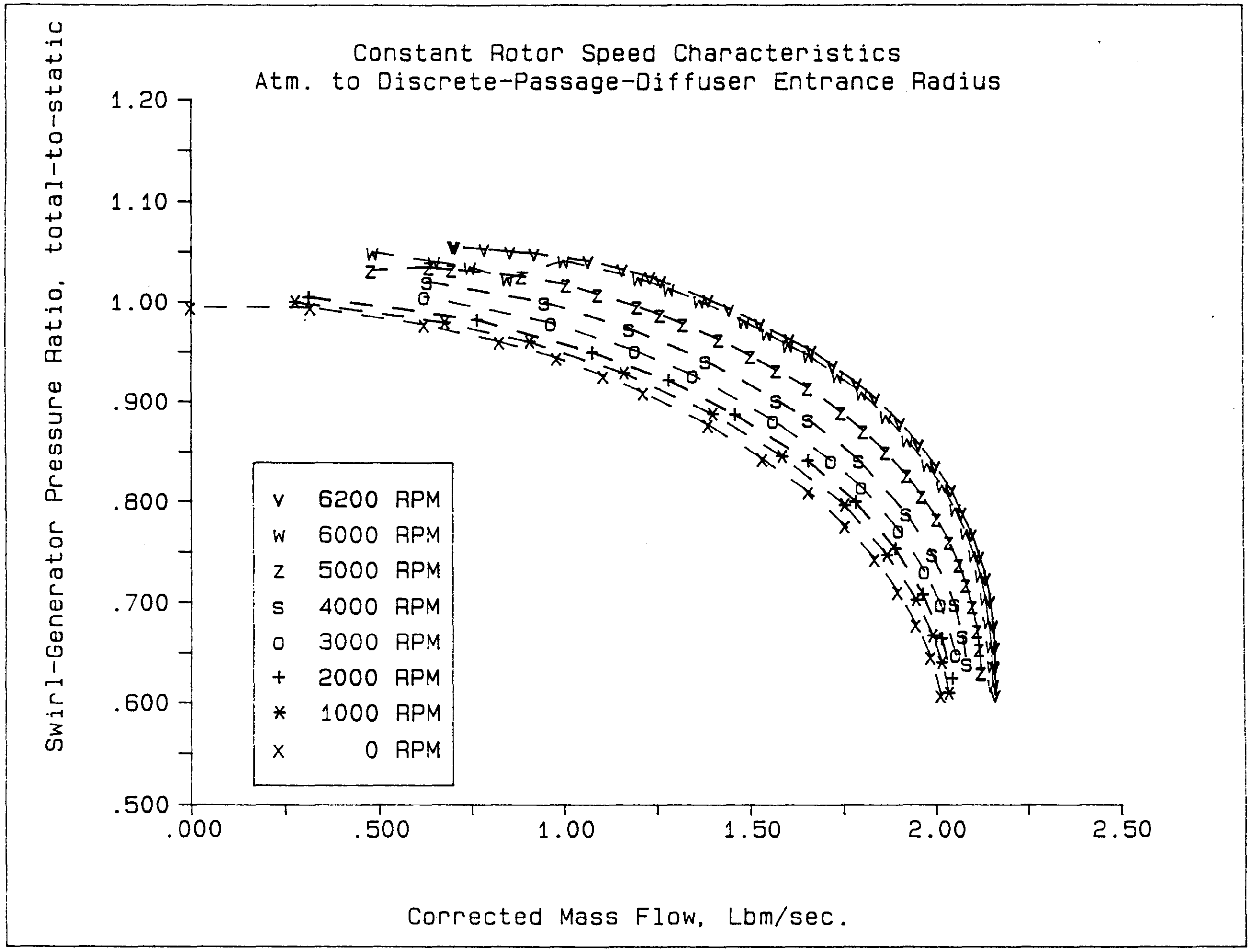

Fig. 3.1 Swirl-Generator Total-to-Static Pressure Ratio
Constant Speed Characteristics

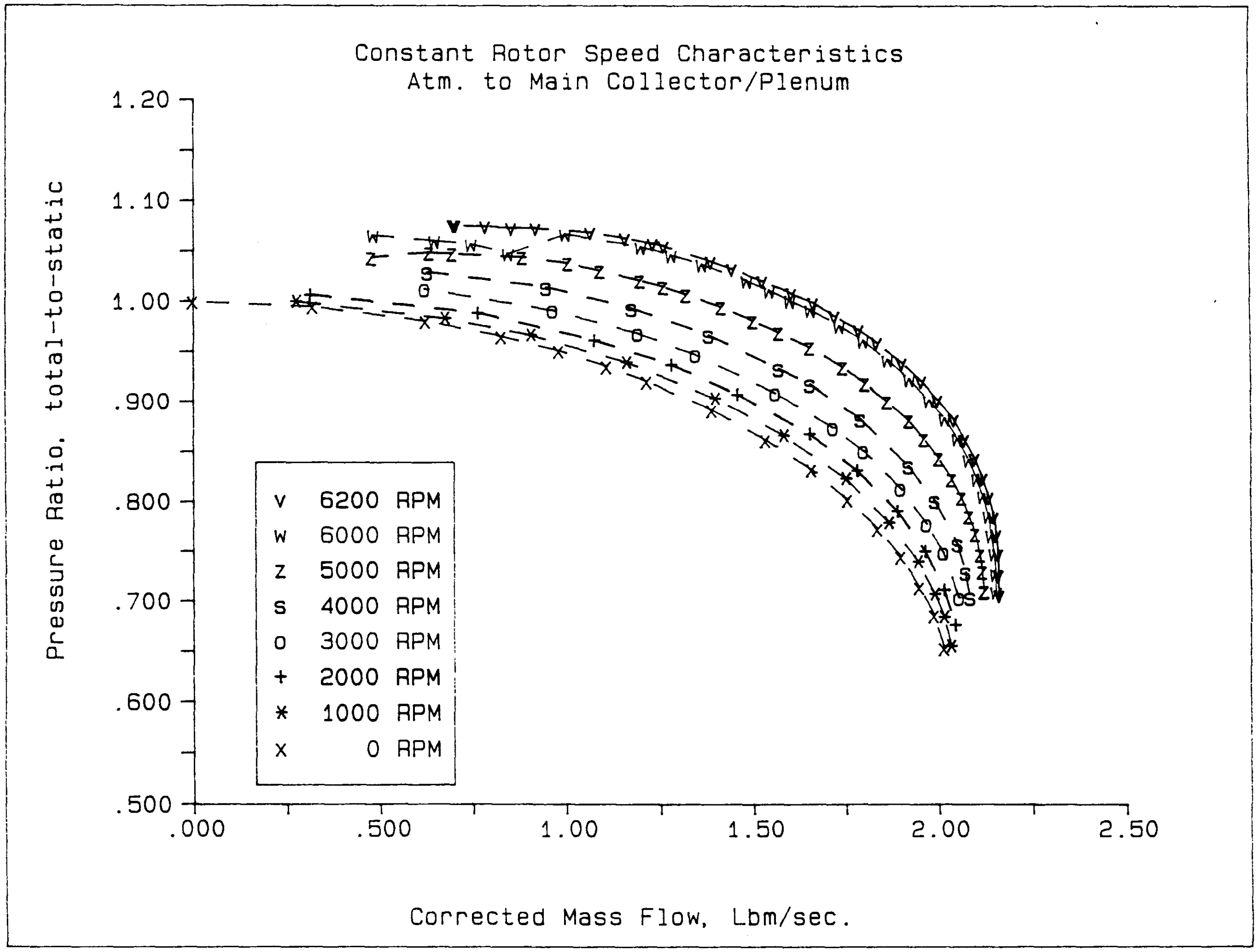

Fig 3.2 Swirl-Generator Atmosphere-to-Plenum Pressure-Ratio Constant Speed Characteristics

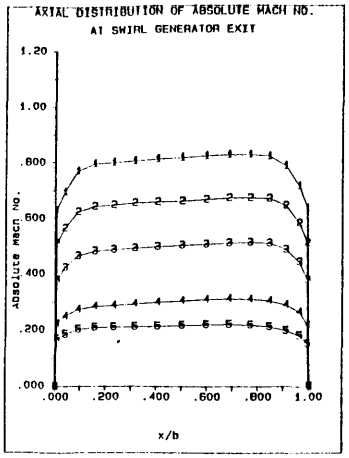

Absolute Mach No.

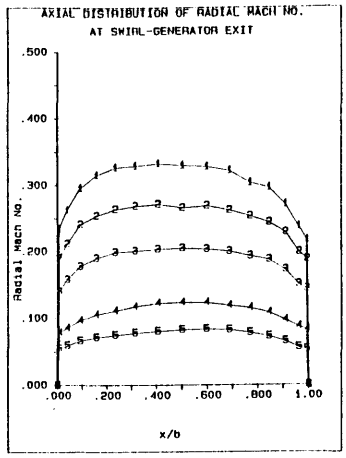

Radial Mach No.

1000 RPM

Curve No.	P_{plenum}/P_{atm}
1	0.65
2	0.75
3	0.85
4	0.95
5	0.98

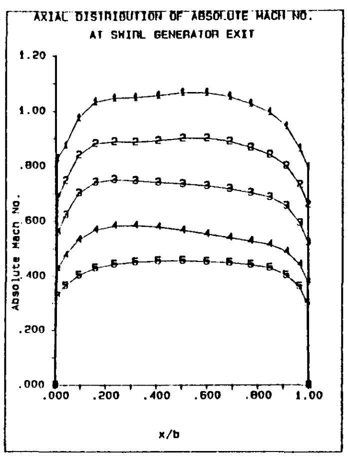

Absolute Mach No.

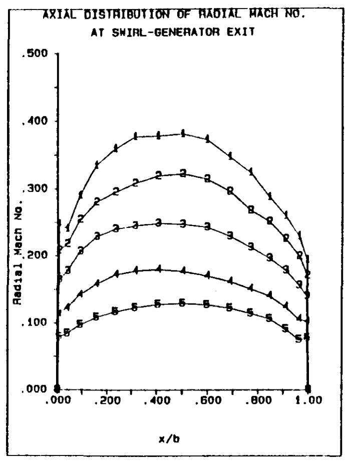

Radial Mach No.

4000 RPM

Curve No.	P_{plenum}/P_{atm}
1	0.65
2	0.75
3	0.85
4	0.95
5	1.00

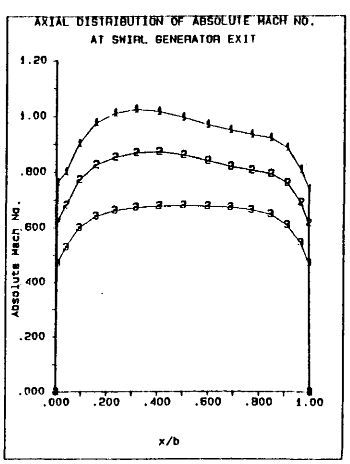

Absolute Mach No.

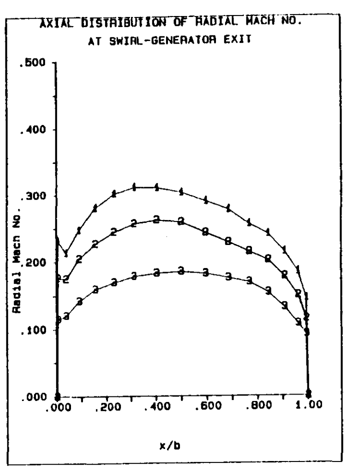

Radial Mach No.

6000 RPM

Curve No.	P_{plenum}/P_{atm}
1	0.80
2	0.90
3	1.00

Fig. 3.3 Absolute and Radial Mach Number Axial Distributions at the Swirl-Generator Exit

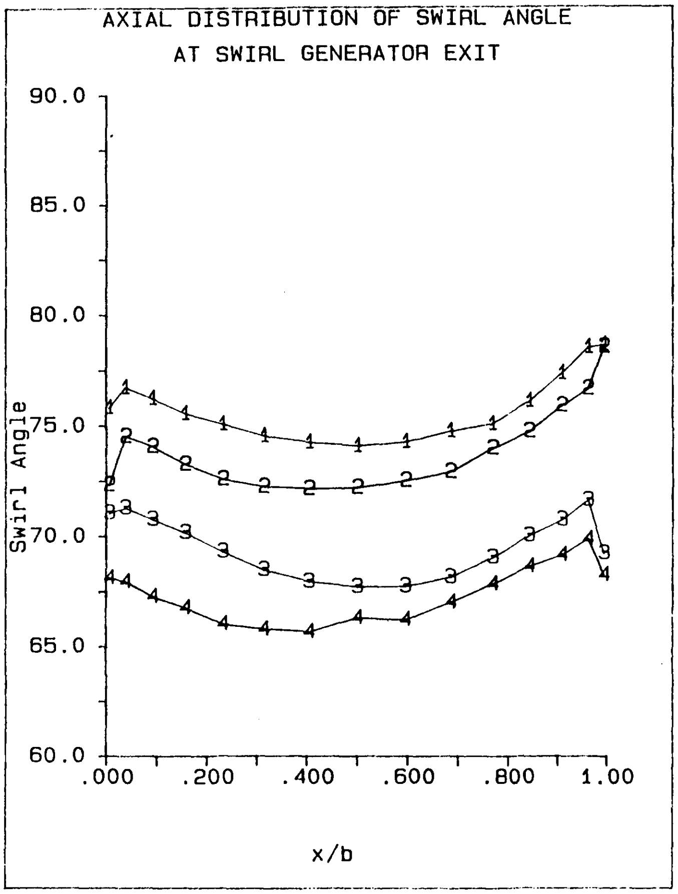

Curve No.	RPM	P_{plenum}/P_{atm}
1	6000	1.000
2	6000	0.800
3	1000	0.980
4	1000	0.750

Fig. 3.4 **Swirl-Angle Axial Distributions at Swirl-Generator Exit**

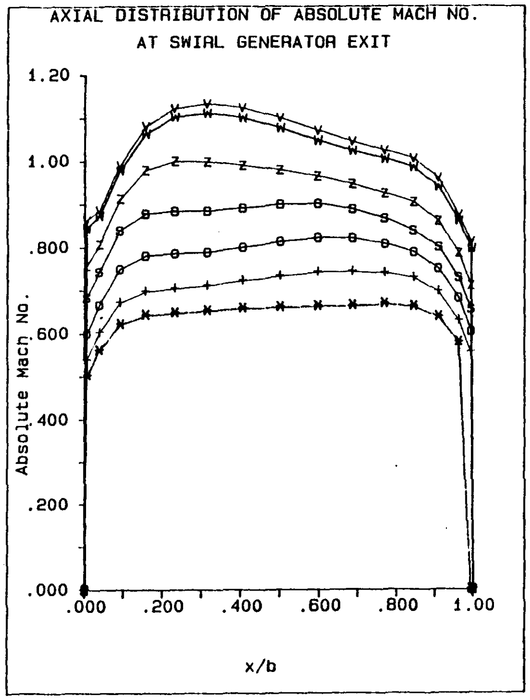

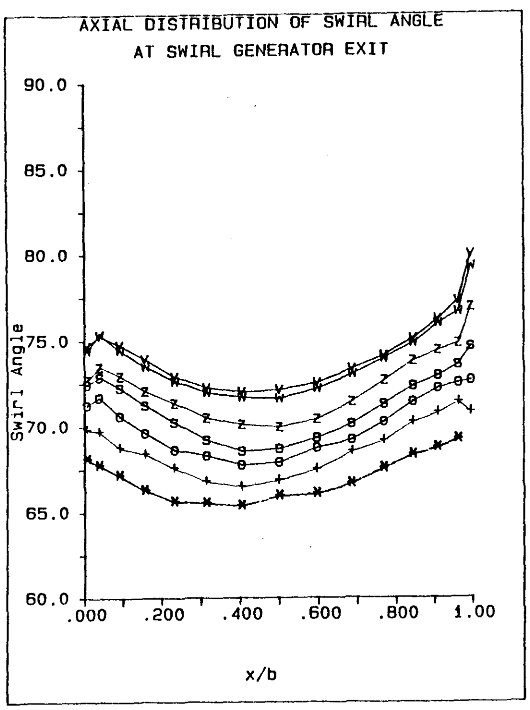

$P_{plenum}/P_{atm} = 0.75$

v 6200 RPM
w 6000 RPM
z 5000 RPM
s 4000 RPM
o 3000 RPM
+ 2000 RPM
* 1000 RPM

Fig. 3.5 Effect of Rotor Speed on Swirl-Generator Exit Mach Number and Swirl-Angle Axial Distributions

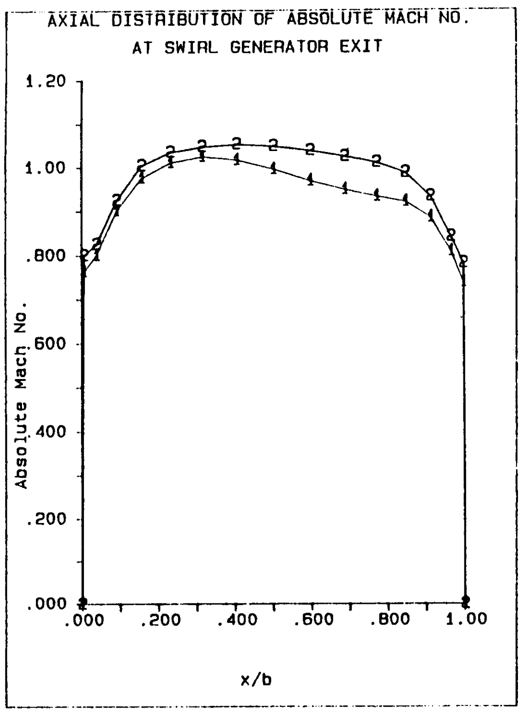

Absolute Mach No.

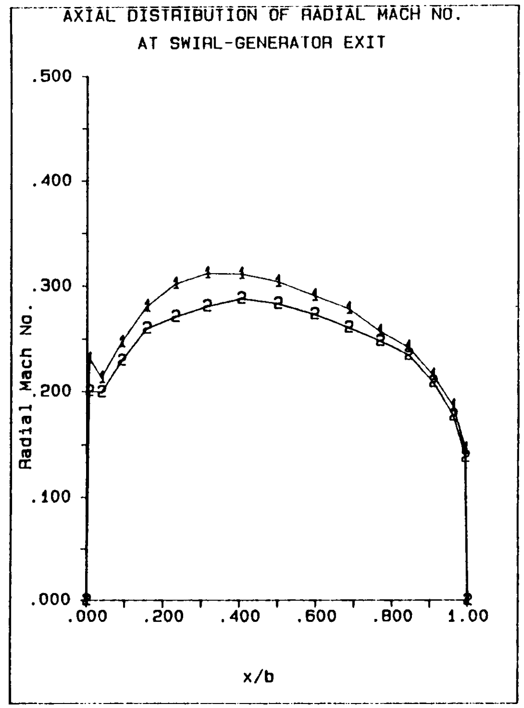

Radial Mach No.

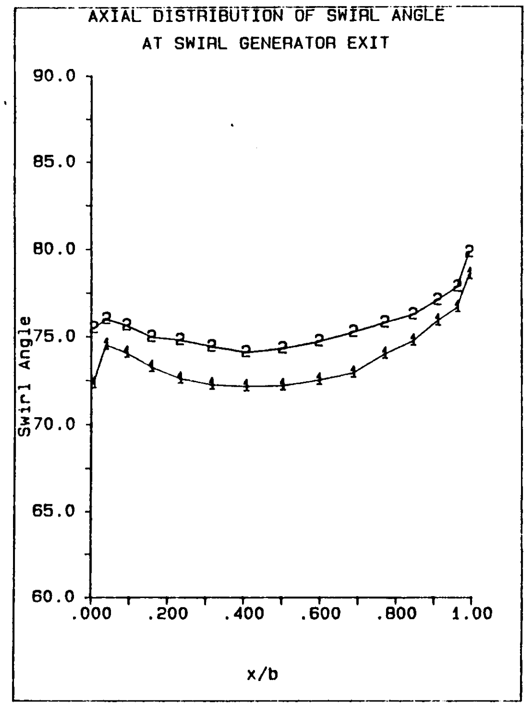

Swirl Angle

N = 6000 RPM
P_{plenum}/P_{atm} = 0.80
Curves 1: No Profile Control
Curves 2: Suction, $P_s3,4/P_{atm}$ = 0.50

Fig. 3.6 Effect of Suction Through Vaneless-Space Slots on the Swirl-Generator Exit Flow Field

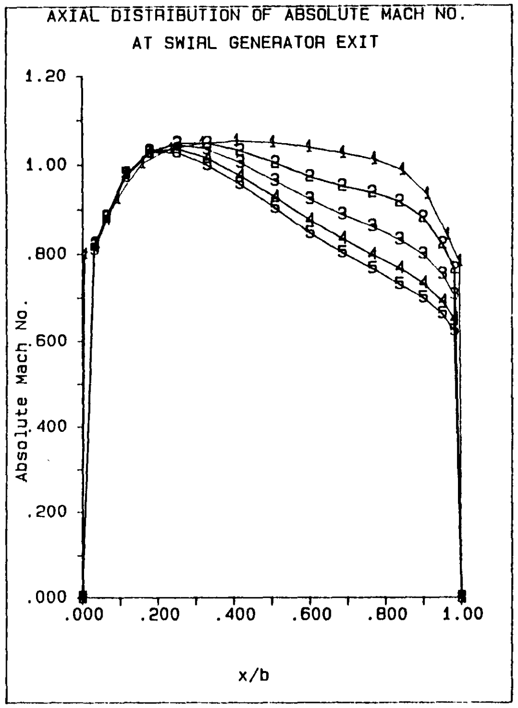

Absolute Mach No.

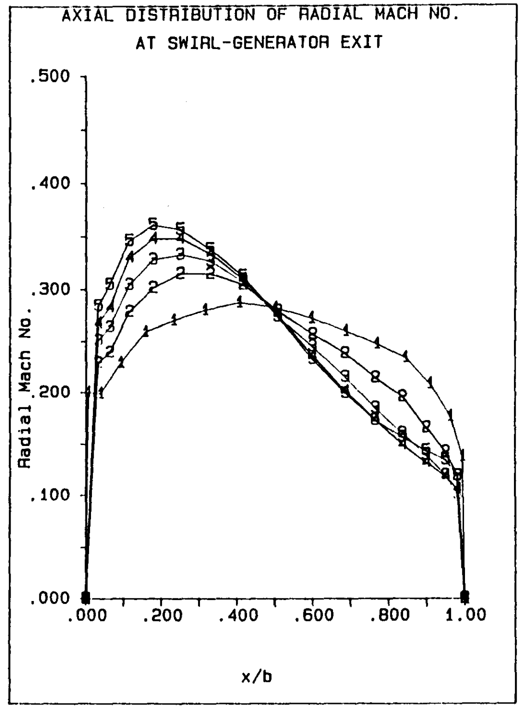

Radial Mach No.

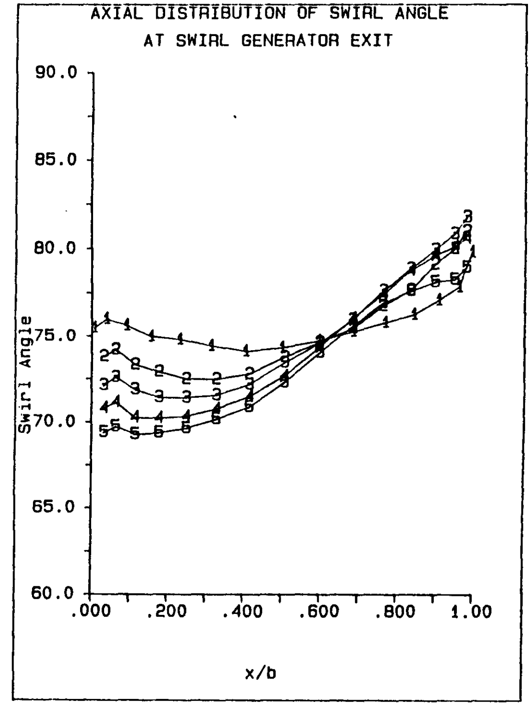

Swirl Angle

N = 6000 RPM, P_{plenum}/P_{atm} =0.80

Fig. 3.7 Effect of Asymmetric Cross-Flow Injection Through the Vaneless-Space Slots on Swirl-Generator Exit Flow Field

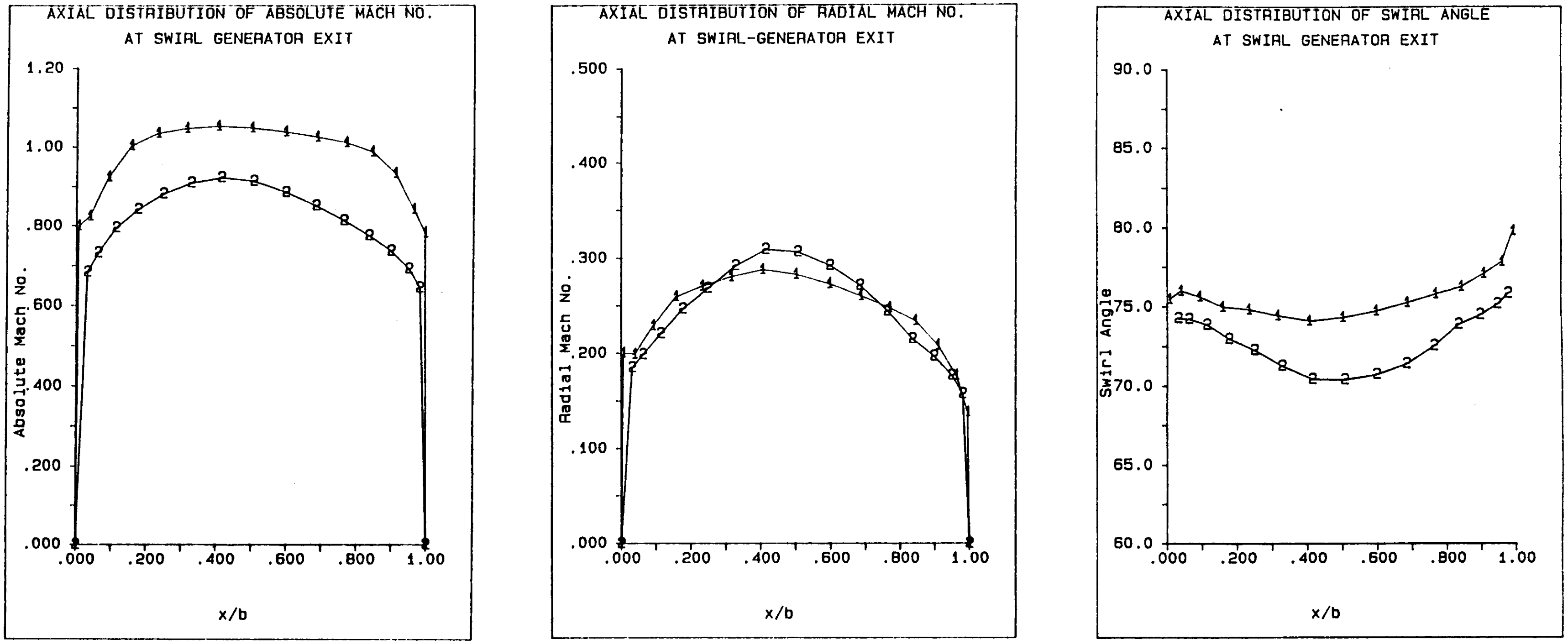

Absolute Mach No. **Radial Mach No.** **Swirl Angle**

N = 6000 RPM

Curves 1: Suction Both Sides (Slots 3 and 4), $P_3/P_{atm} = 0.50$, $P_4/P_{atm} = 0.50$, $P_{plenum}/P_{atm} = 0.80$

Curves 2: Injection Both Sides (Slots 3 and 4), $P_3/P_{atm} = 0.75$, $P_4/P_{atm} = 0.75$, $P_{plenum}/P_{atm} = 0.85$

Fig. 3.8 Effect of Symmetric Cross-Flow Injection Through the Vaneless-Space Slots on Swirl-Generator Exit Flow Field

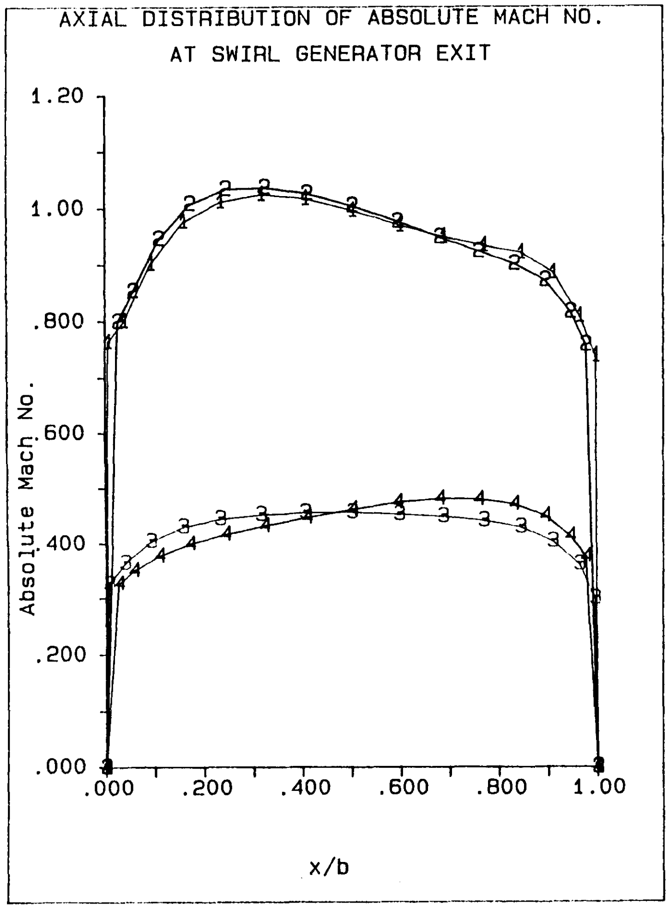

Absolute Mach Number

Curves 1 and 3:
No Injection

Curves 2:
Injection
Thru Slot 1

Curves 4:
Injection
Thru Slot 2

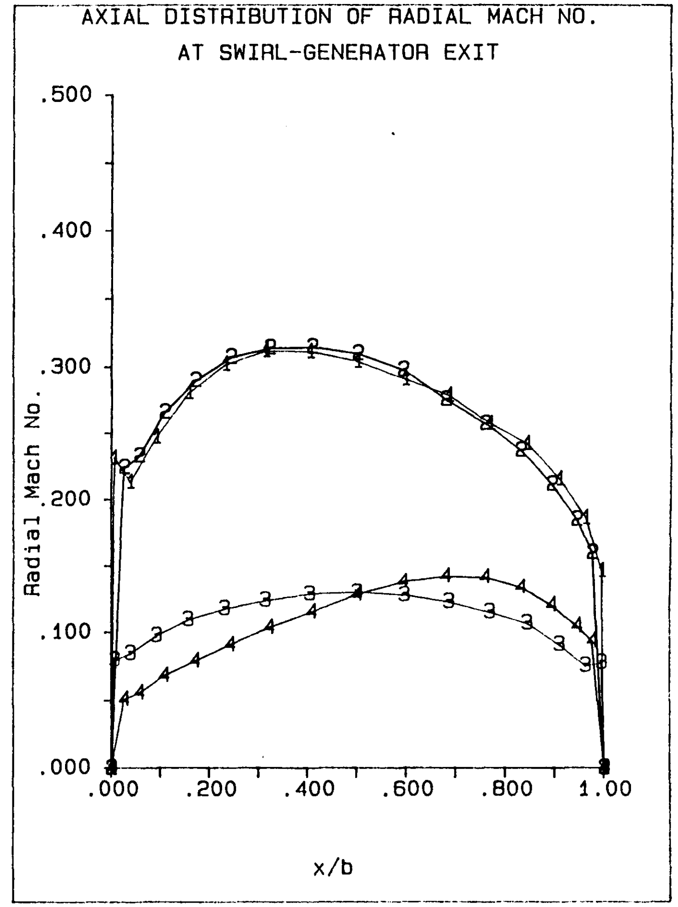

Radial Mach Number

Curves 1 and 2: $N = 6000$ RPM, $P_{plenum}/P_{atm} = 0.80$

Curves 3 and 4: $N = 4000$ RPM, $P_{plenum}/P_{atm} = 1.00$

Fig. 3.9 Effect of Cross-Flow Injection through the Rotor Inlet Slots on Swirl-Generator Exit Flow-Field

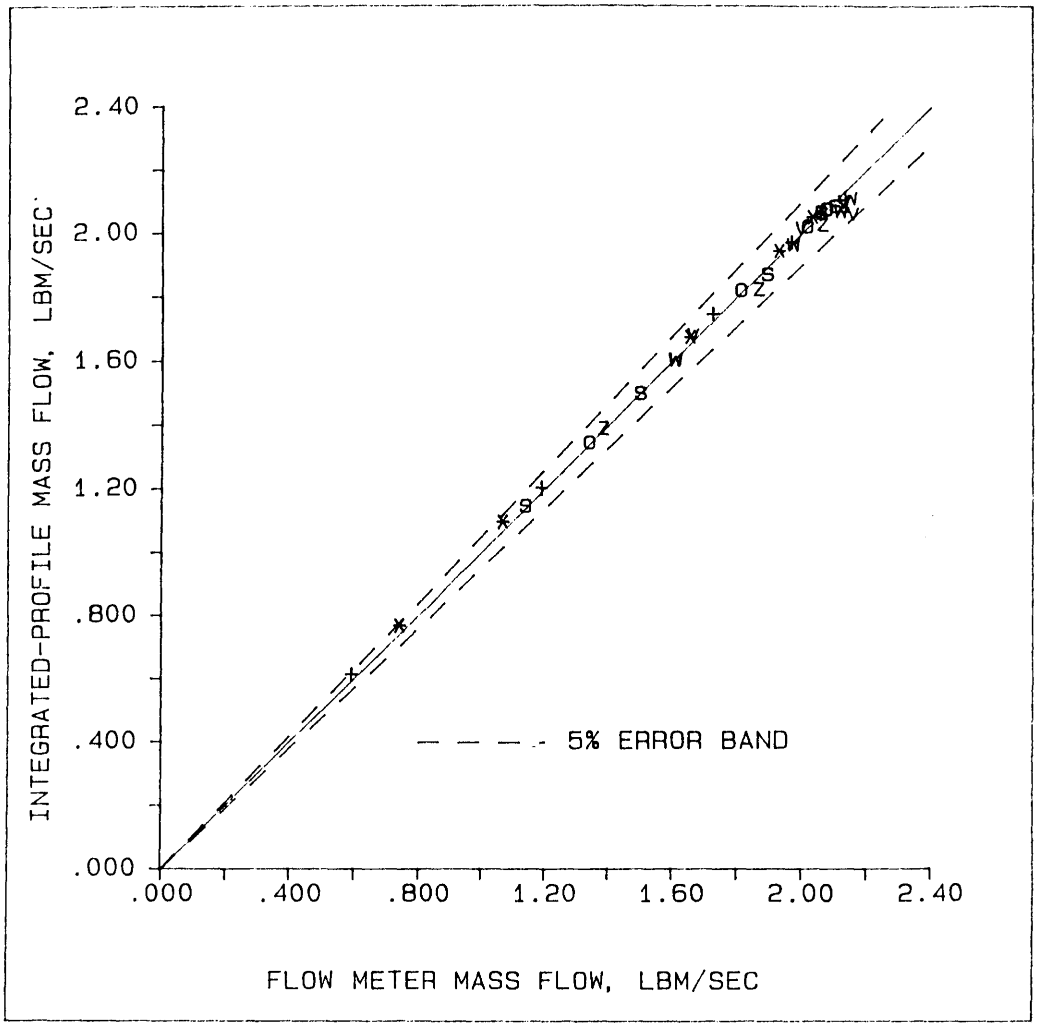

Fig. 3.10 **Mass-Flow Continuity Check Without Slot Injection/Suction**

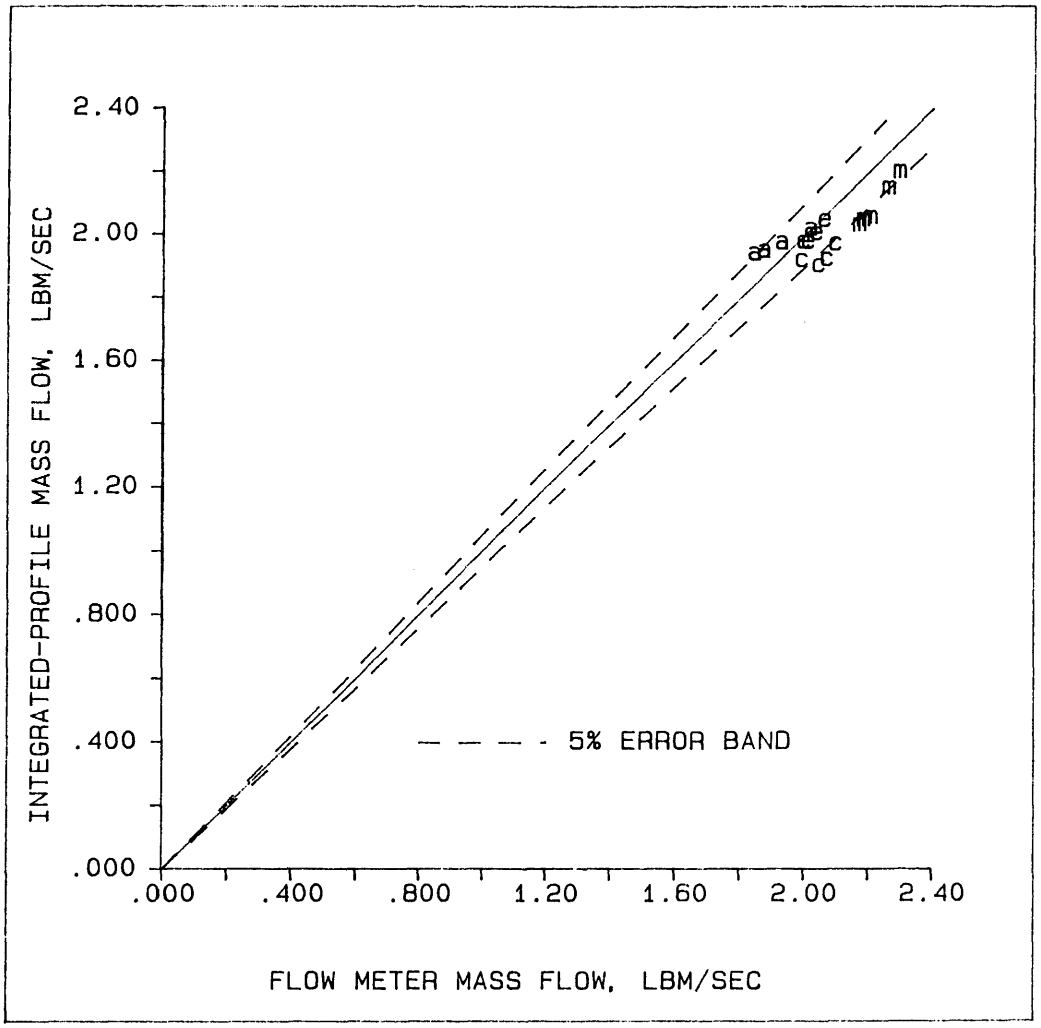

Fig. 3.11 Mass-Flow Continuity Check With Slot Injection/Suction

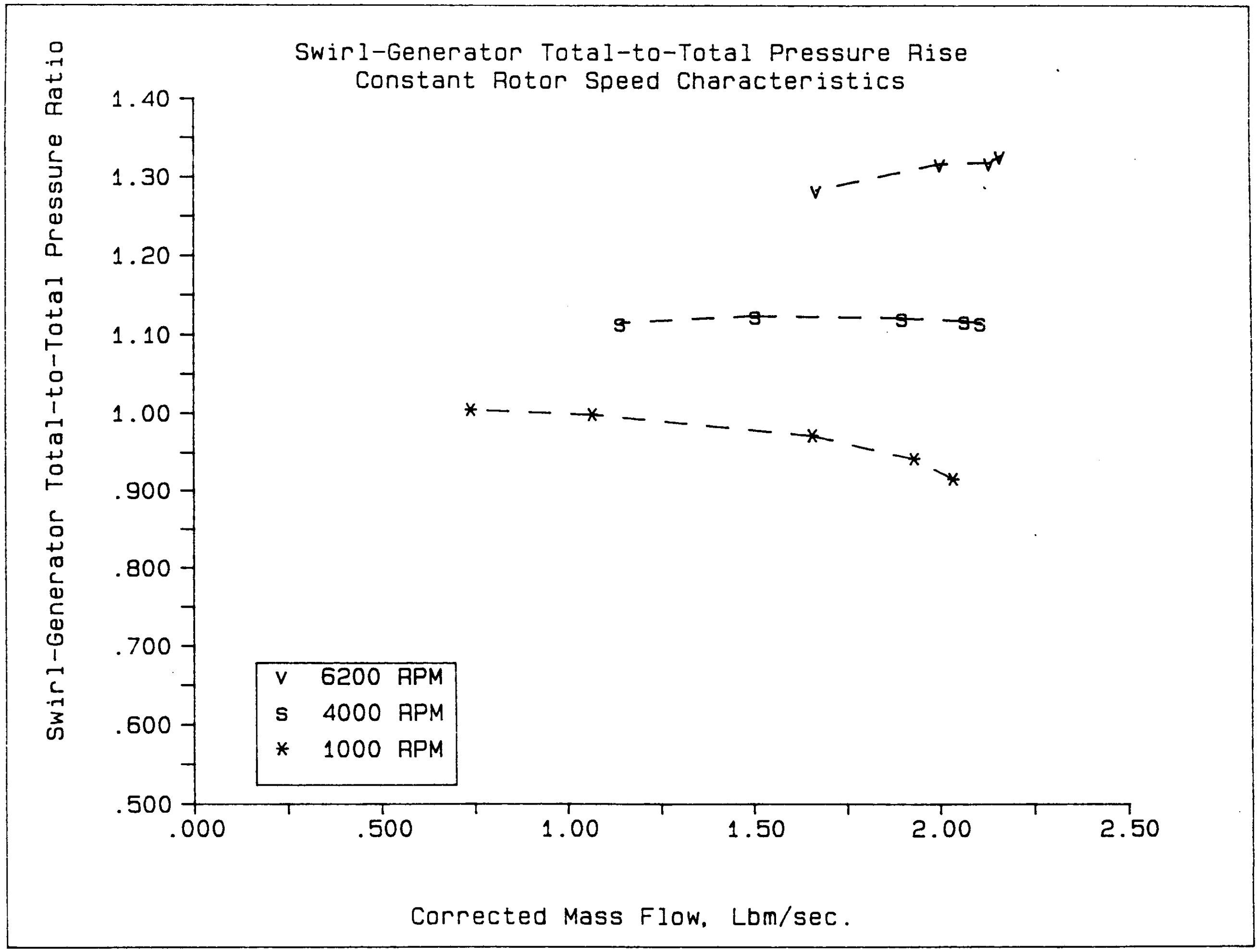

Fig. 3.12 Swirl-Generator Total-to-Total Pressure-Ratio Constant-Speed Characteristics

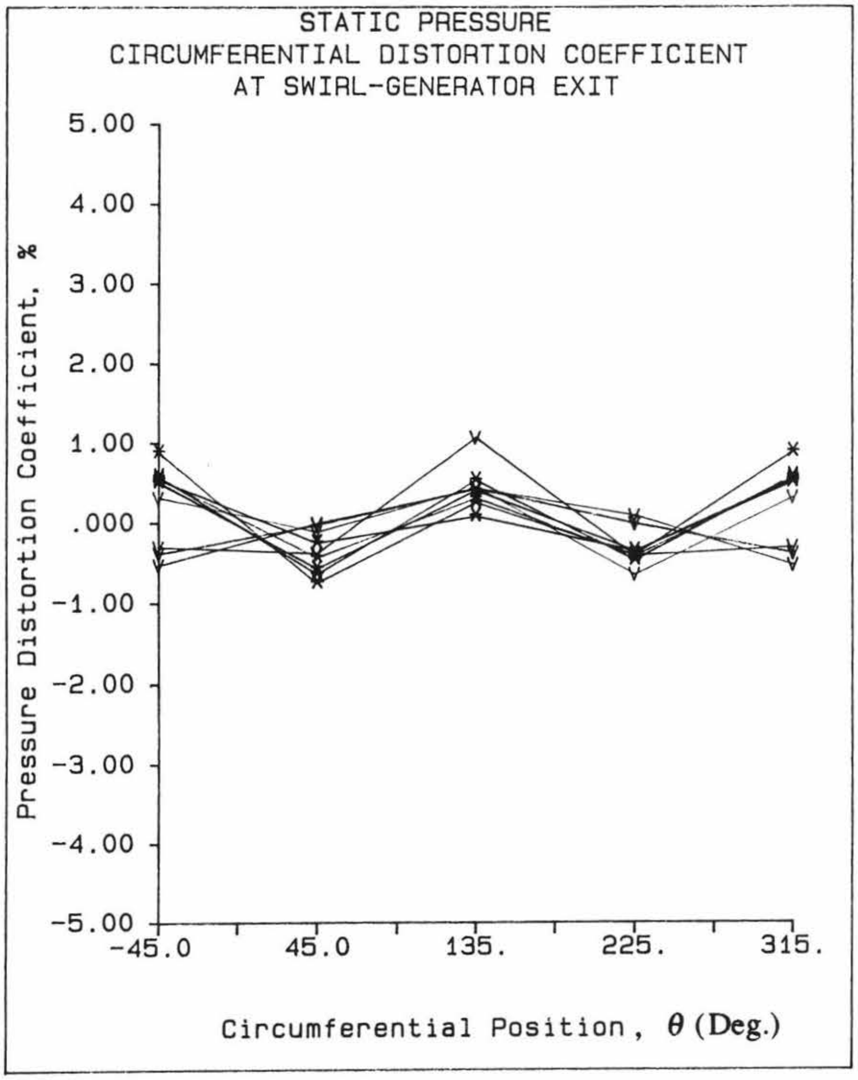

Fig. 3.13 Swirl-Generator Exit Static Pressure Circumferential Distortion Without Slot Injection/Suction

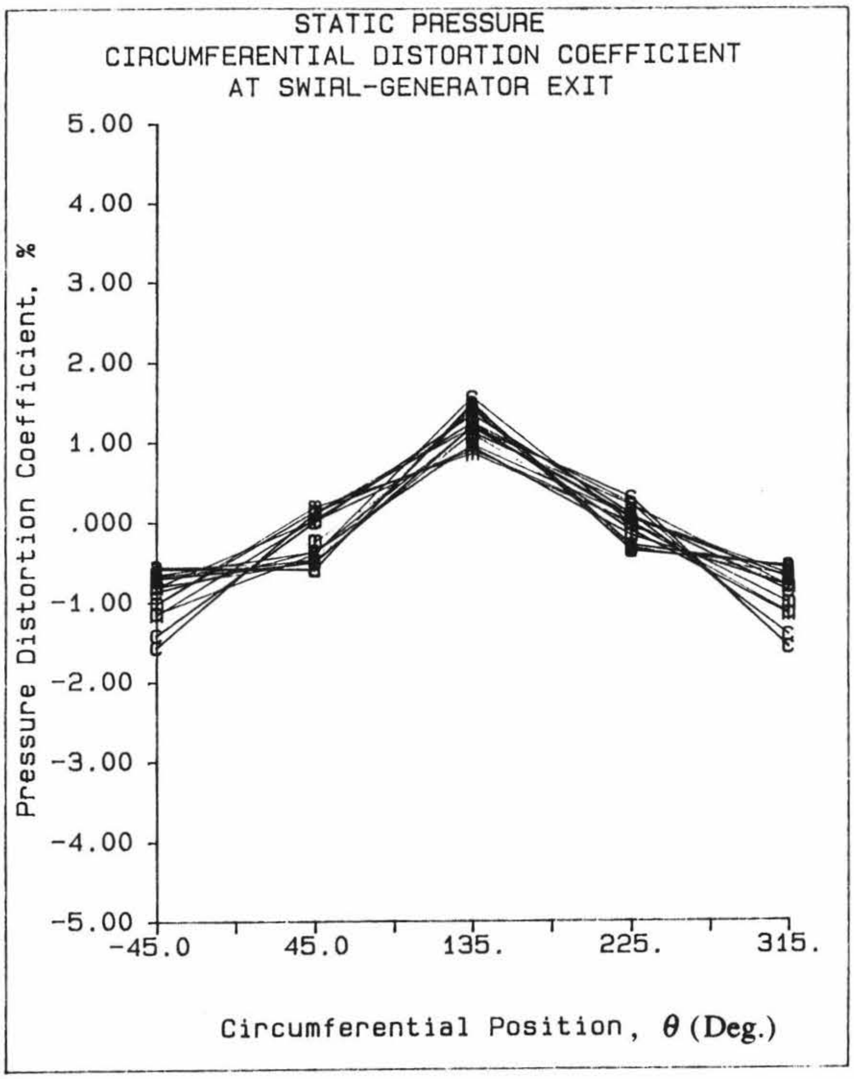

Fig. 3.14 Swirl-Generator Exit Static Pressure Circumferential Distortion With Slot Injection/Suction

CHAPTER 4

DISCRETE PASSAGE DIFFUSER TEST SERIES

4.1 Discrete Passage Diffuser Test Configuration

The 30-passage General-Electric discrete passage diffuser was mounted in the diffuser housing with a 1.10 radius ratio vaneless-space between the swirl generator rotor exit and the discrete passage diffuser inlet as described in sections 2.2.6 and 2.4.2. Three Kulite high frequency response pressure transducers, as described in section 2.5.3, were mounted in the vaneless space elements at circumferential positions of $\theta = 1.25°, 46.25°,$ and $181.25°$ at a radius ratio of 1.077 relative to the rotor exit radius as described in section 2.4.2. The probe actuator mechanism with the single-hole total-pressure/flow-angle probe, as described in section 2.5.1, was mounted at the $\theta = 0°$, $r=r_1$ (test-diffuser inlet) position on the diffuser housing. All of the static pressure taps in the discrete passage diffuser, as described in section 2.4.2, were connected to the Scanivalve pressure-transducer multiplexer.

To determine the overall diffuser pressure recovery performance, it is necessary to measure the diffuser inlet static pressure. This pressure could not be accurately determined by means of simple static pressure wall taps in the present experimental setup because there is a step transition of 0.079 inches (nominal) between the inlet width of the test diffuser (b=0.433) and the width of the swirl generator vaneless space (b = 0.354 inches) as is shown schematically in figure 2.20. (This corresponds to the step transition which exists between the inlet width of the test diffuser and the exit width of the *actual* impeller with which the test diffuser was designed to operate.) The static pressure at the test diffuser inlet (swirl-generator exit) was thus determined by means of a flush probe consisting of a steel tube with a squared-off end (o.d. = 0.039 inches, i.d. = 0.027 inches), inserted into one of the swirl-generator exit probe ports at the test diffuser inlet ($r=r_1$). The axial location of the face of the probe was adjusted to match the atmosphere-to-$r=r_1$ (total-to-static) pressure ratios obtained with the vaneless diffuser (see chapter 3) at corresponding operating points (rotor speed and flow rate).

The axial location of the probe was set at the start of the present tests with the discrete passage diffuser to give the best possible agreement with the vaneless diffuser data over the operating range of the machine and then was not moved for the duration of all of the tests (i.e. all of the data presented in this thesis relating to the discrete passage diffuser was obtained with the static pressure probe at one fixed position). The probe was secured in position using the stationary probe holder described in section 2.2.7 and shown in figures F18.a and F18.b. A schematic diagram of the static pressure probe positioned at the test diffuser inlet, and a discussion of the dependence of the present results on the accuracy of the diffuser inlet static pressure measurements are given in appendix L.

To determine the total temperature of the flow through the test diffuser, a thermocouple-type total temperature probe, as described in section 2.5.4, was mounted at the exit of the discrete passage diffuser with the thermocouple located at $x = b/2$.

4.2 Baseline Inlet-Flow Data

To establish the effect of axial distortion of the diffuser inlet flow field on pressure recovery and operating range of the discrete passage diffuser, diffuser performance data was first obtained with as uniform an inlet flow-field as possible and then with an axially distorted flow field produced using cross-flow injection through the profile control slots in the vaneless space.

As discussed in chapter 3, the swirl generator exit flow field exhibits good uniformity at low and moderate speeds and flow rates but develops some skew at the highest rotor speeds attempted at flow rates near rotor choke. The present baseline tests were performed with and without suction through the vaneless space slots. The use of suction provides a marginal improvement in the uniformity of the swirl generator exit flow field and also shifts the operating point (flow coefficient) of the rotor relative to the diffuser as discussed in chapter 3, aiding in the separation of phenomena that are specific either to the rotor or to the diffuser. The diffuser inlet "average" and distortion parameters are discussed and quantified in chapter 5, and the range of these parameters achieved in the discrete-passage diffuser tests is tabulated in tables 5.1 and 5.2.

The procedure for these tests followed that of the vaneless diffuser tests described in chapter 3. Steady-state operating points were set up giving a range of diffuser inlet Mach numbers and flow angles. Each operating point was defined by rotor corrected speed and atmosphere to swirl-generator-exit (total-to-static) pressure ratio. This establishes the swirl generator operating point independent of the specific diffuser installed in the test rig. The operating point can also be uniquely defined in terms of the rotor speed and any other conveniently measured pressure ratio, say the atmosphere to plenum pressure ratio as is often done, but this makes it difficult to reproduce a given swirl generator operating point if a different diffuser is installed. At each steady-state operating point, a fifteen-point Mach-number/flow-angle axial traverse of the discrete-passage diffuser inlet was made and pressures from all static pressure taps were recorded.

At each rotor speed, the maximum flow was limited by the choking of either the swirl-generator rotor or the test diffuser. The minimum flow limit was marked by breakdown of the axisymmetric flow regime in the rotor/diffuser, signaled by an audible blowdown of the main collector/plenum through the swirl-generator inlet. After the initial plenum blowdown in cases where the downstream slave-compressor was not used, the machine stabilized in operation with rotating stall. This was indicated by distinct circumferentially-traveling pressure disturbances in the vaneless space as seen by monitoring the output of the vaneless-space Kulite pressure transducers on an oscilloscope. The main collector/plenum pressure and flow rate was steady in this regime as indicated by the output signal from the plenum Kulite pressure transducer. It was also found that a surge cycle could be initiated at these same limiting flow rates if the slope of the main collector/plenum discharge-throttle characteristic were adequately increased. (Assuming that the throttle is not choked, this is achieved by means of the downstream slave compressor which in conjunction with the throttle setting, allows the pressure drop across the throttle to be varied independently of the test-rig through-flow rate). The output signals of the Kulite pressure transducers indicated that this operating mode involved a combination of circumferentially traveling pressure disturbances in the vaneless space and cyclic variation of the main plenum/collector pressure and through-flow rate.

Since a major objective of this work was the determination of the effect of inlet distortion on the stable operating range of the discrete-passage diffuser, close attention was given to obtaining the diffuser inlet flow-field and diffuser-passage static pressure distribution data at the "stall threshold" operating point of the machine. It is to be emphasized that, as will be shown in chapter 5, the discrete-passage diffuser was in fact the stability limiting element of the rotor/diffuser system. Operation at the rotating stall threshold was achieved by finding the pressure ratio and throttle position at which rotating stall occurs at each rotor speed, by trial and error, and then setting up an unstalled operating point as close as possible to this to obtain the diffuser inlet stall threshold total-pressure/swirl-angle profile. Because the downstream slave compressor imposes small but detectable pressure disturbances on the test rig flow-system as described in section 2.3.5, all stall threshold data was obtained <u>without</u> the use of the slave compressor.

Figure 4.1 shows the range of distributions of absolute and radial Mach number achieved at the swirl generator exit in the tests with the 30-passage discrete-passage diffuser without the use of profile control injection/suction. Figure 4.2 shows the corresponding swirl-angle distributions. These data were obtained under unstalled steady-state operating conditions. The profiles corresponding to the rotating-stall-threshold operating points are indicated by an asterisk (*).

The static pressure distributions along the axis of an individual diffuser passage corresponding to the data shown in figures 4.1 and 4.2 are shown in figure 4.3. These data represent the operating range of the diffuser from choke to stall. The static pressure in these figures is represented by a pressure coefficient defined as:

$$C_{pr}(\xi/l) = \frac{P_{st}(\xi/l) - P_{st1}}{P_{t_{\psi_1}} - P_{st1}} \tag{4.1}$$

were $P_{t_{\psi_1}}$ is the "availability averaged" diffuser inlet total pressure defined in chapter 5 (In the present experiments, the diffuser inlet dynamic pressure based on the inlet mass averaged total pressure was in the most extreme case 1.6 % greater than the dynamic pressure based on the availability-averaged total pressure).

As can be seen from figure 4.3, at maximum overall-diffuser pressure recovery (rotating stall threshold), over 90% of the overall static pressure rise occurs within the first 60% of the diffuser passage length. The large drop in pressure recovery upstream of the diffuser throat (ζ/l=0.40) seen at 2000 RPM, compared to the 6000 RPM case when the diffuser is choked, occurs because at 2000 RPM, the diffuser chokes (sonic velocity at the throat) when the diffuser inlet angle is still less than the throat centerline angle (69°) and the flow must accelerate as it approaches the throat. At 6000 RPM however, sonic velocity at the throat is attained at a diffuser inlet angle greater than the throat centerline angle, requiring a deceleration of the flow as it approaches the throat. The relationship between the swirl generator exit flow angle, absolute Mach number, and swirl generator rotor speed responsible for this behavior, where the swirl generator exit flow angle (considering the axially uniform case for simplicity) decreases at fixed absolute Mach number as the rotor speed is decreased (as shown in figure 2.6), is due to the forward-leaning rotor blading.

The static pressure distribution in the quasi-vaneless space, as measured at the twelve quasi-vaneless-space static pressure taps shown in figure 2.18 is given in figures 4.4a-4.4c. The static pressure here is again represented in the form of a pressure coefficient defined in a manner analogous to equation 4.1:

$$C_{pr}(\xi,\theta) = \frac{P_{st}(\xi,\theta) - P_{st1}}{P_{t_{\psi_1}} - P_{st1}} \qquad 4.2$$

The operating points at which this data was obtained correspond to those represented by the data shown in figures 4.1, 4.2, and 4.3 and cover the operating range of the diffuser from choke to stall. As can be seen from figures 4.4a through 4.4c, there is a substantial loading on the leading-edge cusps in the quasi-vaneless space with a consistent reversal of the loading from diffuser choke to stall over the range of diffuser inlet Mach numbers investigated. In addition, at any given operating point, there is a reversal of the loading across the leading edge cusps along the axial direction of the passage (between the diffuser inlet inlet and the throat).

4.3 Distorted Inlet-Flow Data

As discussed in chapter 3, the establishment of a swirl-generator operating point in general requires the setting of six independent operating parameters: rotor speed, diffuser through-flow rate (or pressure ratio), and pressure in the four profile-control-slot flow distribution chambers. Since injection or suction through the profile control slots located at the inlet of the rotor proved to have only a minimum influence on the swirl-generator exit flow field as shown in chapter 3, only the vaneless-space slots were used for the present experiments, reducing to four the number of independent operating-point parameters which must be set.

To establish the influence of axial distortion of the diffuser inlet flow field on the diffuser performance, data analogous to that shown in figures 4.1, 4.2, and 4.3 was obtained with cross-flow injection through profile-control slot number 3 (x/b=1 side of the diffuser) and simultaneous suction through profile-control slot number 4 (x/b=0 side of the diffuser). (A schematic diagram of the profile-control slot arrangement is shown in figure 2.15). Based on the swirl-generator performance data obtained with the vaneless diffuser, this combination of injection/suction provides the greatest possible skew-type distortion at the swirl-generator exit.

The maximum theoretical injection mass flow rate (based on the flow-distribution chamber and vaneless-space static pressures) was limited to ≈10% of the diffuser through-flow rate because it was found that when the ratio of the injected mass flow rate to the diffuser through flow rate was increased beyond roughly 20%, the discrepancy between the mass flow rate as determined by means of the downstream venturi flow meter and by integration of the swirl-generator exit velocity profile became substantial (>5%). It is believed that the reason for this is that at high injection cross-flow rates, significant axial velocities occur at the probe traverse location and these can not be resolved with the present instrumentation.

The range of axial distributions of absolute and radial Mach number obtained at the test diffuser inlet with cross-flow injection and suction is shown in figure 4.5 and the corresponding distributions of swirl angle are shown in figure 4.5. The data representing rotating-stall threshold operating points in these figures is indicated by an asterisk (*).

Means of quantifying the flow field distortion together with definitions of "average" flow field parameters will be discussed in chapter 5. To give a qualitative indication of the level of distortion achieved in these test however, a comparison of the "distorted" and the baseline or "undistorted" absolute and radial Mach number profiles is shown in figure 4.7 for the rotating stall threshold operating points. Figure 4.8 shows the corresponding comparison of the distorted and undistorted swirl-angle distributions. As will be discussed quantitatively in chapter 5, the level of distortion achieved is significant, particularly in the radial Mach number and flow angle distributions.

A comparison between the diffuser through-flow mass flow rate as measured by the venturi flow meter and as determined by integrating the swirl-generator flow field data according to equation 3.12 is shown in figure 4.9, to indicate of the quality of the undistorted and distorted flow field data shown in figures 4.1 and 4.5. As can be seen from figure 4.9, the agreement is to within 6% except for two operating points at the highest flow rates. It is believed that the increased discrepancy between the integrated and flow meter flow rates at corrected through-flow rates above 2.0 lbm/sec is due to shock effects which were not taken into account. At lower flow rates, the data consistently falls within the 0% to +6% error range with all of the distorted and undistorted rotating stall threshold operating points (indicated with a circle) lying within one percentage point of the +5% error line. This suggests that there was a bias error of approximately -0.8 degrees in the probe angle setting as can be seen from equation 3.11.

4.4 Flow Instability Phenomena

As indicated in section 4.2, as the flow rate through the test diffuser was decreased at constant rotor speed (resulting in the increase of the diffuser inlet flow angle), a point was reached at which the axisymmetric flow through the diffuser and swirl-generator rotor became unstable, resulting in a operating regime characterized by circumferentially-traveling pressure (and flow) waves (rotating stall). In all cases corresponding to the data shown in figures 4.1 through 4.8, this transition occurred with a single blowdown of the main collector/plenum ending at an operating point in which the main plenum/collector pressure and through-flow rate was steady but the rotor and diffuser were operating in stable rotating stall.

Figure 4.10 shows the time varying static pressure at the three high frequency response pressure transducers in the vaneless space and in the main collector/plenum during a transition to rotating stall at 2000 RPM and 4000 RPM (see section 2.5.3 for a description of the transducers and figure 2.19 for the transducer locations). The time varying static pressure in figure 4.10 is given in terms of a pressure coefficient which for the vaneless space pressures is defined as:

$$Cp = \frac{P(t) - P_{st1_{rts}}}{(P_{t1} - P_{st1})_{rts}} \qquad 4.3$$

In equation 4.3, $P(t)$ is the time resolved absolute static pressure as determined from the transducer output, the subscript rts represents rotating-stall-threshold quantities (as measured just before the onset of rotating stall) and the P_{t1} is the mass averaged total pressure at the test diffuser inlet. (In words, equation 4.3 is the difference between time resolved static pressure and the near stall static pressure, divided by the near stall dynamic pressure.) For the plenum pressure, the pressure coefficient is defined as:

$$Cp = \frac{P(t) - P_{atm}}{(P_{plen} - P_{atm})_{rts}} \qquad 4.4$$

Time in figure 4.10 is normalized by the swirl angular velocity at the swirl generator exit as measured at the rotating-stall threshold:

$$t_n = \frac{t(C_{\theta_1})_{rts}}{2\pi r_1} \qquad 4.5$$

where $(C_{\theta_1})_{rts}$ is the mass averaged swirl velocity at the diffuser inlet at the rotating stall threshold.

The transition to rotating stall shown in figure 4.10 is characteristic of all of the cases seen in the present investigation, with and without distortion of the diffuser inlet flow. As will be shown in chapter 5, the observed transition to operation in rotating stall was the result of loss of flow stability in the test diffuser, and was independent of the rotor operating point. In all cases, at throttle settings corresponding to the onset of rotating stall, the rotating stall was single-celled and the stall cell speed ranged from 23% to 28% of the stall-threshold diffuser inlet tangential velocity. As the throttle was closed further, transition to a two-cell rotating stall was observed.

4.5 Summary of Chapter 4

- Pressure recovery performance data and stable operating flow range of the 30-passage discrete passage diffuser were determined over the operating range of the swirl generator, with and without axial distortion introduced by means of cross-flow injection in the vaneless space. The diffuser inlet Mach number and swirl angle axial profiles, and the wall static pressure distributions in the diffuser quasi-vaneless space and along the centerline of a diffuser passage were measured over a range of steady state operating points from diffuser choke to the limit of stable axi-symmetric operation.
- The minimum flow at which stable operation could be maintained was limited by the onset of rotating stall. Combined rotating stall/surge-cycle mode was also found to be possible, at the same limiting flow rates as the pure rotating stall mode, if the slope of the main throttle were increased by means of the downstream compressor.
- It was found that the character of the rotating stall was independent of rotor speed and the diffuser inlet flow field distortion level. The stall was a single cell with propagation speed approximately equal to 25% of the stall threshold mass-averaged diffuser inlet tangential velocity.
- A reversal of the loading across the leading edge cusps occurs during a transition of operation from near diffuser choke to near diffuser stall and also along the diffuser passage centerline from the diffuser inlet to the diffuser throat at any given operating point.
- Over 90% of the overall-diffuser static pressure rise occurs within the first 60% of the diffuser passage length.

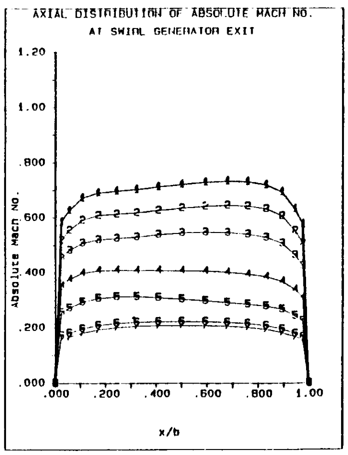

Absolute Mach No.

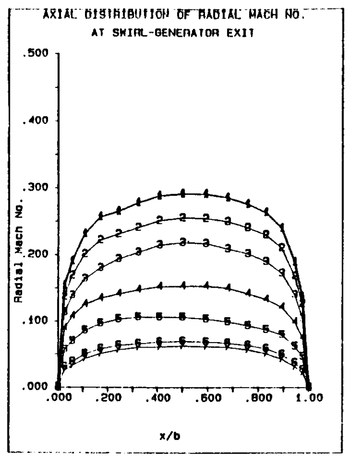

Radial Mach No.

2000 RPM

Curve No.	P_{st1}/P_{atm}
1	0.720+
2	0.781
3	0.840
4	0.920
5	0.970
6	0.995
7	0.998*

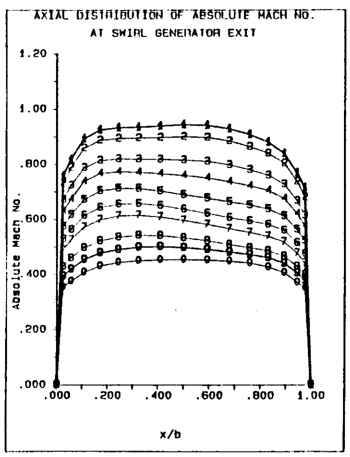

Absolute Mach No.

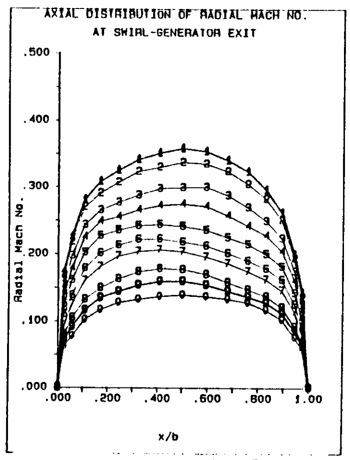

Radial Mach No.

4000 RPM

Curve No.	P_{st1}/P_{atm}
1	0.650+
2	0.680
3	0.740
4	0.780
5	0.830
6	0.870
7	0.900
8	0.940
9	0.960
0	0.980*

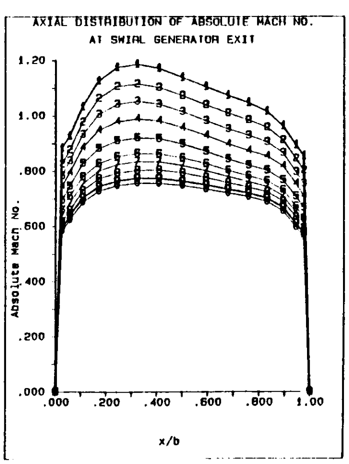

Absolute Mach No.

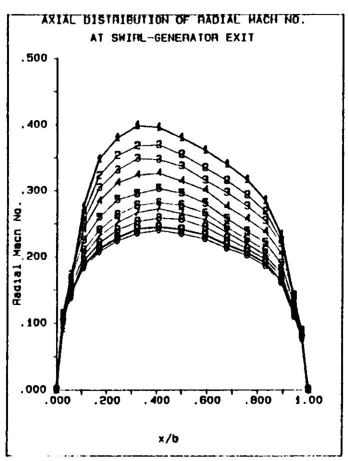

Radial Mach No.

6000 RPM

Curve No.	P_{st1}/P_{atm}
1	0.600+
2	0.650
3	0.700
4	0.750
5	0.800
6	0.840
7	0.860
8	0.880
9	0.900
0	0.910*

+ Diffuser Choke

* Rotating Stall Threshold

Fig. 4.1 Absolute and Radial Mach Number Axial Distributions at the Swirl-Generator Exit Achieved with the 30-Passage Diffuser Without Profile Control Injection/Suction

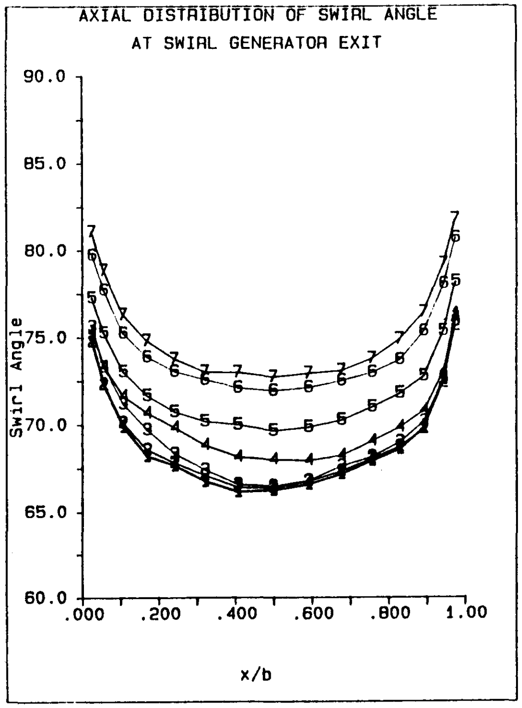

2000 RPM

Curve No.	P_{st1}/P_{atm}
1	0.720+
2	0.781
3	0.840
4	0.920
5	0.970
6	0.995
7	0.998*

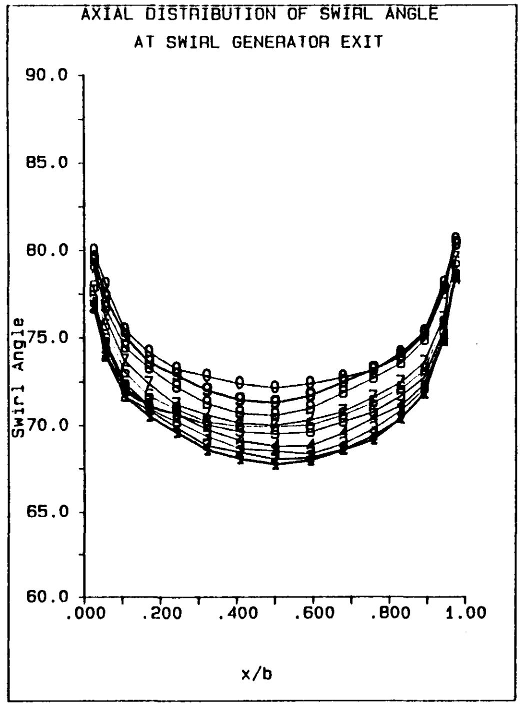

4000 RPM

Curve No.	P_{st1}/P_{atm}
1	0.650+
2	0.680
3	0.740
4	0.780
5	0.830
6	0.870
7	0.900
8	0.940
9	0.960
0	0.980*

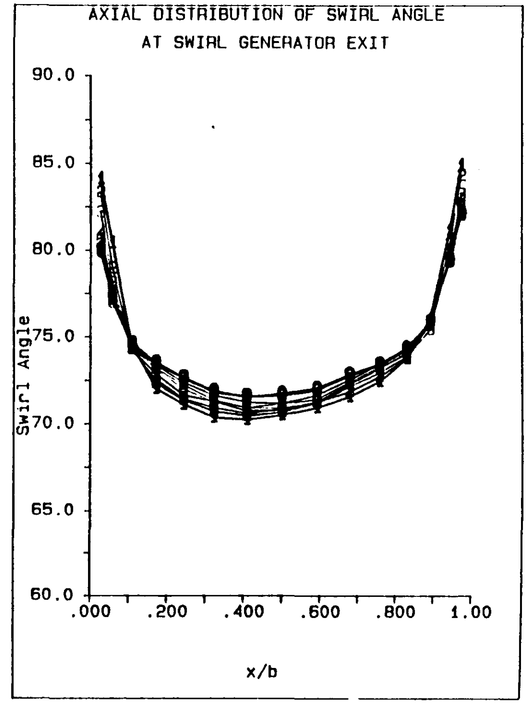

6000 RPM

Curve No.	P_{st1}/P_{atm}
1	0.600+
2	0.650
3	0.700
4	0.750
5	0.800
6	0.840
7	0.860
8	0.880
9	0.900
0	0.910*

+ Diffuser Choke

Fig. 4.2 Swirl-Angle Axial Distributions at the Swirl-Generator Exit Achieved with the 30-Passage Diffuser Without Profile Control Injection/Suction Corresponding to Mach Number Distributions Shown in Figure 4.1

* Rotating Stall Threshold

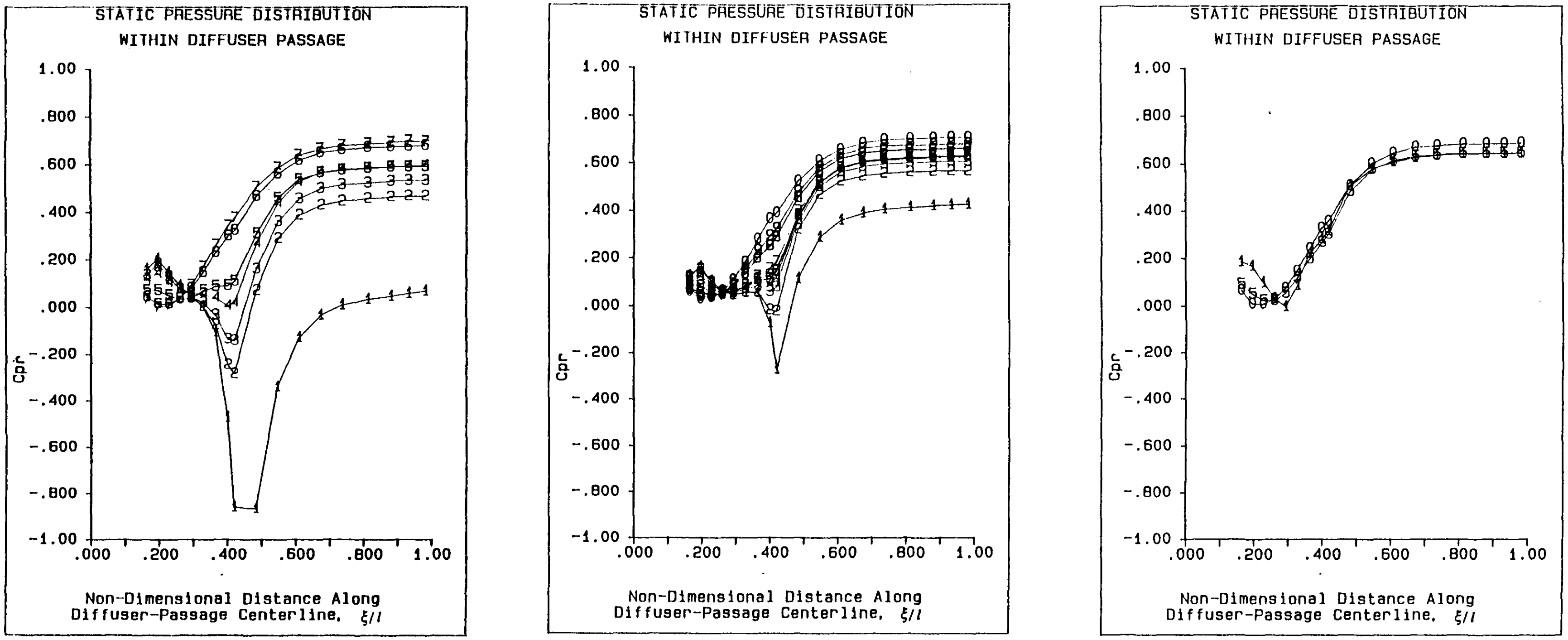

2000 RPM

Curve No.	P_{st1}/P_{atm}
1	0.720+
2	0.781
3	0.840
4	0.920
5	0.970
6	0.995
7	0.998*

4000 RPM

Curve No.	P_{st1}/P_{atm}
1	0.650+
2	0.680
3	0.740
4	0.780
5	0.830
6	0.870
7	0.900
8	0.940
9	0.960
0	0.980*

6000 RPM

Curve No.	P_{st1}/P_{atm}
1	0.600+
5	0.800
0	0.910*

+ Diffuser Choked

* Rotating Stall Threshold

Fig. 4.3 Static Pressure Distribution Along Diffuser Passage Centerline (Measured at the Wall) for Operating Points Corresponding to the Data Shown in Figures 4.1 and 4.2

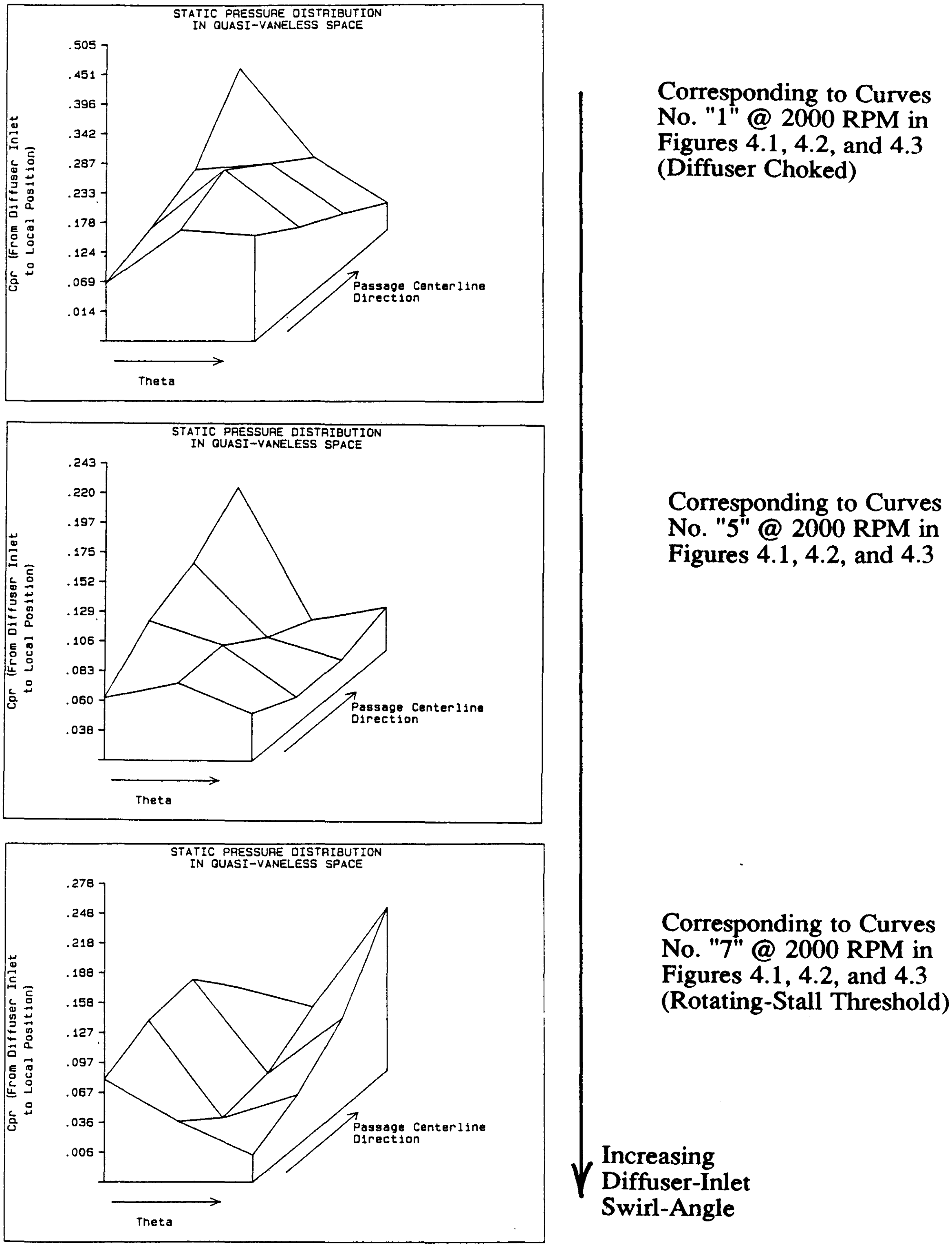

Fig. 4.4a Static Pressure Distribution in the Discrete-Passage Diffuser Quasi-Vaneless Space at Swirl-Generator Rotor Speed = 2000 RPM.

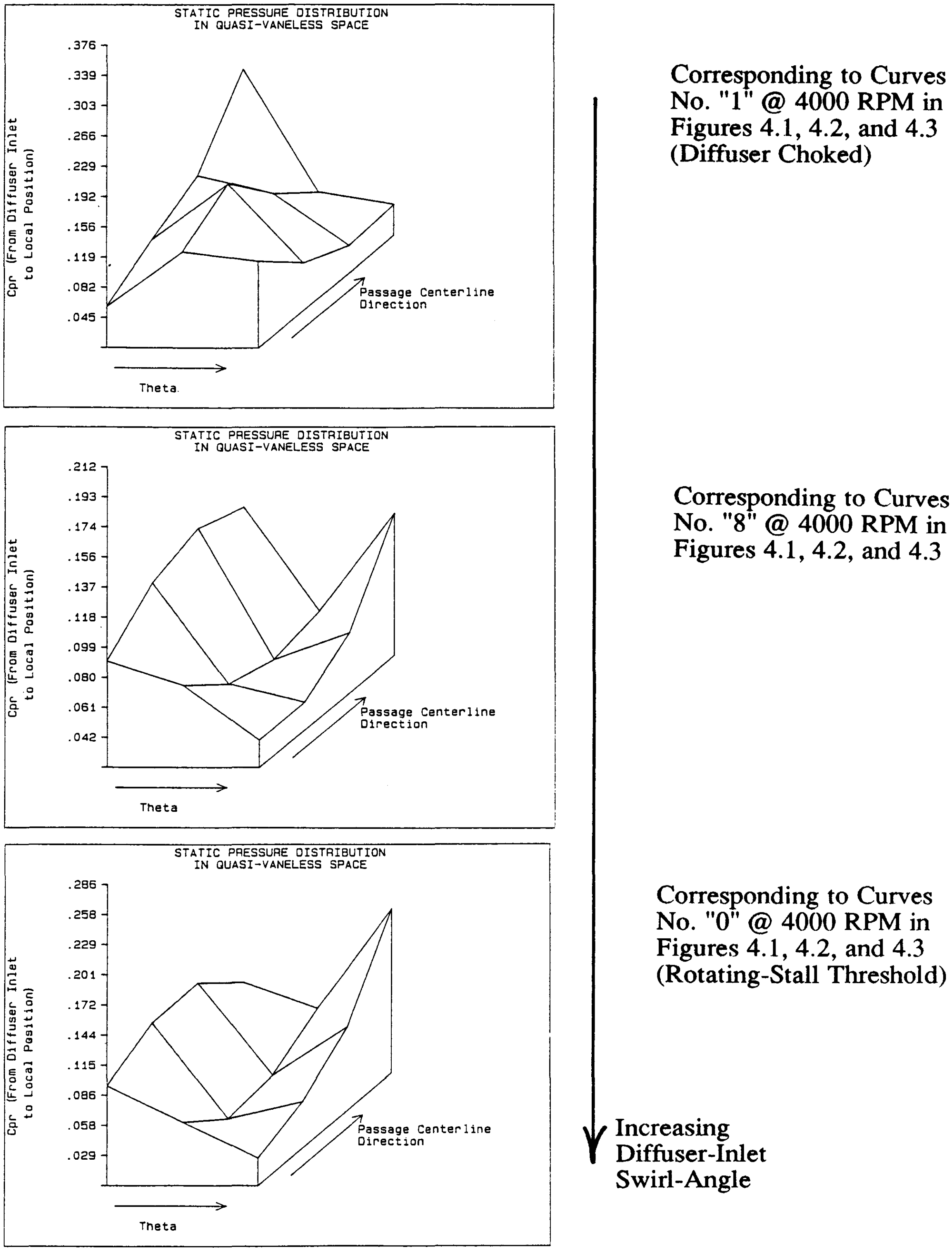

Fig. 4.4b Static Pressure Distribution in the Discrete-Passage Diffuser Quasi-Vaneless Space at Swirl-Generator Rotor Speed = 4000 RPM.

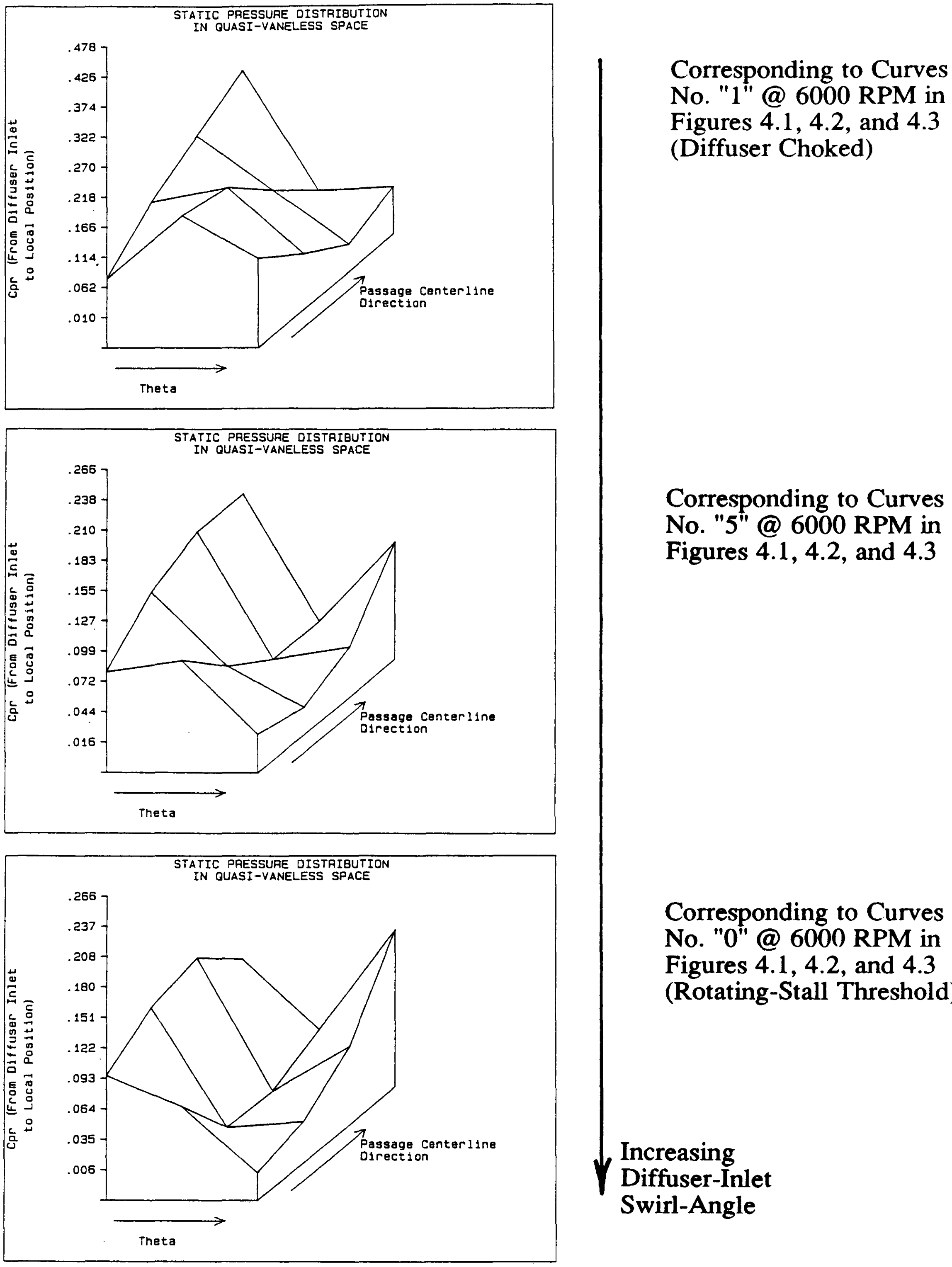

Fig. 4.4c Static Pressure Distribution in the Discrete-Passage Diffuser Quasi-Vaneless Space at Swirl-Generator Rotor Speed = 6000 RPM.

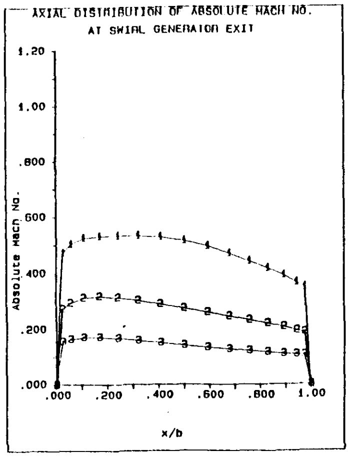

Absolute Mach No.

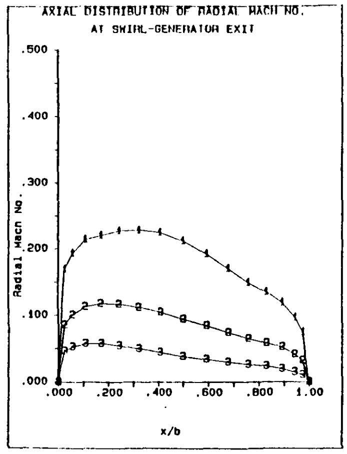

Radial Mach No.

2000 RPM

Curve No.	P_{st1}/P_{atm}
1	0.840
2	0.970
3	1.003*

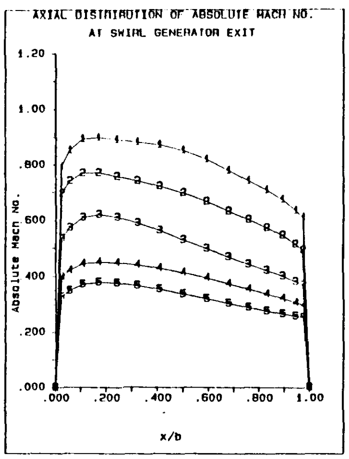

Absolute Mach No.

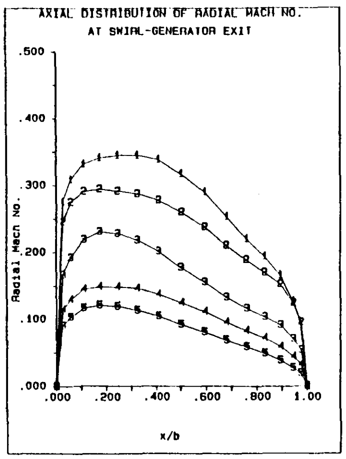

Radial Mach No.

4000 RPM

Curve No.	P_{st1}/P_{atm}
1	0.680
2	0.780
3	0.900
4	0.980
5	1.007*

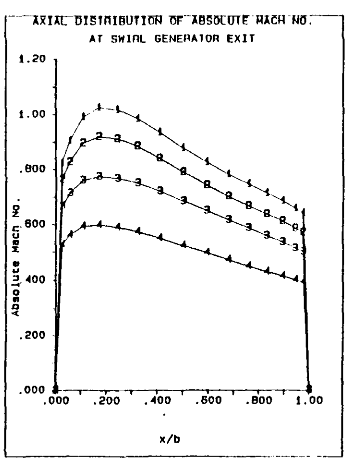

Absolute Mach No.

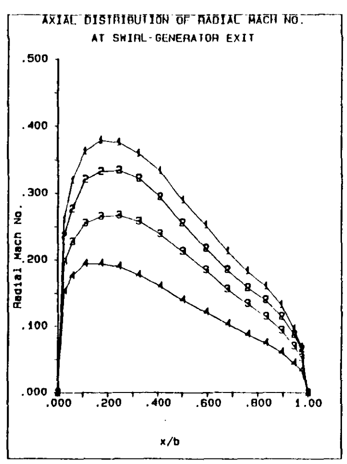

Radial Mach No.

6000 RPM

Curve No.	P_{st1}/P_{atm}
1	0.720
2	0.800
3	0.900
4	1.002*

* Rotating Stall Threshold

Fig. 4.5 Absolute and Radial Mach Number Axial Distributions at the Swirl-Generator Exit Achieved with the 30-Passage Diffuser With ≈10% Cross-Flow Injection Through Profile Control Slot No. 3 and ≈10% Suction Through Slot No. 4.

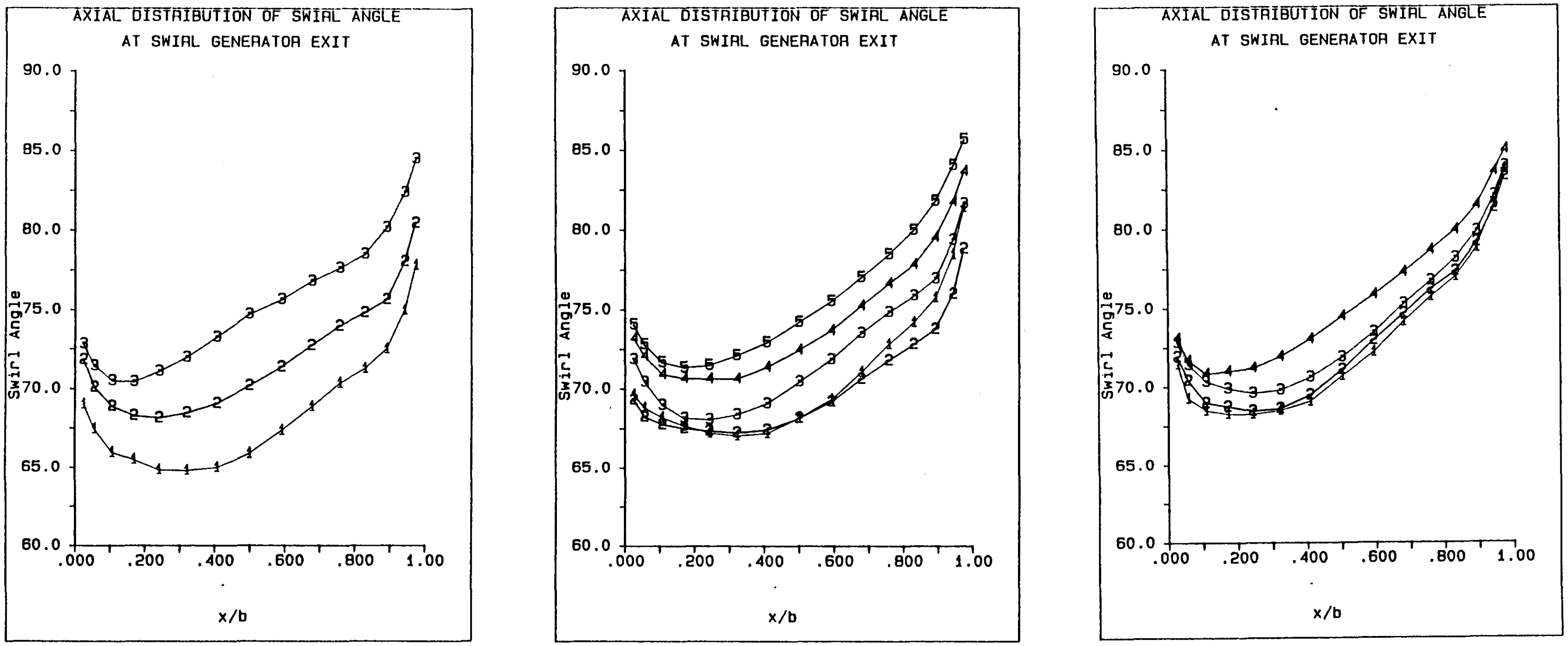

2000 RPM

Curve No.	P_{st1}/P_{atm}
1	0.840
2	0.970
3	1.003*

4000 RPM

Curve No.	P_{st1}/P_{atm}
1	0.680
2	0.780
3	0.900
4	0.980
5	1.007*

6000 RPM

Curve No.	P_{st1}/P_{atm}
1	0.720
2	0.800
3	0.900
4	1.002*

* Rotating Stall Threshold

Fig. 4.6 Swirl-Angle Axial Distributions at the Swirl-Generator Exit Achieved with the 30-Passage Diffuser With Cross-Flow-Injection Through Slot No. 3 and Suction Through Slot 4, Corresponding to the Mach Number Distributions Shown in Figure 4.5

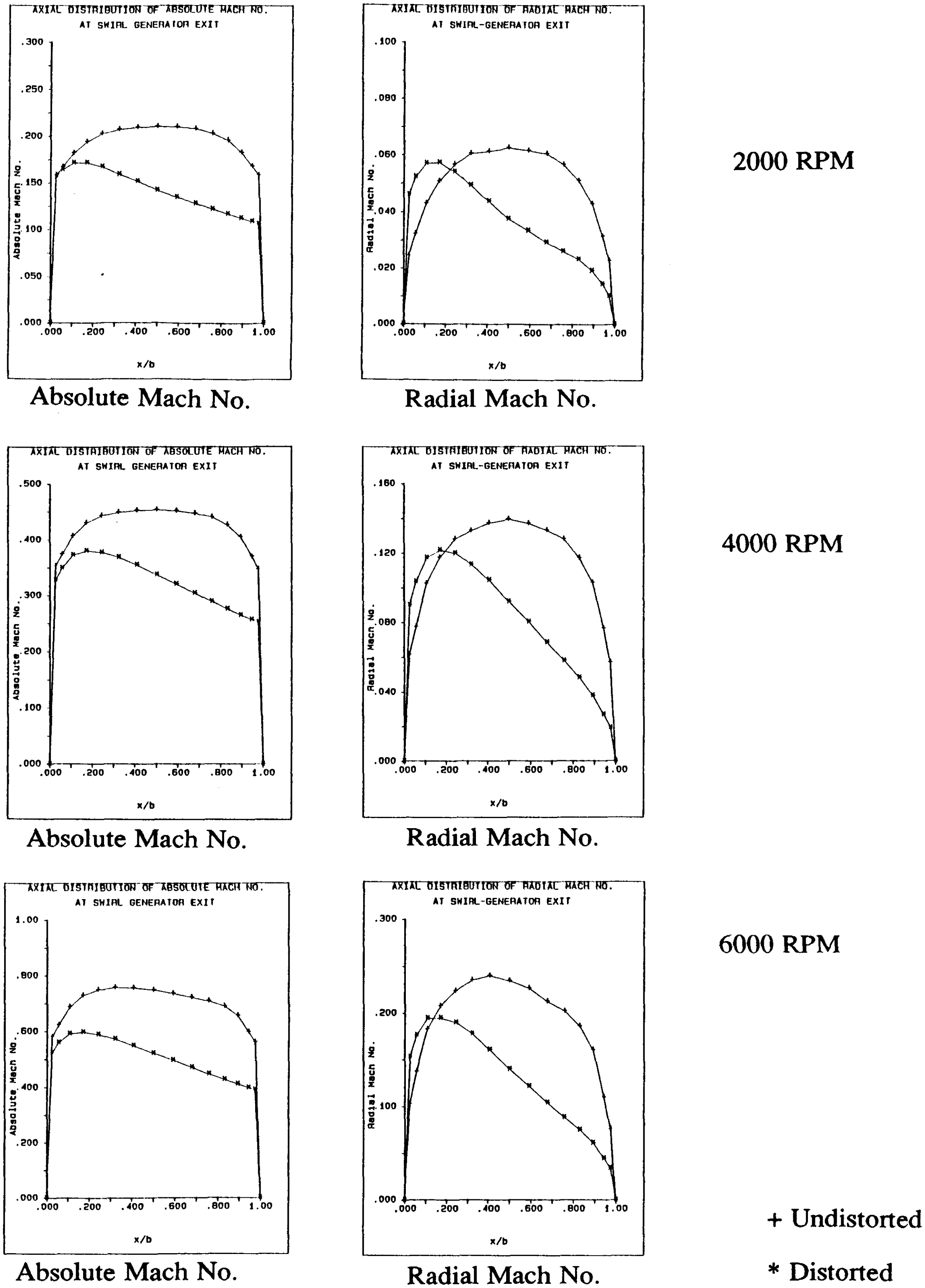

Fig. 4.7 Comparison of "Undistorted" and "Distorted" Discrete-Passage Diffuser Inlet Axial Distributions of Absolute and Radial Mach Number at the Rotating Stall Threshold.

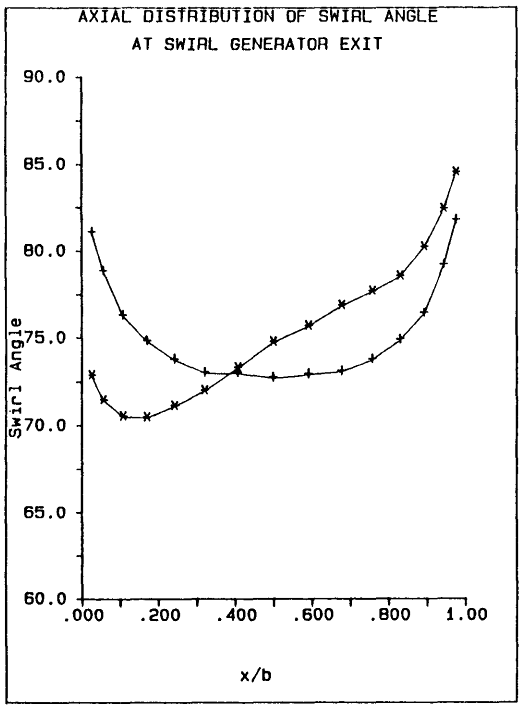

2000 RPM

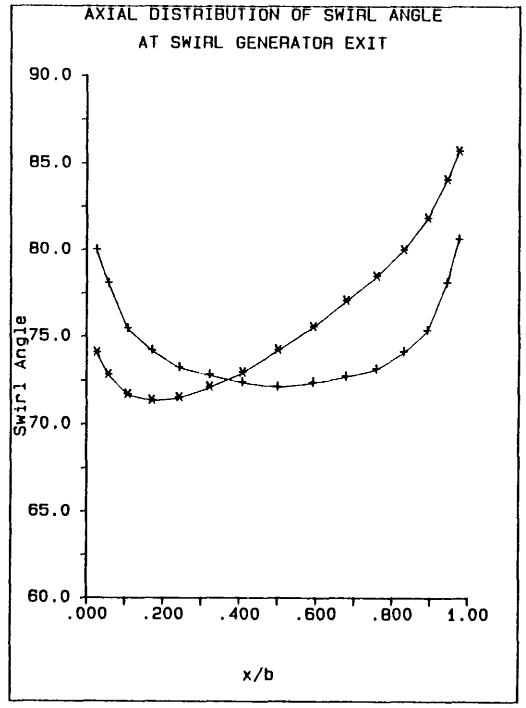

4000 RPM

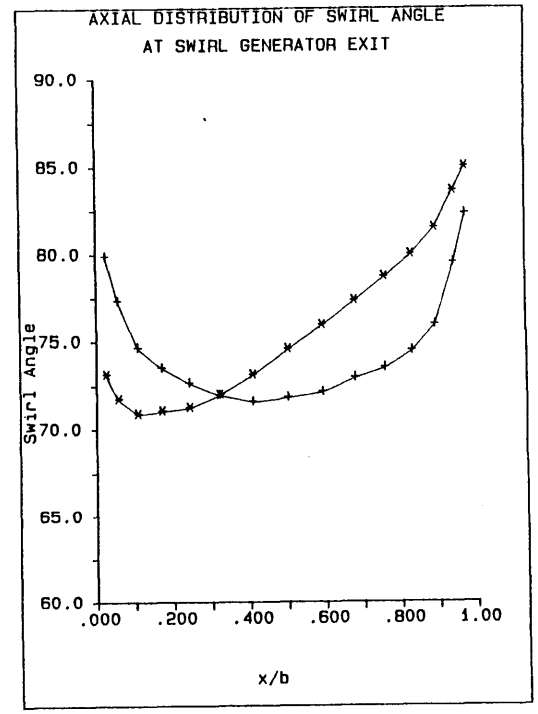

6000 RPM

+ Undistorted

* Distorted

Fig. 4.8 Comparison of "Undistorted" and "Distorted" Discrete-Passage Diffuser Inlet Axial Distributions of Swirl-Angle at the Rotating-Stall Threshold.

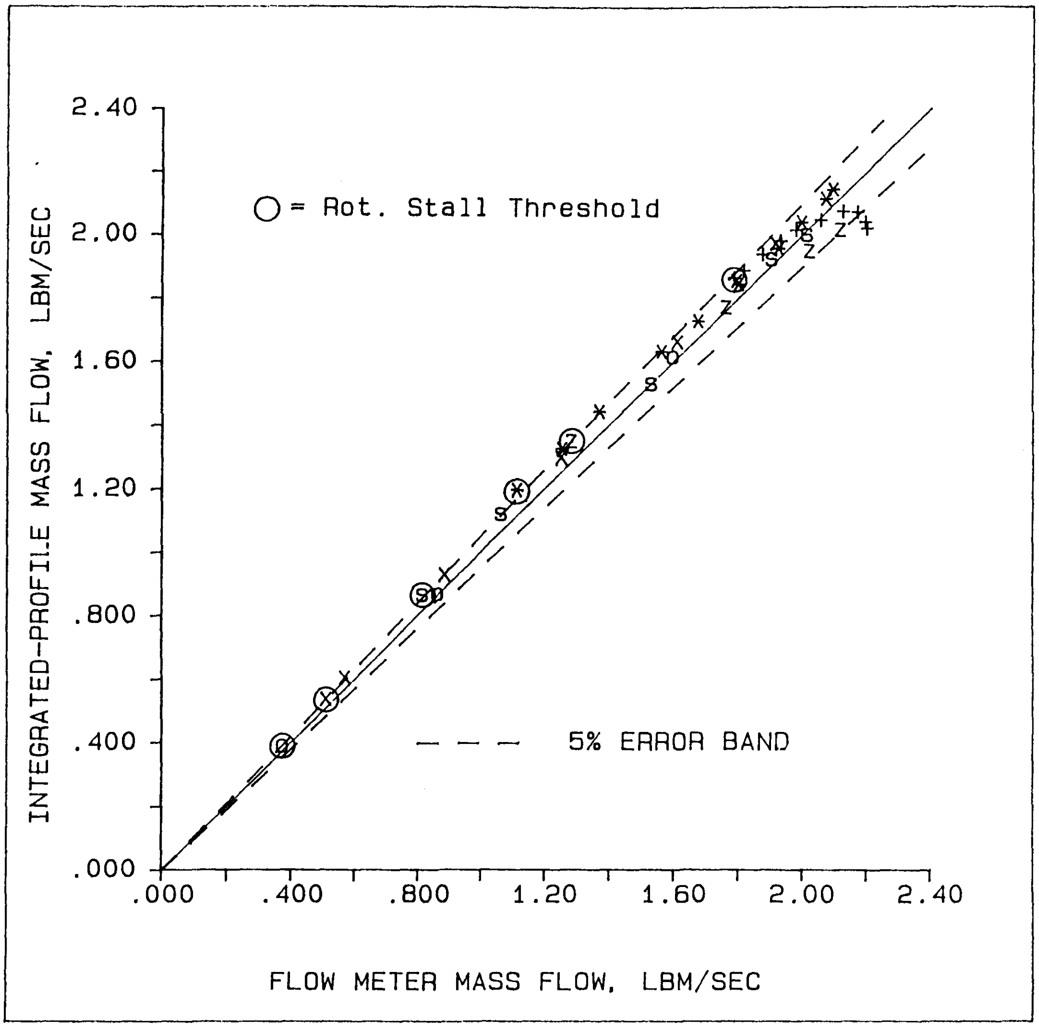

Fig. 4.9 Mass-Flow Continuity Check For Undistorted and Distorted Flow-Field Data Shown in Figures 4.1 Through 4.8

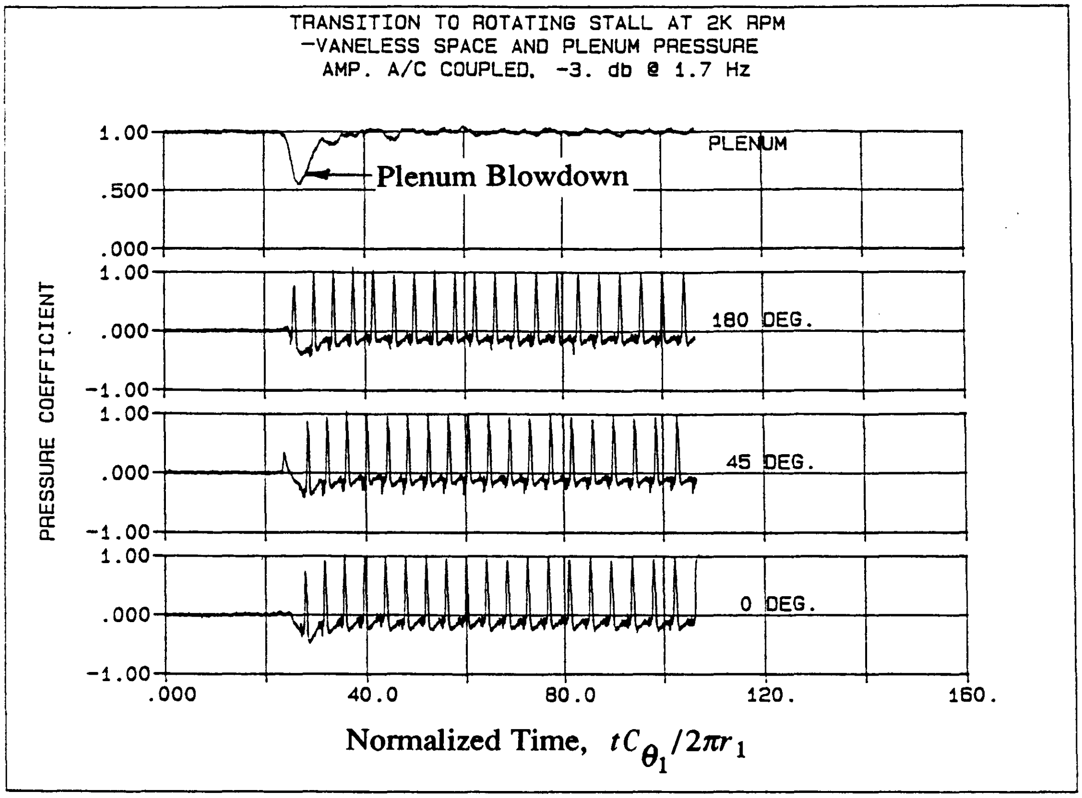

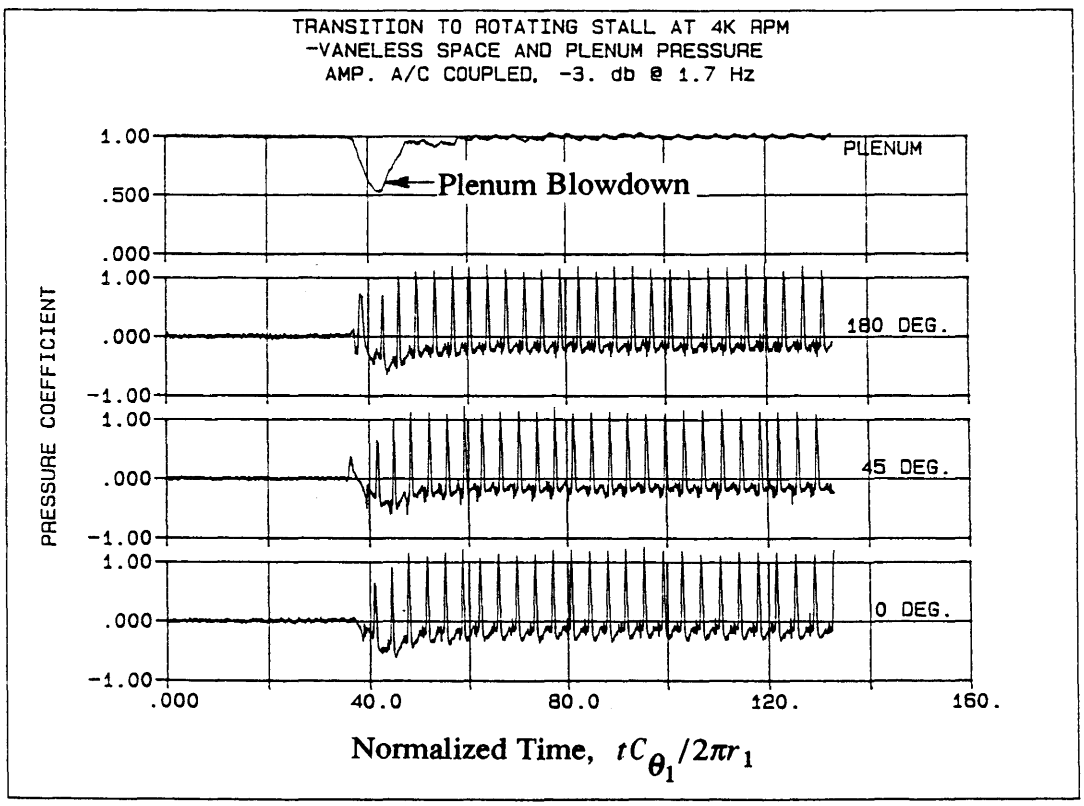

Fig. 4.10 Vaneless Space and Main Plenum Static Pressure During Transition to Rotating Stall (transducers in vaneless space at θ=0, 45, and 180 degrees)

CHAPTER 5

DISCRETE-PASSAGE DIFFUSER DATA ANALYSIS AND DISCUSSION

5.1 Diffuser Pressure Recovery Performance Parameters

To quantify the diffuser performance and relate it to the diffuser inlet conditions, appropriate diffuser performance parameter(s) must be defined and the inlet conditions must be quantified.

The most widely used and useful diffuser performance parameter is the pressure recovery coefficient, defined as the ratio of the diffuser static pressure rise to the diffuser inlet dynamic pressure:

$$Cpr \equiv \frac{P_{st2} - P_{st1}}{P_{t1} - P_{st1}} \tag{5.1}$$

This parameter indicates what fraction of the dynamic pressure of the flow at the inlet to the diffuser is converted into static pressure by the diffuser. For an ideal flow (isentropic, one-dimensional), the maximum value this coefficient can theoretically reach is unity if the flow is decelerated to zero velocity by the diffuser. In such a case, the entropy and total pressure of the flow through the diffuser would be constant and the static pressure at the diffuser exit would be equal to the total pressure at the diffuser inlet. In the case of a real diffuser of finite area ratio, the value of Cpr is less than unity. Other factors which could reduce the diffuser pressure recovery include viscous effects, separation, and the effect of non-uniform velocity as will be shown in section 5.4

Another useful diffuser performance parameter (as discussed in [61] for example) is the diffuser effectiveness, defined as the ratio of the actual pressure recovery coefficient to the theoretical diffuser pressure-recovery coefficient for that particular geometry:

$$\eta_{diff} \equiv \frac{Cpr}{Cpr_{th}} \tag{5.2}$$

The theoretical pressure recovery coefficient, Cpr_{th}, gives the level of pressure recovery which the diffuser of the given area ratio would attain in the case of isentropic one-dimensional flow. This parameter eliminates the direct effect of area ratio, thereby giving a better indication of the fluid dynamic qualities of the diffuser than does Cpr. For non-ideal flows, η_{diff} can take on a range of values, including the possibility of values greater than unity in cases where the diffuser inlet velocity profile is non-uniform as will be discussed in section 5.4.

In the case of a diffuser with uniform inlet conditions, there is no ambiguity in as to the interpretation of definitions 5.1. and 5.2. For the case of non-uniform conditions however, an appropriate representation of the diffuser inlet total pressure must be made. The following section addresses the problem of defining the diffuser inlet conditions in the case of non-uniform diffuser inflow.

5.2 Diffuser Inlet Average and Distortion Flow-Field Parameters

Previous investigators have presented diffuser pressure recovery performance data based on various different definitions of the diffuser inlet dynamic pressure. Masuda et al. [43] investigated the behavior of uniform shear flow in individual channel diffusers and defined the pressure recovery coefficient in terms of the diffuser inlet mass-averaged dynamic pressure while Wolf and Johnston [63], also investigating the influence of non-uniform inlet profiles on the performance of two-dimensional diffusers, based the diffuser inlet dynamic pressure on the area averaged velocity. Bhinder et al. [1], [6] apparently based the definition of pressure recovery on the spatially-averaged diffuser inlet dynamic pressure. In the extensive compilation of channel diffuser performance data by Runstadler et al. [50], the inlet flow was modeled as a potential core with boundary layers and the diffuser Cpr was based on the potential core total pressure as measured at the diffuser throat centerline. Dutton et al. [15] also based the definition of Cpr on the diffuser throat centerline total pressure in their investigation of the performance of radial vaned diffusers. These different methods of specifying the diffuser performance make the interpretation, comparison, and generalization of the data of the different investigators difficult or impossible.

5.2.1 Definition of Inlet Total Pressure

The static pressure at the diffuser inlet and exit is generally quite uniform and the problem of defining the pressure recovery is really one of assigning a relevant value of total pressure to the non-uniform diffuser inlet flow. This can be addressed by asking the question: given a generally non-uniform flow entering the diffuser, what is the maximum static pressure which can possibly be attained by the flow (without any external work or heat interactions)? This is the pressure which would be attained in a reversible, adiabatic, zero work process that ends in a uniform zero-velocity state. Such a process conserves the net thermodynamic availability [29] of the flow ($\dot{\Psi} = const.$), and an appropriate designation of the final total pressure attained is the "availability averaged" total pressure (P_{t_ψ}). An extensive discussion of such a definition of a "mean" total pressure for general non-uniform internal flows for which a physically meaningful measure of the losses is desired is given by Livesey and Hugh [42].

An expression for P_{t_ψ} can be derived by considering a steady, reversible-adiabatic transition process from a non-uniform flow (at say station i) to a uniform flow (station ii). In this case, the net entropy flux at ii is equal to the net entropy flux at i. Thus, assuming that the local properties of the flowing fluid can be specified in terms of bulk-flow states as defined by Gyftopoulos and Beretta [29],

$$\int_{i} s(\rho_{st}\vec{V}\cdot\vec{n})dA = \dot{m}s_{ii} \tag{5.3}$$

If we take the flow to be a simple one-component fluid, the Gibbs relation combined with the definition of enthalpy gives the relation $Tds = dh - vdP$. For a perfect gas (equation of state $Pv = RT$), this can be written as:

$$ds = C_p\frac{dT_t}{T_t} - R\frac{dP_t}{P_t} \tag{5.4}$$

If the stagnation temperature is uniform (as is closely the case in practice for adiabatic duct flows), equation 5.4 can be integrated from a reference state giving:

$$s - s_{ref} = R\,(\ln P_{t_{ref}} - \ln P_t) \tag{5.5}$$

Substituting equation 5.5 into 5.3 with $P_{tii} = P_{t_\psi}$, and assuming axisymmetric flow, an expression for P_{t_ψ} at the diffuser inlet is obtained:

$$P_{t_{\psi_1}} = exp\left[\frac{\int_0^b \ln(P_{t1})\rho_{st1}V_{r1}2\pi r_1 dx}{\int_0^b \rho_{st1}V_{r1}2\pi r_1 dx}\right] \tag{5.6}$$

where axisymmetric flow has been assumed.

The diffuser pressure recovery coefficient is then given by equation 5.1 with P_{t1} replaced by $P_{t_{\psi_1}}$ according to equation 5.6:

$$Cpr_{\psi_1} \equiv \frac{P_{st2} - P_{st1}}{P_{t_{\psi_1}} - P_{st1}} \qquad 5.7$$

The denominator of 5.7 can be defined as the diffuser inlet availability-averaged dynamic pressure. In the case of the present diffuser tests, where the diffuser-inlet profile data is available at discrete points across the diffuser inlet, the integrals in 5.6 were approximated using the trapezoidal rule.

The diffuser inlet swirl angle and Mach number are also parameters which are relevant to the evaluation of the diffuser performance. Since these are also in general non-uniform across the diffuser inlet, physically relevant "average" values must be defined.

5.2.2 Inlet Swirl Angle

The diffuser-inlet "average" flow angle was defined in terms of the tangential and radial mass-averaged velocities at the diffuser inlet:

$$\bar{\alpha}_1 \equiv tan^{-1}\left[\frac{\bar{V}_{\theta 1}}{\bar{V}_{r1}}\right] \qquad 5.8$$

where

$$\bar{V}_{\theta 1} = \frac{\int_0^b \rho_1 V_{r1} V_{\theta 1} 2\pi r_1 dx}{\int_0^b \rho_1 V_{r1} 2\pi r_1 dx} \qquad 5.9$$

and

$$\bar{V}_{r1} = \frac{\int_0^b \rho_1 V_{r1} V_{r1} 2\pi r_1 dx}{\int_0^b \rho_1 V_{r1} 2\pi r_1 dx} \qquad 5.10$$

Since the tangential and radial mass-averaged velocities represent the tangential and radial momentum of the diffuser inlet flow, the average flow angle as given by equation 5.8 is termed the "momentum-average" flow angle.

5.2.3 Inlet Mach Number

The diffuser inlet average Mach number was defined as in [42] to maintain consistency between the diffuser inlet static pressure and the availability averaged total pressure:

$$\bar{M}_1 = \sqrt{\frac{2}{\gamma-1}\left\{\left[\frac{P_{t\psi_1}}{P_{st\,1}}\right]^{\frac{\gamma-1}{\gamma}} - 1\right\}} \qquad 5.11$$

5.2.4 Inlet Mass, Momentum, and Kinetic Energy Deficit and Skew Parameters

In addition to the average diffuser-inlet flow-field quantities described above, diffuser inlet mass, momentum, and kinetic-energy flux "deficit" and "skew" parameters were defined to quantify the severity of the inlet flow field non-uniformity. These are:

mass-flux deficit:

$$\sigma_m \equiv \frac{\delta_m}{b} \qquad 5.12a$$

where

$$\delta_m = \frac{\int_0^b \left[(\rho V_r)_{max} - \rho V_r\right] 2\pi r_1 dx}{(\rho V_r)_{max} 2\pi r_1} \qquad 5.12b$$

The parameter δ_m is essentially the displacement thickness at the diffuser inlet and gives the fraction of the mass flow "lost" relative to the mass flow which would have been attained if the profile were uniform with a value of velocity and flow angle corresponding to the local maximum value of mass flux within the diffuser entrance. Analogous "deficit" parameters can also be defined for the momentum and kinetic energy flows:

momentum-flux deficit:

$$\sigma_p \equiv \frac{\delta_p}{b} \qquad 5.13a$$

where

$$\delta_p = \frac{\int_0^b \left[(\rho V_r V)_{max} - \rho V_r V\right] 2\pi r_1 dx}{(\rho V_r V)_{max} 2\pi r_1} \qquad 5.13b$$

δ_p is analogous to a momentum thickness.

The kinetic-energy-flux deficit can be defined as:

$$\sigma_{ke} \equiv \frac{\delta_{ke}}{b} \qquad 5.14a$$

where

$$\delta_{ke} = \frac{\int_0^b \left[(\rho V_r V^2)_{max} - \rho V_r V^2\right] 2\pi r_1 dx}{(\rho V_r V^2)_{max} 2\pi r_1} \qquad 5.14b$$

δ_{ke} can be viewed as being analogous to a kinetic energy thickness.

Profile skew parameters were also defined to indicate the extent of asymmetry of the inlet flow field relative to the diffuser radial center plane. These parameters were defined in terms of the axial position which divides the diffuser inlet width b into two equal flows of mass, momentum, or kinetic energy (i.e. the center of mass, momentum, or kinetic energy flow). The offset of these positions relative to the diffuser center plane ($x = b/2$), expressed as a fraction of the maximum possible offset ($b/2$), defines the skew parameters:

mass-flux skew:

$$\xi_m \equiv \frac{(x_m^* - b/2)}{b/2} \qquad 5.15a$$

where x_m^* is defined by:

$$\int_0^{x_m^*} \rho V_r 2\pi r_1 dx = \int_{x_m^*}^b \rho V_r 2\pi r_1 dx \qquad 5.15b$$

momentum-flux skew:

$$\xi_p \equiv \frac{(x_p^* - b/2)}{b/2} \qquad 5.16a$$

where x_p^* is defined by:

$$\int_0^{x_p^*} \rho V_r V 2\pi r_1 dx = \int_{x_p^*}^b \rho V_r V 2\pi r_1 dx \qquad 5.16b$$

and kinetic-energy-flux skew:

$$\xi_{ke} \equiv \frac{(x_{ke}^{*} - b/2)}{b/2} \qquad 5.17a$$

where x_{ke}^{*} is defined by:

$$\int_0^{x_{ke}^{*}} \rho V_r V^2 2\pi r_1 dx = \int_{x_{ke}^{*}}^{b} \rho V_r V^2 2\pi r_1 dx \qquad 5.17b$$

The skew parameters have a value of zero for any flow field which is symmetrical about the diffuser center plane and a value of ±1.0 in the hypothetical limiting case when all of the flow is concentrated in an infinitesimally thin layer at one of the vaneless-space walls at the test diffuser inlet.

5.2.5 Inlet Flow Angle Non-Uniformity Parameters

Since the flow angle is a basic feature of the diffuser inlet flow, diffuser inlet flow angle non-uniformity and skew parameters were also defined. The flow angle non-uniformity was represented as the root mean square (*rms*) deviation of the flow angle from the momentum-averaged value:

$$\alpha_n = \sqrt{\frac{1}{b}\int_0^{b} (\alpha - \bar{\alpha})^2 dx} \qquad 5.18$$

while the flow-angle skew was defined as the difference between the area averaged flow angles computed over half of the diffuser inlet width (*b*/2) on each side of the diffuser center plane:

$$\alpha_s = \frac{2}{b}\left[\int_0^{b/2} \alpha\, dx \; - \; \int_{b/2}^{b} \alpha\, dx\right] \qquad 5.19$$

5.2.6 Range of Diffuser Inlet Conditions Examined

The range of diffuser inlet conditions achieved in the present investigation without cross-flow injection/suction is shown in table 5.1 in terms of the average and distortion flow-field parameters defined above. These results correspond to the data shown in figures 4.1 through 4.4. The range of diffuser inlet flow parameters achieved with cross-flow injection, corresponding to the profiles shown in figures 4.5 and 4.6, is shown in table 5.2.

Although data on the exit flow field of the actual matching impeller for the present test diffuser is not available, the range of blockage (equation 5.2a) achieved in the present experiments includes that produced by a typical centrifugal compressor impeller. For example, Mishina et al. [45] measured the exit flow field axial profiles for a range of impellers, all with an exit back-sweep blade angle of 15° but with different hub and shroud contours, exit b/r ratios, and blade loading distributions. The range of blockage for all of the impeller design point exit profile data given in [45] was calculated (according to equation 5.12a) to be from 25% to 33%. As can be seen from tables 5.1 and 5.2, this range of blockage is included in the present experiments. In another example, using the data provided by Kenny [38] for a 6:1 pressure ratio impeller centrifugal impeller, a blockage of 37% was calculated. This is slightly above the range achieved in the present experiments but should be attainable with an increase of cross-flow injection. Since the lowest level of blockage achieved in the present experiments was 13.8%, it can be concluded that the present test apparatus achieves a range of blockage up to and below that of typical conventional centrifugal compressor impellers.

The following section discusses the dependence of the performance and stability of the present radial discrete passage diffuser on the diffuser inlet distortion parameters.

5.3 Influence of Diffuser Inlet Flow Angle, Flow-Field Distortion, and Mach Number on Pressure Recovery and Stable Flow Range

5.3.1 Influence of Inlet Flow Angle and Distortion on Diffuser Pressure Recovery

For an isentropic, quasi-one-dimensional flow through a discrete-passage diffuser, the diffuser inlet flow angle has a direct effect on the overall diffuser pressure recovery. This can be seen simply in the case of incompressible (low Mach number) flow for which the ideal pressure recovery coefficient is a function of the velocity ratio across the diffuser: $Cpr_{\text{ideal}} = 1 - \left[\frac{V_2}{V_1}\right]^2$. In this idealized case, the velocity ratio is obtained directly from continuity which gives, assuming that the diffuser exit flow angle does not depend on the inlet flow angle (as would be the case for a diffuser of infinite solidity), $\frac{V_2}{V_1} = const. \times \cos \alpha_1$. In this idealized case, the overall diffuser pressure recovery coefficient increases monotonically with increasing inlet flow angle, approaching a value of unity as the inlet flow angle approaches 90 degrees.[1]

For the case of the present experiments with the General Electric discrete-passage diffuser (with 30 passages), the overall diffuser pressure recovery coefficient Cpr_{ψ_1} as defined by equation 5.7, was plotted as a function of the diffuser inlet momentum-averaged flow angle as defined by equation 5.8, along curves of constant rotor speed from choke to stall as shown in figure 5.1. The stall points are circled in this figure. This figure contains all of the operating points with undistorted and distorted diffuser inlet profiles as quantified in tables 5.1 and 5.2 respectively and shown in figures 4.1, 4.2, 4.5, and 4.6. From these results it can be concluded that stall of the General Electric discrete passage diffuser occurs at a critical momentum-averaged flow angle and at a corresponding critical value of Cpr_{ψ_1}, independent of the inlet flow-field distortion (the scatter of the flow-angle measurements in figure 5.1 approaches the resolution limits of the present instrumentation). It is also seen that the pressure recovery coefficient Cpr_{ψ_1} correlates well with the momentum averaged inlet flow angle over most of the diffuser operating range, with Cpr_{ψ_1} increasing monotonically with increasing inlet flow angle.

For comparison, figure 5.2 shows the same data as used in figure 5.1 but plotted in terms of a pressure recovery coefficient based on the peak value of the diffuser inlet dynamic pressure as measured across the diffuser inlet width b:

$$Cpr_a \equiv \frac{P_{st2} - P_{st1}}{P_{t1}(x) - P_{st1}} \qquad 5.20$$

(note that the momentum averaged flow angle is still used in figure 5.2). This definition of Cpr is analogous to that based on the diffuser inlet potential core dynamic pressure as used by Runstadler et al. [50] and other investigators. As can be seen from figure 5.2, an apparent sensitivity of the diffuser pressure recovery to inlet distortion is now observed, with a decrease in the pressure recovery with increased inlet distortion. This trend is to be expected since the inlet flow availability-averaged total pressure

[1]This is in contrast to the ideal behavior of a parallel-wall vaneless diffuser for which the pressure recovery coefficient depends only on the square of the diffuser inlet-to-exit radius ratio: $Cpr_{ideal} = 1 - \left[\frac{r_1}{r_2}\right]^2$

decreases with respect to the value of total pressure at the peak of the diffuser inlet total pressure profile as the inlet distortion is increased. As a result, the denominator of 5.20 becomes artificially high when the diffuser inlet flow field is distorted, unjustly penalizing the diffuser.

Similarly, the data used to obtain figure 5.1 also indicates a sensitivity of the diffuser pressure recovery coefficient to inlet distortion if the pressure recovery coefficient is based on the diffuser inlet area-averaged dynamic pressure.This is shown in figure 5.3. This definition of Cpr corresponds to that used by Al-Mudhafar et al. [1] and, assuming uniform static pressure across the diffuser inlet, is given by:

$$Cpr_b \equiv \frac{P_{st2} - P_{st}}{\check{P}_{t1} - P_{st1}} \qquad 5.21$$

were in the present experiments,

$$\check{P}_{t1} = \frac{1}{b}\int_0^b P_{t1}dx \qquad 5.22$$

In this case, as can be seen from figure 5.3, the increase in diffuser inlet flow distortion actually results in an apparent increase in diffuser pressure recovery.

As discussed above, another common approach to quantifying the diffuser pressure recovery performance is to define the diffuser pressure recovery coefficient in terms of a dynamic head based on the diffuser inlet area-averaged velocity (see Wolf and Johnston [63] for example):

$$Cpr_c \equiv \frac{P_{st2} - P_{st1}}{\frac{1}{2}\rho\check{V}_1^2} \qquad 5.23$$

In the present case, with the previously stated assumptions of axisymmetric flow and axially-uniform static pressure:

$$\check{V}_1 = \frac{1}{b}\int_0^b V_1 dx \qquad 5.22$$

Taking the density in 5.23 to be the diffuser inlet area-averaged static density, an apparent sensitivity of the diffuser pressure recovery performance to inlet distortion is also observed using this definition as shown in figure 5.4. In this case however, because static density is used in the definition of the pressure recovery coefficient, it is to be expected that variations in the diffuser inlet Mach number also play a role in the scatter of the data as seen in figure 5.4.

Comparing figures 5.1 through 5.4, it is seen that the common pressure-recovery parameters which have and continue to be used by various investigators for correlating diffuser performance data lead to different conclusions as to the effect of inlet distortion on diffuser pressure recovery. Of the four main definitions of Cpr considered above however, Cpr_{ψ} is the most physically appropriate for use as a diffuser pressure recovery performance parameter because it is based on a comparison of the diffuser pressure recovery to the best possible which could be achieved by an arbitrary zero-work, adiabatic device with the given inlet flow conditions. Data such as presented in [6] (showing a monotonic decrease of diffuser pressure recovery with increased inlet profile-skew) is thus of little use since the definition of the diffuser inlet reference total pressure used in the definition of Cpr was not given.

5.3.2 Effect of Inlet Mach Number on Diffuser Performance

In addition to inlet flow angle and inlet distortion, the diffuser inlet Mach number is also expected to have an effect on the diffuser pressure recovery, based on the idealized case of isentropic flow. This can be seen in figure 5.5 which shows that for isentropic quasi-one-dimensional flow, the diffuser pressure recovery coefficient monotonically increases with increasing diffuser inlet Mach number. The reason for this is that as the diffuser inlet Mach number is increased, the static density ratio across the diffuser (ρ_{st2}/ρ_{st1}) increases, resulting in a decrease in the velocity ratio across the diffuser (V_2/V_1) relative to that which would occur if the static density remained constant.

Since in the present experiments the diffuser inlet Mach number decreases as the flow rate through the swirl generator is decreased at constant rotor speed (because of the forward-leaning blading), the maximum average diffuser inlet Mach number achieved at stall was only 0.72 without injection/suction and 0.54 with cross-flow injection as shown in table 5.3. The diffuser inlet average flow angle can however be increased for any given rotor operating point by means of suction through the vaneless space slots as discussed in section 3.3.2. Thus, to determine the effect of inlet Mach number on the diffuser pressure recovery as the Mach number approaches unity, two rotating-stall threshold operating points were obtained with theoretical suction flow rates of 5% and 10% of the rotor through-flow rate. The average diffuser inlet Mach numbers at these two operating points were 0.86 and 0.95 respectively as defined by equation 5.11 and the corresponding momentum-averaged flow angles were 73.7° and 73.9° respectively. These are in the same critical-angle range as measured for all of the lower Mach number cases shown in table 5.3 (73.2° to 74.1°). The diffuser inlet absolute and radial Mach number and swirl angle distributions for these operating points are shown in figure 5.6 and the corresponding mean and distortion parameters are given in table 5.4.

The effect of $\bar{M}_1$ on the diffuser pressure recovery (Cpr_{ψ_1}) is shown in figure 5.7. This figure contains the high Mach number stall threshold data from table 5.4 and also all of the lower Mach number rotating stall threshold data from the distortion study as given in table 5.3. As can be seen from figure 5.7, the effect of diffuser inlet Mach number on the actual diffuser pressure recovery is minimal but a definite trend is detectable. Below $\bar{M}_1 \approx 0.4$, Cpr_{ψ_1} increases with $\bar{M}_1$, qualitatively as in the ideal (isentropic) case. At the higher values of $\bar{M}_1$ over the range investigated in the present experiments, Cpr drops off slightly with increasing $\bar{M}_1$. This is in contrast to the isentropic case and suggests that the relative loss, $\Delta P_{t1-2}/(P_{t_{\psi_1}} - P_{st1})$, increases with Mach number over the range investigated.

5.4 Effect of Flow-Field Mixing on the Diffuser Pressure Recovery Performance

5.4.1 Idealized Cases of Mixing in Diffusers

The effect of mixing of the diffuser inlet flow field on the diffuser pressure recovery was investigated to determine what role mixing may have in the observed insensitivity of the diffuser performance to inlet distortion. Three idealized cases were considered:

a.) No mixing
b.) Complete mixing in a constant-area mixing section at the diffuser inlet followed by isentropic quasi-one-dimensional flow in an increasing-area section (this approximates the case of very rapid mixing at the actual diffuser inlet)
c.) Increasing-area section in which no mixing takes place followed by a constant-area mixing section in which complete mixing occurs.

The following idealizations were made in the analysis:

- No wall shear stress

- The flow is completely mixed out at the exit of the mixing sections (uniform profile)
- The flow is irrotational in the diverging sections
- The flow is steady and incompressible

In each of the three cases, a distorted inlet flow was represented by a step velocity profile with half of the inlet at a uniform velocity vj (the "jet" velocity) and the other half of the inlet at a uniform velocity vw (the "wake" velocity). The analysis is straightforward (the continuity and momentum equations are applied to the constant area mixing sections and the continuity and Bernoulli equations are applied to the increasing-area sections) and will not be repeated here.

The calculated pressure recovery coefficient (as defined by equation 5.1) is plotted as a function of the inlet velocity distortion parameter 1-vw/vj for several different area ratios for the three cases in figures 5.8a, 5.8b, and 5.8c respectively. In the case of no mixing, the diffuser pressure recovery decreases monotonically with inlet distortion for all area ratios greater than unity. In the case of complete mixing upstream of the diverging section (case b) however, the pressure recovery coefficient increases with inlet distortion at low area ratios but decreases with inlet distortion at higher area ratios. At intermediate area ratios, *Cpr* is relatively insensitive to the inlet distortion. Similarly, in the case C, when the mixing section is placed after the diffuser, there is an area ratio for which the pressure recovery coefficient is insensitive to inlet distortion, although the area ratio (and corresponding pressure recovery) is lower than for the case when the mixing section is placed ahead of the diffuser.

5.4.2 Discrete-Passage Diffuser Pressure Recovery Performance Insensitivity to Inlet Distortion Due to Mixing

The reason for the effect of mixing on diffuser pressure recovery seen in section 5.4.1 can be understood by considering two limiting cases: 1.) a constant area mixing duct by itself and 2.) a constant area mixing duct followed by an ideal diffuser of infinite area ratio. In the first limiting case, with a uniform inlet velocity profile, no change occurs and the static pressure in the duct remains constant (*Cpr*=0). For values of distortion parameter 1-vw/vj greater than zero, conservation of momentum in the mixing process results in a rise in the static pressure across the duct so *Cpr* increases with increasing inlet non-uniformity.

In the second limiting case, with a uniform inlet profile the static pressure remains constant in the constant area mixing section and the downstream ideal diffuser recovers of all of the total pressure at the inlet to the mixing section. The overall Cpr (mixing section plus ideal diffuser) is thus equal to unity. As the inlet velocity distortion parameter is increased, the mixing results in an increase in the static pressure across the mixing duct. However, because of the reduction of the availability-averaged total pressure due to the mixing, the overall rise in static pressure in the mixing duct plus the ideal diffuser must be less than the availability-averaged dynamic pressure at the inlet to the mixing section. Cpr for the mixing section combined with the ideal infinite area ratio diffuser is thus less than one and monotonically decreases with increasing inlet distortion.

For cases where the mixing duct is followed by a diffuser of finite area ratio, the effects described for the two limiting cases combine to various degrees resulting in the behavior seen in figure 5.8b. Where the overall Cpr is insensitive to inlet distortion, at low distortion, most of the pressure rise occurs in the diverging section. As the distortion is increased, the static pressure rise due to mixing increases but because of the reduction of total pressure in the mixing process, the static pressure rise in the diverging section decreases.

Based on the above discussion, the effect of mixing can be seen in the present diffuser data by considering the static pressure distributions along the centerline of a diffuser passage at the rotating stall threshold with undistorted and distorted inlet flow fields as shown in figure 5.9 (see figures 4.7 and 4.8 for corresponding diffuser inlet Mach number and swirl angle profiles). At rotor speeds of 4000 RPM and 6000 RPM, for the cases of high inlet distortion, the static pressure increases more than for the cases of low inlet distortion over the initial portion of the diffuser passage but the static pressure rise for the overall passage is essentially independent of the level of distortion. This behavior is particularly prominent at the highest rotor speed attempted (6000 RPM) where at the throat (ξ/l=0.4), as shown in figure 5.9, the static pressure rise relative to the diffuser inlet was 27% higher for the case of high inlet distortion than for the case of low distortion, although the pressure recovery for the overall diffuser was unaffected by distortion. In the case of the lowest rotor speed (2000 RPM), the static pressure distribution in the diffuser passage from the diffuser inlet to the throat was essentially identical for the high and low distortion cases. In the diverging section of the diffuser downstream of the throat however, the rate of increase of Cpr along the passage was initially greater for the lower distortion case (for $0.4 < \xi/l < 0.6$) and then became greater for the high distortion case (for $\xi/l > 0.6$) so that the overall diffuser Cpr was the same for the low and high distortion cases. The difference between the static pressure distributions in the diffuser passage for the high and low rotor speeds suggests that the degree of mixing in the initial portion of the passage increased as the rotor speed (and Reynolds number) was increased. The Reynolds numbers (based on the diffuser inlet width *b* and the inlet mass-averaged properties) for the low and high distortion cases corresponding to figure 5.9 were:

	Low Distortion	High Distortion
2000 RPM	3.6×10^4	2.6×10^4
4000 RPM	7.6×10^4	6.0×10^4
6000 RPM	1.2×10^5	9.2×10^4

5.4.3 Mixing Enhancement Due to Streamwise Vorticity

The flow angles in the quasi-vaneless space of the test diffuser are such that there is cross-flow across the leading edge cusps over the diffuser operating range. This results in a pressure loading on the cusps as seen from the static pressure distributions in the quasi-vaneless space shown in figures 4.4a through 4.4c. At the sharp edge of each cusp the flow separates and streamwise vorticity is shed into the flow. The strength of this vorticity increases with pressure difference across the cusps. Since streamwise vorticity can play a major role in enhancing mixing, it is interesting to note that the loading across the leading-edge cusps (and therefore the shed vorticity) in the quasi-vaneless space increased in all cases with increased inlet distortion. This can be seen from figure 5.10 which compares the distribution of the static pressure coefficient in the diffuser quasi-vaneless space at the rotating stall threshold corresponding to the pressure distributions along the passage centerline shown in figure 5.9. The difference in loading was most prominent at the maximum rotor speed (6000 RPM) where at low distortion, the pressure coefficients on the suction and pressure surfaces just upstream of the throat were 0.206 and 0.237 respectively while at high inlet distortion they were 0.204 and 0.333 respectively. However, as can be seen from figure 5.10 and also figures 4.4a through 4.4c (which show the variation in the pressure distribution in the quasi-vaneless space in the case of low inlet distortion, from choke to stall), there is significant loading on the leading edge cusps at all operating conditions with a reversal of the loading in the region between the diffuser inlet and the throat. This suggests that although streamwise vorticity resulting from the cross-flow at the leading edge cusps may be advantageous to diffuser performance in the case of a distorted inlet flow, it may result in undesirable losses in the case when the diffuser inlet profile is uniform.

5.5 Discussion of the Stable-Flow Breakdown Phenomena

To demonstrate that the onset of rotating stall as described in section 4.4 and shown in figure 4.10 is triggered by flow instability in the discrete-passage diffuser and not by the rotor, different levels of injection and suction through the vaneless space slots were used so that the diffuser inlet momentum-averaged flow angle reaches the critical value at different rotor operating points as the main throttle is closed, as described in section 3.3.2. This is illustrated in figure 5.11 which shows rotor total-to-static pressure ratio characteristics at several rotor speeds obtained using the vaneless diffuser. The four circled points (labeled *a*, *b*, *c*, and *d*) on the 6000 RPM corrected speed line are rotor operating points corresponding to the onset of rotating stall as detected using the high frequency response pressure transducers in the vaneless space. The stall point at the lowest of these flows (point *a*) corresponds to the case of cross-flow injection through the vaneless space slots. Stall point b was obtained without injection or suction through the slots and points c and d were obtained with progressively increasing suction through the slots. In all four cases, the onset of rotating stall occurred as soon as the diffuser inlet momentum-averaged flow angle reached the critical range shown in figure 5.1 (73.6, 73.2°, 73.7°, and 73.9° for operating points a, b, c, and d respectively). Since each time stall occurred the rotor was operating at a different operating point (as well as on the negatively sloped portion of its total-to-static pressure rise characteristic), it can be concluded that the onset of rotating stall was triggered by the diffuser.

It was also found that if the diffuser inlet flow angle is reduced sufficiently by means of cross-flow injection through the vaneless space slots as the main throttle is closed, overall compression system instability (surge) can occur without the onset of rotating stall. This is illustrated in figure 5.12 which shows the growth of a surge cycle without the onset of rotating stall (note that the pressure fluctuations at the three vaneless space transducers and in the main plenum are all in phase). After stabilization in a surge limit cycle, transition to rotating stall could be achieved by closing the main throttle further. As the rotating stall developed in such a case, the surge mode seen in figure 5.12 was damped out (the plenum pressure became steady) and the rotating stall took on the characteristics shown in figure 4.10. This behavior again supports the conclusion that the diffuser is responsible for the onset of rotating stall since as the throttle is closed starting in a surge limit cycle, the diffuser inlet cycle peak (and time averaged) flow angle is driven into the critical range shown in figure 5.1.

5.6 Summary of Chapter 5

- The influence of the inlet flow field axial distortion on the pressure recovery performance and stability of the 30-passage General Electric discrete-passage diffuser was investigated. It was found that the pressure recovery coefficient defined in terms of the diffuser inlet availability-averaged total pressure correlates with the diffuser inlet momentum-averaged flow angle over the majority of the operating range. Other commonly used representations of diffuser pressure recovery were also examined but these did not result in as tight a correlation of the data.
- The diffuser performance is insensitive to inlet Mach number, contrary to the increase in performance with increased Mach number predicted from a consideration of adiabatic-isentropic quasi-one-dimensional flow. It was hypothesized that the losses increase with Mach number at a rate which just offsets the favorable effect of compressibility on pressure recovery.
- The observed onset of rotating stall is directly linked to flow instability in the discrete-passage diffuser. Rotating stall is triggered at a critical diffuser-inlet "momentum averaged" flow angle and corresponding overall diffuser pressure recovery coefficient based on the availability-averaged diffuser inlet total pressure.
- The effect of mixing on diffuser pressure recovery was considered for several idealized cases. From these results, and from the static pressure distributions along a diffuser passage centerline, it was concluded that mixing plays a major role in the observed insensitivity of the test diffuser performance to inlet distortion. It was suggested that vorticity generation due to the loading on the leading edge cusps may be associated with enhancement of mixing within the diffuser, since loading increases with increased inlet distortion.

Table 5.1- Discrete-Passage Diffuser Inlet Flow Field Parameters Achieved without Injection/Suction (See figures 4.1 and 4.2 for corresponding profiles identified by rotor speed and profile ref. no.)

N (RPM)	Profile Ref. No.	$\bar{M}_1$	$\bar{\alpha}_1$ (Deg.)	σ_m (%)	σ_p (%)	σ_{ke} (%)	ξ_m (%)	ξ_p (%)	ξ_{ke} (%)	α_n (Deg.)	α_s (Deg.)
2000	1	0.702	67.9	13.8	16.6	19.2	0.8	1.9	3.0	2.2	-0.3
2000	2	0.618	68.1	14.0	16.7	19.5	1.0	2.0	3.1	2.0	-0.2
2000	3	0.527	68.4	15.8	18.5	21.1	0.9	1.3	1.8	2.2	0.2
2000	4	0.396	69.5	13.6	16.0	18.2	-0.7	-2.1	-3.3	1.9	0.5
2000	5	0.296	71.1	15.1	20.1	24.4	-3.2	-5.7	-8.0	1.9	-0.1
2000	6	0.214	73.3	17.4	21.4	25.0	-0.2	-0.3	-0.3	2.0	0.0
2000	7*	0.200	74.1	18.5	22.5	26.1	-0.1	0.1	0.2	2.2	-0.1
4000	1	0.907	69.5	16.9	19.5	22.0	-1.3	-1.9	-2.5	2.3	-0.1
4000	2	0.867	69.7	16.2	18.8	21.2	-1.2	-2.0	-2.8	2.2	0.1
4000	3	0.788	70.1	15.4	17.8	20.0	-1.7	-3.0	-4.1	2.1	0.1
4000	4	0.735	70.5	15.6	18.0	20.7	-2.4	-4.2	-5.8	2.0	0.0
4000	5	0.670	70.9	15.4	19.4	23.3	-3.7	-6.0	-8.1	2.0	-0.2
4000	6	0.616	71.3	16.8	21.5	25.7	-3.9	-6.4	-8.6	2.0	-0.3
4000	7	0.575	71.6	17.9	22.1	26.2	-3.6	-6.2	-8.5	2.2	-0.1
4000	8	0.510	72.4	19.2	23.4	27.1	-3.3	-5.0	-6.6	2.2	-0.4
4000	9	0.475	73.0	18.4	22.2	25.6	-2.0	-2.9	-3.8	2.1	-0.3
4000	0*	0.434	73.5	17.0	20.4	23.3	-0.2	-0.4	-0.5	2.0	0.0
6000	1	1.100	72.1	24.8	29.2	33.1	-5.8	-7.8	-9.6	3.6	-1.1
6000	2	1.036	72.3	23.4	27.8	31.9	-5.9	-7.9	-9.7	3.2	-1.1
6000	3	0.978	72.3	22.9	27.5	31.7	-5.8	-7.9	-9.8	2.9	-1.1
6000	4	0.922	72.4	22.1	26.3	30.4	-5.9	-8.0	-9.9	2.8	-1.1
6000	5	0.862	72.5	22.0	26.2	30.0	-5.5	-7.3	-9.0	2.7	-1.1
6000	6	0.814	72.6	20.9	25.0	28.6	-4.9	-6.5	-7.9	2.6	-1.0
6000	7	0.788	72.8	21.3	25.3	28.9	-4.7	-6.1	-7.5	2.5	-1.0
6000	8	0.761	72.9	20.2	24.1	27.6	-4.3	-5.5	-6.7	2.4	-0.9
6000	9	0.735	73.1	19.5	23.3	26.6	-4.1	-5.3	-6.4	2.3	-0.9
6000	0*	0.719	73.2	19.7	23.3	26.5	-4.1	-5.2	-6.2	2.3	-1.0

* Rotating Stall Threshold

Table 5.2- Discrete-Passage Diffuser Inlet Flow Field Parameters Achieved with Distorted Diffuser Inlet Flow Field (See figures 4.5 and 4.6 for corresponding profiles identified by rotor speed and profile ref. no.)

N (RPM)	Profile Ref. No.	$\bar{M}_1$	$\bar{\alpha}_1$ (Deg.)	σ_m (%)	σ_p (%)	σ_{ke} (%)	ξ_m (%)	ξ_p (%)	ξ_{ke} (%)	α_n (Deg.)	α_s (Deg.)
2000	1	0.499	67.0	21.5	26.8	31.2	-14.7	-18.9	-22.2	3.2	-4.6
2000	2	0.280	70.3	28.1	36.7	43.4	-20.5	-27.5	-33.3	3.2	-4.8
2000	3*	0.151	73.3	35.4	43.4	49.6	-27.5	-35.4	-41.2	3.9	-6.0
4000	1	0.832	69.2	22.5	27.0	31.2	-16.9	-20.8	-24.0	3.6	-5.1
4000	2	0.693	68.9	22.9	30.1	36.0	-17.3	-23.1	-28.0	2.8	-4.1
4000	3	0.544	70.4	31.2	39.5	45.9	-23.1	-30.0	-35.7	3.7	-5.6
4000	4	0.411	72.6	27.4	33.6	38.8	-21.1	-26.0	-30.1	3.6	-5.4
4000	5*	0.343	73.8	32.7	39.2	44.5	-25.1	-30.3	-34.7	4.2	-6.3
6000	1	0.903	70.6	32.9	39.9	45.7	-24.8	-30.1	-34.7	4.5	-6.7
6000	2	0.812	71.0	32.6	39.5	45.2	-25.1	-30.6	-35.4	4.4	-6.7
6000	3	0.694	72.0	30.8	37.0	42.4	-23.6	-28.7	-33.1	4.2	-6.3
6000	4*	0.537	73.6	33.9	40.4	45.7	-27.1	-32.7	-37.3	4.3	-6.6

* Rotating Stall Threshold

Table 5.3- Comparison of Discrete-Passage Diffuser Inlet Flow Field Parameters with Distorted and Undistorted Diffuser Inlet Profiles at Rotating Stall Threshold (See figures 4.7 and 4.8 for corresponding Mach number and swirl angle profiles)

N (RPM)		$\bar{M}_1$	$\bar{\alpha}_1$ (Deg.)	σ_m (%)	σ_p (%)	σ_{ke} (%)	ξ_m (%)	ξ_p (%)	ξ_{ke} (%)	α_n (Deg.)	α_s (Deg.)
2000	Undistorted	0.200	74.1	18.5	22.5	26.1	-0.1	0.1	0.2	2.2	-0.1
2000	Distorted	0.151	73.3	35.4	43.4	49.6	-27.5	-35.4	-41.2	3.9	-6.0
4000	Undistorted	0.434	73.5	17.0	20.4	23.3	-0.2	-0.4	-0.5	2.0	0.0
4000	Distorted	0.343	73.8	32.7	39.2	44.5	-25.1	-30.3	-34.7	4.2	-6.3
6000	Undistorted	0.719	73.2	19.7	23.3	26.5	-4.1	-5.2	-6.2	2.3	-1.0
6000	Distorted	0.537	73.6	33.9	40.4	45.7	-27.1	-32.7	-37.3	4.3	-6.6

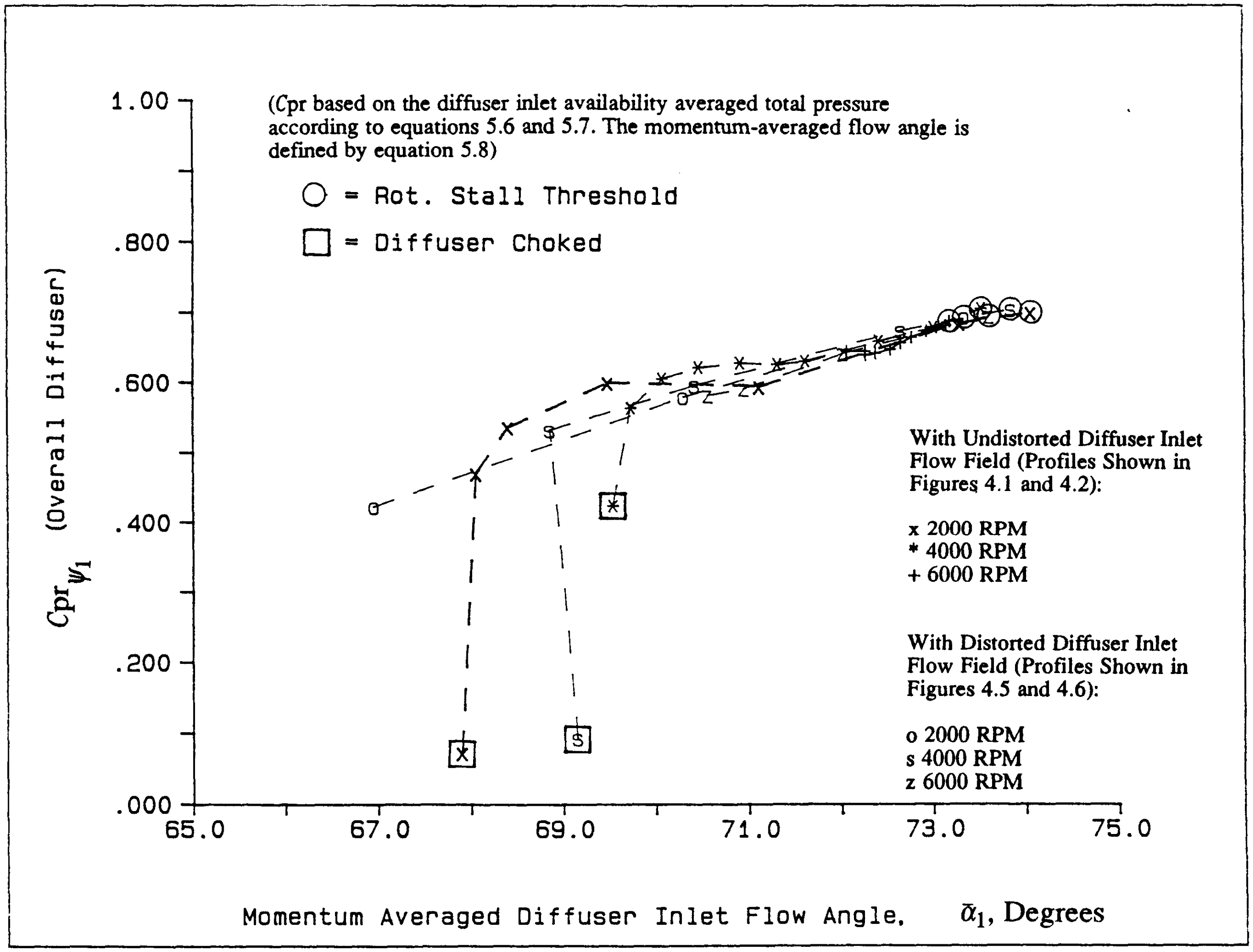

Fig. 5.1 Overall Discrete-Passage Diffuser Pressure Recovery (Cpr_{ψ_1}) as a Function of the Diffuser Inlet Momentum-Averaged Flow Angle

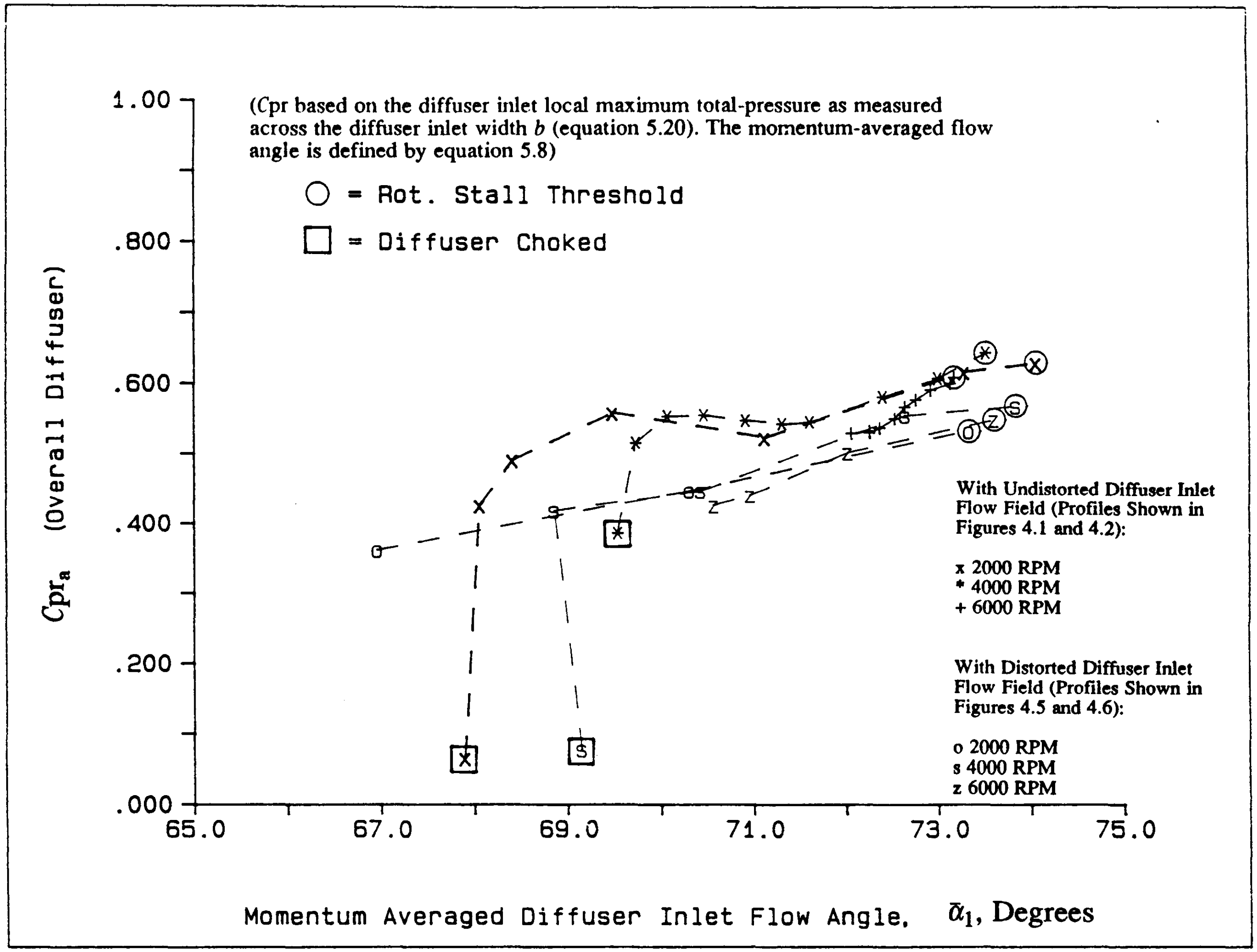

Fig. 5.2 Overall Discrete-Passage Diffuser Pressure Recovery (Cpr_a) as a Function of the Diffuser Inlet Momentum-Averaged Flow Angle

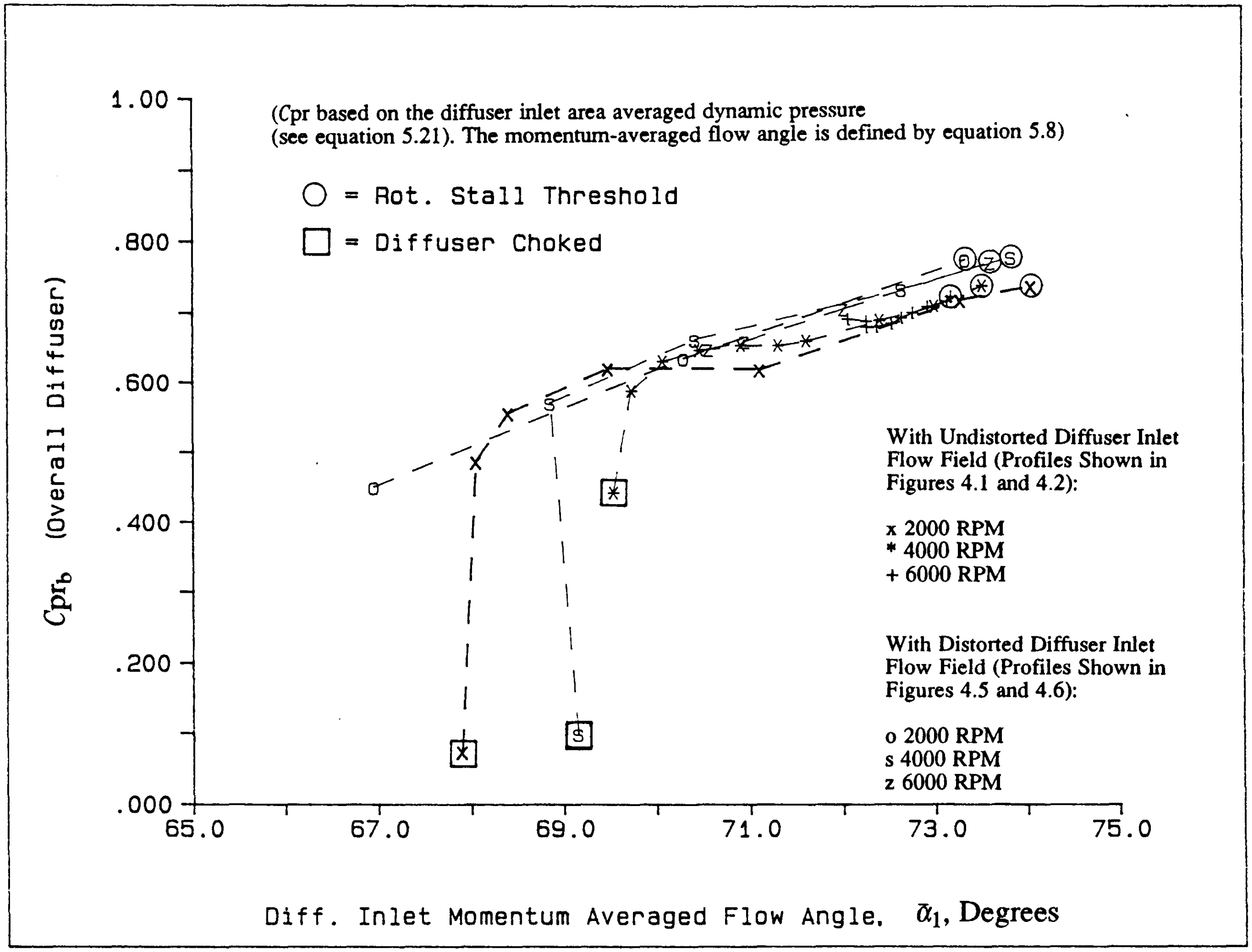

Fig. 5.3 Overall Discrete-Passage Diffuser Pressure Recovery (Cpr_b) as a Function of the Diffuser Inlet Momentum-Averaged Flow Angle

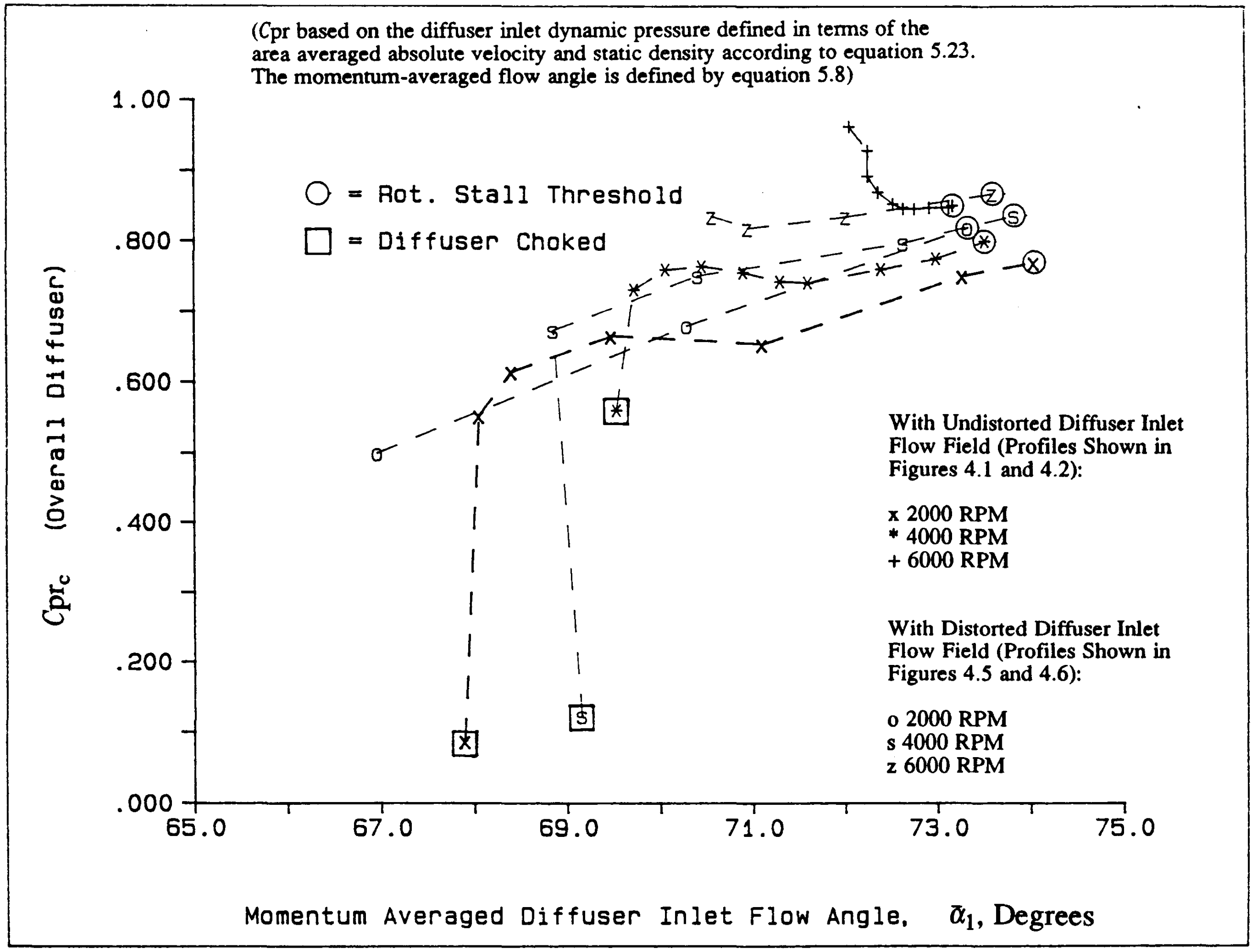

Fig. 5.4 Overall Discrete-Passage Diffuser Pressure Recovery (Cpr_c) as a Function of the Diffuser Inlet Momentum-Averaged Flow Angle

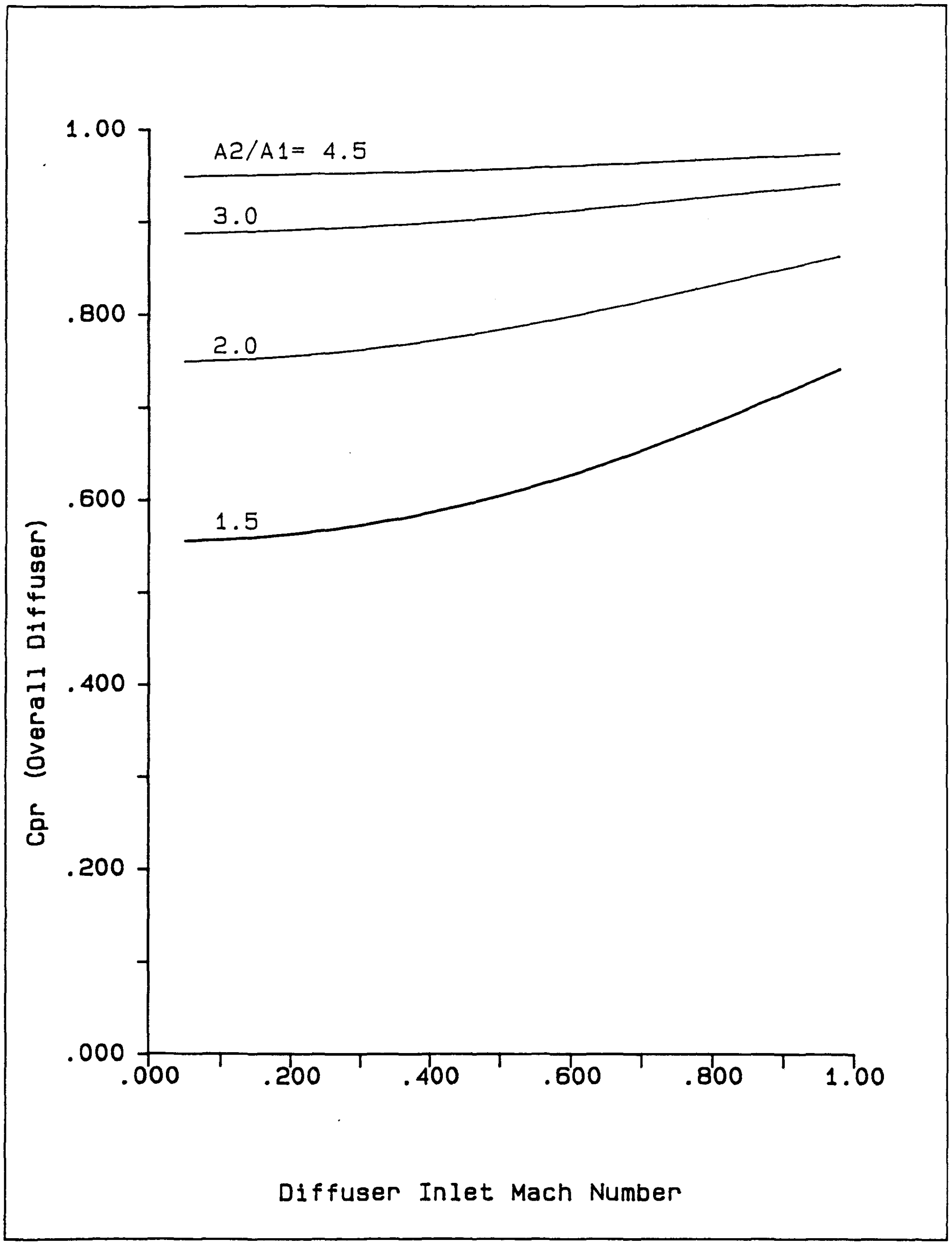

Fig. 5.5 Effect of Inlet Mach Number on Diffuser Pressure Recovery in the Ideal Case of Isentropic Quasi-One-Dimensional Flow

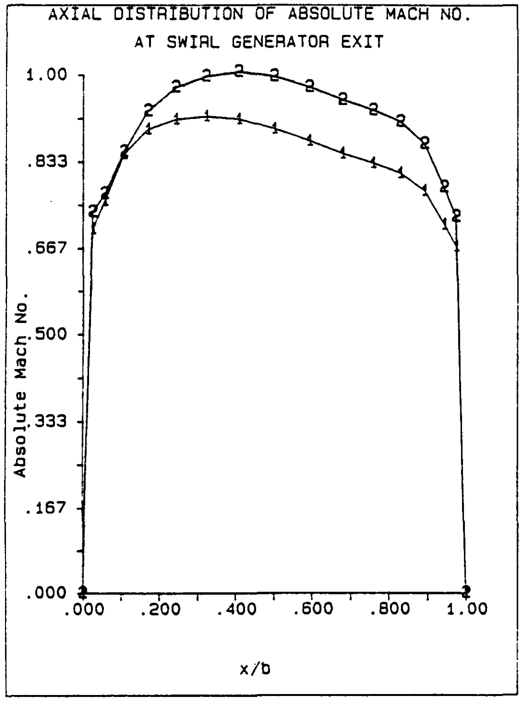

Absolute Mach No.

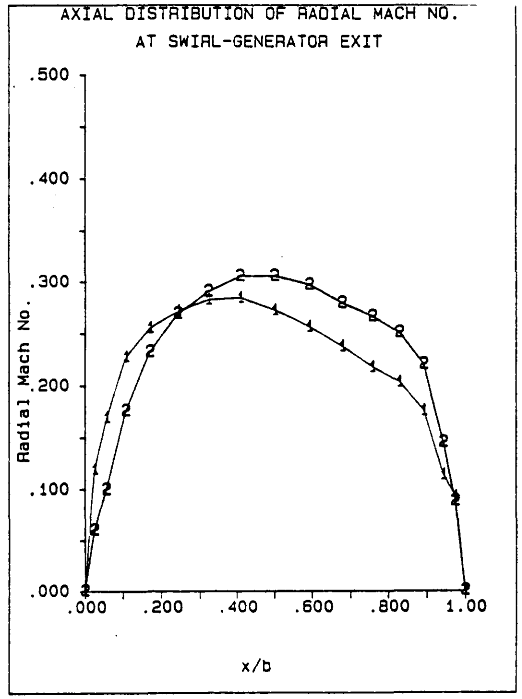

Radial Mach No.

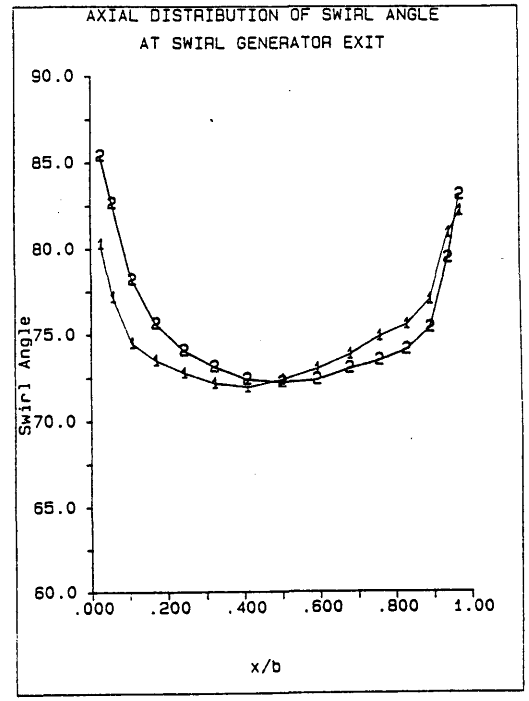

Swirl-Angle

$N = 6000$ RPM

Curves 1: Suction on Slots 3 and 4, $P_3/P_{atm} = 0.74$, $P_4/P_{atm} = 0.74$, $P_{st1}/P_{atm} = 0.81$

Curves 2: Suction on Slot 3, $P_3/P_{atm} = 0.63$, $P_{st1}/P_{atm} = 0.74$

Fig. 5.6 Swirl-Generator Exit Absolute Mach Number, Radial Mach Number, and Swirl-Angle Distributions at Rotating Stall Threshold for High Mach Number Cases Achieved by Means of Suction Through Vaneless Space Slots

Table 5.4- Discrete-Passage Diffuser Inlet Flow Field Parameters for High Mach Number Cases at Rotating Stall Threshold, Achieved Using Suction Through Vaneless Space Slots (See figure 5.6 for corresponding Mach number and swirl angle profiles)

N (RPM)	Profile Ref. No.	$\bar{M}_1$	$\bar{\alpha}_1$ (Deg.)	σ_m (%)	σ_p (%)	σ_{ke} (%)	ξ_m (%)	ξ_p (%)	ξ_{ke} (%)	α_n (Deg.)	α_s (Deg.)
6000	1	0.86	73.7	21.6	25.3	29.0	-7.4	-9.3	-10.9	2.4	-1.8
6000	2	0.95	73.9	22.6	26.4	29.9	1.3	0.2	-0.8	3.1	1.0

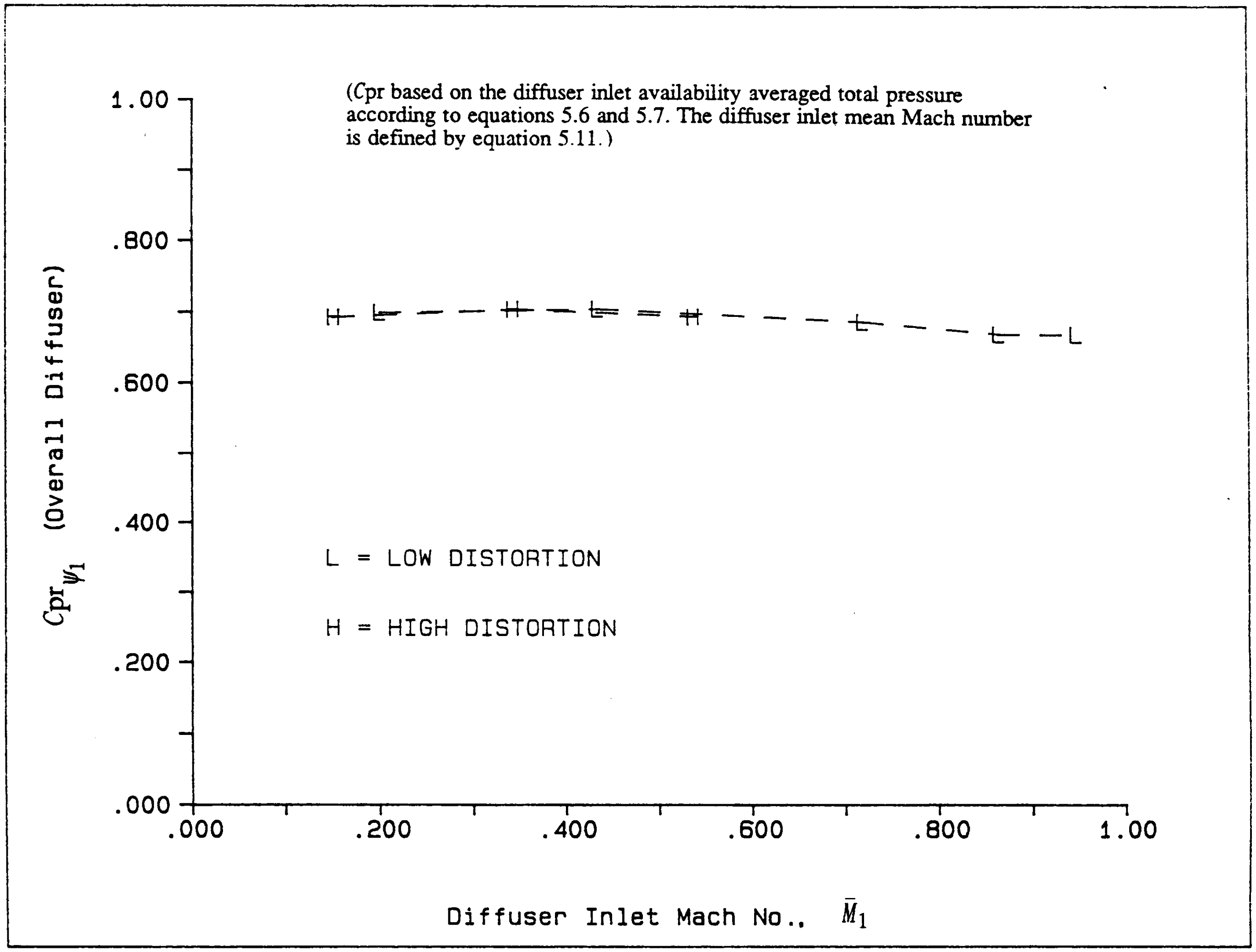

Fig. 5.7 Effect of Diffuser Inlet Mach Number on the Diffuser Peak Pressure Recovery (at Rotating Stall Threshold)

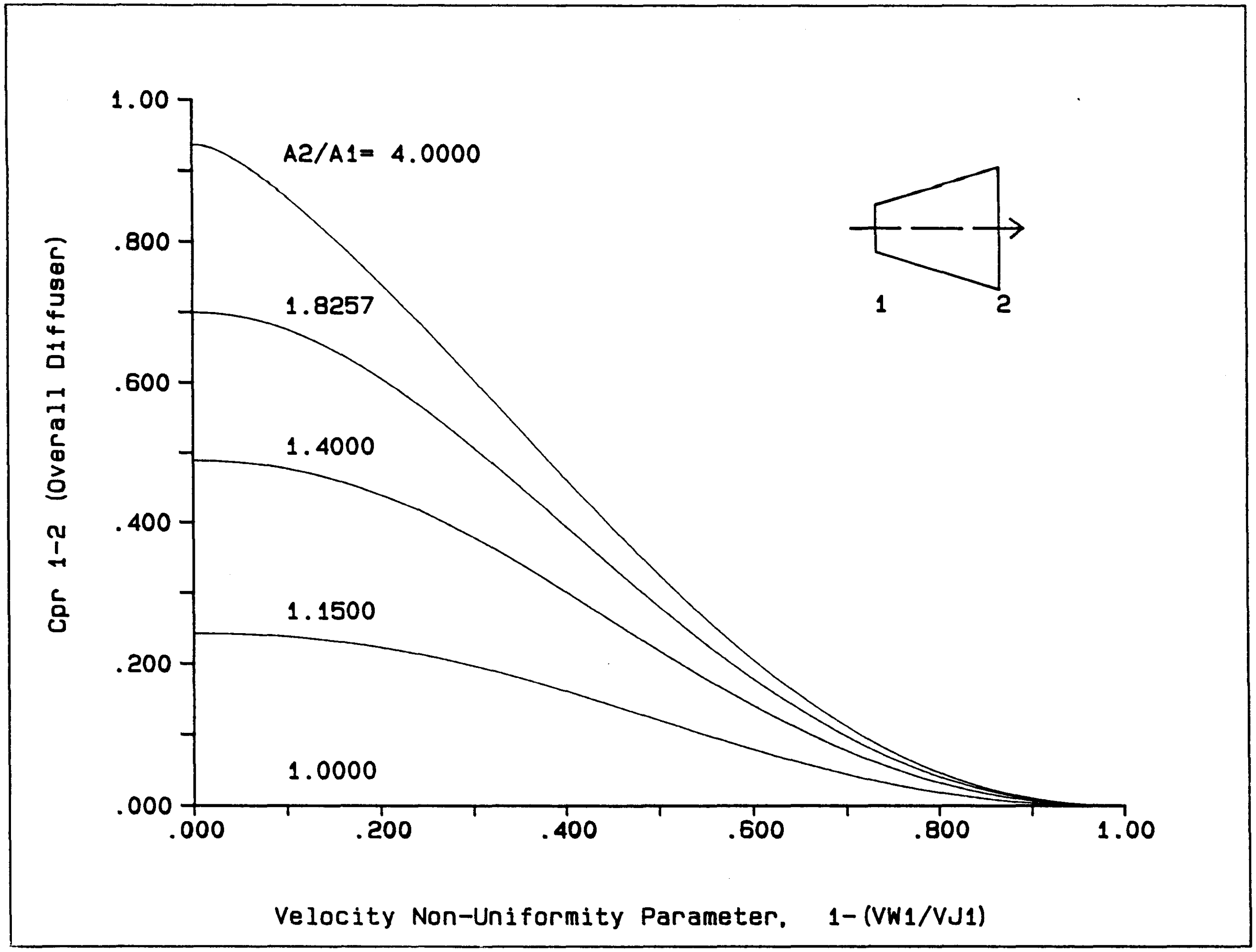

Fig. 5.8a Pressure Recovery in a Diffuser with Inlet Distortion: Case a)- No Mixing

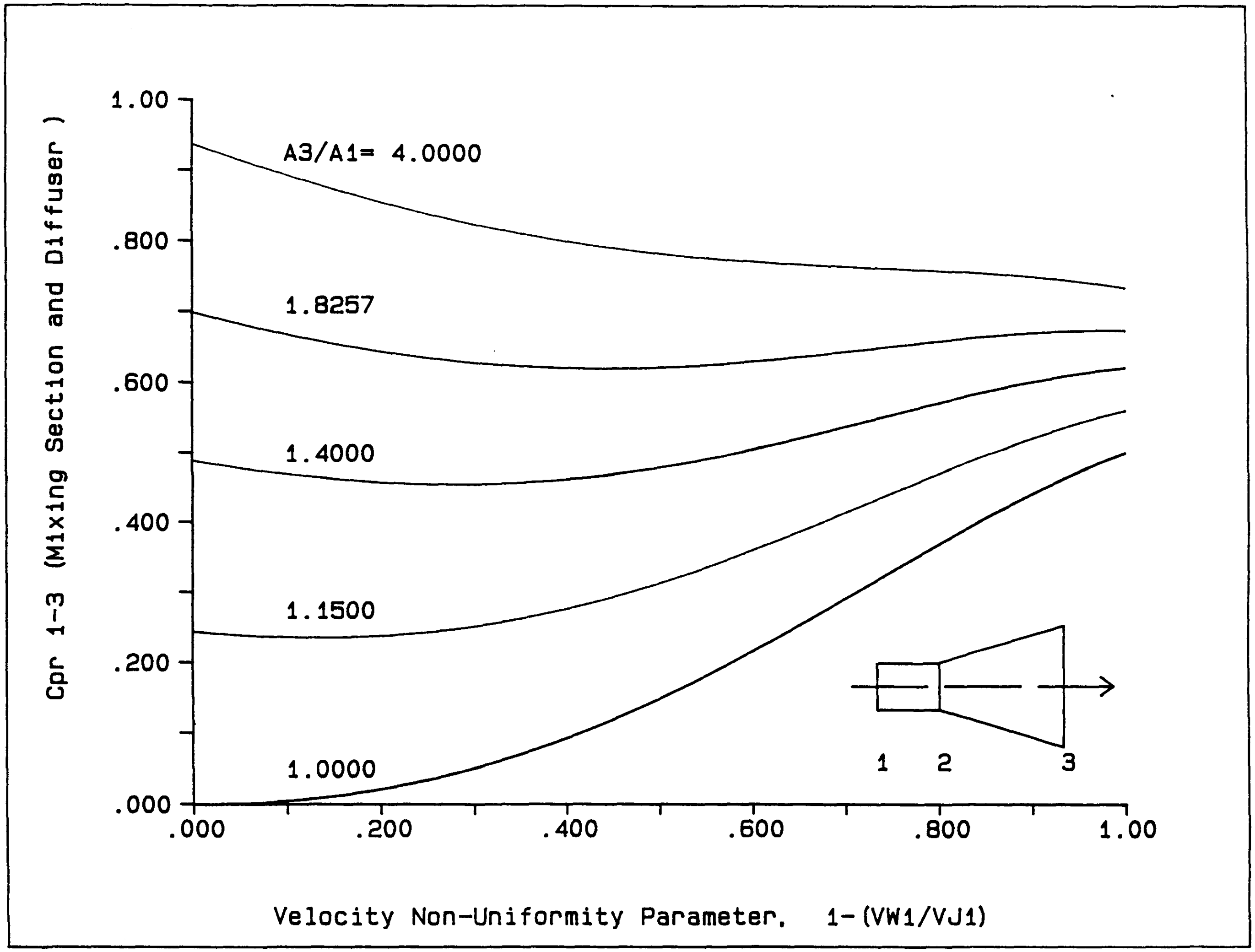

Fig. 5.8b Pressure Recovery with Inlet Distortion: Case b)- Constant-Area Mixing Section in which Mixing is Complete, Followed by a Diverging-Section Diffuser

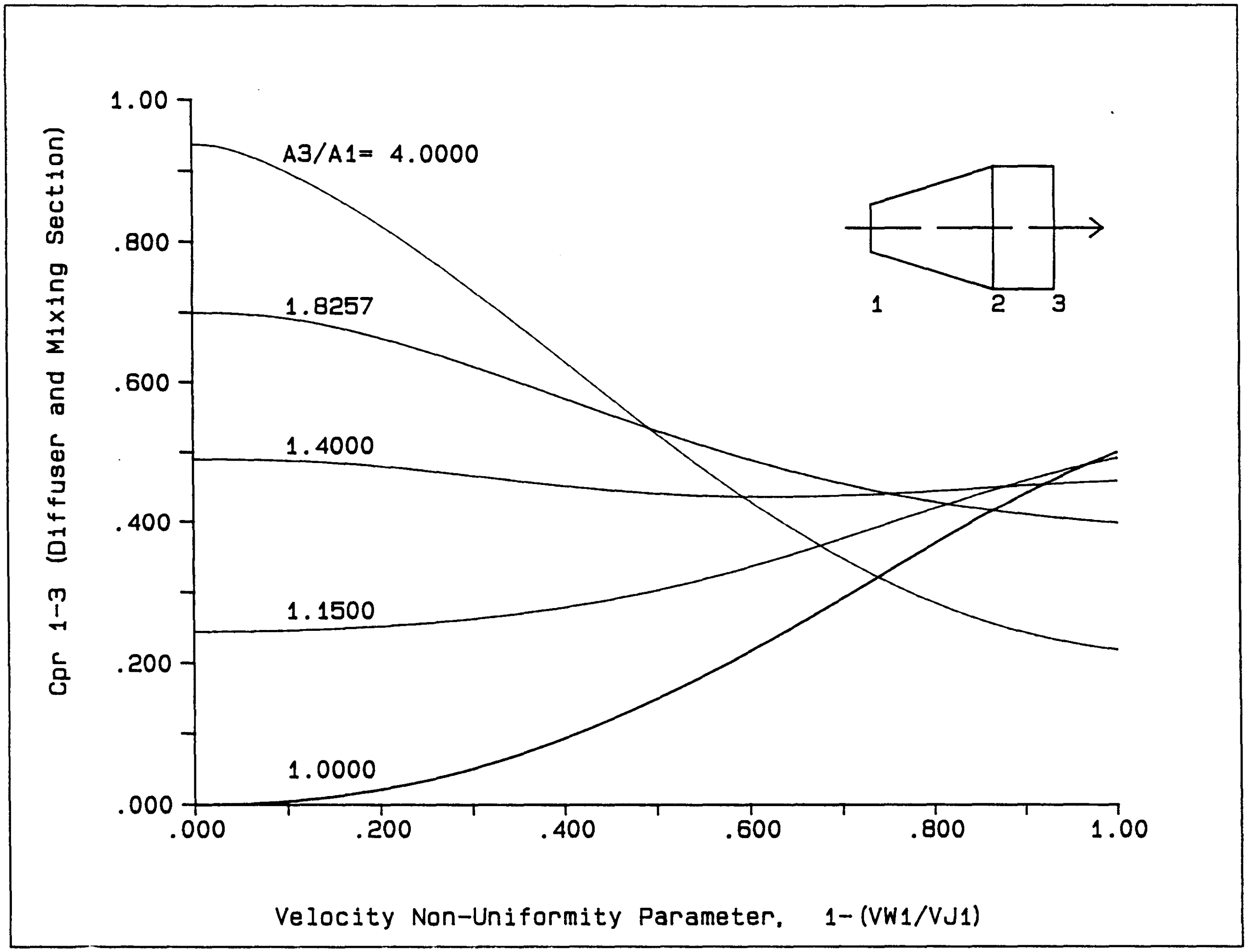

Fig. 5.8c Pressure Recovery with Inlet Distortion: Case c)- Diverging Section in which no Mixing Occurs, Followed by a Constant-Area Mixing Section in which Mixing is Complete

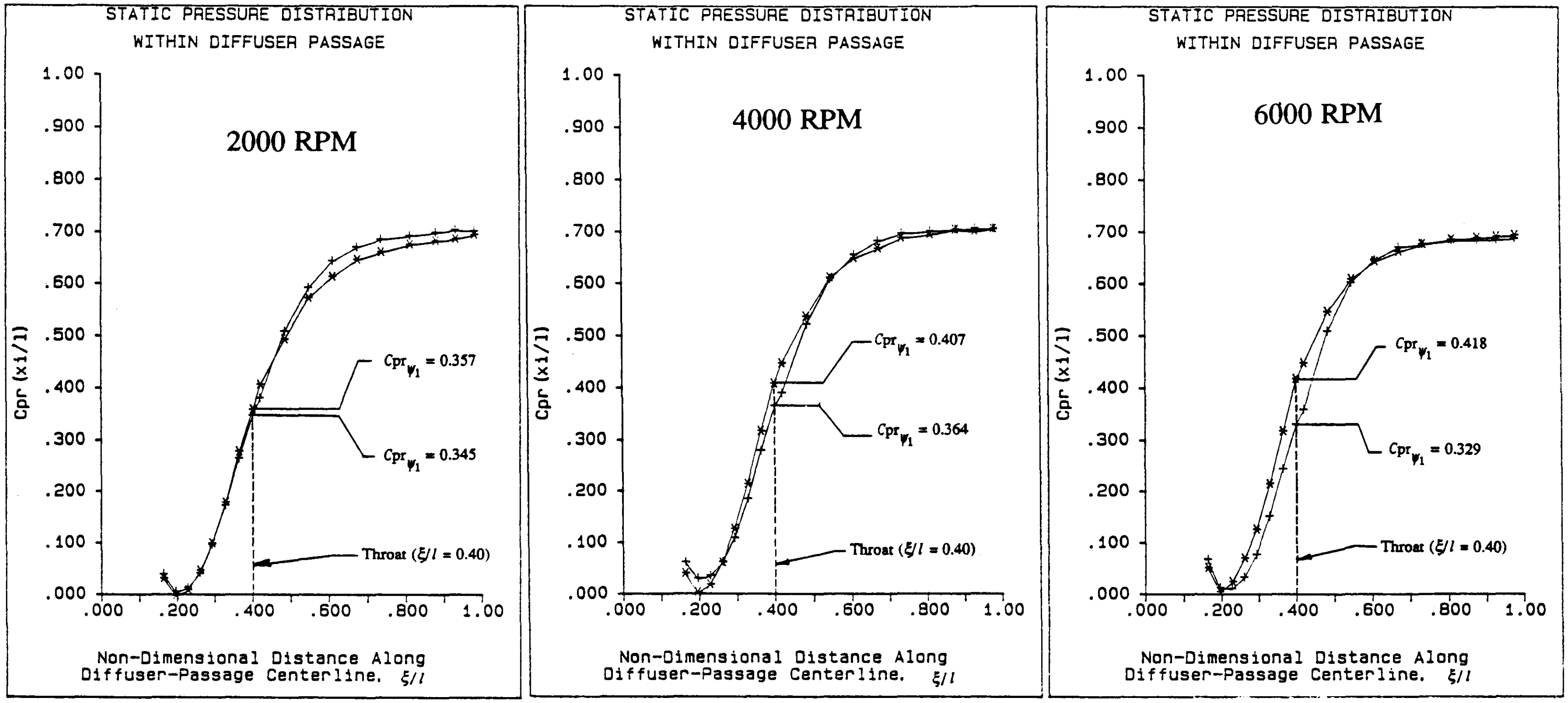

+ Undistorted Inlet Flow

* Distorted Inlet Flow

(See figures 4.7 and 4.8 for corresponding inlet Mach number and swirl-angle profiles)

Fig. 5.9 Static Pressure Distribution Along the Centerline of an Individual Diffuser-Passage at the Rotating Stall Threshold with Low and High Diffuser-Inlet Flow Field Distortion

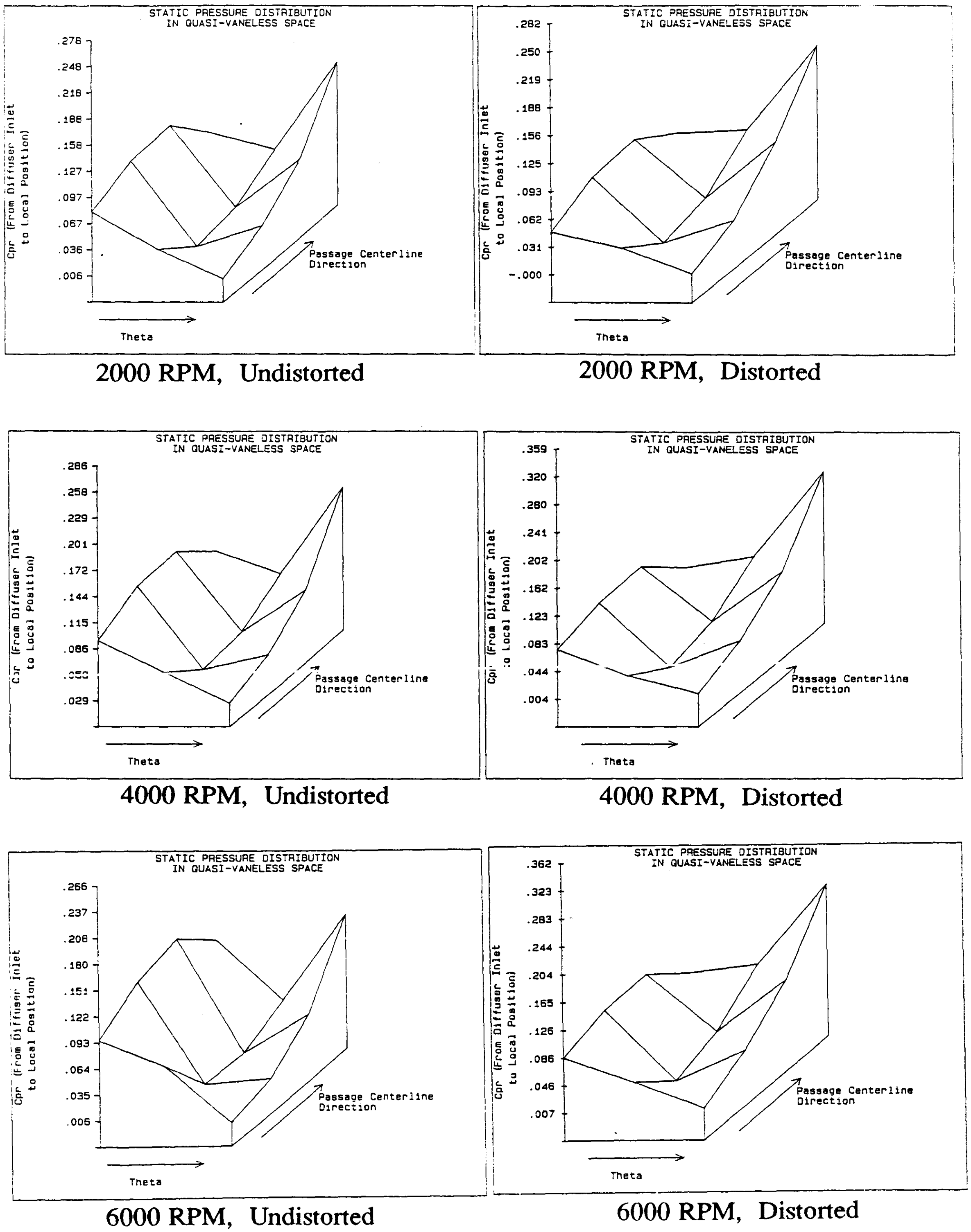

Fig. 5.10 Static Pressure Distribution in the Quasi-vaneless Space at the Rotating Stall Threshold with Undistorted and Distorted Diffuser Inlet Flow Field

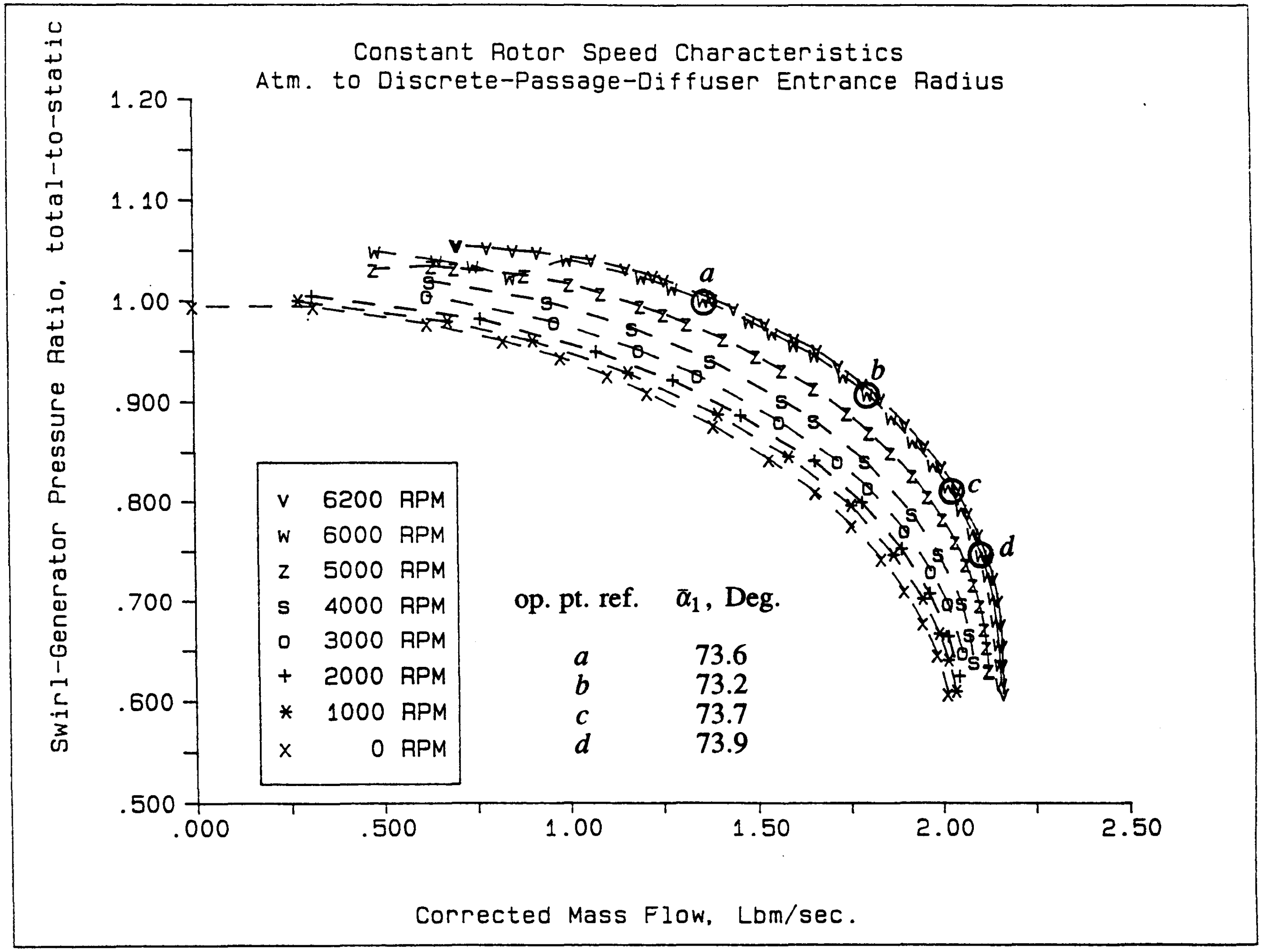

Fig. 5.11 Range of Rotor Operation Achieved at Onset of Rotating Stall

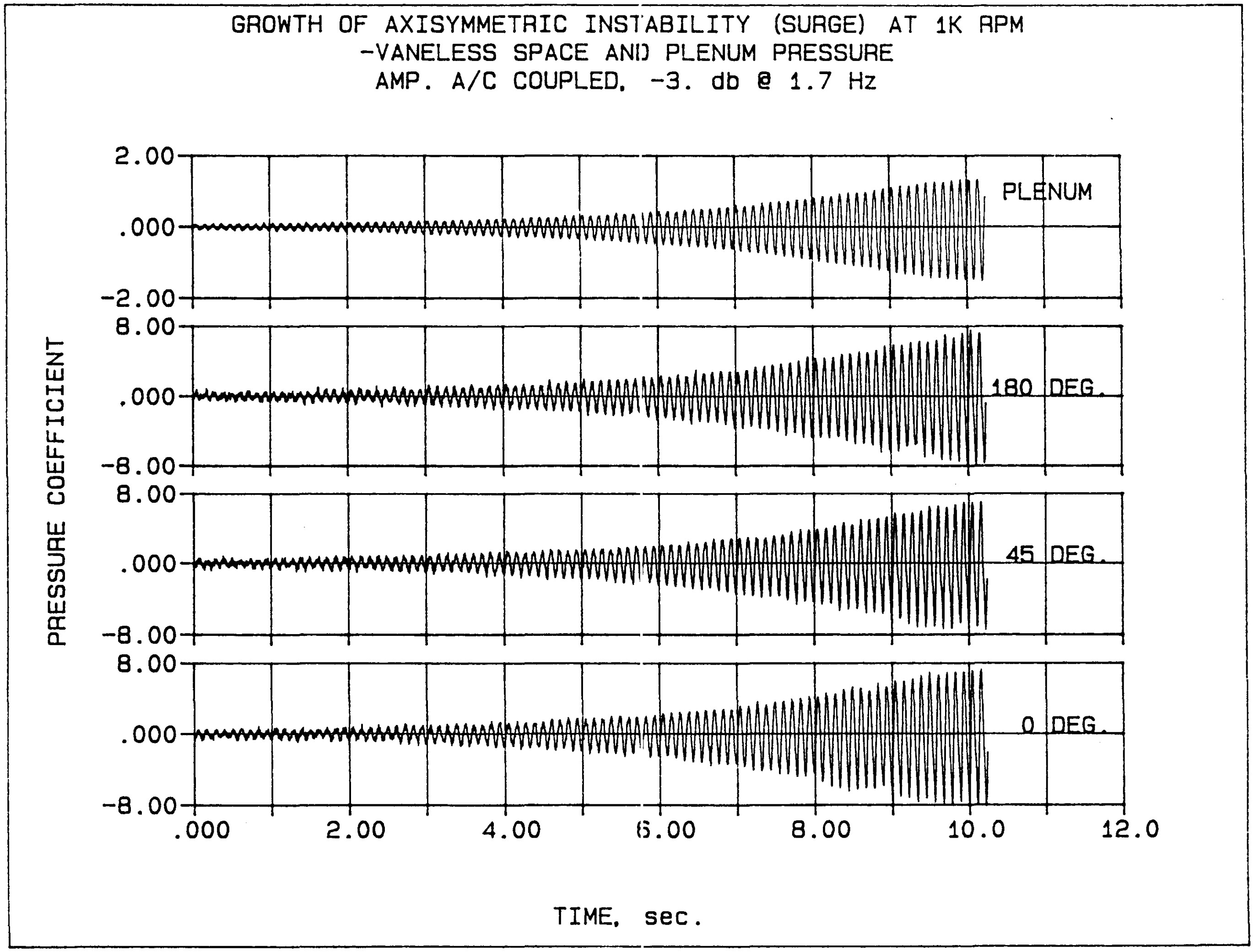

Fig. 5.12 Growth of Surge Cycle in the Case of Overall Compression System Instability

CHAPTER 6

SUMMARY AND CONCLUSIONS

6.1 Summary of the Radial-Diffuser Test Facility Development

The present research effort was initiated with the objective of investigating the fluid mechanics of a modern, high performance radial discrete passage diffuser for a centrifugal compressor. Specific questions to be answered were:

- How does diffuser pressure recovery performance and operating range depend on inlet Mach number and swirl angle?
- What is the sensitivity of the diffuser pressure recovery and operating range to inlet flow-field blockage and skew?
- What is the nature of flow breakdown process limiting the operating range of the diffuser and how is this sensitive to the diffuser inlet conditions?

To address these questions, a complete diffuser test facility, based on a radial, negative-reaction rotor swirl generator concept, was developed for the study of radial diffuser fluid mechanics over a wide range of inlet conditions.

The facility allows for the study of radial diffusers at Mach numbers up to unity and a swirl angles of 66 to 75 degrees from radial (additional flow angle range may be obtained by replacing the rotor which is easily removable). A unique feature of the facility is the ability to control the diffuser inlet flow-field axial distortion by means of annular cross-flow injection and/or suction in the vaneless space between the rotor and the diffuser inlet.

A significant initial effort in the facility development process was investigation of the suitability of various techniques for generating the required highly- swirling, high Mach number, controlled diffuser-inlet flow-field. One approach which was initially proposed consisted of a subsonic radial-inflow swirl-nozzle cascade, in conjunction with a contoured, axisymmetric radial-to-axial-to-radial turnaround duct and this was examined in detail. Although attractive because of mechanical simplicity, analysis showed that boundary layer separation will occur in the axial-to-radial portion of the turnaround duct due to the required diffusion in this region. The radial, negative-reaction rotor concept was then proposed as the best means for generating the required diffuser-inlet swirl flow-field and an experimental test facility was designed and constructed based on this concept.

The following points summarize the features and advantages of the diffuser test facility which was developed as a major part of this thesis:

- A radial-outflow rotor with lightly loaded, high solidity, two-dimensional, forward leaning blading was designed to generate the required highly-swirling flow-field at the test diffuser inlet. The light loading, in conjunction with a favorable streamwise static pressure gradient and subsonic relative flow through the blading results in low circumferential and axial non-uniformity of the flow field at the diffuser inlet, compared to actual centrifugal compressor impellers and various stationary-nozzle swirling-flow generation schemes. In addition, the high blade solidity results in an "integrated throttle" effect, producing losses which compensate for the de-stabilizing positively-sloped pressure rise v.s. flow rate characteristic typical of compressors with forward leaning blading. An oversized drum collector/plenum surrounding the test section aids in maintaining a low circumferential flow field non-uniformity over a wide flow range compared to volute collectors typically used in centrifugal compressors.
- An auxiliary flow injection/suction system allows for the control of the diffuser inlet flow field axial distortion by means of flow injection and/or suction through annular slots in both walls of the vaneless space between the rotor exit and the test diffuser inlet.
- The provision for flow injection/suction through annular slots in the vaneless space allows for operation of the diffuser over an inlet flow angle range independent of the operating point of the rotor on its operating characteristic. This facilitates the isolation of phenomena specific to either component.
- Three high-frequency-response, flush-mounted static-pressure transducers in the 1.10 radius-ratio vaneless space between the rotor exit and test-diffuser inlet allow for detection of any circumferentially-traveling and general pressure disturbances. Another high frequency response pressure transducer in the collector/plenum detects system unsteadiness such as that resulting from surge. Additional transducers can easily be mounted in the vaneless space for greater spatial resolution.
- Twelve circumferentially-distributed axial-probe ports are provided at the test diffuser inlet radius and twelve at the test diffuser exit radius. Mounting

rings are provided for mounting probe traverser-mechanisms or stationary probe-holders.

- A direct-drive induction motor, in conjunction with a variable frequency power supply, allows for the continuous variation of rotor tip speed from 30. ft/sec. to 460. ft/sec. while keeping rotor speed variations due to changes in load (such as result from flow transients) to a minimum.
- An independent compressor, downstream of the test rig plenum, allows for the control of flow through the test section independently of rotor speed.
- A personal computer based data acquisition system, an auto-shutdown safety monitoring system, and specially designed test section handling/assembly devices allow for one-person operation of the entire test facility.
- Although designed for a specific radial discrete-passage diffuser, the facility can be easily adapted to various other radial diffuser configurations.

6.2 Summary of the Radial-Diffuser Test Facility Performance

The performance of the test facility was initially examined using a 1.2-radius-ratio vaneless diffuser alone. It was determined that the performance of the rig was satisfactorily close to design.

The diffuser inlet flow-field parameter range obtained is as follows:

Mach number:	0.0-1.0
Swirl angle:	66°-75°
Mass flux deficit:	14-35%
Mass flux skew:	0.1-28%
Momentum flux deficit:	17-43%
Momentum flux skew:	0.1-35%
Kinetic energy deficit:	19-50%
Kinetic energy skew:	0.2-41%

The range of blockage (mass flux deficit) achieved includes values below and up to those produced by typical centrifugal compressor impellers.

The circumferential non-uniformity of the flow-field was negligibly small, with a maximum circumferential static pressure deviation from the average of less than 1 % of the dynamic pressure.

6.3 Summary of the Diffuser Performance Correlation Parameters

Various definitions of diffuser pressure-recovery coefficient for cases of non-uniform diffuser inlet conditions were considered. It was concluded that basing the definition of the diffuser pressure-recovery coefficient on the diffuser inlet "availability-averaged" total pressure is most physically meaningful as this is the highest pressure that could possible be obtained using a reversible, adiabatic, zero-work-interaction device "operating" on the given inlet velocity profile. The availability-averaged total pressure is equal to the mass-averaged total pressure for an ideal incompressible fluid but a different expression, which was derived, must be used for a perfect gas. For the Mach numbers and levels of flow-field non-uniformity in the present investigation, the pressure recovery coefficient based on the mass averaged total pressure was, in the most extreme case, 1.6% less than the pressure recovery coefficient based on the availability-averaged total pressure. The diffuser-inlet "effective" Mach-number was defined based on the diffuser inlet static pressure and the availability-averaged total pressure.

Several means of specifying an "average" diffuser-inlet flow angle for the case of a non-uniform flow-field were also considered. It was concluded that the diffuser inlet momentum-averaged flow angle gives the best correlation of the discrete-passage diffuser performance, as discussed in the following section.

6.4 Summary of the Radial Discrete-Passage Diffuser Performance

The pressure-recovery and stability performance of a General-Electric, 30-passage centrifugal-compressor diffuser, representing modern, high-performance aircraft engine diffuser geometry, was investigated. This diffuser is characterized by straight centerline passages which are circular in cross-section from the impeller exit to the diffuser throat (and conical in form) and then transition to a semi-rectangular cross-section between the throat and the diffuser exit. Between the impeller exit and the diffuser throat, the intersection of the conical passages forms a quasi-vaneless space with highly swept back cusp-like leading edges.

The dependence of the diffuser pressure recovery coefficient on Mach number and swirl angle was initially established over the stable operating range of the machine with an as uniform as possible diffuser inlet flow-field and then again with an axially skewed flow field. This was done by measuring the Mach number and swirl angle axial distributions at the diffuser inlet and applying the above-described averaging techniques. To determine the effect of diffuser inlet flow field distortion and Mach number on the onset of stable-flow breakdown, special attention was given to establishing stable operating points as close as possible to the onset of unstable operation.

It was shown that in the operating range between choke and stable-flow breakdown, the diffuser pressure-recovery coefficient (*Cpr*) correlates well (to within ±2.8% of the mean) with the diffuser inlet flow angle, independently of inlet distortion, when *Cpr* is based on the availability-averaged diffuser inlet total pressure and the flow angle is taken to be the momentum-averaged flow angle. It was found that for the test diffuser, the stable, axi-symmetric flow transitioned to rotating stall at a critical diffuser-inlet momentum-averaged flow angle and corresponding overall diffuser pressure recovery coefficient (based on the availability-averaged total pressure) independently of the inlet flow-field distortion and Mach number. By altering the matching between the swirl generator rotor and the diffuser by means suction or injection through the vaneless-space slots, it was shown that the onset of rotating stall was due to the loss of stability within the diffuser alone.

For the test diffuser, the critical momentum-averaged diffuser inlet flow angle and corresponding overall diffuser pressure recovery coefficient, evaluated at the limits of inlet distortion described in the previous section, and over a Mach number range of 0.15-0.80 were determined to be:

$$\alpha_{crit} = 73.6° \pm 0.5° \ , \quad Cpr_{crit} = 0.70 \pm 0.02$$

A drop-off of Cpr_{crit} to 0.67 at an inlet Mach number of .95 was found, although α_{crit} remained in the above range.

Analysis of time-resolved signals from the three high frequency response static pressure transducers in the vaneless space showed that the breakdown of stable operation can result in either a rotating stall, a combined rotating-stall/surge-cycle, or a a pure surge mode characterized by axi-symmetric pressure and flow fluctuations in the rotor/diffuser. Rotating stall always occurred when the diffuser inlet angle reached the critical value. If the slope of the main collector/plenum throttle was made adequately high by means of downstream suction, however, the onset of rotating stall in the diffuser developed into a surge cycle with rotating stall occurring over part of each cycle. If overall system instability occurred (due to operation on the atmosphere-to-plenum pressure ratio characteristic in a region where the slope is adequately positive) before the diffuser inlet flow angle reached the critical value, a pure surge cycle mode developed with axisymmetric pressure and flow oscillations in the rotor/diffuser. Operation in this mode can be achieved with the present facility by the injection of mass through the annular slots in the vaneless space. This drives the rotor to a lower-flow operating point on its characteristic (more positively sloped) while driving the diffuser inlet flow angle to lower values (away from α_{crit}). When the overall (rotor plus diffuser) system total-to-static characteristic becomes sufficiently positively sloped, a surge cycle develops.

It was shown that the insensitivity of the diffuser performance to inlet distortion can be due to mixing in the quasi-vaneless space and throat region of the diffuser. Measurements of static-pressure distribution along a diffuser passage centerline qualitatively support this conclusion. It was suggested that the generation of streamwise vorticity due to the loading across the leading edge cusp can aid in the mixing of a non-uniform diffuser inlet flow-field.

Analysis of the static pressure distribution in the quasi-vaneless space of the diffuser showed a distinct loading reversal on the leading edge cusps as the operating range between choke and stall was traversed. Near choke, the pressure and suction surfaces of the leading-edge cusp immediately at the diffuser inlet are loaded in the correct direction (higher pressure on the pressure surface) while the loading is reversed near the throat entrance. Near stall, the situation reverses, with higher pressure on the suction surface immediately at the diffuser inlet and correct loading near the throat entrance. This trend was found to be independent of inlet distortion although the loading across the leading edge just upstream of the throat was found to increase with increased inlet distortion.

6.5 Recommendations for further research

The main areas where further research is recommended are as follows:

1.) Investigation of diffuser sensitivity to the jet-wake structure of actual impeller exit flows

Since the present research focused on the influence of axial flow field distortion on radial discrete-passage diffuser performance, a very lightly loaded, high solidity swirling flow generator rotor was designed to achieve a circumferentially uniform weak-wake diffuser inlet flow field. In actual centrifugal compressors however, flow separation on the suction surface of the impeller blading well upstream of the impeller exit results in a jet-wake flow structure at the impeller exit (see Eckardt [16] for example). This circumferentially-periodic non-uniformity in the rotating frame of reference is seen as a periodic unsteady flow by the diffuser. In an investigation of the influence of these strong circumferential non-uniformities of the impeller exit flow on radial diffuser performance, Baghdadi [4] compared the performance and stability of a radial wedge-type diffuser as measured using the vortex-nozzle swirling flow generator [2,3] with that obtained using an actual centrifugal impeller. The diffuser performance and stability for the two cases was found to "agree within the range of experimental accuracy". Since the vortex nozzle produced a circumferentially uniform flow while the impeller produced a jet-wake type flow at the diffuser inlet, it was concluded that the diffuser performance is insensitive to the jet-wake structure of the impeller exit flow. It was suggested that a combination of rapid mixing and the high frequency of the unsteadiness as seen by the diffuser relative to the flow response time of the diffuser were responsible for this insensitivity. Since Baghdadi's comparison involved a diffuser geometry different from that used in the present investigation and only one impeller/diffuser combination was investigated, an in-depth investigation of the effect of rotor blade wakes on the performance of the present diffuser geometry is suggested to verify the generality of his results.

The present apparatus can be modified to simulate the jet-wake flow structure produced by actual impellers by blocking some of the rotor passages with individual inserts. Since a prime-number of blades was used (71) in the present rotor, complete circumferential periodicity can not be achieved but this should not pose serious problems with proper balancing. An alternative approach would be to use a ring insert supported by the leading edges of the present rotor and perforated in such a way as to produce the desired circumferentially-periodic variation of blockage. If neither of these options proves satisfactory, a new rotor with the required circumferential variation of blockage can be manufactured.

2.) The investigation of mixing and losses in the quasi-vaneless space

In the present research it was shown that the performance of the test diffuser was insensitive to axial distortions of the diffuser inlet flow field and that mixing plays an important role in this. Since mixing also results in losses (entropy generation), it is important to obtain a more in-depth understanding of the mixing and loss processes within the diffuser. It was suggested in the present research for example that the flow across the leading-edge cusps results in the generation of vorticity which aids in the mixing process and makes the diffuser insensitive to inlet distortion. Does the vorticity shedding off of the leading edge cusps therefore result in unnecessary losses if the diffuser is provided with a uniform inlet flow (when mixing is not required)?. The possibility of this is suggested from the measured peak diffuser effectiveness (Cpr/Cpr_{th}) which ranged from 70% to 72% in all cases of low and high distortion in the present experiments.

It is suggested that the possibility of using a laser velocimeter to "look into" the quasi-vaneless space from the diffuser exit be investigated. This will only allow for the resolution of the cross-flow velocity components (normal to the passage centerline) but it is these components which are important in the mixing process. Such an approach would eliminate the complexity of an access window in the highly curved walls of the quasi-vaneless space.

3.) Investigation of other radial diffuser configurations.

Since the present investigation focused on a specific diffuser geometry, the influence of inlet distortion on the performance and stability of other radial diffuser geometries should be investigated to evaluate the universality of the present results. In particular, it is suggested that the influence of inlet distortion on the performance and stability of a diffuser without a quasi-vaneless space (such as a vane-island diffuser) be investigated. This would give insight into the suggested importance of the flow phenomena in the quasi-vaneless space of the present diffuser in the observed insensitivity of the diffuser performance to inlet distortion and its role in loss generation. The present diffuser test facility can be easily adapted to any other radial diffuser configuration.

4.) Detection of stall precursors and investigation of stall cell development

The current interest in the implementation of active control schemes to extend the operating range of dynamic compressors requires a detailed understanding of stall inception dynamics for the effective design of control laws. In the present investigation it was shown that rotating stall can be triggered by the diffuser completely independently of the rotor, and a detailed investigation of the dynamic development of rotating stall in the diffuser should be undertaken. Due in part to the relatively "clean" flow produced by the high solidity swirl generator rotor, the present diffuser test facility offers the advantage of a high signal-to-noise ratio for studying stall pre-cursors and the dynamic development of rotating stall as compared to actual centrifugal compressor impellers. In the present experimental setup, only three high frequency response pressure transducers were mounted in the vaneless space between the rotor and the test diffuser. This is adequate for the detection of rotating stall and the determination of the number of stall cells but gives inadequate spatial resolution for a detailed investigation of stall cell development. This problem can be easily overcome by mounting additional transducers in the vaneless space although a more elegant means of routing the wiring than used in the present setup is required.

REFERENCES

1. Al-Mudhafar, M. M., Ilyas, M., and Bhinder, F. S., "Investigation of Flows in Rectangular Diffusers with Inlet Flow Distortion", ASME paper No. 82-GT-67, 1982.

2. Baghdadi, S., "A Study of Vaned Radial Diffusers Using Swirling Transonic Flow Produced by a Vortex Nozzle", Ph.D. Thesis, School of Mechanical Engineering, Purdue University, December 1973.

3. Baghdadi, S., and McDonald, A. T., "The Performance of Three Radial Vaned Diffusers With Swirling Transonic Flow", Journal of Fluids Engineering, June, 1975, pp. 155-173.

4. Baghdadi, S., "The Effect of Rotor Blade Wakes on Centrifugal Compressor Diffuser Performance -A Comparative Experiment", in Centrifugal Compressor and Pump Stability, Stall, and Surge, copyright by ASME, 1976, pp. 121-138.

5. Bammert, K., Jansen, M., and Rautenberg, M., "On the Influence of the Diffuser Inlet Shape on the Performance of a Centrifugal Compressor Stage", ASME paper No. 83-GT-9, 1983.

6. Bhinder, F.S., Al-Mudhafar, M. M., and Ilyas, M., "Further Data on The Performance of a Rectangular Diffuser in Distorted Inlet Flows", ASME paper No. 84-GT-64, 1984.

7. Bryer, D. W., and Pankhurst, R.C., Pressure-Probe Methods for Determining Wind Speed and Direction, Her Majesty's Stationary Office, London, 1971.

8. Creare Technical Note No. 366, section 4 (regarding swirl generator design), "Test Facility Design and Evaluation", author unknown, provided by Bharatan R. Patel.

9. Dean, R. C., Jr., "The Centrifugal Compressor", Parts 1 and 2, Gas Turbine International, March-April 1973, and May-June 1973, respectively.

10. Dean, R. C., Jr., "On the Unresolved Fluid Dynamics of the Centrifugal Compressor", in Advanced Centrifugal Compressors, copyright by the ASME Gas Turbine Division, 1971, pp. 1-55.

11. Den Hartog, J. P., Advanced Strength of Materials, McGraw-Hill, 1952, pp. 49-69

12. Den Hartog, J. P., Mechanical Vibrations, Dover Publications, New York, 1985, pp. 225-281.

13. Denton, J., Private Communication

14. Dixon, S. L., Fluid Mechanics, Thermodynamics of Turbomachinery, Pergamon Press Ltd., Oxford, England, 1978, pp. 87-89.

15. Dutton, J. C., Piemsomboon, P., and Jenkins, P. E., "Flowfield and Performance Measurements in a Vaned Radial Diffuser", Journal of Fluids Engineering, Vol. 108, June 1986, pp. 141-147.

16. Eckardt, D., "Instantaneous Measurements in the Jet-Wake Discharge Flow of a Centrifugal Compressor Impeller", Journal of Engineering for Power, Transactions of ASME, July 1975, pp. 337-346.

17. Eckardt, D., "Detailed Flow Investigations Within a High-Speed Centrifugal Compressor Impeller", Journal of Fluids Engineering, Transactions of ASME, September 1976, pp. 390-402.

18. Elder, R. L., and Gill, M. E., "A Discussion of the Factors Affecting Surge in Centrifugal Compressors", ASME paper No. 84-GT-194, 1984.

19. Erwin, J. R., and Vitale, N. G., "The Radial Outflow Compressor", in Advanced Centrifugal Compressors, copyright by the ASME Gas Turbine Division, 1971, pp. 56-117.

20. Faulders, C., "Experimental and Theoretical Study of Vaneless Diffuser Flow with Supersonic Entry", MIT Gas Turbine Laboratory Report, June 1952.

21. Filipenco, V., and Greitzer, E. M., "Conceptual Design of a Swirl Generator for the Study of Discrete Passage Diffusers", report submitted to the General Electric Company, June 26, 1985.

22. Fink, D. A., "Surge Dynamics and Unsteady Flow Phenomena in Centrifugal Compressors", Ph.D. Thesis, Department of Aeronautics and Astronautics, M.I.T., May 1988.

23. Fink, D. A., Private Communication

24. Goldberg, T. J., and Erwin, J. R., "Performance of an Impulse-Type Supersonic-Compressor Rotor Having a Mean Turning of 114°", NACA RM L56J01, 1957.

25. Greitzer, E. M., "The Stability of Pumping Systems-The 1980 Freeman Scholar Lecture", ASME Journal of Fluids Engineering, June 1981, Vol. 103, pp. 193-242.

26. Greitzer, E. M., "Discrete Passage Diffuser Performance and Stability", proposal submitted to the General Electric Company, October 1, 1984.

27. Greitzer, E. M., Paterson, R. W., and, Tan, C. S., "An Approximate Substitution Principle for Viscous Heat Conducting Flows, Proc. Royal Society, London, 1985, A 401, pp. 163-193

28. Griffel, W., Plate Formulas, Frederick Ungar Publishing Co., N.Y., 1968.

29. Gyftopoulos, E. P., and Beretta, G. P., Thermodynamics: Foundations and Applications, Macmillan Publishing Co., New York, 1991

30. Halmi, D., "Metering Performance Investigation and Substantiation of the "Universal Venturi Tube" (U.V.T.), Part 1- Hydraulic Shape and Discharge Coefficient", Journal of Fluids Engineering, Transactions of ASME, Vol 96, 1974, pp. 124-131.

31. Handbook of Chemistry and Physics, 70th Edition, CRC Press, Inc., 198? p. F-6.

32. Haupt, U., Seidel, U., Abdel-Hamid, A. N., and Rautenberg, M., "Unsteady Flow in a Centrifugal Compressor with Different Types of Vaned Diffusers", ASME paper No. 88-GT-22, 1988.

33. Horowitz, P. and Hill, W., The Art of Electronics, Cambridge University Press, Cambridge, 1980.

34. Jansen, W., "Rotating Stall in a Radial Vaneless Diffuser", Journal of Basic Engineering, Transactions of ASME, Vol 86, 1964, pp. 750-758.

35. John, J. E. A., Gas Dynamics, Allyn and Bacon, Inc., Boston, 1969.

36. Katsanis, T., "Velocity Gradient Method for Calculating Velocities in an Axisymmetric Annular Duct", NASA Technical Paper 2029, 1982.

37. Kenny, D.P., "A Novel Low-Cost Diffuser for High-Performance Centrifugal Compressors", Journal of Engineering for Power, Transactions of ASME, January 1969, pp. 37-47.

38. Kenny, D. P., "A Comparison of the Predicted and Measured Performance of High Pressure Ratio Centrifugal Compressor Diffusers", ASME Paper No. 72-GT-54, 1972.

39. Kerrebrock, J. L., Aircraft Engines and Gas Turbines, The M.I.T. Press, Cambridge, Massachusetts, 1989, pp. 116-163.

40. Klein, A., "REVIEW: Effects of Inlet Conditions on Conical-Diffuser Performance", ASME Journal of Fluids Engineering, Vol. 103, June 1981, pp. 250-257.

41. Kline, S. J., and Johnston, J. P., "Diffusers- Flow Phenomena and Design", in Advanced Topics in Turbomachinery Technology, Principal Lecture Series No. 2, Chapter 6, copyright by Concepts ETI, Inc., Norwich, Vt, 1986.

42. Livesey, J. L. and Hugh, T., " 'Suitable Mean Values' in One-Dimensional Gas Dynamics", Journal Mechanical Engineering Science, Vol. 8 No. 4 1966, pp. 374-383.

43. Masuda, S., Ariga, I., and Watanabe, I., "On the Behavior of Uniform Shear Flow in Diffusers and its Effects on Diffuser Performance", Journal of Engineering for Power, Transactions of ASME, October 1971, pp. 377-385.

44. Meyer, C. A., and Lowrie, J. A., "The Leakage Thru Straight and Slant Labyrinths and Honeycomb Seals", ASME paper No. 74-WA/PTC-2, 1974.

45. Mishina, H., and Nishida, H., "Effect of Relative Velocity Distribution on Efficiency and Exit Flow of Centrifugal Impellers", ASME Paper No. 83-GT-74, 1984.

46. Moore, F. K., "Weak Rotating Flow Disturbances in a Centrifugal Compressor with a Vaneless Diffuser", ASME Journal of Turbomachinery, Vol. 111, October 1989, pp. 442-449.

47. Oberg, E., Jones, F. D., and Horton, H. L., Machinery's Handbook, Industrial Press Inc., N.Y., 1984.

48. Rodgers, C., "The Performance of Centrifugal Compressor Channel Diffusers", ASME paper No. 82-GT-10, 1982.

49. Runstadler, P. W., Jr., and Dean, R. C., Jr., "Straight Channel Diffuser Performance at High Inlet Mach Numbers", Journal of Basic Engineering, Transactions of ASME, September 1969, PP. 397-422.

50. Runstadler, P. W., Jr., Dolan, F. X., and Dean, R. C., Diffuser Data Book, Technical Note TN-186, copyright by Creare Inc., Hanover, N.H., 1975

51. Russo, C. J., and Blair, L. W., "Effects of Size and Reynolds' Number on Centrifugal Diffuser Performance", ASME paper No. 81-GT-8, 1981.

52. Sakamoto, Y., Suyari, M., Nagata, A., Kinoshita, S., Ishigami, H., and Kobayashi, T., "A Data Analysis Method for Centrifugal Compressors (Mean Velocity at the Inlet of Vaneless Diffusers)", Kobelco Technical Bulletin 1066, Kobe Steel, Ltd., March, 1985.

53. Schorr, P. G., Welliver, A.D., and Winslow, L. J., "Design and Development of Small, High Pressure Ratio, Single-Stage Centrifugal Compressors", in Advanced Centrifugal Compressors, copyright by the ASME Gas Turbine Division, 1971, pp. 147-217.

54. Senoo, Y., Kinoshita, Y., and Ishida, M., "Asymmetric Flow in Vaneless Diffusers of Centrifugal Blowers", in Centrifugal Compressor and Pump Stability, Stall, and Surge, pp. 139-155, copyright 1976 by ASME.

55. Shapiro, A. H., The Dynamics and Thermodynamics of Compressible Fluid Flow, Vol. 2, pp. 1117-1124, The Ronald Press Company, New York, 1954.

56. Shreeve, R. P., Schulz, H. D., Erwin, J. R., and Schumann, L., "A Novel Centrifugal Diffuser Test Device", ASME. Paper No. 85-IGT-135

57. Stenning, A. H., Kriebel, A. R., and Montgomery, S.R., "Stall Propagation in Axial Flow Compressors", NACA Technical Note #3580, June 1956.

58. Stocker, H. L., "Advanced Labyrinth Seal Design Performance for High Pressure Ratio Gas Turbines", ASME paper No. 75-WA/GT-22, 1975.

59. Stodola, A., Steam and Gas Turbines, vol. 1, Peter Smith, N.Y., 1945, pp. 416-437.

60. Vitting, T., Flow Measurements in a Centrifugal Diffuser Test Device, -Final Report, Exotech, Inc., Campbell, CA., Report No: TR-8501.

61. Wilson, D. G., The Design of High-Efficiency Turbomachinery and Gas Turbines, The M.I.T. Press, Cambridge, Massachusetts, 1984, pp. 147-187 and pp. 241-243.

62. Wittig, S. L. K., Dörr, L., and Kim, S., "Scaling Effects on Leakage Losses in Labyrinth Seals", ASME paper No. 82-GT-157, 1982.

63. Wolf, S., and Johnston, J. P., "Effects of Nonuniform Inlet Velocity Profiles on Flow Regimes and Performance in Two-Dimensional Diffusers", Journal of Basic Engineering, Transactions of ASME, September 1969, pp. 462-474.

PHOTOGRAPHS

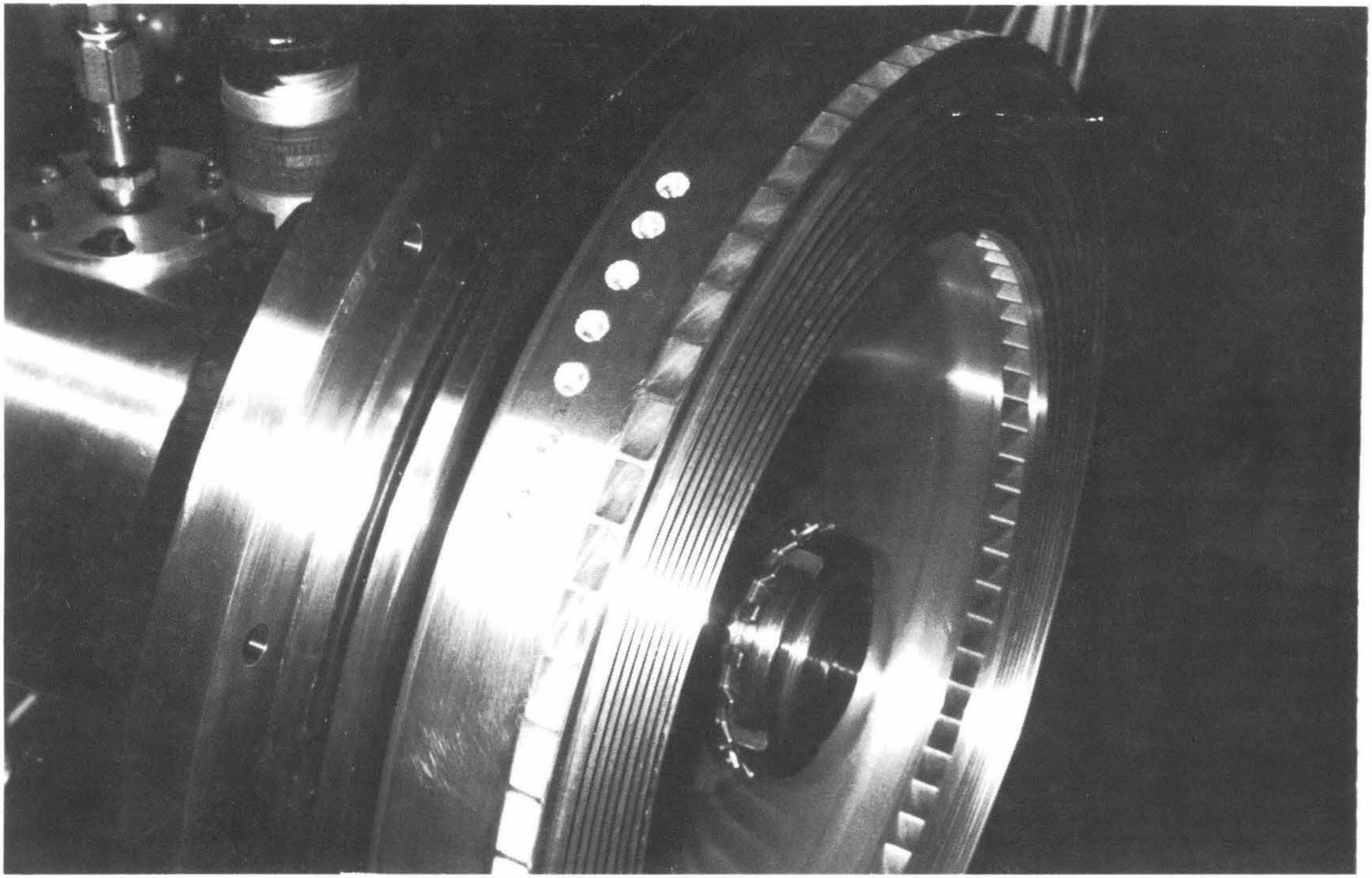

Photo. 1   Swirl-Generator Blisk

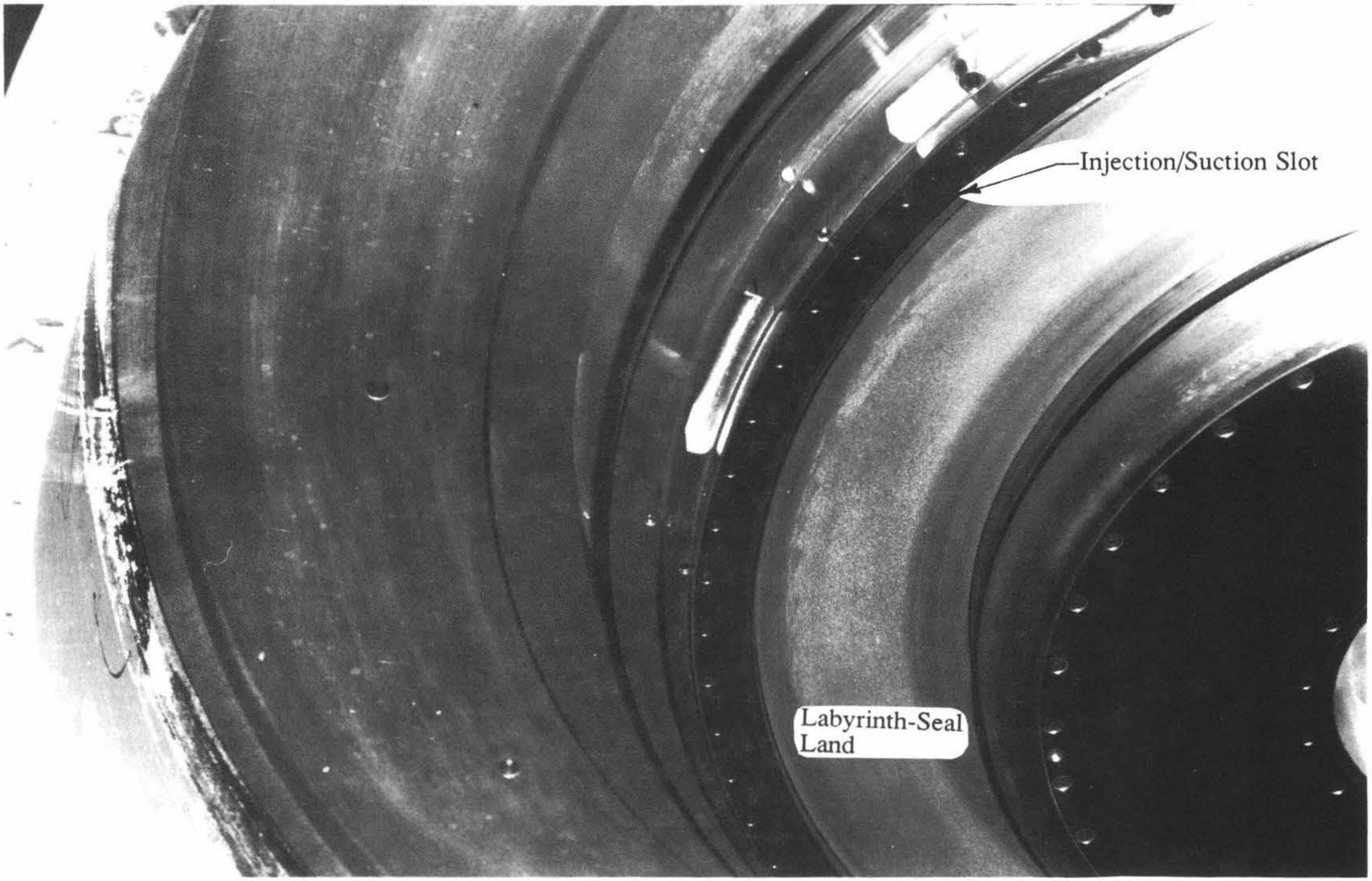

Photo. 2 Close-up View of Front-Downstream Injection/Suction Slot and Labyrinth-Seal Land

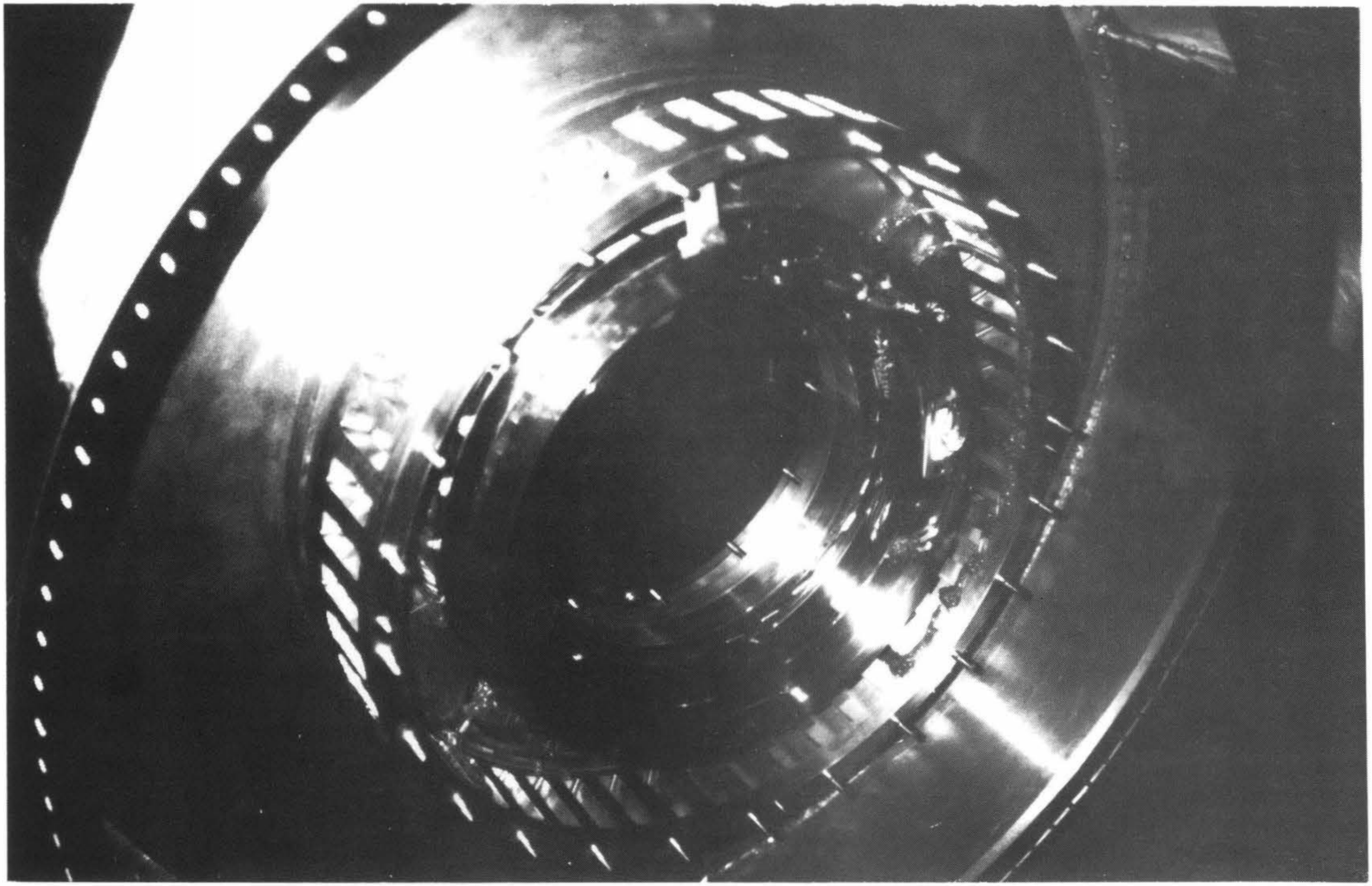

Photo. 3a Discrete Passage Diffuser Shown Mounted In Test Section Housing

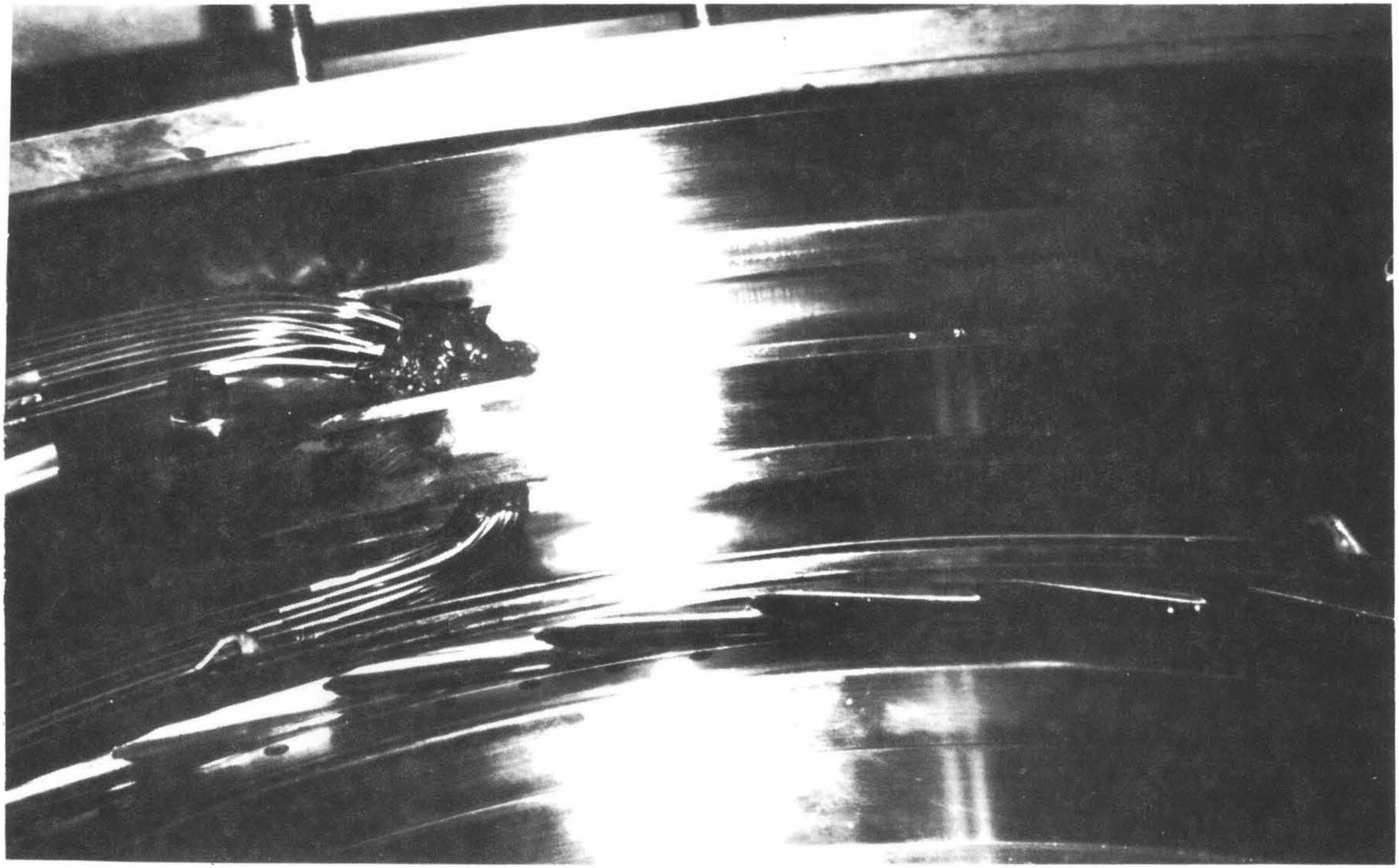

Photo. 3b Close-up View of Discrete-Passage Diffuser Inlet Showing the Leading Edge Cusps

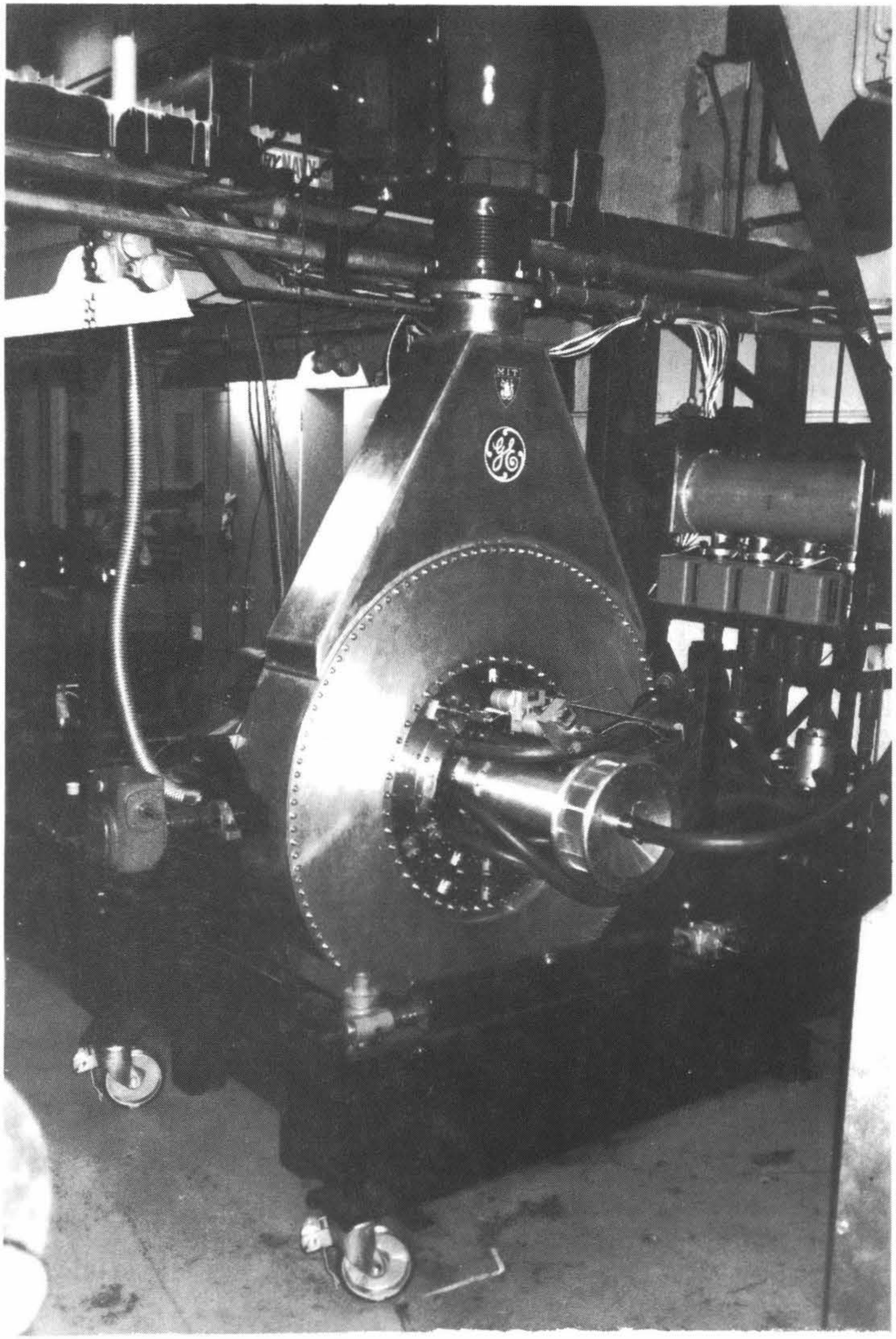

Photo. 4 Test Facility, Viewed From Inlet End

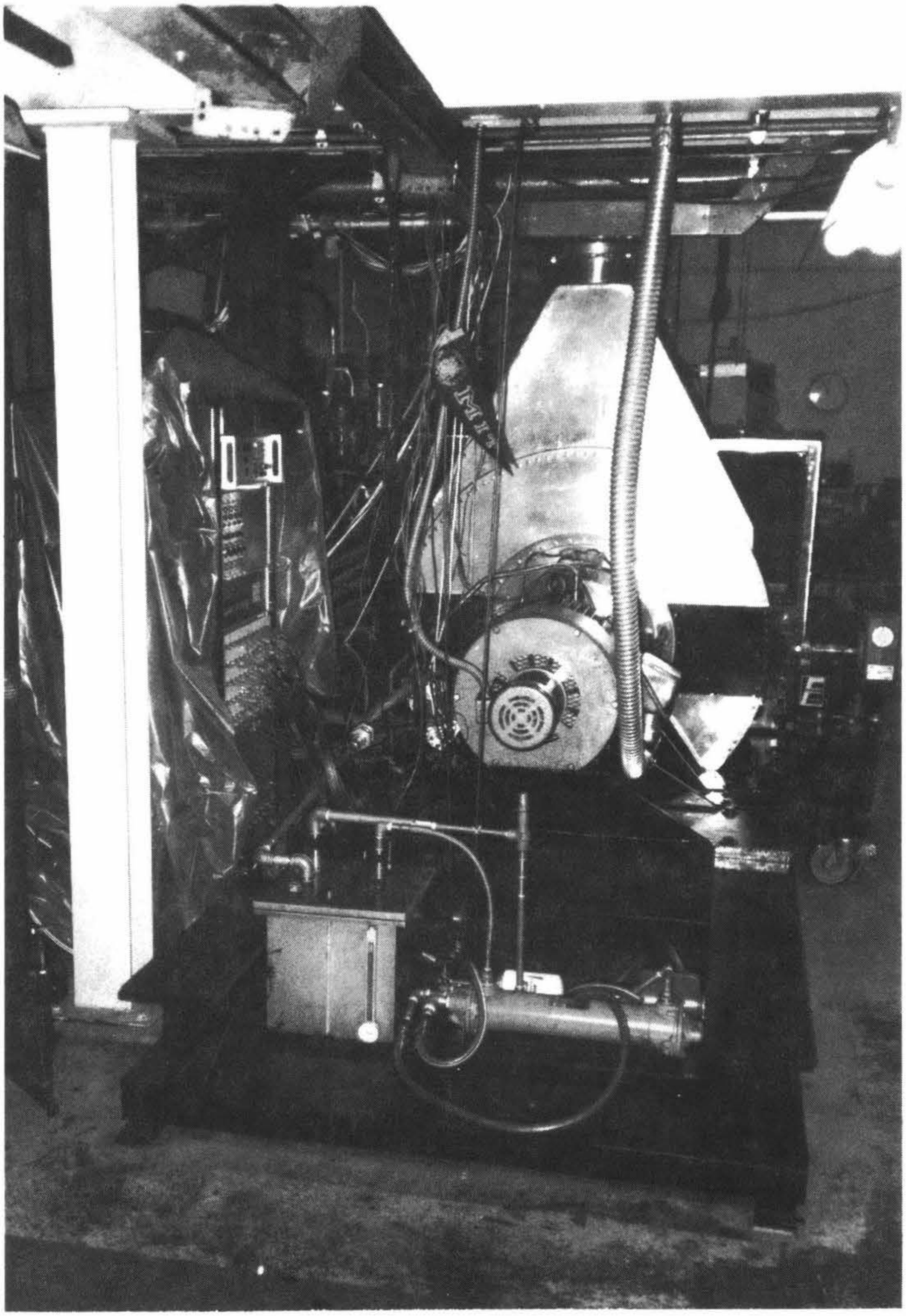

Photo. 5   Test Facility, Viewed From Drive-Motor End

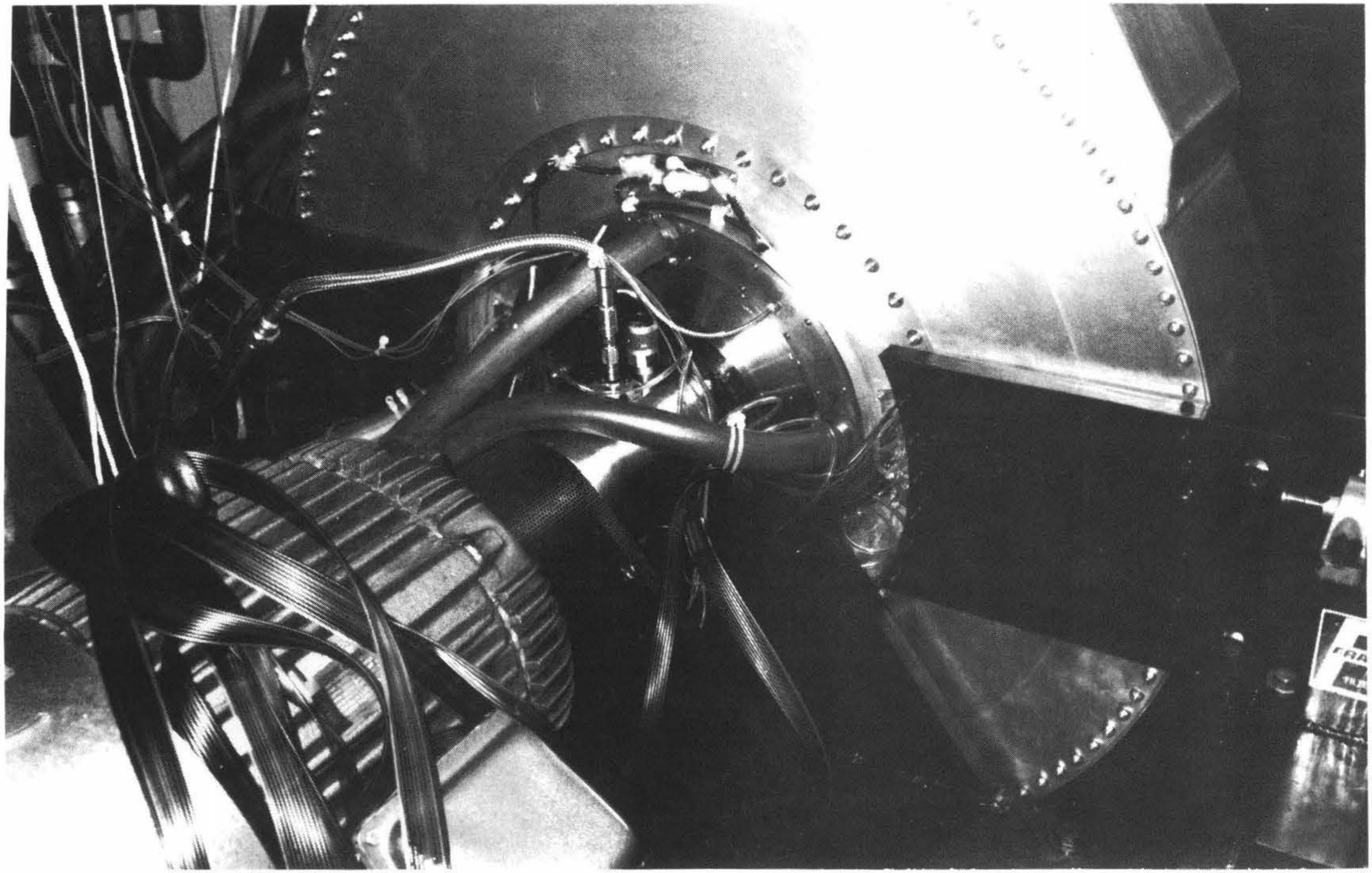

Photo. 6 Close-Up View of Swirl Generator, Shown From Drive-Motor End

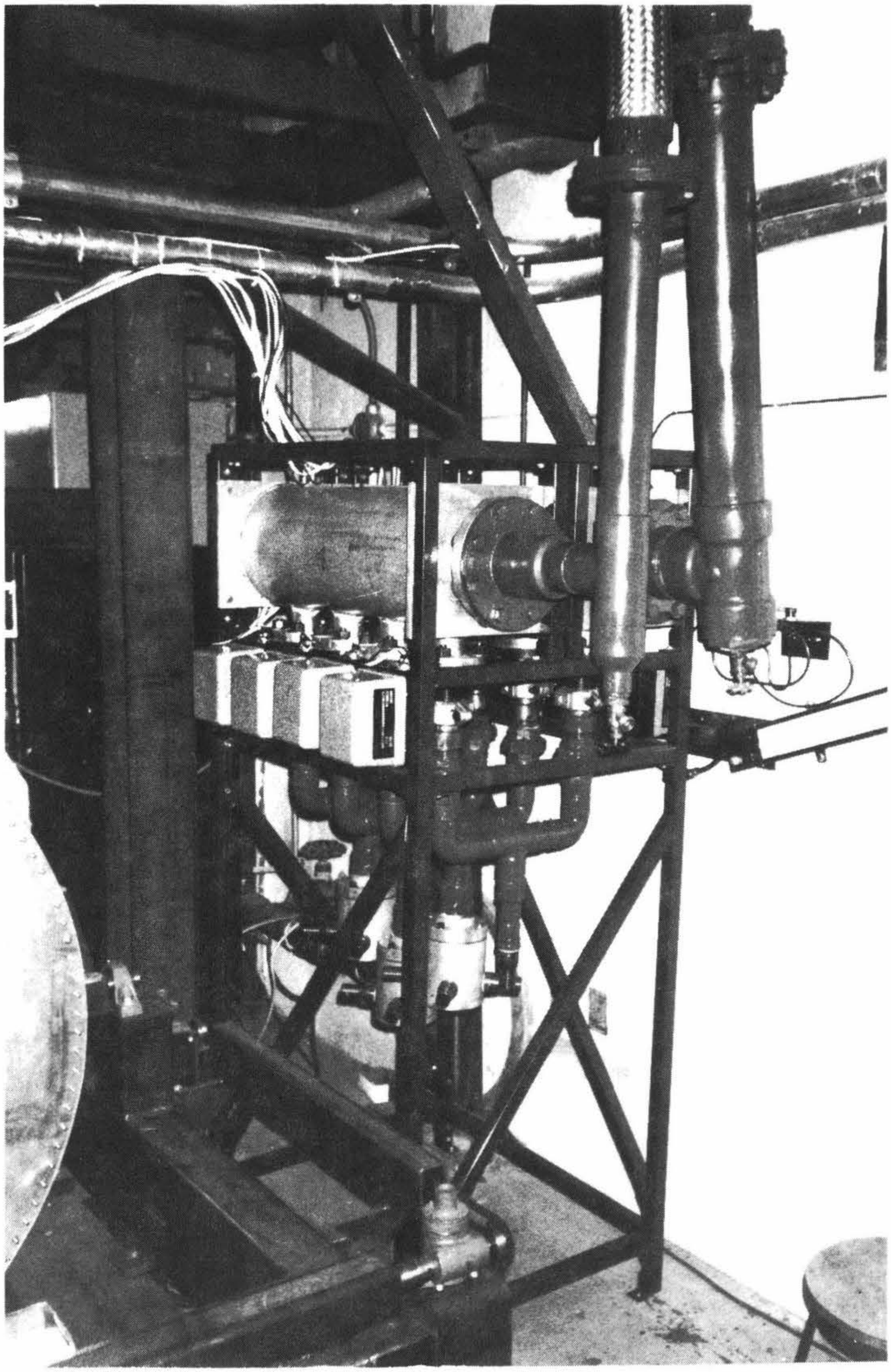

Photo. 7 Injection/Suction Flow Control System

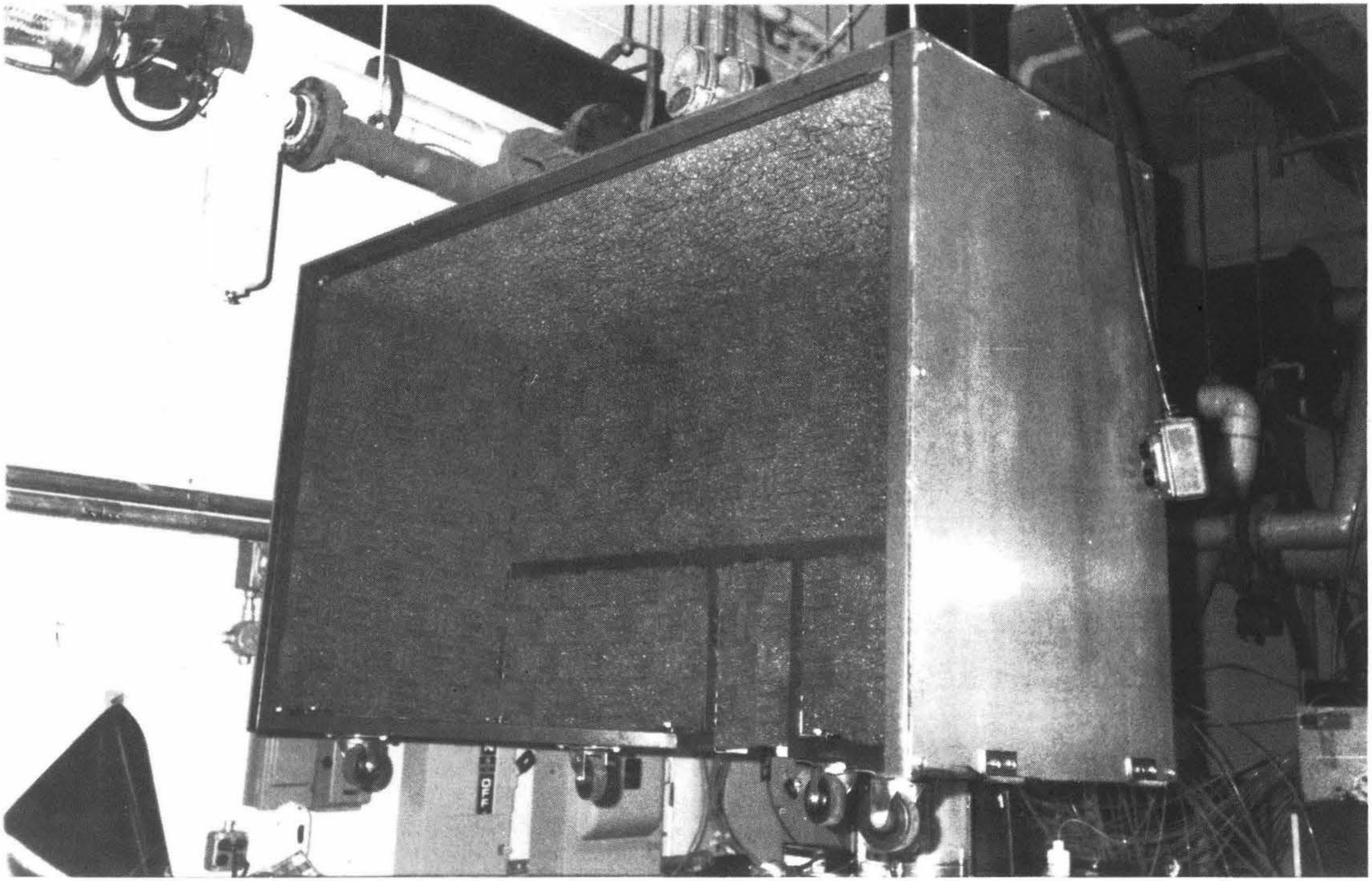

Photo. 8 Inlet Noise-Attenuator/Protector

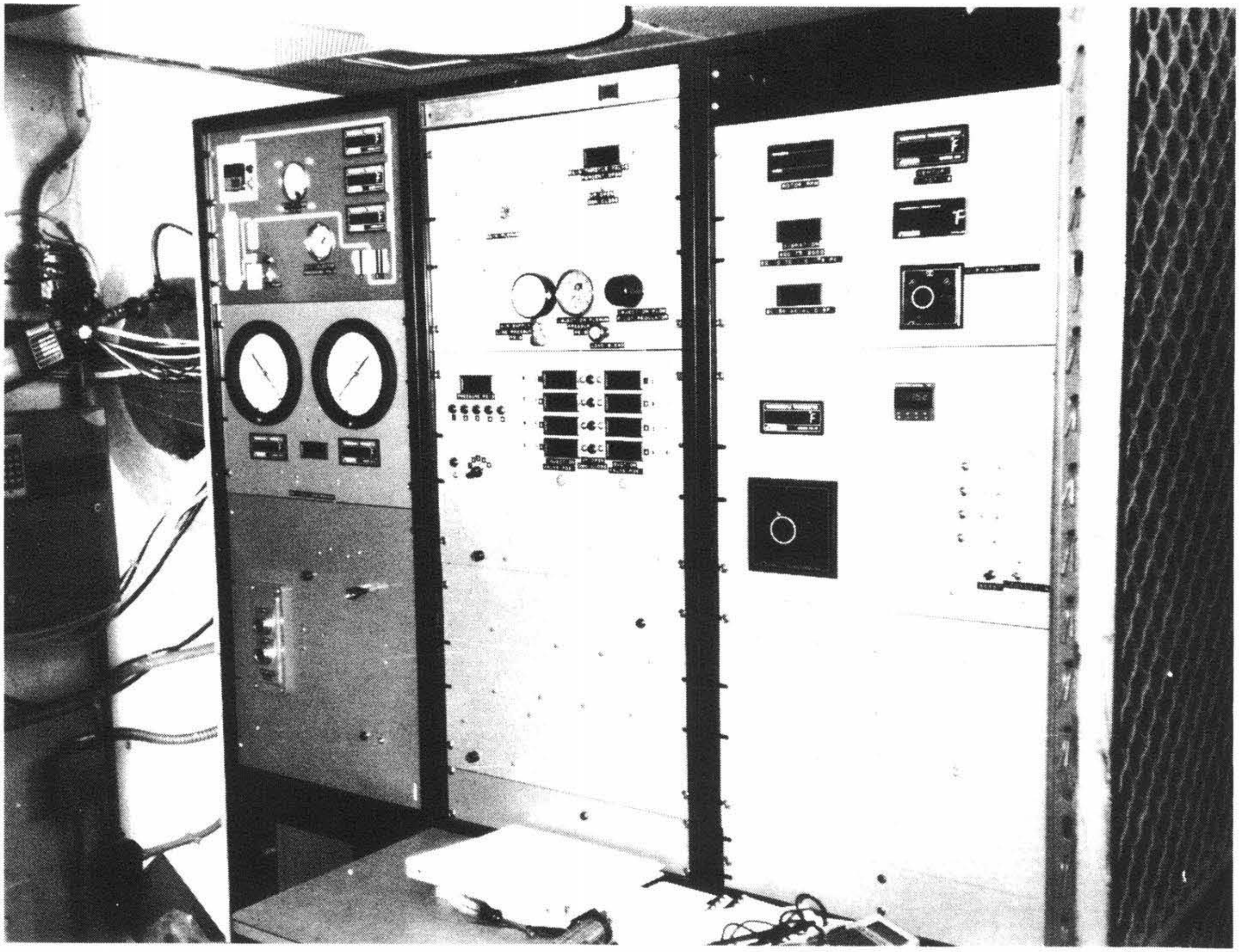

Photo.9 Main Facility-Control Panel

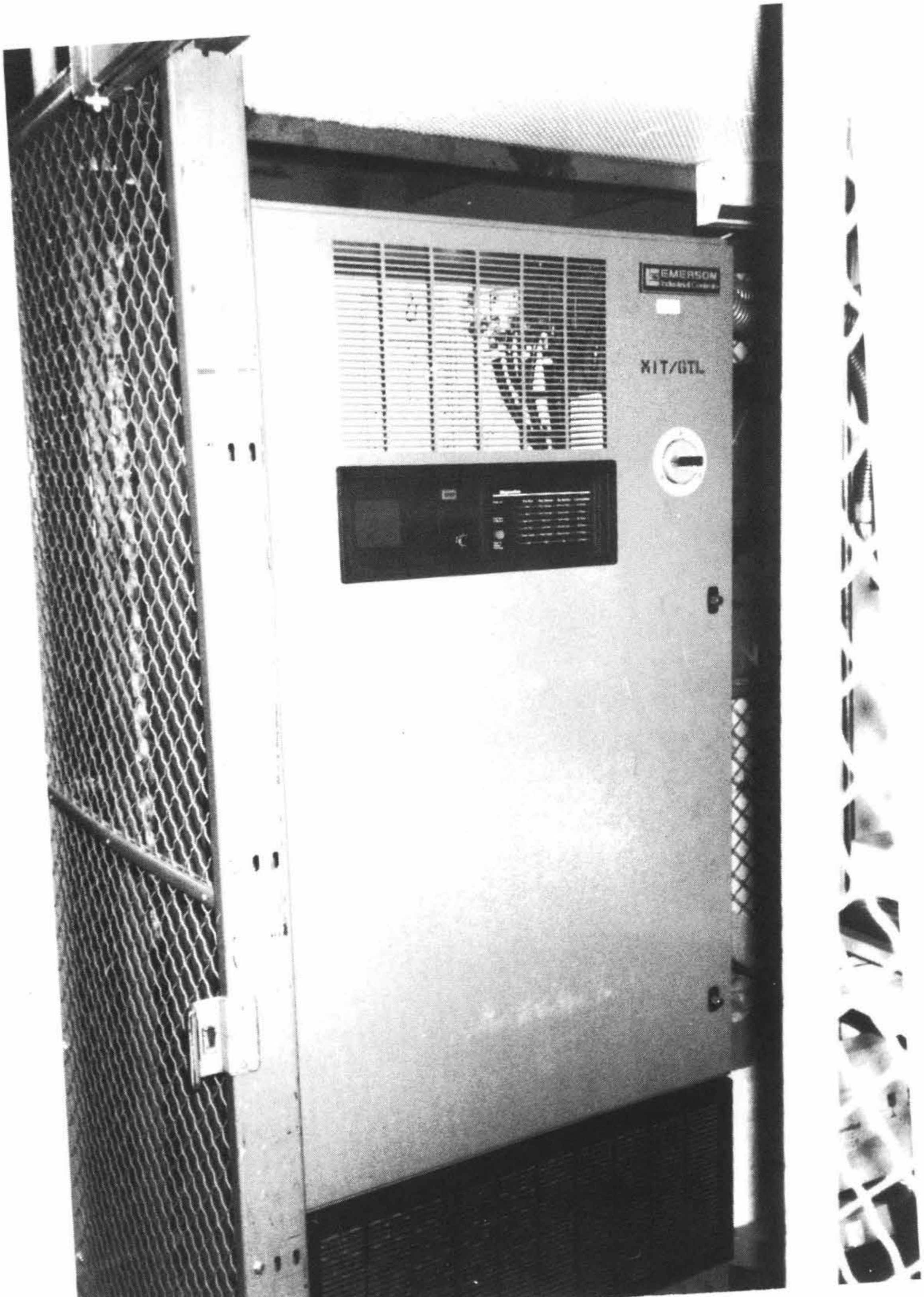

Photo. 10 Swirl-Generator Drive Motor Variable Frequency Power Supply

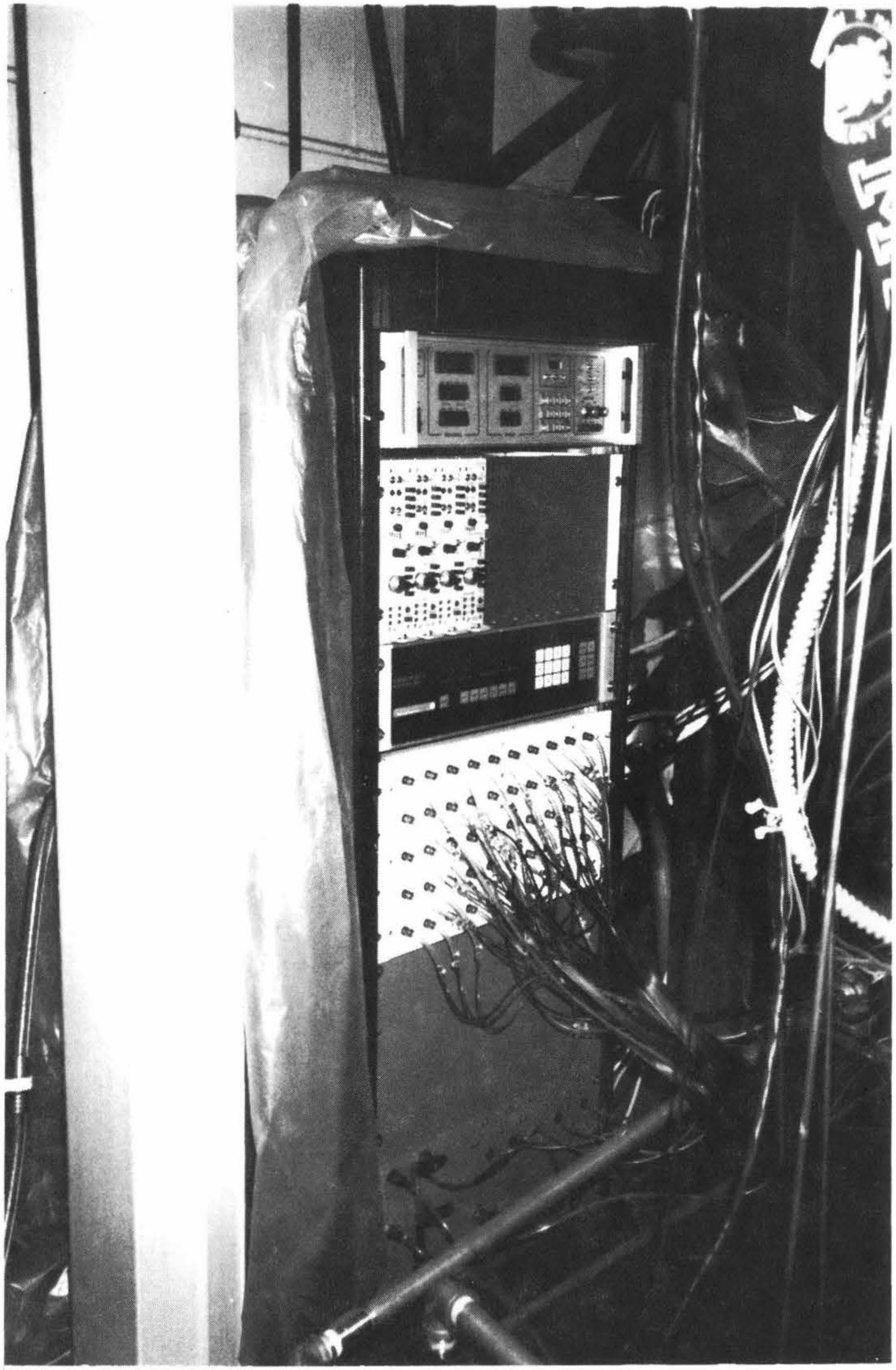

Photo. 11 Data Acquisition Instrumentation

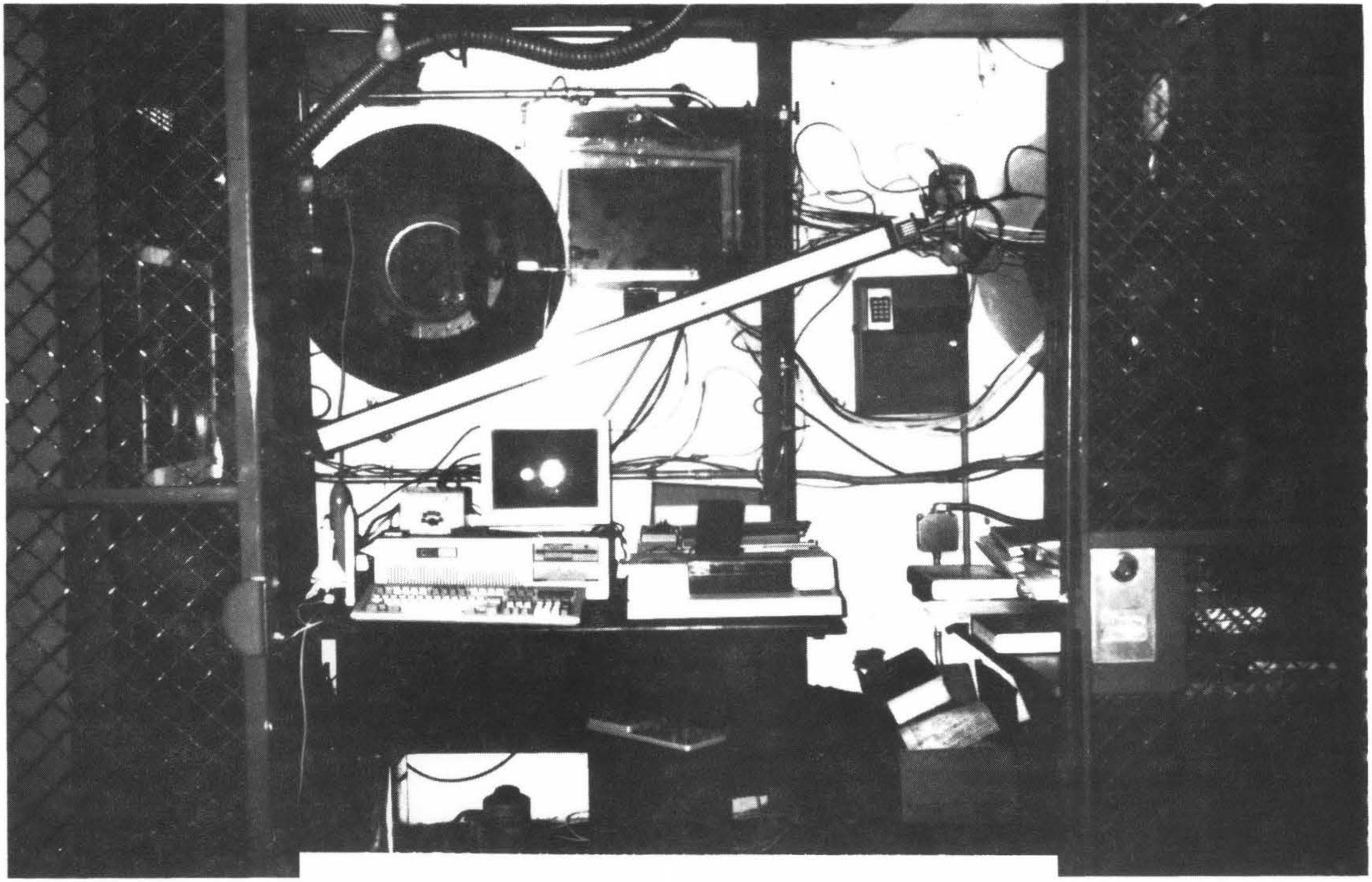

Photo. 12 Data Acquisition Station

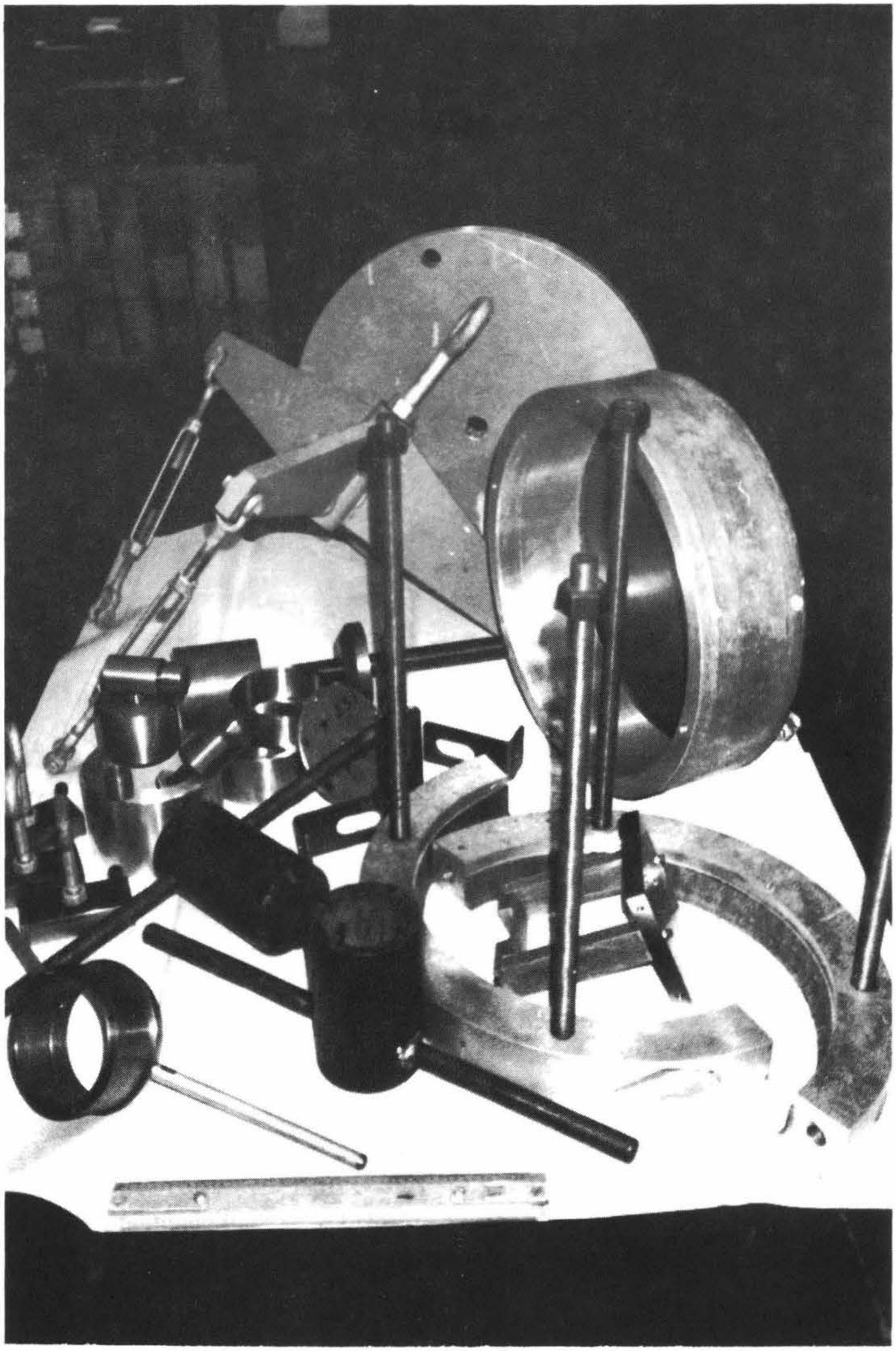

Photo. 13 Assembly/Disassembly Tools

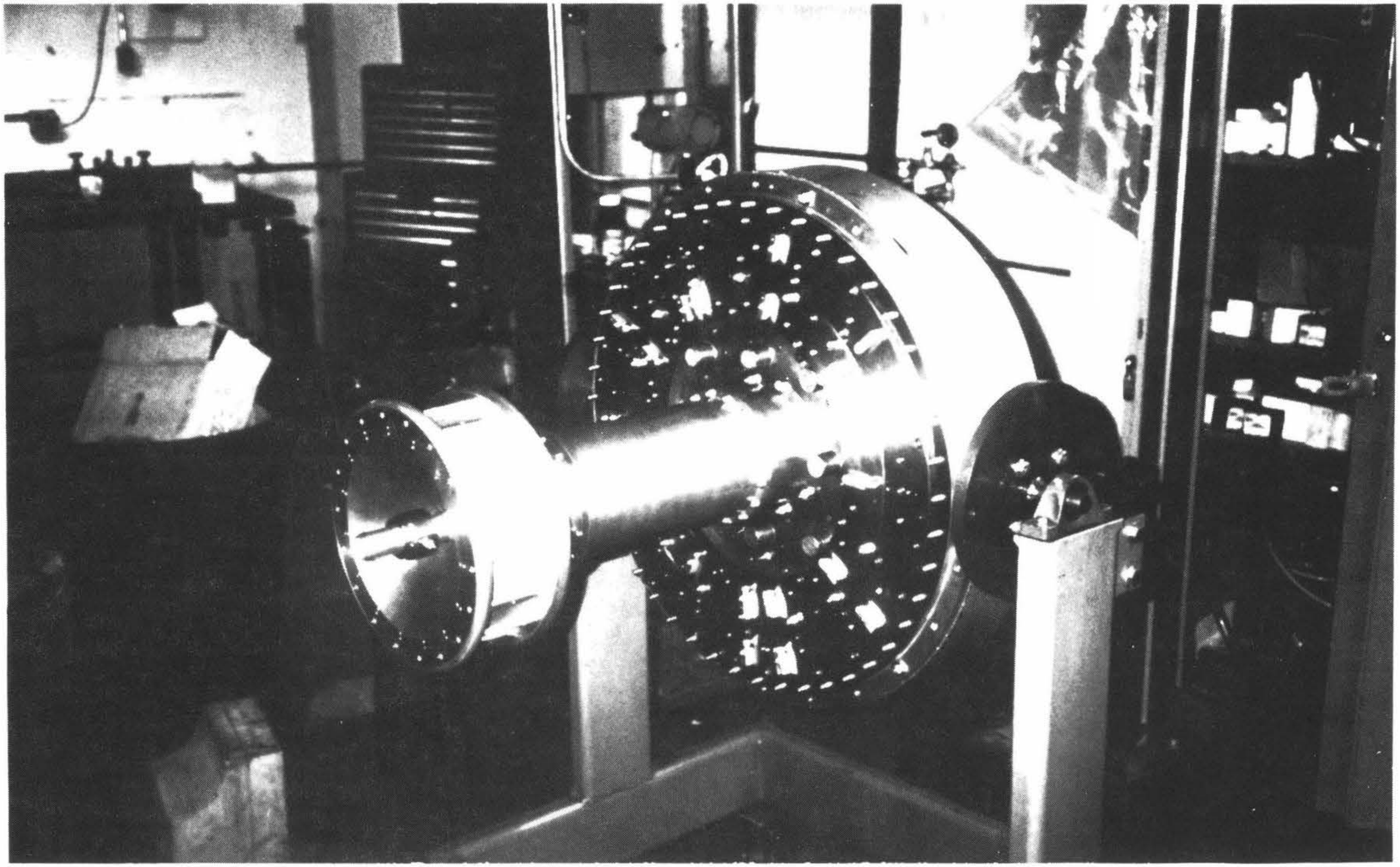

Photo. 14 Auxiliary Assembly/Disassembly Pivot-Stand With Diffuser Housing Front Section

APPENDIX A

VORTEX-NOZZLE/CONTOURED DUCT SWIRL GENERATOR BOUNDARY-LAYER ANALYSIS

The vortex-nozzle/contoured-duct swirl-generator concept was initially considered for generating the required swirling radial-outflow for the present diffuser studies as described in chapter 1. Because of the required diffusion in the radial-to-axial turn of the contoured axi-symmetric duct, an analysis was performed to estimate the boundary-layer thickness and wall flow-angle distributions along the duct wall. This analysis was patterned after a momentum-integral approach taken by Senoo et al. [54] for radial vaneless diffusers, generalized to the case of an axi-symmetric duct of arbitrary meridional shape.

With the assumptions that the boundary layer is axi-symmetric and that the radius of curvature of the duct wall in the meridional plane is small compared with the boundary layer thickness, the resulting momentum-integral boundary-layer equations are:

s-Momentum:

$$\left[\frac{dr_0}{ds}\right] \int_0^\delta \rho w^2 dz + \hat{U}\frac{d}{ds}\int_0^\delta \rho u(r_0 \pm z\cos\varphi)dz$$
$$= \frac{d}{ds}\int_0^\delta \rho u^2(r_0 \pm z\cos\varphi)dz + \left[\frac{dP}{ds}\right]\int_0^\delta (r_0 \pm z\cos\varphi)dz + \tau_{w_s} r_0 \quad \text{(A.1)}$$

θ-Momentum:

$$\frac{d}{ds}\int_0^\delta \rho wu(r_0 \pm z\cos\varphi)^2 dz$$
$$= \hat{W}(r_0 \pm \delta\cos\varphi)\frac{d}{ds}\int_0^\delta \rho u(r_0 \pm z\cos\varphi)dz - \tau_{w_\theta} r_0^2 \quad \text{(A.2)}$$

In these equations, where $\pm$ is shown, the (+) sign is used for the hub (inner wall) and the (-) sign is used for the shroud (outer wall). The local coordinate z is orthogonal to the duct wall at any location s and is zero at either wall with the positive sense being away from the wall into the flow.

The assumed boundary layer meridional and tangential velocity profiles are:

$$\frac{u}{\hat{U}} = \left[\frac{z}{\delta}\right]^{1/n} \left[1 - \left[1 - \frac{z}{\delta}\right]^{m} \tan\gamma \tan\hat{\alpha}\right] \tag{A.3}$$

$$\frac{w}{\hat{W}} = \left[\frac{z}{\delta}\right]^{1/n} \left[1 + \left[1 - \frac{z}{\delta}\right]^{m} \tan\gamma \cot\hat{\alpha}\right] \tag{A.4}$$

Here, $m = 3$ and $n = 2.667 Re_{\delta}^{0.125}$ as in [54].

A linear variation in boundary layer density from the wall to the boundary layer edge was assumed:

$$\rho = \frac{\hat{\rho}}{\left[1 + \mathcal{R}\left[\frac{\gamma-1}{2}\right]\hat{M}^2\right]} \left[1 + \mathcal{R}\left[\frac{\gamma-1}{2}\right]\hat{M}^2\left[\frac{z}{\delta_T}\right]\right] \tag{A.5}$$

where $\mathcal{R}$ is the recovery factor and δ_T is the thermal boundary layer thickness.

From Shapiro [55], for Mach numbers less than $\simeq 2$, a good approximation for $\mathcal{R}$ is:

$$\mathcal{R} \cong \sqrt[3]{Pr} \tag{A.6}$$

Also from [55],

$$\frac{\delta}{\delta_T} = \sqrt{\frac{Pr}{\mathcal{R}}} \tag{A.7}$$

Empirical relationships for wall shear stress as used by Senoo et al. [54] were assumed to apply to the present configuration:

$$\tau_{w_s} = \frac{\hat{\rho}\hat{U}^2_{tot}}{2} k_f \lambda Re_{\delta}^{-0.25} (\cos\hat{\alpha} - \sin\hat{\alpha}\tan\gamma) \tag{A.8}$$

and,

$$\tau_{w_\theta} = \frac{\hat{\rho}\hat{U}^2_{tot}}{2} k_f \lambda Re_{\delta}^{-0.25} (\sin\hat{\alpha} + \cos\hat{\alpha}\tan\gamma) \tag{A.9}$$

where,

$$\hat{U}^2_{tot} \equiv \hat{U}^2 + \hat{W}^2, \tag{A.10}$$

$$Re_\delta \equiv \frac{\hat{\rho}\hat{U}\delta}{\mu}, \tag{A.11}$$

$$\lambda \equiv 1.0 - 0.07\hat{M} + 0.009\hat{M}^2 - 0.017\hat{M}^3, \tag{A.12}$$

and, k_f is an empirical constant taken to be 0.045 based on the discussion in [54].

Substituting eq's. (A.3) through (A.12) into (A.1) and (A.2) and performing the integration and differentiation results in two coupled non-linear ordinary differential equations for de/ds and $d\delta/ds$.

These equations were solved for e and δ as a function of s by means of a fourth order Runge-Kutta numerical integration scheme with $\hat{U}_{tot}$, $\hat{\alpha}$, $\hat{M}$, and $\hat{\rho}$ imposed at the boundary layer edge by the inviscid core streamline-curvature solution described in chapter 1. The calculated boundary-layer thickness and wall flow angle distributions are shown in figure 1.5. These results correspond to the inviscid streamline-curvature solution shown in figure 1.4.

APPENDIX B

SWIRL-GENERATOR PRELIMINARY DESIGN ANALYSIS

Once the basic swirl-generator concept was defined as described in chapter 1, various geometric and operating-point design parameters had to be selected. As discussed in chapter 2, section 2.1, the basic requirement that the swirl-generator blading be of constant span and untwisted was imposed to simplify design and manufacturing. With this constraint, the basic design and operating-point parameters which had to be selected prior to the detailed design of the machine included the vaneless-space radius ratio, the rotor-exit relative Mach number, the rotor-blade radius ratio, the number of blades, and the rotor pre-whirl angle. Selection of these parameters defines the rotor inlet and exit velocity triangles.

Since the complexity and cost of the test facility increases with the required shaft power and since it is desirable for the entire operating-speed envelope of the swirl generator to be below the first critical-speed as discussed in section 2.2.6, the main objective of the preliminary design analysis was to determine the dependence of the required shaft speed and power on the vaneless space radius ratio, rotor-exit design-point relative Mach number, and pre-whirl angle. In addition, the dependence of the blade loading on these parameters and on the number of blades and blade radius-ratio had to be determined. To study these basic relationships, the following idealizations were made:

1.) The flow in the vaneless-space is axi-symmetric, axially uniform, and adiabatic-isentropic.

2.) The flow upstream and downstream of the rotor blading is axi-symmetric and axially-uniform.

3.) The flow in the laboratory frame of reference is steady upstream and downstream of the rotor blading.

4.) The air behaves as a perfect gas with constant specific heat C_p.

In this analysis, the target diffuser-inlet-condition is specified by a Mach number of 1.0 and a swirl angle of 75°. Using assumptions 1 and 3, above, the rotor exit absolute Mach number and swirl angle required to obtain this diffuser inlet condition is determined as follows:

From assumptions 1 and 3, the tangential component of the Navier-Stokes equation reduces to (in cylindrical coordinates):

$$C_r \frac{dC_\theta}{dr} + \frac{C_r C_\theta}{r} = 0 \tag{B.1}$$

and the continuity of mass-flow equation simplifies to:

$$\frac{d}{dr}(\rho r b C_r) = 0 \tag{B.2}$$

Integrating equation B.1 gives:

$$rC_\theta = const. \tag{B.3}$$

or,

$$r_{1'} C_{\theta 1'} = r_1 C_{\theta 1} \tag{B.4}$$

where $1'$ designates the vaneless-space inlet radius and 1 designates the discrete-passage diffuser inlet radius.

From equation B.2 and the isentropic compressible flow relations: $\dfrac{\rho_{st_1}}{\rho_{st_{1'}}} = \left[\dfrac{T_{st_1}}{T_{st_{1'}}}\right]^{\frac{1}{\gamma-1}}$ and $\dfrac{T_{st_1}}{T_{st_{1'}}} = \dfrac{1 + \frac{\gamma-1}{2}M_{1'}^2}{1 + \frac{\gamma-1}{2}M_1^2}$, the following relationship is obtained:

$$\frac{C_{r_{1'}}}{C_{r_1}} = \frac{r_1}{r_{1'}} \frac{b_1}{b_{1'}} \left(\frac{1 + \frac{\gamma-1}{2}M_{1'}^2}{1 + \frac{\gamma-1}{2}M_1^2} \right)^{\frac{1}{\gamma-1}} \tag{B.5}$$

Using assumption 4, the definitions of total temperature and Mach number, the basic velocity vector relations, and the assumption of adiabatic flow, equations B.4 and

B.5 are be combined to give the following implicit equation for the rotor exit absolute Mach number in terms of the diffuser inlet Mach number and swirl angle and the vaneless-space radius and width ratios:

$$\frac{M_1^2}{M_{1'}^2}\left(\frac{1+\frac{\gamma-1}{2}M_{1'}^2}{1+\frac{\gamma-1}{2}M_1^2}\right)\left(\frac{b_1}{b_{1'}}\cos^2\alpha_1\left(\frac{1+\frac{\gamma-1}{2}M_{1'}^2}{1+\frac{\gamma-1}{2}M_1^2}\right)^{\frac{2}{\gamma-1}}+\sin^2\alpha_1\right)=\frac{r_{1'}^2}{r_1^2} \qquad \text{B.6}$$

where b is the axial spacing between the front and rear walls of the vaneless space.

Similarly, since $\tan\alpha = \frac{C_\theta}{C_r}$, equations B.4 and B.5 can be combined to obtain a relationship between the diffuser inlet absolute flow angle and the rotor exit absolute flow angle:

$$\frac{\tan\alpha_{1'}}{\tan\alpha_1}=\frac{b_{1'}}{b_1}\left(\frac{1+\frac{\gamma-1}{2}M_1^2}{1+\frac{\gamma-1}{2}M_{1'}^2}\right)^{\frac{1}{\gamma-1}} \qquad \text{B.7}$$

Given the discrete-passage diffuser inlet Mach number and swirl angle and the radius and width ratios of the vaneless space, equations B.6 and B.7 are used to determine the required rotor-exit absolute Mach number and swirl angle. The rotor speed, power, and blade angles can then be determined as follows:

The required blading power can be determined from Euler's equation, which invoking assumption 2, can be written as:

$$\dot{W}=\dot{m}\left[U_{1'}C_{\theta_{1'}}-U_0C_{\theta_0}\right] \qquad \text{B.8}$$

where location 0 is at the inlet to the rotor and location 1′ is at the exit of the rotor as defined in figure B.1.

Assuming adiabatic flow, equation B.8 together with the energy equation gives the total-temperature rise through the rotor blading :

$$T_{t1'} - T_{t0} = \frac{1}{C_p}\left[U_{1'}C_{\theta_{1'}} - U_0 C_{\theta_0}\right] \qquad \text{B.9}$$

Using the basic relations:

$$U = \Omega r \ , \qquad \text{B.10}$$

$$a = \sqrt{\gamma R T_{st}} = \frac{C}{M} \ , \qquad \text{B.11}$$

$$\frac{T_t}{T_{st}} = 1 + \frac{\gamma-1}{2}M^2 \ , \qquad \text{B.12}$$

and the velocity triangle geometry relations according to the nomenclature defined in figure B.1, together with equation B.9, gives a quadratic expression for $C_{\theta_{1'}}$ in terms of $M_{1'}$, $\alpha_{1'}$ $M_{rel1'}$, C_{θ_0}, and T_{t0} :

$$\left\{\frac{C_p\left[1 + \frac{1-\gamma}{2}M_{1'}^2\right]}{\gamma R M_{1'}^2 \sin^2\alpha_{1'}} - \left[1 - \frac{M_{rel1'}}{M_{1'}}\frac{\sin\beta_{1'}}{\sin\alpha_{1'}}\right]\right\} C_{\theta_{1'}}^2 \ +$$

$$C_{\theta_0}\frac{r_0}{r_{1'}}\left\{1 - \frac{M_{rel1'}}{M_{1'}}\frac{\sin\beta_{1'}}{\sin\alpha_{1'}}\right\} C_{\theta_{1'}} - C_p T_{t0} = 0 \qquad \text{B.13}$$

where $\beta_{1'} = \cos^{-1}\left[\frac{M_{1'}}{M_{rel1'}}\cos\alpha_{1'}\right]$ as can be seen from figure B.1.

From continuity,

$$\dot m_{1'} = \dot m_0 = \dot m = \left[\frac{P_t}{RT_t}\right]\frac{\sqrt{\gamma R T_t}\ M\ 2\pi r b\ \cos\alpha}{\left[1 + \frac{\gamma-1}{2}M^2\right]^{\frac{\gamma+1}{2(\gamma-1)}}} \qquad \text{B.14}$$

or,

$$\frac{\dot{m}_{1'}}{\dot{m}_0} = 1 = \left[\frac{P_{t1'}}{P_{t0}}\right] \left[\frac{T_{t0}}{T_{t1'}}\right]^{\frac{1}{2}} \left[\frac{M_{1'}}{M_0}\right] \left[\frac{r_{1'}}{r_0}\right] \left[\frac{b_{1'}}{b_0}\right] \left[\frac{\cos\alpha_{1'}}{\cos\alpha_0}\right] \left(\frac{1 + \frac{\gamma-1}{2}M_0^2}{1 + \frac{\gamma-1}{2}M_{1'}^2}\right)^{\frac{\gamma+1}{2(\gamma-1)}} \qquad \text{B.15}$$

A polytropic blading-efficiency was assumed to relate the total pressure and total temperature ratios across the rotor blading:

$$\frac{P_{t1'}}{P_{t0}} = \left[\frac{T_{t1'}}{T_{t0}}\right]^{\frac{\gamma}{\gamma-1}\eta_{tt_p}} \qquad \text{B.16}$$

In addition, as can be seen from figure B.1, the following velocity-triangle relation can be written:

$$\Omega r_{1'} = C_{\theta_{1'}}\left(1 - \left[\frac{M_{rel_{1'}}}{M_{1'}}\right] \left[\frac{\sin\beta_{1'}}{\sin\alpha_{1'}}\right]\right) \qquad \text{B.17}$$

and the relationship between the absolute tangential velocity and absolute Mach number at the rotor inlet is:

$$C_{\theta_0} = \frac{\sqrt{\gamma R T_{t0}}\; M_0 \; \sin\alpha_0}{\left[1 + \frac{\gamma-1}{2}M_0^2\right]^{\frac{1}{2}}} \qquad \text{B.18}$$

Given the desired diffuser-inlet Mach number and swirl angle, together with the radius ratios of the vaneless space and the rotor blading and with $b_0 = b_{1'} = b_1$, equations B.6 through B.9 and B.13 through B.18 are solved simultaneously to determine the required rotor speed and blading power.

As discussed in chapter 2, a lift-coefficient was used as an indication of the blade loading for selection of the blade radius-ratio and the number of blades.

As in the analysis in [61], the blade lift coefficient is defined as:

$$C_L = \frac{\text{tangential aerodynamic force}}{\text{tangential blade area} \times \text{rotor-exit relative dynamic pressure}} \qquad \text{B.19}$$

This can be expressed in terms of the relevant rotor-blade geometric and operating parameters as follows:

The torque required to spin the swirl-generator rotor at a steady speed is obtained from the conservation of angular momentum across the rotor (neglecting disk windage, and seal and bearing drag):

$$Tq = \dot{m}_1 \left[r_{1'} C_{\theta_{1'}} - r_0 C_{\theta_0} \right] \qquad \text{B.20}$$

The torque can also be represented as:

$$Tq = \frac{r_{1'} - r_0}{2} \times F_{t_{bl}} \times Z \qquad \text{B.21}$$

where $F_{t_{bl}}$ is the tangential lift on a single blade, assumed to act at the mean blade radius and Z is the number of blades.

The tangential blade area is:

$$A_{b_t} = b \left[r_{1'} - r_0 \right] \qquad \text{B.22}$$

and the rotor exit relative dynamic pressure can be expressed as:

$$\left[P_{t_{rel_{1'}}} - P_{st_{1'}} \right] = P_{t_{1'}} \frac{\left[1 + \frac{\gamma - 1}{2} M^2_{rel_{1'}} \right]^{\frac{\gamma}{\gamma - 1}} - 1}{\left[1 + \frac{\gamma - 1}{2} M^2_{1'} \right]^{\frac{\gamma}{\gamma - 1}}} \qquad \text{B.23}$$

Using equations B.20 through B.23, the blade lift coefficient as defined by B.19 can be expressed in terms of the basic geometric parameters of the blade and the upstream and downstream flow parameters:

$$C_L = \frac{2\dot{m}\left[r_{1'}C_{\theta_{1'}} - r_0 C_{\theta_0}\right]\left[1 + \frac{\gamma-1}{2}M_{1'}^2\right]^{\frac{\gamma}{\gamma-1}}}{P_{t1'}b\left[r_{1'} + r_0\right]\left[r_{1'} - r_0\right]\left[\left[1 + \frac{\gamma-1}{2}M_{rel\,1'}^2\right]^{\frac{\gamma}{\gamma-1}} - 1\right]Z} \qquad \text{B.24}$$

The results and discussion of this analysis are given in chapter 2.

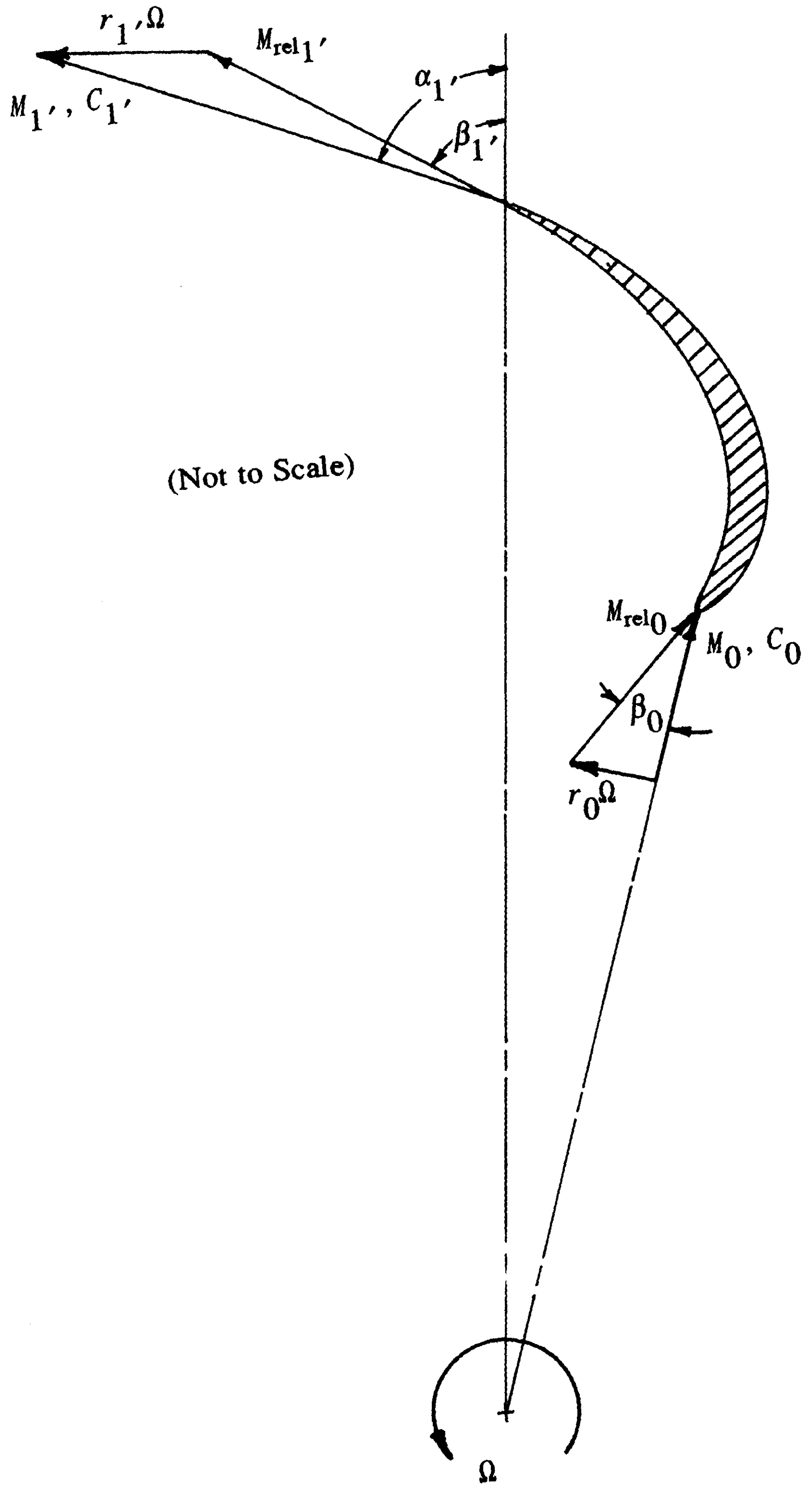

Fig. B.1 Swirl Generator Rotor Blading Velocity Vector Diagrams

APPENDIX C

STRESS ANALYSIS OF THE BLISK AND SHAFT

The stress analysis of the blisk was carried out based on the ordinary differential equations developed in [11] for a variable thickness rotating disk:

$$r^2 \frac{d^2}{dr^2}(tr\sigma_r) + r\frac{d}{dr}(tr\sigma_r) - (tr\sigma_r) - \frac{r}{t}\frac{dt}{dr}\left[r\frac{d}{dr}(tr\sigma_r) - \nu\,(tr\sigma_r)\right] + (3+\nu)\,\rho\Omega^2 r^3 t = 0 \qquad \text{C.1}$$

$$\frac{d}{dr}(tr\sigma_r) - t\sigma_t + \rho\Omega^2 r^2 t = 0 \qquad \text{C.2}$$

$$\frac{du}{dr} = \frac{1}{E}\,(\sigma_r - \nu\sigma_t) \qquad \text{C.3}$$

where u is the radial displacement.

The analysis assumes axial symmetry and no variation of stress in the axial direction (i.e. it is assumed that the component of stress in the axial direction of the rotor is zero). The effect of the blading and shroud on the stress distribution within the disk was approximated by a distributed mass in the form of an additional thickness added over the radius range covered by the blading.

The disk stress analysis was done assuming a rotor rotational speed of 7200 RPM. This is the maximum possible rotor rotational speed with the current facility setup. The modulus of elasticity, E, for 6061-T6 aluminum was taken to be 10.0×10^6 psi and Poisson's ratio, ν, was taken to be 0.34. The corresponding calculated tangential and radial stress distributions are shown in figure C.1a and the radial displacement distribution is given in figure C.1b.

To verify structural integrity of the disk, the failure criterion of von Mises was applied, which for the present case can be written as:

$$\sqrt{\sigma_r^2 + \sigma_t^2 - \sigma_r\sigma_t} < \sigma_{yp} \qquad \text{C.4}$$

for safe operation, where σ_{yp} is the yield strength of the material.

From the results shown in figure C.1a, the greatest value of the left side of inequality C.4 occurs at the bore of the blisk and is equal to 6079 psi. Since the yield strength of 6061-T6 aluminum is 38000 psi at the present maximum operating temperature of 150°F, the factor of safety on yield strength is 6.25, not taking into account the stress concentration in the bore keyways. The endurance limit for 6061-T6 aluminum is however only 14000 psi, giving a factor of safety of 2.3 on fatigue strength.

The prediction of the stress concentration in the corners of the keyways is difficult. Typically, for a sharp-cornered keyway in a ductile material, local yielding occurs upon initial application of load providing a "natural" stress relief. Initial over-spinning of the disk could be used to yield these high-stress regions in the bore so that they then normally operate in compression, inhibiting crack growth. In the present case, to reduce the stress concentration in the keyway corners, a somewhat unconventional keyway design was used, with the keyway corners rounded to a 0.0625 inch radius.

A simple estimation of the maximum stress level in the blading and shroud/blading interface was made to verify that these parts of the blisk are of adequate strength.

The stress distribution within the blade is the result of a combination of the effects of the centripetal-acceleration body force acting on the blade, the static pressure difference across the blade, the loading imposed on the blade at the hub and shroud, pre-stress remaining from the manufacturing processes, and thermal stress. In the present analysis, only the first two effects were considered, although the blisk was stress relieved during manufacturing. Modeling an element of the blade as a beam spanning the distance from the hub to the shroud with fixed supports at the ends, it can be easily shown that the maximum normal stress in the blade element due to centripetal acceleration and aerodynamic loading occurs at the ends and is equal to:

$$\sigma_{max} = \frac{\rho_{al}\Omega^2 b^2 r}{2t}\sin\beta + \frac{\Delta P_{st} b^2}{2t^2} \qquad \text{C.5}$$

where ρ_{al} is the density of aluminum, t is the thickness of the blade element, b is the span and β is the blade angle.

The first term in equation C.5 represents the centripetal acceleration loading and is an approximation in that it assumes that the blade element is constrained to deflect only in the direction normal to the camber line. The second term in equation

C.5 represents the effect of aerodynamic loading.

As can be seen from equation C.5, the highest stress due to centripetal acceleration can be expected at the trailing edge in the present design as this is where r is greatest, t is smallest, and β is greatest. The effect of aerodynamic loading according to equation C.5 is that for a given ΔP_{st}, the maximum stress occurs at the thinnest portion of the blade. Although ΔP_{st} vanishes at the trailing edge, if it can be shown that the calculated stress level at the trailing edge is acceptably low with the assumption that the maximum possible ΔP_{st} acts at the trailing edge, then according to equation C.5, the stress level will be acceptably low throughout the rest of the blade.

With a trailing edge thickness of 0.50 mm, the first term of equation C.5 gives a maximum centripetal acceleration stress of 3026 psi at the maximum possible speed of 7200 RPM. As can be seen from figure 2.12a, the maximum design point value of ΔP_{st} across the rotor blade is approximately 2. psid. Using a very conservative value of 4. psid to account for flow unsteadiness and the increase of ΔP_{st} with approximately the square of the speed from the design point value to that which would occur at the maximum speed of 7200 RPM, the second term of equation C.5 gives a stress value of 647 psi for a combined centripetal-acceleration/aerodynamic maximum stress level of 3673 psi within the blade. This is a very conservative value since the modeling of the trailing edge as an isolated beam spanning the distance between the hub and shroud does not take into account the support the trailing edge receives from the thicker portion of the blade. Since the yield strength of 6061-T6 aluminum at the operating temperature of 150° F is 38000 psi with an endurance limit of 14000 psi, the structural integrity of the swirl generator blading is assured.

A simple conservative-estimate of the average shear-stress level in the brazed interface between the blading and the shroud/labyrinth-seal was also made. The shroud, if unsupported by the blading and spinning at the same speed as the blisk, would have a greater radial growth than the blisk. With the shroud brazed onto the blading, this radial growth is restrained by the shear stress at the blading/shroud brazed interface and by the hoop stress within the shroud. An upper limit of the average shear stress at the blading/shroud interface can be found by neglecting the hoop stress. It can then be easily shown that for a large number of blades ($Z >> 1$), the average shear stress at the blade/shroud interface is:

$$\tau_{ave} \simeq \frac{2\pi\rho_{a1}\Omega^2 t}{ZA_{b1}}\left[\frac{r_0^{\,3} - r_i^{\,3}}{3}\right] \qquad \text{C.6}$$

where t is the average thickness of the shroud and A_{bl} is the blade cross-section area.

The calculated average shear stress at the blading/labyrinth-seal interface for the present blisk design according to equation C.6 is 740 psi at the maximum blisk speed of 7200 RPM. Considering the conservative assumption of no hoop stress in the shroud, this is a very safe calculated stress level since the shear strength of 6061-T6 aluminum is 30000 psi and a conservative estimate for the braze material joining the shroud to the blading is half this value.

A check for the adequate strength of the swirl-generator rotor shaft was also made. The shaft is primarily subjected to shearing stress due to the torque resulting from the aerodynamic loading on the rotor blading. (During rotor speed transients there is additional torsional loading on the shaft due to the inertia of the blisk, but this was reduced to a negligible level by setting the motor controller speed ramp-up/ramp-down time constants to values of approximately fifteen seconds). As discussed in section 2.2.5, the dimensions of the swirl-generator rotor shaft were set by the stiffness required to place the first critical speed above the operating speed range. This resulted in a very lightly stressed shaft.

From [47] (for example), the maximum shear stress at any given section in the shaft is given by:

$$\tau_{max} = \frac{Tq\,r_o}{J} \qquad \text{C.7}$$

where Tq is the torque and r_o is the outer radius of the shaft at the given section. Since in the present case the entire shaft is subjected to the same torque, the maximum stress in the shaft occurs at the section of smallest diameter which in the present case is 2.2 inches. From the analysis given in appendix B (equation B.20), the maximum torque due to aerodynamic loading was estimated to be 500 inch-pounds. This results in τ_{max}=240 psi which is very low compared to the shear strength (85000$^+$ psi) of the 4340 low-alloy-steel shaft material.

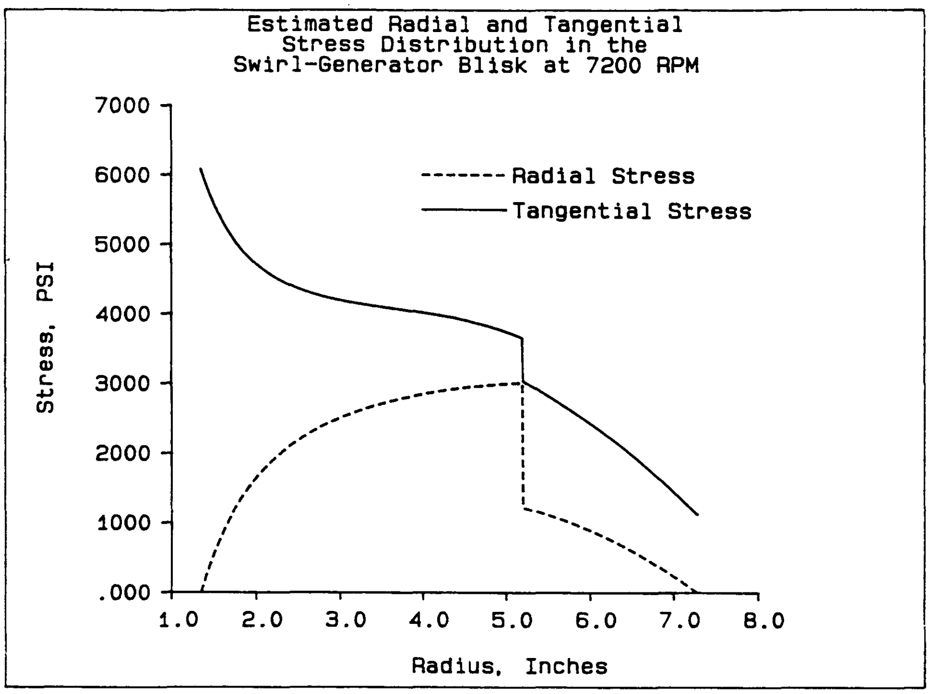

Fig. C.1a Calculated Radial and Tangential Stress distribution in Blisk

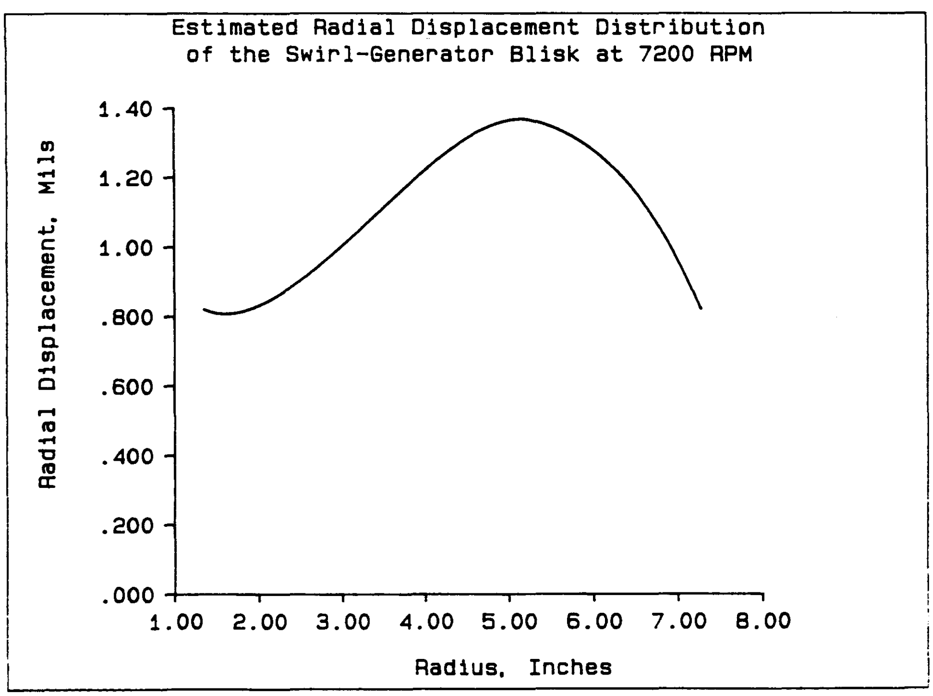

Fig. C.1b Calculated Radial Displacement Distribution in Blisk

APPENDIX D

CRITICAL SPEED ANALYSIS

As discussed in section 2.2.6, a key objective in the design of the swirl generator rotor was the placement of the first critical speed at least 30% above the maximum operating speed of 7200 RPM so that the machine can be operated without any speed restrictions in the range from 0 to 7200 RPM. Both shaft flexing and torsional modes were considered in the analysis which was based on the analysis presented by Stodola [59].

The lowest frequency shaft-flexing critical speed for the present overhung blisk configuration is the lower synchronous backward-precession critical speed as discussed by Stodola [59]. In this mode, the shaft/bearing deflection is as shown schematically in figure D.1. Here, it is assumed that the section of the shaft between the front and rear bearings has infinite stiffness compared to the overhung potion and that the precession of the shaft occurs about the rear bearing (point *0* figure D.1). (This is an improvement over the analysis presented by Stodola which assumed infinite stiffness for the bearings closest to the overhung disk). To simplify the present analysis, the mass and diametral moment of inertia of the shaft was taken into account by adding the mass of the shaft to the blisk as a point mass located at the center of mass of the blisk. This results in a conservative (lower than actual) estimate of the critical speed.

For equilibrium, the sum of the moments acting on the shaft about point *0* must be zero. In terms of the notation of figure D.1, this can be written as:

$$\Sigma M_o = 0 = 3I_d\Omega^2\varepsilon_2 + \Delta_d\Omega^2(L_1+L_2)m - \Delta_1 k_{br} L_1 \qquad \text{D.1}$$

were I_d is the blisk diametral moment of inertia and $3I_d\Omega^2\varepsilon_2$ is the moment acting on the shaft due to the rate of change of angular momentum of the blisk in synchronous backward precession. This moment, in combination with the transverse force on the shaft due to the centripetal acceleration of the center of mass of the blisk, results in the deflection of the cantilevered portion of the shaft, Δ_2, and the change in the slope, ε_1:

$$\Delta_2 = \frac{1}{JE}\left[\frac{F_d L_2^3}{3} + \frac{M_d L_2^2}{2}\right] \qquad \text{D.2a}$$

$$\varepsilon_1 = \frac{1}{JE}\left[\frac{F_d L_2^2}{2} + M_d L_2\right] \qquad \text{D.2b}$$

were $F_d = m\Delta_d\Omega^2$ and $M_d = 3I_d\Omega^2\varepsilon_2$.

The total deflection and slope of the shaft at the blisk is the combined result of the shaft deflection and the bearing deflection:

$$\Delta_d = \Delta_1\frac{(L_1+L_2)}{L_1} + \Delta_2 \qquad \text{D.3a}$$

$$\varepsilon_2 = \frac{\Delta_1}{L_1} + \varepsilon_1 \qquad \text{D.3b}$$

Equations D.1, D.2a,b, and D.3a,b can be combined to give two coupled linear equations in Δ_d and ε_2:

$$\left(1 - \frac{m\Omega^2 L_2^3}{3JE} - \frac{m\Omega^2}{k_{br}}\left[\frac{L_1+L_2}{L_1}\right]^2\right)\Delta_d - \left(\frac{3I_d\Omega^2 L_2}{2JE} + \frac{3I_d\Omega^2}{k_{br}}\left[\frac{L_1+L_2}{L_1^2 L_2}\right]\right)L_2\varepsilon_2 = 0 \qquad \text{D.4}$$

$$\left(\frac{m\Omega^2 L_2^2}{2JE} + \frac{m\Omega^2(L_1+L_2)}{k_{br}L_1^2}\right)\Delta_d + \left(\frac{3I_d\Omega^2}{JE} + \frac{3I_d\Omega^2}{k_{br}L_1^2 L_2} - \frac{1}{L_2}\right)L_2\varepsilon_2 = 0 \qquad \text{D.5}$$

Equations D.4 D.5 are satisfied when the determinant of their coefficients equals zero. This results in a quadratic equation in Ω^2, the roots of which give the upper and lower synchronous backward precession critical speeds.

The relevant parameters for the present rotor spindle design are:

I_d	0.1032 kg-m^2
m	22.72 kg
k_{br}	7.69×10^8 N/m
J	5.24×10^{-7} m^4
E_{steel}	2.07×10^{11} N/m^2
L_1	0.196 m
L_2	0.104 m

Substituting these values into equations D.4 and D.5 and solving for the roots gives a lower synchronous backward-precession critical speed of 1570 rad/sec. This is over twice the maximum operating speed of 754 rad/sec., satisfying the requirement that the the lowest critical speed be at least 30% above the maximum operating speed.

A check of the lowest shaft torsional vibration mode critical speed was also made. For this purpose, the present rotor configuration can be modeled as a two degree of freedom system consisting of the motor rotor inertia I_m and the blisk inertia I_b connected by a torsional spring of stiffness K_t representing the shaft and coupling stiffness. The lowest natural frequency of this system is:

$$\Omega = \sqrt{K_t \frac{I_m + I_b}{I_m I_b}} \qquad \text{D.6}$$

as given in [12].

In the present case, $I_m = 0.155$ slugs-ft^2, $I_b = 0.147$ slugs-ft^2, and the overall shaft and coupling torsional stiffness was estimated to be 1.14×10^5 ft-lb$_f$/rad. This gives a first torsional critical speed of 1229 rad/sec. which is 63% greater than the maximum operating speed, satisfying the design criterion.

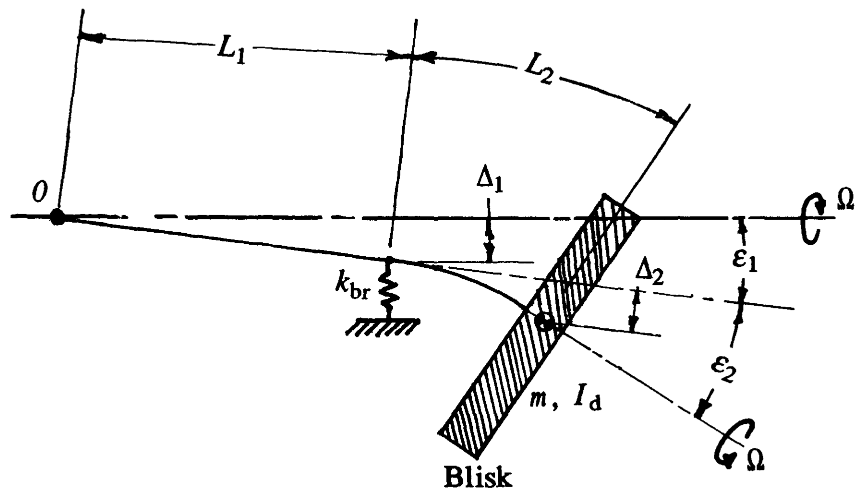

Fig. D.1 Swirl-Generator Rotor In Synchronous Backward Precession

APPENDIX E

DEFLECTION ANALYSIS OF THE TEST SECTION HOUSING

As discussed in section 2.2.7, the axial spacing between the front and rear vaneless space rings (which are supported by the diffuser housing end plates) must be maintained to within ±0.002 inches of the nominal width of 0.354 inches. The manufacturing tolerances were specified to allow this spacing to be set to within ±0.0005 inches with shimming. Due to the pressure loading on the diffuser housing plates, deflection of the diffuser housing must be taken into account.

Using the plate deflection formulas given in reference [28], the deflection of the diffuser housing end plates due to pressure loading was estimated with the assumption that the plates are of constant thickness, clamped on the outer edge (to the diffuser housing ring), and constrained at the inner edge so that there is no rotation at the inner edge. This corresponds to case 14 of reference [28] (pg. 19), which gives the maximum deflection of the plate as:

$$y_{max} = \frac{\beta^3 D_{14} w a^4}{E t^3} \qquad \text{E.1}$$

were: $\beta = \frac{a - b}{a}$ (a is the outer radius of the plate, b the inner radius), D_{14} is a constant which is a function of β (from ref. [28], figure 5), w is the pressure difference across the plate, and t is the plate thickness.

The diffuser housing rear plate has a thickness of 1.3 inches, an outer edge diameter of 28.7 inches, and an inner edge diameter of 14.6 inches. The front plate thickness was taken to be 1.0 inches, with an outer edge diameter of 28.7 inches and an inner edge diameter of 10.4 inches. E, the modulus of elasticity for aluminum is 10.4×10^6 psi. In the worst case, the pressure difference across the plates is 6 psi. According to equation E.1, this results in a deflection of 0.0002 inches for the rear plate and 0.0014 inches for the front plate, for a total maximum relative axial deflection of 0.0016 inches. This satisfies the design criteria as stated above and is a conservative value in that the stiffening provided by the 0.75 inch thick stainless steel probe mounting plates, attached to the front of the diffuser housing, was neglected.

APPENDIX F

SWIRL-GENERATOR COMPONENT DRAWINGS

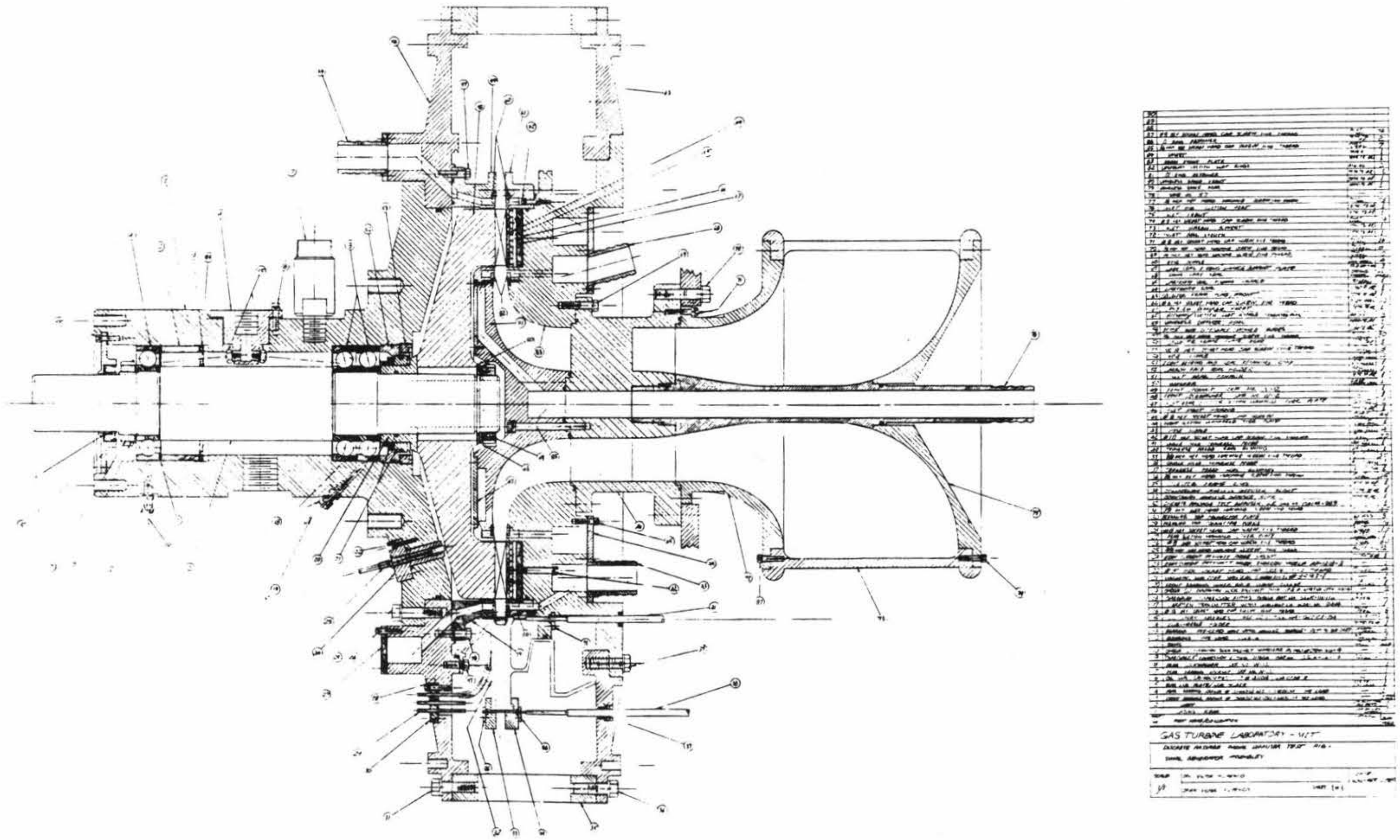

Fig. F.1 Swirl-Generator Assembly Drawing

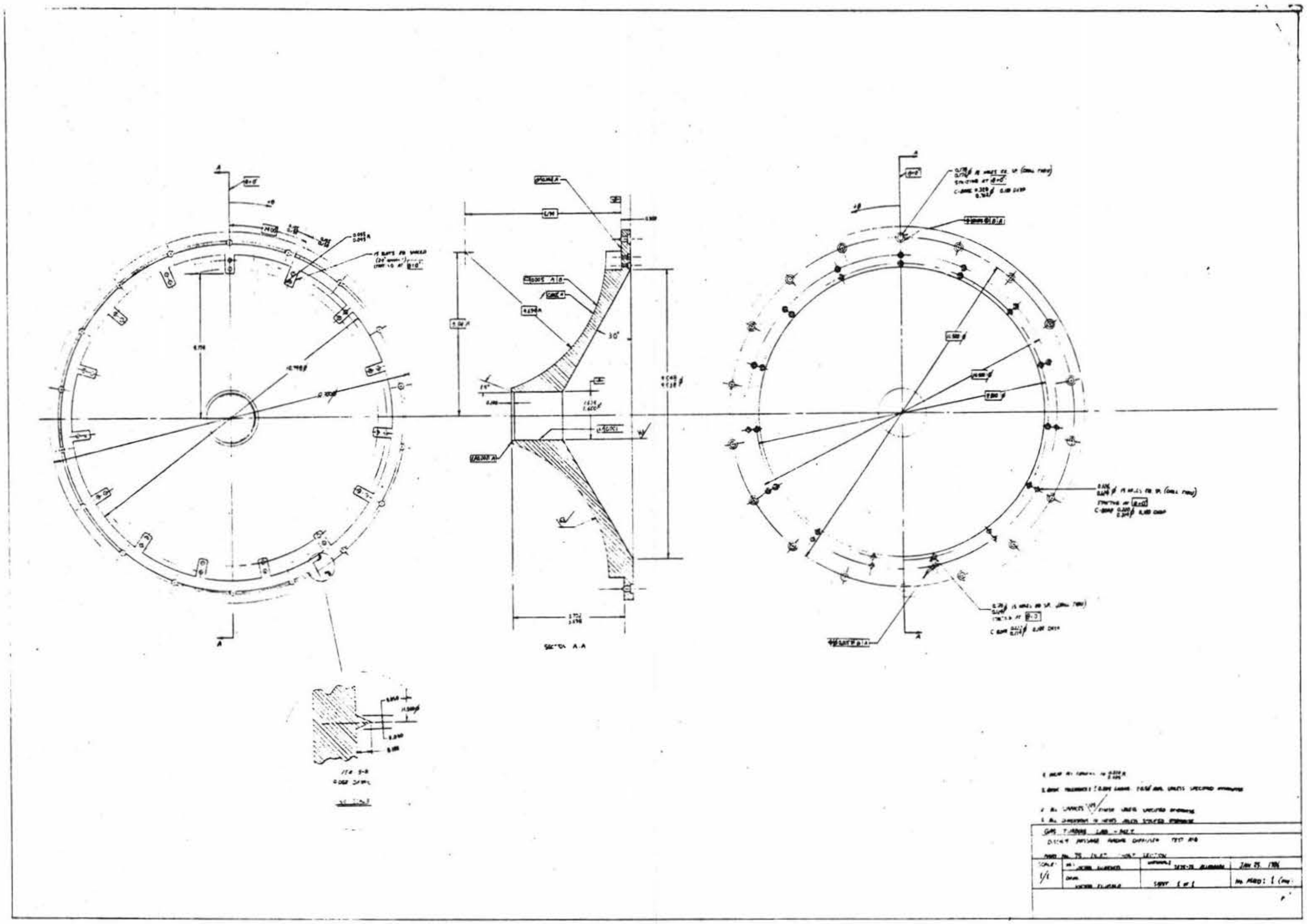

Fig. F.2a Inlet Front Contour

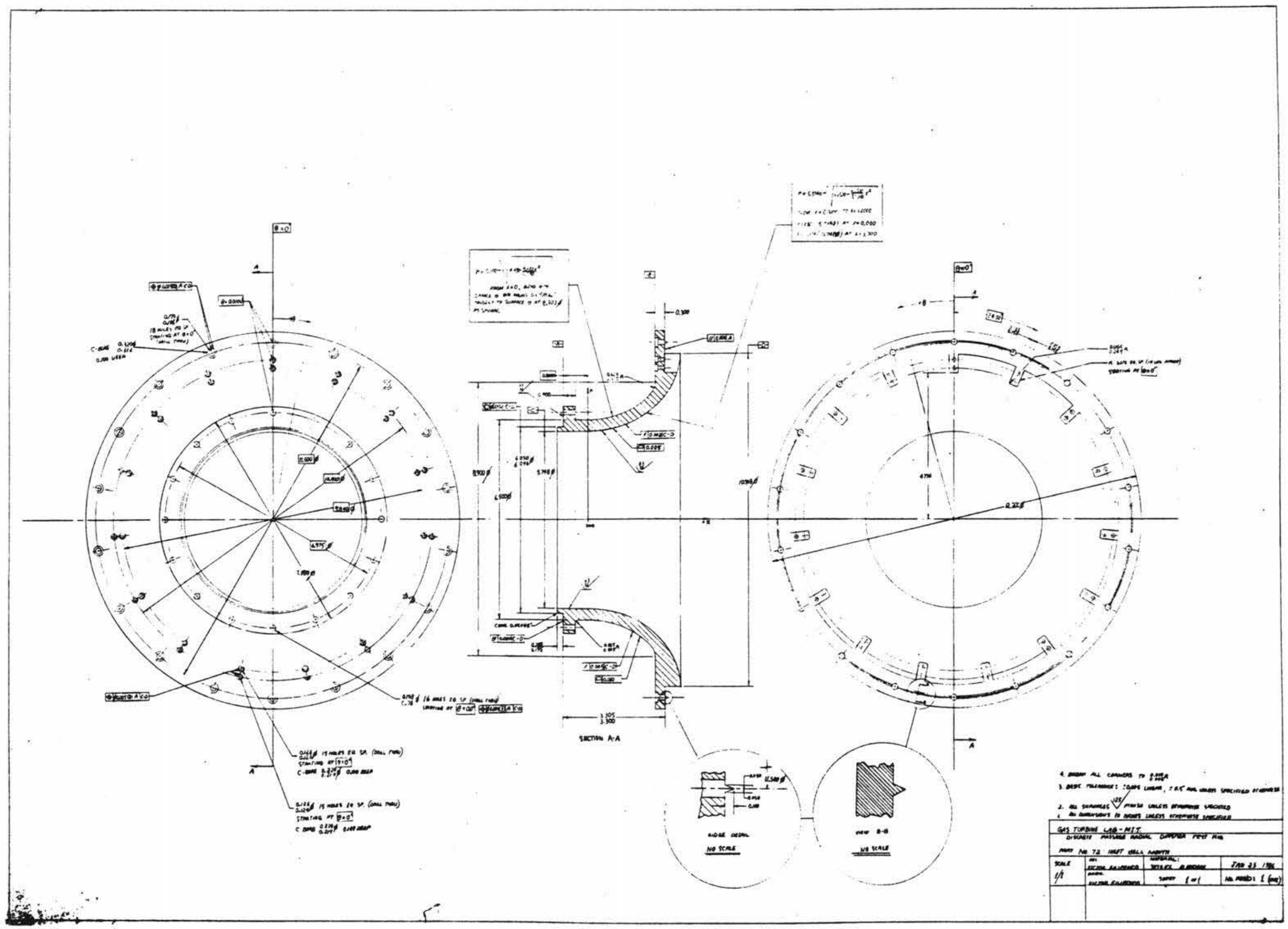

Fig. F.2b Inlet Bell-Mouth Contour

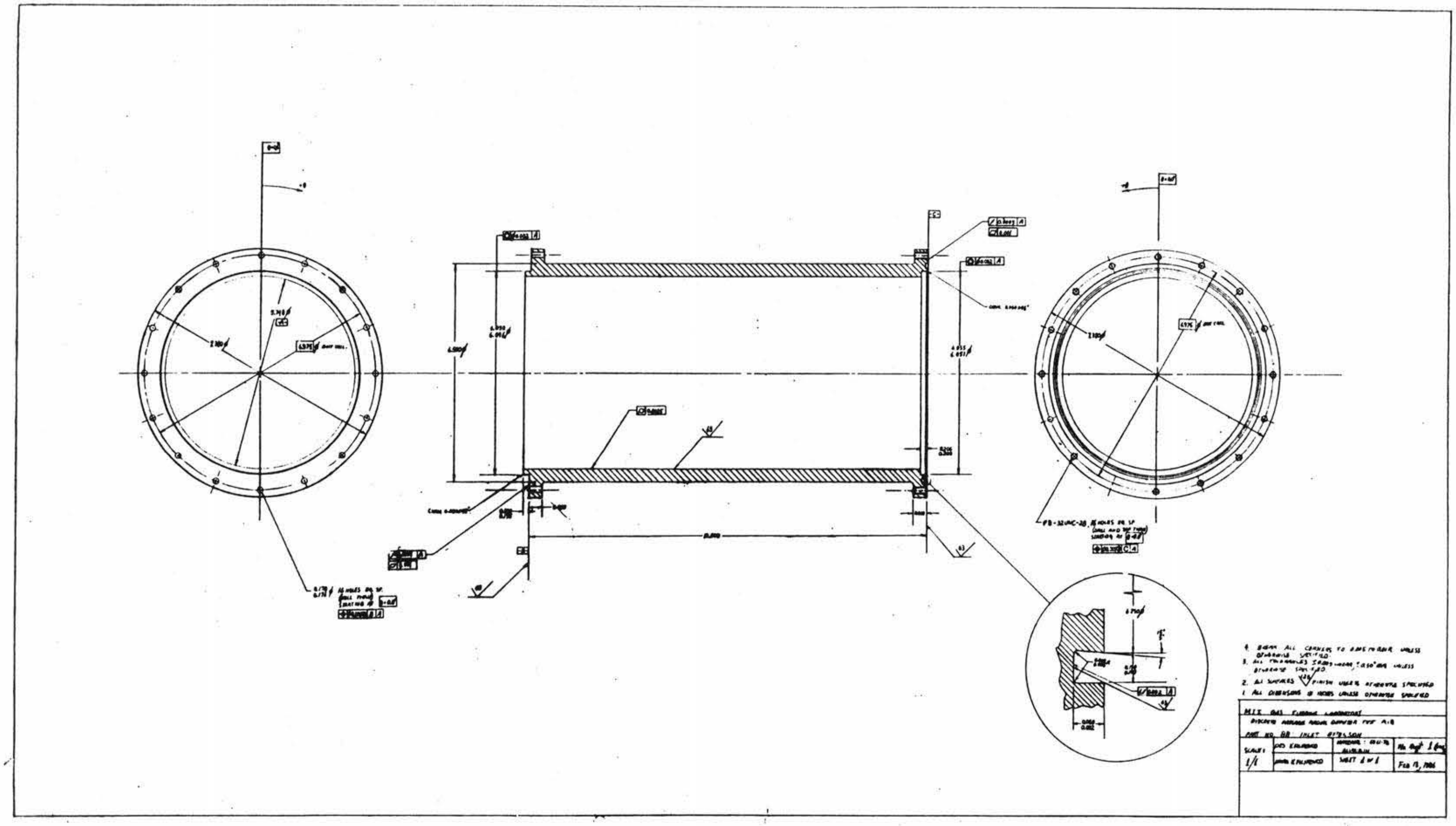

Fig. F.2c Inlet Extension

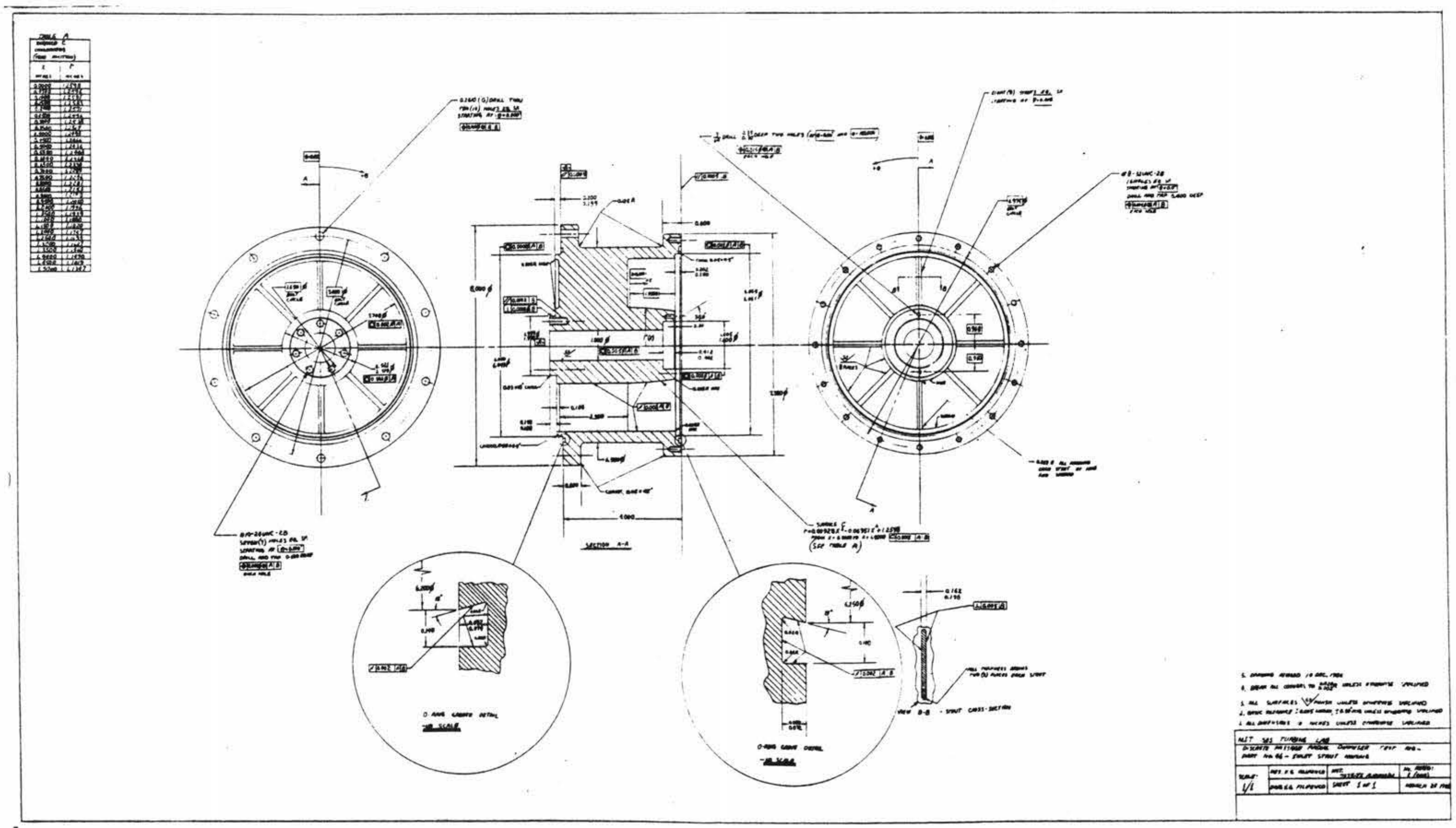

Fig. F.2d Inlet Strut Housing

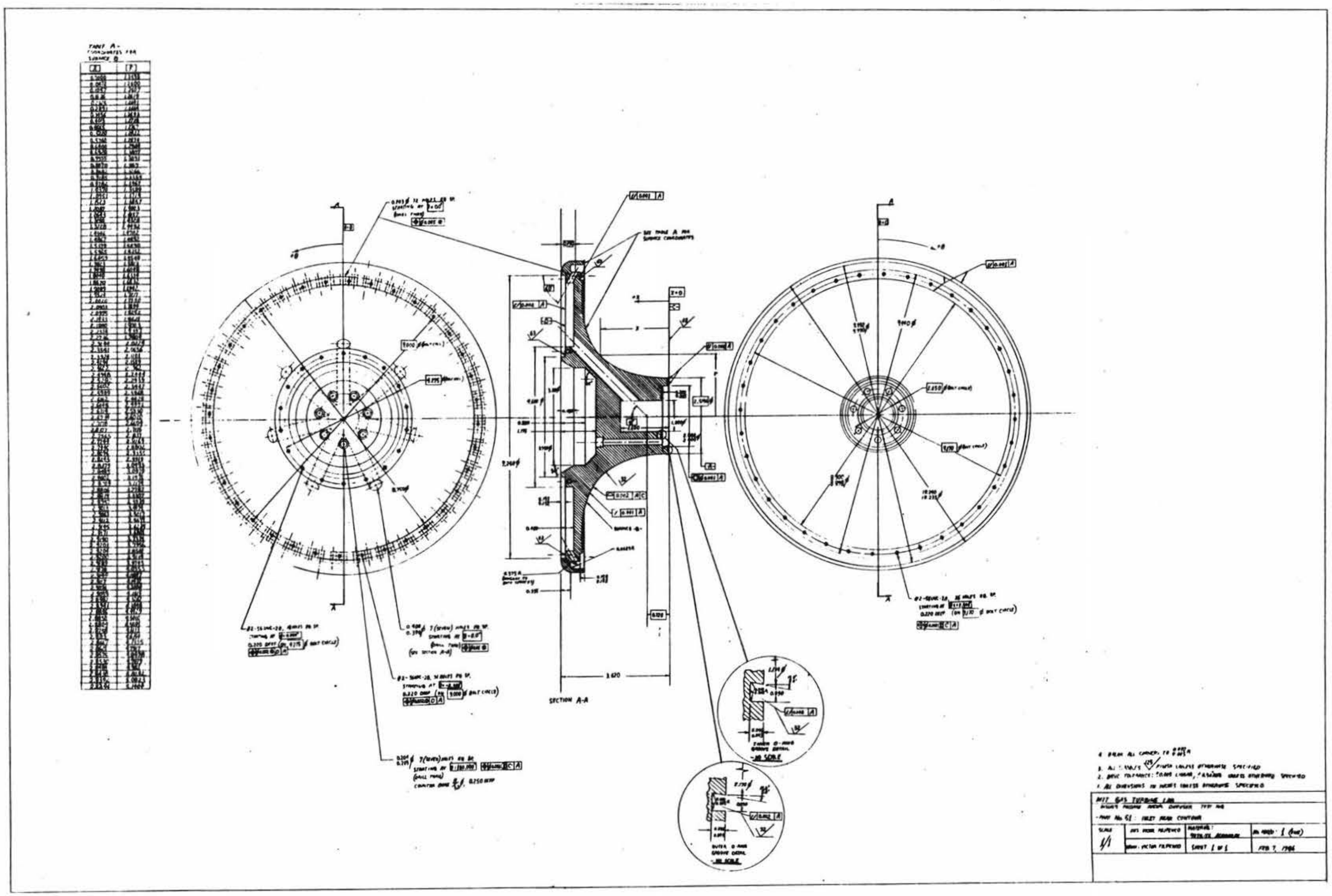

Fig. F.2e Inlet Axial-to-Radial Turn Hub Contour

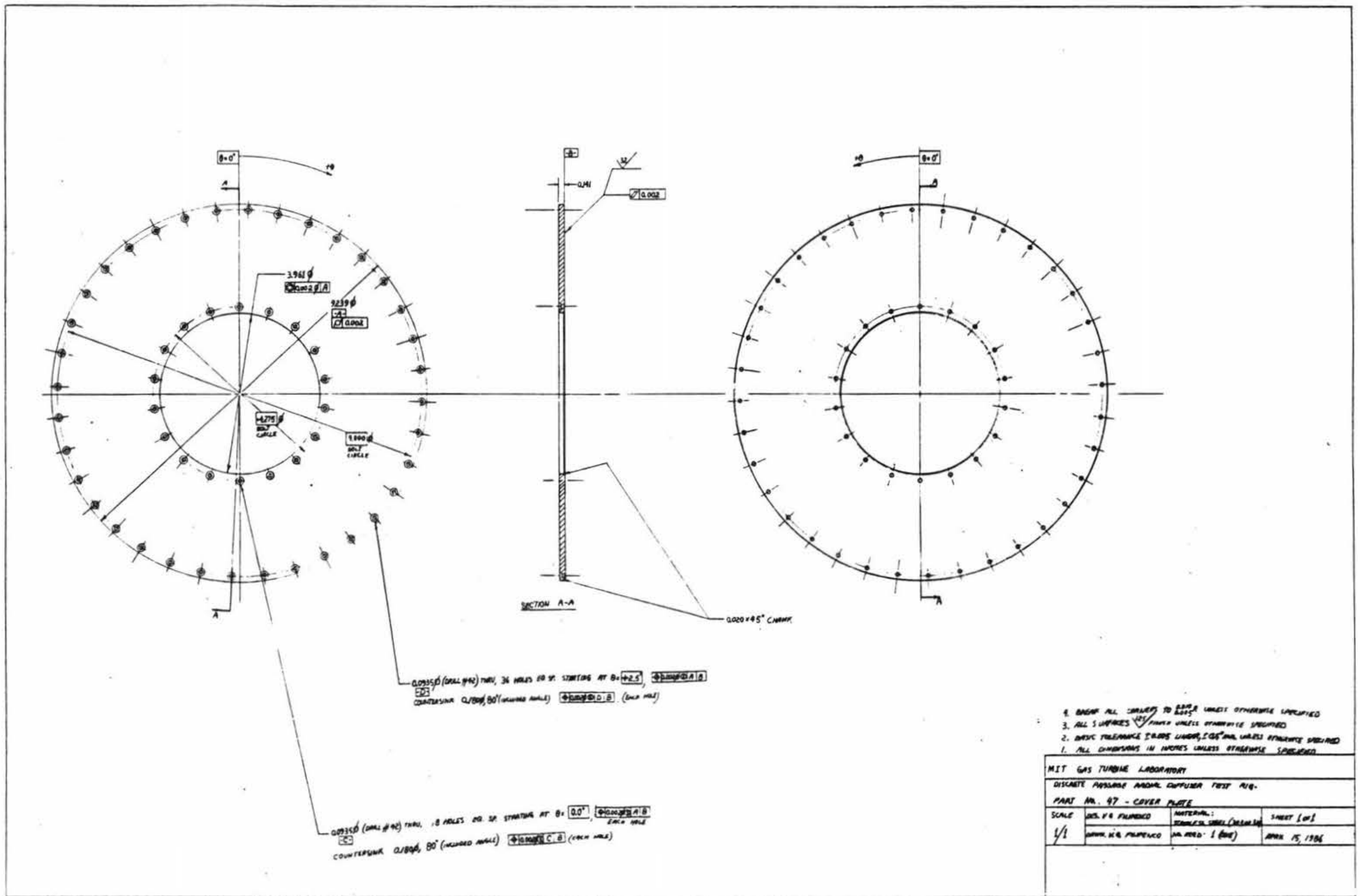

Fig. F.2f Inlet Axial-to-Radial Turn
Hub Contour Rear Cover

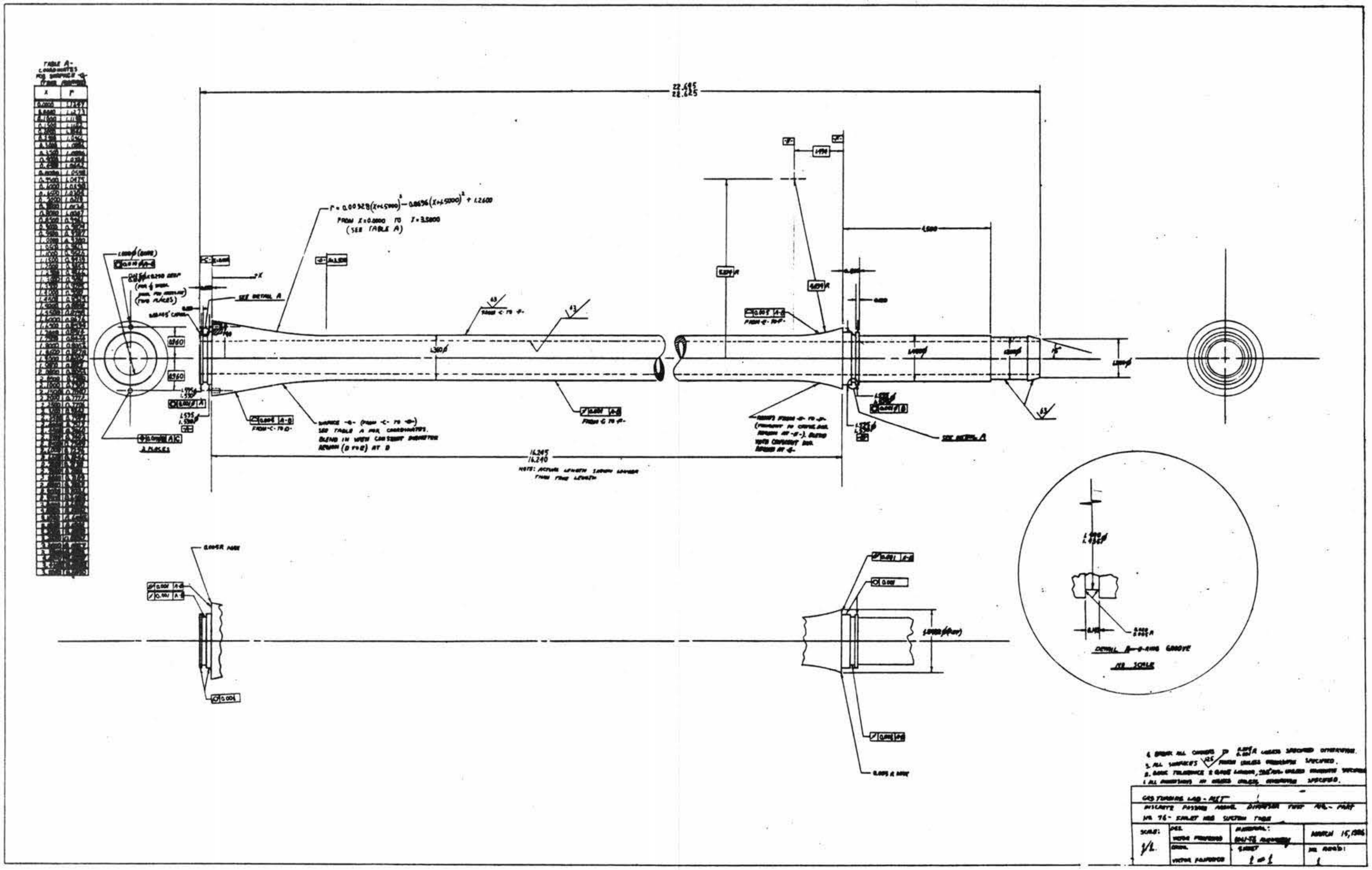

Fig. F.2g Inlet Injection/Suction Center Tube

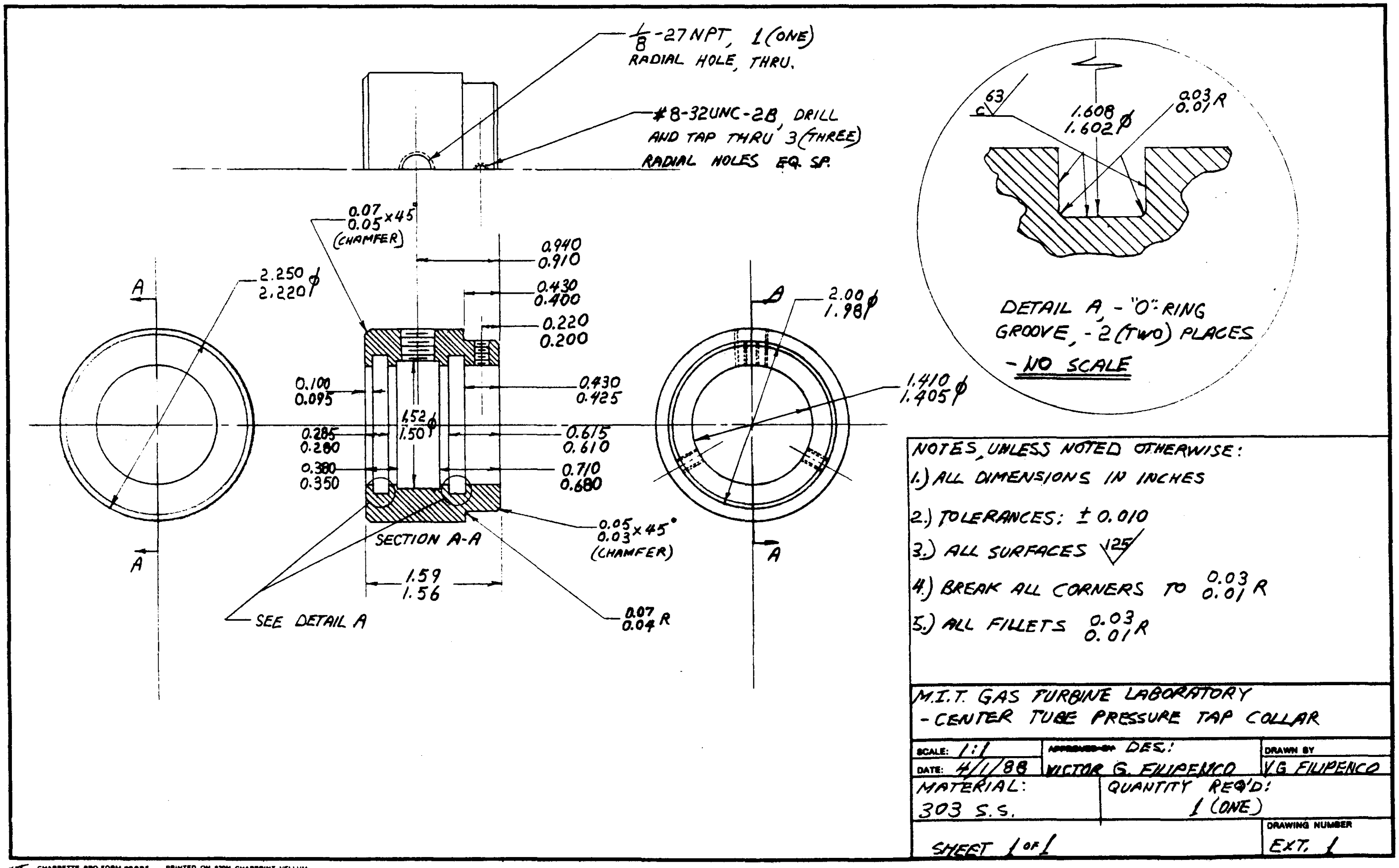

Fig. F.2h Inlet Center Tube Pressure-Tap Collar

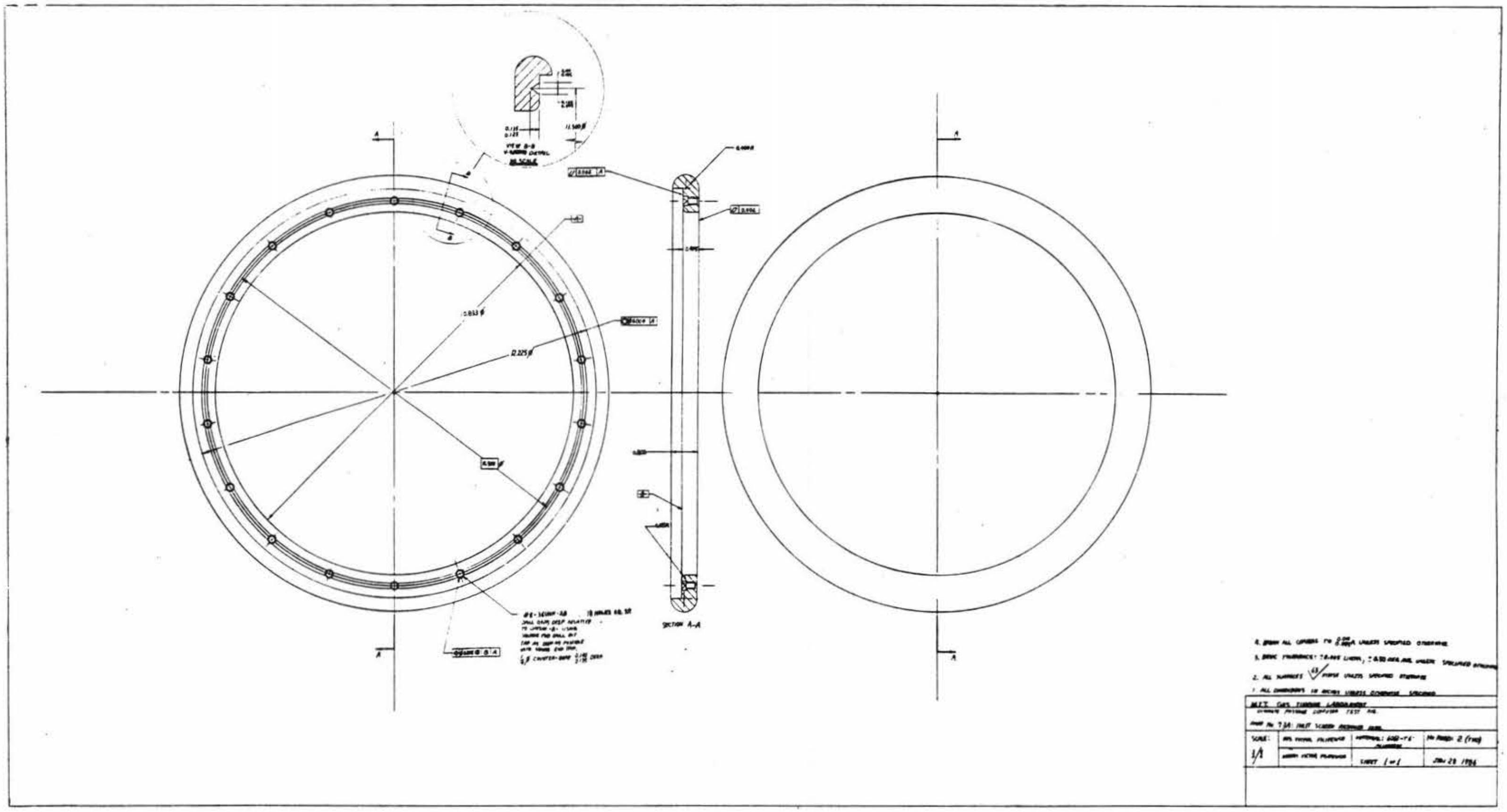

Fig. F.2i Inlet-Lip Ring

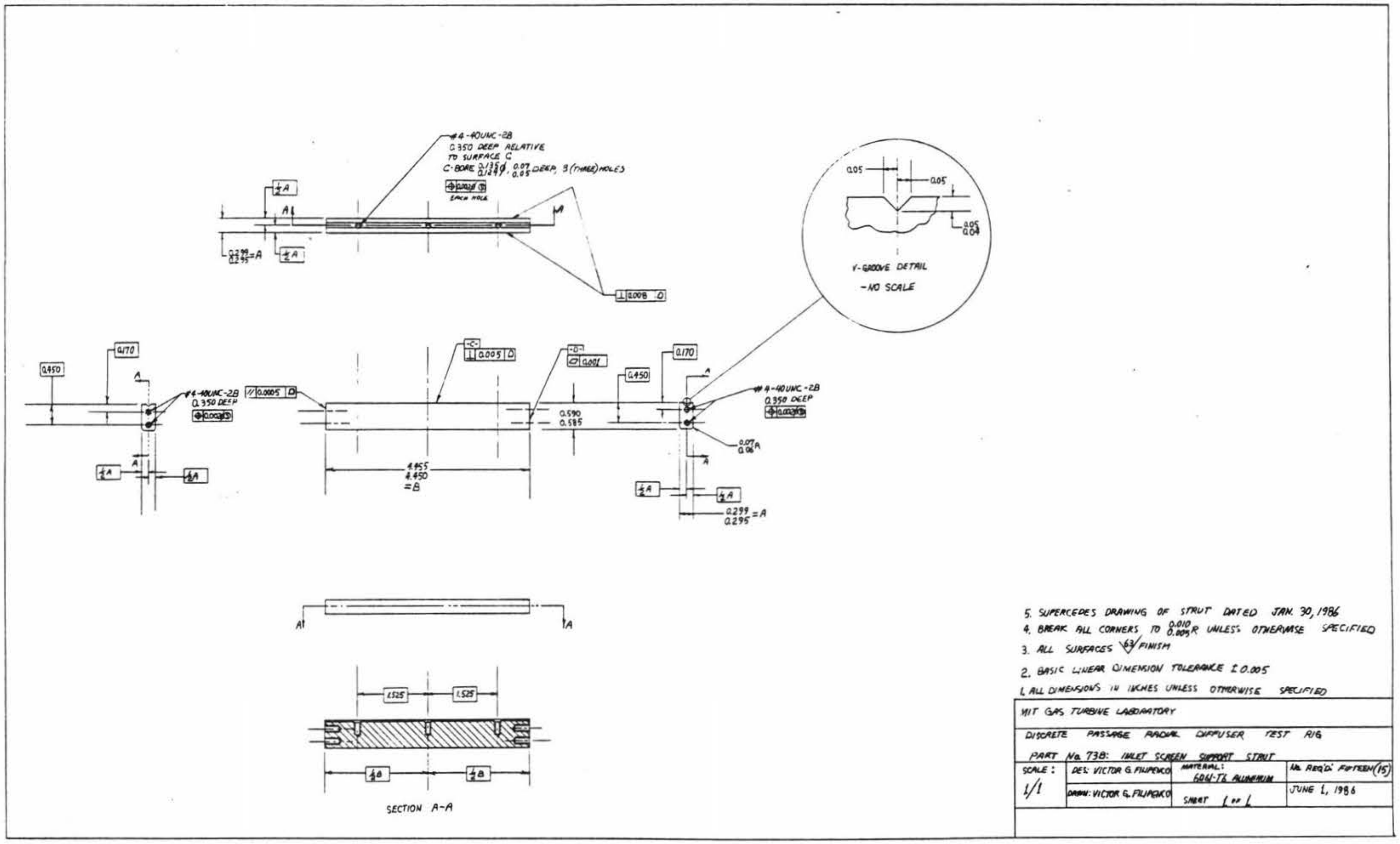

Fig. F.2j Inlet Screen Support Strut

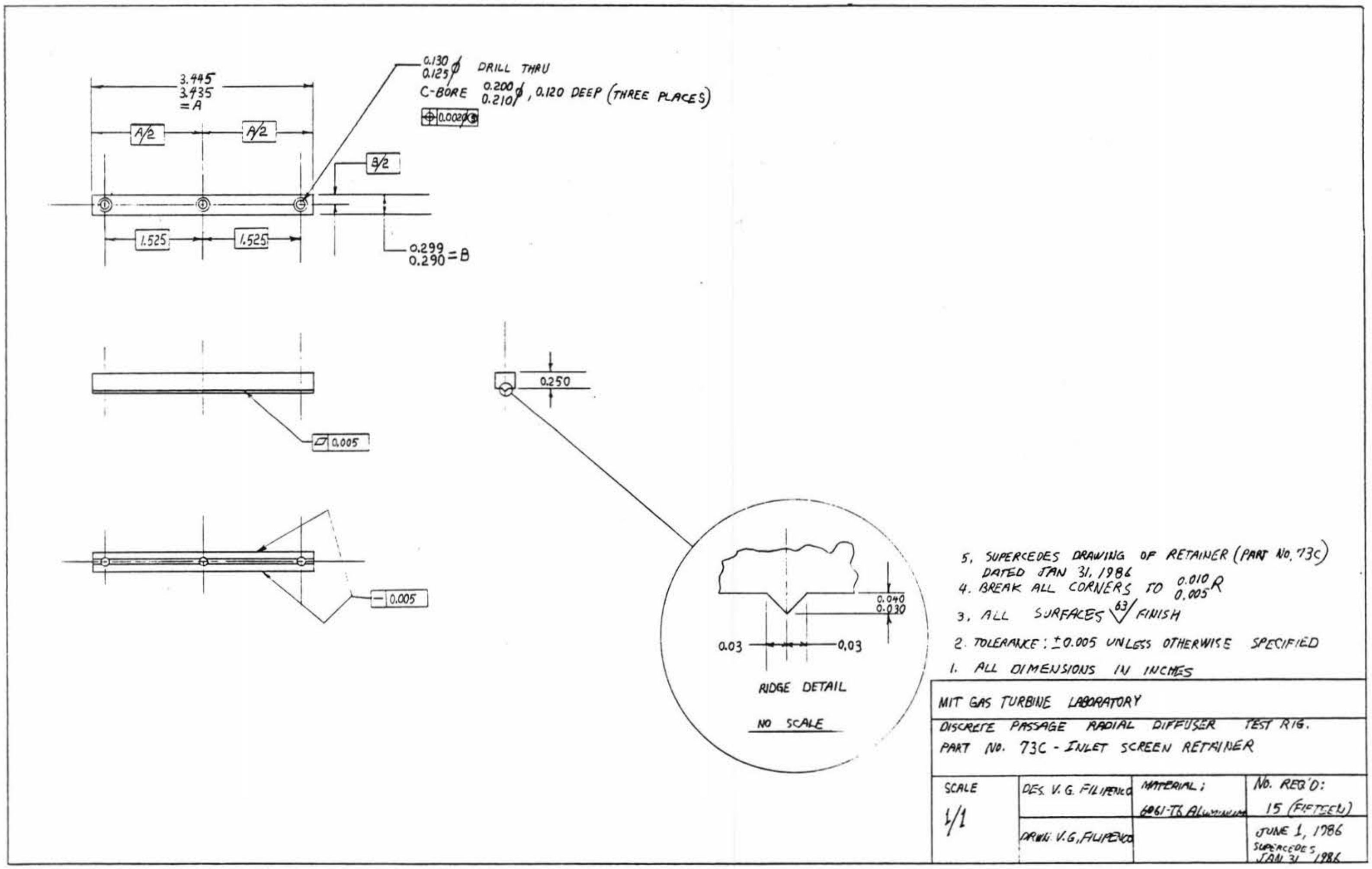

Fig. F.2k Inlet Screen Support Strut Cap

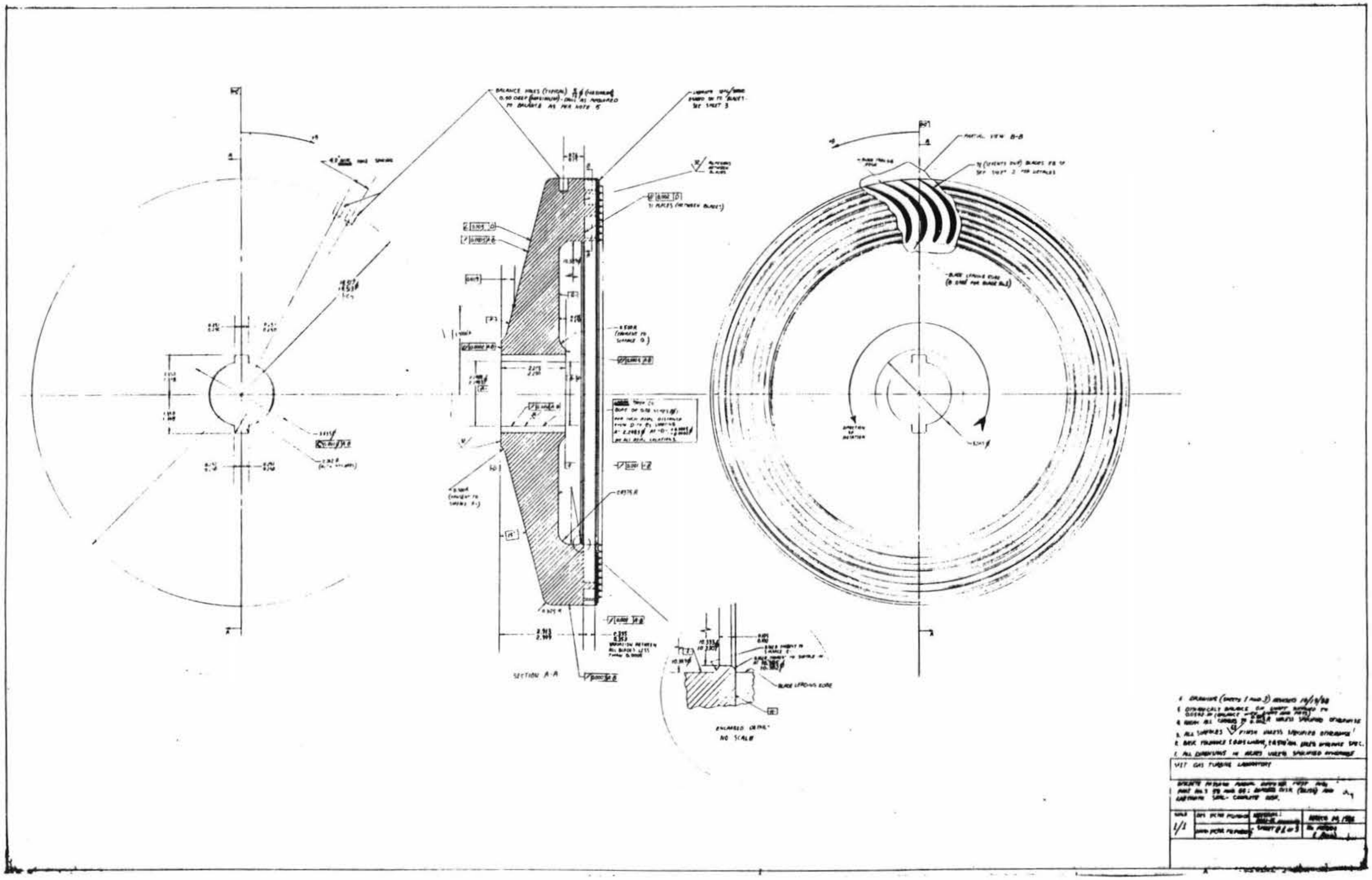

Fig. F.3a Blisk and Shroud/Labyrinth-Seal Assembly

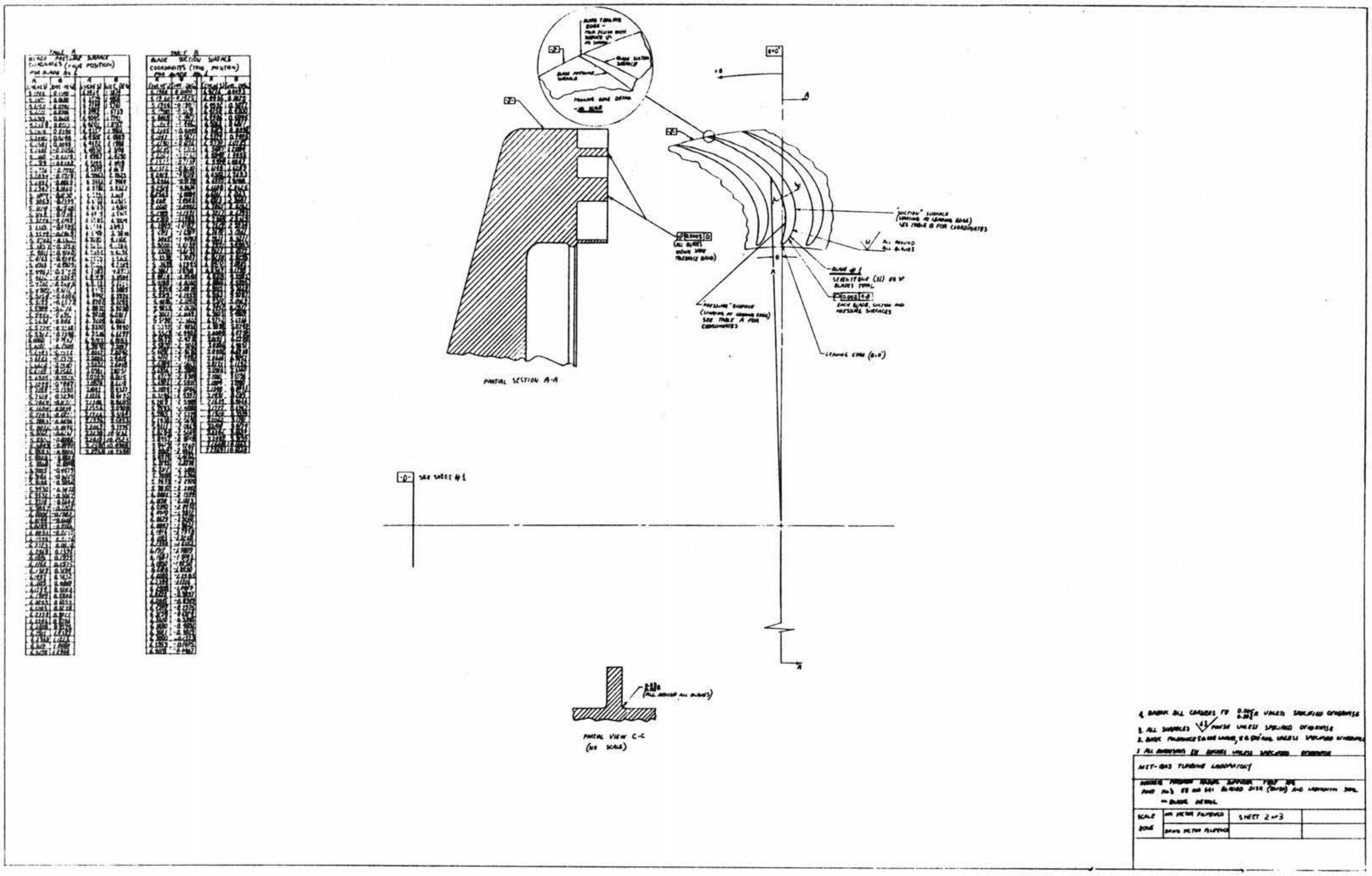

Fig. F.3b Rotor Blading Detail

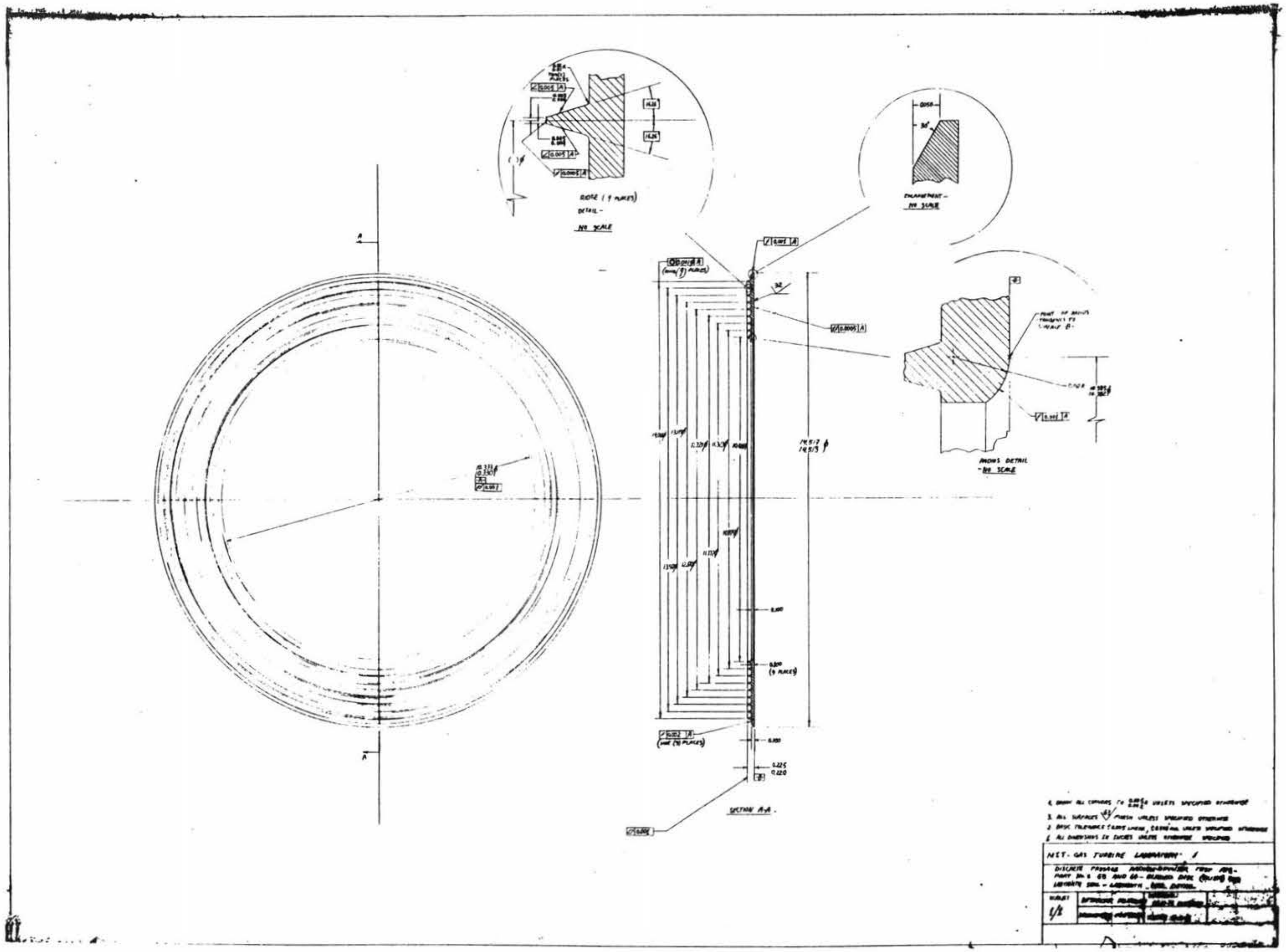

Fig. F.3c Rotor Shroud/Labyrinth-Seal Detail

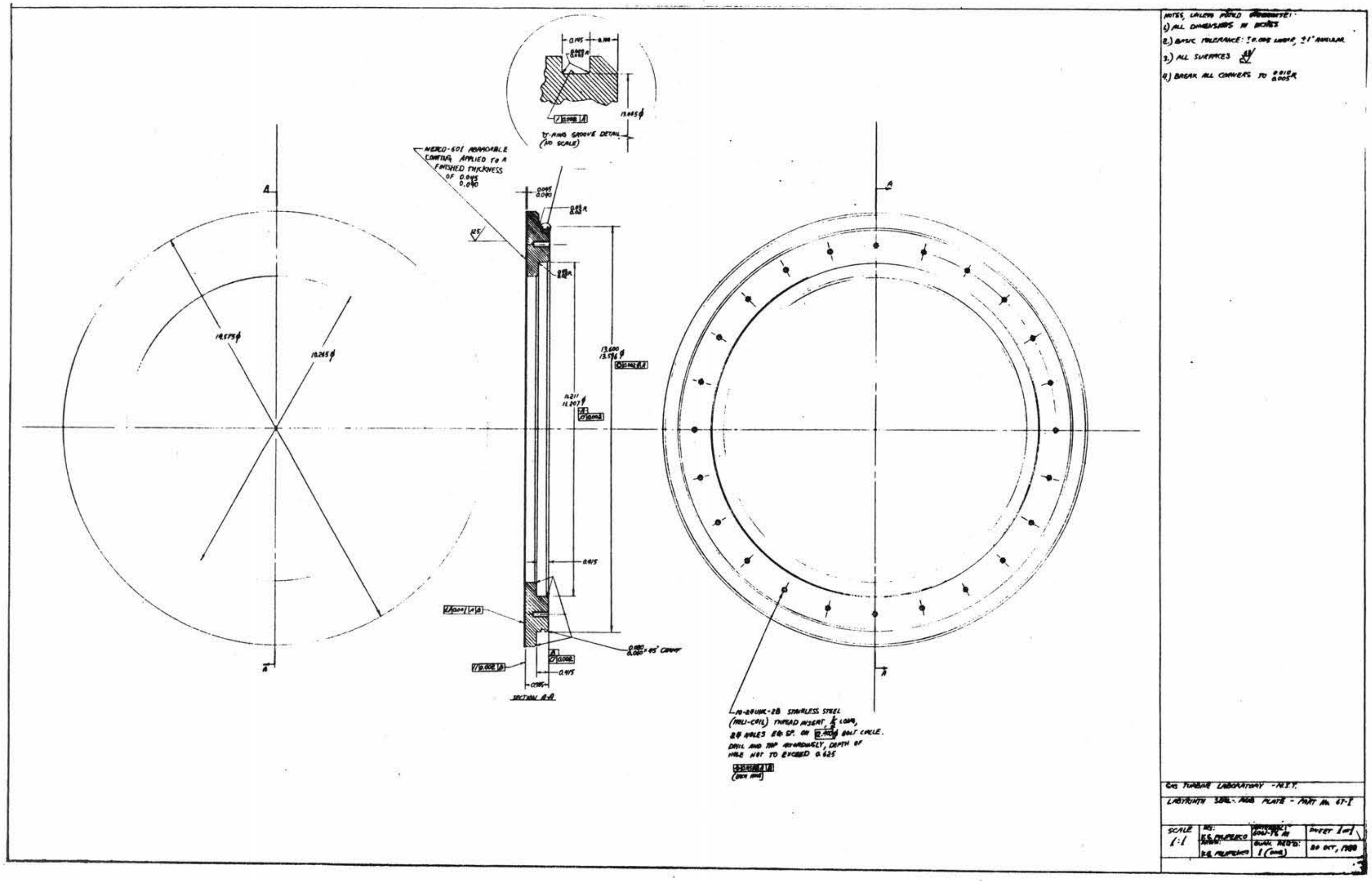

Fig. F.4 Labyrinth Seal Abradable Land Ring

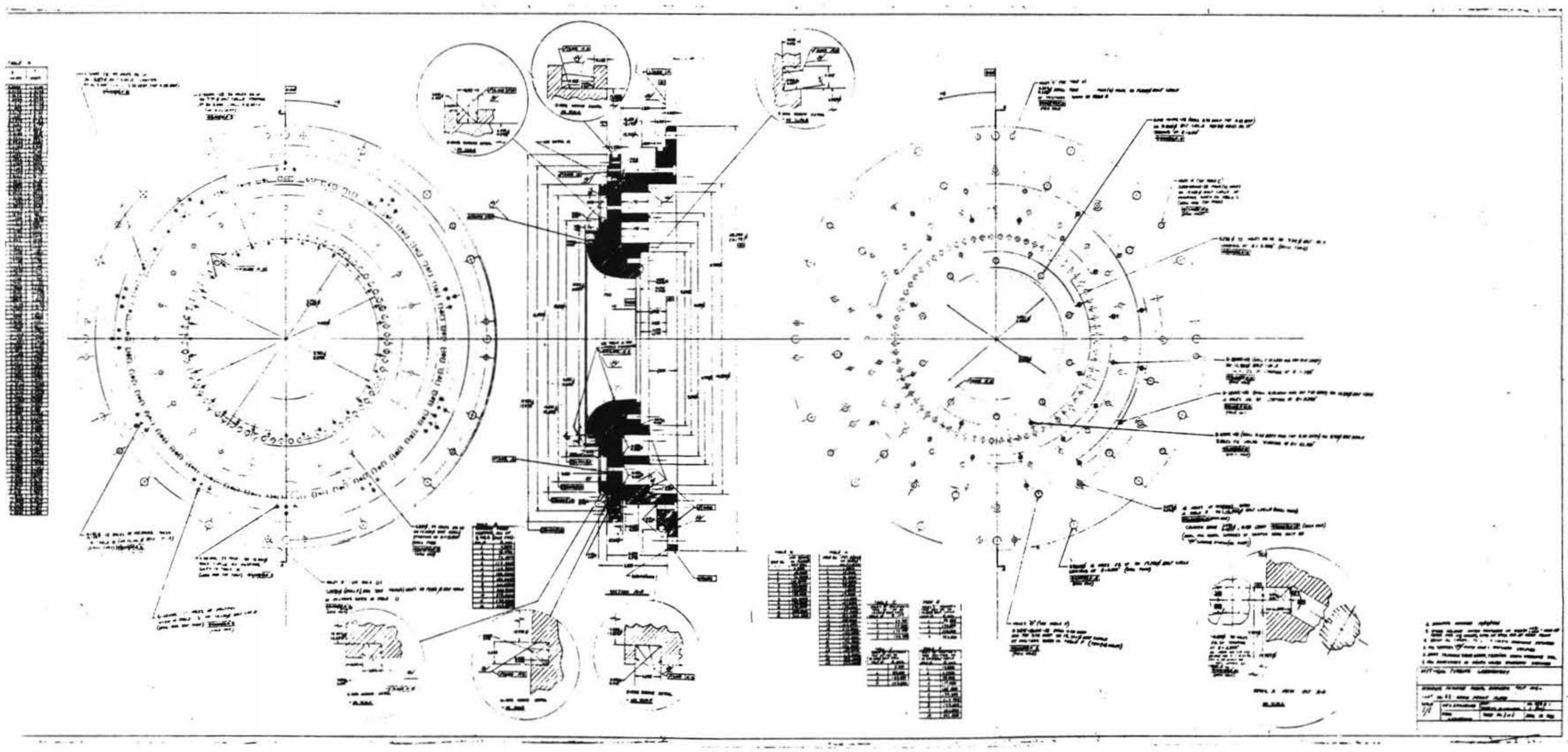

Fig. F.5a   Diffuser Housing Front Inner Section

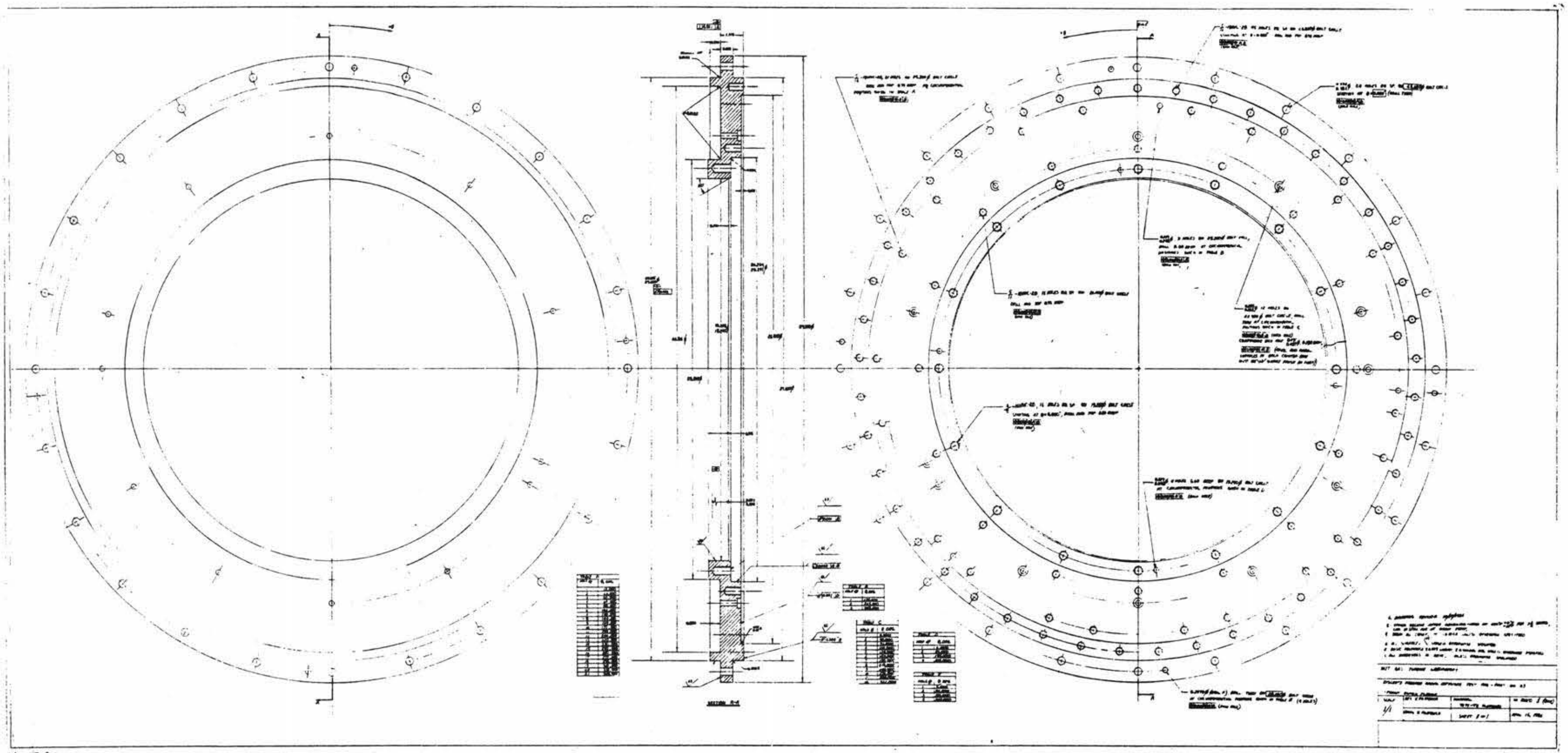

Fig. F.5b Diffuser Housing Front Outer Plate

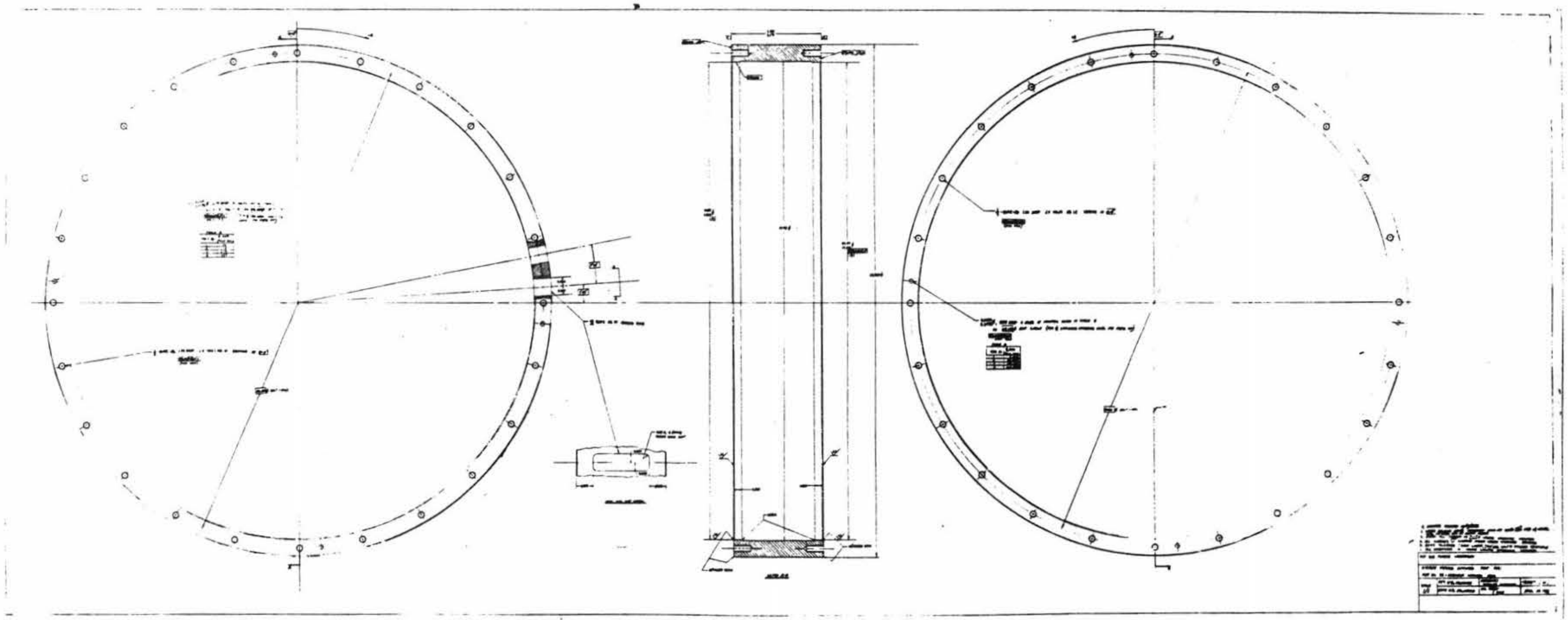

Fig. F.5c Diffuser Housing Outer Structural Ring

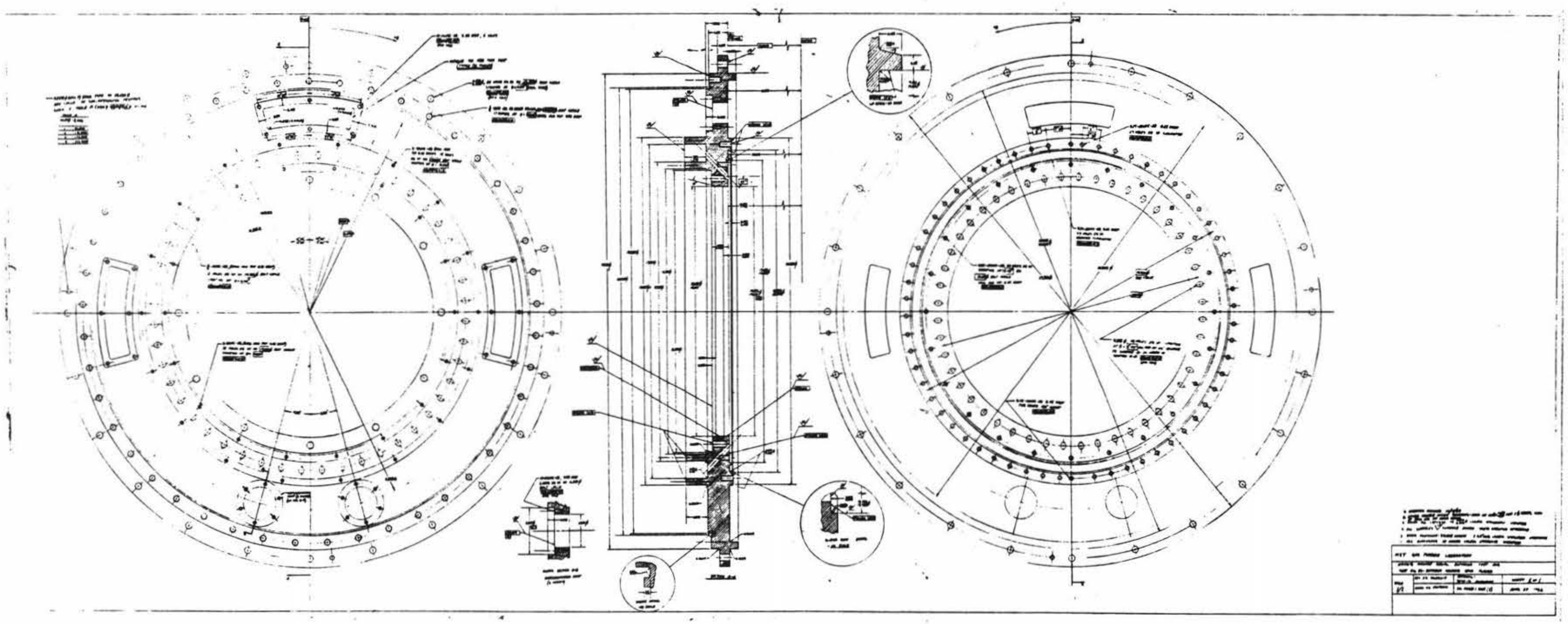

Fig. F.5d Diffuser Housing Rear Plate

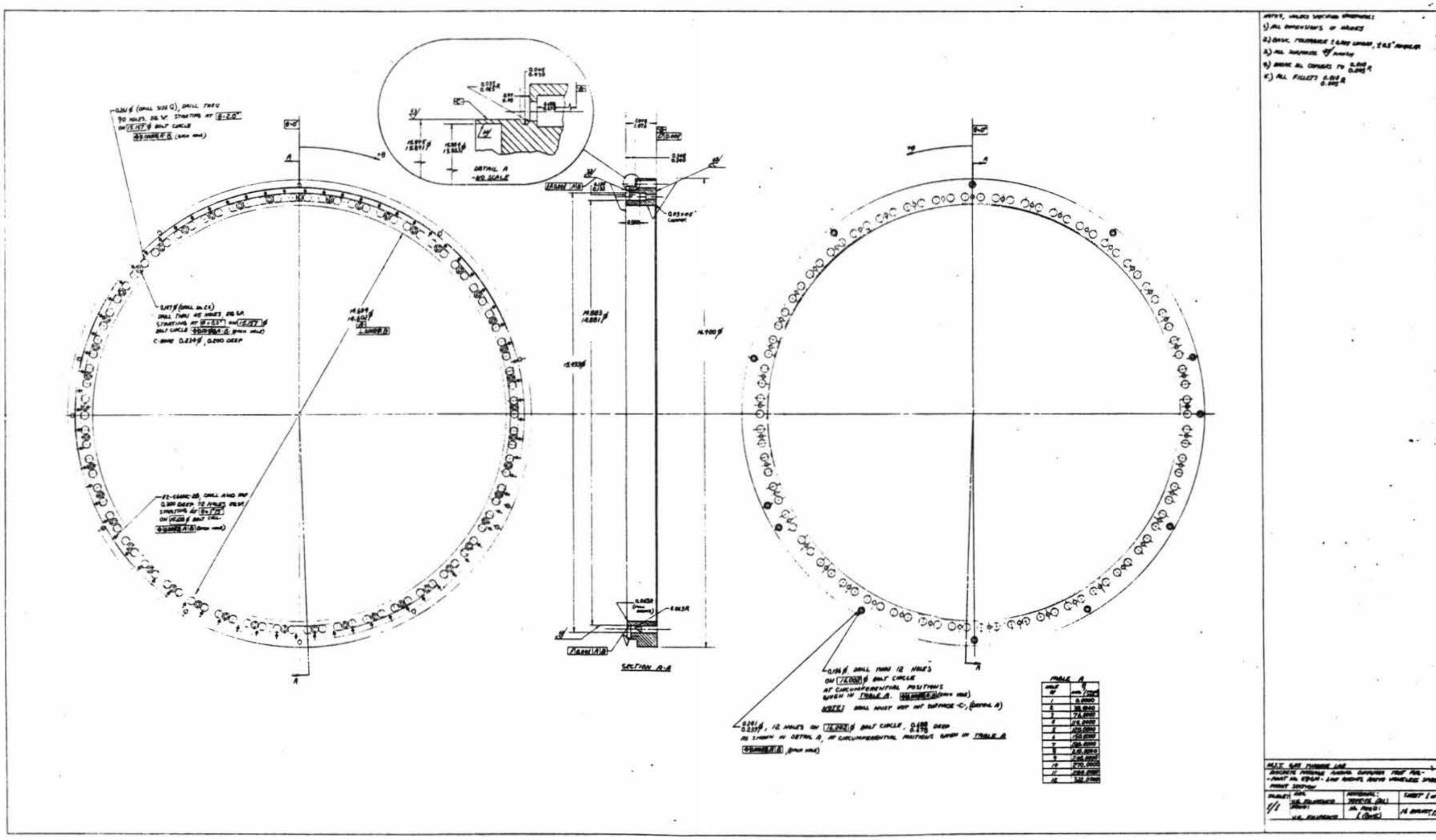

Fig. F.6a   1.10 Radius Ratio Vaneless-Space Front-Ring

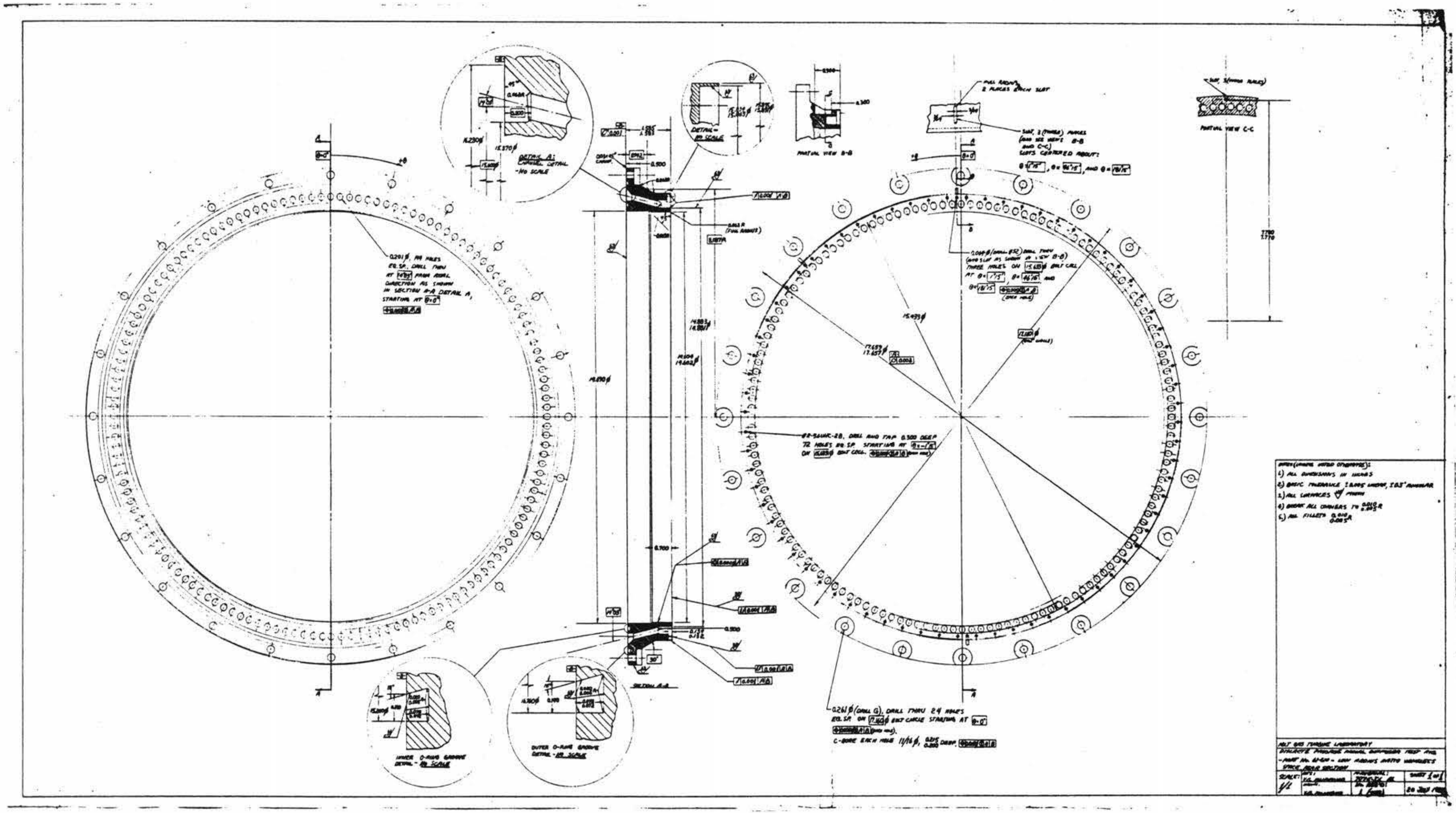

Fig. F.6b 1.10 Radius Ratio Vaneless-Space Rear-Ring

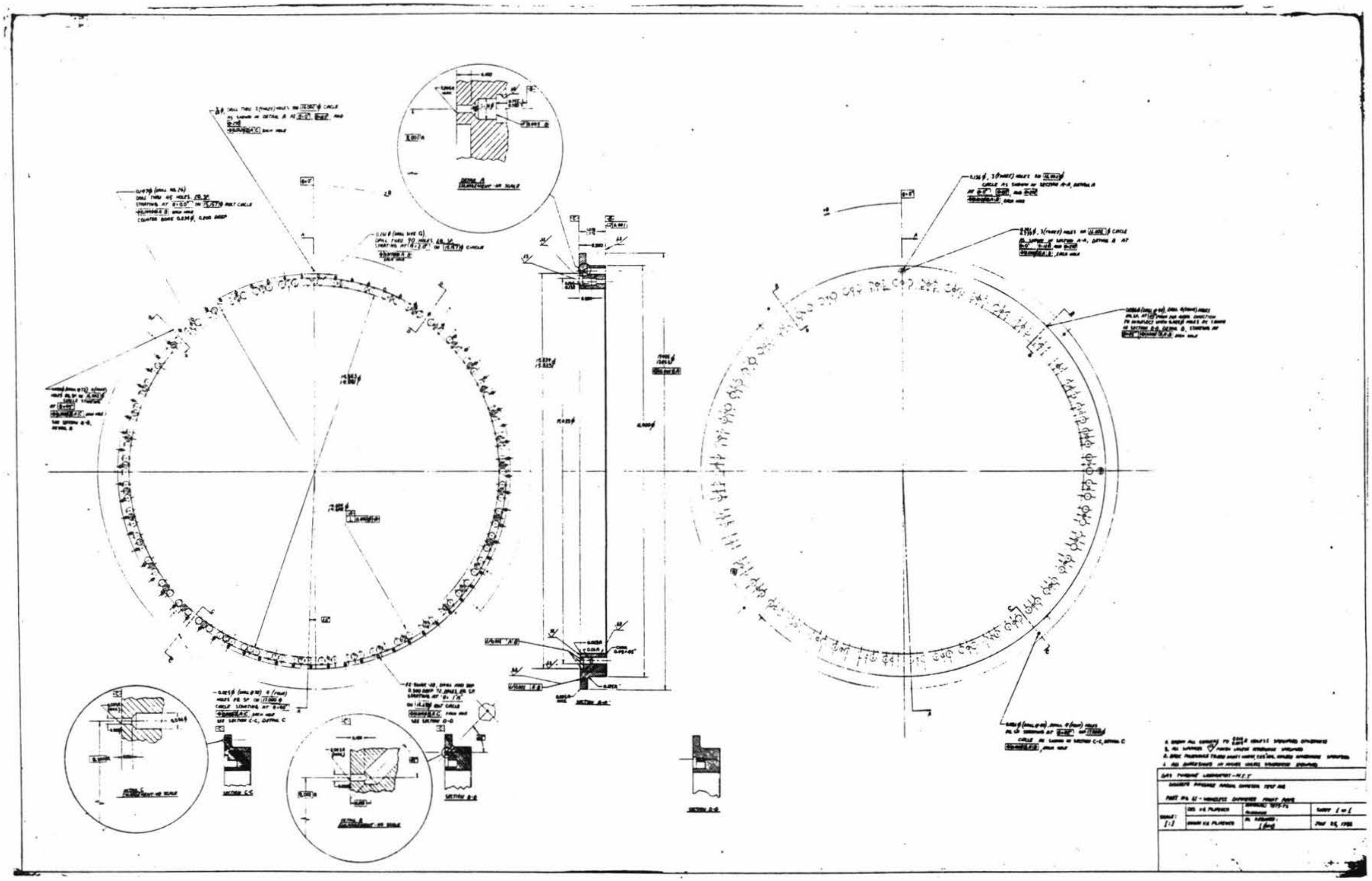

Fig. F.7a 1.20 Radius Ratio Vaneless-Diffuser Front-Ring

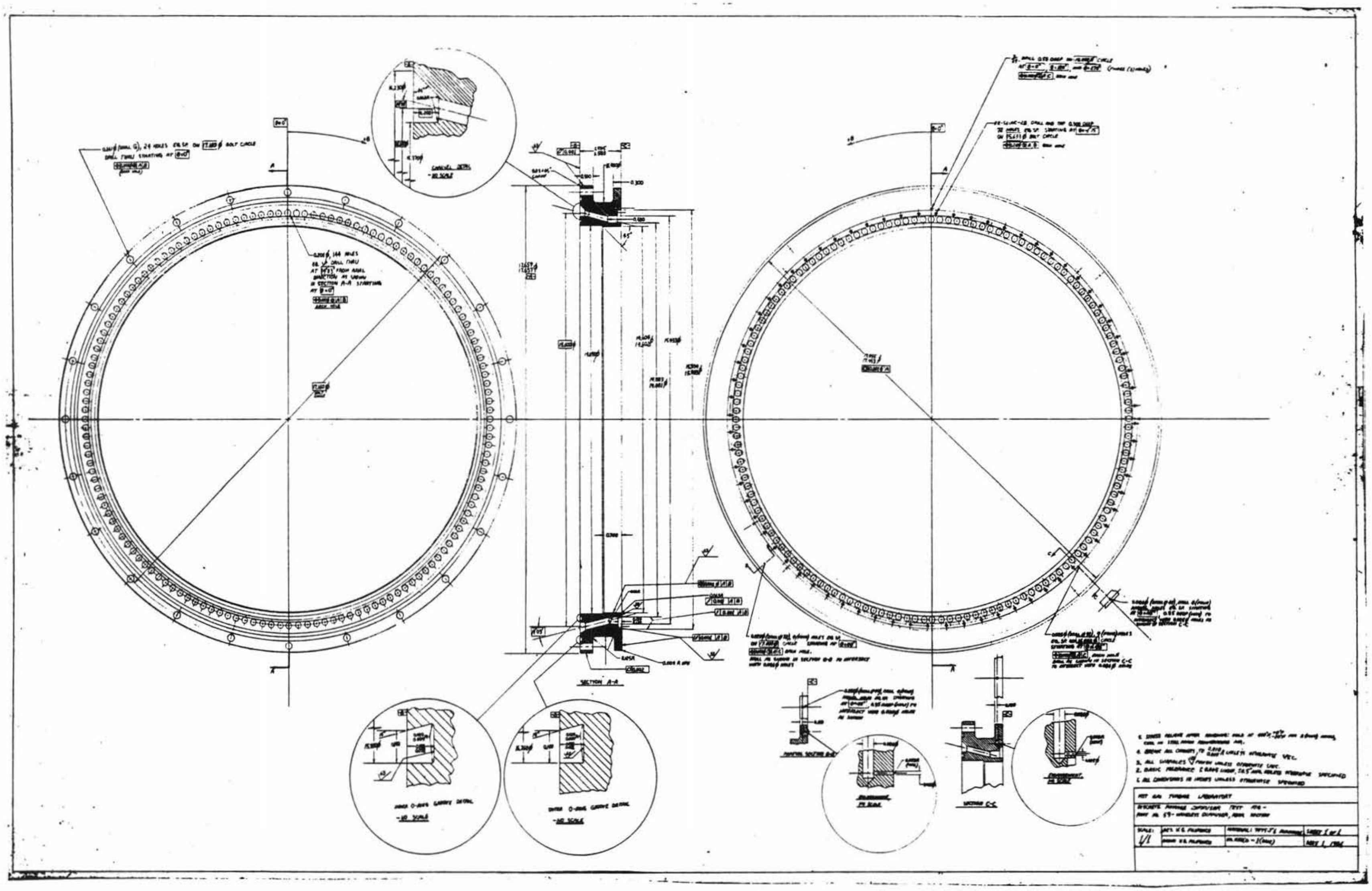

Fig F.7b 1.20 Radius Ratio Vaneless-Diffuser Rear-Ring

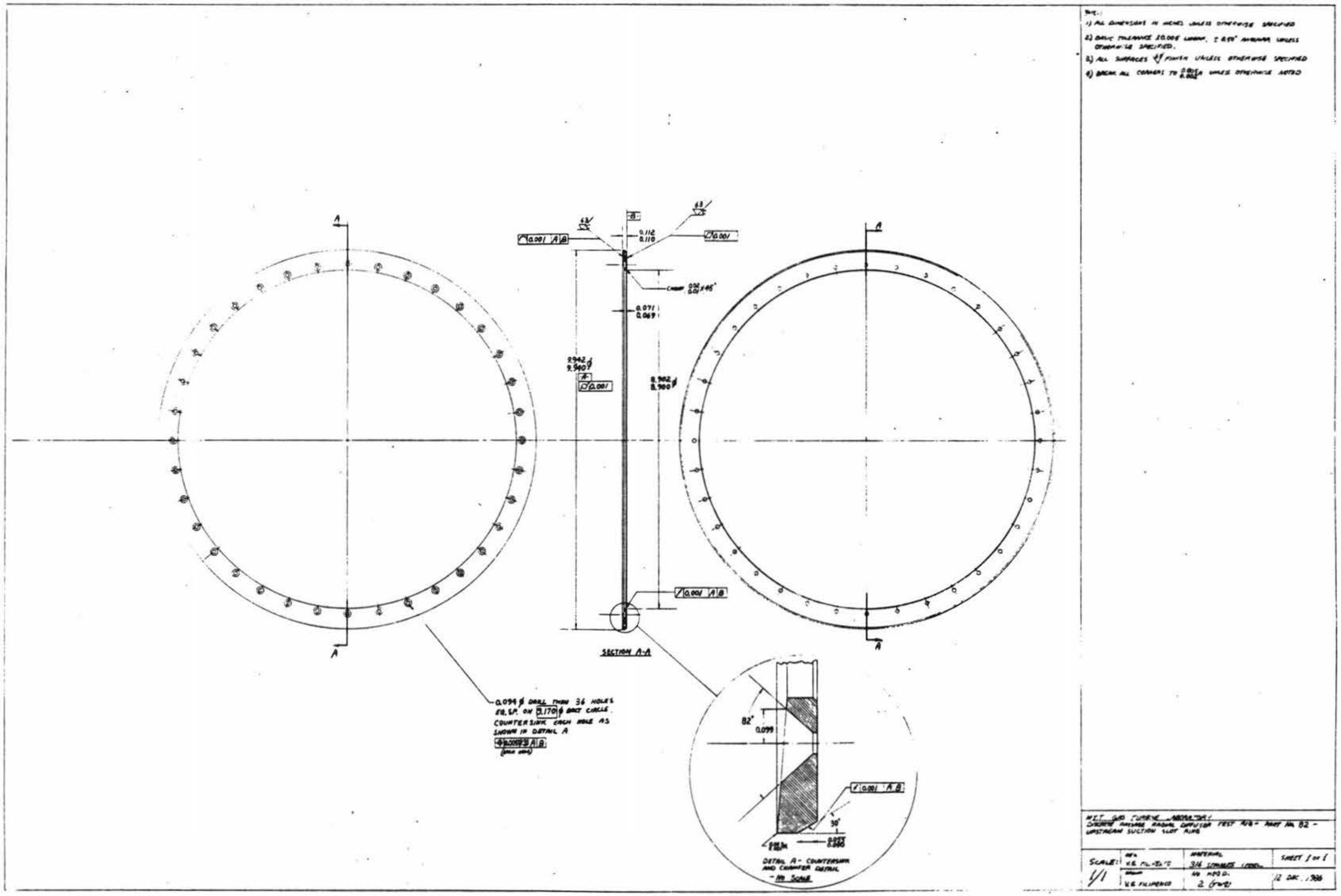

Fig. F.8a Upstream Injection/Suction-Slot Ring

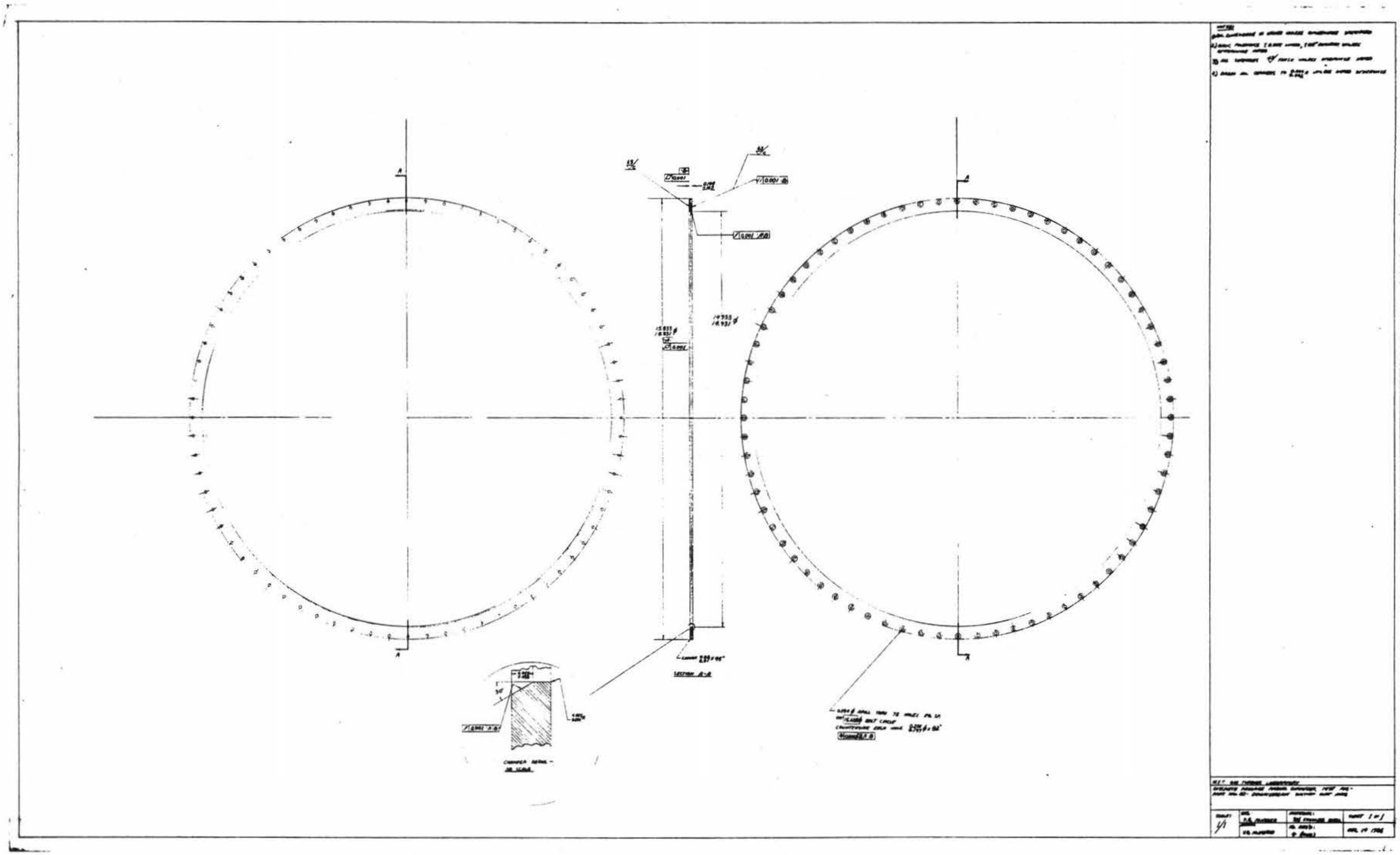

Fig. F.8b Downstream Injection/Suction-Slot Ring

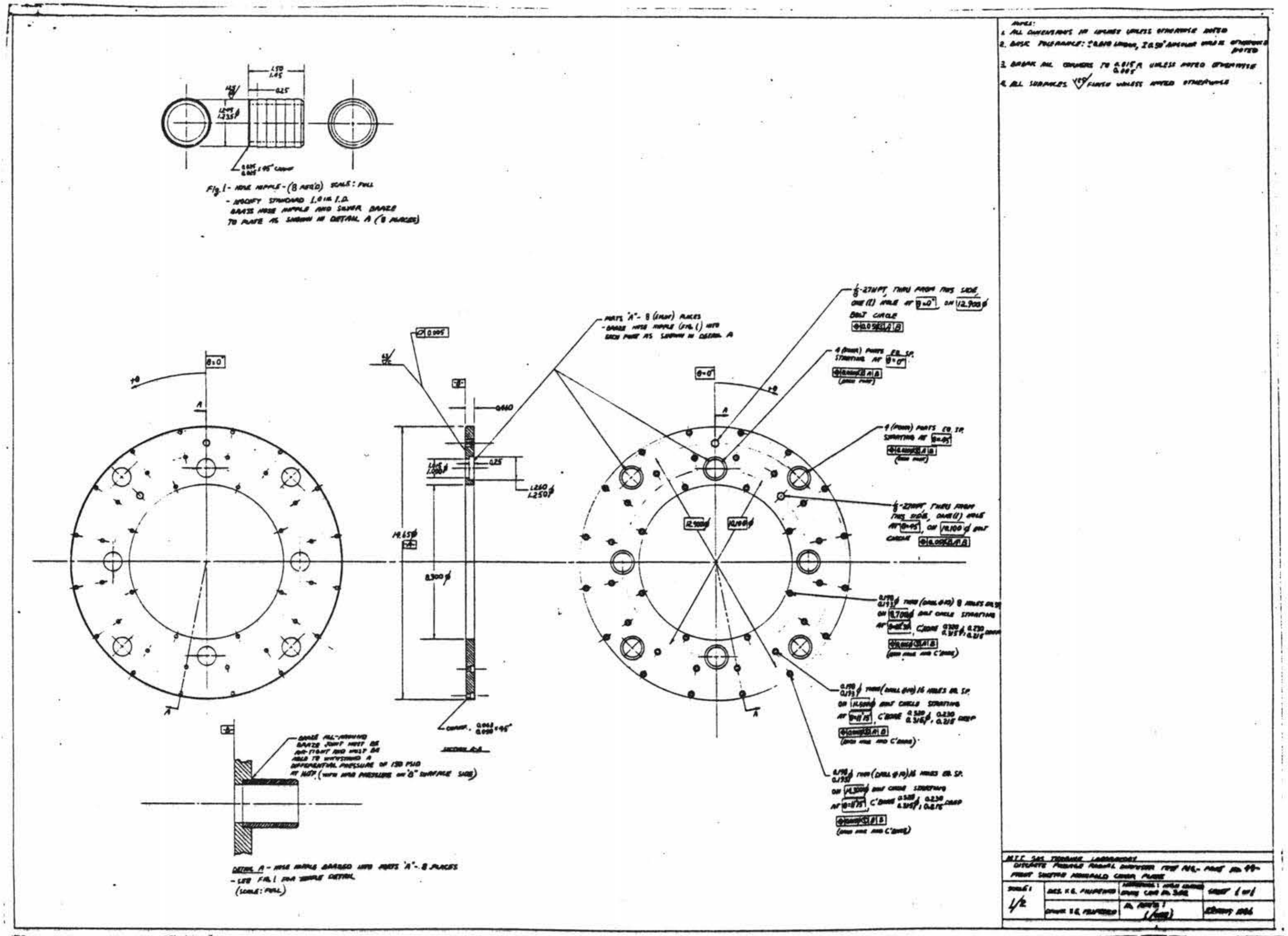

Fig. F.9a Front Secondary Injection/Suction Plenum Cover

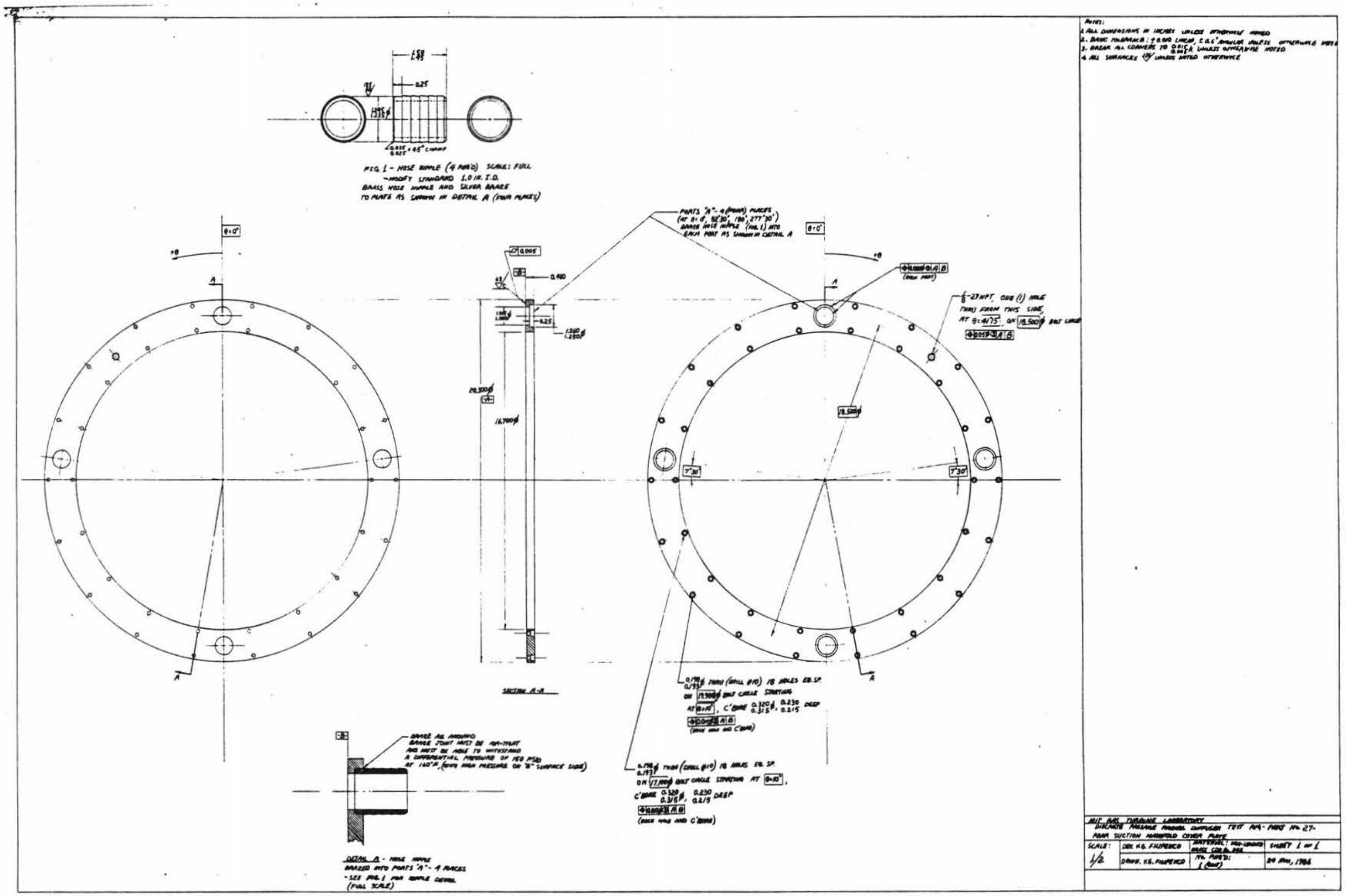

Fig. F.9b Rear Secondary Injection/Suction Plenum Cover

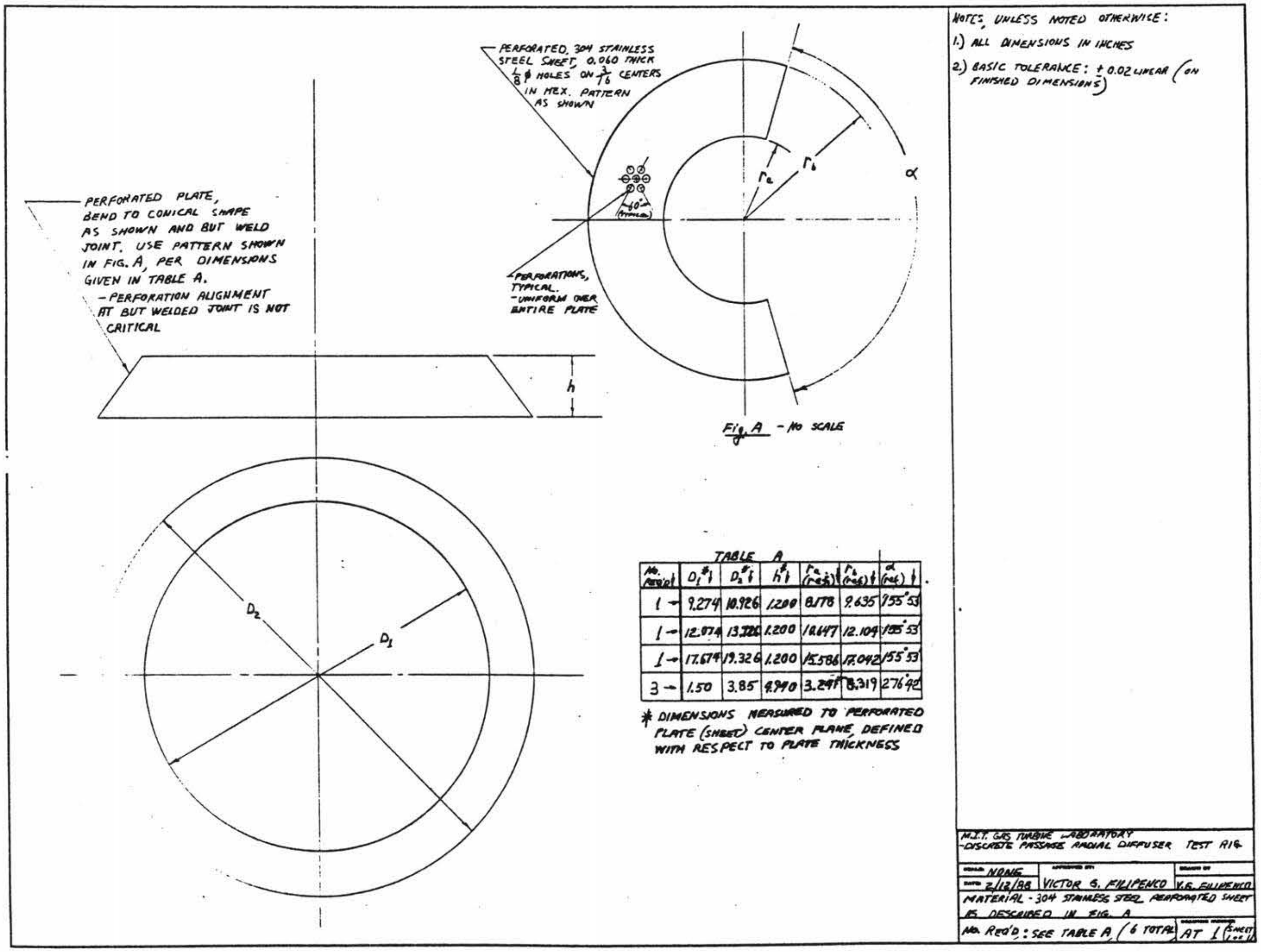

TABLE A

No. Req'd	D_1*	D_2*	h*	r_a (ref.)	r_b (ref.)	α (ref.)
1 →	9.274	10.926	1.200	8.178	9.635	155°53'
1 →	12.974	13.326	1.200	10.647	12.109	155°53'
1 →	17.674	19.326	1.200	15.586	17.042	155°53'
3 →	1.50	3.85	4.940	3.291	8.319	276°42'

* DIMENSIONS MEASURED TO PERFORATED PLATE (SHEET) CENTER PLANE, DEFINED WITH RESPECT TO PLATE THICKNESS

Fig. F.10 Secondary Injection/Suction Plenum Flow Distribution Screen

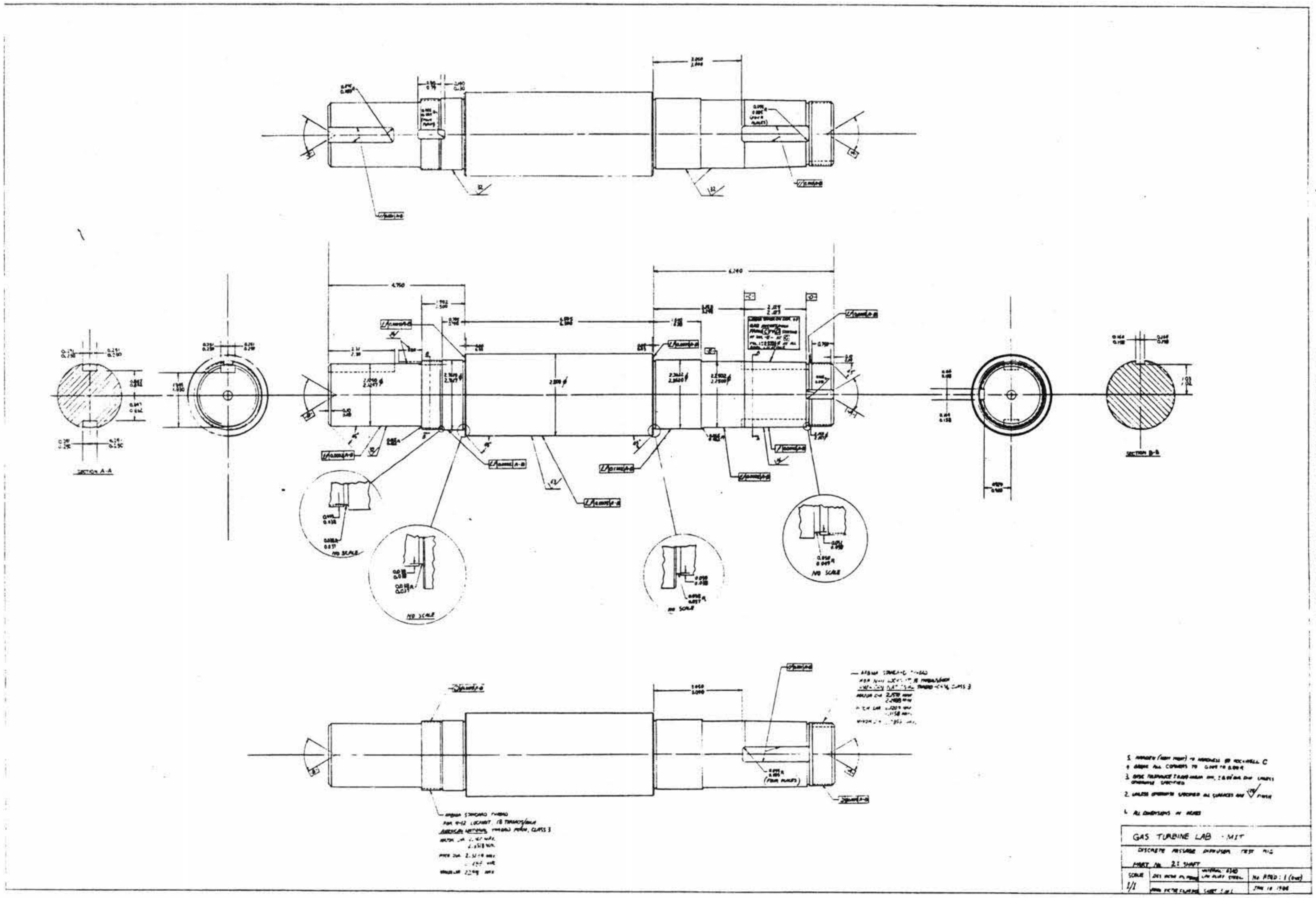

Fig. F.11a Swirl-Generator Main Shaft

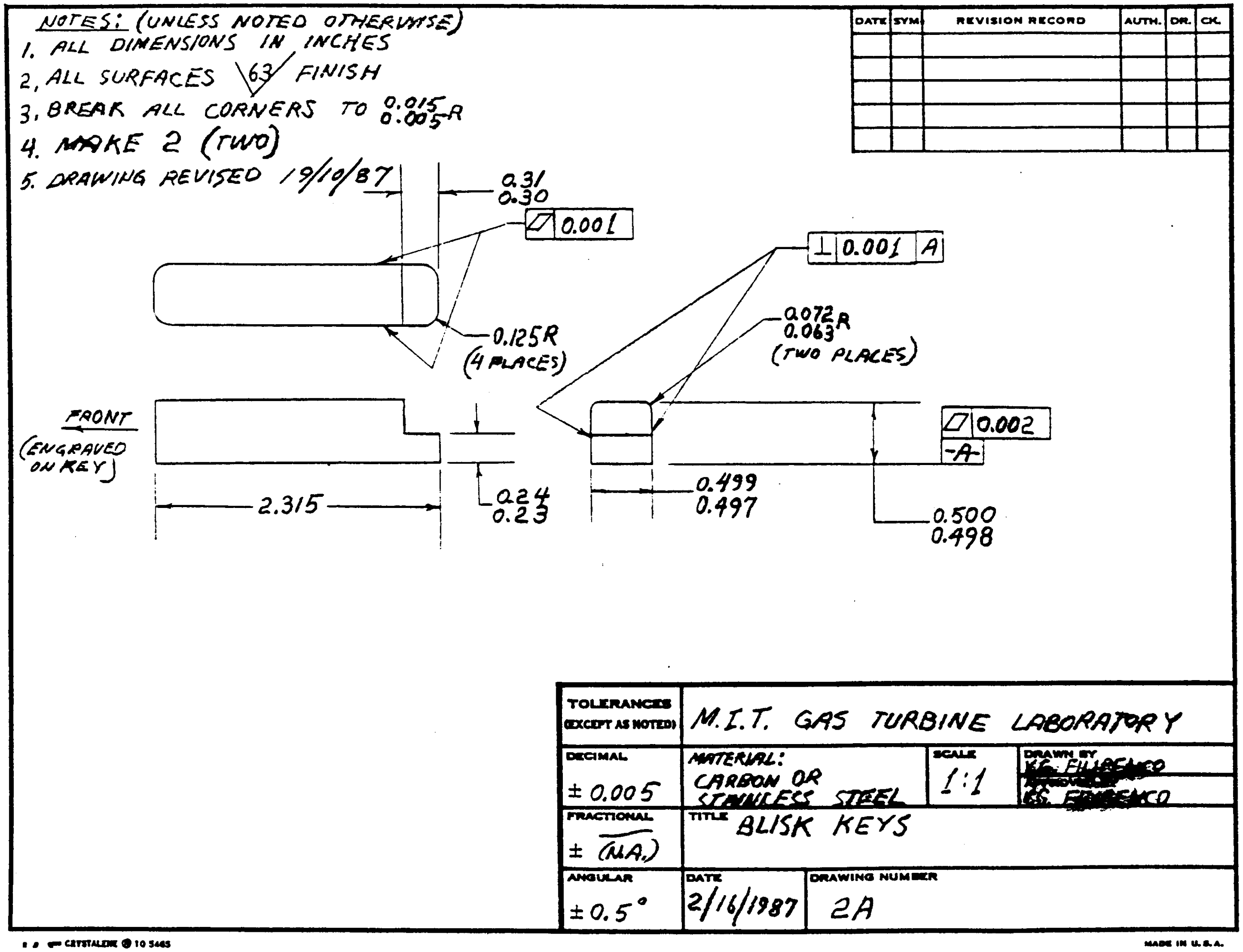

Fig. F.11b Blisk Mount Keys

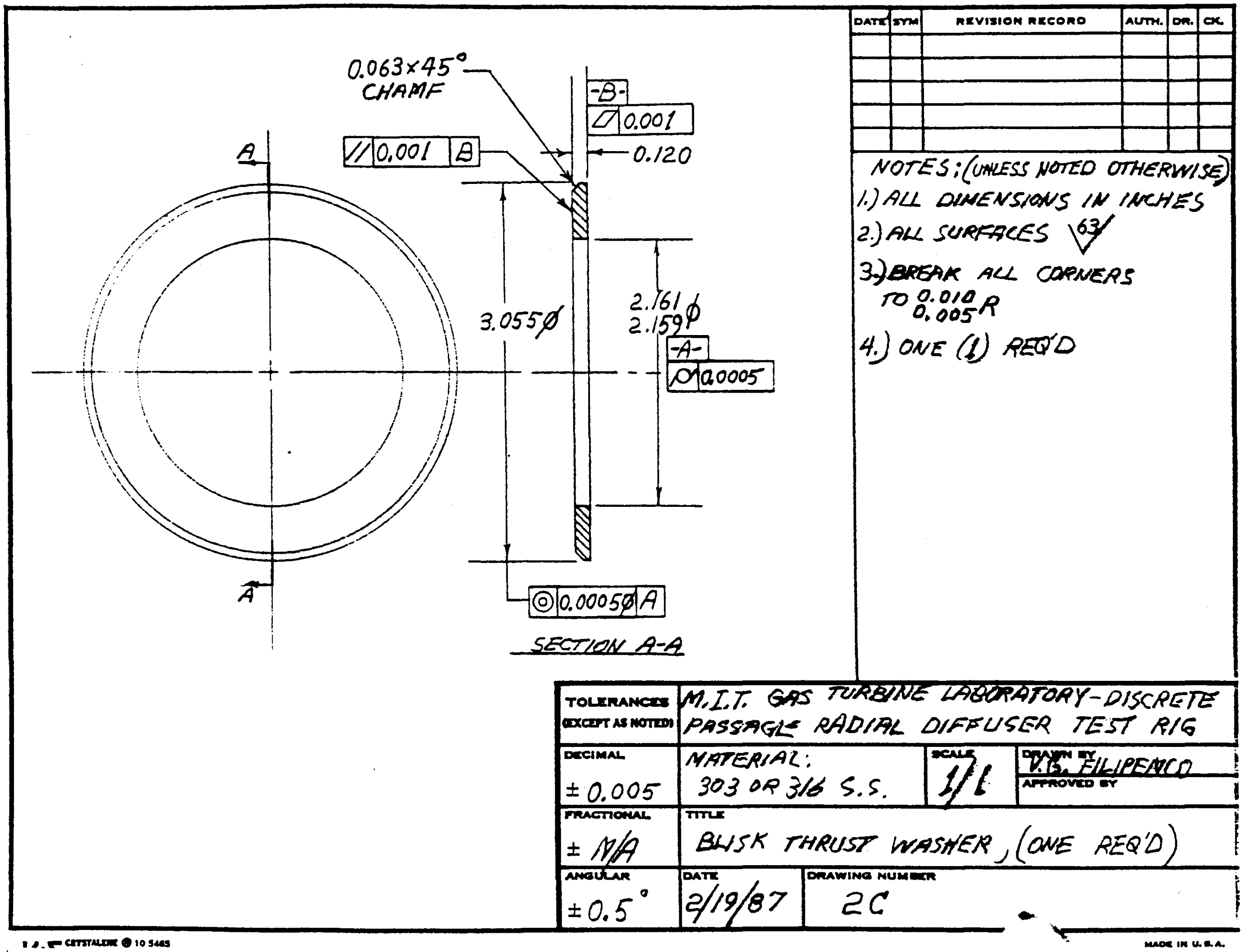

Fig. F.11c Blisk Locknut Thrust-Washer

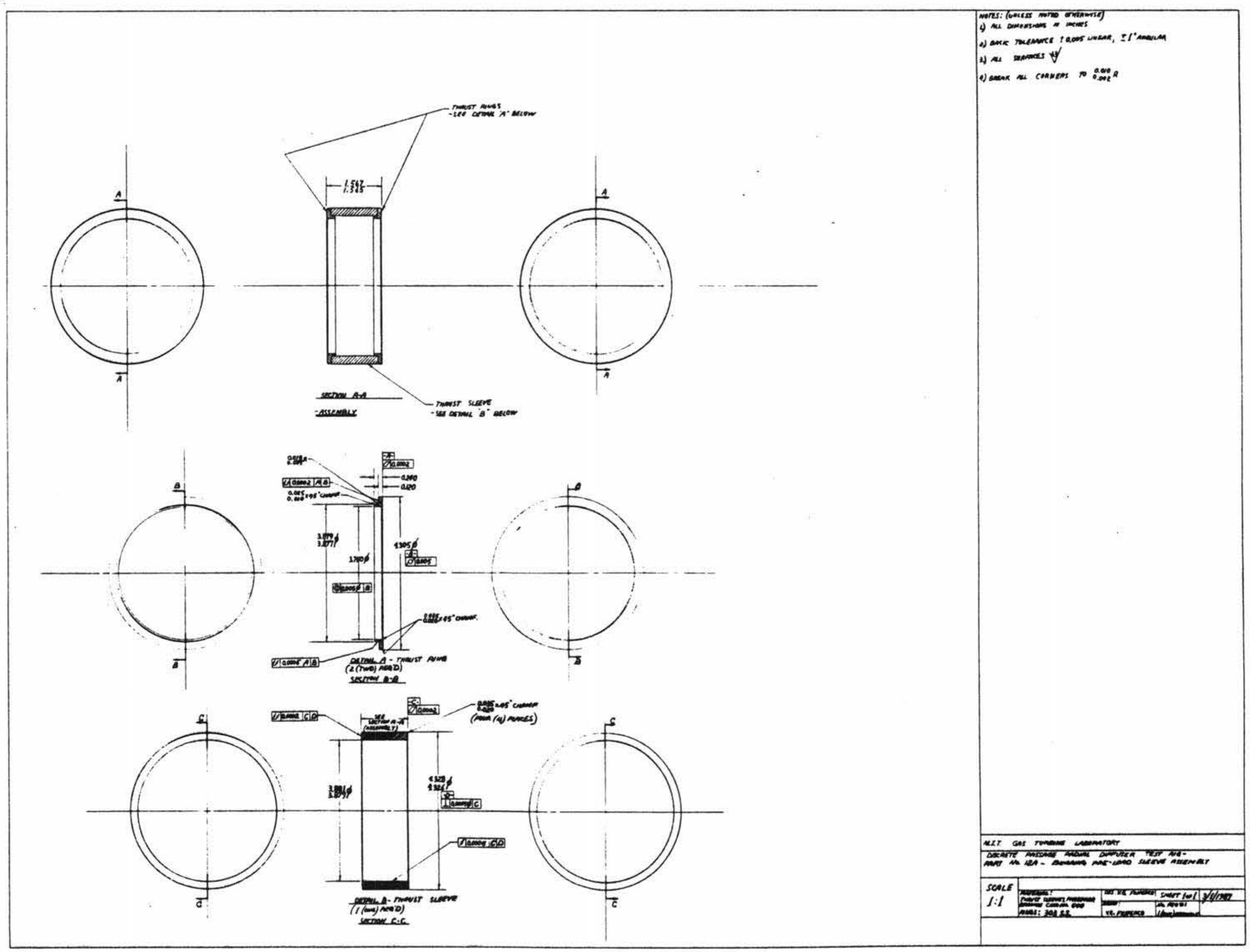

Fig. F.12 Bearing Pre-Load Sleeve

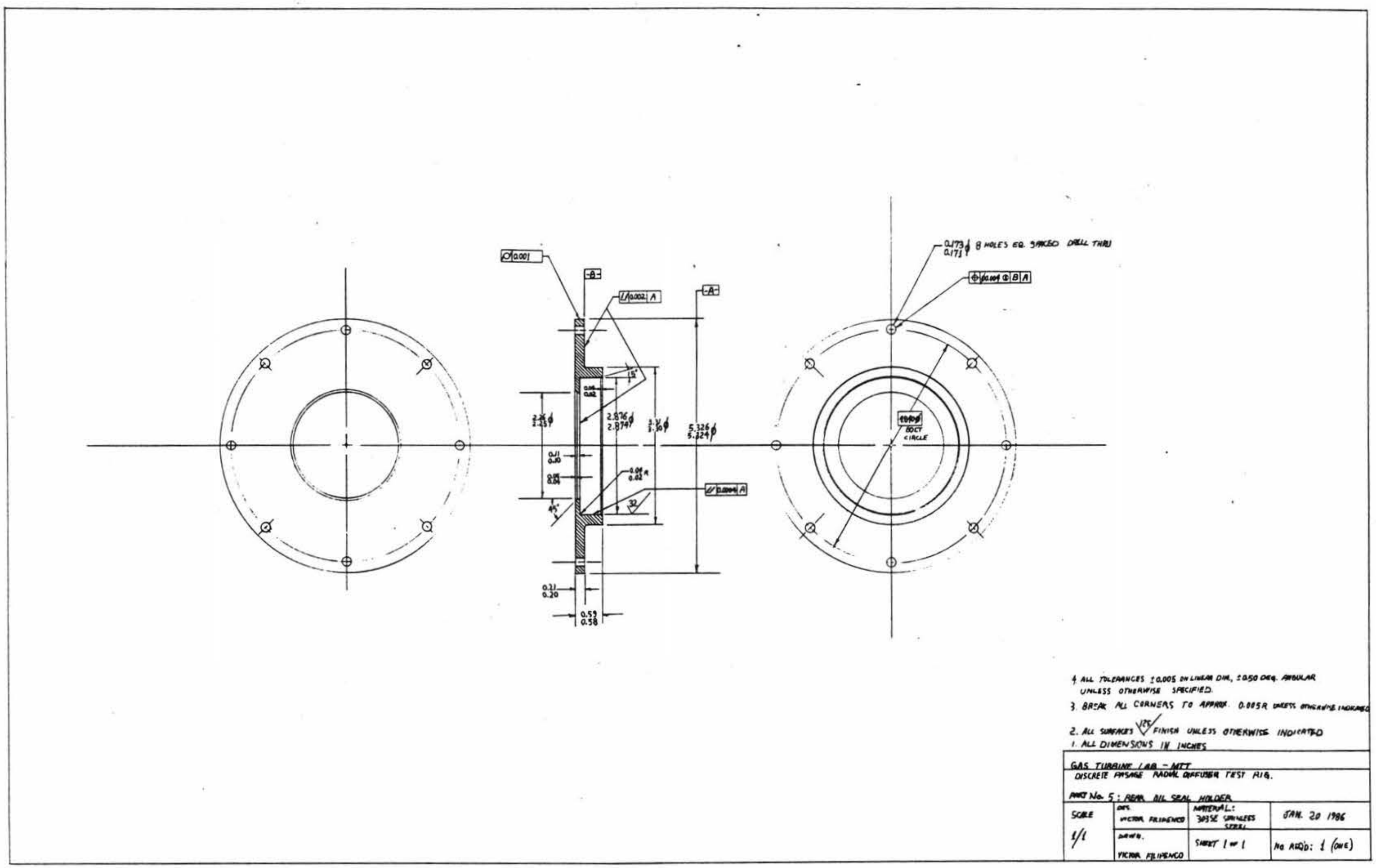

Fig. F.13 Bearing Housing Rear Cover

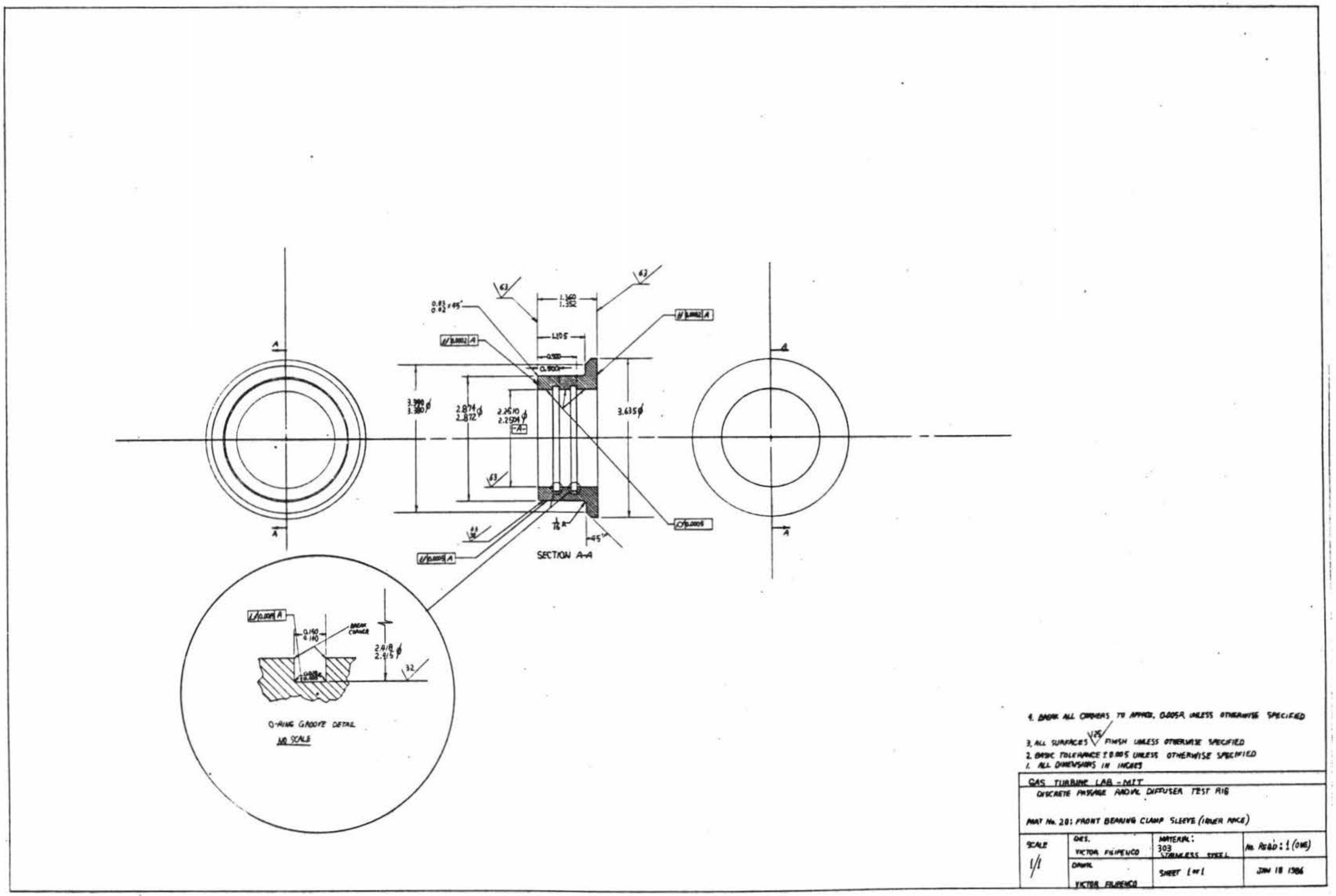

Fig. F.14a Carbon Face Seal Shaft-Sleeve

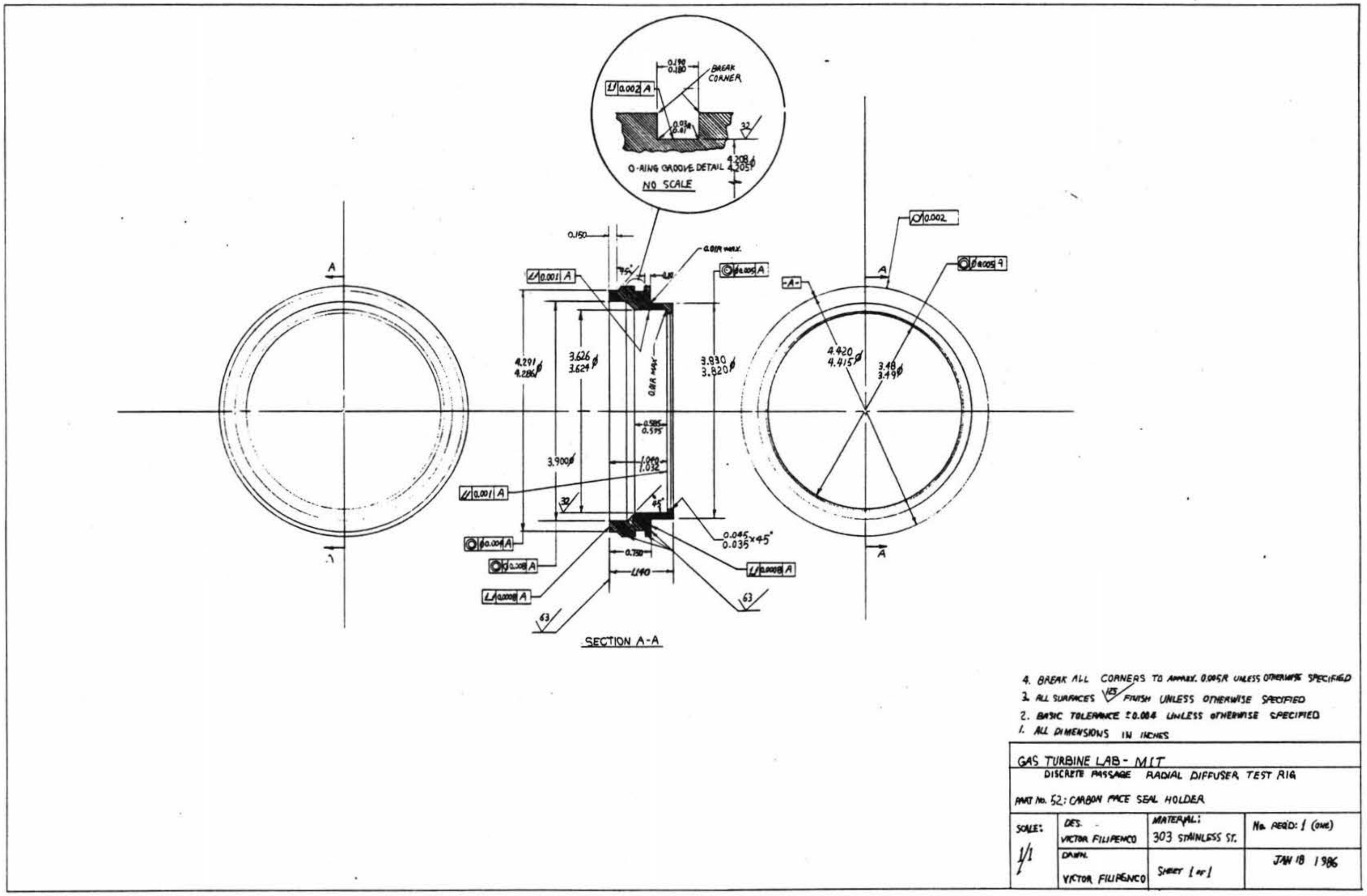

Fig. F.14b Carbon Face Seal Magnet-Ring Holder

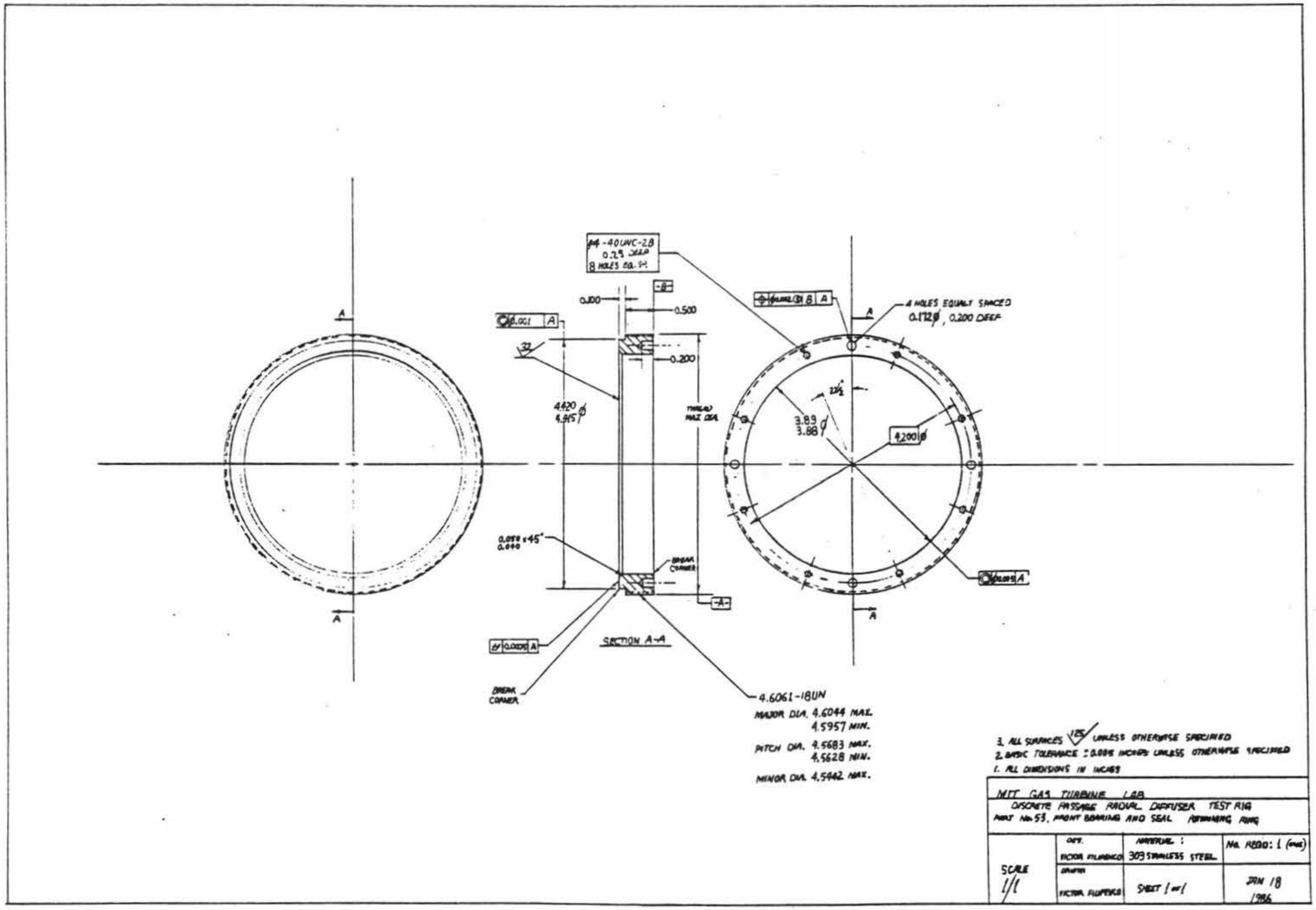

Fig. F.14c Front-Bearing and Oil-Seal Retaining Ring

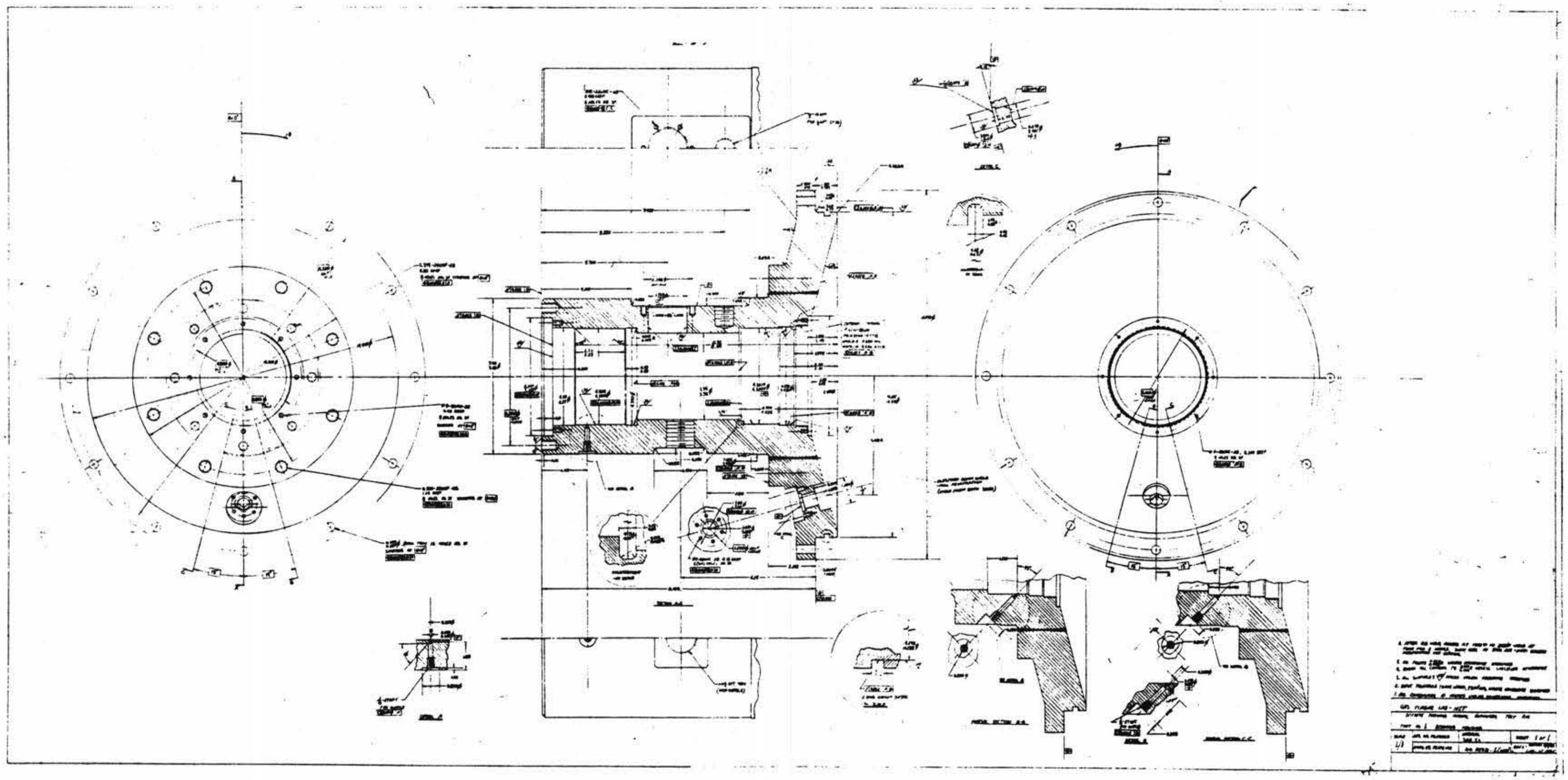

Fig. F.15 Swirl-Generator Bearing Housing

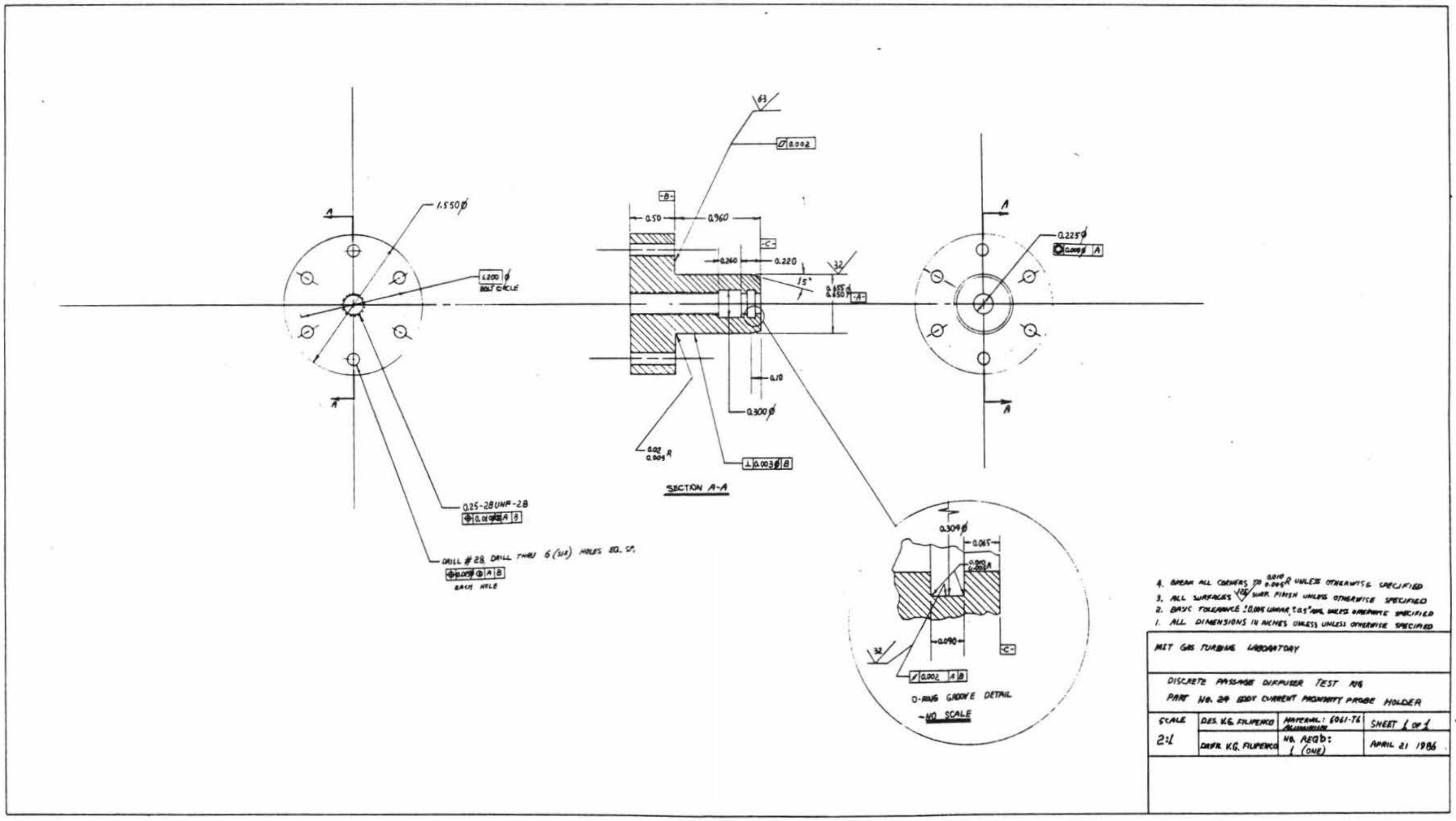

Fig. F.16 Eddy-Current Proximity Probe Holder

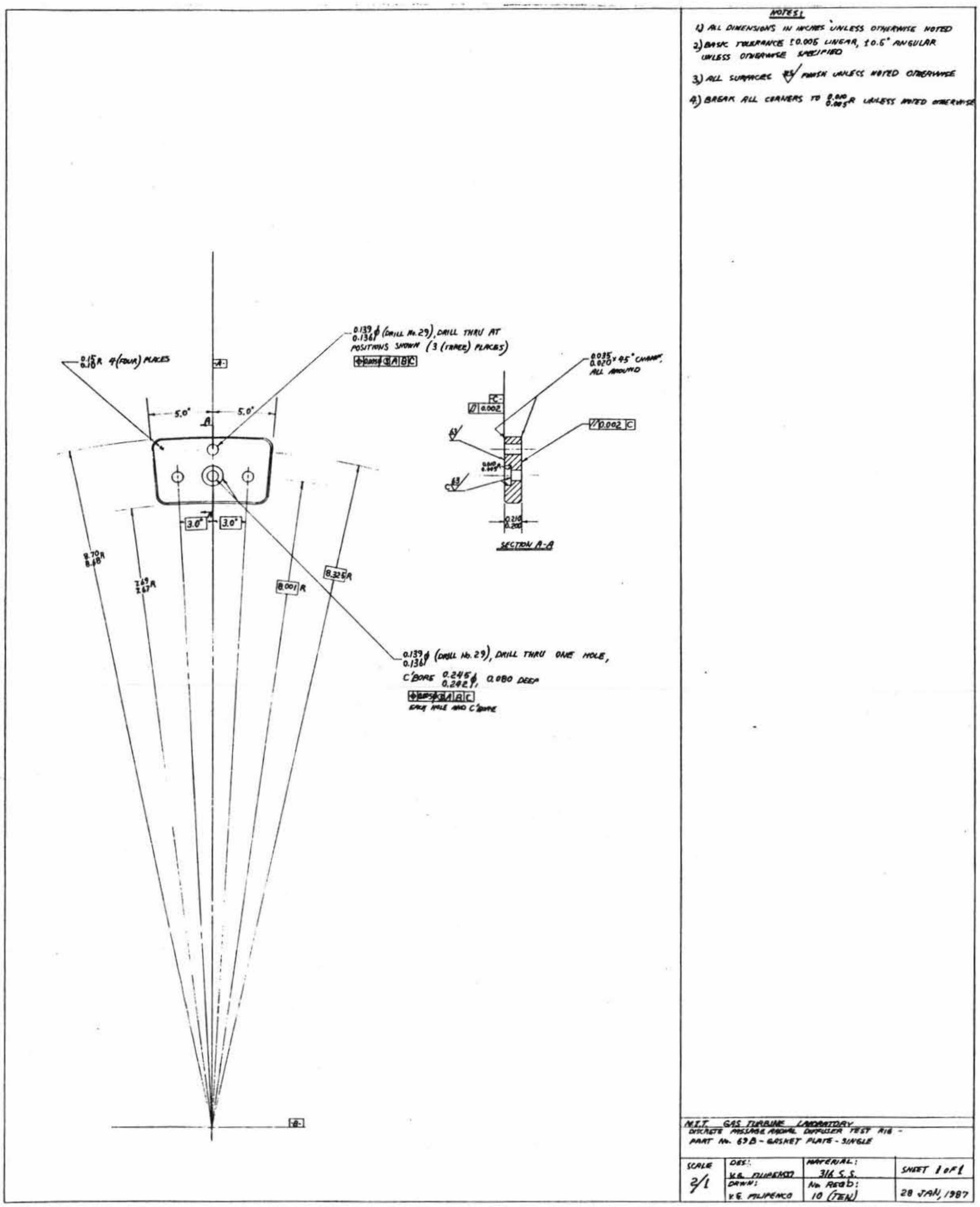

Fig. F.17 Probe O-Ring Retaining Plates

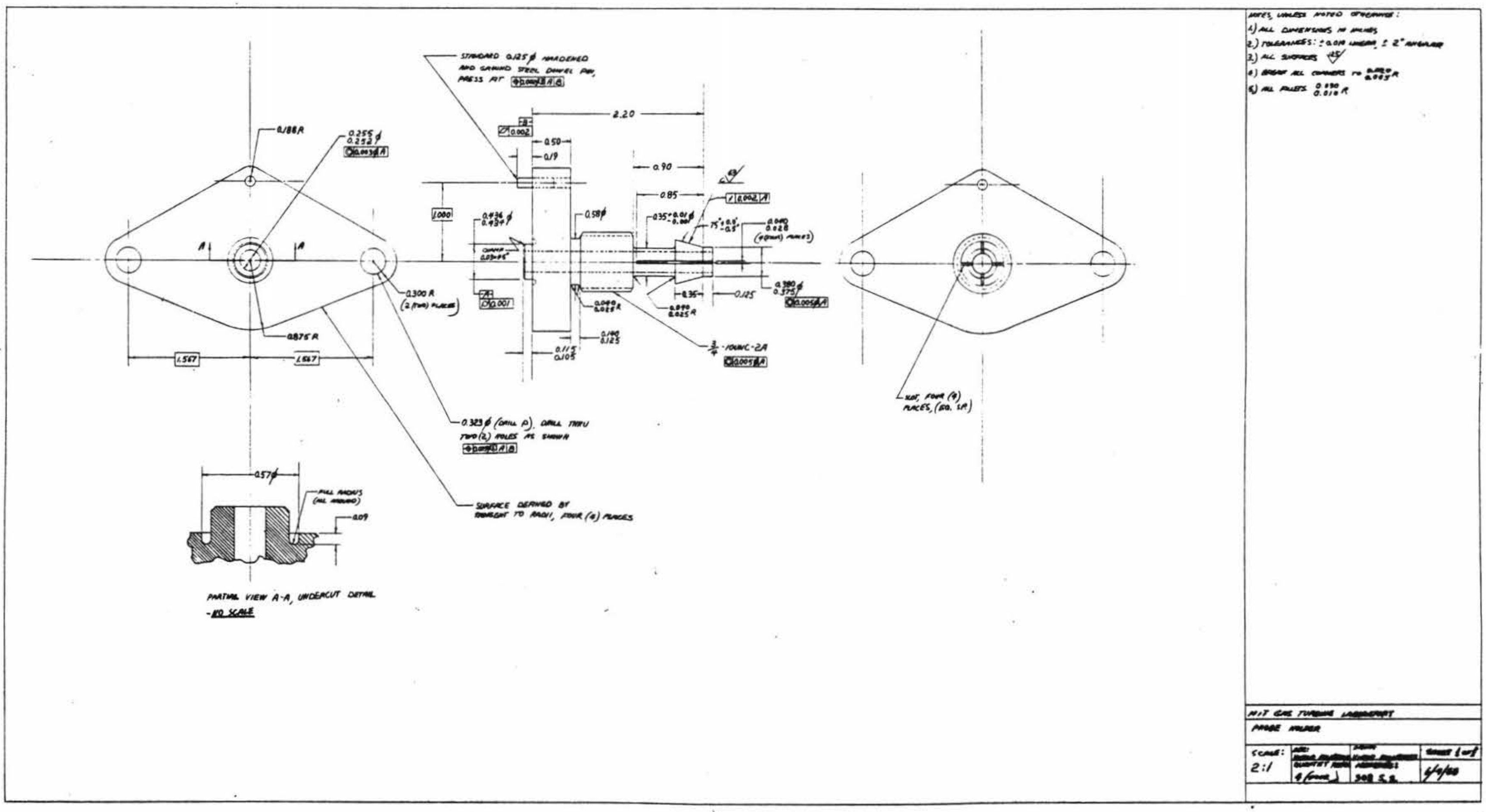

Fig. F.18a Stationary Probe Mounting Fixture

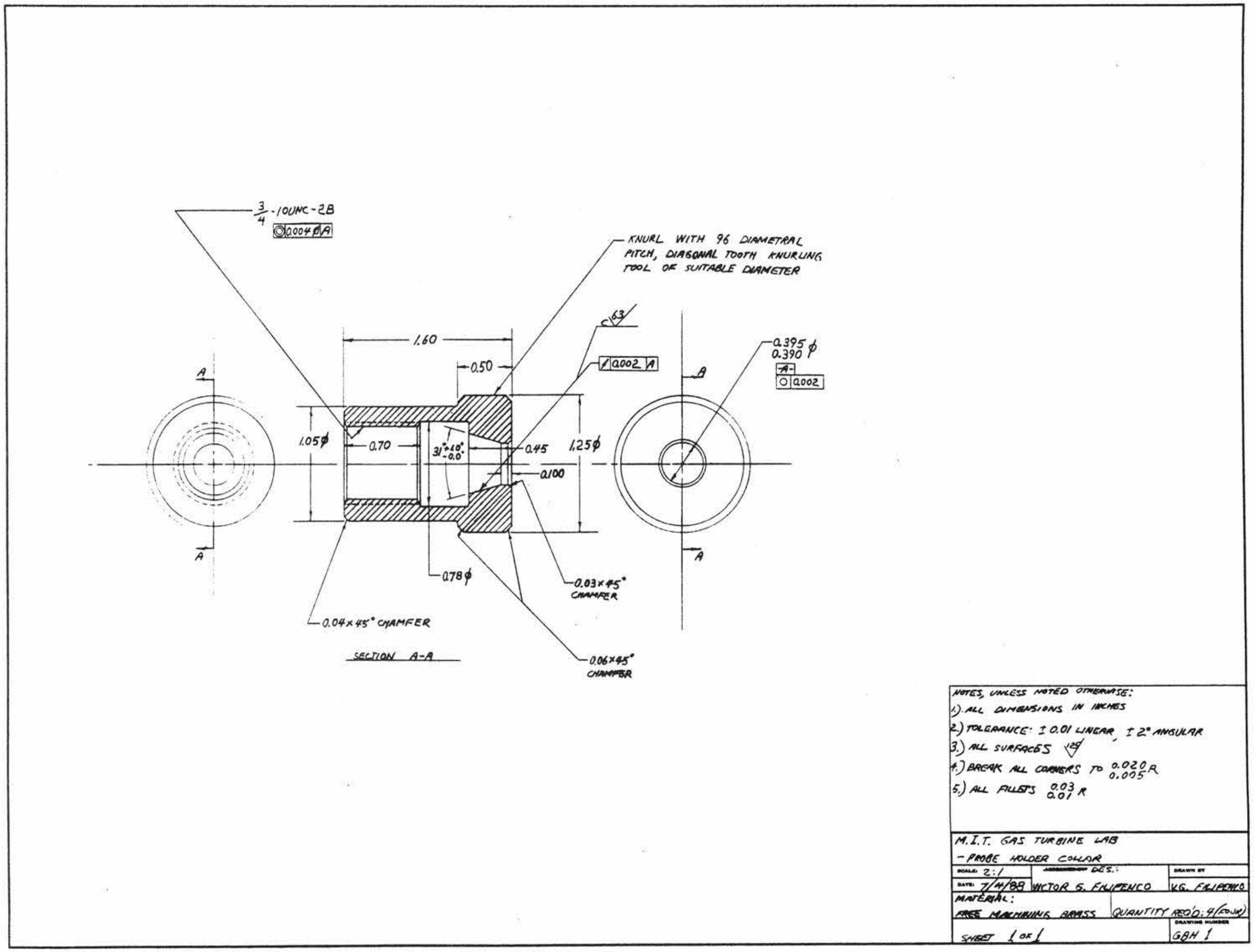

Fig. F.18b Stationary Probe Mounting Fixture Collar

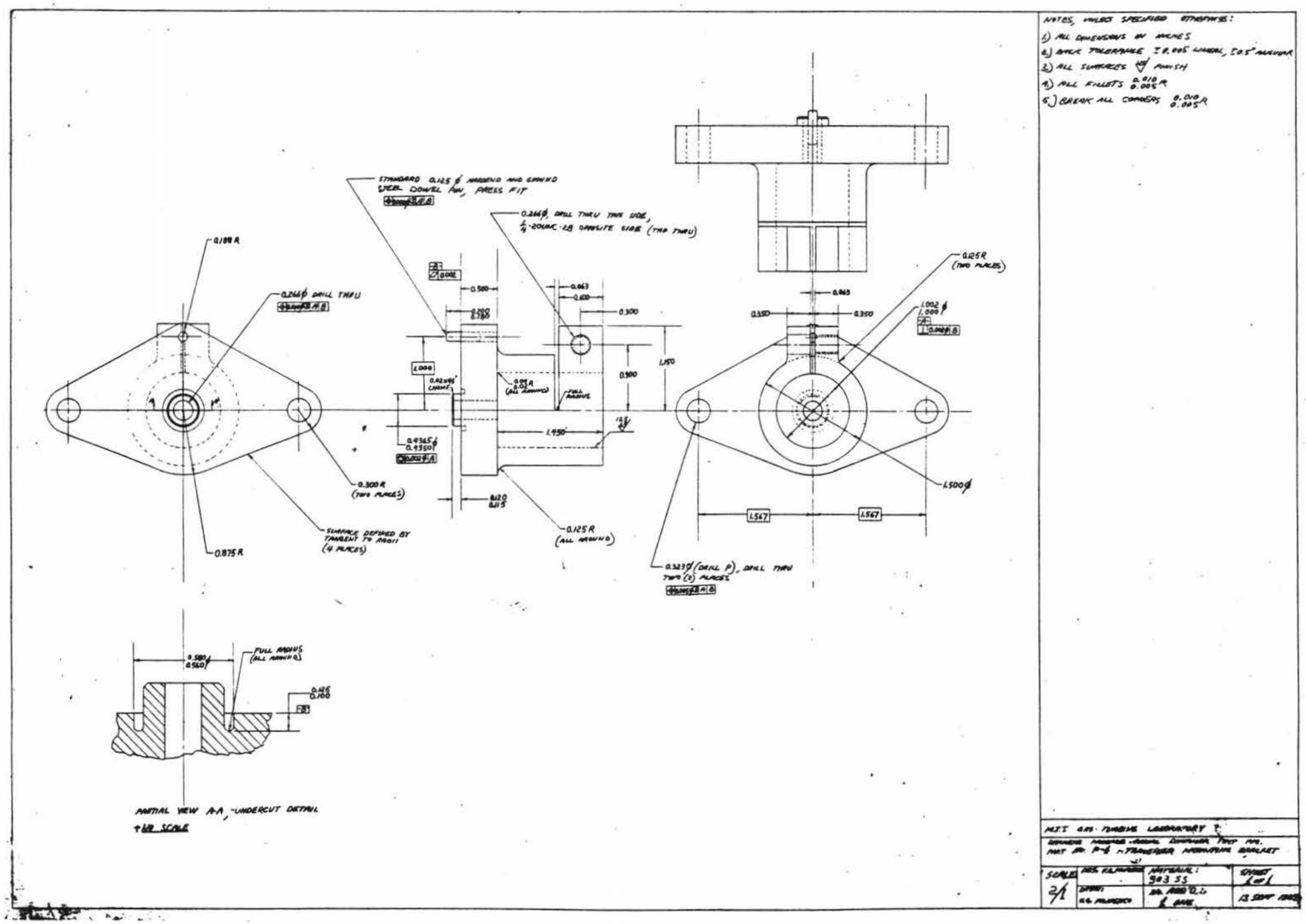

Fig. F.19 Probe Actuator Mechanism Mounting Fixture

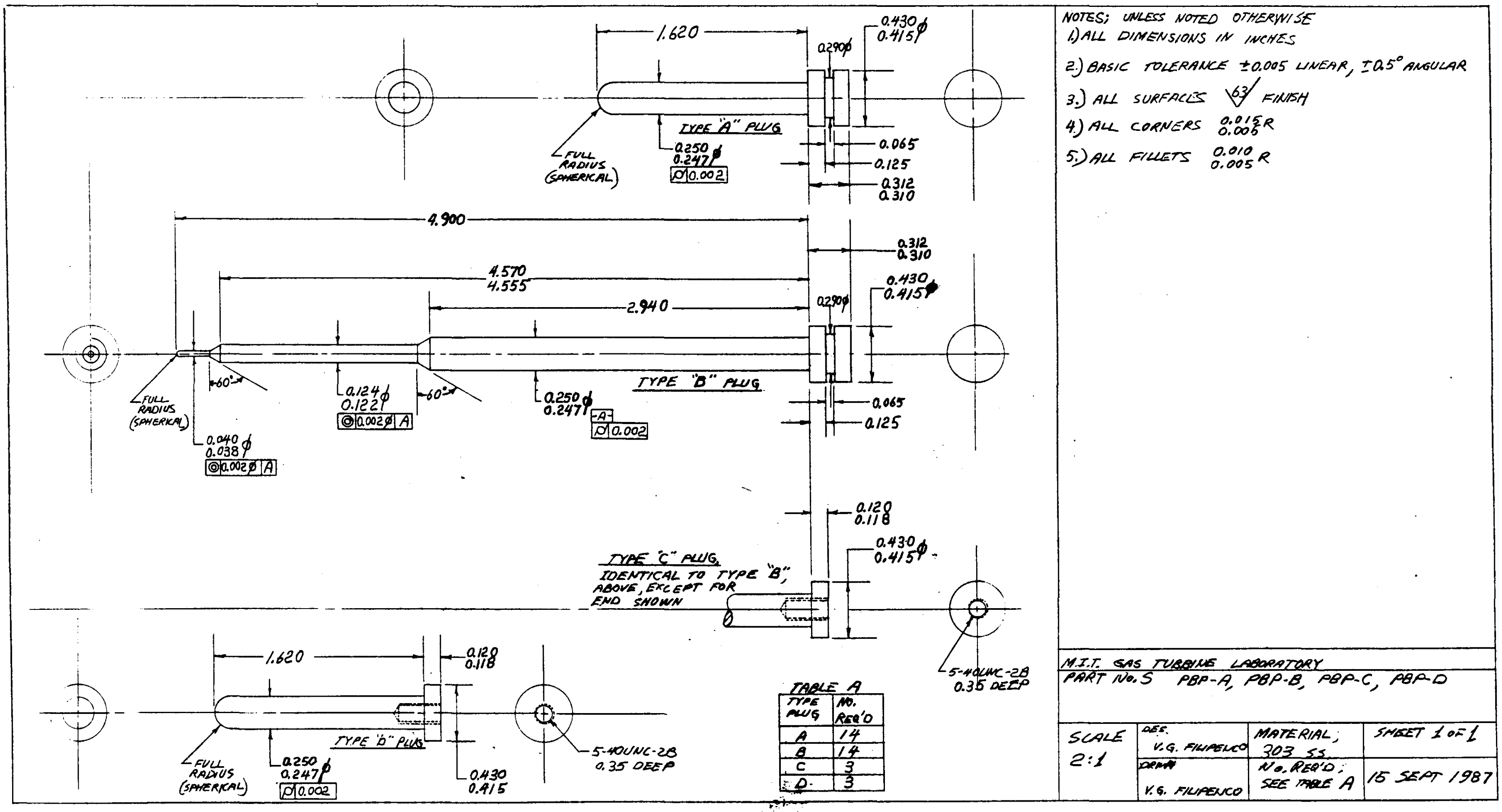

Fig. F.20 Dummy Probes

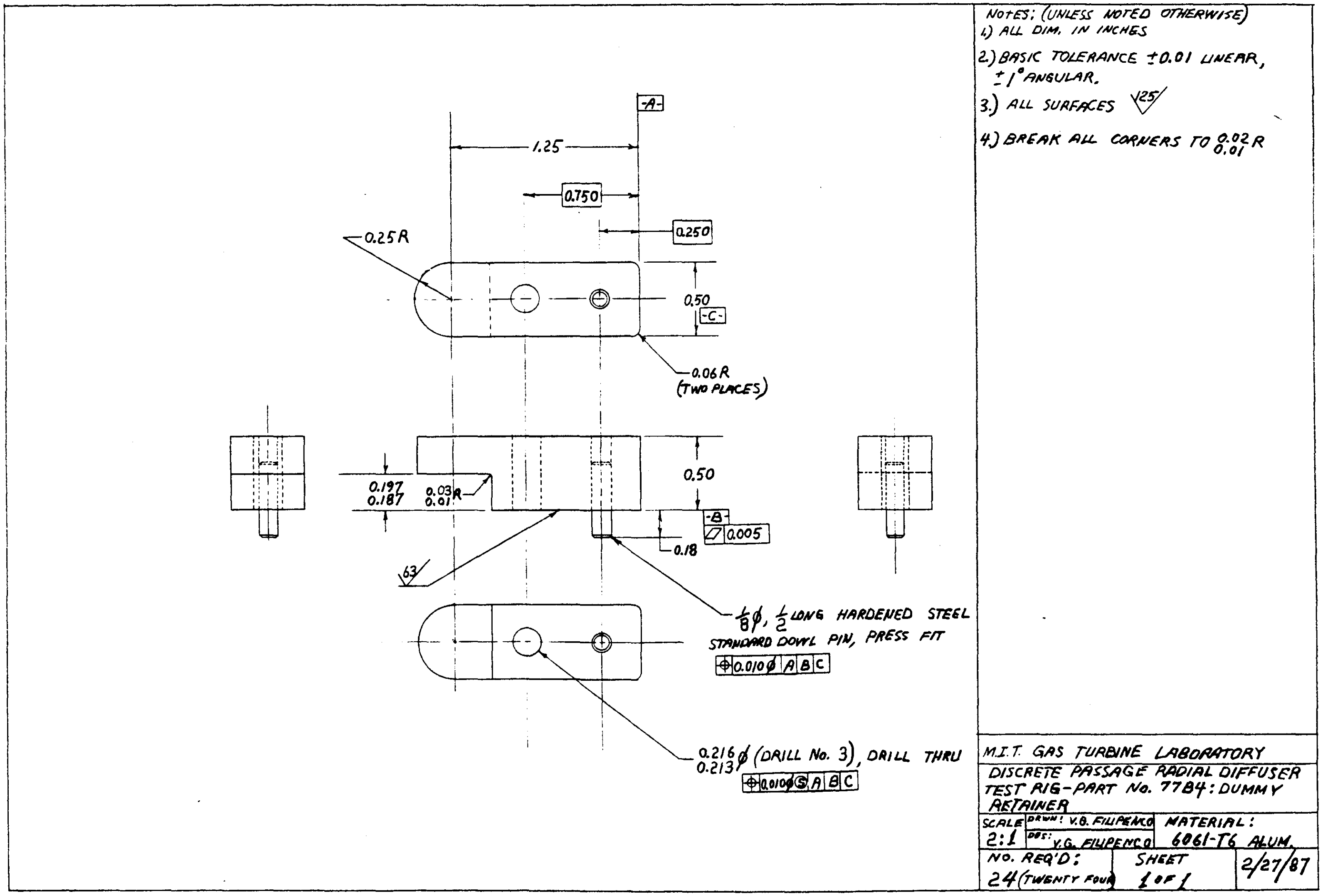

Fig. F.21 Dummy-Probe Retainer

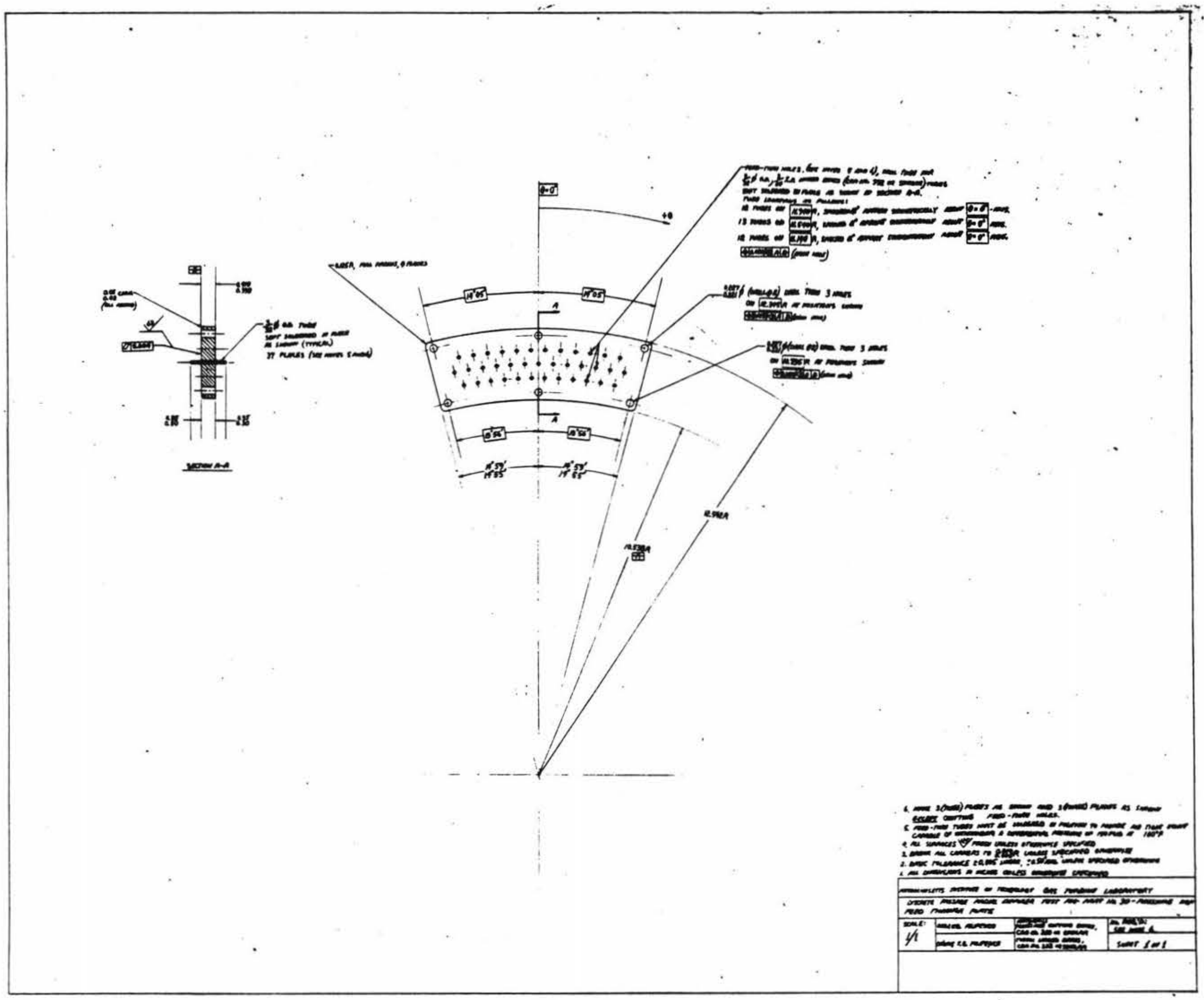

Fig. F.22 Pressure-Line Feed-Through Block

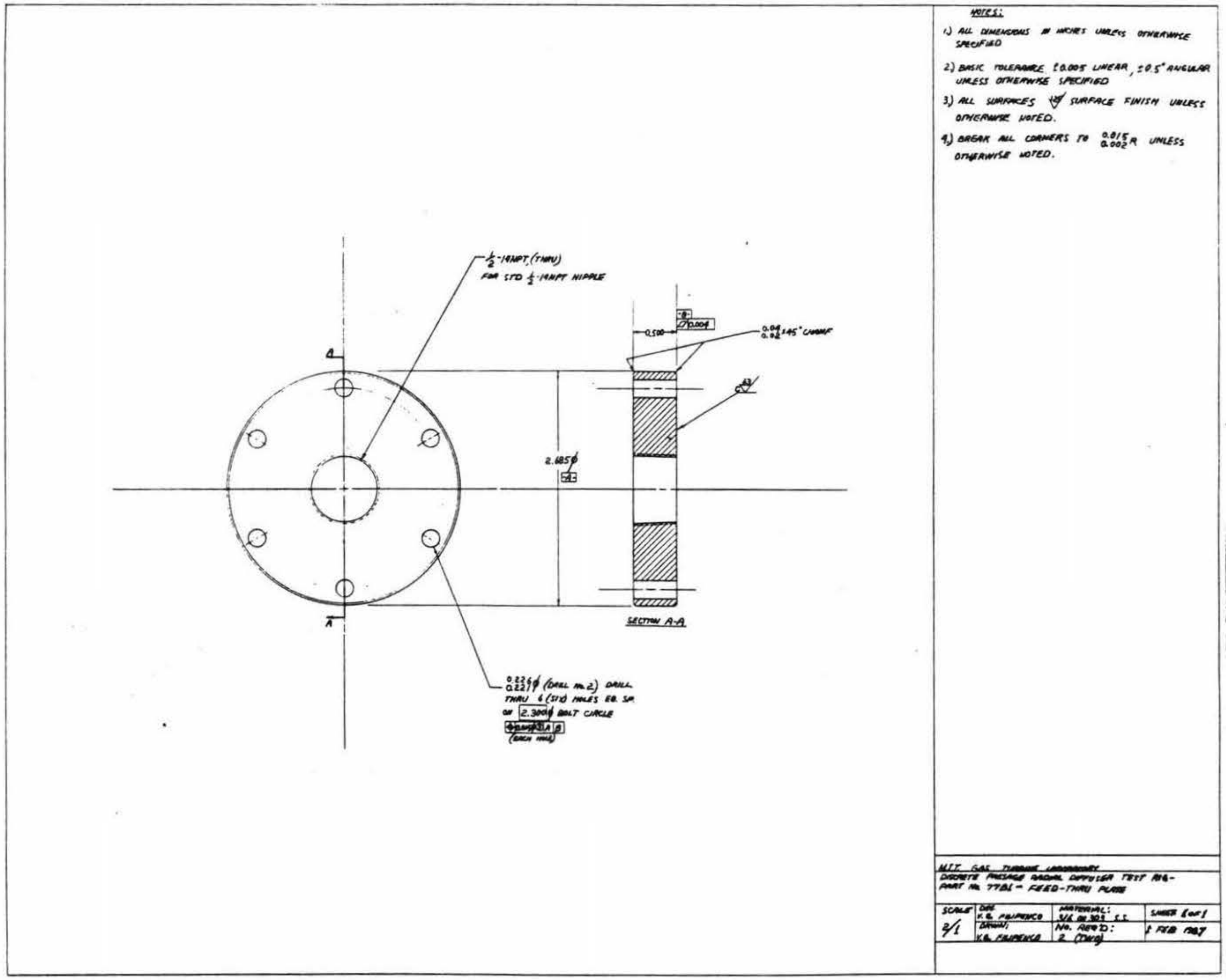

Fig. F.23 Electrical Feed-Through Fixture

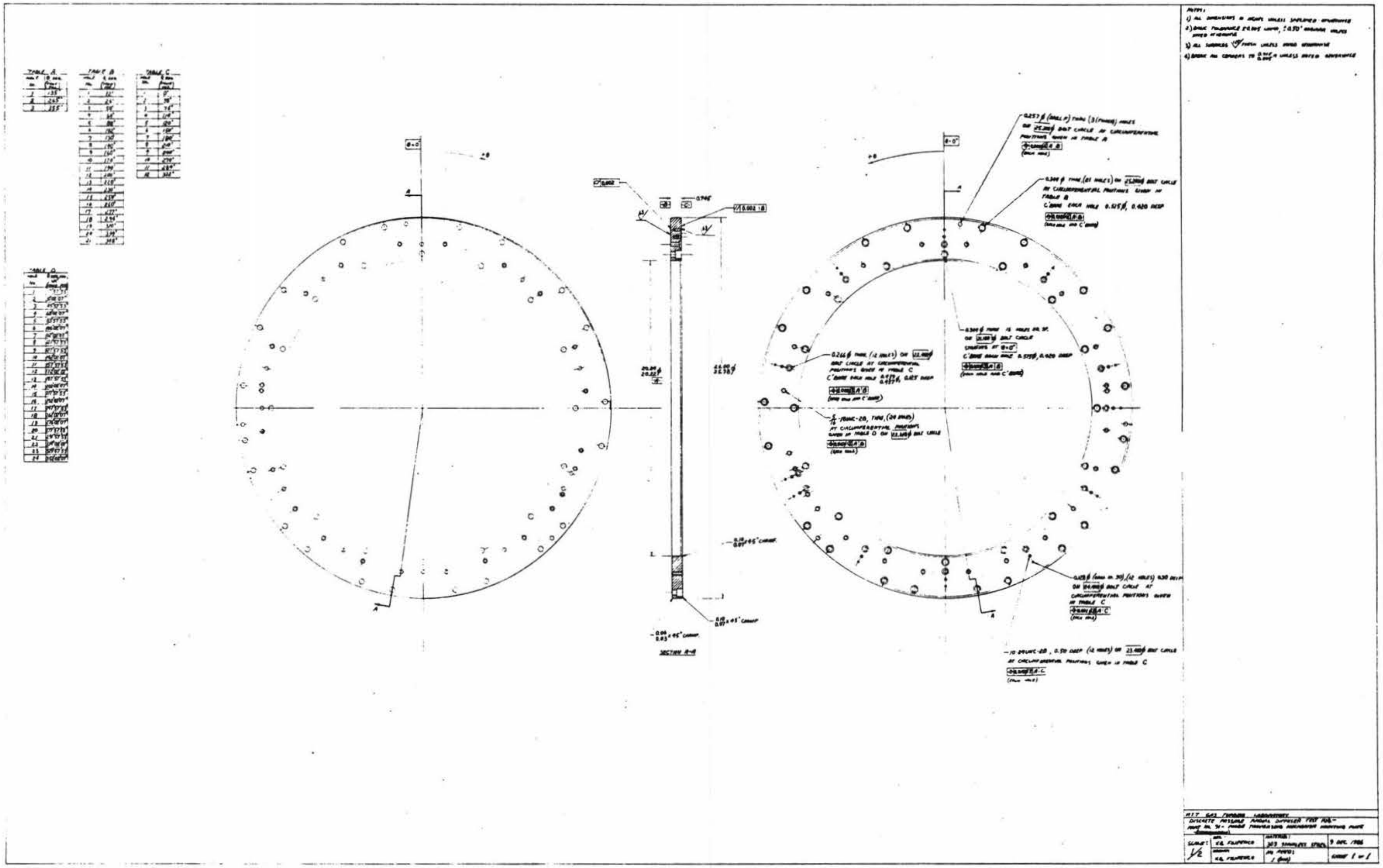

Fig. F.24 Outer Probe-Mount Plate

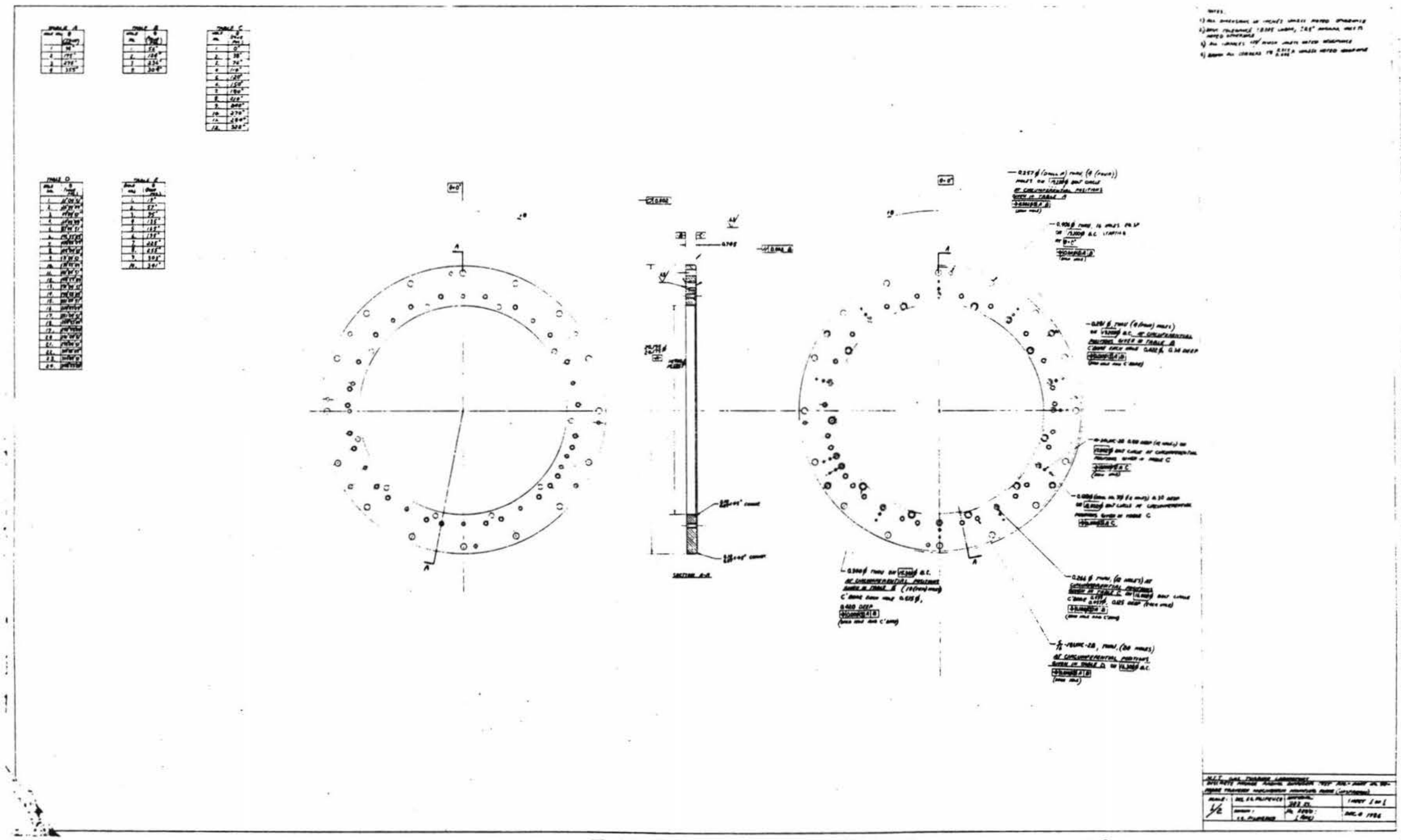

Fig. F.25 Inner Probe-Mount Plate

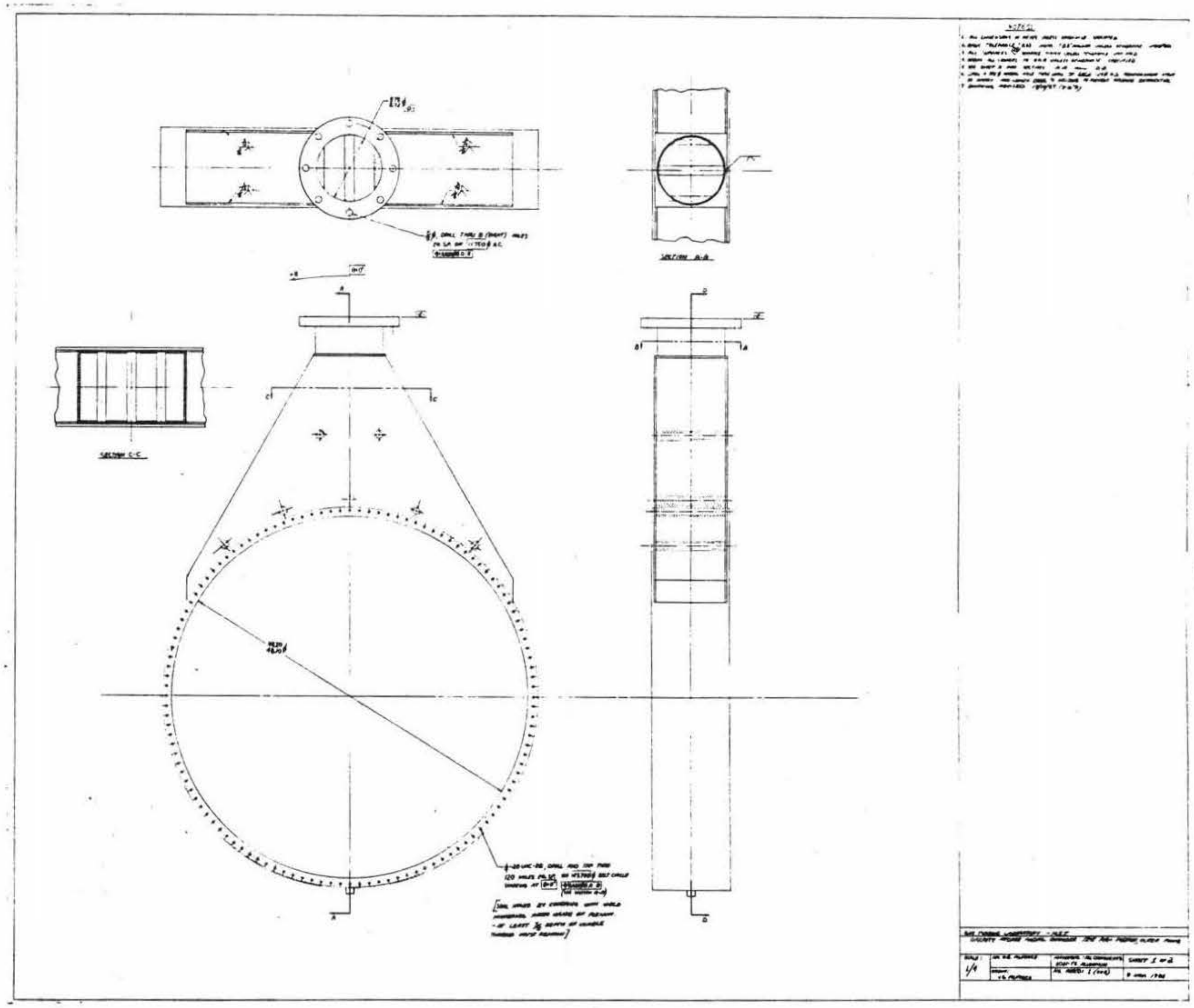

Fig. F.26a Main Plenum/Collector, General View

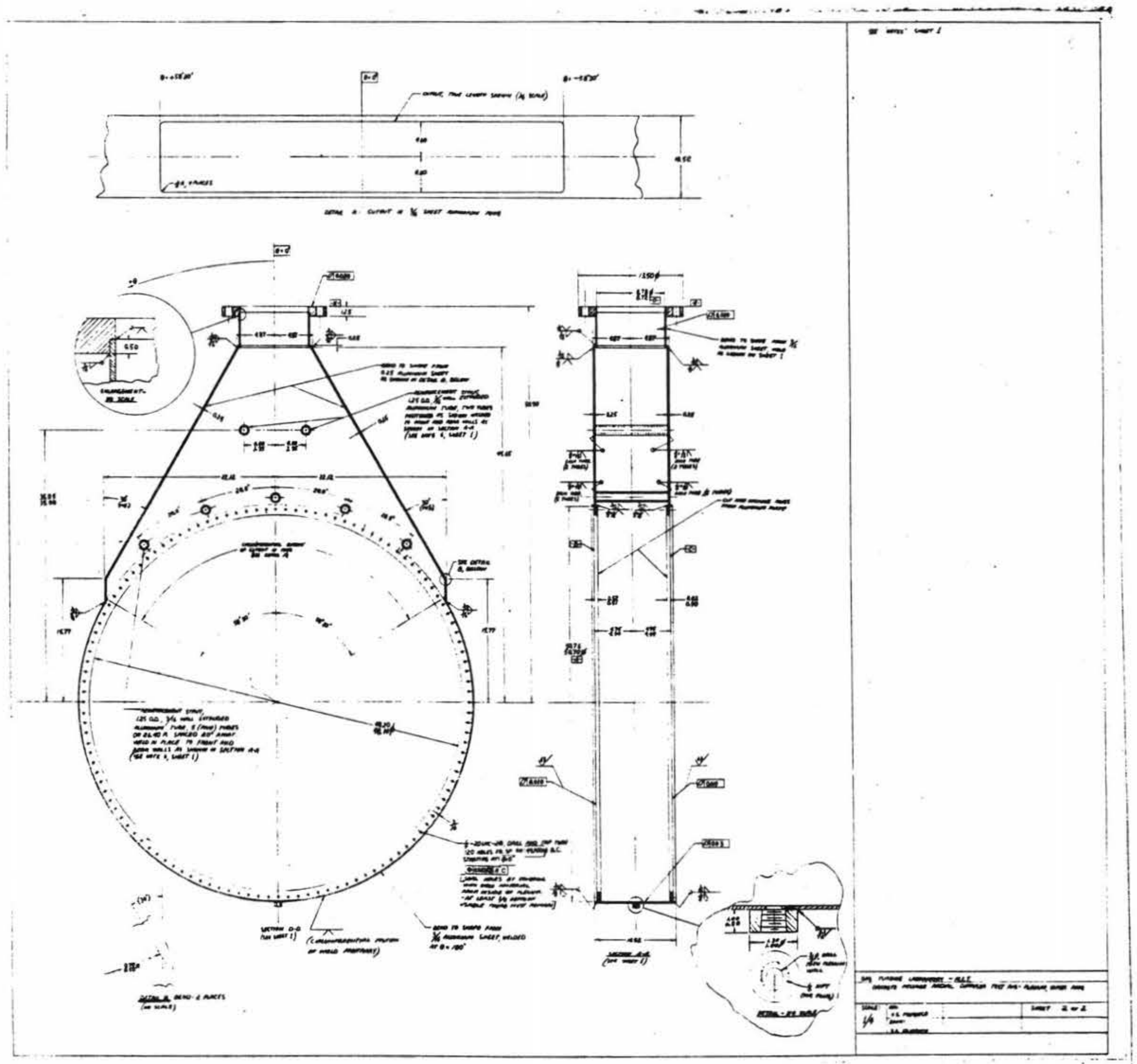

Fig. F.26b Main Plenum/Collector, Cross Section View

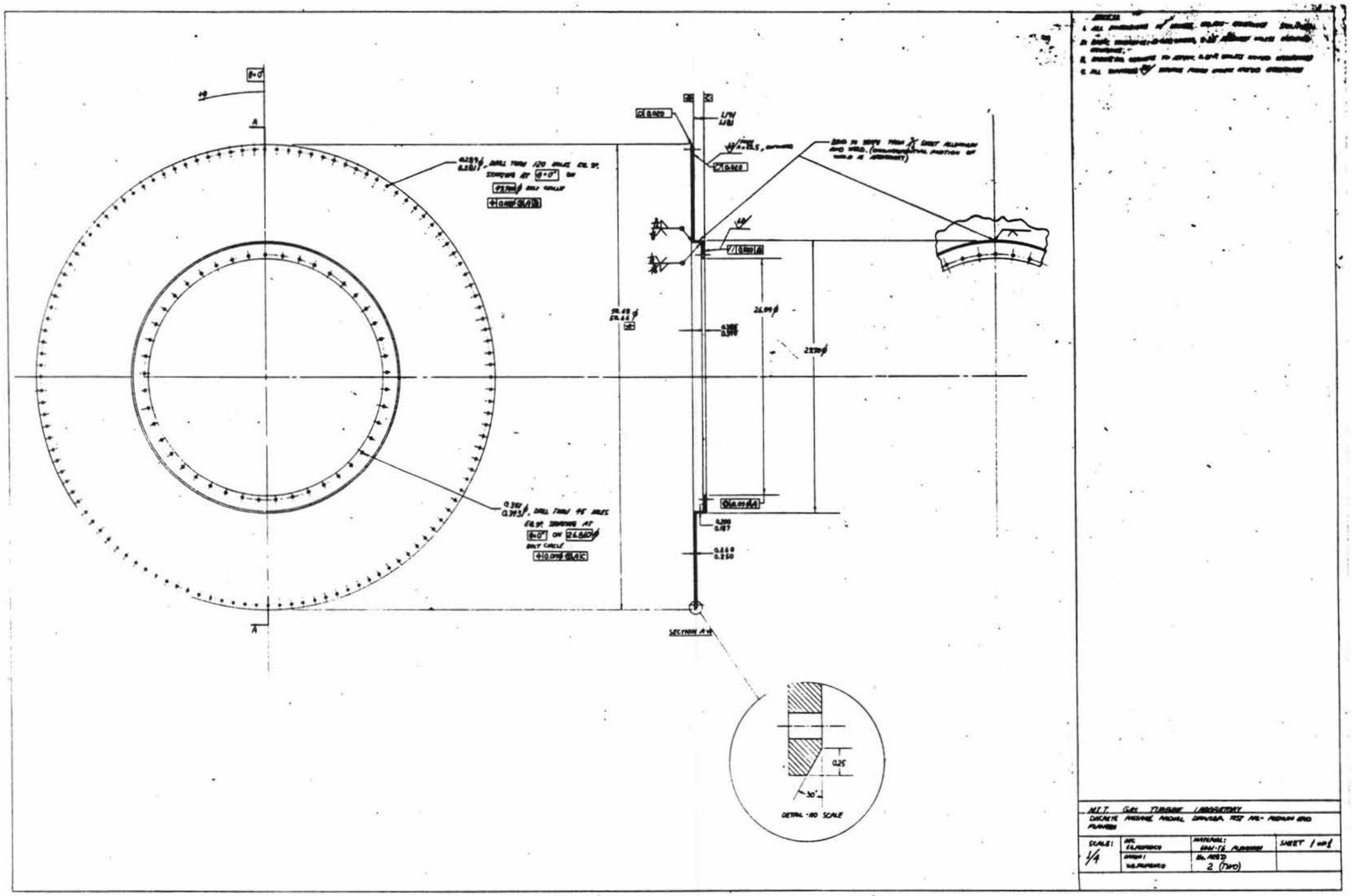

Fig. F.27 Main Plenum/Collector End Plates

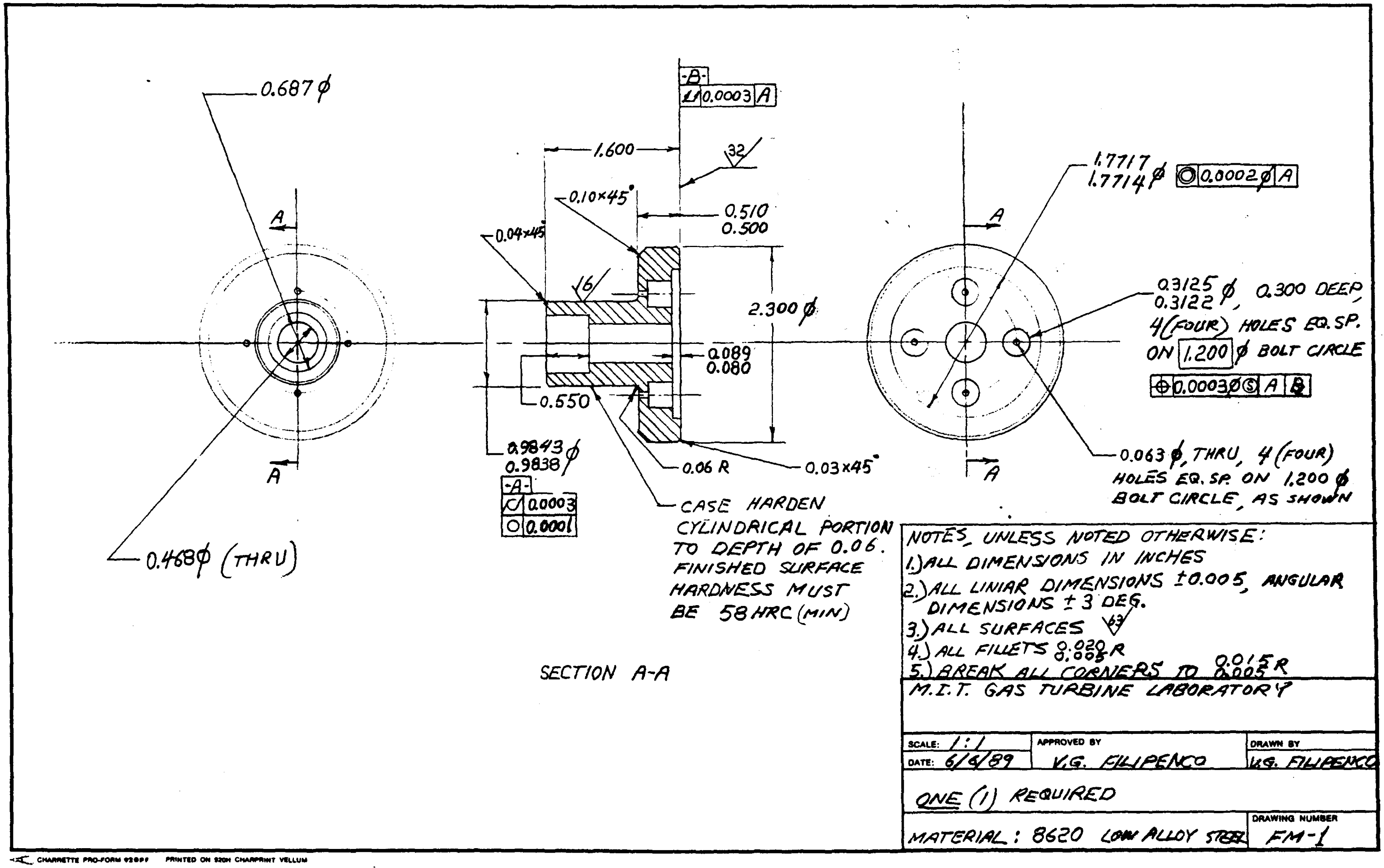

Fig. F.28 Motor Roller-Clutch Shaft Extension

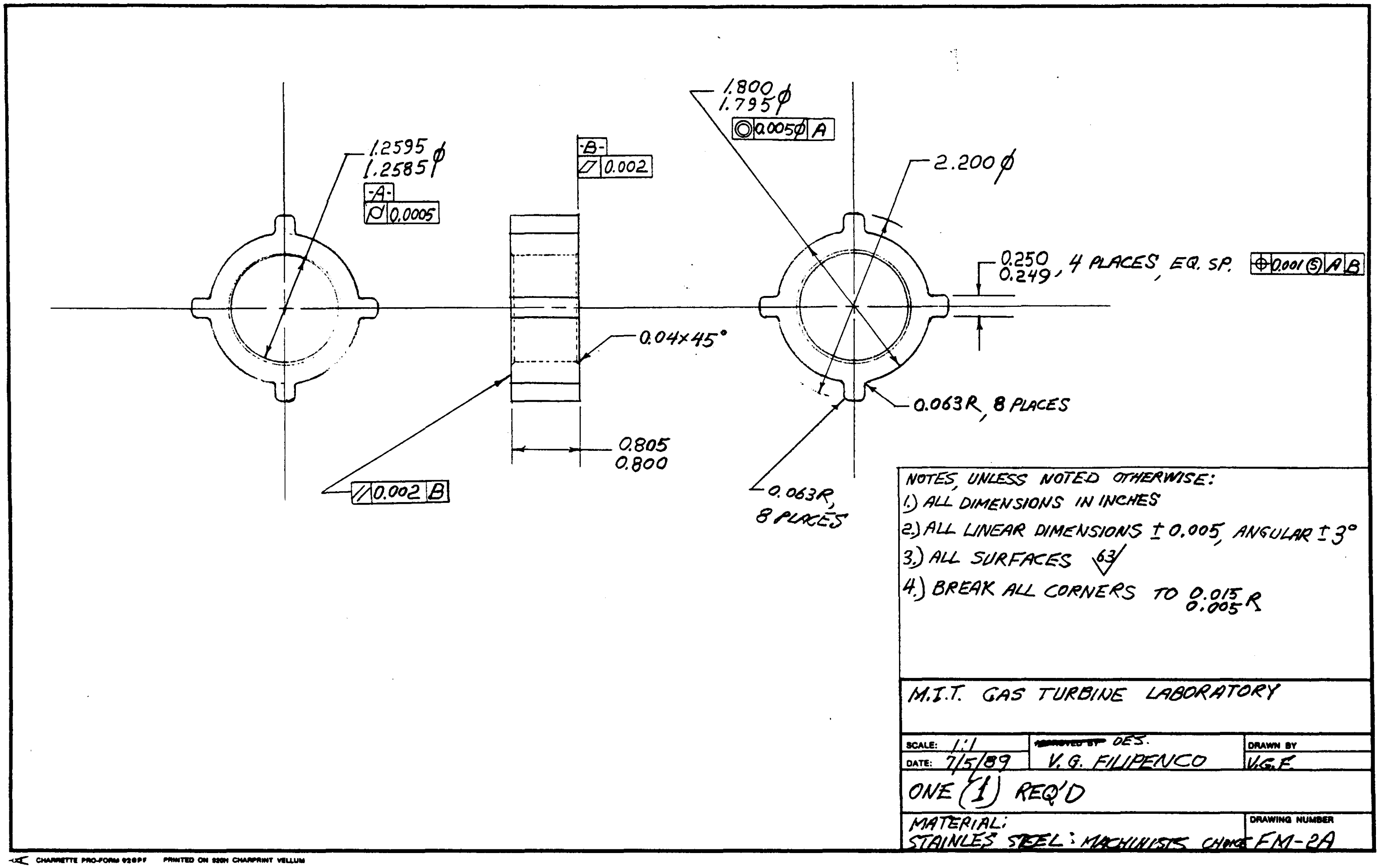

Fig. F.29a Roller-Clutch Floating Spider

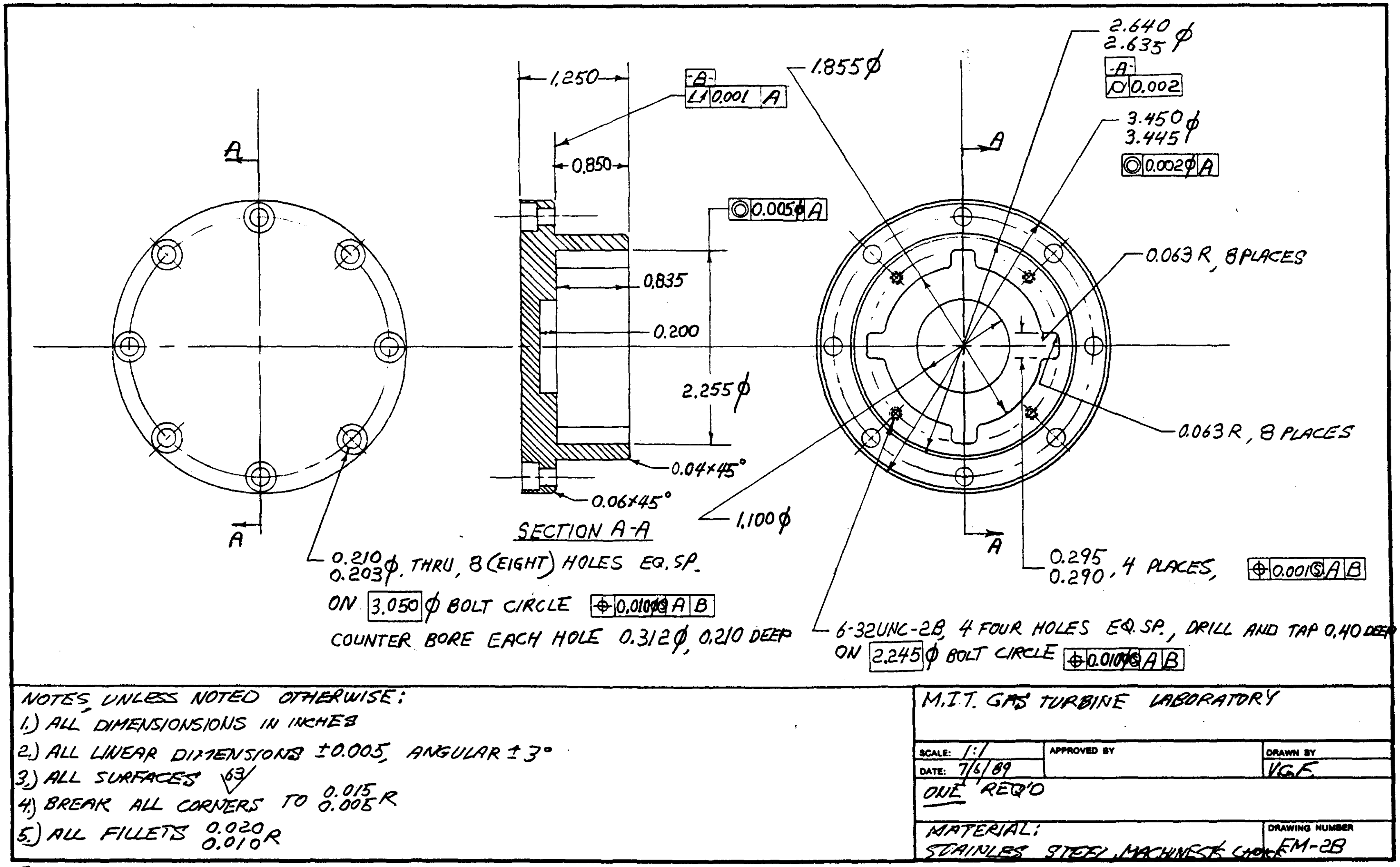

Fig. F.29b Roller-Clutch Socket-Cap

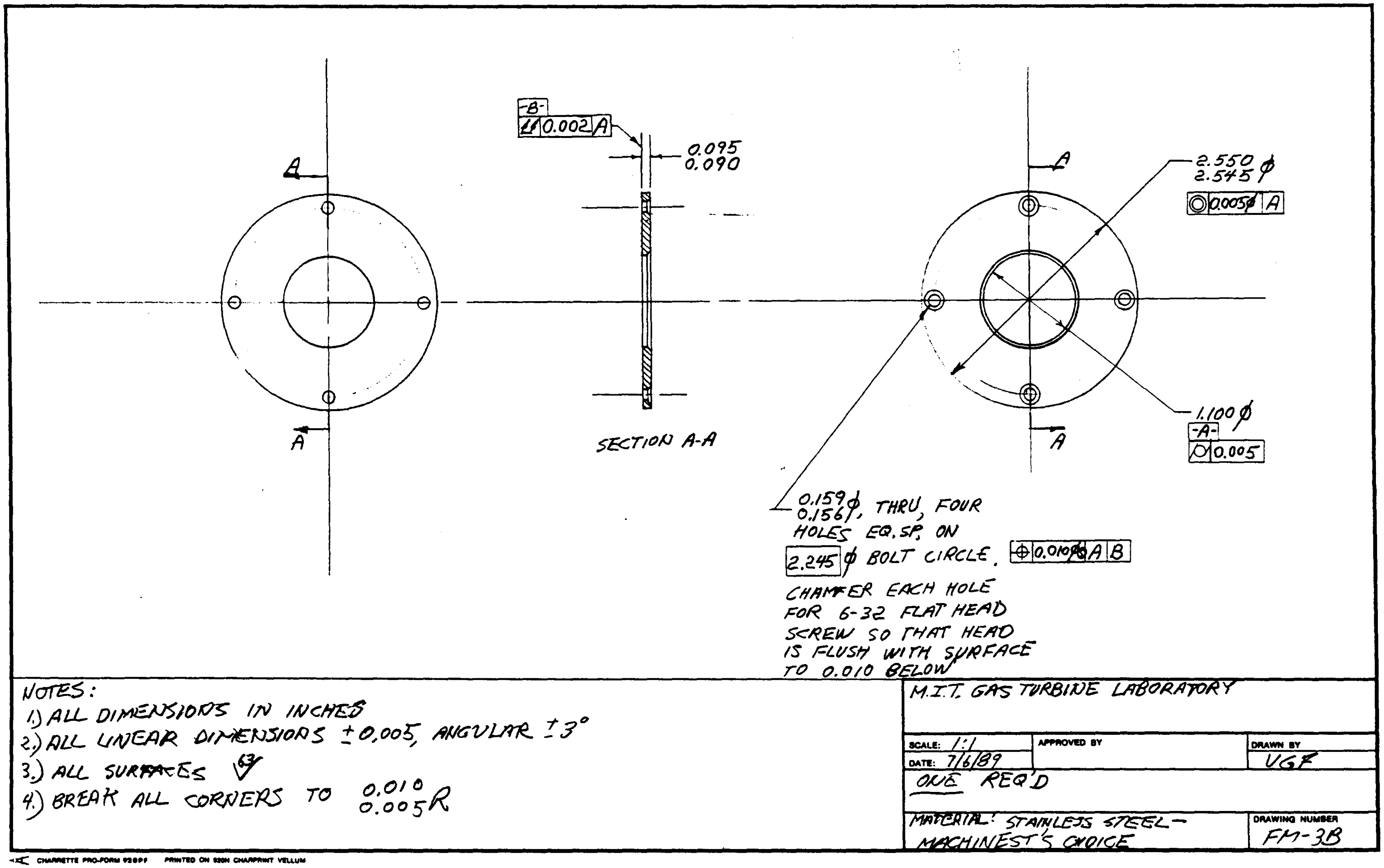

Fig. F.29c Roller-Clutch Spider Retainer

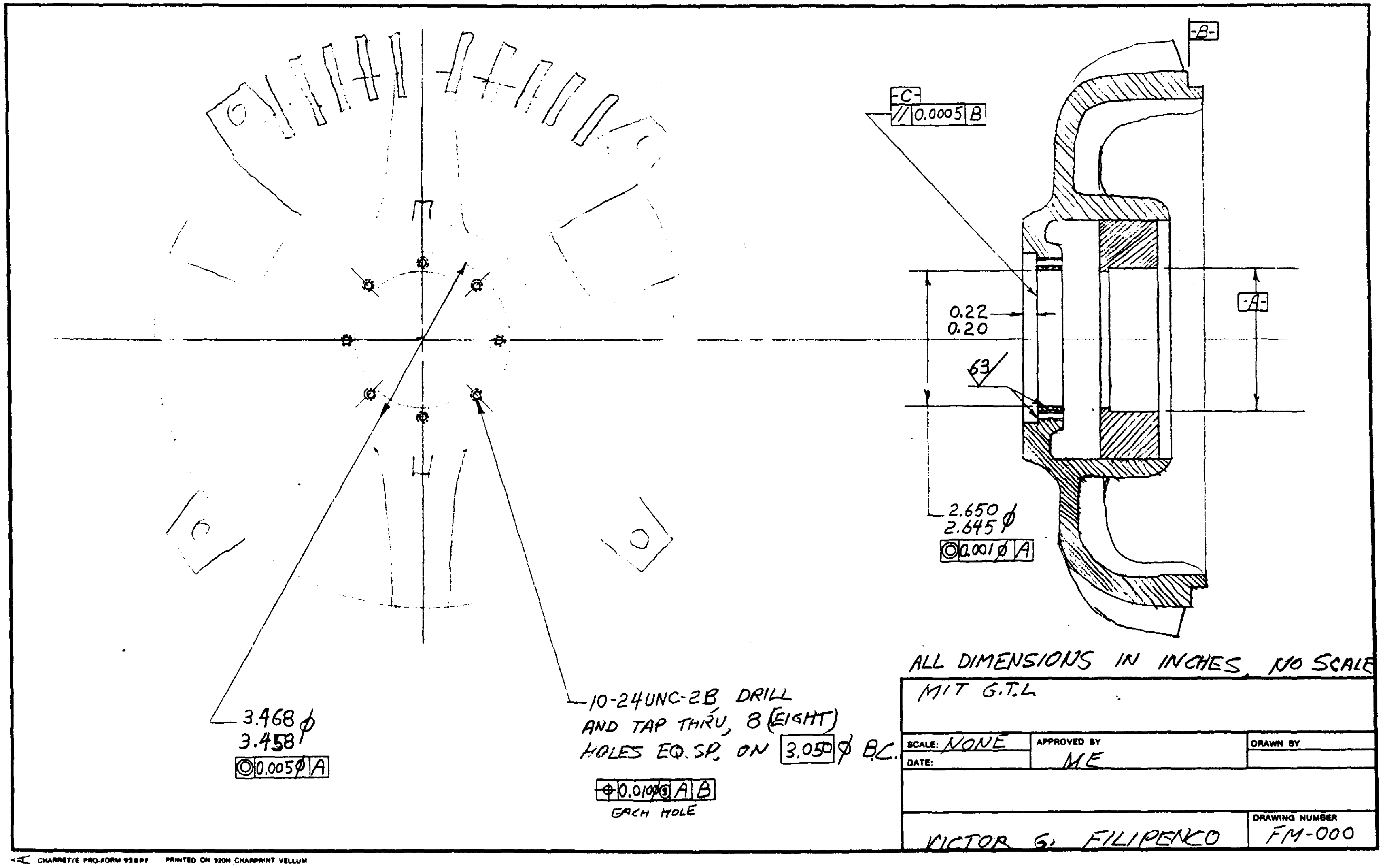

Fig. F.30 Modification of Main-Motor Rear Cover

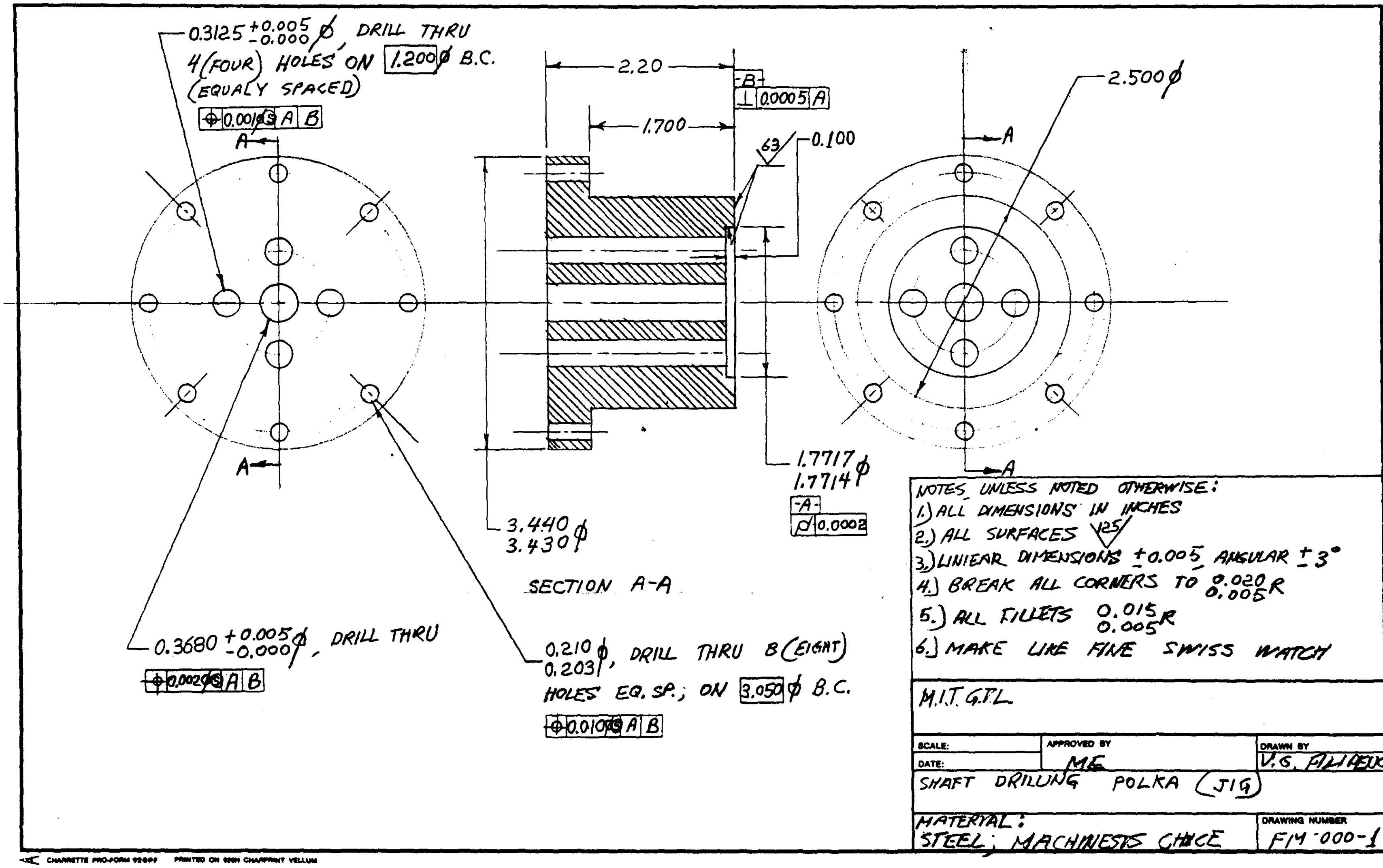

Fig. F.31 Motor Shaft Drill Jig

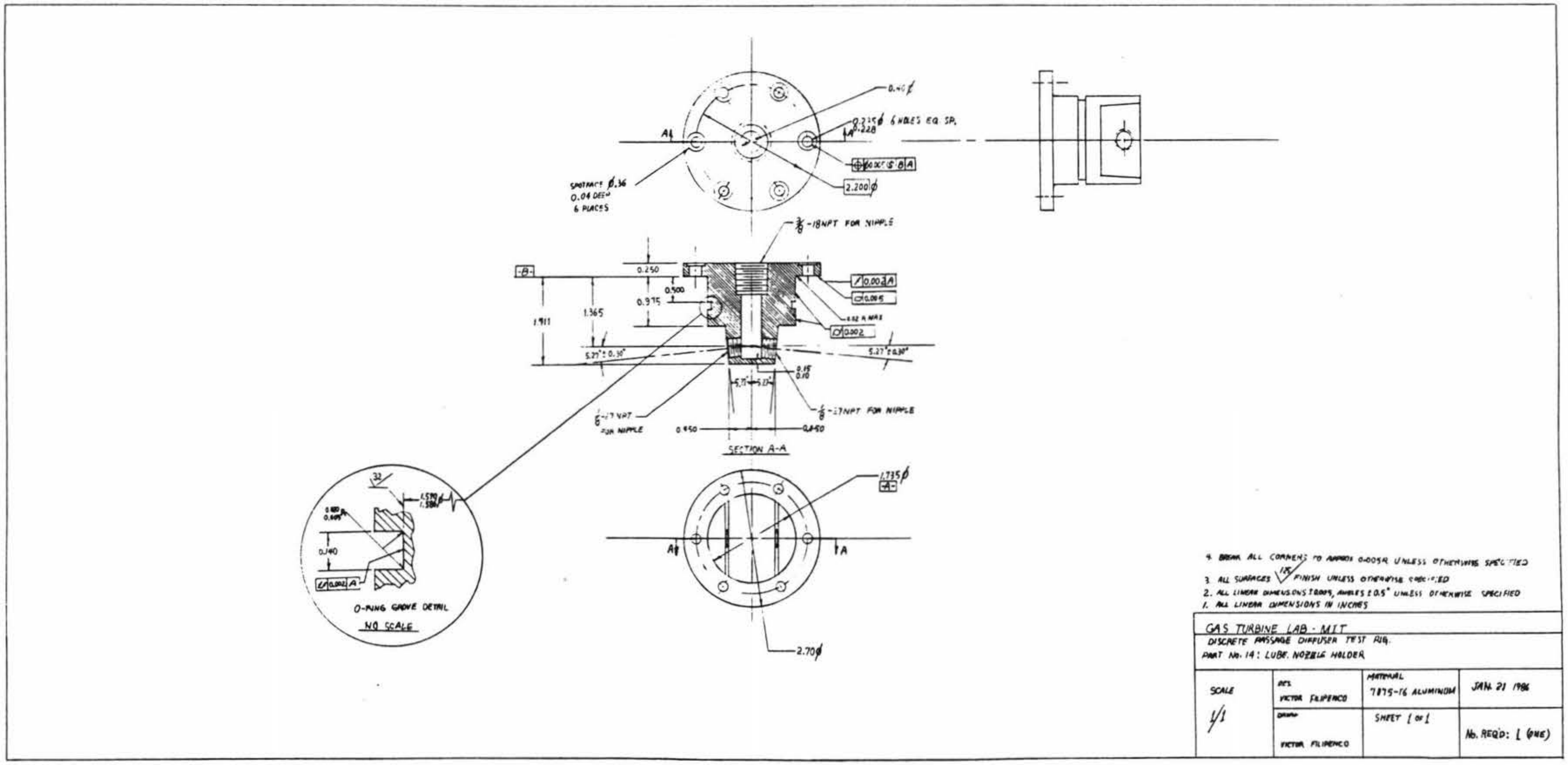

Fig. F.32 Oil Nozzle Holder

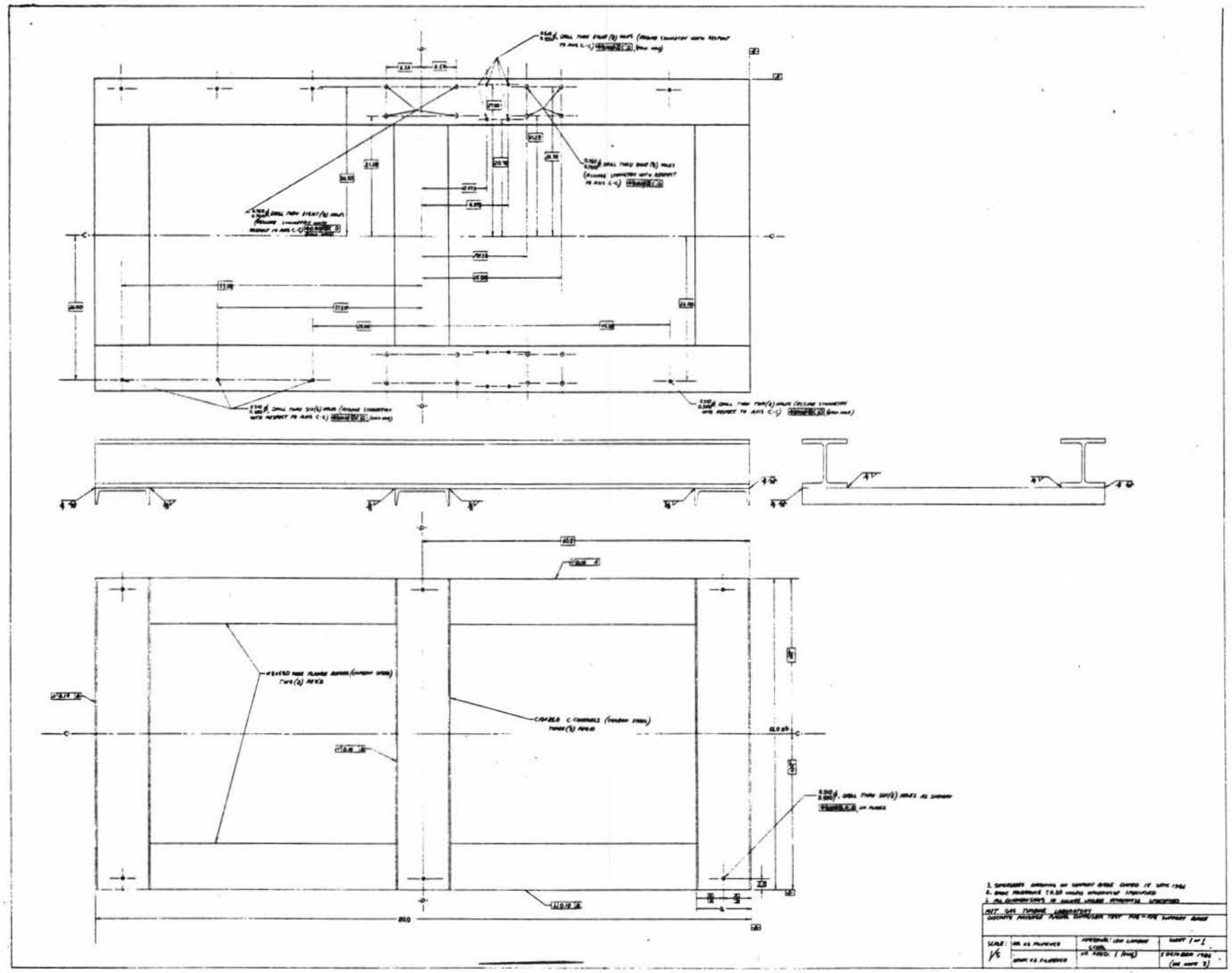

Fig. F.33a Test Stand Foundation Assembly

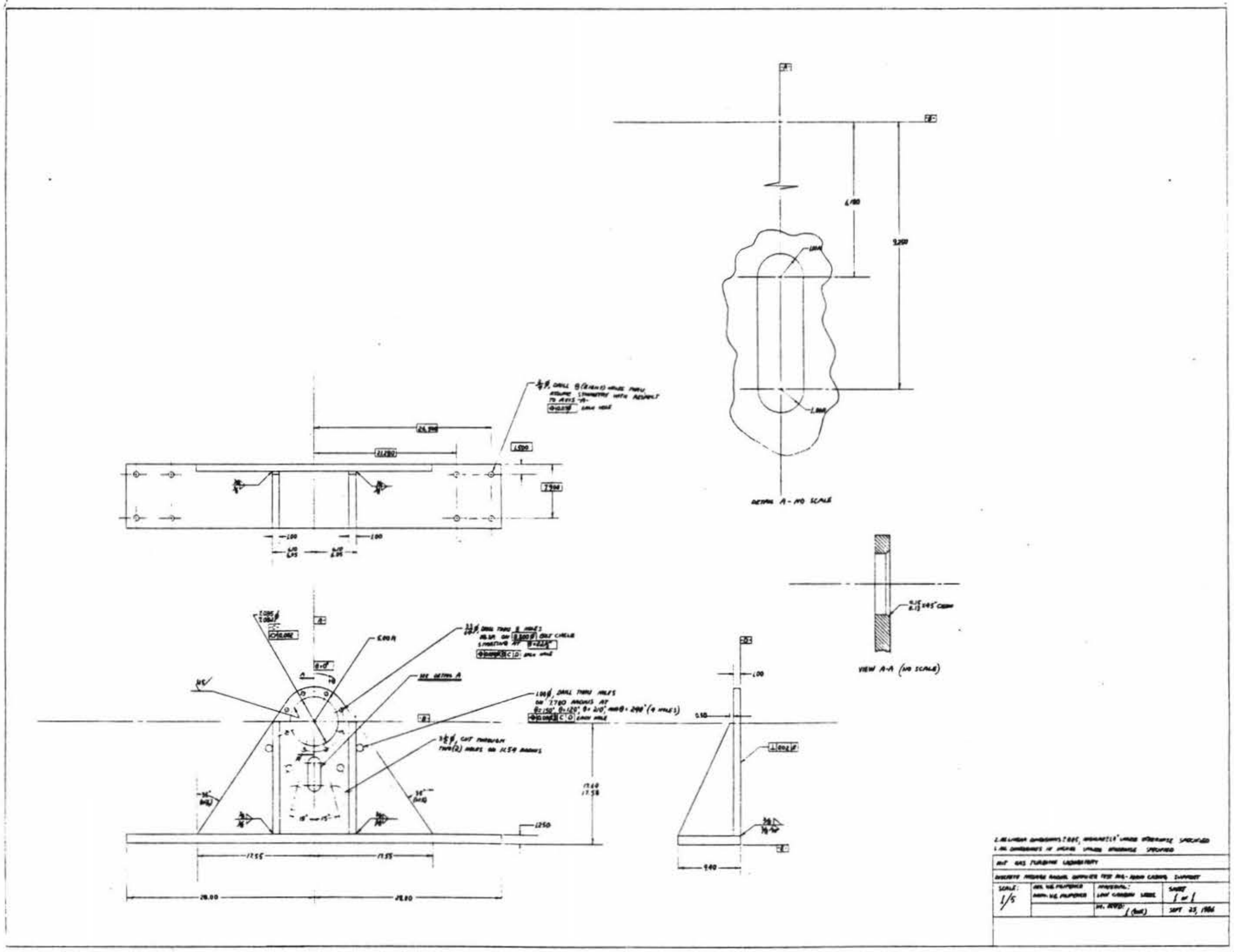

Fig. F.33b Swirl-Generator Front Mounting Bracket

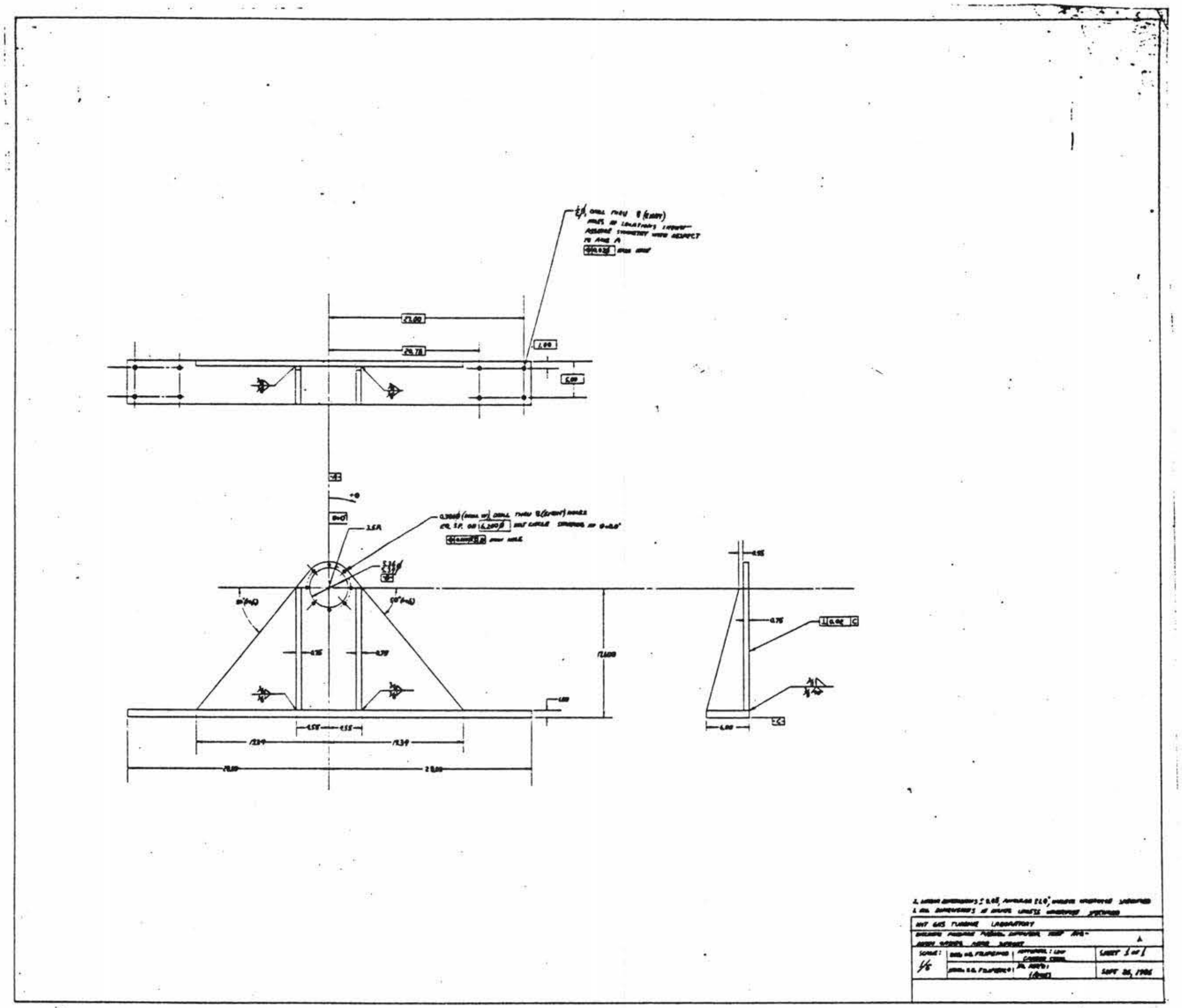

Fig. F.33c Swirl-Generator Rear Mounting Bracket

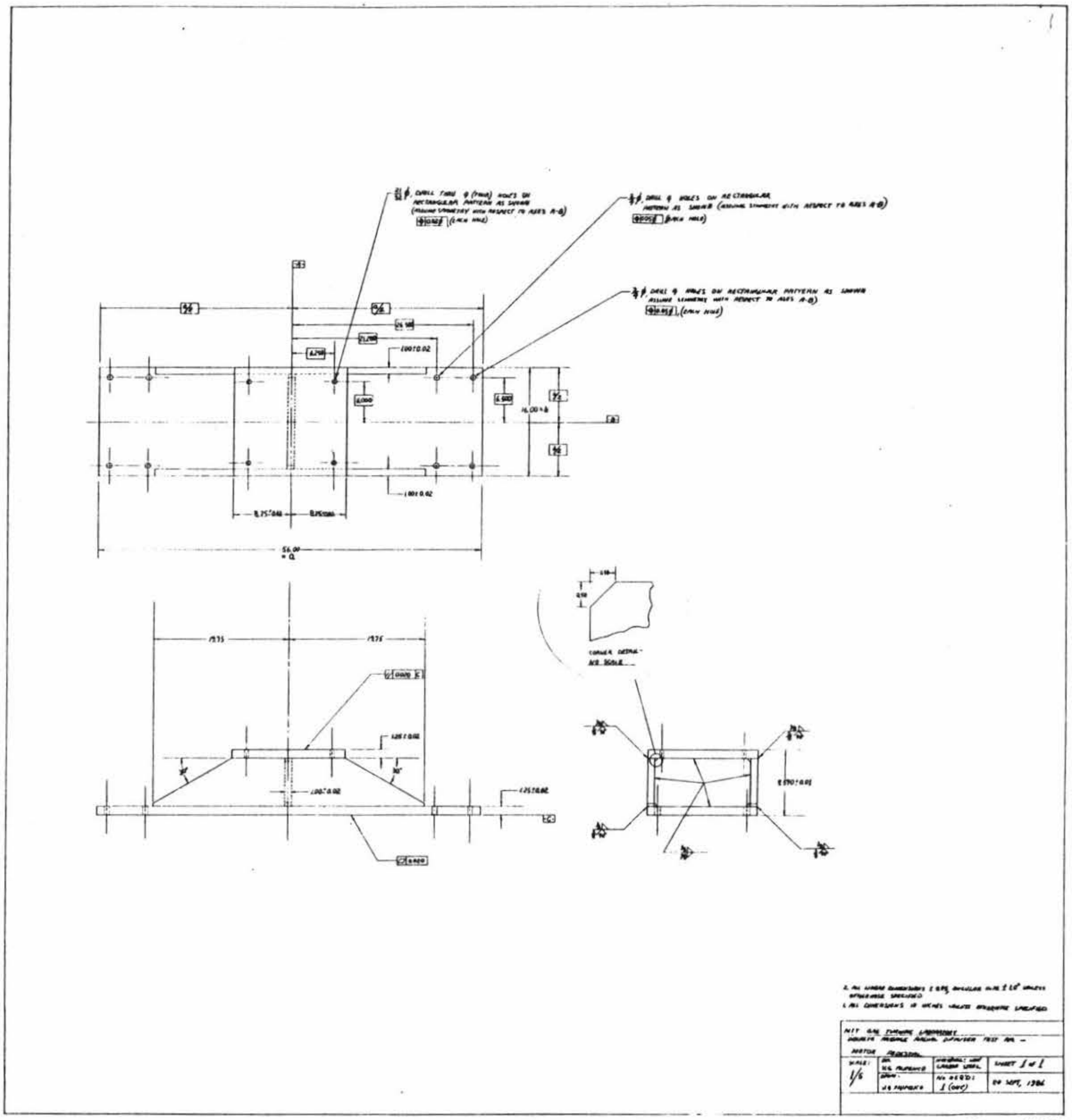

Fig. F.33d Drive-Motor Mounting Pedestal

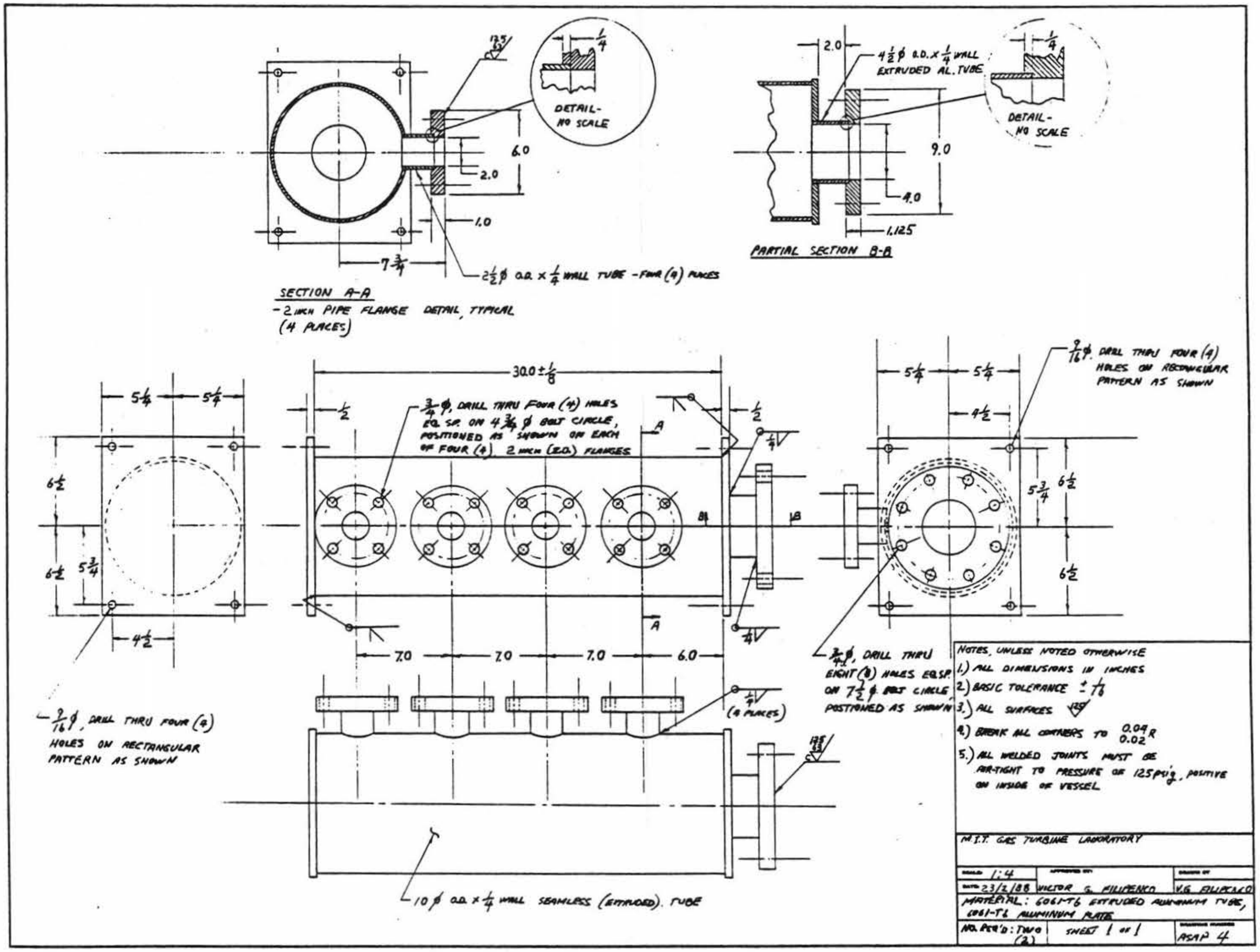

Fig. F.34 Profile Control System Main Suction/Feed Plenum

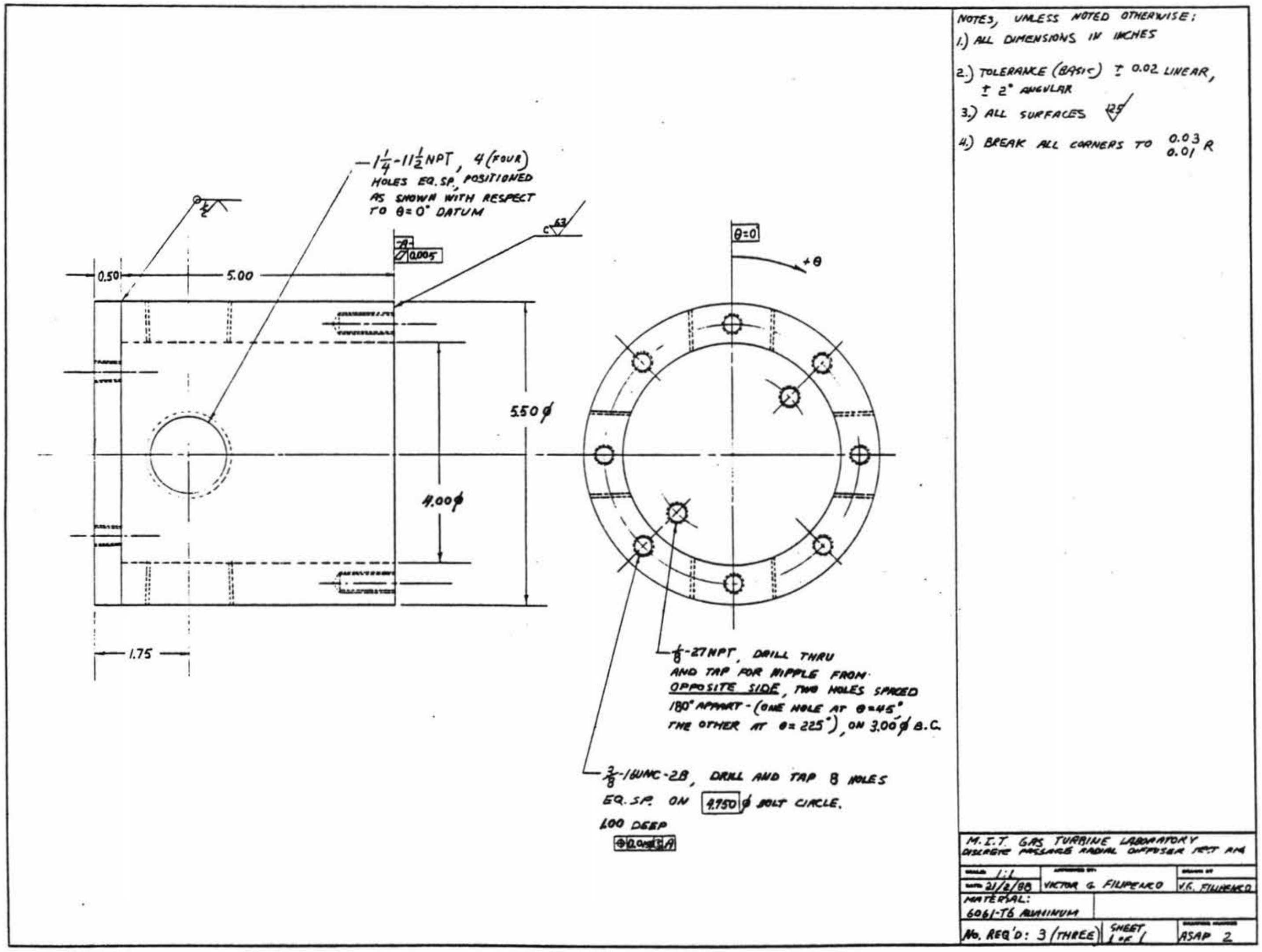

Fig. F.35a Profile Control System Flow Distributor

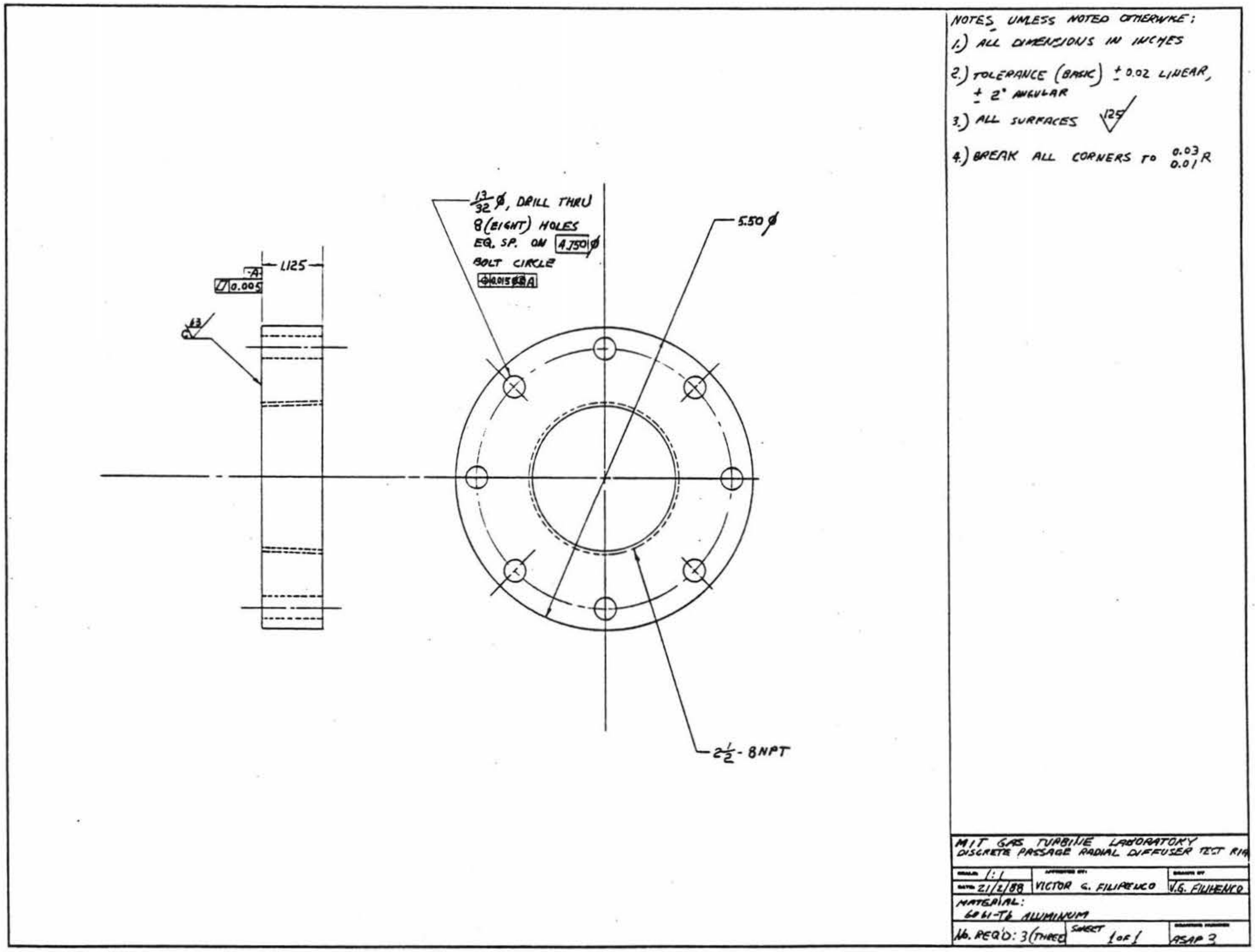

Fig. F.35b Profile Control System Flow Distributor Cover

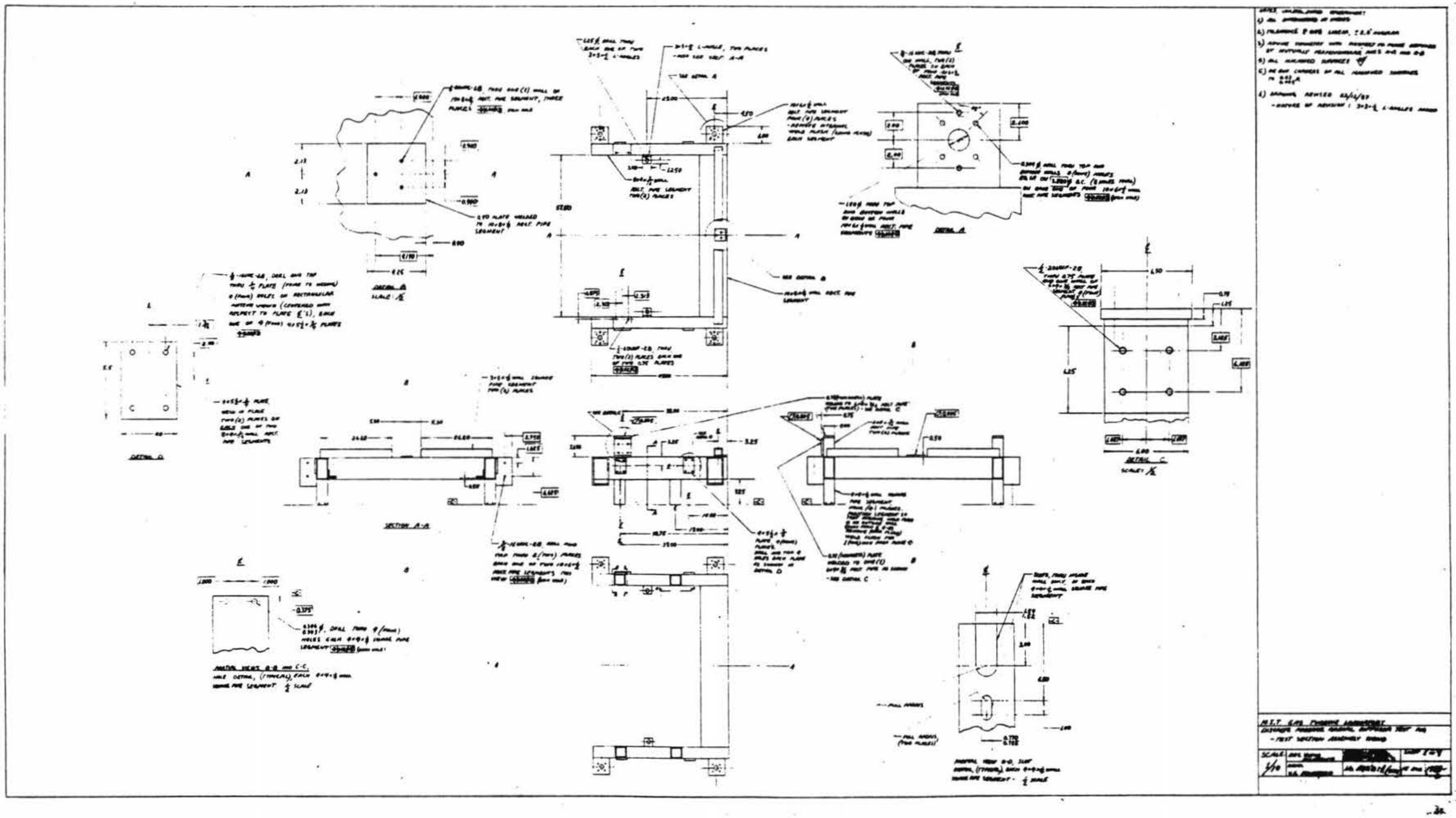

Fig. F.36a Main Pivot-Stand Frame

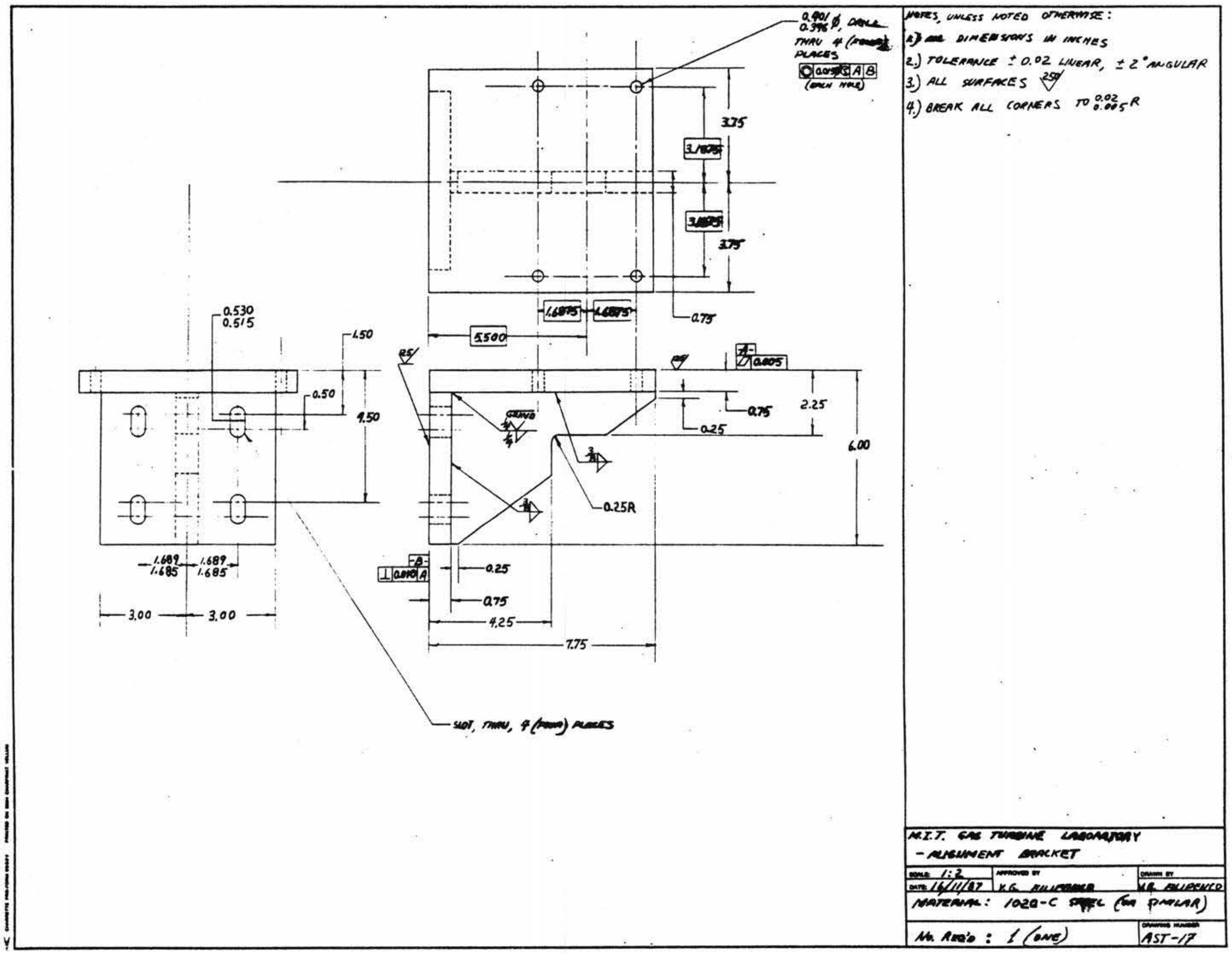

Fig. F.36b Main Pivot-Stand Worm-Gear-Drive Mounting Bracket

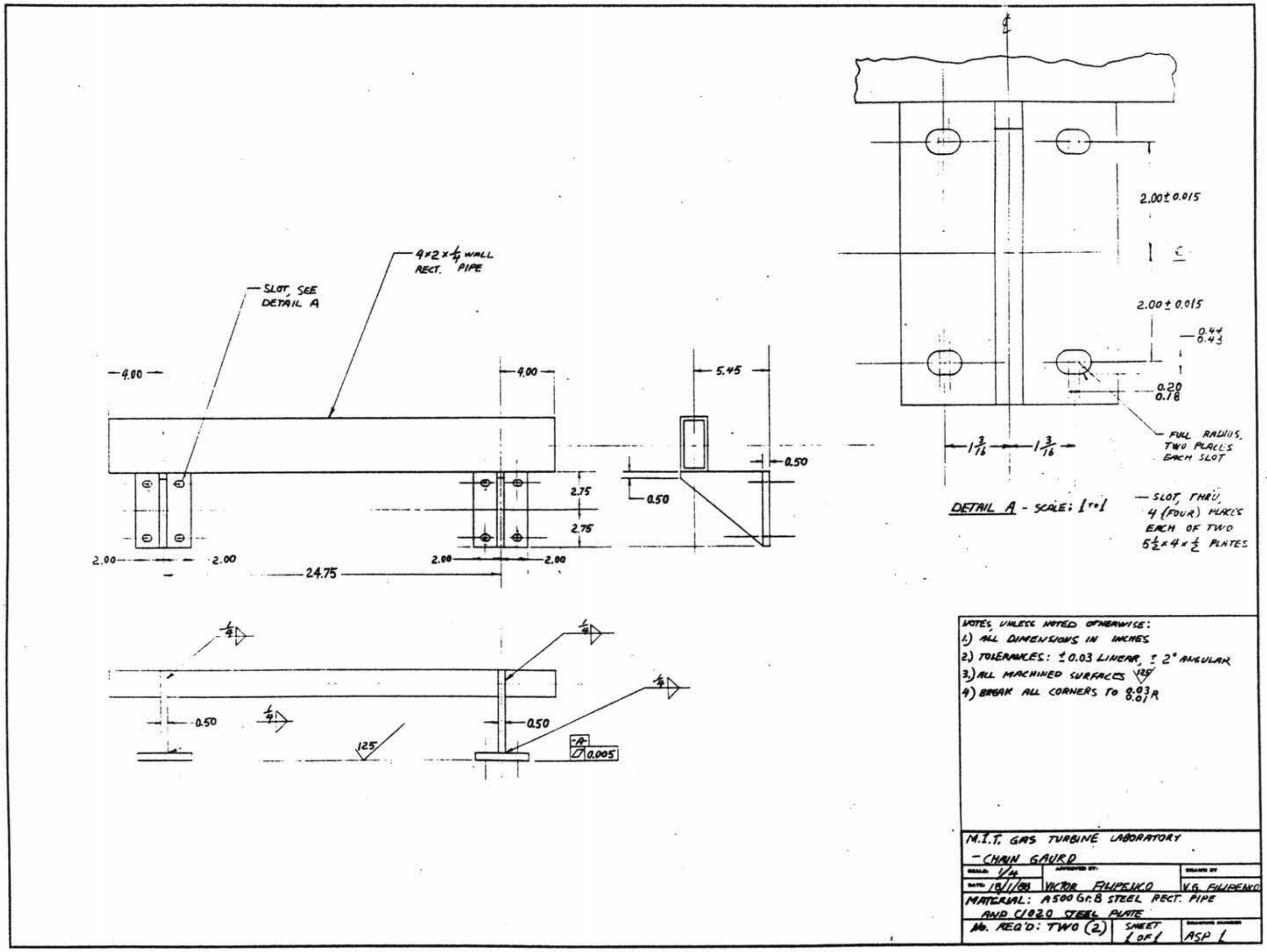

Fig. F.36c Main Pivot-Stand Chain Guard

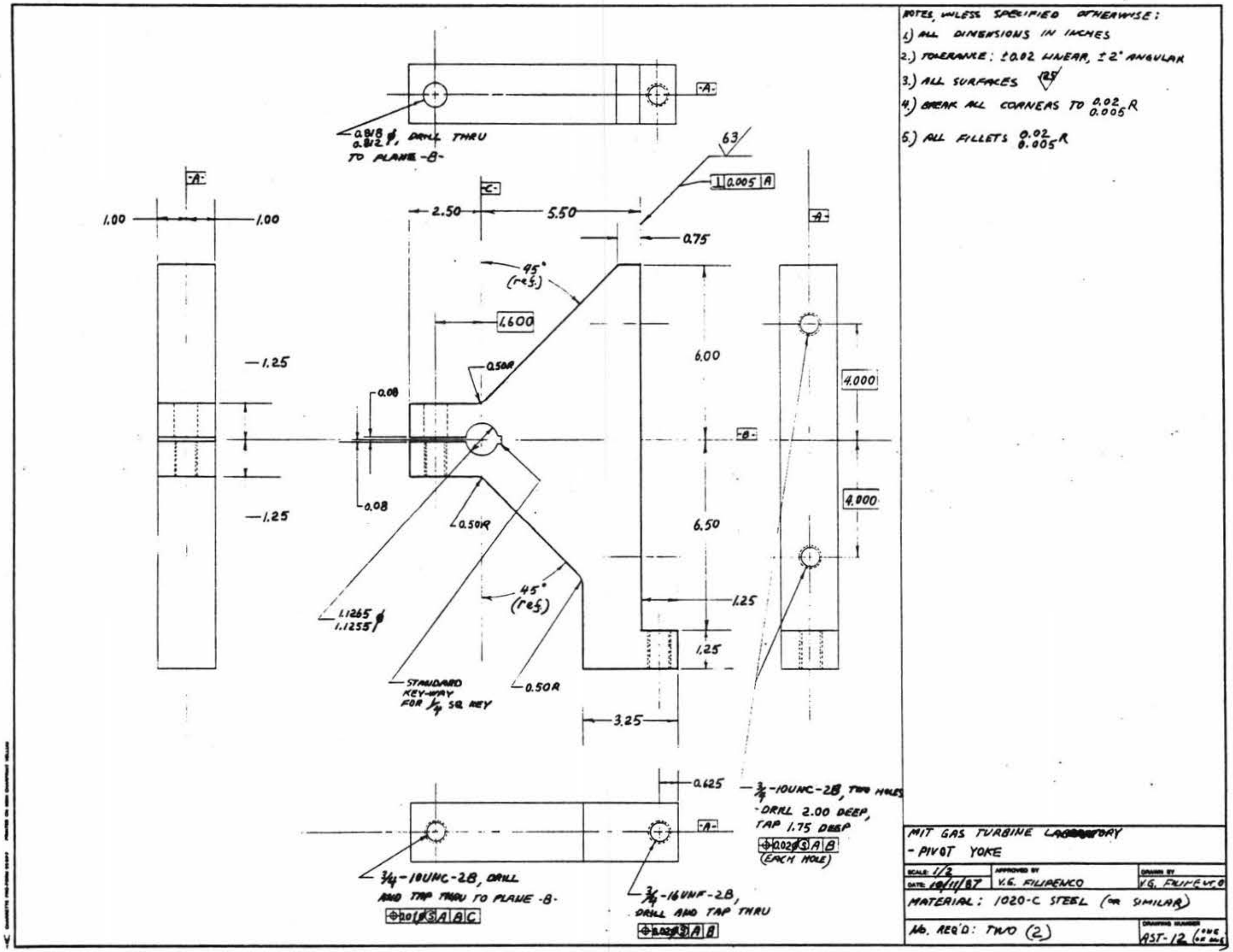

Fig. F.36d Main Pivot-Stand Pivot-Lug

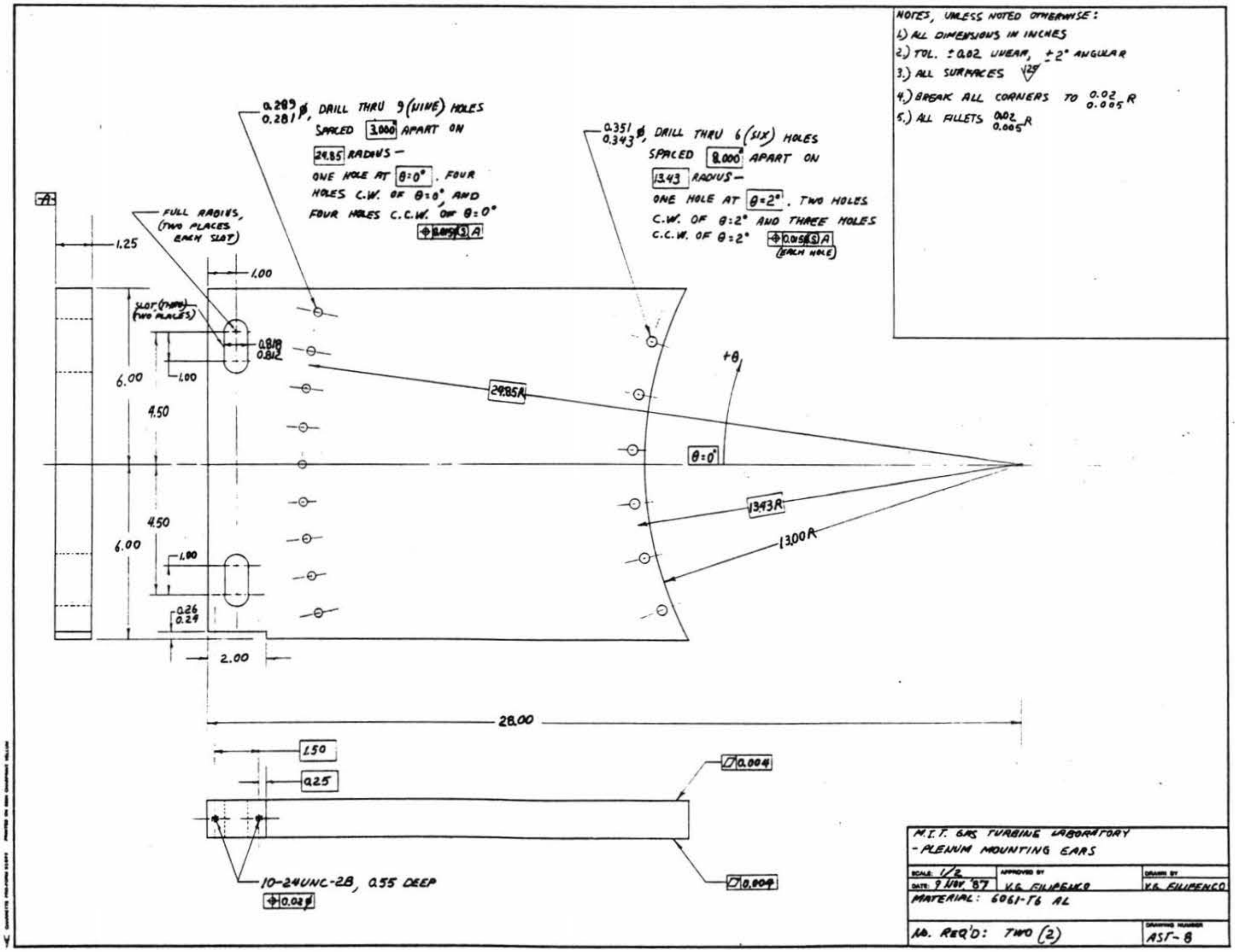

Fig. F.36e Main-Plenum/Test-Section Assembly Mounting Ears

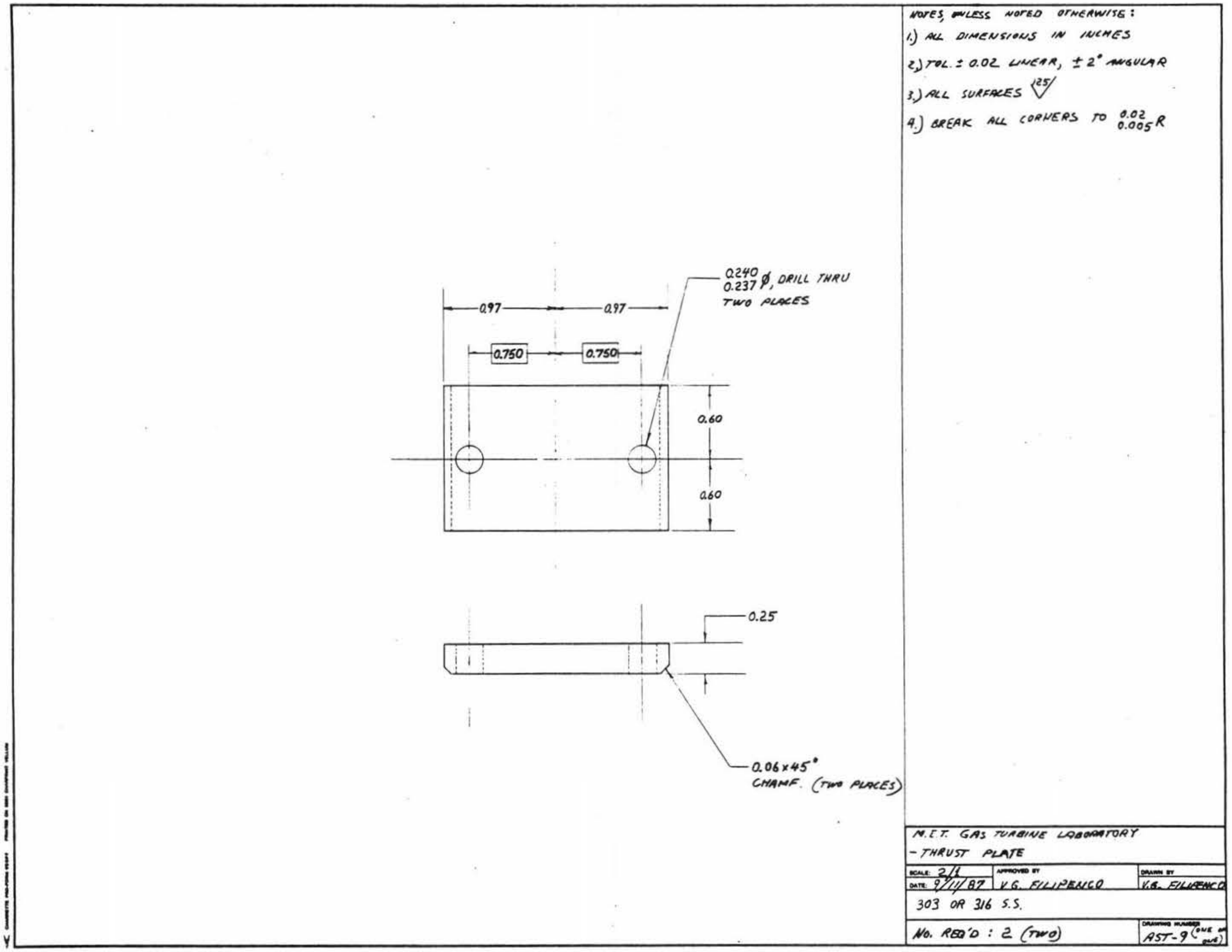

Fig. F.36f Main Pivot Stand Height Adjustment Thrust Plate

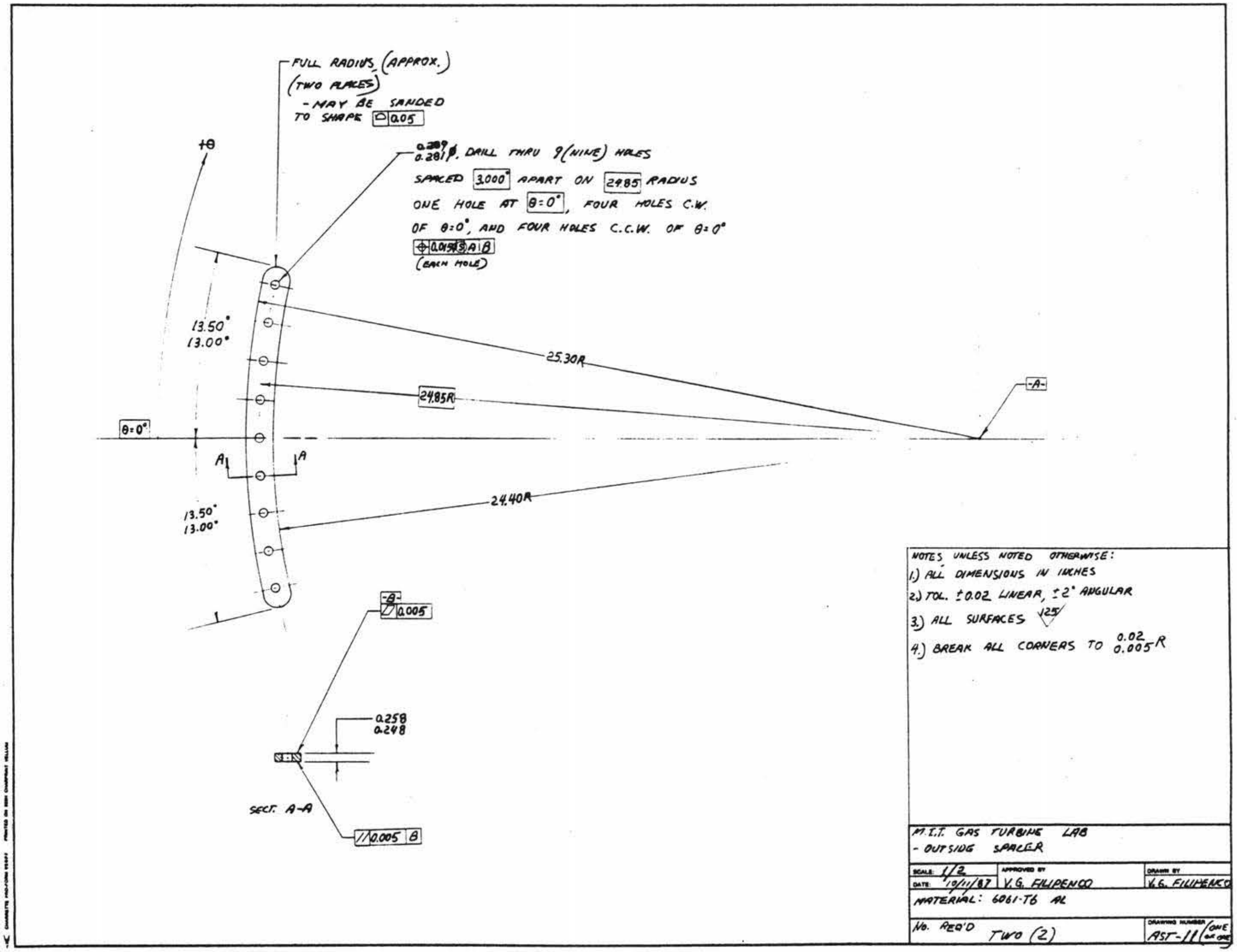

Fig. F.36g Test-Section Mounting Ear Outer Spacer

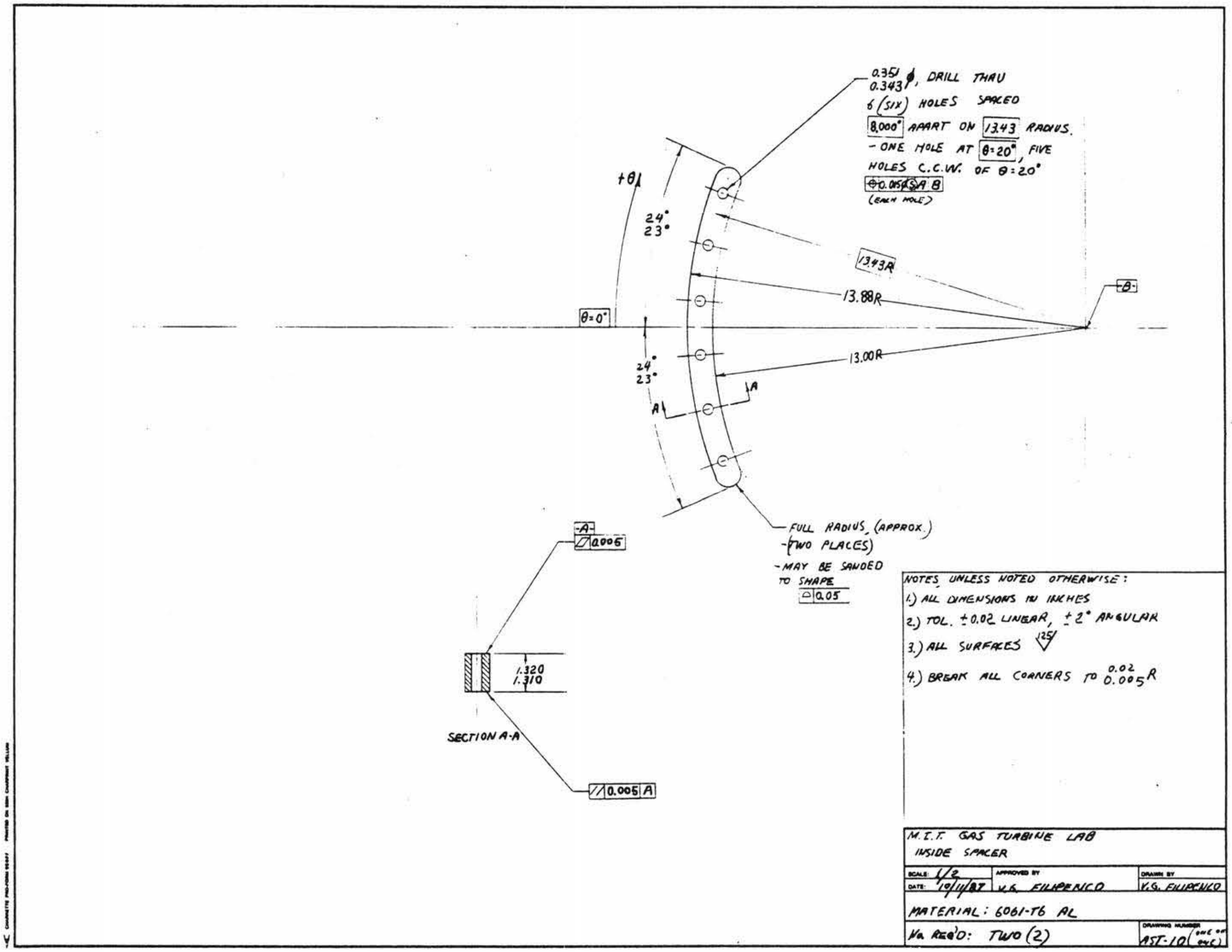

Fig. F.36h Test-Section Mounting Ear Inner Spacer

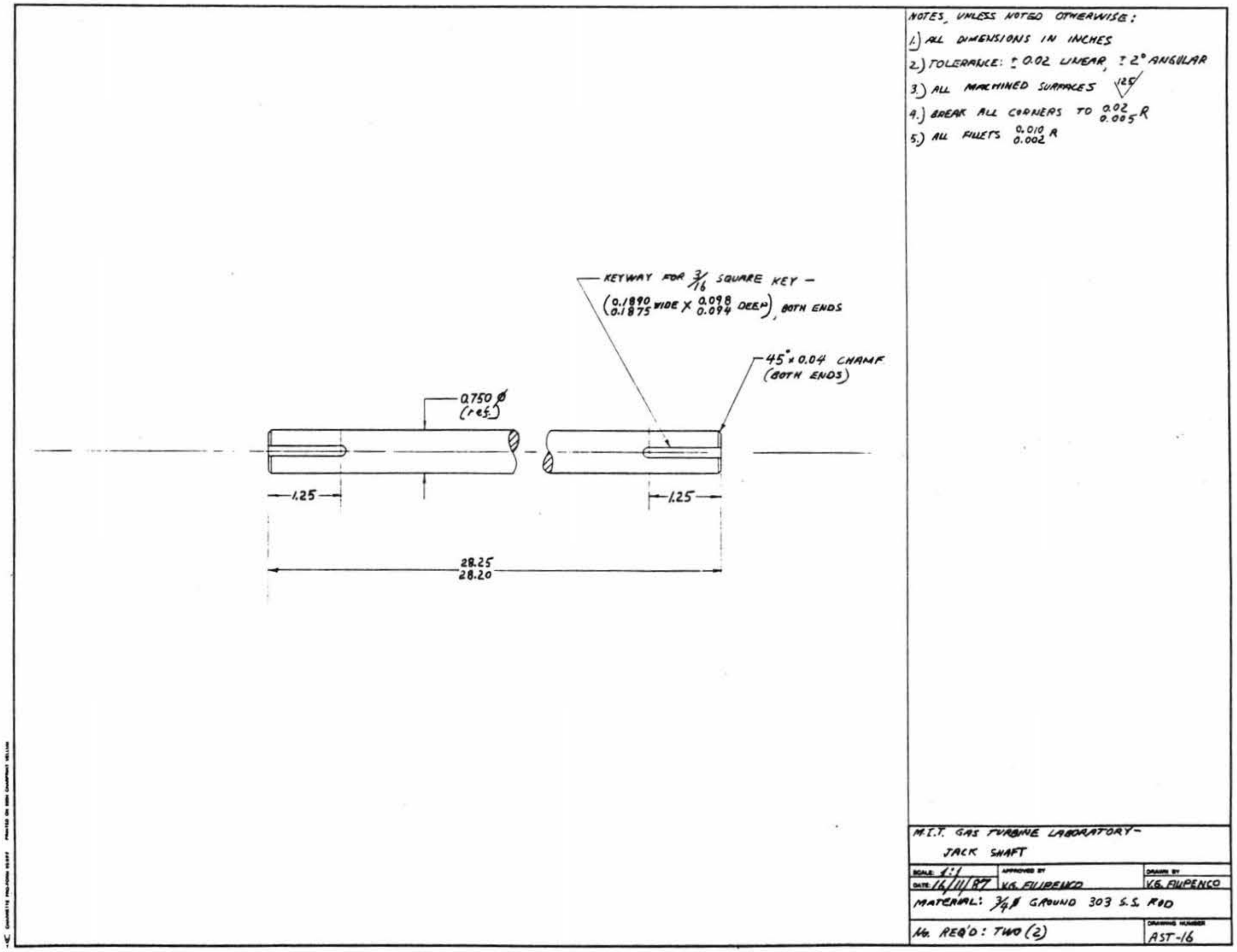

Fig. F.36i Main Pivot Stand Jack Drive-Shaft

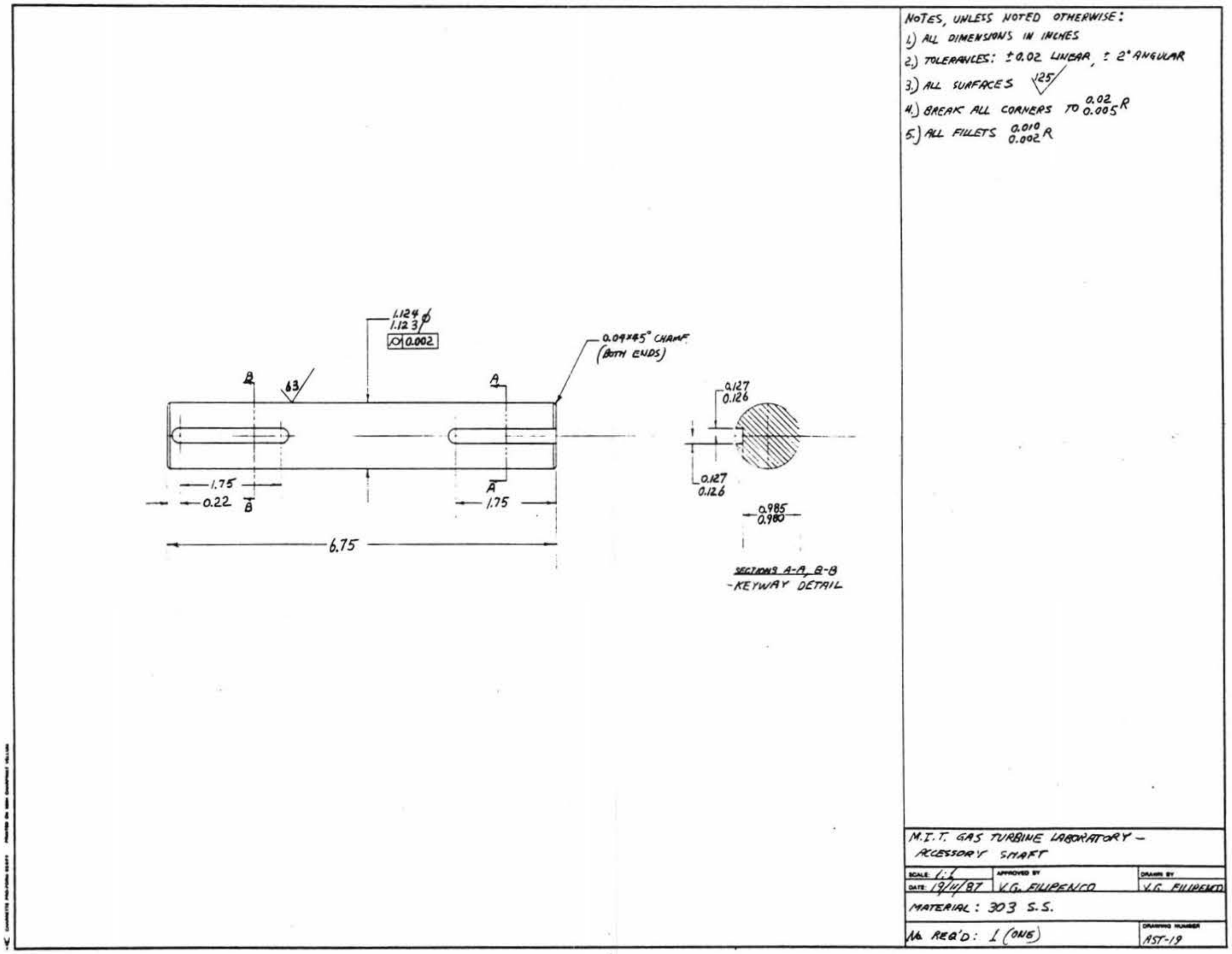

Fig. F.36j Main Pivot Stand Worm-Gear-Drive Shaft

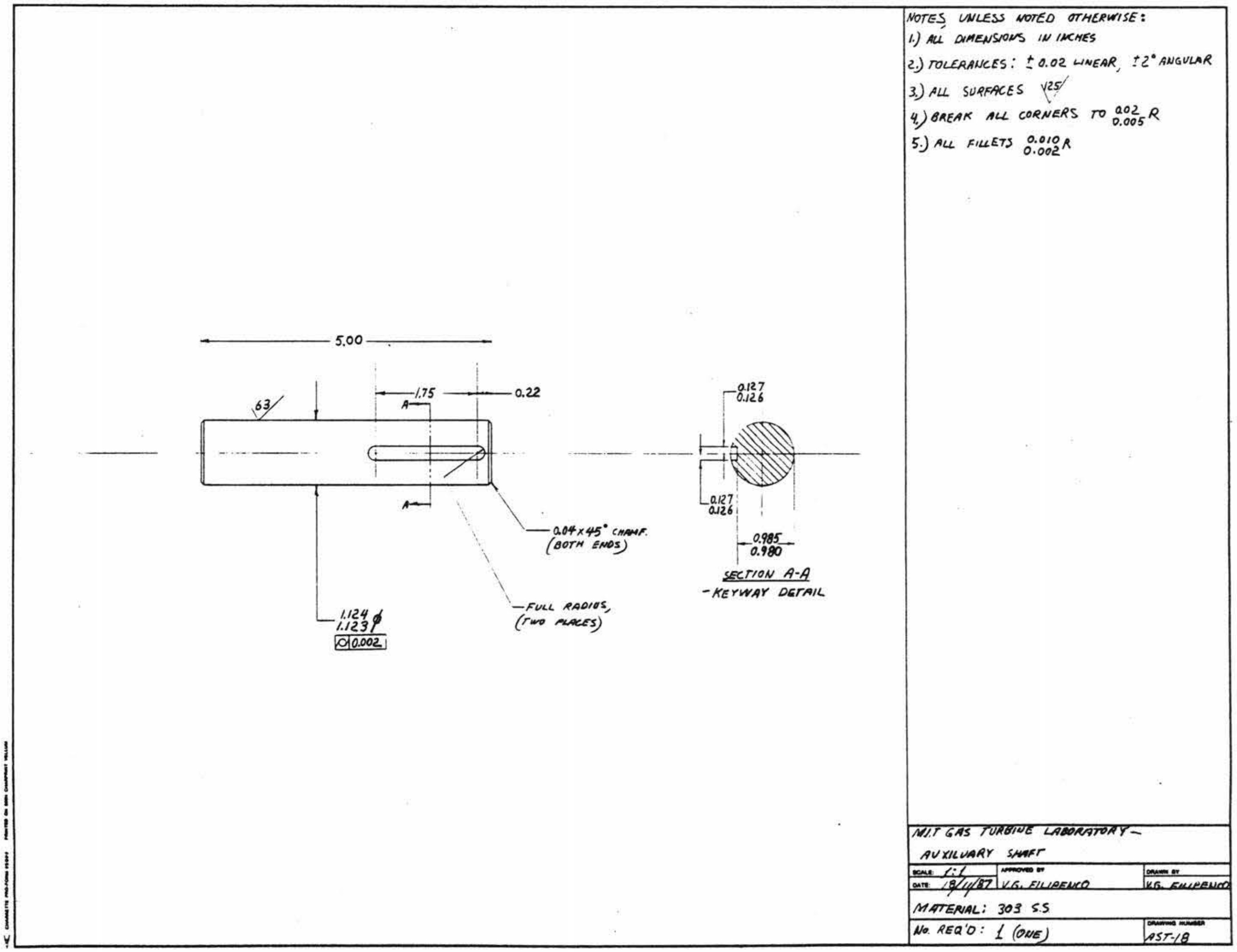

Fig. F.36k Main Pivot Stand Pivot Shaft

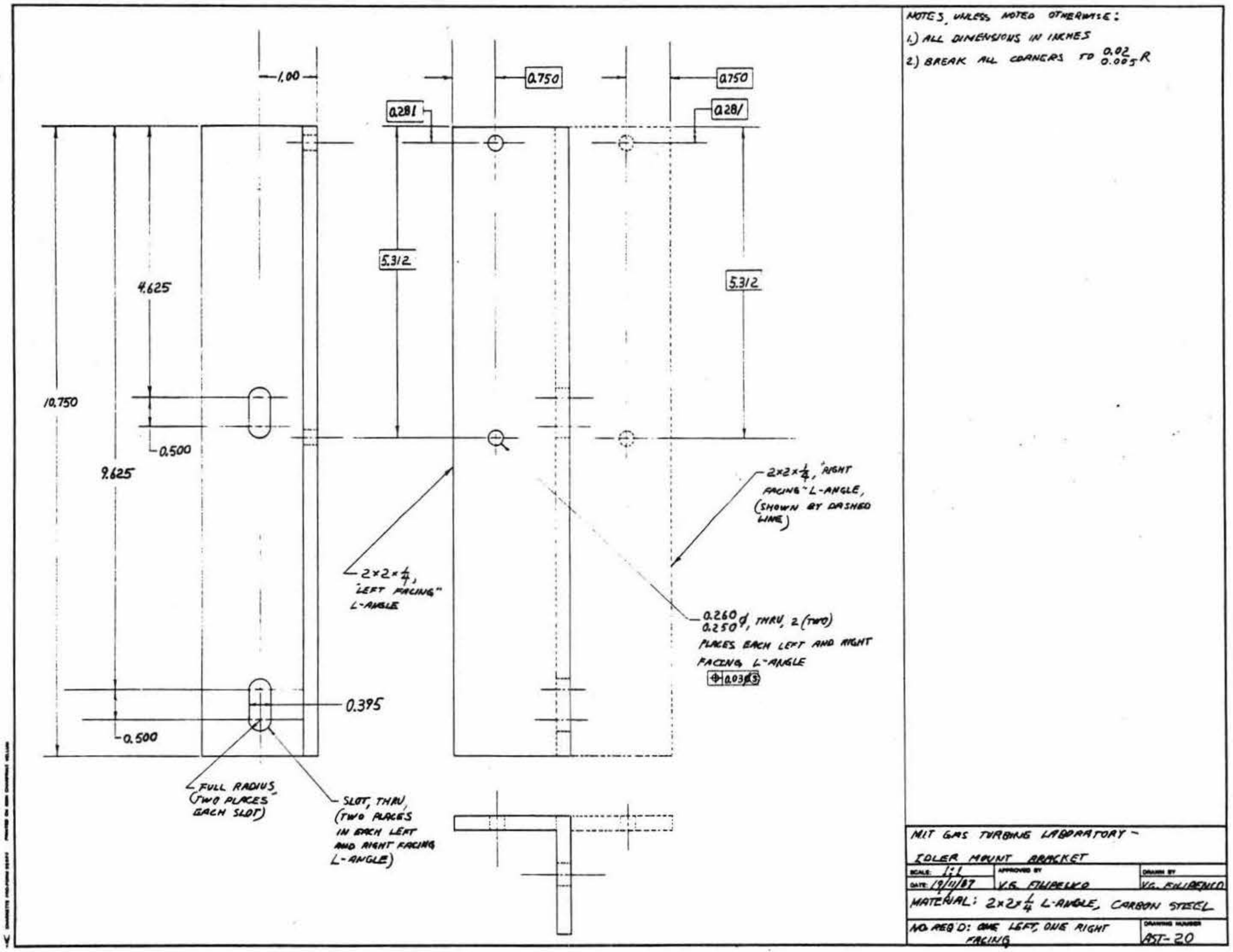

Fig. F.361 Main Pivot Stand Idler-Sprocket Mounting Bracket

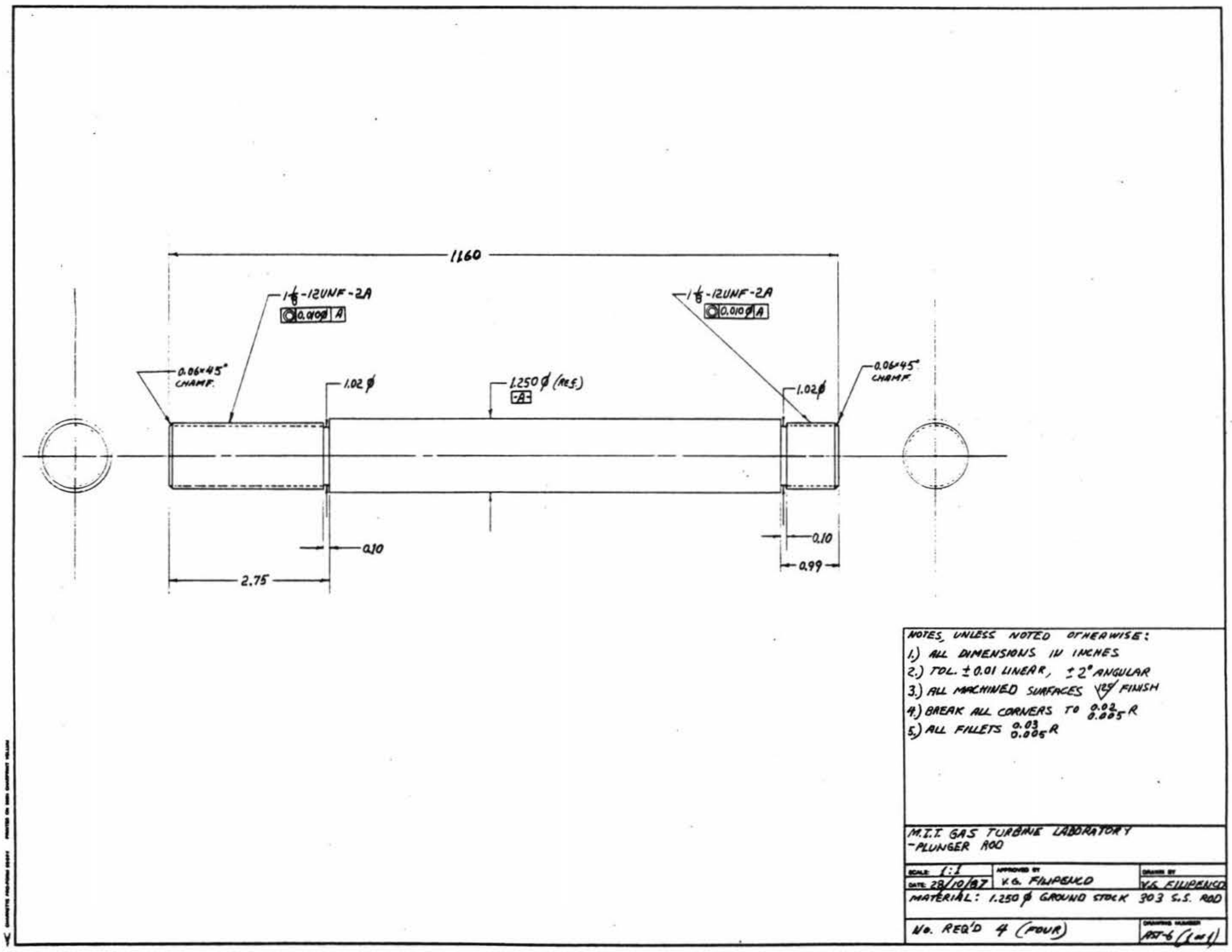

Fig. F.36m Main Pivot Stand Ball-Bushing Rod

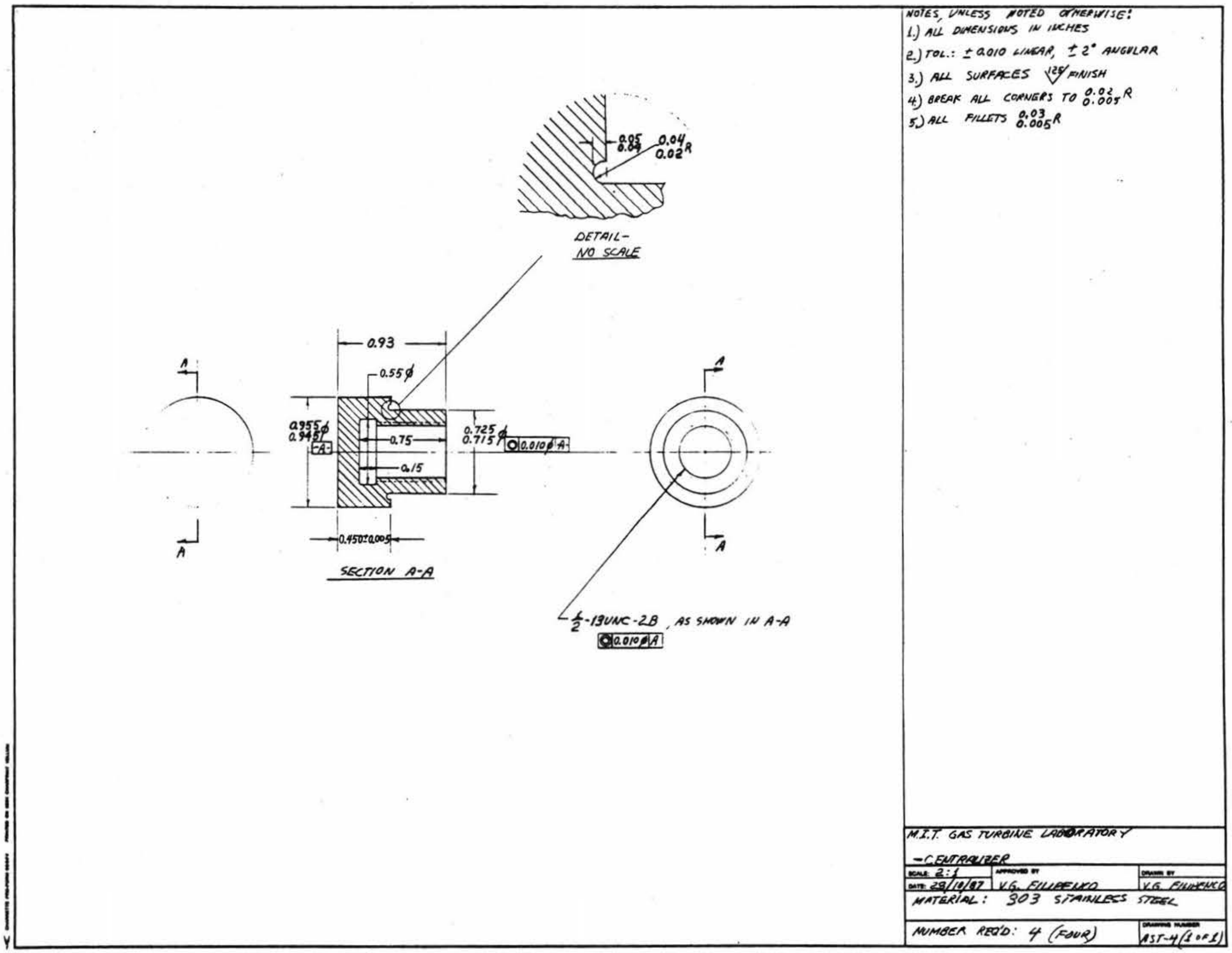

Fig. F.36n Main Pivot Stand Ball-Bushing Rod Coupling Plug

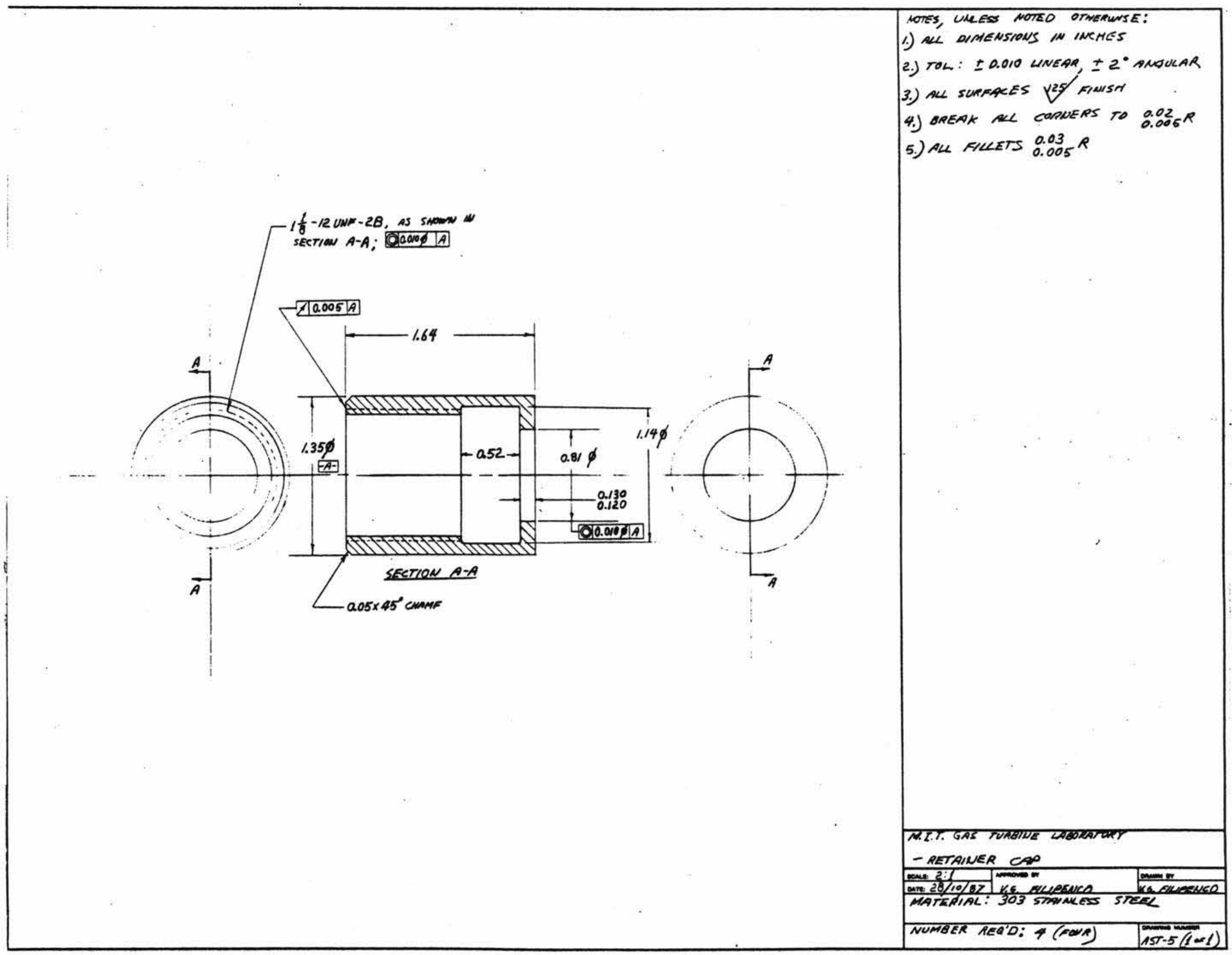

Fig. F.36o Main Pivot Stand Ball-Bushing Rod Coupling Plug Cap

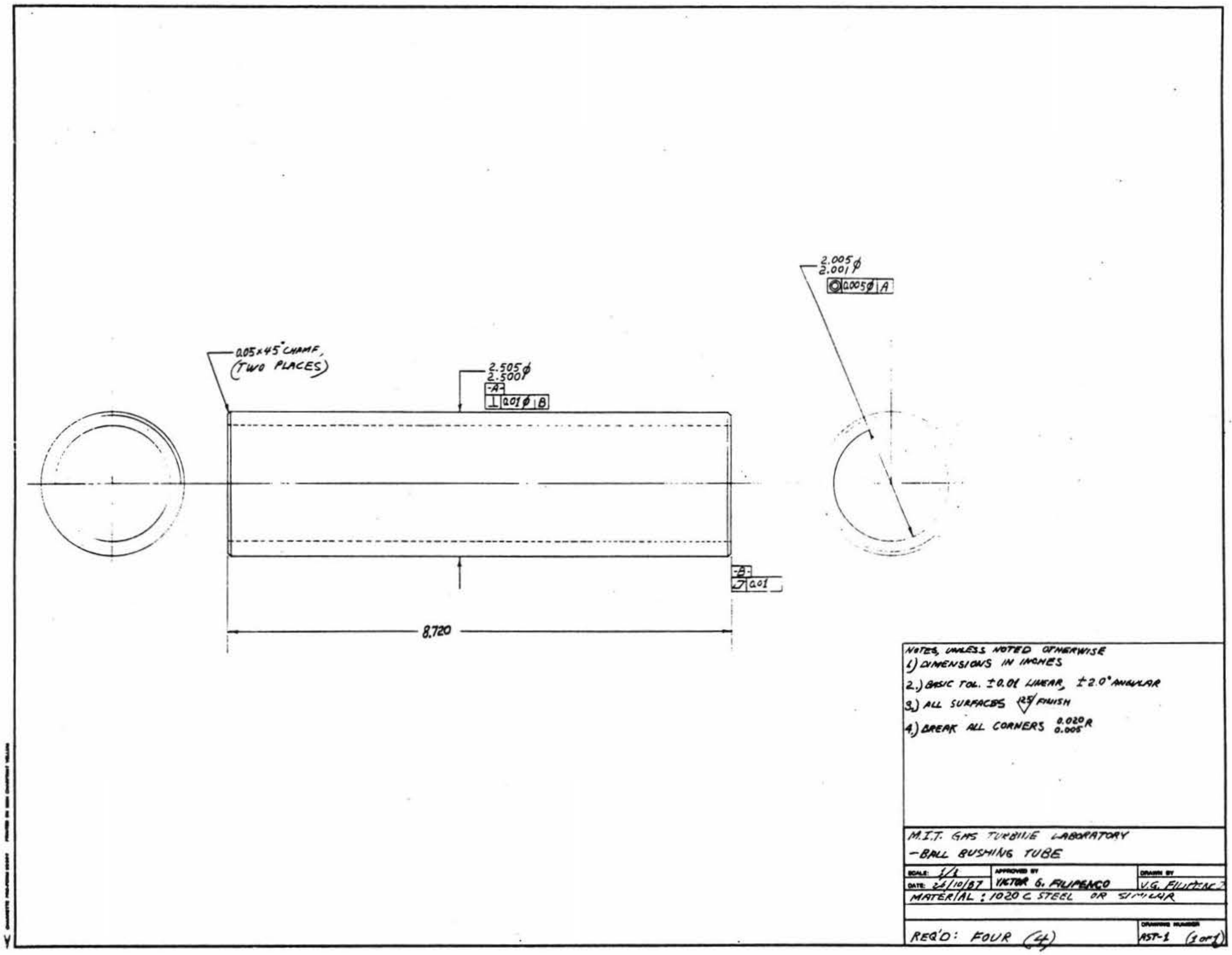

Fig. F.36p Main Pivot Stand Ball-Bushing Housing

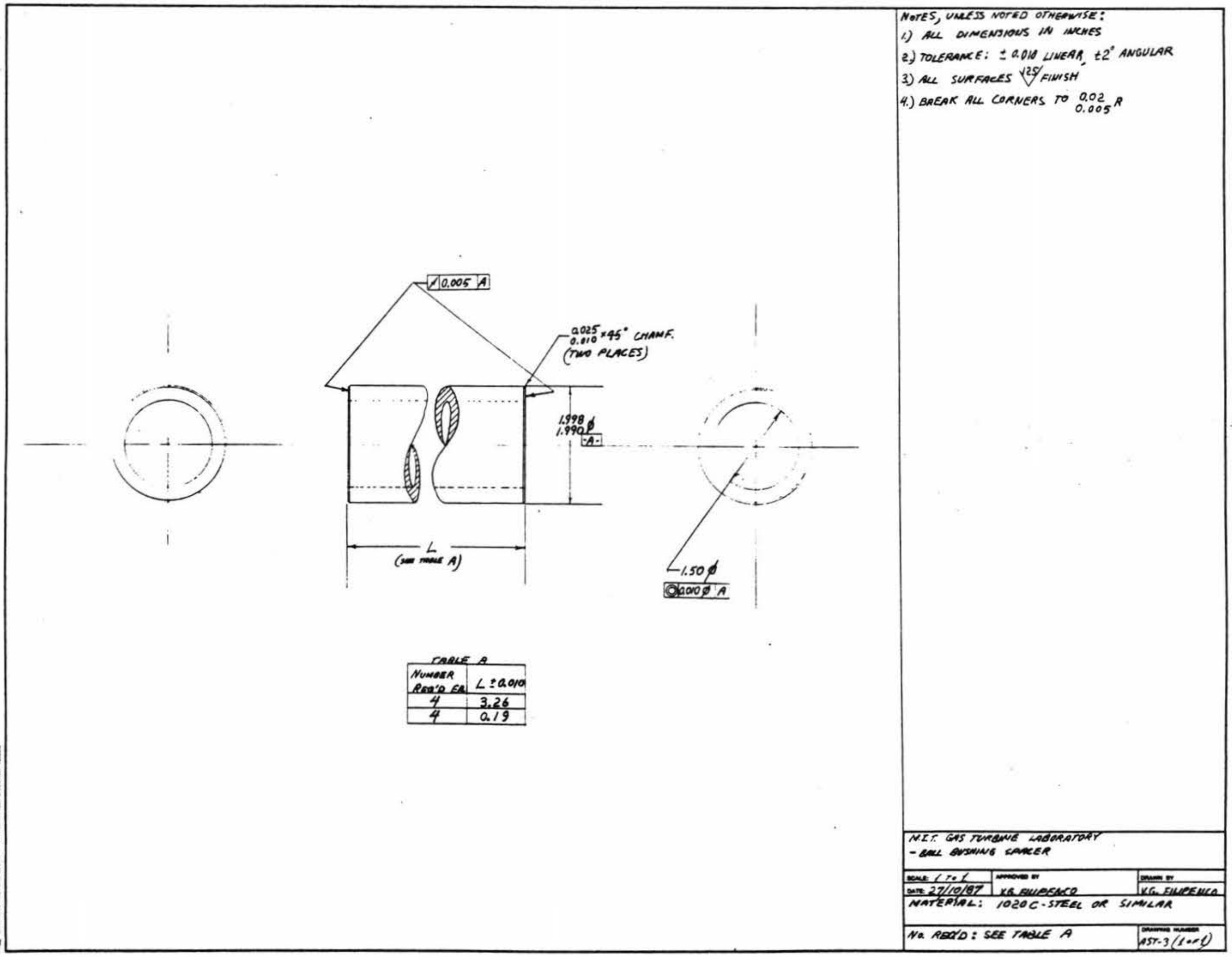

Fig. F.36q Main Pivot Stand Ball-Bushing Spacer-Ring

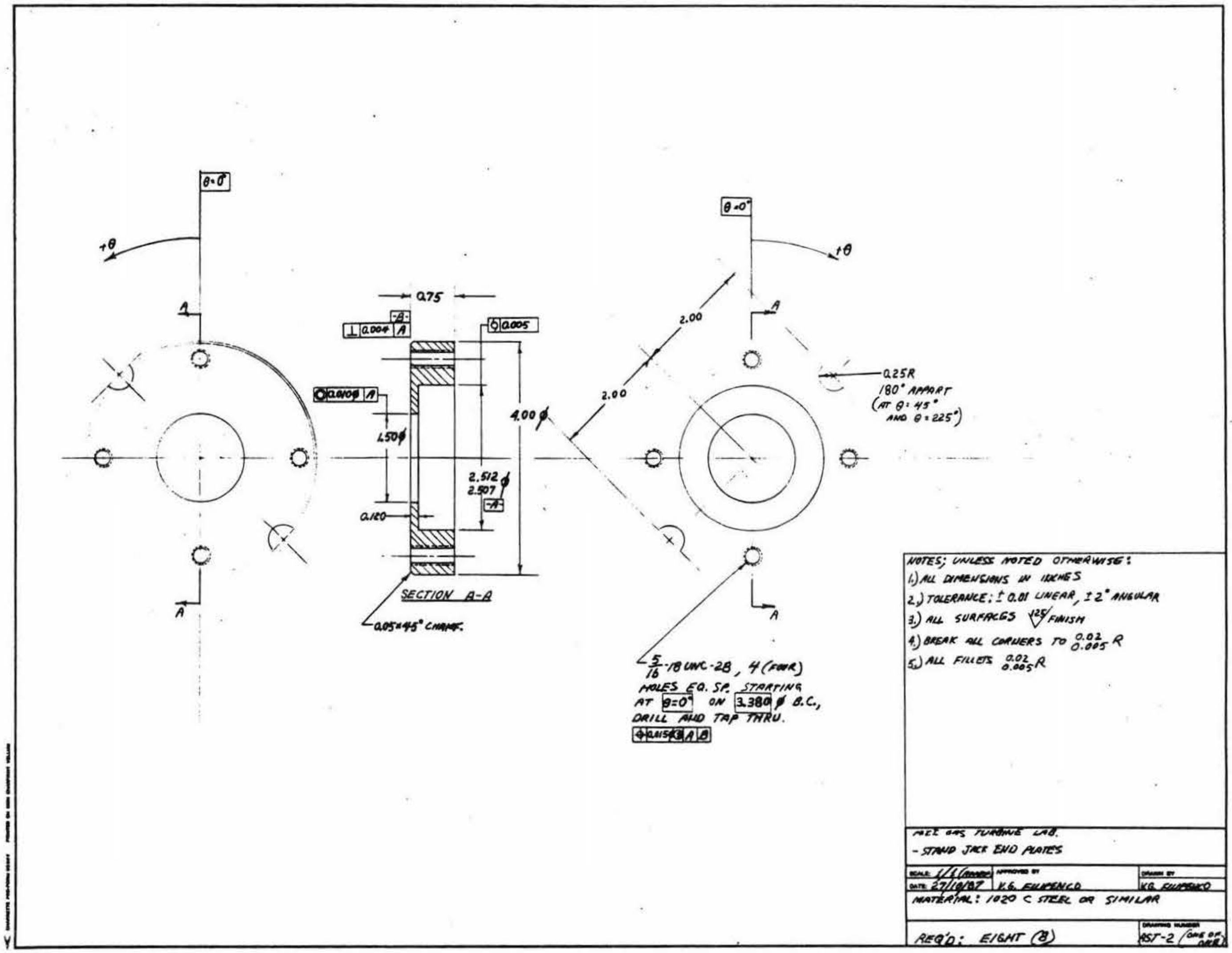

Fig. F.36r Main Pivot Stand Ball-Bushing-Housing End Cap

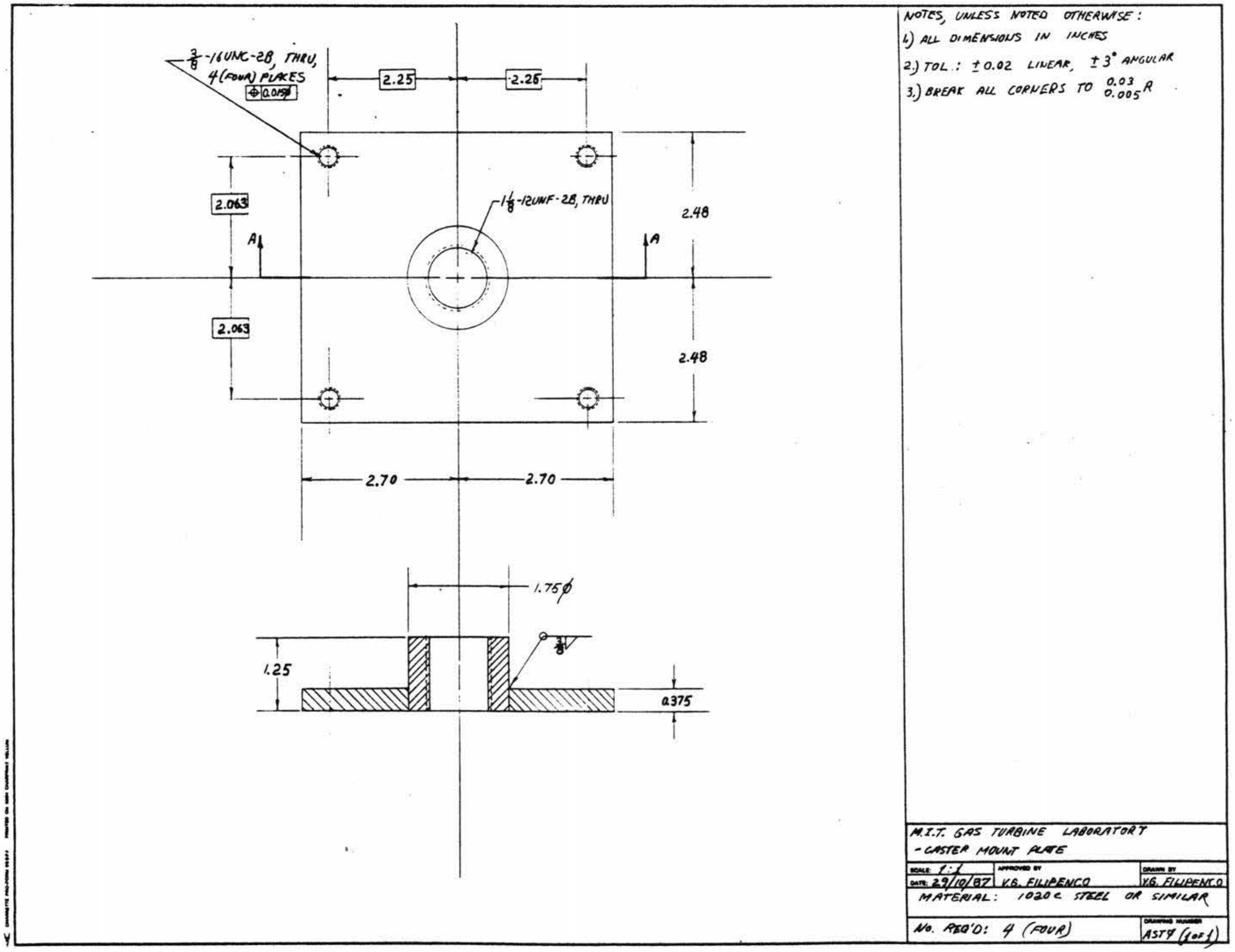

Fig. F.36s Main Pivot Stand Caster Mount Pad

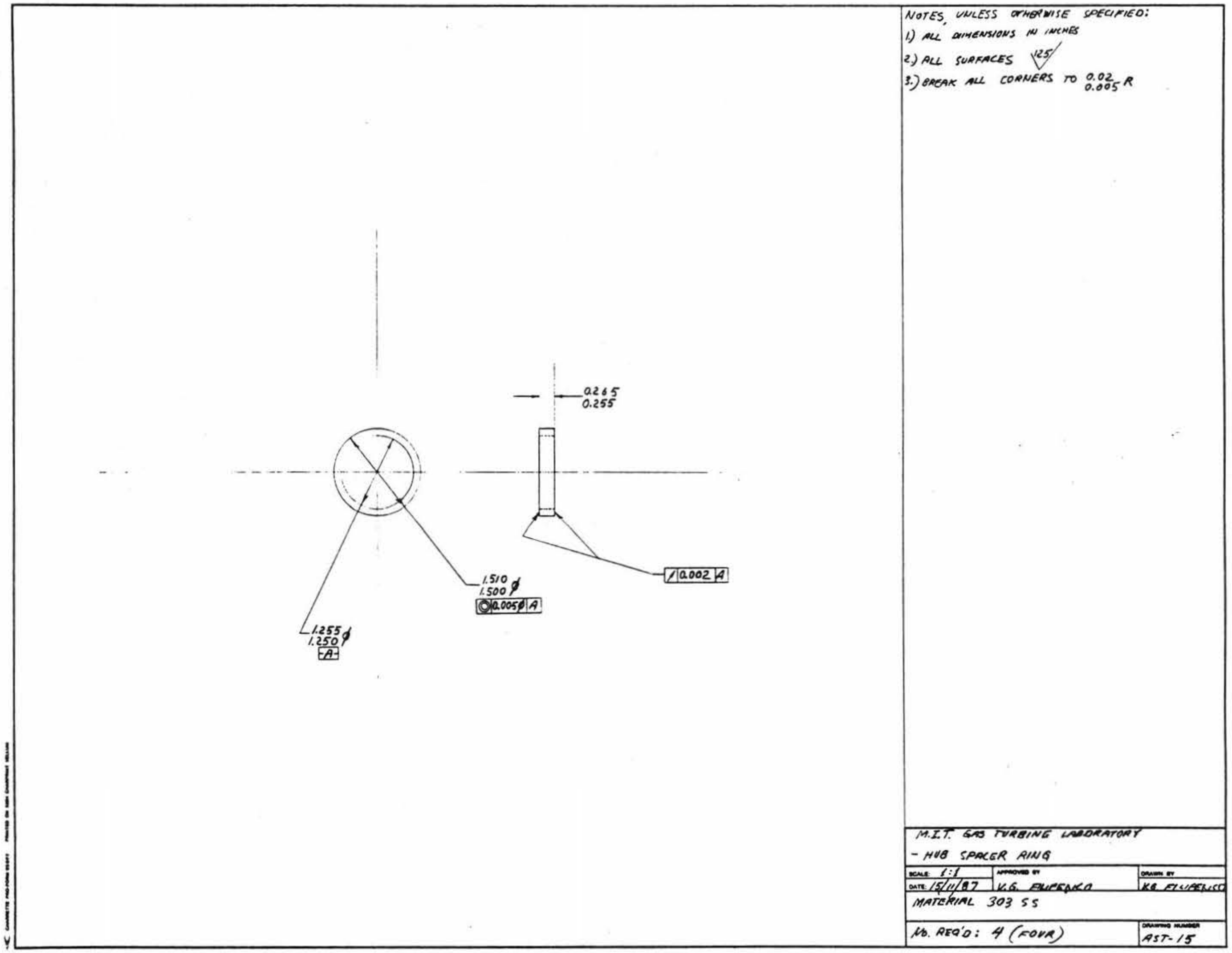

Fig. F.36t Main Pivot Stand Roller Spacer

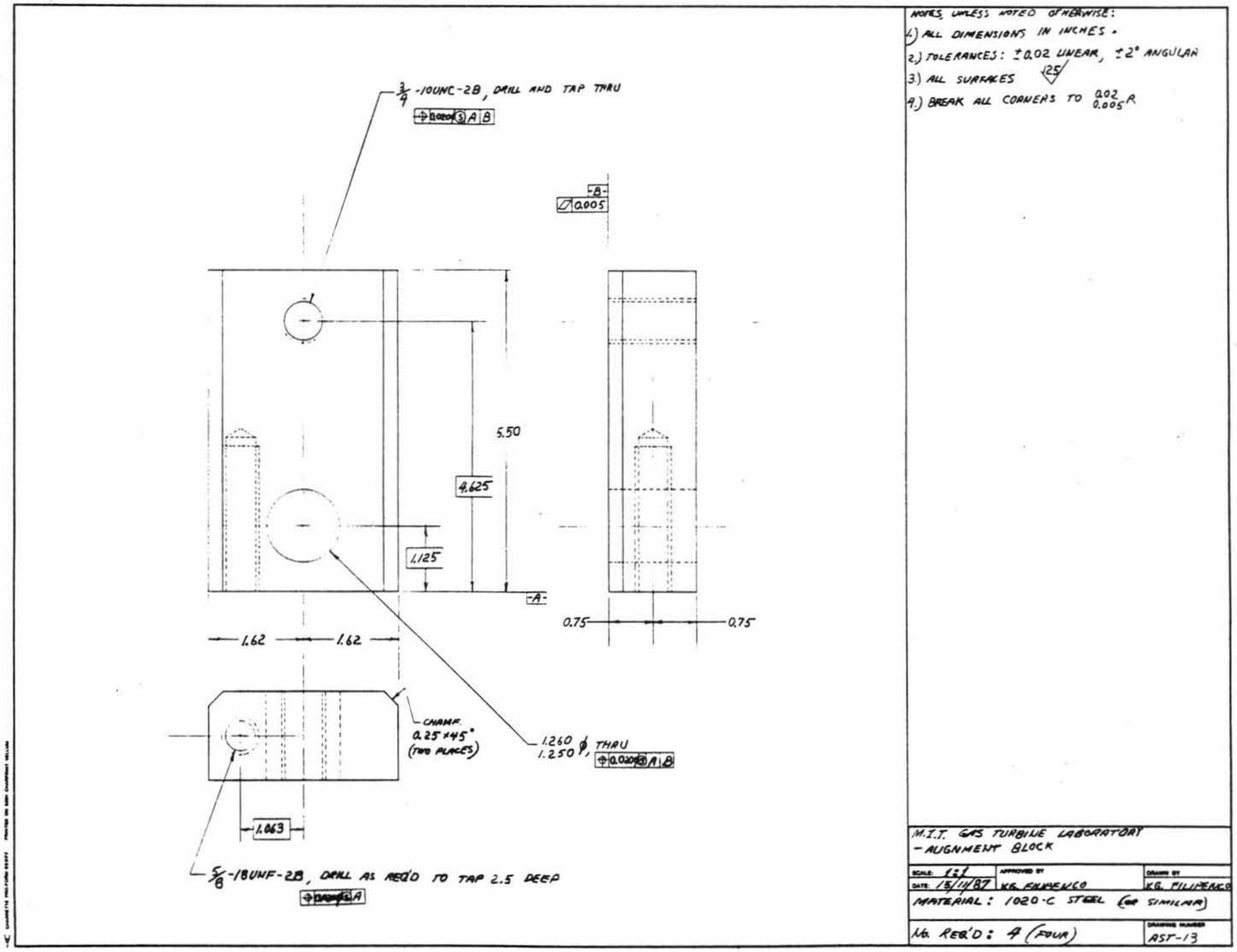

Fig. F.36u Main Pivot Stand Roller Mount Block

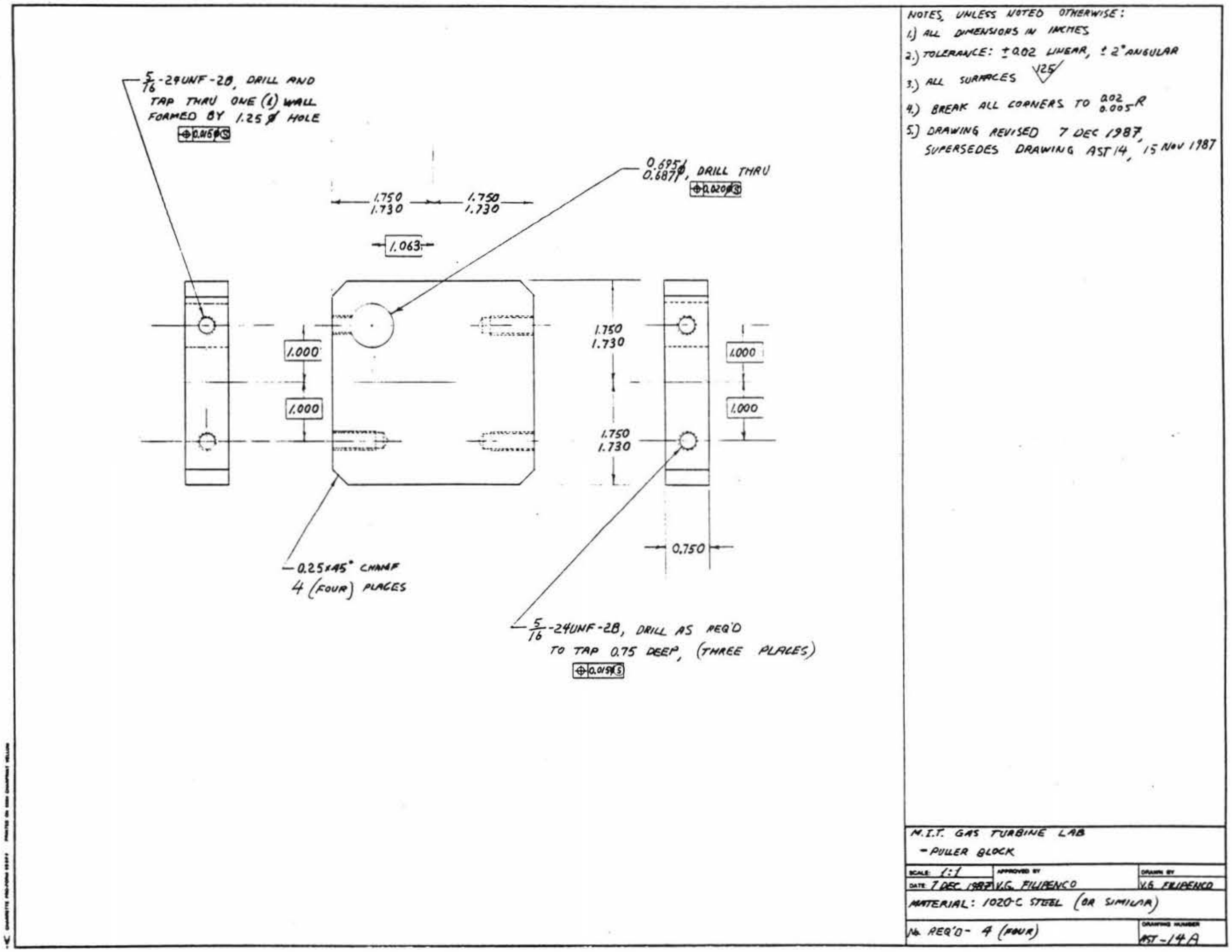

Fig. F.36v Main Pivot Stand Roller Mount Block
Height-Adjustment End Cap

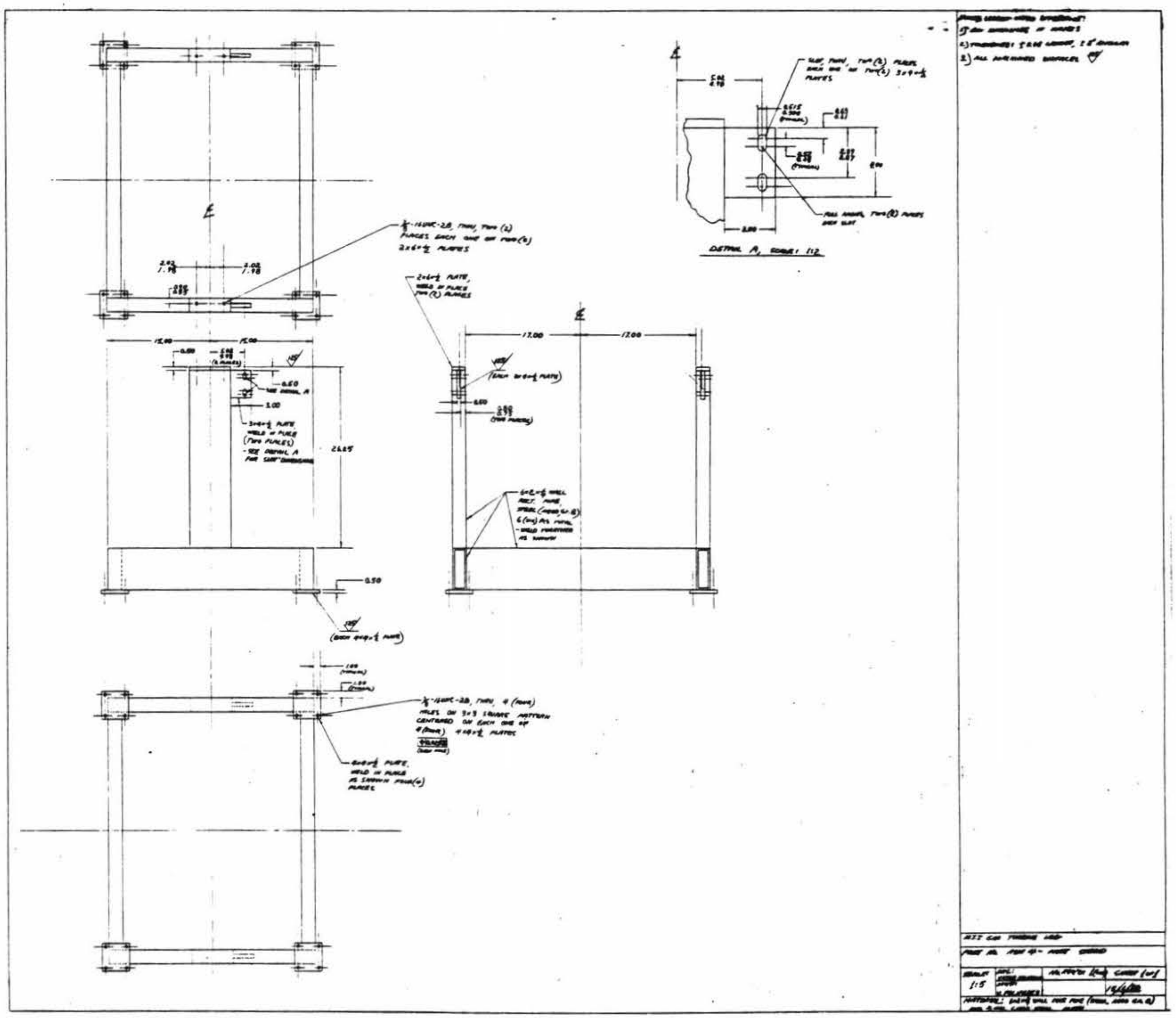

Fig. F.37a Auxiliary Pivot-Stand Frame

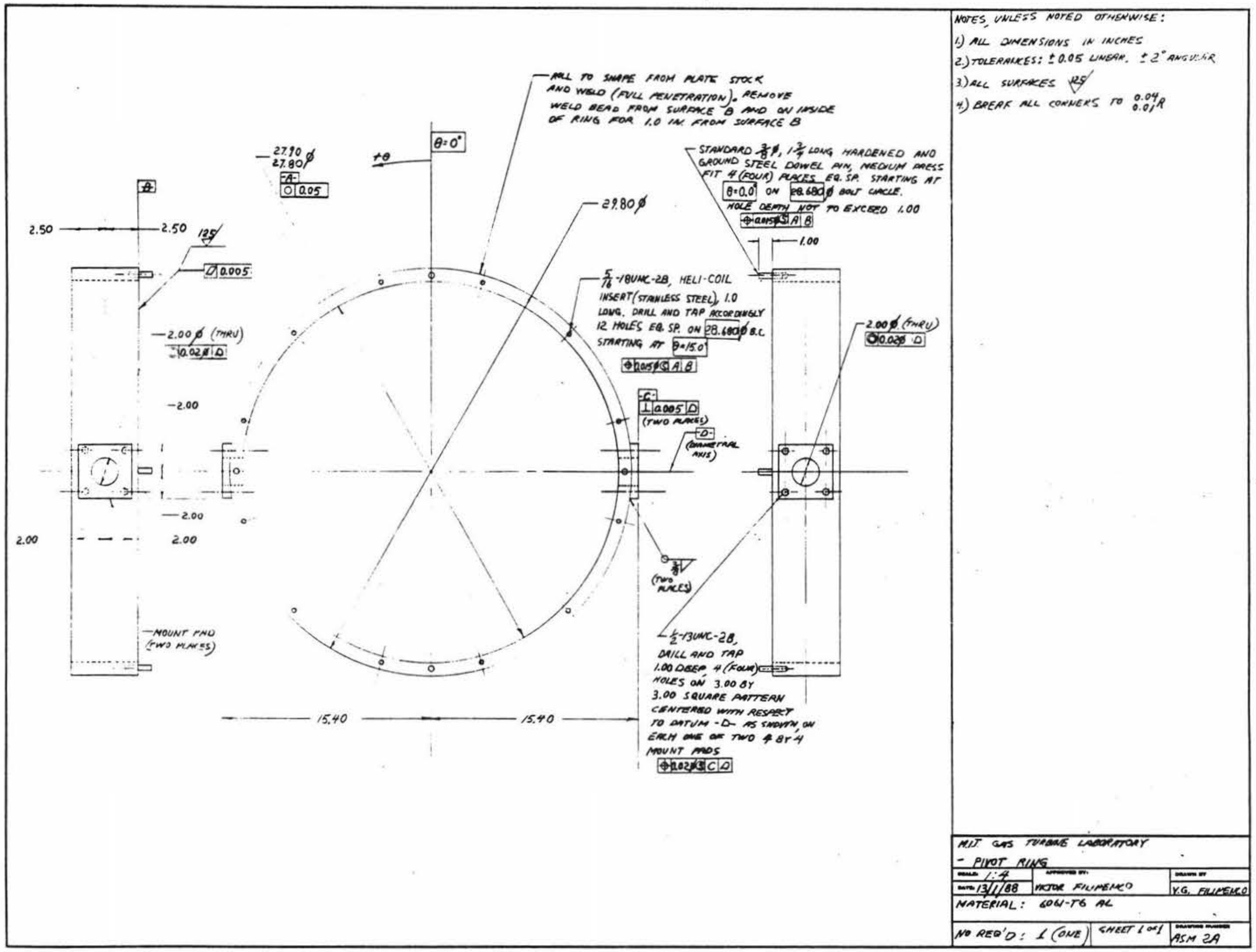

Fig. F.37b Auxiliary Pivot-Stand Diffuser Housing
Front-Section Mounting Ring

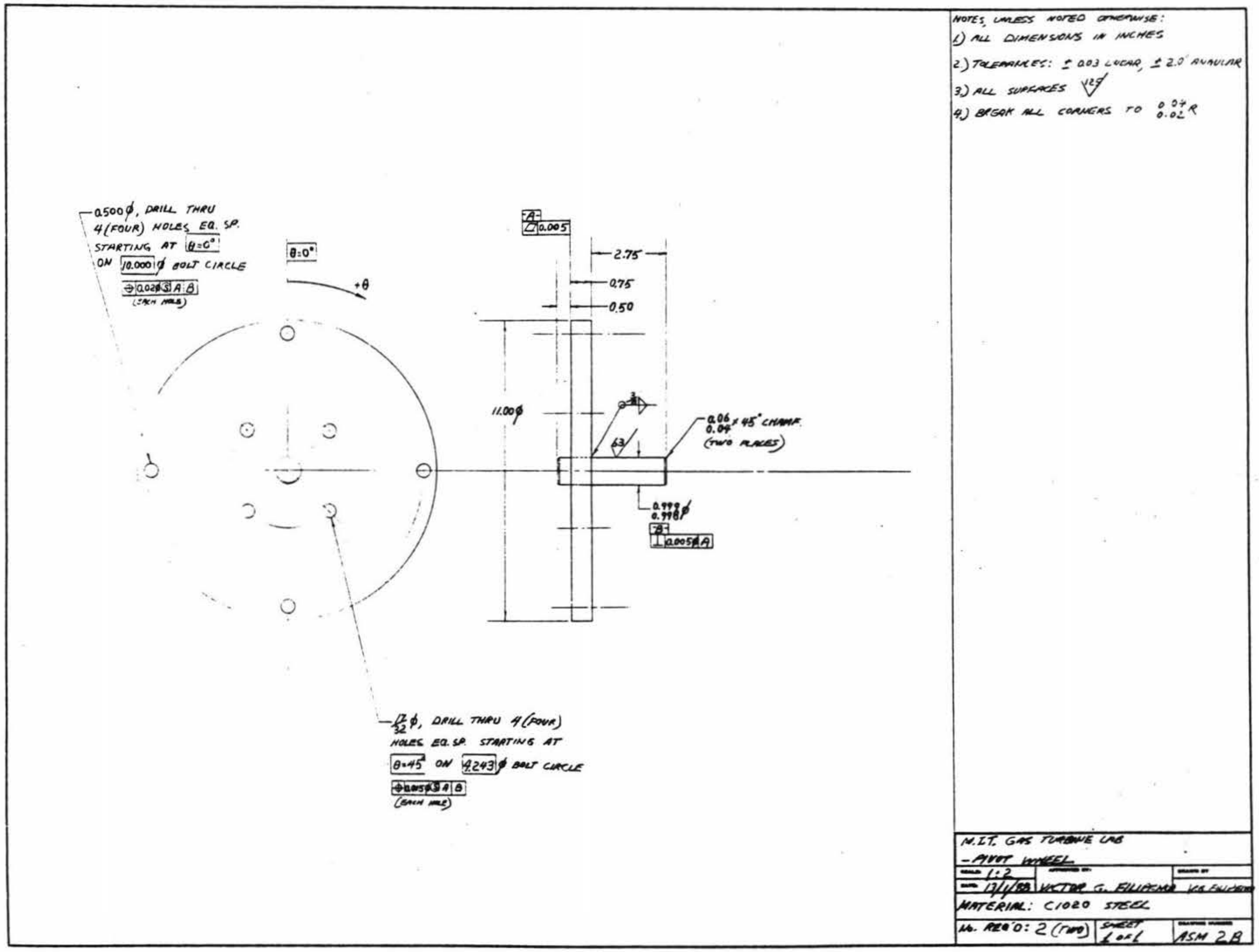

Fig. F.37c Auxiliary Pivot-Stand Index Wheel

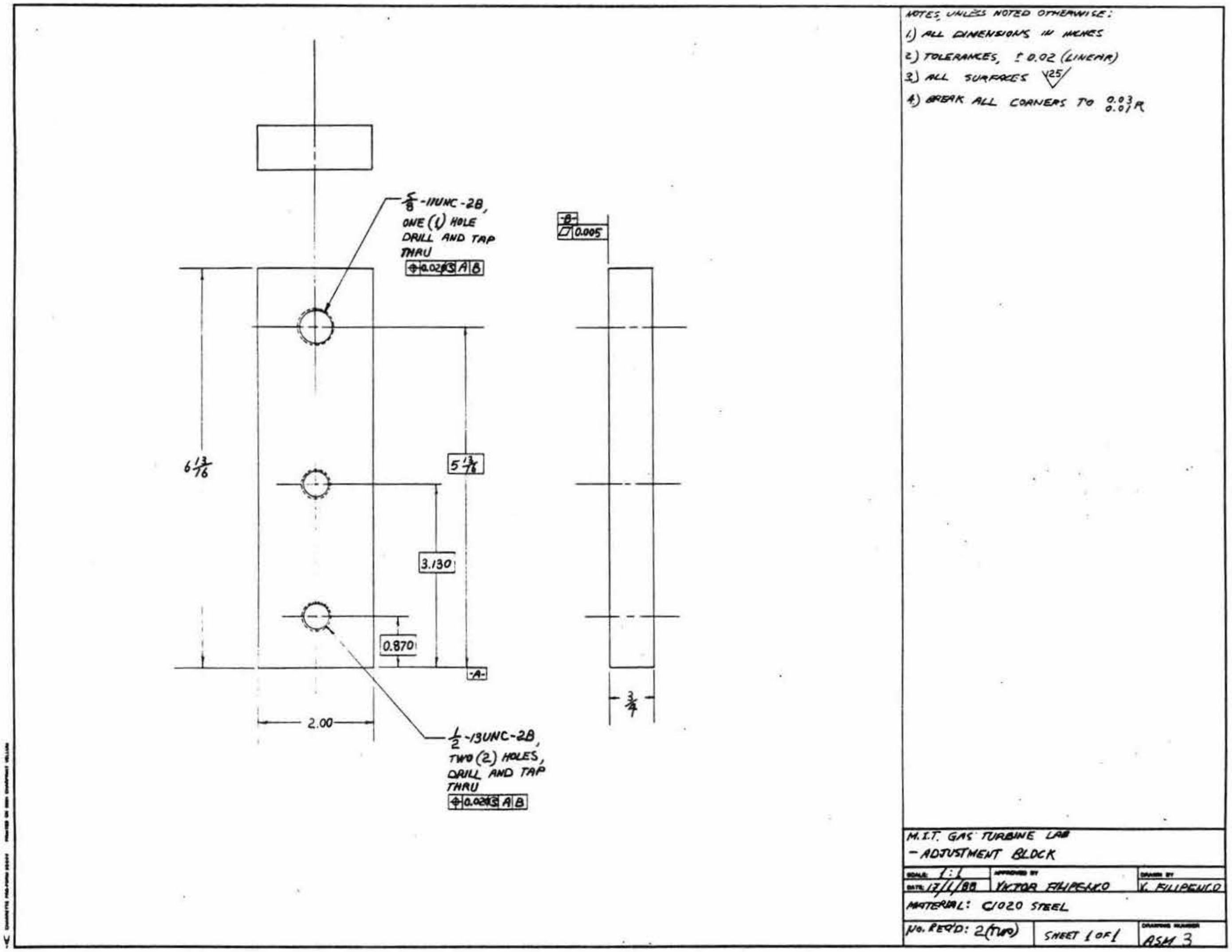

Fig. F.37d Auxiliary Pivot-Stand Index-Pin Block

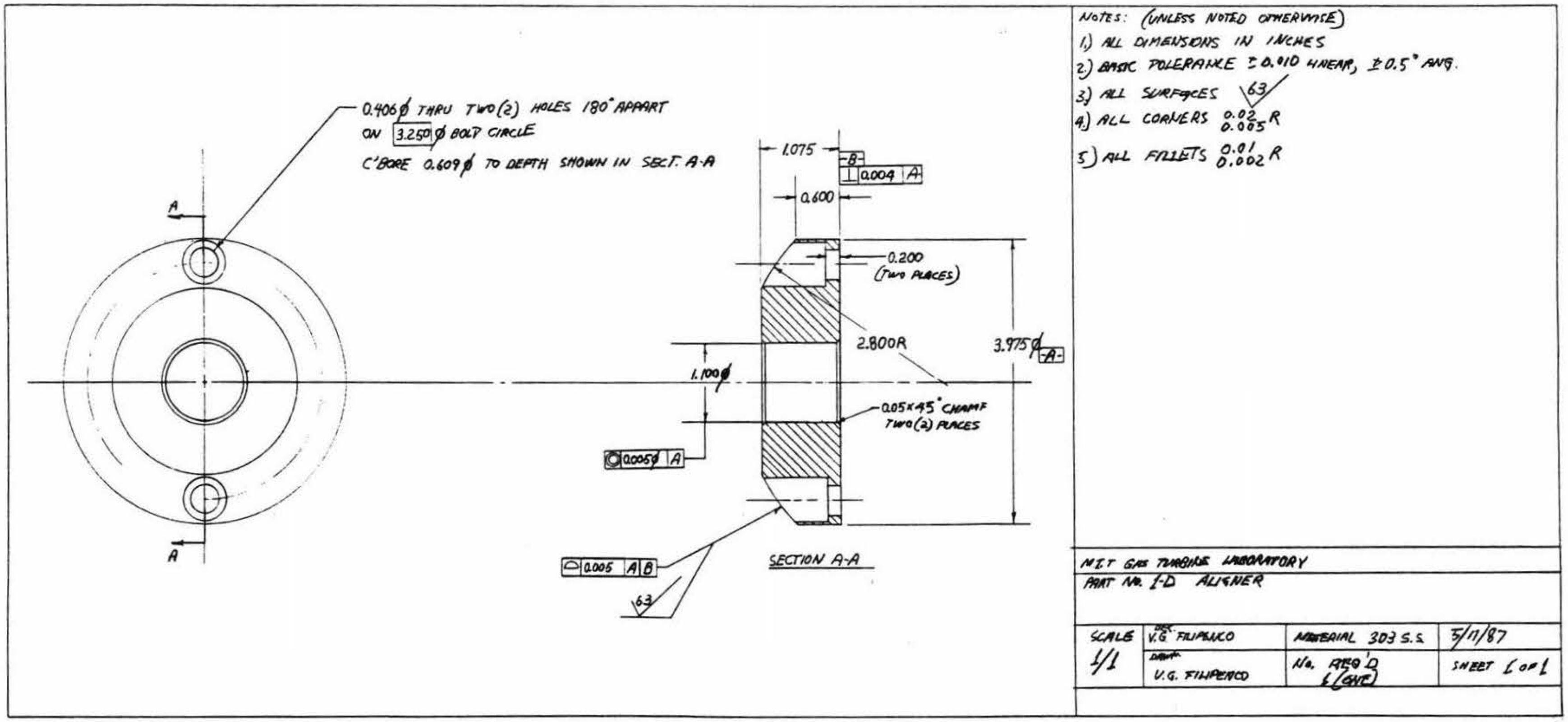

Fig. F.38a Blisk-Mounter Swivel Pad

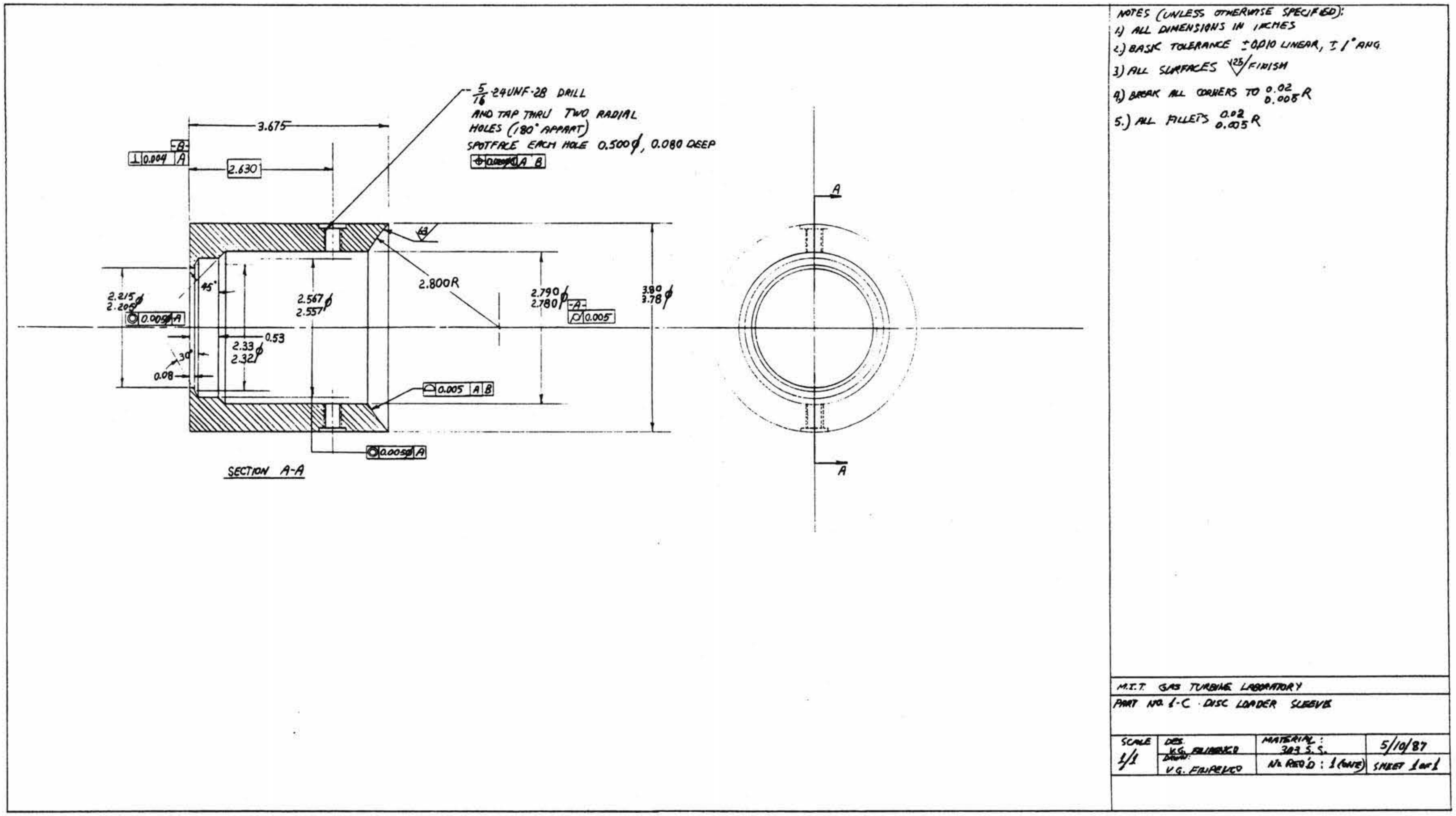

Fig. F.38b Blisk-Mounter Main Sleeve

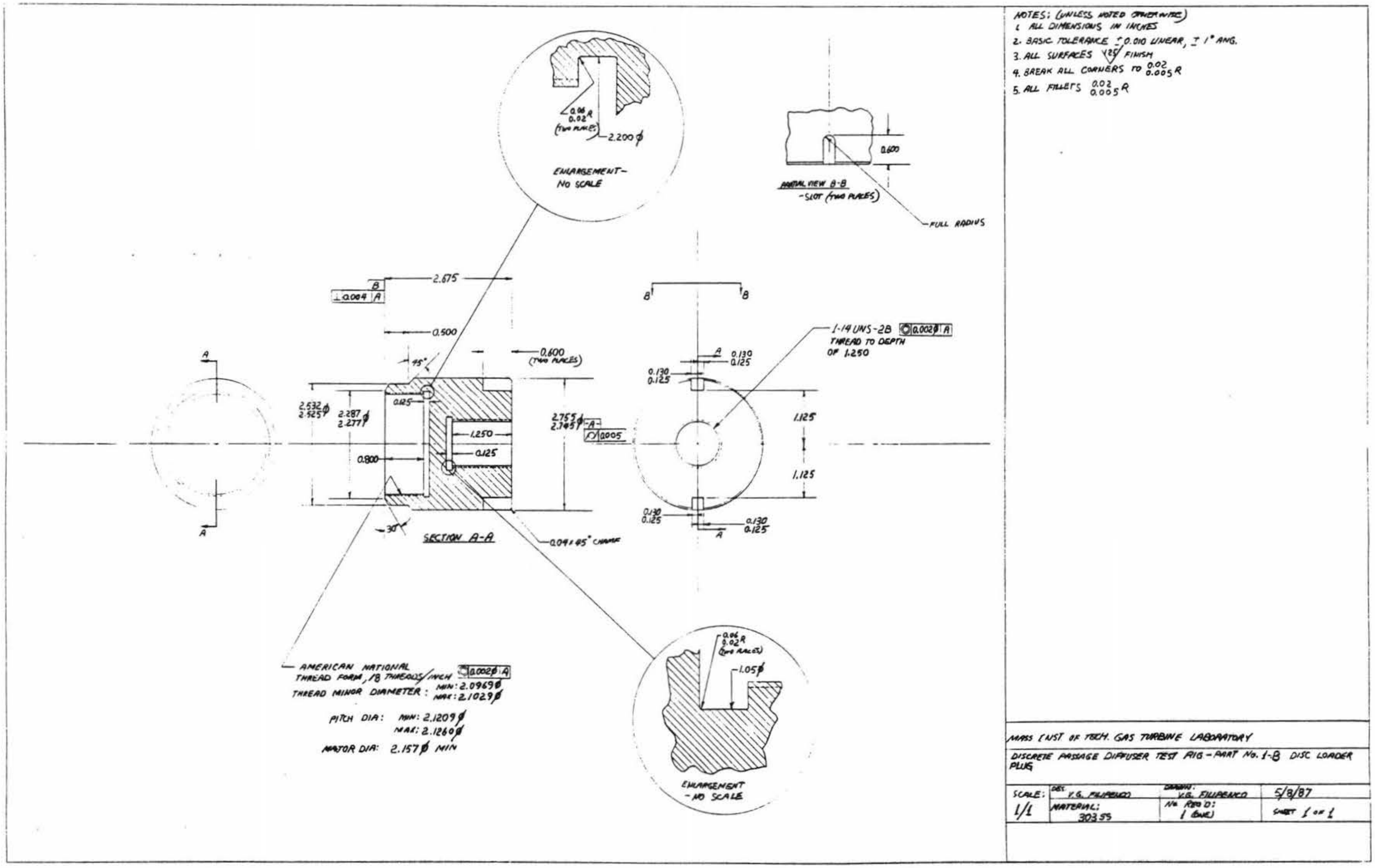

Fig. F.38c Blisk-Mounter Shaft Attachment Collar

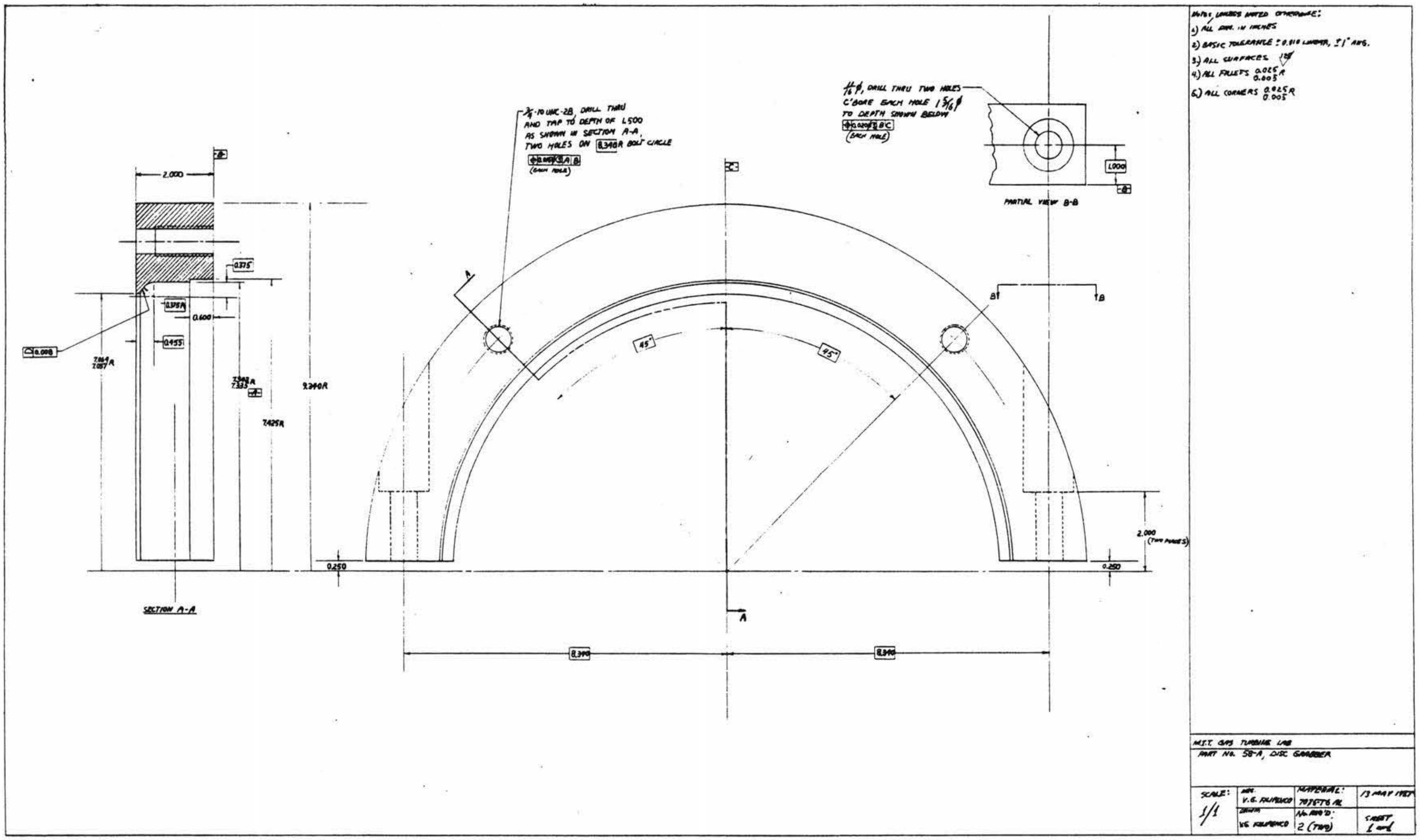

Fig. F.39a Blisk-Dismounter Clamp

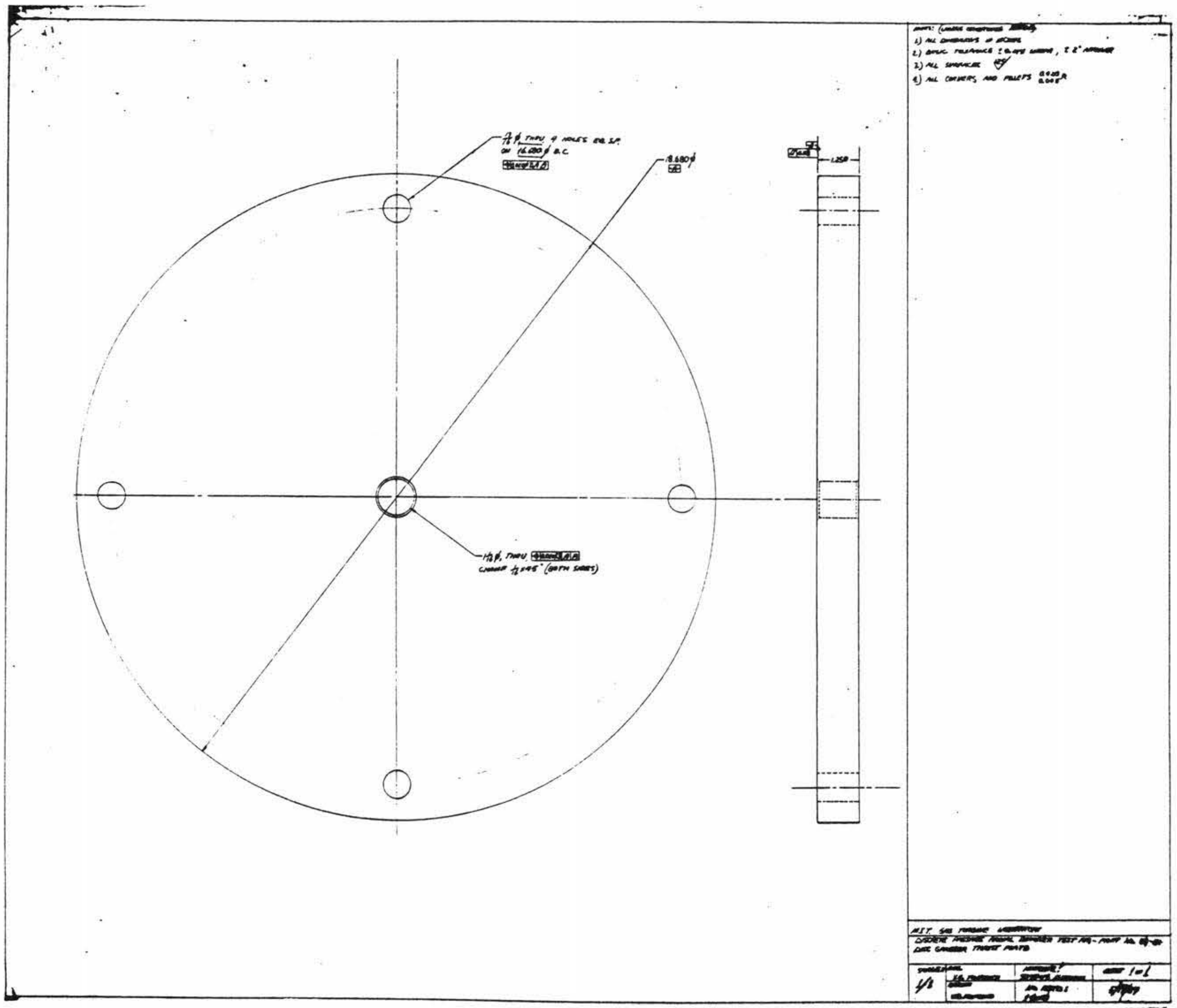

Fig. F.39b Blisk-Dismounter Puller Disk

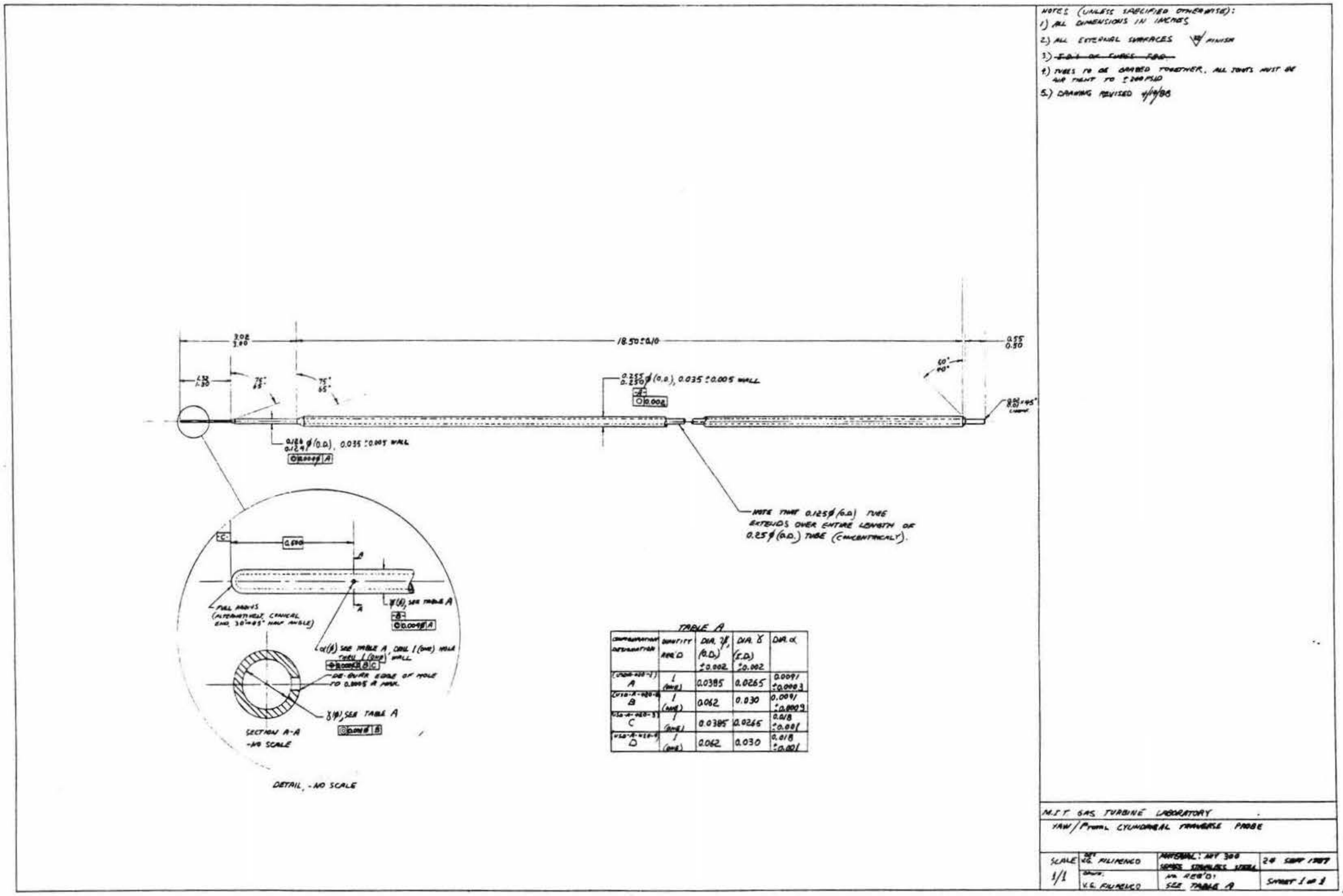

Fig. F.40 *P*-Total/Flow-Angle Probe

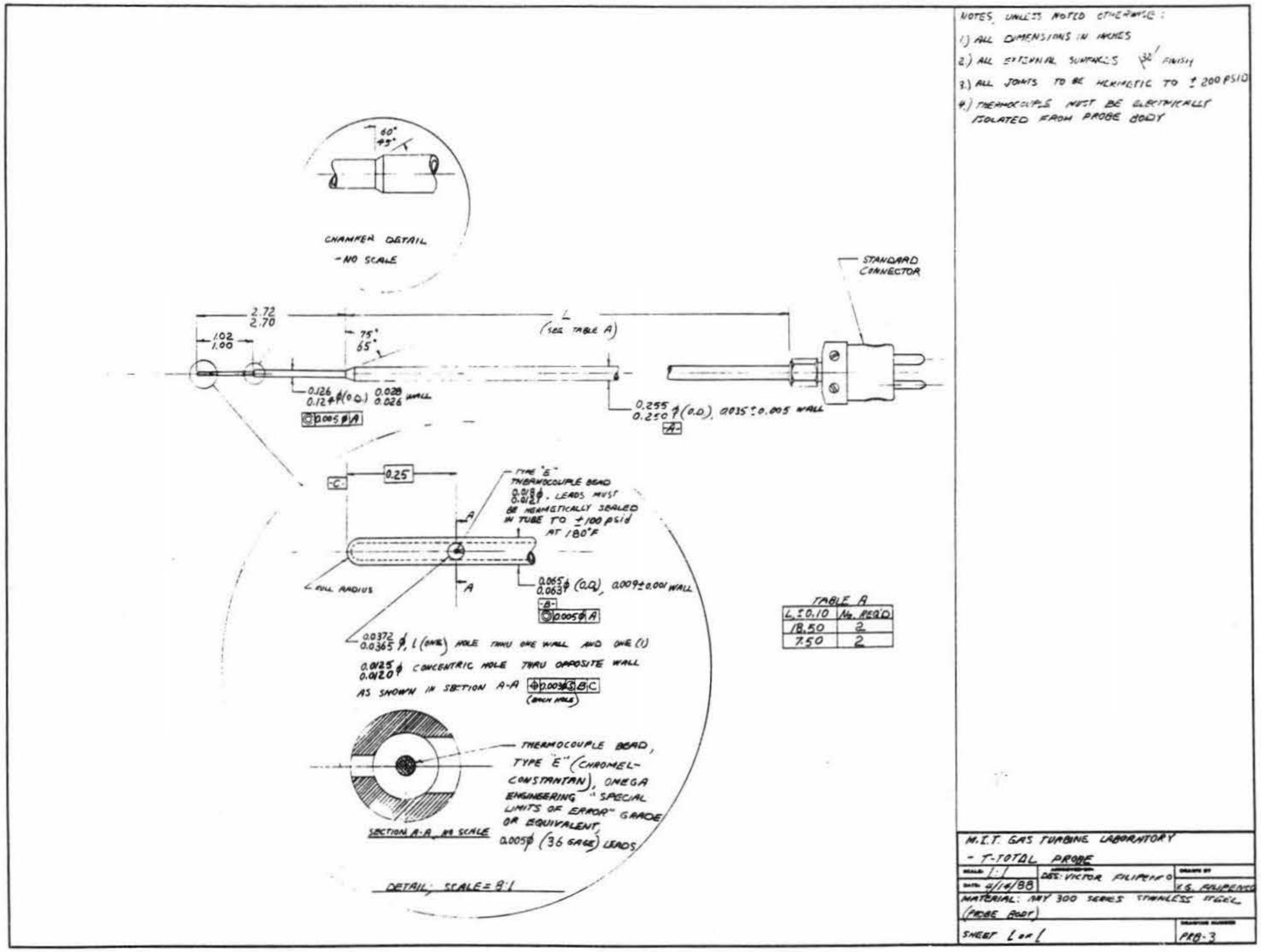

Fig. F.41 Total-Temperature Probe

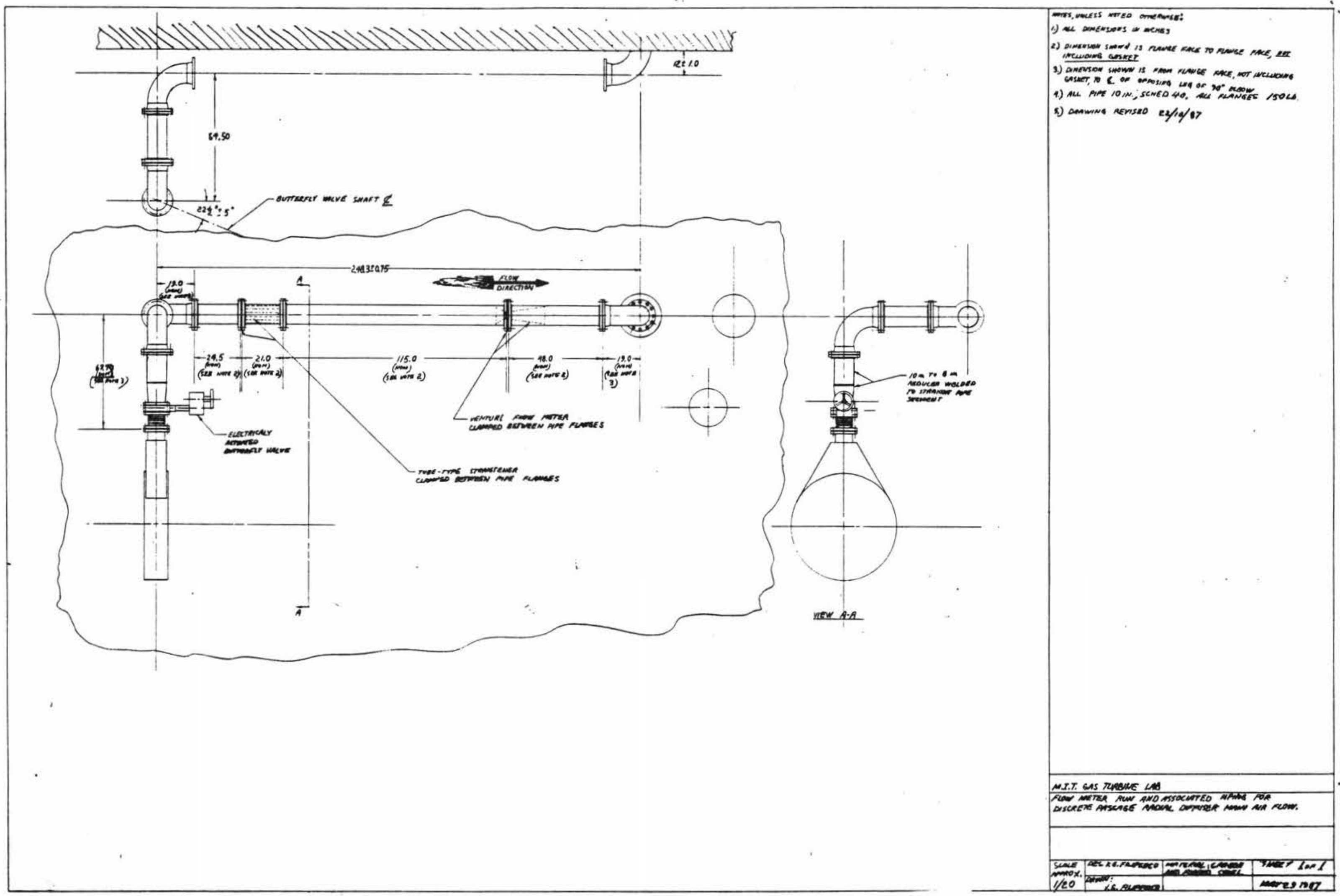

Fig. F.42 Diffuser Test Rig Discharge Piping Layout

APPENDIX G

PROBE AND TRANSDUCER CALIBRATION CURVES

A calibration of the flow-angle/total-pressure probe described in section 2.5.1 was performed using a calibration jet to establish an angular position reference for the probe in the traverser mechanism (the probe was secured in the traverser mechanism prior to calibration and remained undisturbed for the duration of the present experiments). The measured probe output pressure as a function of the angular offset of the probe sensing hole centerline from the jet centerline is given in figure G.1.

The pressure transducers used in the present experiments were calibrated using a standard mercury manometer to set the applied pressure ($\Delta P_{\text{applied}} = g\rho_{Hg}\Delta h$). The density of mercury corresponding to the room temperature at the time of calibration was obtained from [31]. The transducers, which include the Druck pressure transducer in the Scanivalve multiplexer, the Setra pressure transducer, the three Kulite pressure transducers in the vaneless space, and the main plenum/collector Kulite were calibrated simultaneously using a system of manifolds and a pressure/vacuum vessel. Figures G.2 and G.3 show the calibration curves for the Druck and Setra pressure transducers respectively and the calibration curves for the vaneless space pressure transducers located at $\theta = 1.25°$, $46.25°$, and $181.25°$ and the main plenum Kulite are shown in figures G.4a through G.4d respectively.

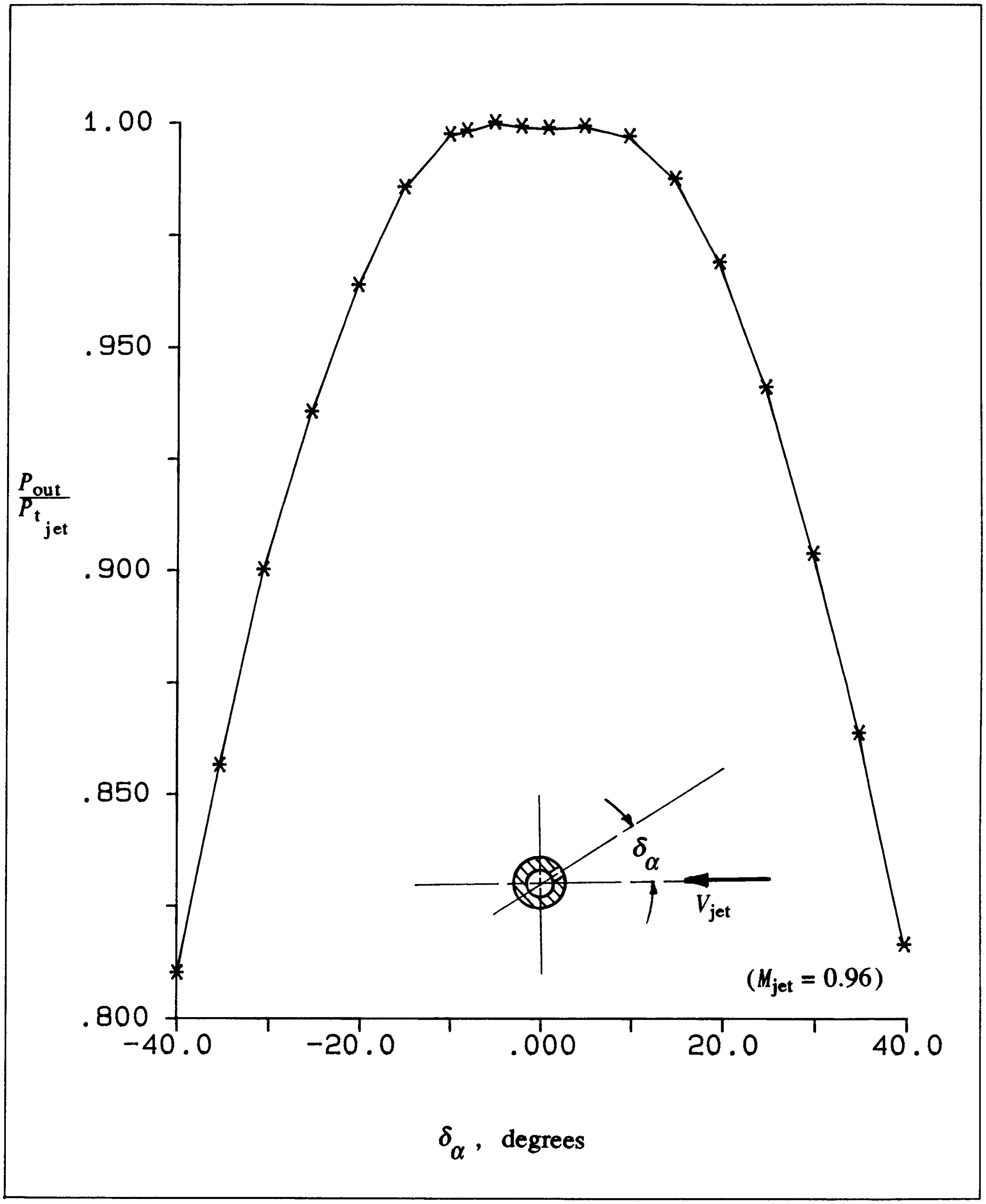

Fig. G.1 Total-Pressure/Flow-Angle Probe Calibration

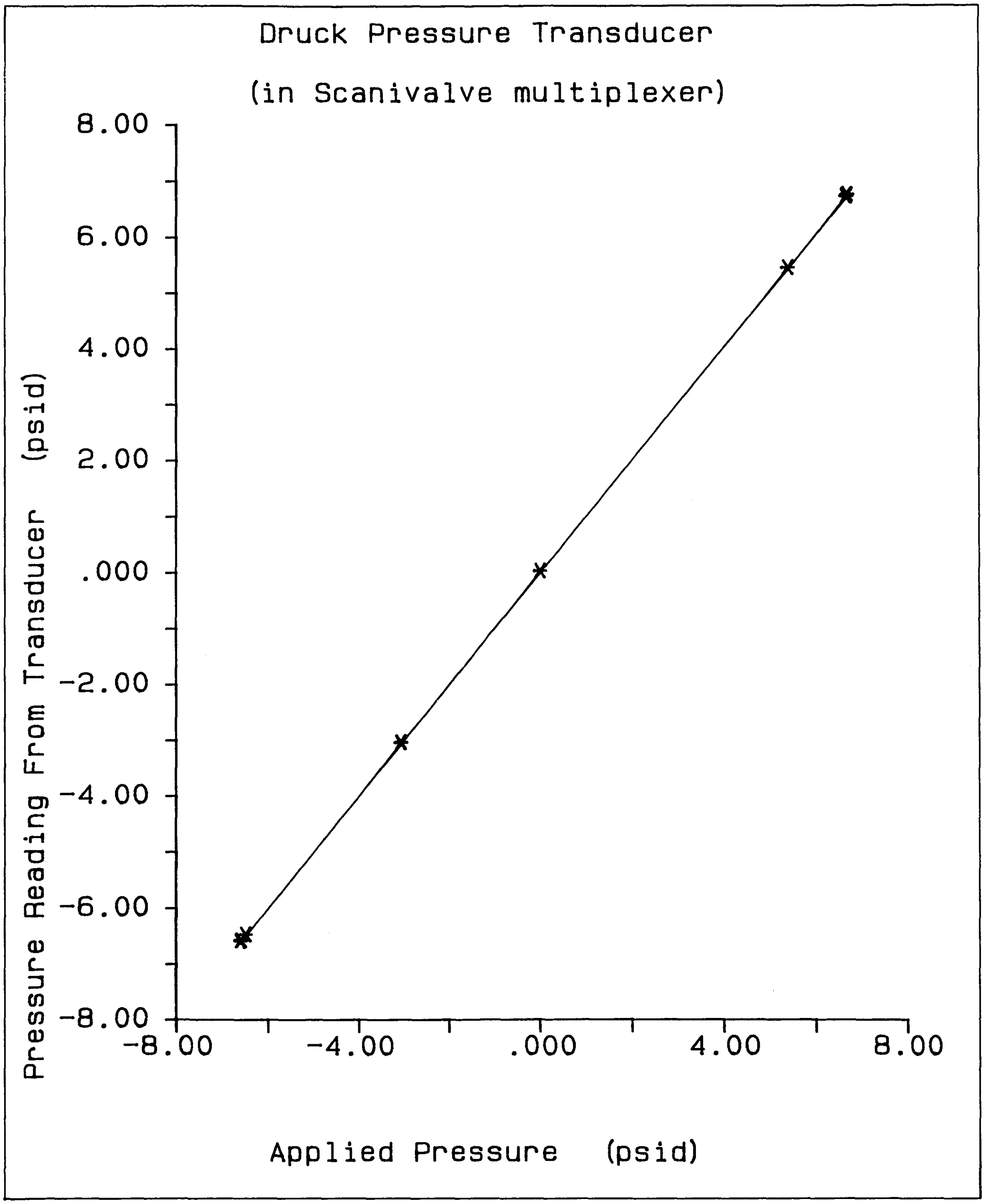

Fig. G.2 Calibration Curve for the Druck Pressure Transducer

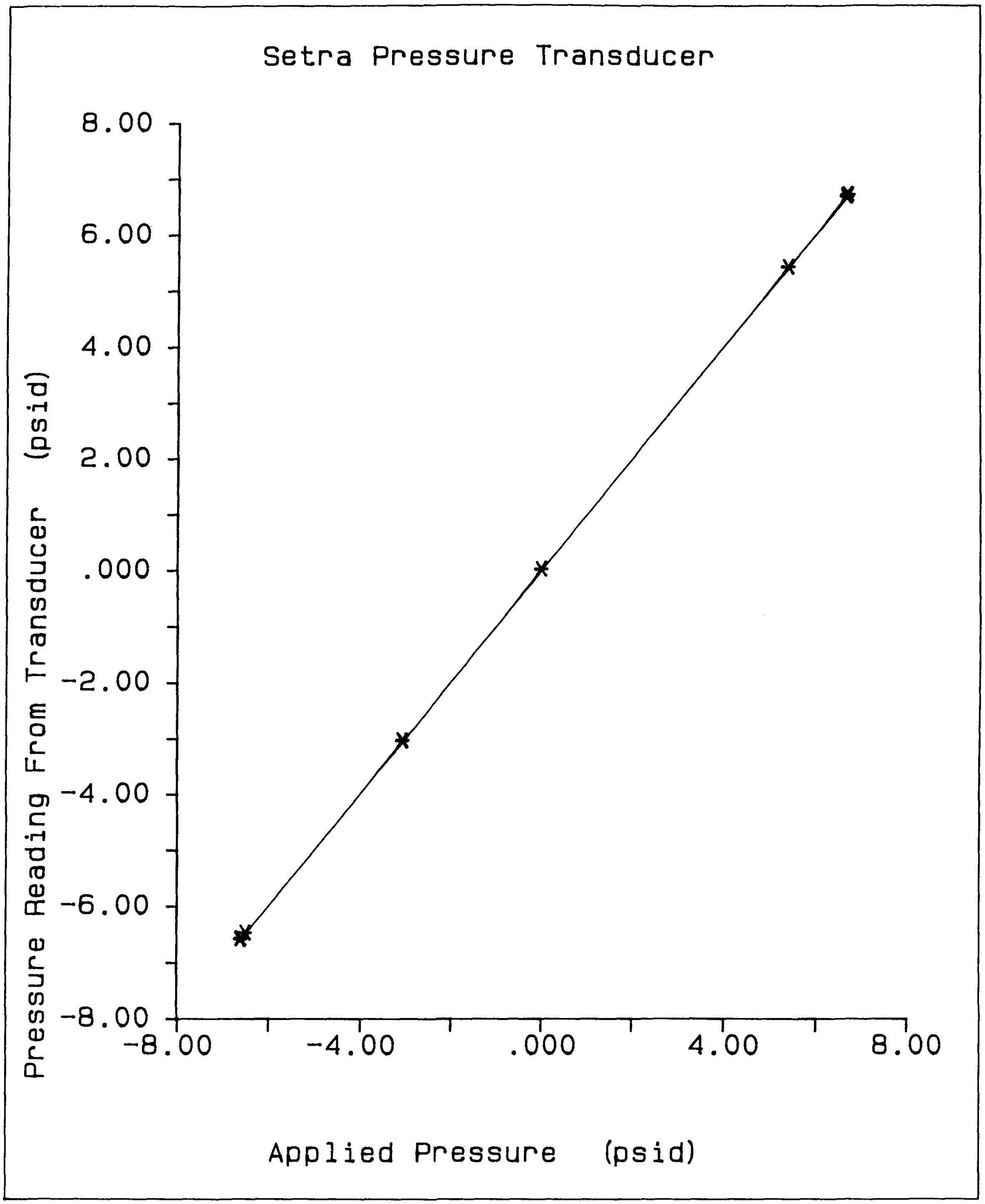

Fig. G.3 Calibration Curve for the Setra Pressure Transducer

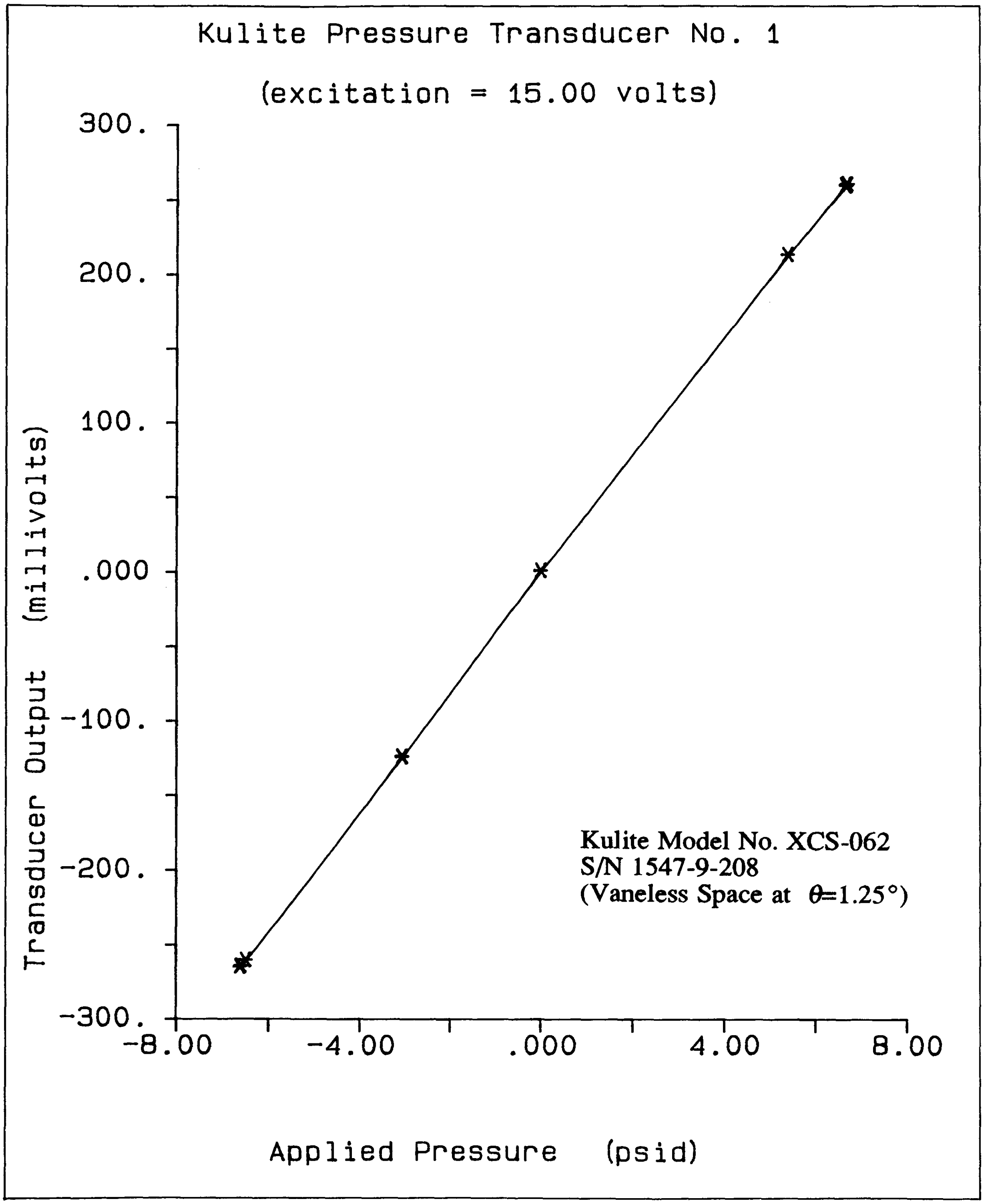

Fig. G.4a Calibration Curve for the Vaneless Space Pressure Transducer No. 1

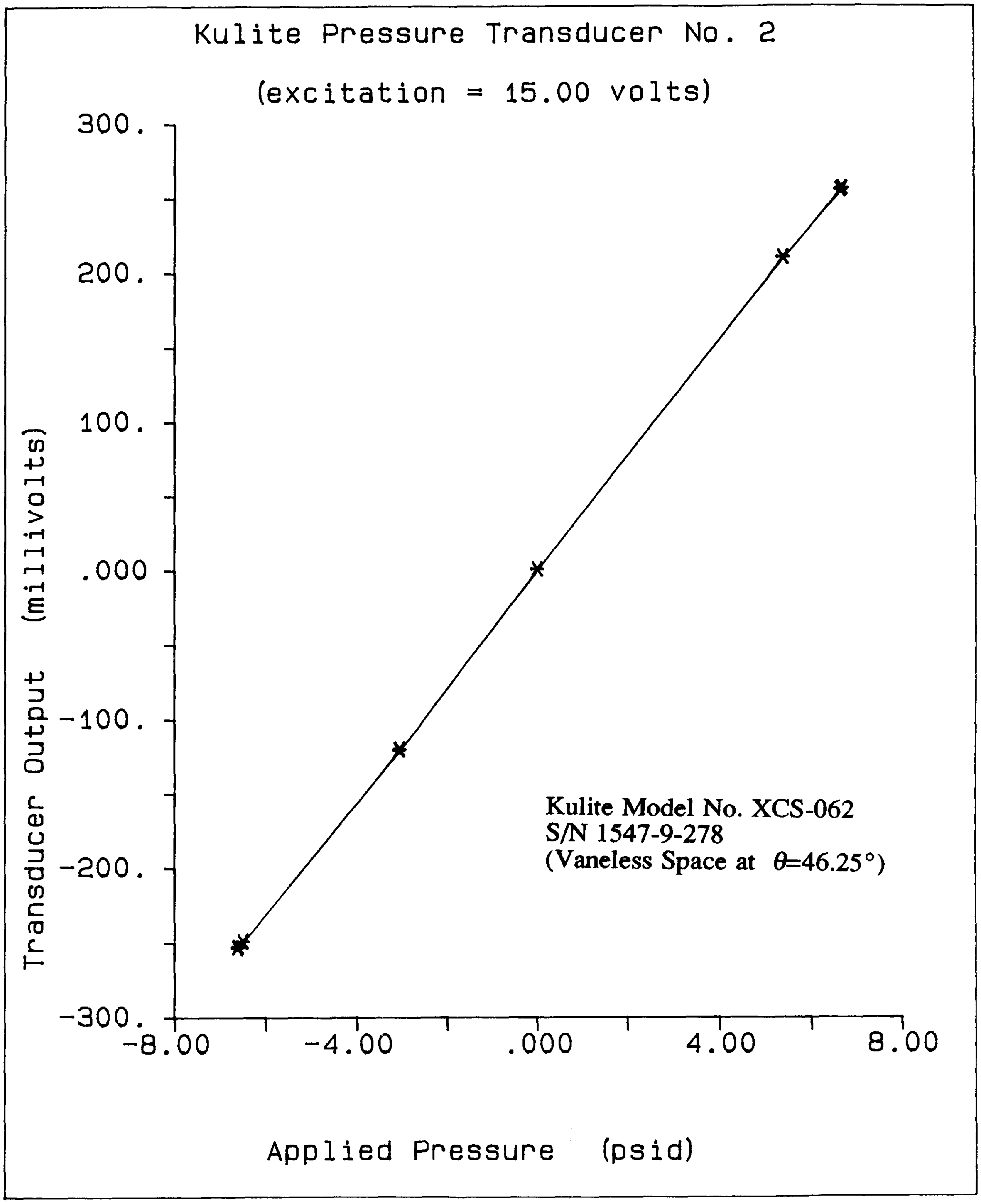

Fig. G.4b Calibration Curve for the Vaneless Space Pressure Transducer No. 2

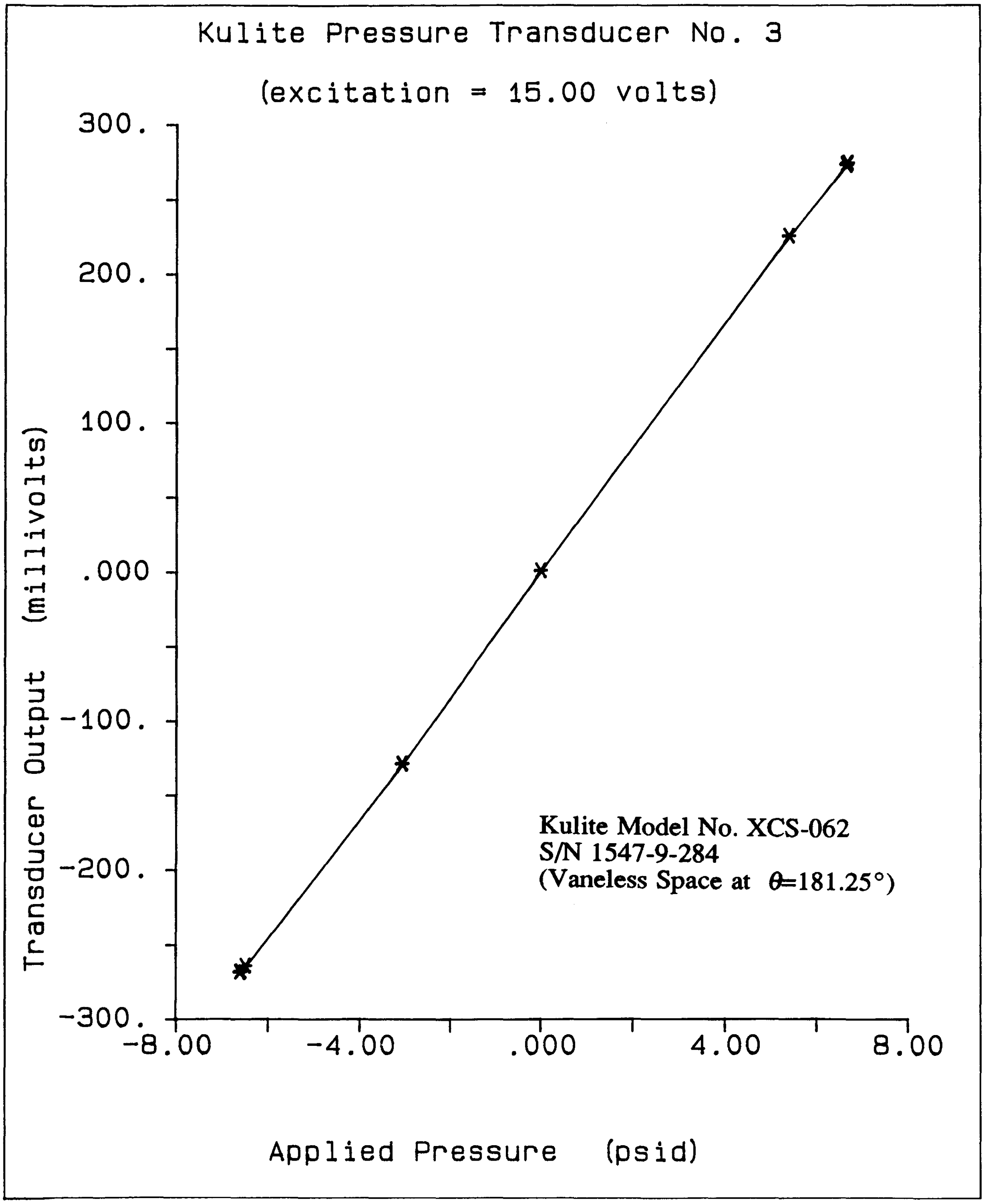

Fig. G.4c Calibration Curve for the Vaneless Space Pressure Transducer No. 3

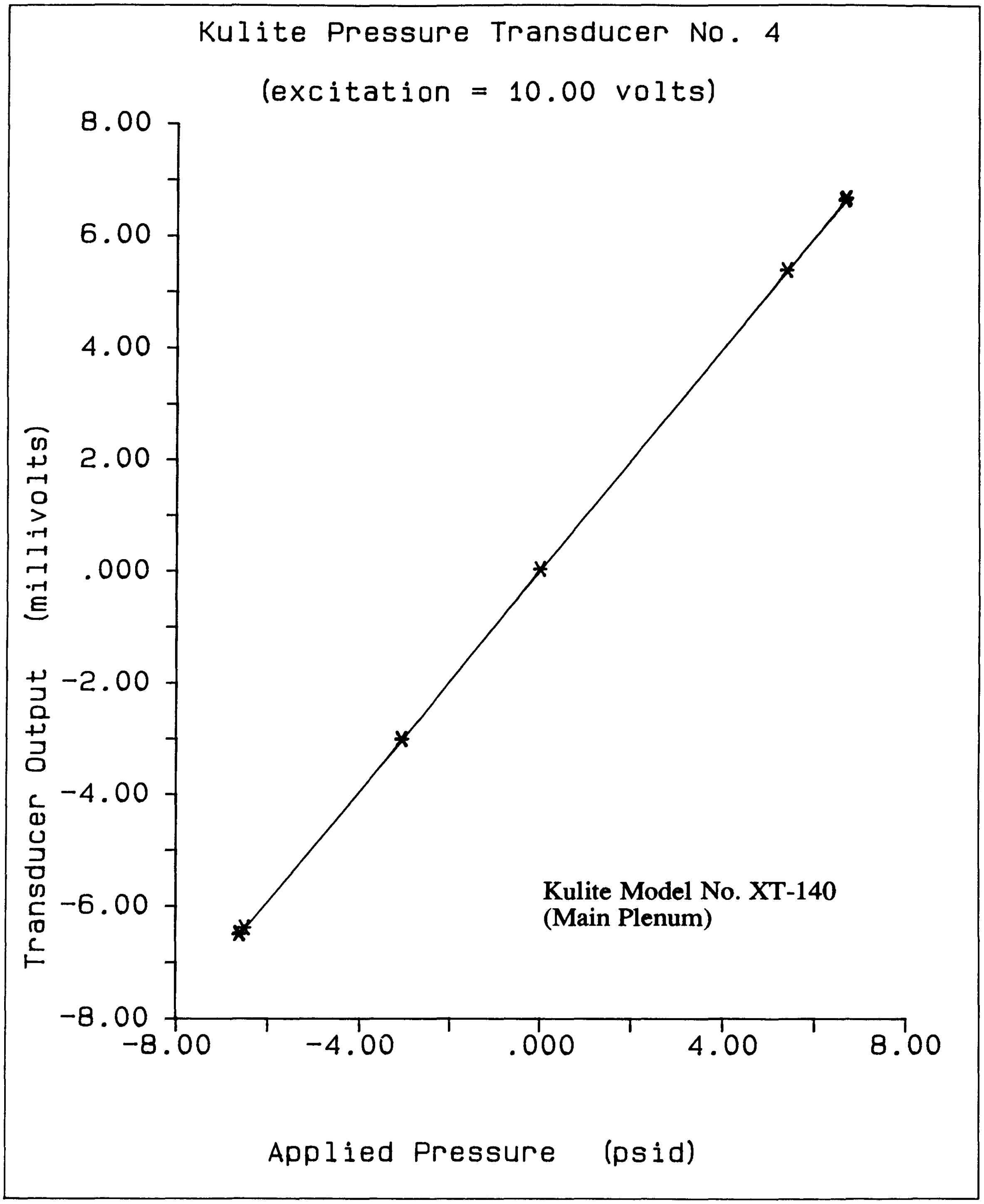

Fig. G.4d Calibration Curve for the Main-Plenum Pressure Transducer

APPENDIX H

VENTURI-FLOWMETER MASS FLOW RATE CALCULATION

The mass flow rate through the test diffuser was measured by means of a BIF "universal venturi tube" (U.V.T.) [30] part number 0182-10-2291 with a throat diameter of 5.81 inches. The venturi was mounted in the ten-inch diffuser-tester discharge line leading to the downstream slave compressor.

An upstream static-pressure tap, a venturi-throat static-pressure tap, and a temperature probe (see section 2.5.4) provided the measured quantities from which the flow rate was calculated. The venturi upstream-to-throat static pressure difference was measured by means of a Meriam Instrument inclined manometer with a range of 0-20 inches of water and a resolution of 0.02 inches using Meriam "green 1000" manometer fluid (specific gravity =1.000). The venturi upstream static pressure was determined using a Setra model number 271, ±15 psid pressure transducer, as described in section 2.5.2.

As shown in [30], the discharge coefficient of the U.V.T., defined as the ratio of the actual mass flow-rate to the theoretical mass flow-rate, is constant at 0.980 to within ±0.5% for Reynolds numbers (based on the pipe diameter) of 75,000 and above. This covers the range of the present experiments down to ≈29% of the swirl-generator maximum (choke) corrected flow rate of ≈2.2 lbm/sec. The rated uncalibrated accuracy of the U.V.T. is to within ±1.0%.

The theoretical mass flow rate is calculated on the assumptions of uniform flow properties at the upstream and throat static-pressure-tap locations, constant total pressure between the locations of the taps, and constant and uniform total temperature between the locations of the upstream static tap and the downstream temperature probe. Given the upstream (station 1) static pressure, the throat (station 2) static pressure, and the total temperature of the flow, the theoretical mass-flow-rate was calculated as follows:

By continuity between stations 1 and 2 and the above stated assumptions, the theoretical mass flow rate is:

$$\dot{m}_{1_{th}} = \rho_1 V_1 A_1 = \dot{m}_{2_{th}} = \rho_2 V_2 A_2 = \dot{m}_{th} \qquad \text{H.1}$$

were ρ, V, and A are the static density, the flow velocity, and the cross-section flow area, respectively.

Equation H.1, combined with the equation of state for a perfect gas:

$$Pv = RT \ , \qquad \text{H.2}$$

the definition of Mach number and the relation for the acoustic velocity in a perfect gas:

$$M = \frac{V}{a} = \frac{V}{\sqrt{\gamma RT}} \ , \qquad \text{H.3}$$

and the relationship between static and total temperatures in a flow of a perfect gas:

$$\frac{T_t}{T} = 1 + \frac{\gamma-1}{2}M^2 \ , \qquad \text{H.4}$$

can be written as:

$$\dot{m}_{th} = \frac{P_2}{RT_t}\sqrt{\gamma RT_t}\, M_2\left[1 + \frac{\gamma-1}{2}M_2^2\right]^{\frac{1}{2}} A_2 \qquad \text{H.5}$$

Applying the basic relations for the adiabatic-isentropic flow of an ideal gas, an expression for M^2 in terms of the upstream-to-throat static pressure and area ratios is obtained:

$$M_2^2 = \frac{\dfrac{2}{\gamma-1}\left[\left[\dfrac{P_1}{P_2}\right]^{\frac{\gamma-1}{\gamma}} - 1\right]}{1 - \left[\dfrac{A_2}{A_1}\right]^2\left[\dfrac{P_1}{P_2}\right]^{\frac{-2}{\gamma}}} \qquad \text{H.6}$$

Using equation H.6 to eliminate M_2 in equation H.5, the theoretical mass flow rate can be calculated given only the upstream and throat static pressures, the total temperature, and the throat-to-pipe area ratio. The actual mass flow rate is then determined by applying the discharge coefficient:

$$\dot{m}_{actual} = C_D\, \dot{m}_{theoretical} \qquad \text{H.7}$$

APPENDIX I

BEARING PRE-LOAD SPRING CALIBRATION

As described in section 2.2.6, the angular contact bearings selected to support the swirl generator rotor had to be axially pre-loaded to 320. lb_f to obtain the required radial and axial bearing stiffness. This was accomplished using a stack of five (5) wave-washer springs (Smalley Steel Ring Company part no. SSR-0437-N).

The force v.s. displacement characteristic of the spring stack was determined by applying known loads to the stack by means of a materials testing machine and measuring the spring displacement using a dial indicator. For purposes of this calibration, the spring stack was positioned in a cylindrical holder with a bore diameter equal to that of the spring-locating bore of the actual bearing housing. The spring stack was loaded using a sleeve with inside and outside diameters equal to those of the actual pre-load sleeve. The resulting calibration curve is shown in figure I.1 from which it is seen that a spring compression of 0.083 inches is required to give the required pre-load of 320 lb_f. The length of the actual pre-load sleeve (see figures F.1 and F.12) was machined accordingly after measurement of the relevant axial dimensions of the actual bearing housing and shaft.

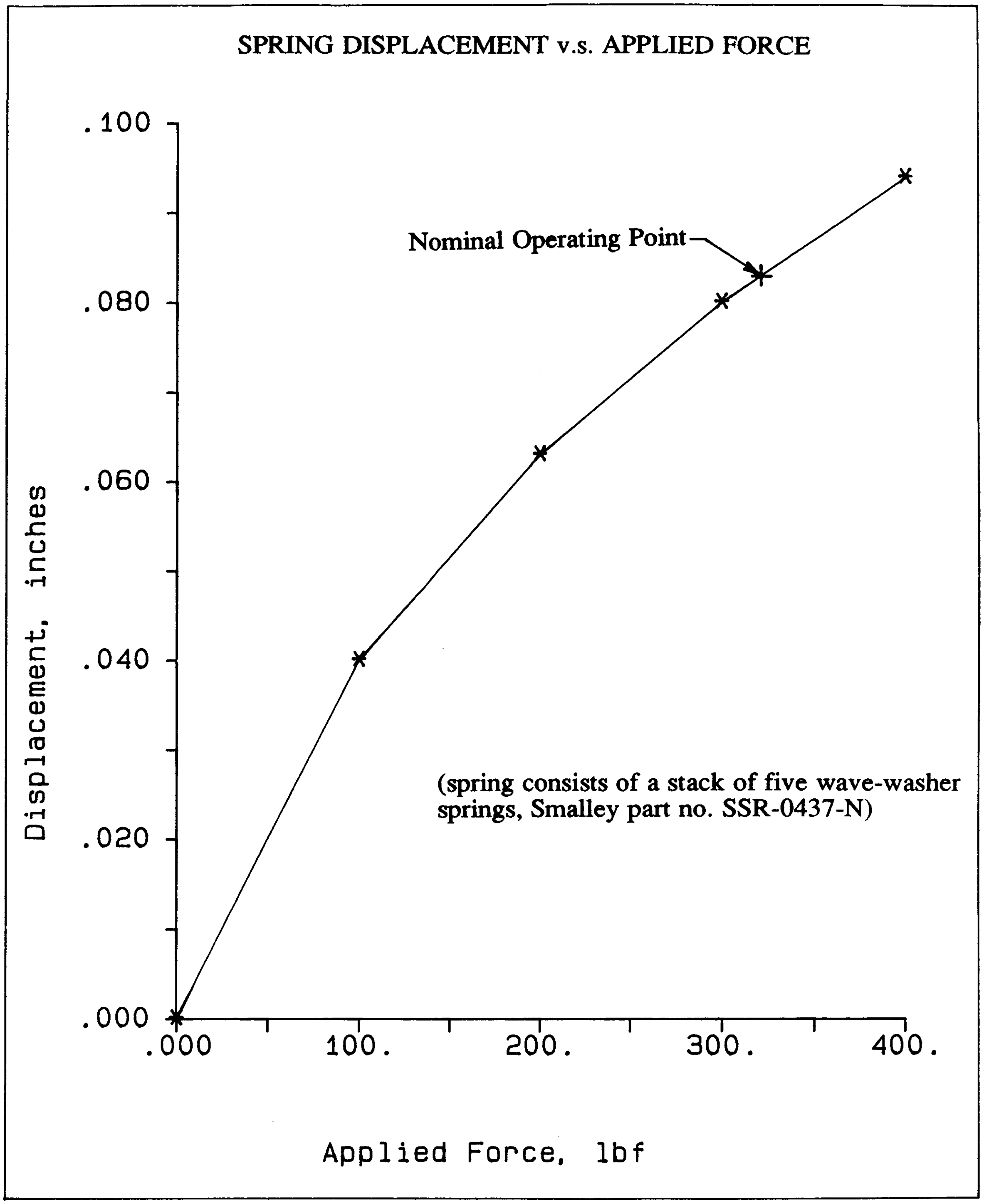

Fig. I.1 Bearing Pre-Load Spring Calibration

APPENDIX J- BEARING LUBRICATION SYSTEM SCHEMATIC

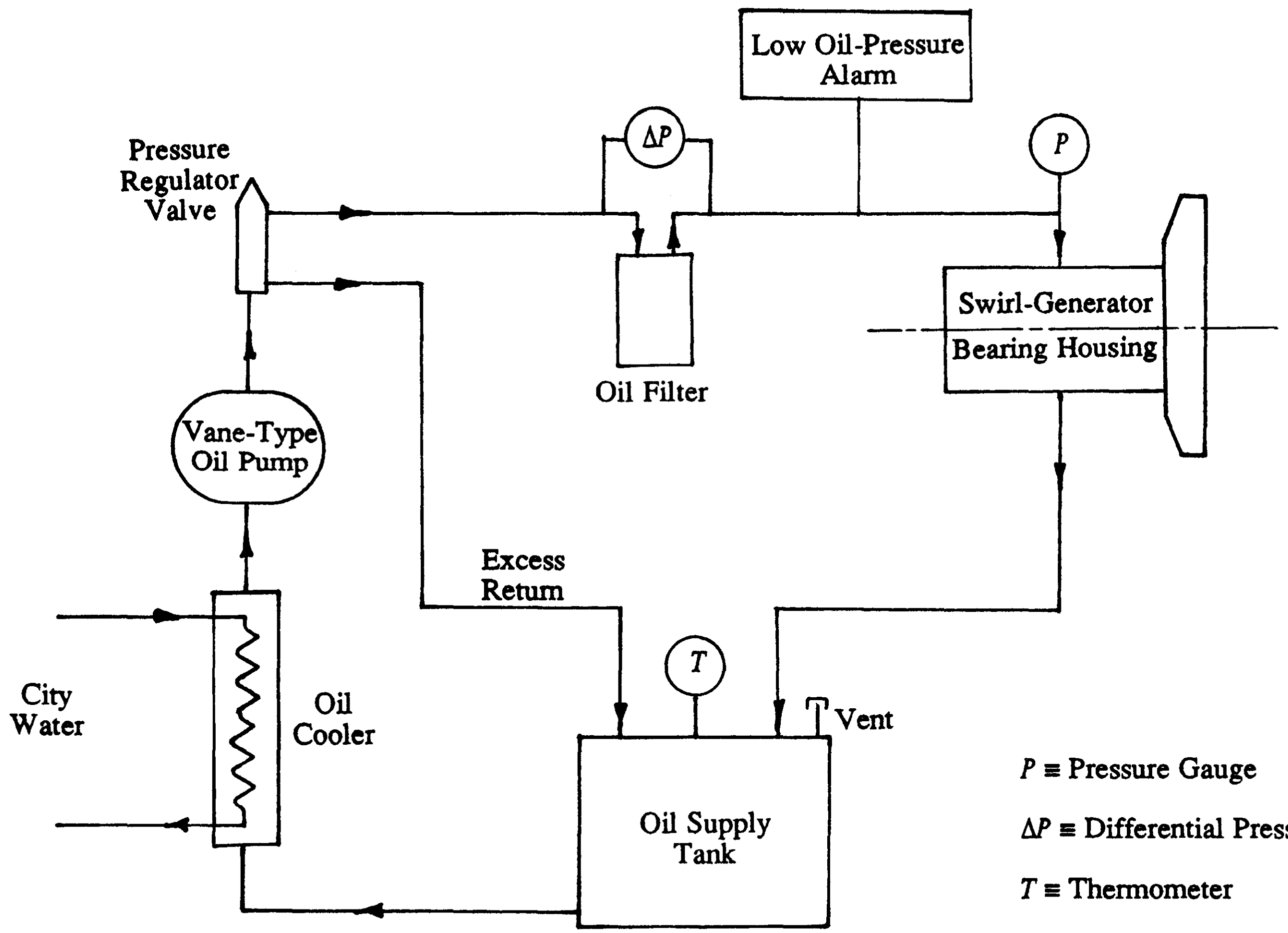

$P \equiv$ Pressure Gauge

$\Delta P \equiv$ Differential Pressure Indicator

$T \equiv$ Thermometer

Fig. J.1 Bearing Lubrication System Schematic

APPENDIX K

OPERATION MONITORING AUTO SHUTDOWN SAFETY CIRCUIT SCHEMATICS

Circuits were designed and constructed to trip the swirl generator drive motor if any of several facility operating parameters exceed pre-set limits as described in section 2.3.6. The monitored parameters include the swirl generator flow temperature (measured at the test diffuser exit), the swirl generator vibration level (measured at the swirl-generator bearing housing), the pressure downstream of the venturi flow meter, and the differential pressure across the venturi flow meter.

The venturi flow meter differential pressure threshold circuit is shown in figure K.1. The circuit consists of a high input-impedance amplifier which amplifies the output of the venturi flow meter differential pressure transducer (BR1), coupled to a Schmitt trigger. The output of the Schmitt trigger (at B) switches from a "low" to "high" TTL state when the output of the pressure transducer drops below a value selected by adjusting R3 and R9. R9, in conjunction with R8, can be adjusted to set the hysteresis for the threshold levels. Figure K.2 shows the vibration threshold circuit. The design of this circuit is essentially identical to that of the differential pressure threshold circuit described above. The input to the circuit is the voltage across R23, where R23 is used as a current sensor in the vibration transducer current loop described in section 2.3.6. The output of the circuit (at D) switches from a "high" to "low" TTL state when the vibration level exceeds a value set by means of R16 and R20. R20, in conjunction with R19, sets the hysteresis.

The logic circuit designed to trip the swirl generator drive motor when any of the monitored parameters exceed preset values is shown in figure K.3. In this circuit diagram, TS1 is a digital thermostatic switch (Omega Engineering Catalogue No. CN900) and is in the open position when the diffuser exit flow temperature is greater than a pre-set value. PS1 is a pressure switch (Omega Engineering Catalogue No. PSW-354) and is in the open position when the static pressure downstream of the venturi flow meter is below a preset value. Terminals B and D are connected to the corresponding outputs from the venturi differential pressure threshold and the bearing housing vibration threshold circuits described above.

The function of the logic circuit is to open the contacts of relay RL1 (and thereby shutdown the main drive motor) if one or more of the following conditions develop:

1.) The diffuser exit flow temperature exceeds a preset value.
2.) The venturi differential pressure drops below a preset value.
3.) The pressure downstream of the flow meter exceeds a preset value.
4.) The vibration of the bearing housing exceeds a preset value.

The above shutdown criteria can be deactivated individually by closing switches SW2 through SW5 respectively. The entire circuit can be deactivated by closing switch SW6.

Green LED's, one for each shutdown criteria, indicate "safe" conditions while red LED's, (also one for each shutdown criteria) indicate a trip condition. Once a trip has occurred, the circuit must be reset by pressing SW1.

The design of the threshold and logic circuits described above followed the basic guidelines given in reference [33].

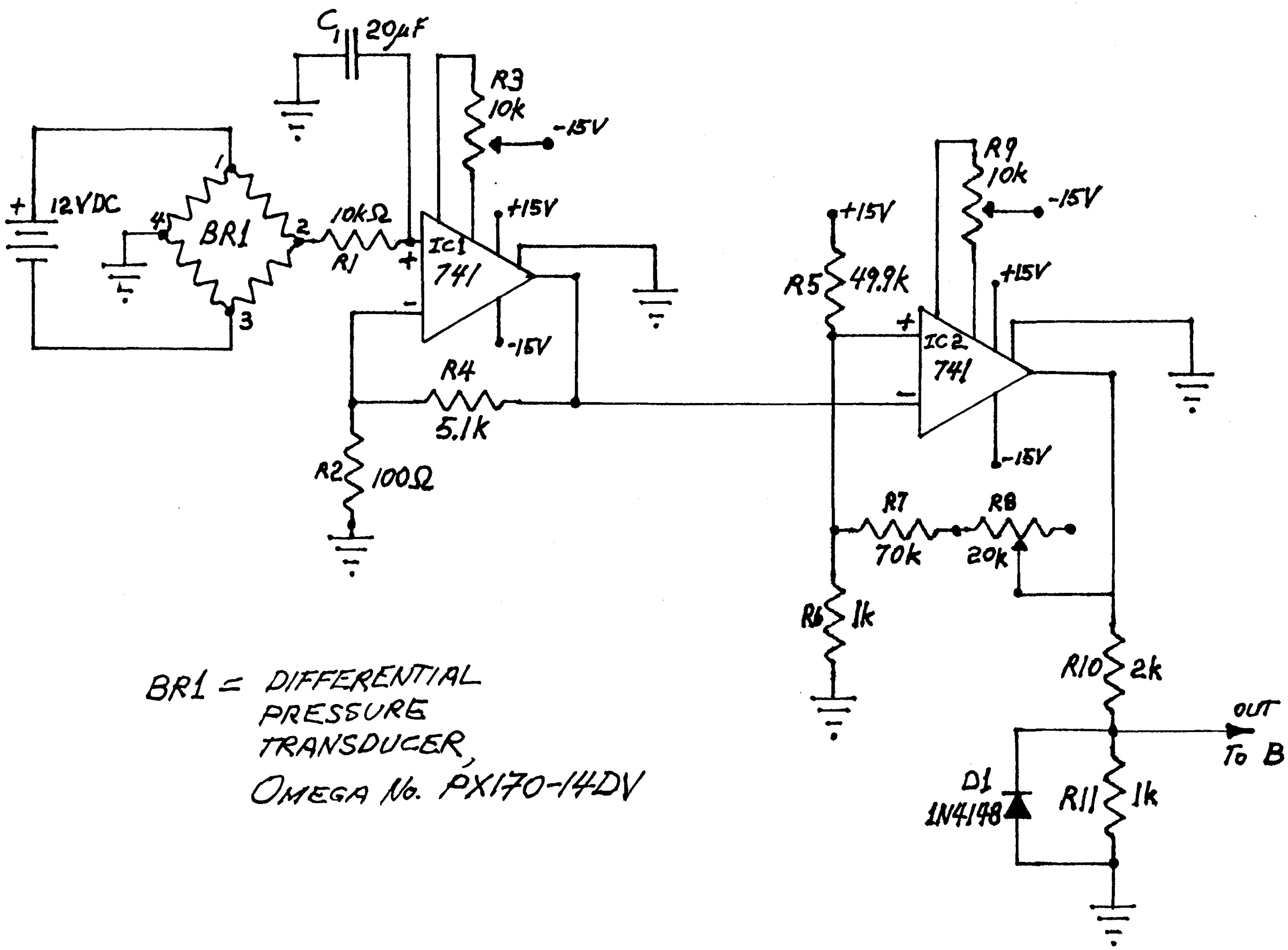

Fig. K.1 Venturi Flow Meter Differential Pressure Threshold Circuit

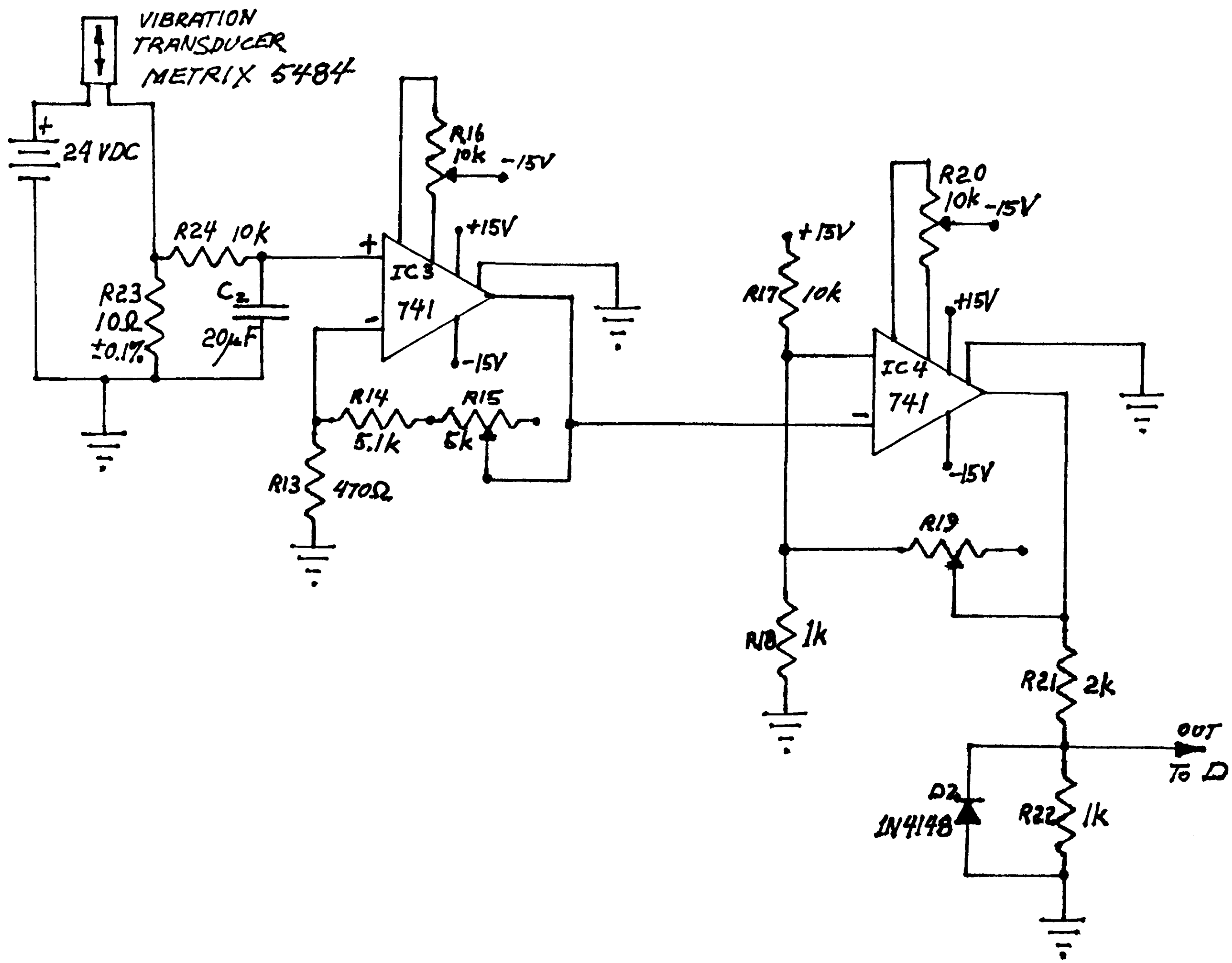

Fig. K.2 Vibration Transducer Threshold Circuit

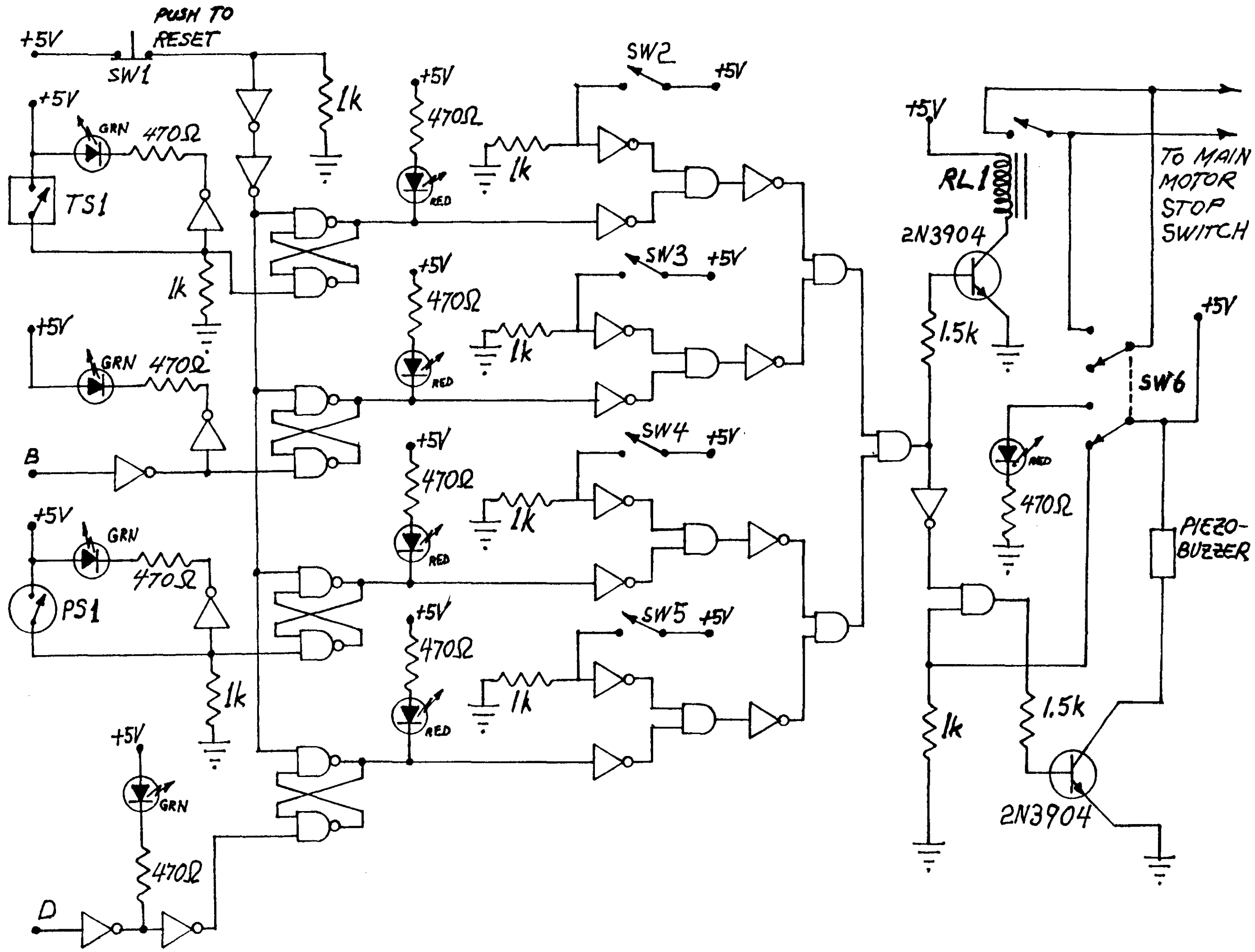

Fig. K.3 Drive Motor Trip Logic Circuit

APPENDIX L

DISCUSSION OF THE DISCRETE PASSAGE DIFFUSER INLET STATIC PRESSURE MEASUREMENTS

As discussed in section 4.1, the static pressure at the inlet to the discrete passage diffuser was determined using a flush probe inserted into a traverse port at the diffuser inlet. The axial position of the probe was adjusted to match the data obtained with the vaneless diffuser (see chapter 3) at corresponding swirl generator operating points. This was done at the start of the present tests with the discrete passage diffuser and then the probe was not moved for the duration of the tests. A schematic diagram illustrating the placement of the static pressure probe at the discrete passage diffuser inlet is shown in figure L.1. All of the data presented in chapters 4 and 5 was obtained using this probe.

The good agreement obtained between the mass flow rate as calculated by integration of the diffuser inlet profile and that determined by means of the venturi flow meter (see figure 4.9) suggests that the measurement of the static pressure by means of the flush probe was reliable (since this calculation depends on the measurement of the diffuser inlet static pressure). To check the reliability of the measurements of the diffuser inlet static pressure using the flush probe as relating to the conclusions of this thesis, the diffuser pressure recovery performance was also calculated with the diffuser inlet static pressure taken as that measured at twelve (12) circumferentially distributed static pressure wall taps in the quasi-vaneless space. The taps are located on the axial projection of the centerlines of passages 1, 6, 11, 16, 21, and 26, at a radius ratio $r/r_1 = 1.025$, with six taps on the front wall of the diffuser (swirl-generator inlet side) and six taps on the rear wall (drive motor side). The radial location of these taps is depicted schematically in figure L.1. To determine the severity of the circumferential non-uniformity of the static pressure at this radius, a circumferential pressure distortion coefficient, analogous to that given by equation 3.15, was defined:

$$\Psi_{d_i} = \frac{P_{st_i} - \bar{P}_{st_i}}{P_{t1_{ref}} - \bar{P}_{st_i}} \qquad \text{L.1}$$

where P_{st_i} is the static pressure as measured at tap i (i = 1,2...12) at radius r/r_1 = 1.025, $P_{t1_{ref}}$ is the diffuser inlet mass averaged total pressure (see equation 3.14), and $\bar{P}_{st_i}$ is the numerical average of the static pressure readings from all 12 taps at r/r_1 = 1.025:

$$\bar{P}_{st_i} = \frac{1}{12}\sum_{i=1}^{12} P_{st_i}\Big|_{\frac{r}{r_1} = 1.025} \qquad \text{L.2}$$

Figure L.2 shows the circumferential distribution of the static pressure distortion coefficient obtained from the taps at r/r_1 = 1.025 at the rotating stall threshold operating points shown in figure 5.1.

The overall diffuser pressure recovery coefficient (based on the diffuser inlet availability averaged total pressure) as defined by equation 5.7 can be approximated by replacing P_{st1} in equation 5.7 with the numerical average of the static pressure readings from the twelve wall taps at r/r_1 = 1.025 as given by equation L.2. Figure L.3 shows the overall diffuser pressure recovery performance (based on the diffuser inlet availability averaged total pressure and the static pressure defined by equation L.2) plotted as a function of the diffuser inlet momentum averaged flow angle. Comparing this to the performance shown in figure 5.1 (which was based on the diffuser inlet availability averaged total pressure and the static pressure measured using the flush probe), it is seen that the differences between the two measurements of the diffuser inlet static pressure (at the rotating stall threshold) are roughly 1% of the inlet dynamic pressure and hence negligible in the context of the conclusions of this thesis.

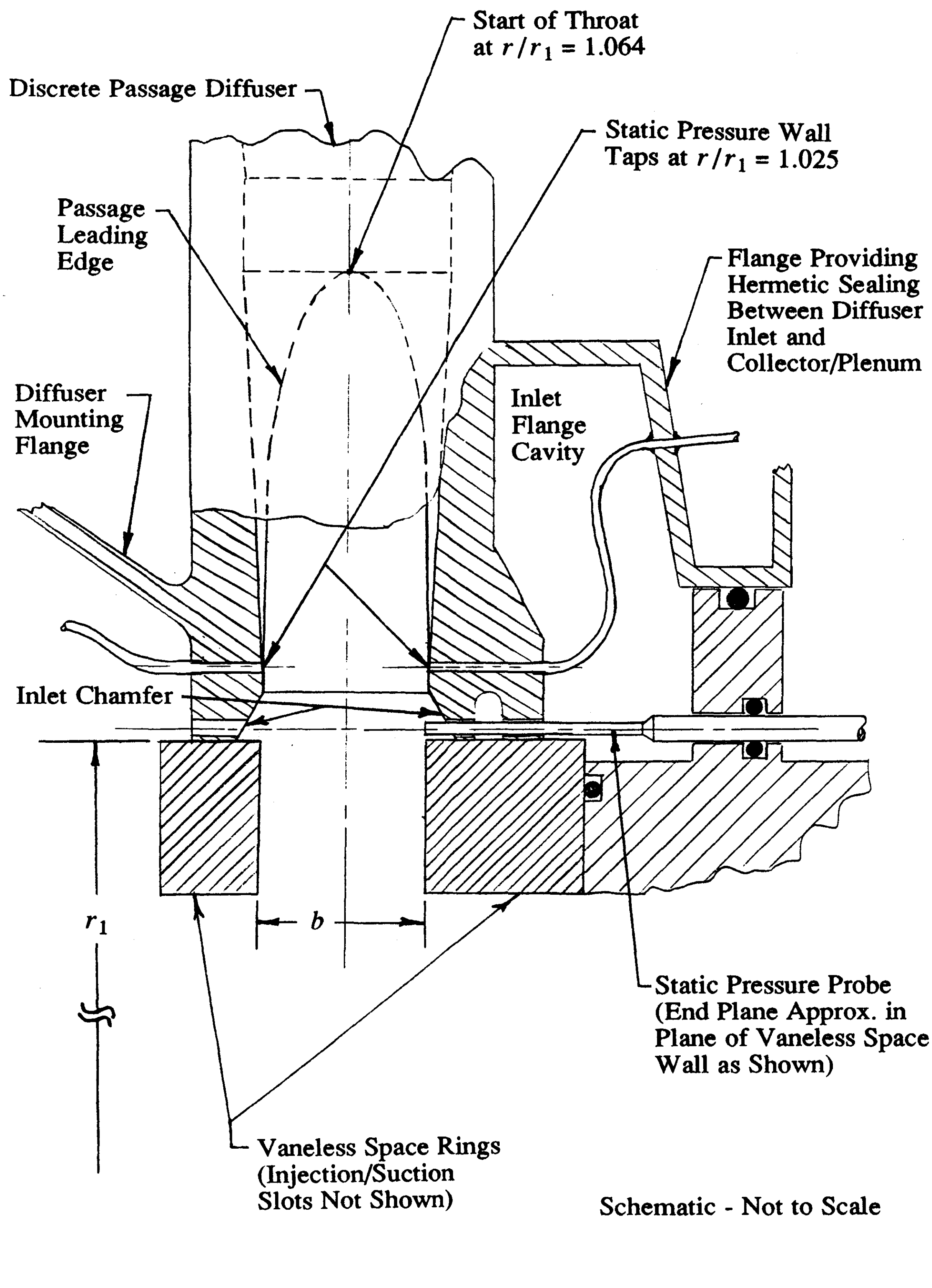

Fig. L.1 Discrete Passage Diffuser Inlet Static Pressure Probe Arrangement

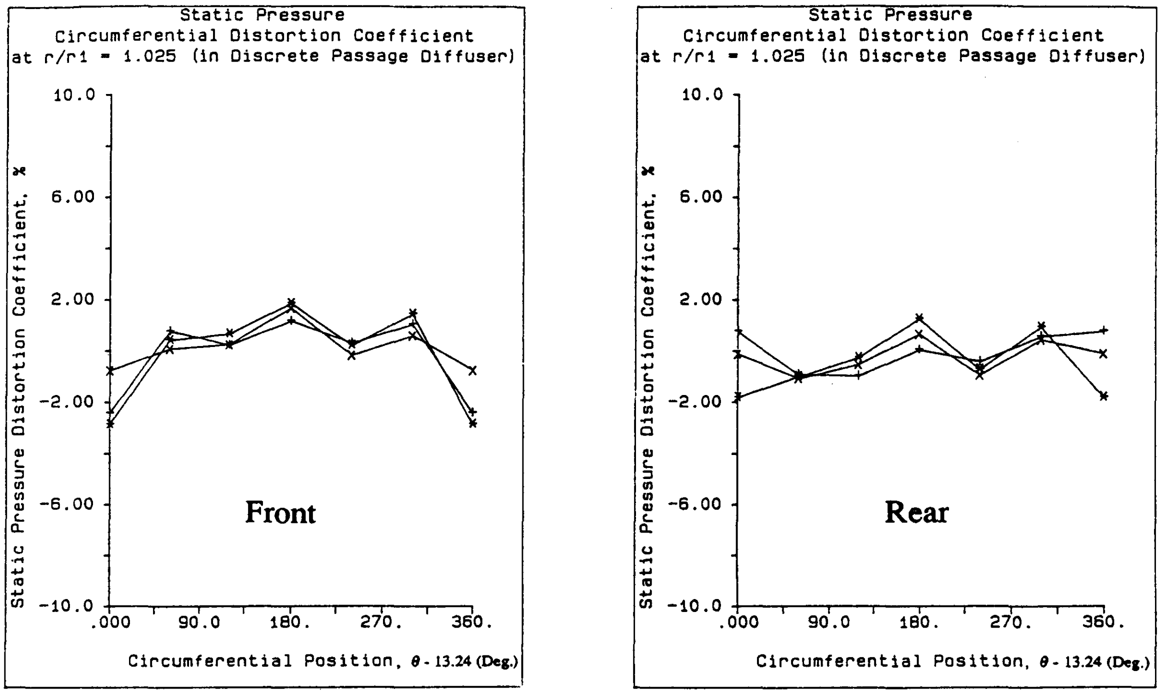

With Undistorted Inlet Flow Field- x 2000 RPM, * 4000 RPM, + 6000 RPM

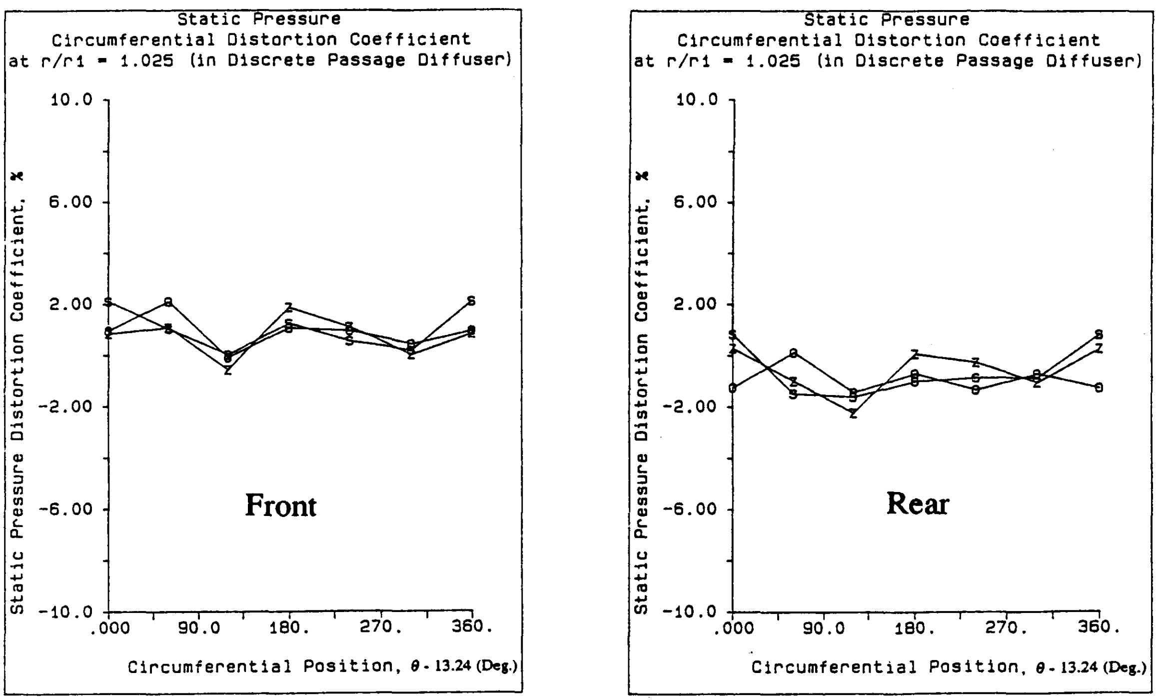

With Distorted Inlet Flow Field- o 2000 RPM, s 4000 RPM, z 6000 RPM

Fig. L.2 Circumferential Distribution of the Static Pressure Distortion Coefficient (see eq. L.1) in the Discrete Passage Diffuser at $r/r_1 = 1.025$ at Rotating Stall Threshold (Corresponding to Stall Points Shown in Figure 5.1)

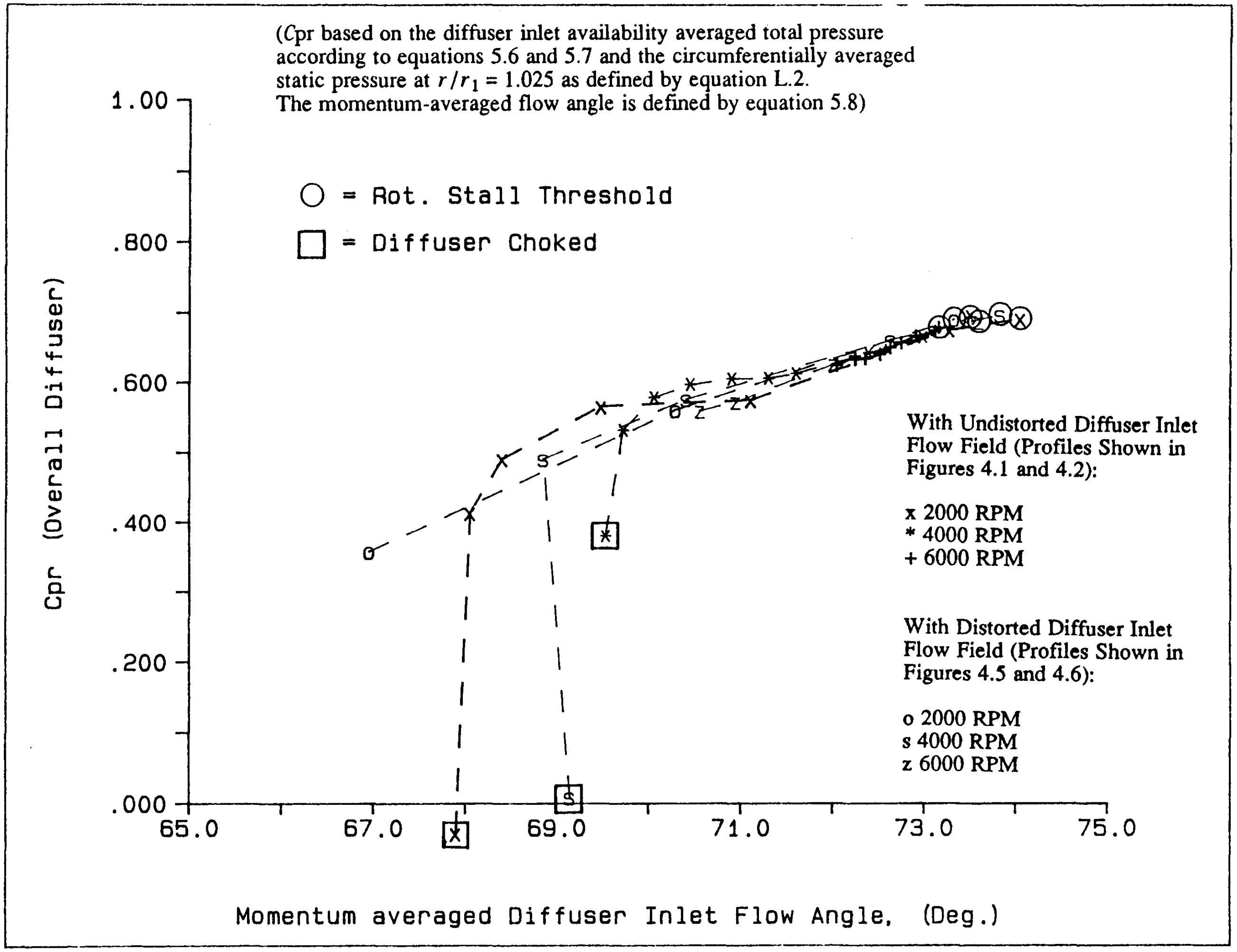

Fig. L.3 Overall Discrete-Passage Diffuser Pressure Recovery (Cpr_{ψ_1}) as a Function of the Diffuser Inlet Momentum-Averaged Flow Angle, with Diffuser Inlet Static Pressure Defined by Equation L.2

AUG 3 1 '95